



Pontificia Universidad Católica del Perú

Escuela de Posgrado

Grandes deslizamientos en el flanco occidental de los Andes Centrales: inventario, caracterización y Factores temporales

Tesis para obtener el grado académico de Doctor en Ingeniería
que presenta:

Gabino Fabrizio Delgado Madera

Asesor PUCP: ***Carlos Lenin Benavente Escobar***

Co-Asesor UGA: ***Stéphane Schwartz***

Co-Asesor UGA: ***Swann Zerathe***

Lima, 2024



THÈSE

Pour obtenir le grade de

DOCTEUR DE L'UNIVERSITE GRENOBLE ALPES

**préparée dans le cadre d'une cotutelle entre
l'Université Grenoble Alpes et la Pontificia
Universidad Católica del Perú**

Spécialité : **Sciences de la Terre et de l'Univers et de
l'Environnement**

Arrêté ministériel : le 25 mai 2016

Présentée par

Gabino Fabrizio DELGADO MADERA

Thèse dirigée par **Stéphane SCHWARTZ**
co-encadrée par **Swann ZERATHE** et **Carlos BENAVENTE
ESCOBAR**

préparée au sein du **laboratoire Institut des Sciences de la Terre
(ISterre) et de la Pontificia Universidad Católica del Perú (PUCP)**
dans l'école doctorale **Sciences de la Terre de
l'environnement et des planètes (STEP)** et l'**Escuela Doctoral
Franco-Peruana en Ciencias de la Ingeniería y Geociencias
(EDFPCIG)**

Grands glissements de terrain du flanc Ouest des Andes Centrales : inventaire, caractérisation et contraintes temporelles

Thèse soutenue publiquement le « **22 Août 2024** »,
devant le jury composé de :

Madame Stella MOREIRAS

PROFESSEURE ASSOCIEE, University of Mendoza, Rapportrice

Monsieur Jan KLIMES

CHARGE DE RECHERCHE, Czech Academy of Sciences, Rapporteur

Monsieur Laurent BAILLET

PROFESSEUR DES UNIVERSITES, Université Grenoble Alpes, Examineur

Monsieur Andres FOLGUERA

DIRECTEUR DE RECHERCHE, CONICET, Examineur

Monsieur Jose MACHARÉ

PROFESSEUR, Universidad Nacional de Ingeniería de Lima, Examineur

Monsieur Stéphane SCHWARTZ

MAITRE DE CONFERENCE, HDR, Université Grenoble Alpes, Directeur de Thèse




Informe de Similitud

Yo, Carlos Lenin Benavente Escobar, docente de la Escuela de Posgrado de la Pontificia Universidad Católica del Perú, asesor(a) de la tesis titulada(o) Grandes deslizamientos en el flanco occidental de los Andes Centrales (15-20°S): inventario, caracterización y Factores temporales, de el autor Gabino Fabrizio Delgado Madera, dejo constancia de lo siguiente:

- El mencionado documento tiene un índice de puntuación de similitud de 59%. Así lo consigna el reporte de similitud emitido por el software *Turnitin* el 11 de septiembre de 2024.
- He revisado con detalle dicho reporte y la Tesis o Trabajo de investigación, y no se advierte indicios de plagio.
- Las citas a otros autores y sus respectivas referencias cumplen con las pautas académicas.

Lugar y fecha:

Lima, 22 de enero de 2025.

Apellidos y nombres del asesor / de la asesora: <u>Benavente Escobar, Carlos Lenin</u>	
DNI: 40790626	Firma 
ORCID: 0000-0002-2237-0016	

INFORME

A : Secretaría Académica
Pontificia Universidad Católica del Perú

ASUNTO : Observación sobre la similitud detectada en la tesis doctoral de Fabrizio Delgado

REFERENCIA : Correo electrónico de Srta. Paola Virreyra similitud del 13/09/24

FECHA : Lima, 23 de setiembre de 2024

1. Introducción

En respuesta a la observación emitida por la Secretaría Académica respecto al porcentaje de similitud del 59 % detectado en la tesis doctoral de mi asesorado, Fabrizio Delgado, mediante el programa Turnitin, presento el siguiente informe. El objetivo es detallar la procedencia de dicha similitud y justificar un ajuste en el porcentaje basado en la correcta identificación de los artículos incluidos en la tesis.

2. Artículos incluidos en la tesis

La tesis doctoral de Fabrizio Delgado incluye investigaciones publicadas durante su doctorado, en las cuales participó como primer autor o coautor. Los capítulos y anexos relevantes son los siguientes:

- **Capítulo II:** Artículo titulado *“Inventory of large landslides along the Central Western Andes (ca. 15°–20°S): Landslide distribution patterns and insights on controlling factors”*, donde Fabrizio Delgado es el primer autor. Turnitin reporta erróneamente un 6 % de similitud en este capítulo.
- **Capítulo III:** Artículo *“Giant landslide triggerings and paleoprecipitations in the Central Western Andes: The Aricota rockslide dam (South Peru)”*, con un 2 % de similitud errónea, en el que también es primer autor.
- **Anexos:** Contienen artículos científicos y resúmenes de congresos donde participó como coautor, entre ellos:
 - *“¹⁰Be dating reveals a one-million-years record of landslide activities in the Central Western Andes”*.
 - *“Earthquake surface ruptures on the altiplano and geomorphological evidence of normal faulting in the December 2016 (Mw 6.1) Parina earthquake, Peru”*.
 - Otros artículos científicos colaborativos.

Estos artículos fueron publicados durante el doctorado de Fabrizio Delgado, lo que explica la similitud detectada.

3. Análisis del porcentaje de similitud

Del total de **59 %** de similitud identificado por Turnitin, **50 %** corresponde a artículos en los que Fabrizio Delgado es autor o coautor. Turnitin no ha reconocido correctamente que estos trabajos forman parte de sus publicaciones previas, por lo que la similitud

detectada en gran parte es errónea. Estos artículos fueron publicados antes de la presentación de su tesis.

4. Propuesta

El porcentaje de similitud real atribuible a coincidencias legítimas, tales como citas y referencias correctamente utilizadas, sería solo del **9 %**, una vez excluida la similitud relacionada con las publicaciones originales del autor. Es importante resaltar que la similitud que detecta Turnitin se ubica en las secciones de introducción y metodologías correctamente referenciados.

5. Conclusión

El programa Turnitin ha detectado incorrectamente como copia una serie de artículos que son de la autoría o coautoría de Fabrizio Delgado, publicados previamente durante su doctorado. En consecuencia, el porcentaje de similitud debe ajustarse para reflejar con mayor precisión la originalidad de su trabajo. Se adjunta un análisis detallado de los artículos y sus porcentajes de similitud.

Anexos

- Cuadro con el desglose detallado del porcentaje de similitud detectado.



Documento firmado digitalmente

PhD. CARLOS L. BENAVENTE ESCOBAR

ABSTRACT

Landslides are responsible for economic losses and deaths around the world. Large landslides also play an active role in the erosion and geomorphological evolution of mountains. They can be triggered by multiple factors including climatic and tectonic forcing's. However, the respective roles climate variations and long-term tectonic on landslide processes remain poorly known because of a lack of chronological data on landslide occurrences over suitable time-scales. The western flank of the Central Andes presents interesting possibilities to study those questions because it offers landscapes and old sequences of mass movements that have been well preserved since hundreds of thousand years due to a dominant arid climate. In this context the aim of this thesis was to conduct a pluri-disciplinary work to better understand the factors controlling and triggering the large landslides in the Central arid Andes. For this purpose, we combined field geomorphology, SIG analysis and absolute dating at different spatial scales (i) a regional-scale landslide inventory; (ii) a local focus on an emblematic giant landslide for dating and geomorphological reconstructions, and (iii) a more systematic dating of landslides at the scale of a valley.

Firstly, in order to identify the factors controlling landslide formation at a regional scale along the Central Andes, we inventoried all the large landslides (areas $>0.1 \text{ km}^2$) between the latitude 15 and 20°S . A thousand landslides were mapped, identifying two dominant typologies: rockslides (86%) and rock avalanches (14%). By statistical exploring this landslide database, it was identified a dominant lithological and relief control. The spatial distribution of the landslides reveals the presence of landslide clusters close to the crustal faults.

Secondly, we conducted a focused study on the giant Aricota landslide, located in the southern Peru, in order to know when and in which conditions this large mass movement occurred. Detailed geomorphological mapping and cosmogenic nuclide dating (^{10}Be) were applied revealing the occurrence of two failure events: (i) first a rockslide of $\sim 2 \text{ km}^3$ dated at $17.9 \pm 0.7 \text{ ka}$, which dam the the valley and formed the Aricota lake ($\sim 6 \text{ km}$ long), (ii) second a smaller rock-avalanche dated at $12.1 \pm 0.2 \text{ ka}$, which was deposited on top of the first event. This chronology correlates well with two major paleo wet periods recorded on the Altiplano during the Younger Dryas and the Henrich 1st stadial, suggesting that the transition from arid to more humid climate may have influenced the formation of this landslide.

Thirdly, in order to document more patterns of landslide occurrence though time and to further investigate their triggering, we replicated the dating procedure on eight other large landslides located all around the Aricota rockslide (the Locumba landslide cluster). The results indicated that they all occurred during the Pleistocene. Precise ages were obtained for four cases: the Cotana rock-avalanche at ca. 16 ka, the Antavilca rock-avalanche at ca. 18 ka, the Quilahuani rock-avalanche at ca. 114 ka and the Angostura rockslide at ca. 205 ka. However, strong ages dispersion attributed to problems due cosmogenic nuclide inheritance have affected the others hampering robust dating. Those additional chronological constraints did not favor the hypothesis that the Locumba landslide cluster formed during a single event such as a single mega earthquake. Alternatively, the almost systematic correlation of landslide timing with paleo wet periods, including the "Ouki humid event" (ca. 100-120 ka) during the MIS5, rather support a dominant climate forcing although the co-effect of local seismicity cannot be ruled out.

RESUMEN

Los deslizamientos son responsables de pérdidas económicas y muertes en todo el mundo. Los grandes deslizamientos también desempeñan un papel activo en la erosión y la evolución geomorfológica de las montañas. Estos pueden ser provocados por múltiples factores, entre ellos los climáticos y tectónicos. Sin embargo, los roles que desempeñan las variaciones climáticas y tectónicas a largo plazo en los procesos de deslizamiento siguen siendo poco conocidos debido a la falta de datos cronológicos sobre la ocurrencia de deslizamientos en escalas de tiempo adecuadas. El flanco oeste de los Andes Centrales presenta interesantes posibilidades para estudiar estas cuestiones porque ofrece paisajes y antiguas secuencias de movimientos en masa que se han conservado bien desde hace cientos de miles de años debido al clima árido dominante. En este contexto, el objetivo de esta tesis fue realizar un trabajo pluridisciplinar para comprender mejor los factores que controlan y desencadenan los grandes deslizamientos en los Andes Áridos Centrales. Para ello, combinamos la geomorfología de campo, el análisis SIG y la datación absoluta a diferentes escalas espaciales: (i) un inventario de deslizamientos a escala regional; (ii) un enfoque local sobre un gran deslizamiento para su datación y reconstrucciones geomorfológicas, y (iii) una datación más sistemática de los deslizamientos a escala de un valle.

En primer lugar, para identificar los factores que controlan la formación de deslizamientos a escala regional a lo largo de los Andes Centrales, se hizo el inventario de todos los grandes deslizamientos (áreas $>0,1 \text{ km}^2$) entre la latitud 15 y 20°S . Se cartografiaron mil deslizamientos de tierra, identificando dos tipologías dominantes: deslizamientos de roca (86%) y avalanchas de rocas (14%). Mediante la exploración estadística de esta base de datos de deslizamientos, se identificó que la litología y el relieve son factores dominantes para su formación. La distribución espacial de los deslizamientos revela la presencia de agrupaciones de deslizamientos cerca de las fallas corticales.

En segundo lugar, realizamos un estudio enfocado en el gran deslizamiento Aricota, situado en el sur de Perú, para saber cuándo y en qué condiciones se produjo este gran evento. Se aplicó un mapeo geomorfológico detallado y datación con nucleidos cosmogénicos (^{10}Be), los resultados revelaron la ocurrencia de dos eventos: (i) primero un deslizamiento de rocas de $\sim 2 \text{ km}^3$ fechado en $17,9 \pm 0,7 \text{ ka}$, que represó el valle y formó el lago de Aricota (de $\sim 6 \text{ km}$ de longitud), (ii) segundo una avalancha de rocas más pequeña fechada en $12,1 \pm 0,2 \text{ ka}$, que se depositó sobre el primer evento. Esta cronología se correlaciona bien con dos importantes períodos paleohúmedos registrados en el Altiplano durante el Younger Dryas y el Henrich 1st stadial, lo que sugiere que la transición de un clima árido a uno más húmedo puede haber influido en la formación de este deslizamiento.

En tercer lugar, para documentar los patrones de ocurrencia de deslizamientos a lo largo del tiempo e investigar más a fondo su desencadenamiento, replicamos el procedimiento de datación en otros ocho grandes deslizamientos situados alrededor del deslizamiento de Aricota (enjambre de deslizamientos de Locumba). Los resultados indicaron que todos ellos se produjeron durante el Pleistoceno. Se obtuvieron edades precisas para cuatro casos: el deslizamiento de rocas Cotana a ca. 16 ka , la avalancha de rocas Antavilca a ca. 18 ka , la avalancha de rocas Quilahuani a ca. 114 ka y la avalancha de rocas Angostura hacia 205 ka . Sin embargo, la fuerte dispersión de las edades, atribuida a problemas debidos a la herencia de los nucleidos cosmogénicos, ha afectado a los demás, dificultando una datación sólida. Estas limitaciones cronológicas adicionales no favorecen la hipótesis de que el conjunto de desprendimientos de Locumba se formara durante un único evento, como un único megaterremoto. Por el contrario, la correlación casi sistemática de la cronología de los deslizamientos con los períodos paleohúmedos, incluido el "evento húmedo de Ouki" (ca. $100\text{-}120 \text{ ka}$) durante el MIS5, apoya más bien un forzamiento climático dominante, aunque no se puede descartar el efecto conjunto de la sismicidad local.

LIST OF FIGURES

Figure	Description	Page
Chapter I: State of the art		
1	Geographic map of the world with country boundaries (a) The location of non-earthquake triggered fatal landslide events from 2004 to 2016. Individual landslide events shown by a black dot. (b) Number of non-seismically triggered fatal landslide events from 2004 to 2016 by country (Froude and Petley (2018)).	10
2	Location of fatal landslides in Latin America and the Caribbean (black dots) in the period 2004–2013 according to the EDFLD. (Sepúlveda and Petley 2015)	12
3	Main triggers of fatal landslides in the period studied (2004-2013). It is observed that the distribution of fatal landslides was mostly triggered by hydraulic controls (torrential rains and by hurricanes or tropical storms). A lower percentage (4%) of landslides were triggered by earthquakes. (Sepúlveda and Petley 2015).	12
4	Earthquake-induced debris avalanche on Nevados Huascarán in the 1970 th (Peru). Town of Yungay is buried beneath the landslide in middle foreground. The avalanche had a height difference of ~3,500 m from the rupture zone to the Santa. The displacement of the avalanche was 14 km (Plafker et al. 1971) (Photo courtesy of the National Aerophotographic Service of Peru: June 13, 1970).	13
5	Before (A) and after (B) the lahar of the 1985 eruption of Nevado del Ruiz. The population of Armero (30,000 inhabitants) was almost totally destroyed, causing the loss of some 25,000 people. Situation of the area affected by the lahar just after the eruption (C) and today (D). Since the event the affected land has been used exclusively for agriculture. (Carracedo, J. C. 2015).	14
6	A) Oblique view of slide looking west, showing rockslide source on upper southwest margin, reactivated rotational slides on upper northwest margin, extensive banding in middle reach of debris flow and splatter zone on lower northwest margin (June 1974). B) View of breached landslide dam looking northwest, showing scour zone on right margin of mouth of Quebrada Tinte and associated fall-back ridges (Servicio Aerofotografico Nacional, 9 June 1974). (Modified from Kojan and Hutchinson (1978)).	15
7	(a) Panoramic view of the landslide that occurred on 15 March this year in the village of Retamas. The white line and the dotted line limit the Retamas landslide (Base Photo Aldair Mejia/PRESIDENCIA PERUANA/AFP). (b) Image of the precise moment that the landslide begins (Video capture). The white circle is the location of the houses that were covered by the landslide debris and the red polygon are the houses located at the base of the landslide, these houses were affected.	16
8	Mechanisms of largescale rock-slope failure proposed in the literature, ordered on the basis of failure geometry and structural controls. (a), (b), (c), (f) Bois et al. (2008); (d) Mahr (1977); (e), (g), (h), (i) Ambrosi and Crosta (2006); (j) Agliardi et al. (2001); (k), (l) Hutchinson (1988); (m), (n) Zischinsky (1966); (o), (p), (t) Chigira (1992); (q), (r) Nemcok (1972); (s) Agliardi et al. (2009b); (u), (v), (w) Kieffer (1998). (Agliardi et al., 2012).	17

9	Morpho-structural features diagnostic of deep-seated gravitational slope deformation (DSGSD) phenomena, related kinematic significance, and typical associations (modified after Agliardi et al., 2001). (Agliardi et al., 2012)	19
10	Schematic model of typical deep-seated landslide (Cruden and Varnes 1996; Highland and Bobrowsky 2008).	20
11	View of the La Josefina landslide that occurred in March 1993 in Ecuador. The landslide of about 20 Mm ³ created a natural dam 100 m high, 300 m wide and 1.1 km long. This landslide filled the Paute river valley. (A) Head scarp, (B) Direction of movement; (C) Partial accumulation of debris, (D) Excavated channel, (E) Dammed lake. (Modified from Plaza et al., 2011).	21
12	Oblique view of the rock avalanche deposit that fills the valley of the Melado river. The slide mass forms a large dike and gives rise to Dial Lake, Chile (Modified from Hermanns et al., 2011).	22
13	Example of long-lasting horizontal movements and opening of tensile cracks within the La Clapière Sack (French Alps), 3 stages are observed: first a stage of continuous evolution of the landslide that in a second stage (mid-Holocene) transforms into an increase of the deformation rate, finally in the third stage becomes a predominantly vertical and accelerated shearing, which as a result formed a landslide occurred in the last 50 years (Modified from El Bedoui et al., 2009).	23
14	Main dating methods used to date landslides (Modified from Pánek, 2015).	25
15	Probability distributions and variability of ages expressed as box-whisker plots for published DSGSDs and DSLs situated in formerly glaciated terrains and in non-glaciated settings. Gray box indicates no data due to lack of landslide studies and dating. (Modified from Pánek and Klimeš (2016)).	26
16	Focus of the Western Flank of the Central Andes divided into geomorphological zones. Large landslides are observed in this part of the Andes: Chuquibamba (Margirier et al., 2015), Caquilluco landslide (Zerathe et al., 2017), Lluta landslide (Wörner et al., 2002; Strasser and Schlunegger, 2005), Miñimiñi and Latagualla landslides (Pinto et al., 2008). There is a rugged topography with mountains, valleys and deep canyons (Cotahuasi, Colca, Tambo). This part has intense seismicity, we consider surface seismicity <30 km (red circle) for subduction and cortical earthquakes (http://ds.iris.edu/seismon/index.phtml).	28
17	Global precipitation conditions along the Pacific side of the Central Andes. (a) Tropical Rainfall Measuring Mission (TRMM 2B31). The international borders are in grey. The Annual rainfall of the Andes is averaged for the period of 1998 to 2006 (9 years) with a spatial resolution of ~5 × 5 km ² . We note that the eastern flanks of the Andes represent an important orographic barrier which prevents the overflow of rainfall from the Amazon basin to the west. International borders in gray. (b) and (c) Swath profiles of the Andes, precipitation is in blue (TRMM 2B31) and green (TRMM 3B42); SRTM topography is in black and gray; and 3 km radius relief is in red. (Bookhagen and Strecker, 2008).	30
18	Caquilluco landslide (Rock avalanche). It has a drop between the headscarp and the foot of the landslide of ~3250 m and a strike length of ~41 km. Note that the landslide mass is preserved.	31

19	3D view of the Lluta landslide, the 37 km long landslide mass disturbed the topography which was probably like the relief of the right flank of the Lluta valley.	32
20	Chuquibamba landslide block diagram (modified Margirier et al., 2015) with digital elevation model (GeoMapApp, SRTM data, 90 m resolution) and the ages obtained by cosmogenic nuclide dating method.	32

<p>Chapter II: Inventory of large landslides along the Central Western Andes (ca. 15°–20° S): Landslide distribution patterns and insights on controlling factors</p>
--

1	(a) Study area location and major climatic features of South America showing the Intertropical Convergence Zone (ITCZ), El Niño wings and the Humboldt oceanic current, (b) focus on the study area showing the different geomorphotectonic areas of the Central Western Andes and the location of giant landslides documented in the literature (Chuquibamba landslide - Margirier et al., 2015; Thouret et al., 2017; Aricota landslide - Delgado et al., 2020; Caquilluco landslide - Zerathe et al., 2017; Lluta landslide - Worner et al., 2002; Strasser and Schlunegger, 2005; Minimiñi and Latagualla landslides - Pinto et al., 2008; El Magnifico landslide - Mather et al., 2014; Crosta et al., 2017), (c) and (d) AA' topographic profile of the western flank of the Central Andes and its geological interpretation (adapted from Armijo et al., 2015), respectively. CC: Coastal Cordillera, CD: Central Depression, WC: Western Cordillera, AL: Altiplano.	51
2	Lithostratigraphy and main structural features of the Central Western Andes (adapted from http://geocatmin.ingemmet.gob.pe/geocatmin for Peru and https://portalgeominbeta.sernageomin.cl/ for Chile).	52
3	Settings of the western flank of the Central Andes. (a) fault and seismicity (faults database: http://neotec-opendata.com and http://geocatmin.ingemmet.gob.pe/geocatmin ; instrumental earthquakes from http://ds.iris.edu/seismon/index.phtml and historical earthquakes from Villegas-Lanza et al., 2016). (b) and (c) topography and slope, respectively (both derived from SRTM DEM of 30 m of resolution), (d) mean annual rainfall (TRMM 3B43 annual rainfall of the Andes averaged for the period of 1998–2019). The white dashed line marks the eastern limit of our study area.	53
4	Morphological criteria used for landslide recognition and mapping along the Central Western Andes. We classified the landslides according to two main typologies (rockslide and rock avalanche) and also attempted to ascribe a qualitative state of activity (paleo or recent) to each identified case (see text for details). Illustrated examples are from (a) the Aricota paleo rockslide (Delgado et al., 2020) (b) the Caquilluco paleo rock avalanche (Zerathe et al., 2017), (c) the Siguas active landslide (Lacroix et al., 2019) and (d) an active landslide from this study (landslide n°109. RRIM: Red Relief Image Map).	55
5	Landslide sketch illustrating data collection procedure. (a) plan view and b cross-section. The green polygon delimits the whole landslide area (headscarp and slided mass). The yellow dot locates the centroid of the headscarp, considered as the origin of the landslide where several data are extracted (see text for details).	56
6	Landslides inventory along the Western Central Andes between ca. 15 and 20°S. A) Distribution of landslides by typology: rockslide and rock	57

	avalanche. B) Landslides distribution according to their state of activity: recent (or active) and paleo. CC: Coastal Cordillera, CD: Central Depression, WC: Western Cordillera. The black grid corresponds to cells of 50 × 100 km that were explored one by one for the landslide mapping (see text for details).	
7	Results of the Ripley's L-function for our landslide inventory. Grey bar is the range of maximum distribution frequency and is similar for the whole dataset and the two different typologies.	57
8	Spatial distribution analysis of landslides along the western flank of the Central Andes computed through kernel density analysis using a searching radius 20 km for (a) the whole inventory, (b) the rockslide type and (c) the rock avalanche type.	58
9	(a) Spatial distribution of landslides according to their size. Histograms showing the frequency of landslide areas and corresponding cumulative areas in percentage, (b) for the whole dataset using a 10 km ² bin width and (c) for the sub-range 0.1–10 km ² using a bin of 1 km ² . CC: Coastal Cordillera, CD: Central Depression, WC: Western Cordillera.	59
10	Frequency area density distributions of landslides in the Central Western Andes given for the whole dataset (ALL) and the sub datasets rockslide (RS) and rock avalanche (RA). The best parameters and associated uncertainties for the power-law fit of the distribution tails are given from the method of Clauset et al. (2009).	59
11	Morphometric parameters of the landslides for each typology. Relationship between (a) landslide height (ΔH) versus landslide length (L) and (b) landslide length (L) versus landslide area (A). r is the coefficient of correlation of Pearson.	60
12	a) Landslides frequency (in percent) for each lithological unit considering: (a) the whole landslide inventory; (b) the rockslide type and (c) the rock avalanche type. QD: Quaternary deposits (colluvial, fluvial, glacial, eolian); QV: Quaternary volcanic (andesitic lava, volcanic deposits); V-C: Volcanic rock (lava, toba, ignimbrite); SC-C: Sedimentary conglomerate; VS-C: Volcano-Sedimentary (ignimbrite, toba) I-C: Intrusive rocks (granite); V-M: Volcanic rocks (andesite, rhyolite); SM-M: Sediment Marine (limestone and shells); I-M: Intrusive (granite); SM-P: Sedimentary marine; I-P: Intrusive (granite); MR-PP: Metamorphic rocks.	60
13	Landslide statistics versus topography considering (a) and (b) landslide frequency versus elevation, (c) and (d) landslide frequency versus local relief (calculated with cells of 2 × 2 km), (e) and (f) landslide frequency versus slope (calculated with a cell of 2 × 2 km).	62
14	Landslides density (from Fig. 8a) along the Central Western Andes confronted to the instrumental seismic catalogues for the last 50 years from USGS (earthquakes >M _w 5 and depth <30 km), the available historical seismicity and to the main neotectonics crustal faults (see references on the caption of Fig. 3).	64
15	a) Landslide inventory along the Central Western Andes compared to the mean rainfall of the last two decades; b) and c) Frequency of recent and ancient landslides, respectively, versus rainfall patterns.	65
16	Anthropic reactivation of paleo landslides induced by irrigation for agriculture along (a) the Sigüas valley modified from Graber et al. (2021). See location on Fig. 13. a. The Identification of the landslides reactivated by irrigation comes from Lacroix et al. (2020) while the location of the	66

paleo landslides is from this study. Of importance is the fact that the re-activation of those paleo landslides has need more than 40 years of constant irrigation to increase sufficiently the groundwater level, suggesting that a very different climate must have been acting there at past to produce similar conditions.

Chapter III: Giant landslide triggerings and paleoprecipitations in the Central Western Andes: The aricota rockslide dam (South Peru)

1 Morpho-tectonic context of the Central Western Andes and location of the study area. Hillshade and elevation are produced using the ASTER DEM (resolution 30 m). Main faults are reported from Hall et al. (2012); Armijo et al. (2015) and Benavente et al. (2017). The database of giant landslides is compiled from Audin and Bechir (2006); Crosta et al. (2014); Mather et al. (2014); Zerathe et al. (2017) and adding personal mapping from this study. 94

2 Geological settings around the Aricota rockslide (see frame location on Fig. 1). The geological map is adapted from INGEMMET (2011) and draped above hillshade produced using the TanDEM-X DEM (resolution 12 m). Quaternary crustal faults are reported (e.g. Incapuquio-Purgatorio fault system; Hall et al., 2012; Benavente et al., 2017). Giant landslides reported were mapped during this study. 96

3 The Aricota giant rockslide (see frame location on Fig. 2). (A) Raw hillshade and elevation image derived from high resolution (2 m) Pléiades DEM (see text for details). The bathymetry of the Aricota lake (resolution 1 m) has been provided by the company EGESUR. (B) Geomorphological map of the Aricota rockslide showing the two failure events. The first and main event that generated the dam in the valley is mapped in yellow. Note the regressive erosion affecting southwestern part of the slipped mass and the infill of the secondary valley located at the southern center of the map. The second event, a rock-avalanche that have affected the main scarp of the first event, is depicted in orange. Yellow points correspond to samples extracted for ¹⁰Be cosmic ray exposure dating (1 above the rockslide scarp, 3 on the free face of the rockslide scarp and 13 on boulders distributed over the landslide mass). Outside of the rockslide area, the geology is the same as Fig. 3. 97

4 Panoramic views illustrating the main structures of the Aricota giant rockslide area. (A) Panoramic view from the downstream part of the Locumba valley (see location on Fig. 4C). Note the general V-shape of the valley and the contact between the giant Aricota rockslide and the flank underlined by a dotted white line. (B) Westward view taken from the road along the lake (see location on Fig. 3B) and showing the dam generated by the first giant event. Along the dam, two bodies can be discriminated. On the central part, pre-rockslide topographic surfaces and large ignimbrite blocks are preserved (see also Fig. 5A). On the south-eastern part, mixed and highly deformed material are outcropping. Rock-avalanche deposits overly the top the rockslide dam. (C) Southward view of the whole rockslide area taken from the top of the scarp (see location on Fig. 4B). Note on the opposite Locumba valley flank, the lateral valley infilled by accumulation of deposits reflecting its obstruction by the main Aricota rockslide dam. 98

5	Detailed morphologies of the Aricota rockslide. (A) Preserved large ignimbrite boulders outcropping in the central part of the rockslide dam. (B) Large boulders from the Tarata formation (bedded silt and shales) aligned in the rock-avalanche deposit. (C) Boulders of the rock-avalanche partially covered by diatomite. This zone was immersed before the hydroelectric lake drop. (D) Boulder (AR29) sampled to tentatively track the paleo-lake level variations. (E) Boulder of sample AR15. (F) Ignimbrite surface located on the plateau at the top of rockslide scarp and sampled to estimate the long-term local denudation rate (see location on Fig. 3B). On all pictures, see the persons for scale and their location on Fig. 4.	99
6	Main scarp morphologies of the Aricota rockslide. (A) 3D view of the Aricota rockslide area (Google Earth). The scarp of the rockslide dam (first event) is depicted in yellow while the rock-avalanche scarp (second event) is in orange. Dashed orange line highlights the boundary of the rock-avalanche deposit. Small landslides (in black) affect the southwestern slope of the rockslide dam. (B) Preserved scarp surface of the first failure event and location of samples AR4 and AR5. (C) Vertical scarp generated by the second failure event and cutting through alternating silts and black shales of the Tarata formation. Sample AR3 was extracted from the scarp toe. See also location of the sample AR1 at the top of the slope, dedicated to constrain long-term denudation rate. (D) Layer corresponding to a regional paleo weathering profile interbedded in Cretaceous series. (E) Same weathered material (yellow) reworked and transported by the rock-avalanche.	100
7	Exposure durations results on the Aricota giant rockslide. (A) Rockslide map and sample ages (1σ internal uncertainty, Table 1, supplementary data). Legend is the same as Fig. 3B. (B) Probability density plot and statistics over exposure durations (1σ internal uncertainty, Table 1, supplementary data). Yellow curves and orange curves correspond to the rockslide dam (event 1) and the rock-avalanche (event 2), respectively. Thin lines correspond to individual exposure durations. Dashed lines refer to exposure durations interpreted as outliers (see text for details). Exposure duration from sample AR17 (32.7 ± 1.9 ka) is considered as an outlier (out of frame). Thick curves refer to the summed probability density function for each event (excluding outliers).	101
8	Morphological context around the sample AR29. (A) Geomorphological map of the north-eastern part of the Aricota dam showing the location of the sample AR29 and the main variations of the Aricota lake shorelines (the probable highest paleo-lake level was reconstructed according to diatomite deposits (Placzek et al., 2001)). (B) Topographic profile extracted from the Pléiades DEM (see location on Fig. 8B). The legend of the rockslide morphologies is the same as Fig. 3B.	102
9	Interpretative cross-sections of the Aricota giant rockslide. See locations on Fig. 3B. (A) Perpendicular to the Locumba valley. The pre-rockslide topography, before the first event, is reconstructed considering the volume estimation of the rockslide dam and interpolating the slope of the valley flanks (Delgado et al., 2018). Samples for ^{10}Be cosmic ray exposure dating are projected on the cross-section. (B) Parallel to the Locumba valley. The pre-rockslide dam river profile is indicated from Delgado et al. (2018).	103

10	Worldwide compilation of landslide dams modified from Korup et al. (2004) showing the relations between the landslide volumes and heights (n is the number of landslides of the database). The Aricota rockslide (grey circle) stands within the 3 largest landslide dams and the highest height reported worldwide.	104
----	--	-----

Chapter IV: Pleistocene chronicles of large landslides triggering on the western flank of the Central Andes revealed by cosmogenic nuclide dating		
--	--	--

1	a) Location of the study area in the Central Andes. b) Density of large landslides along the Western flank of the Central Andes compared with the seismic catalog of the last 50 years by USGS (earthquakes > 5 Mw and depth < 30 km) and the main active crustal faults (from Delgado et al., 2022). The study area, located in the central part of the Locumba catchment (blue outline) is indicated by a red box.	117
2	Lithostratigraphic map of the study area, where the Locumba cluster is located, with more than 30 landslides inventoried (Delgado et al., 2022). Eight landslides (Pondera, Angostura, Antavilca, Quilahuani, Huanara, Olleria 1, Olleria 2 and Cotana) were chosen for study. The red box marks the Aricota landslide (Delgado et al., 2020) and the other Black box shows the post-Inca rockslide.	119
3	(A) Locumba catchment, the red stripe is the swath profile box. (B) Swath profile of the Locumba river, showing the correlation between knickpoints and landslides. (C) Relationship between landslide location and valley incision. (modified from Mathieux, B. 2021)	120
4	3D Google Earth view of the Aricota rockslide (modified from Delgado et al., 2020). It is observed that the first event (17.9 ± 0.7 ka) filled the valley and formed a big dam and the second event (12.1 ± 0.2 ka) was deposited on top of the first event.	121
5	(a) Geomorphological map of the Pondera rockslide that filled the valley and formed a large dam. This is currently eroded. (b) Cross section of Pondera rockslide.	124
6	a) Panoramic view of the eroded dam of the Pondera rockslide. Note to the north, the perched lacustrine deposits that are outcropping along a tributary dammed by the rockslide deposit, (b) Samples collection for cosmogenic nuclide dating (^{10}Be), (c) Close up on the perched lacustrine deposits, (d) Thick lacustrine deposits located along the main stream, ~2 km upstream to the dam along the Locumba valley.	125
7	Probability density plot of the exposure ages obtained on boulders on top of the Pondera rockslide deposits.	126
8	(a) Geomorphological map of the Angostura rockslide that filled the valley and formed a large dam. Part of this rockslide dam is currently eroded. (b) Cross section of the Angostura rockslide.	127
9	(a) Google Earth 3D image, showing the Angostura rockslide, the preserved deposit, and the eroded mass by the Locumba river, (b) Panoramic view to the northeast, upstream of the dam, location of lacustrine deposits ~2km away, (c) Samples collection for cosmogenic nuclide dating (^{10}Be), (d) Thick lacustrine and fluvial deposits located along the main stream, ~2km upstream to the dam along the Locumba valley.	128
10	Probability density plot of the exposure-ages obtained on boulders on top of the Angostura rockslide deposit.	129

11	(a) Geomorphological map of the Antavilca landslide showing the typical morphology of DSGSD, as well as the two rock avalanches that have developed at the southern extremity of the landslide. (b) Cross section of the Antavilca landslide, showing the first and second rock-avalanche.	130
12	(a) Google Earth 3D image, showing the Antavilca landslide (DSGSD), and two rock avalanches located to the south of the landslide, (b) view of the headscarp of the first event and the deposit of the first avalanche. (c) and (d) Samples collection for cosmogenic nuclide dating (^{10}Be).	131
13	Probability density plot of the exposure ages obtained on boulders on top of the second rock avalanche deposit.	132
14	a) Geomorphological map of the Quilahuani rock avalanche. We observed levees (frontal and lateral) and an erosional process at the foot of the avalanche. b) Cross section of the Quilahuani rock avalanche.	133
15	(a) Panoramic view of the Quilahuani rock avalanche main scarp and the avalanche deposit, (b) Lateral levees channeling the rock avalanche deposit, (c) Detail of the size of ignimbrite blocks, (d) Boulder sampled for cosmogenic nuclide dating (^{10}Be).	134
16	Probability density plot of the exposure ages obtained on boulders on top of the Quilahuani rock avalanche deposit.	134
17	(a) Geomorphological map of the Huanara landslide, four internal events were identified as rock-avalanche. (b) Cross section of the internal avalanches (second and third event) of the Huanara landslide.	136
18	(a) Panoramic view of Huanara landslide, showing the deposits of the successive rock-avalanche generations, (b) Headscarp and slide surface of the third event, (c) Lateral levee channeling the deposits from the second rock-avalanche, (d) and (e) Sampling on top of boulders for cosmogenic nuclide dating (^{10}Be).	137
19	Probability density plot of the exposure-ages obtained on boulders from rock avalanche deposits.	138
20	(a) Geomorphologic map of the Olleria 1 landslide, three internal events were observed, the first and second event are rockslides and the third event corresponds to a rock avalanche deposited on top of the first event. (b) Cross section of the internal events.	139
21	(a) Google Earth 3D image of the Olleria 1 landslide where the three internal events are observed, (b) view of the headscarp of the Olleria 1 landslide. The deposits of the first event (rockslide) and the third event (avalanche rock) can be observed (Figure. 15a). (c) sample collection for cosmogenic nuclide (^{10}Be) dating. (d) Epigenetic process and river incision of bedrock due to blockage of the main channel of the Huanuara river.	140
22	Probability density plot of the exposure ages obtained on boulders from rockslide deposits.	141
23	(a) Geomorphological map of the Olleria 2 rockslide. The rockslide deposit that filled the valley and formed a dam are observed, also the lacustrine deposits of the formed palaeolake are observed, (b) Cross section of Olleria 2 rockslide.	142
24	(a) Panoramic view to the north of the Olleria 2 rockslide, showing the landslide mass. The deposits are observed on the opposite flank of the river and the dam is eroded, (b) sample collection for cosmogenic nuclide dating (^{10}Be) dating. (c) Detail of the rockslide dam incised and eroded by the Huanuara river, (d) lacustrine deposits located along the main stream. The lake is formed by the Olleria 2 rockslide.	143

25	Probability density plot of the exposure ages obtained on boulders on top of the Olleria 2 rockslide deposit.	144
26	(a) Geomorphological map of the Cotana landslide, up to four events are observed: the first event corresponds to a rockslide and the other three events are rock avalanches, (b) Cross section showing the first (rockslide) and second event (rock avalanche).	145
27	(a) Panoramic view to the Cotana landslide, this landslide has several internal events, the main event is a rockslide and the others are rock avalanches, (b) Detail of the headscarp and rock avalanche deposit of the second event, (c) Detail of the avalanches of the second and third events (Figure 18a), (d) sample collection for cosmogenic nuclide dating (^{10}Be).	146
28	Probability density plot of the exposure ages obtained on boulders on top of the second event (rock avalanche).	146
29	(a) and (b) Setting the inheritance problem from Hilger et al. (2019), (c) the Aricota rockslide dam (modified from Delgado et al., 2020) where steady-state concentration was measured on the plateau at the landslide top (AR1) and where an intact relict of this paleo-plateau was mapped in the slided-mass and on which sampled boulders (AR14 and AR15) provided steady-state similar concentrations.	150
30	Theoretical depth profiles and related apparent exposure ages (adapted from Hilger et al., 2019) calculated for two different configurations: i) hillslopes after LGM glacier retreat, considering an exposure duration of ~ 20 ka; (ii) the steady-state arid Andes, considering an « infinite time ». ^{10}Be concentrations and exposure ages were calculated following equations described in Martin et al. (2017), parametrization described in Delgado et al. (2020), using production rate scaled at the elevations and latitude of the Locumba cluster and accounting for the muogenic productions.	151
31	Morphological similitudes between (A) a post-Inca rockslide mapped near Candarave (see location in Figure 2) and (B) the Olleria 2 paleo-rockslide sampled for TCN dating. (C) Tilted, but preserved, Inca terraces as evidences of preserved pre-failure hillslope in the slided-mass.	152
32	Summary map of landslide dating in the Locumba cluster. Paleoseismological studies (Benavente et al. 2017; 2021) with (A) Purgatorio fault and (B) Incapuquio fault. (*) Previous study (Delgado et al., 2020).	154
33	Compilation of landslide exposure ages for the Locumba cluster and comparison with climatic proxies. (a) Exposure ages of the present study. (b, c, d) Previous landslide studies (Caquilluco landslide - Zerathe et al., 2017, 2018; Chuquibamba Landslide - Margirier et al., 2015; Aricota landslide - Delgado et al., 2020). (e) Paleoclimatic study in the Altiplano (Placzek et al., 2013). (f) Paleoclimatic study in lakes in the Altiplano (Martin et al., 2018, 2020). (g) Paleoclimatic study in the Atacama Desert (Ritter et al., 2018). (h, i, j) dated terraces on the western flank of the Andes (Hall et al., 2008; Steffen et al., 2010; McPhillips et al., 2013). (k) climatic fluctuations in the Atacama Desert (Ritter et al., 2019).	156
Chapter V: Conclusions and Perspectives		
1	(a) Google Earth perspective view of the Antavilca rockslide, the dotted lines are main scarp though the mass affected by progressive failure. The yellow stars are the locations where sampling profiles were performed.	169

	(b) and (c) examples of sample collection along the scarps of the Antavilca rockslide.	
2	(a) Example of surface displacement map produced by FLATSIM by the massive processing of multi-temporal Sentinel-1 data (positive displacements are away from the satellite). Landslide polygons (in blue) are reported for comparison from Delgado et al. (2022). (b) Close up view on some large landslides where InSAR results indicate some active cases. (c) Close up view on the Locumba landslide cluster where a large landslide below orrelation of landslide mapping with deformation areas recorded in the InSAR model.	171

LIST OF TABLES

Table	Description	Page
Chapter II: Inventory of large landslides along the Central Western Andes (ca. 15°–20° S): Landslide distribution patterns and insights on controlling factors		
1	Main statistics of the landslide inventory.	61
2	Statistic of landslides versus lithology.	61
3	Supplementary data: Landslides database	70
Chapter III: Giant landslide triggerings and paleoprecipitations in the Central Western Andes: The aricota rockslide dam (South Peru)		
1	Supplementary data	110
Chapter IV: Pleistocene chronicles of large landslides triggering on the western flank of the Central Andes revealed by cosmogenic nuclide dating		
1	Samples parameters, cosmogenic ^{10}Be data and results. Z is the sample thickness, St is the topographic shielding factor. All the uncertainties reported are 1 sigma (σ).	147

TABLE OF CONTENTS

- INTRODUCTION	1
- CHAPTER I: STATE OF THE ART	8
1 Landslides hazards and issues	9
1.1 Worldwide setting	9
1.2 Focus in South America	11
1.3 Large scale historical failure	13
2 Large landslides: state of the art	16
2.1 Definition	16
2.2 Geomorphology and type (DSGSD and DSL)	18
2.3 Long term evolution and controlling factors	22
2.3.1 Concept of progressive failure: creep to collapse	22
2.3.2 Controlling factor (temporal evolution)	23
2.4 Synthesis of large landslide dating in the worldwide (landslide dating in mountainous areas)	24
3 Western Flank of the Central Andes (WFCA)	26
3.1 The WFCA a perfect place to study the large landslide activity over 1Ma time window	26
3.2 Geodynamic and tectonic setting	28
3.3 Climate and geomorphological setting	29
3.4 Western Andean large landslides	31
4 Main problematics of the PhD and strategy	33
4.1 Scientific questions	33
4.2 Strategy methods and data	33
References	34
- CHAPTER II: INVENTORY OF LARGE LANDSLIDES ALONG THE CENTRAL WESTERN ANDES (CA. 15°–20° S): LANDSLIDE DISTRIBUTION PATTERNS AND INSIGHTS ON CONTROLLING FACTORS	48
- Abstract	49
1 Introduction	49
2 Settings of the western flank of the Central Andes	50
2.1 Geodynamic and large-scale morphology	50
2.2 Lithostratigraphy	52
2.3 Tectonic setting	53
2.4 Seismicity	54
2.5 Topography	54
2.6 Current and past climate	54
3 Methods	55
3.1 Landslide mapping strategy	55
3.2 Dimensional and geological landslide parameters	55
3.3 Landslide spatial density analysis	56
3.4 Frequency-area relationships	56
4 Results	57
4.1 Landslide inventory, typology and morphology	57
4.2 Landslide spatial distributions	57
4.3 Landslide size distribution	58
4.4 Landslide morphometry	59
5 Interpretation and discussion	59

5.1	Study limitations	59
5.2	Landslide controlling factors	60
5.2.1	Landslides versus lithostratigraphy	60
5.2.2	Landslides versus relief	62
5.2.3	Landslides versus seismicity and active faults	63
5.2.4	Landslides versus rainfall	64
6	Conclusion	65
	References	66
	Supplementary data	70
-	CHAPTER III: GIANT LANDSLIDE TRIGGERINGS AND PALEOPRECIPITATIONS IN THE CENTRAL WESTERN ANDES: THE ARICOTA ROCKSLIDE DAM (SOUTH PERU)	92
-	Abstract	93
1	Introduction	93
2	Geological context and landslide setting	94
3	Methods	95
3.1	Pléiades DEM elaboration and mapping	95
3.2	Cosmogenic nuclide surface exposure dating	95
4	Results and interpretations	96
4.1	Rockslide morphology	96
4.2	Denudation rate and exposure duration results	101
5	Discussion	102
6	Conclusions	105
	References	105
	Supplementary data	108
-	CHAPTER IV: PLEISTOCENE CHRONICLES OF LARGE LANDSLIDES TRIGGERING ON THE WESTERN FLANK OF THE CENTRAL ANDES REVEALED BY COSMOGENIC NUCLIDE DATING	113
-	Abstract	114
1	Introduction	115
2	Settings	117
2.1	Geological context	117
2.2	Geomorphology and landslides of the Locumba región	119
3	Methodology	121
3.1	Mapping of landslides	121
3.2	Cosmogenic nuclide surface exposure dating	122
4	Results and interpretations	122
4.1	Locumba river	122
4.1.1	Pondera landslide	122
4.1.2	Angostura landslide	126
4.1.3	Antavilca landslide	129
4.1.4	Quilahuani landslide	132
4.2	Huanuara river	135
4.2.1	Huanara landslide	135
4.2.2	Olleria 1 landslide	138
4.2.3	Olleria 2 landslide	141
4.3	Ilabaya river	144
4.3.1	Cotana landslide	144
5	Discussion	149
5.1	Exposure ages scattering	149
5.2	Implication of landslide timings for the triggering factors	153

6	Conclusion	157
7	Acknowledgments	157
8	References	158
-	CHAPTER V: CONCLUSIONS AND PERSPECTIVES	165
1	Conclusions	166
2	Perspectives	168
-	ANNEXES (Participation in conferences)	173
-	ANNEXES (Participation in papers)	180



INTRODUCTION



INTRODUCTION

Landslides play an important role in the erosion and geomorphological evolution of mountain ranges. Every year, these processes constitute a major risk to human activities, generating worldwide economic losses and in some cases also human losses (Froude and Petley, 2018; Wallemacq and House, 2018). Landslides form especially along active margins and reliefs such as the Himalayas and also in intertropical regions. Landslides are mainly predisposed by topography and lithology, while their triggering factors are mainly external forcings such as earthquakes (Rosser et al., 2021; Valagussa et al., 2021), precipitation events (Strom, 2013; Qiu et al., 2016) and anthropogenic factors (Lacroix et al., 2020).

Currently, small to moderate-sized landslide formation processes are well known because they are triggered by earthquakes in arid environments (Lacroix et al., 2013) or in locations with rainfall (Zhao et al., 2020), seasonal rainfall (Kirschbaum et al., 2020) and/or anthropogenic factors (Lacroix et al., 2020; Graber et al., 2021), but comparatively few case studies and documentation exist for large landslides (> million cubic metres in volume). This is due to the fact that larger events have longer recurrence times (thousands of years) but there is a lack of chronological data for such large time scales.

Studies were conducted to date landslides on larger time scales in mountain ranges around the world (Dortch et al., 2009; Hermanns et al., 2013; Zerathe et al., 2014; Pánek, T., 2015; Schwartz et al., 2017) in order to investigate possible relationships between landslide formation and climatic and/or tectonic triggers. The dating results show that the landslides are restricted to the Holocene (Pánek et al. 2017; Pánek 2019), there are no morphologies of landslides older than the last glacial advance, because the signal was erased. Similarly, in the Himalayas landslides are triggered by monsoon rains (Dikshit et al., 2019; 2020) and also by tectonic activity such as the landslides that occurred after the 7.8Mw earthquake in Gorka in 2015 (Roback et al., 2018).

On the other hand, focusing on another important mountain range such as the Andes, which is also located on an active tectonic margin where subduction between the Nazca Plate beneath the South American crust is constant and occurs since ~50 Ma (Pardo-Casas and Molnar, 1987) at a convergence rate of ~62 mm.yr⁻¹ (Villegas-Lanza et al., 2016), this process produces the uplift of the Andes and seismicity. This continuous uplift of the Andes caused this long mountain range to behave as a large orographic barrier that does not allow rainfall from the east and the Amazon to cross to the western flank (Houston and Hartley, 2003, Bookhagen and Strecker, 2008). This lack of rainfall on the western flank of the Andes has been an arid environment for millions of years (Dunai et al., 2005). This arid western fringe has the presence of large landslides where their geomorphological features are preserved. Previous studies on landslides with plurikilometric volumes such as the Chuquibamba landslide (Margirier et al., 2015), Caquilluco (Zerathe et al., 2017), Lluta (Strasser and Schlunegger, 2005), among others, indicate the presence of large paleo-landslides in this part of the Andes. But, although there have been some studies of landslides in the Andes, there are still many questions related to the occurrence and formation of landslides. How many giant landslides are found in this part of the Andes? Or what are the factors that control the formation of such landslides in this sector? Also, there are questions about the distribution of these landslides, whether these landslides follow a common pattern or trigger. Other questions focus on the chronology of the landslides: when did these large paleo-landslides occur, what are the triggers for these landslides, and what are the causes of these landslides? Although some landslides have already been dated (Chuquibamba (Margirier et al., 2015), Caquilluco (Zerathe

et al., 2017), Lluta (Strasser and Schlunegger, 2005), Miñimiñi and Latagualla landslides (Pinto et al., 2008), El Magnifico landslide (Mather et al., 2014; Crosta et al., 2017) there are different points of view. Some researchers point out that landslides in arid environments are linked to the seismotectonic context of the Andes (Mc Philips et al., 2014; Crosta et al., 2017; Junquera-Torrado et al., 2021). In the Andes, seismic activity is an important triggering factor for landslides. In the case of earthquakes linked to subduction dynamics, they generate small landslides (Lacroix et al., 2013). Fault activity related to main fault system development represent also a source for the triggering landslides (e.g. the Purgatorio fault, the Incapuquio fault system, among others) but there are no recent records for comparison. Benavente et al., (2017; 2021) detected that these faults can produce earthquakes larger than 7Mw. Other studies point out that landslides have correspondences with prolonged climatic events, for example the Chuquibamba landslide (Margirier et al., 2015), the Caquilluco landslide (Zerathe et al., 2017) that can be correlated with the Ouki phase identified in the Altiplano (80-120 ka) (Placzek et al., 2013).

In this understanding and with the purpose of contributing to the knowledge of landslides in the Andes, it was proposed to carry out a study of large-scale gravitational processes on the Western Flank of the Central Andes (WFCA). The main objective is to understand what are the conditioning and triggering factors for the formation and/or occurrence of these landslides. The previously mentioned conditions of this part of the Andes and the need for further study to contribute to the knowledge of landslides and disaster risk management, are the main motivation to carry out the thesis project.

The study area of the PhD project is located on the Western Flank of the Central Andes (southern Peru and northern Chile), between 15°-20° South latitudes, from the Pacific coast (0 metres) to the Altiplano (~5000 masl). In order to carry out a study to answer all the questions that motivated this thesis, it was proposed to focus the PhD on three main tasks: (1) To study landslides, carrying out a regional scale mapping and inventory, to understand the factors that control landslide formation. (2) To carry out a detailed study of a landslide and use cosmogenic nuclides to determine the age of exposure of this landslide and determine the triggering factor. (3) To go to an area with a high concentration of landslides to date each landslide using cosmogenic nuclides, with the objective of obtaining a chronology of events in order to have a complete history of landslide formation at this site. In order to perform each task in detail and to answer the scientific questions regarding the landslides, each one was developed in a chapter.

In that understanding, for a better development of the thesis, the manuscript is organised in five chapters:

- **Chapter I: State of the art**

In this first part, a description is made of the knowledge of landslides, from a general point of view in the world and then what is the current state of knowledge of landslides in the Western Flank of the Central Andes (WFCA), setting out the problems in the study area and the strategy for ways of approaching the scientific questions.

- **Chapter II: Inventory of large landslides along the Central Western Andes (ca. 15°-20°S): Landslide distribution patterns and insights on controlling factors.**

This part is a regional study of landslides located between 15°-20° South latitudes. The objective is to identify which are the conditioning factors for landslides in the WFCA. The

methodology applied consists of the recognition and mapping of landslides, using tools such as Google Earth and high-precision DEMs. Based on the inventory, a database is proposed that includes data on typology, dimensions and spatial distribution, in order to carry out statistical analyses to identify the conditioning factors. More than 1000 landslides were inventoried (Rockslide - 86%; Rock avalanches - 14%). The results indicate that the main factors contributing to slope destabilisation are related to factors including lithology and local relief. Furthermore, by analysing the spatial distribution of landslides, it was possible to identify places where there is a high concentration of landslides. Finally, it is suggested that large landslides cannot form under arid conditions. Providing chronological constraints on large paleo-landslides are necessary to explore possible links of their activity to paleoclimatic variations.

- **Chapter III: Giant landslide triggerings and paleoprecipitations in the Central Western Andes: The aricota rockslide dam (South Peru)**

This is a local study, focusing on one landslide. The landslide under study is the Aricota landslide which is located on the right flank of the Locumba river. This landslide is large and filled the Locumba valley forming an important dam which blocked the river's downstream flow and formed a lagoon of approximately 6 km length. The objective of this study is to find out when this landslide occurred and what the triggering factor was. The methodology applied was to carry out a detailed geomorphological mapping of the landslide, in order to identify the internal events. Then, a strategic sampling was carried out to identify the age of exposure using the cosmogenic nuclide methodology (^{10}Be), to then compare the results with paleoclimatic and tectonic proxies close to the study area in order to determine the triggering factor: The first is a rockslide that is dated at 17.9 ± 0.7 ka, this landslide filled the valley and formed a large dam, the second is rock avalanche dated at 12.1 ± 0.2 ka, this event was deposited on top of the deposits of the first event. Comparison of ages with tectonic and paleoclimatic proxies suggests a correlation with paleoclimatic events identified in the Altiplano (Heinrich's Stadial 1a and the Younger Dryas), suggesting that climate played an important role in triggering these landslides.

- **Chapter IV: Pleistocene chronicles of large landslides triggering on the western flank of the Central Andes revealed by cosmogenic nuclide dating.**

The study area focuses on a specific location with a high concentration of landslides (Locumba cluster). This area of interest is located in the central part of the Locumba watershed in the WFCA. The objective of this study is to find patterns of landslide occurrence or periodicity, and then to investigate which triggers (earthquakes or paleoclimatic events) have caused these landslides. For this study, 8 landslides were chosen for detailed geomorphological mapping, then boulder sampling was carried out on each landslide to obtain the age of exposure. As a result, the exposure ages were obtained for half of the landslides, the others showing a dispersion of ages. The landslides occurred during the Pleistocene: the Cotana rock avalanche (ca. 16 ka), the Antavilca rock-avalanche (ca. 18 ka), the Quilahuani rock-avalanche (ca. 114 ka) and the Angostura rockslide (ca. 205 ka), i.e. they have different periods of occurrence. When combined with tectonic proxies, no correlation could be found, because there are no broad proxies, but there are studies of active faults that can produce earthquakes of $M_w \sim 7$. Comparing with paleoclimatic events, it was observed that the ages obtained are compatible with the Younger Dryas, the Heinrich Stadial 1a and another event during the MIS 5, called the "Ouki event". So we can say that probably wet events were responsible for triggering landslides in arid environments.

- Chapter V: Conclusions and Perspectives

This chapter is the last part of the manuscript where the final conclusions obtained during the thesis are presented, as well as some perspectives of future investigations that would complete the studies carried out during this work and would contribute to a better understanding of the activity of large landslides in the Andes.

- Annexes

In this part, all the studies in which I participated during the PhD project are included, as well as the abstracts of the congresses in which I participated.

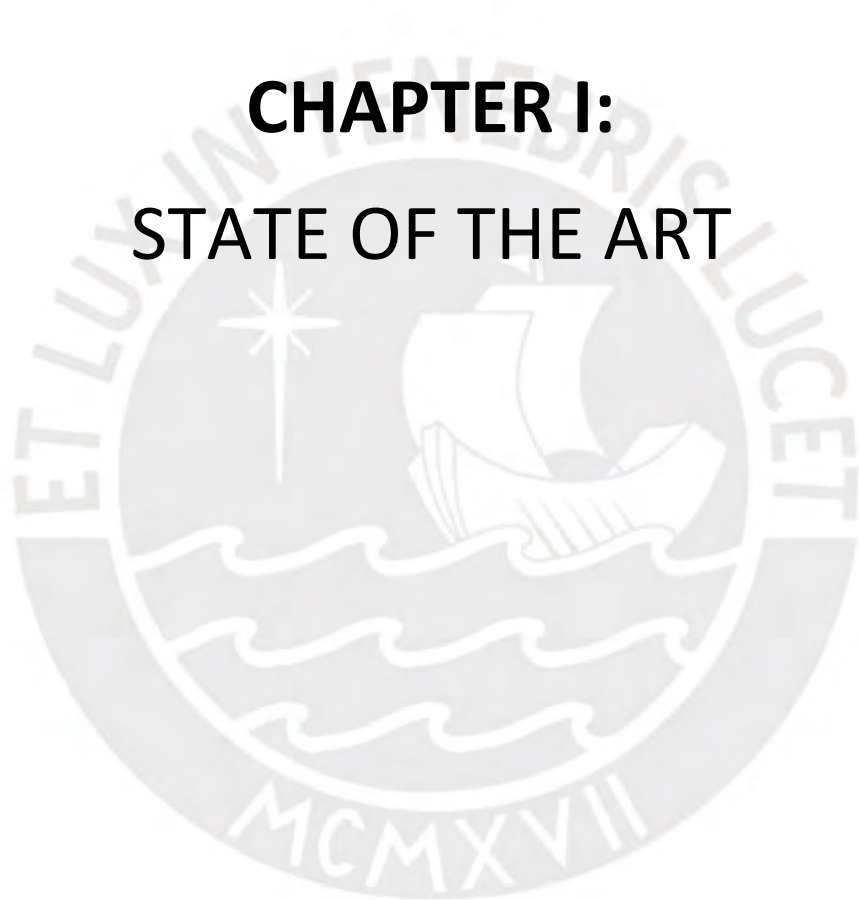
References

- Benavente, C., Wimpenny, S., Rosell, L., Robert, X., Palomino, A., Audin, L., ... & García, B. (2021). Paleoseismic Evidence of an Mw 7 Pre-Hispanic Earthquake in the Peruvian Forearc. *Tectonics*, 40(6), e2020TC006479.
- Benavente, C., Zerathe, S., Audin, L., Hall, S., Robert, X., Delgado, F., Farber, D.L., ASTER Team., 2017. Active compressional tectonics in the Andean forearc of southern Peru evidenced by direct ¹⁰Be surface exposure dating of an active fault scarp. *Tectonics* 36 (9), 1662–1678.
- Bookhagen, B., & Strecker, M. R. (2008). Orographic barriers, high-resolution TRMM rainfall, and relief variations along the eastern Andes. *Geophysical Research Letters*, 35(6).
- Crosta, G. B., Hermanns, R. L., Dehls, J., Lari, S., & Sepulveda, S., 2017. Rock avalanches clusters along the northern Chile coastal scarp. *Geomorphology*, 289, 27-43.
- Dikshit, A., Sarkar, R., Pradhan, B., Acharya, S., & Dorji, K. (2019). Estimating rainfall thresholds for landslide occurrence in the Bhutan Himalayas. *Water*, 11(8), 1616.
- Dikshit, A., Sarkar, R., Pradhan, B., Segoni, S., & Alamri, A. M. (2020). Rainfall induced landslide studies in Indian Himalayan region: a critical review. *Applied Sciences*, 10(7), 2466.
- Dortch, J., Owen, L.A., Haneberg, W.C., Caffee, M.W., Dietsch, C. & Kamp, D.U. 2009. Nature and timing of large landslides in the Himalaya and Transhimalaya of northern India. *Quaternary Science Reviews*, 28, 1037–1054.
- Dunai, T.J., Lopez, G.A.G., and Juez-Larre, J., (2005). Oligocene-Miocene age of aridity in the Atacama Desert revealed by exposure dating of erosion-sensitive landforms: *Geology*, v. 33, p. 321–324, doi: 10.1130/G21184.1.
- Froude, M. J., & Petley, D. N. (2018). Global fatal landslide occurrence from 2004 to 2016. *Natural Hazards and Earth System Sciences*, 18(8), 2161-2181.
- Graber, A., Santi, P., & Meza Arestegui, P. (2021). Constraining the critical groundwater conditions for initiation of large, irrigation-induced landslides, Sigüas River Valley, Peru. *Landslides*, 18(12), 3753-3767.
- Hermanns, R., Oppikofer, T., Dahle, H., Eiken, T., Ivy-Ochs, S., Blikra, L., (2013). Understanding long-term slope deformation for stability assessment of rock slopes: the case of the Oppstadhornet rockslide, Norway. *Ital. J. Eng. Geol. Environ. Book Ser. 6*, 255–264

- Houston, J., Hartley, A.J., (2003). The Central Andean west-slope rainshadow and its potential contribution to the origin of hyper-aridity in the Atacama Desert. *Int. J. Climatol.* 23, 1453–1464.
- Junquera-Torrado, S., Moreiras, S.M., Rodriguez-Peces, M.J., Sepulveda, S.A., 2021. Linking earthquake-triggered paleolandslides to their seismic source and to the possible seismic event that originated them in a portion of the Argentine Precordillera (31°–33°S). *Nat. Hazards* 106, 43–78. <https://doi.org/10.1007/s11069-020-04447-1>.
- Kirschbaum, D., Kapnick, S. B., Stanley, T., & Pascale, S. (2020). Changes in extreme precipitation and landslides over high mountain Asia. *Geophysical research letters*, 47(4), e2019GL085347.
- Lacroix, P., Dehecq, A., & Taipe, E. (2020). Irrigation-triggered landslides in a Peruvian desert caused by modern intensive farming. *Nature Geoscience*, 13(1), 56-60.
- Lacroix, P., Zavala, B., Berthier, E., & Audin, L. (2013). Supervised method of landslide inventory using panchromatic SPOT5 images and application to the earthquake-triggered landslides of Pisco (Peru, 2007, Mw8. 0). *Remote Sensing*, 5(6), 2590-2616.
- Margirier, A. Audin, L., Carcaillet, J., Schwartz, S., (2015). Tectonic and climatic controls on the Chuquibamba landslide (western Andes, southern Peru). *Earth Surf. Dynam. Discuss.* 2, 1129–1153.
- Mather, A. E., Hartley, A. J., & Griffiths, J. S., 2014. The giant coastal landslides of Northern Chile: Tectonic and climate interactions on a classic convergent plate margin. *Earth and Planetary Science Letters*, 388, 249-256.
- McPhillips, D., Bierman, P. R., & Rood, D. H. (2014). Millennial-scale record of landslides in the Andes consistent with earthquake trigger. *Nature Geoscience*, 7(12), 925-930.
- Pánek, T. (2015). Recent progress in landslide dating: a global overview. *Progress in Physical Geography*, 39(2), 168-198.
- Pánek, T., 2019. Landslides and Quaternary climate changes—the state of the art. *Earth Sci. Rev.* 196, 102871.
- Pánek, T., Mentlík, P., Engel, Z., Braucher, R., Zondervan, A., & Team, A. (2017). Late Quaternary sackungen in the highest mountains of the Carpathians. *Quaternary Science Reviews*, 159, 47-62.
- Pardo-Casas, F., Molnar, P., (1987). Relative motion of the Nazca (farallon) and south-American plates since late cretaceous time. *Tectonics* 6, 233–248.
- Pinto, L., Hérail, G., Sepúlveda, S. A., & Krop, P., 2008. A Neogene giant landslide in Tarapacá, northern Chile: A signal of instability of the westernmost Altiplano and palaeoseismicity effects. *Geomorphology*, 102(3-4), 532-541.
- Placzek, C.J., Quade, J., Patchett, P.J., 2013. A 130 ka reconstruction of rainfall on the Bolivian Altiplano. *Earth and Planetary Science Letters*, 363, 97-108
- Qiu H, Regmi AD, Cui P, Cao M, Lee J, Zhu X. 2016. Size distribution of loess slides in relation to local slope height within different slope morphologies. *Catena* 145: 155– 163. <https://doi-org.sid2nomade-2.grenet.fr/10.1016/j.catena.2016.06.005>

- Roback, K., Clark, M. K., West, A. J., Zekkos, D., Li, G., Gallen, S. F., ... & Godt, J. W. (2018). The size, distribution, and mobility of landslides caused by the 2015 Mw7. 8 Gorkha earthquake, Nepal. *Geomorphology*, 301, 121-138.
- Rosser N, Kinsey M, Oven K, Densmore A, Robinson T, Pujara DS, Dhital MR (2021) Changing significance of landslide Hazard and risk after the 2015 Mw 7.8 Gorkha, Nepal Earthquake. *Progress Disaster Sci* 10:100159
- Schwartz, S., Zerathe, S., Jongmans, D., Baillet, L., Carcaillet, J., Audin, L., ... & Lebrouc, V. (2017). Cosmic ray exposure dating on the large landslide of Séchilienne (Western Alps): A synthesis to constrain slope evolution. *Geomorphology*, 278, 329-344.
- Strasser, M., & Schlunegger, F., (2005). Erosional processes, topographic length-scales and geomorphic evolution in arid climatic environments: the 'Lluta collapse', northern Chile. *International Journal of Earth Sciences*, 94(3), 433-446.
- Strom A. 2013. Geological prerequisites for landslide dams' disaster assessment and mitigation in Central Asia. In *Progress of Geo-Disaster Mitigation Technology in Asia*, F Wang, M Miyajima, T Li, W Shan, TF Fathani (eds). Springer: Berlin; 17– 53
- Valagussa, A., Frattini, P., Valbuzzi, E., & Crosta, G. B. (2021b). Role of landslides on the volume balance of the Nepal 2015 earthquake sequence. *Scientific reports*, 11(1), 1-12.
- Villegas-Lanza, J.C., Chlieh, M., Cavali'e, O., Tavera, H., Baby, P., Chire-Chira, J., Nocquet, J.M., (2016). Active tectonics of Peru: heterogeneous interseismic coupling along the Nazca megathrust, rigid motion of the Peruvian Sliver, and Subandean shortening accommodation. *J. Geophys. Res. Solid Earth* 121 (10), 7371–7394.
- Wallemacq, P., & House, R., 2018. Economic losses, poverty & disasters. Centre for Research on the Epidemiology of Disasters and United Nations Office for Disaster Risk Reduction, Geneva, 1-30.
- Zerathe S., Blard P-H., Audin L., Braucher R., Bourles D., Carcaillet J., Benavente C., Delgado F., AsterTeam., 2017. Toward the feldspar alternative for cosmogenic ¹⁰Be exposure dating. *Quaternary Geochronology* 41, 83-96. <https://doi.org/10.1016/j.quageo.2017.06.004>.
- Zerathe, S., Lebourg, T., Braucher, R., & Bourlès, D. (2014). Mid-Holocene cluster of large-scale landslides revealed in the Southwestern Alps by ³⁶Cl dating. Insight on an Alpine-scale landslide activity. *Quaternary Science Reviews*, 90, 106-127.
- Zhao, B., Wang, Y., Feng, Q., Guo, F., Zhao, X., Ji, F., ... & Ming, W. (2020). Preliminary analysis of some characteristics of coseismic landslides induced by the Hokkaido Iburi-Tobu earthquake (September 5, 2018), Japan. *Catena*, 189, 104502.

**CHAPTER I:
STATE OF THE ART**



CHAPTER 1: STATE OF THE ART

1 Landslides hazards and issues

1.1 Worldwide setting

Landslides are gravitational phenomena that constitute one of the main components of natural hazards. They can be triggered by climatic and/or tectonic events and are responsible for thousands of deaths worldwide (Froude and Petley, 2018). These events also cause substantial economic losses in the billions of dollars (Petley, 2012; Shuster, 1996; Froude and Petley, 2018; Wallemacq and House, 2018). Most studies show a relationship between current climate change (rainfall) and landslides (Gariano and Guzzetti 2016). Froude and Petley (2018) conducted a worldwide database of disasters (landslides resulting in fatalities) between 2004 and 2017 based on media reports, government reports and academic articles. This inventory does not take into consideration landslides triggered by earthquakes. In spite of this they identified more than 5300 landslides that caused fatalities, the triggers were rainfall, mining and human activity.

According to this worldwide record, Asia is one of the regions with the highest concentration of landslides (~75%) that generated fatalities (Figure 1), other areas most affected are Central and South America, Africa and Europe. Likewise, Froude and Petley, (2018) indicate that anthropogenic activity related to inadequate construction, irrigation and/or logging on slopes influences the increase of current and future landslides (example Lacroix et al., 2020; Graber et al., 2021). Moreover, the landslide activity is located mostly on mountain fronts (Figure 1). These areas present high topographic relief with steep slopes. These places present high seismic activity triggering landslides that generate fatalities (Collins and Jibson 2015; Rosser et al., 2021; Valagussa et al., 2021). In addition, mountain fronts have presence of abundant rainfall in part of the year, this factor increases the risk for villages located in these places (Havenith et al., 2006; Strom, 2013; Qiu et al., 2016). the database made by Froude and Petley, (2018) covers a very short observation time window (<10 years). This database doesn't fit a broader time window associated with the formation of an orogenic zone (> 10⁶yr), because it does not take into account gravity instabilities associated with landform formation related to geodynamic activity in mountain ranges.

More specific studies of historical landslides occurring on different mountain fronts development (Korup (2005); Hewitt et al., (2011); Pánek et al., (2016), Fan et al., (2018); Zhao et al., (2019); Pánek et al., (2019)) have been conducted to understand what are the controlling and triggering mechanisms, landslide types and characteristic morphology.

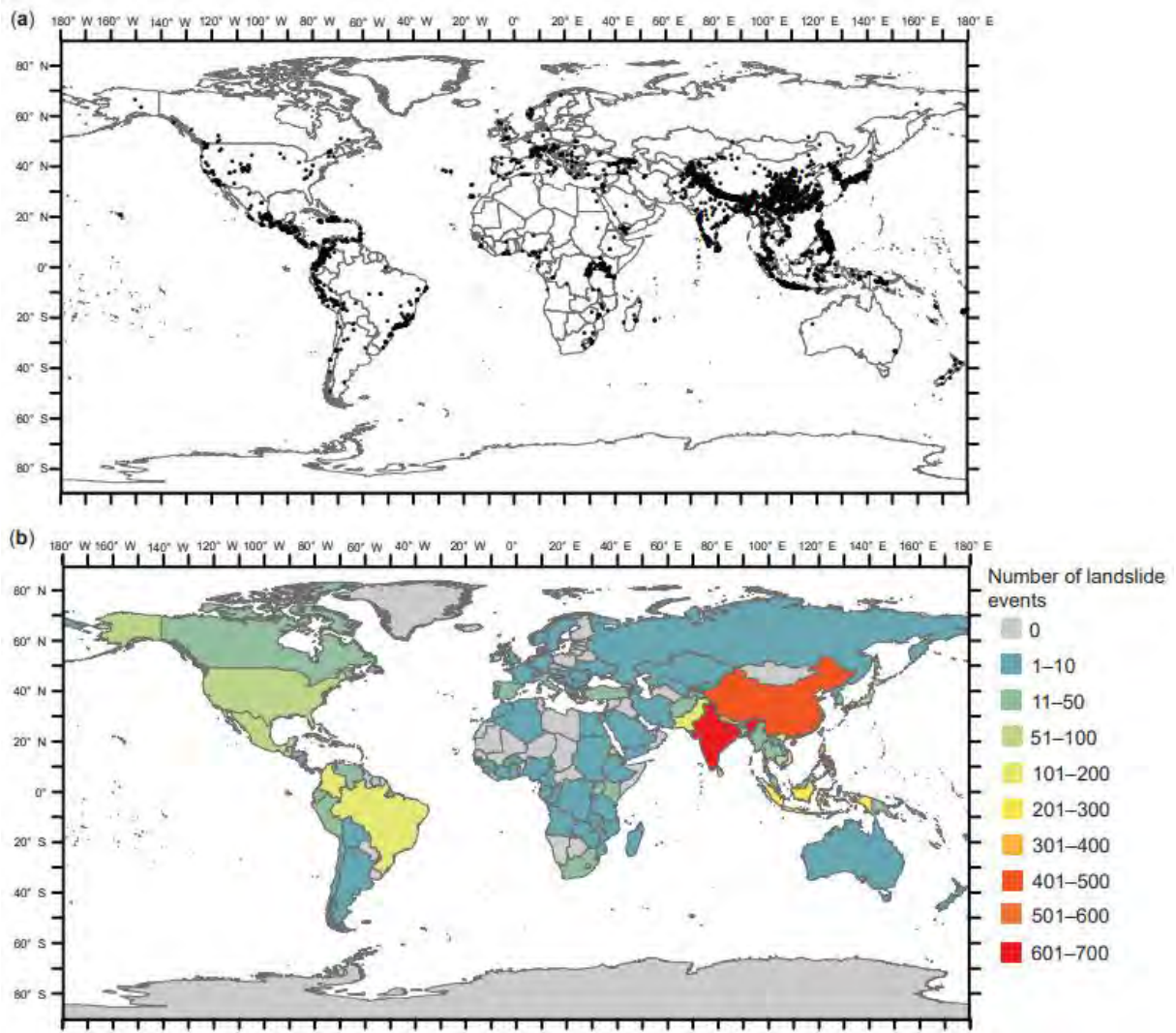


Figure 1. Geographic map of the world with country boundaries (a) The location of non-earthquake triggered fatal landslide events from 2004 to 2016. Individual landslide events shown by a black dot. (b) Number of non-seismically triggered fatal landslide events from 2004 to 2016 by country (Froude and Petley (2018)).

According to Froude and Petley, (2018) show that the countries with the highest concentration of landslides that generated fatalities come to be China and India (Figure 1). At the boundary of these countries are the Himalayan mountain range and the Tibetan plateau. These two orogenic zones record many landslides, due to extreme precipitation events (Wulf et al., 2010; Van der Geest, 2018). Another important orogenic zone in South America is the Andes, which are located within the intertropical convergence domain, an area where trade winds from the southeast and northeast converge. Due to the high temperatures the air masses ascend forming a lot of cloudiness and ending in abundant rainfall. In this sector there is a moderate concentration of landslides (Figure 1), although we can indicate that the high relief of the Andes mountain range plays an important role in the amount, intensity, spatial distribution and duration of precipitation for the formation of landslides.

1.2 Focus in South America

The Andes mountain range is located in South America and corresponds to one of the most important mountain belts in the world, related to the global convergence between the Nazca oceanic plate to the west and the South American plate to the east (subduction process). This shortening is accommodated by subduction of the Nazca plate below the South America plate. This dynamic process has been active from the Cretaceous period and is responsible for the construction of one of the world's most important mountain ranges. It has a length of ~7500 km and the highest point is located in the snowy Aconcagua at 6961 m asl. The western flank has the presence of important valleys as a result of the incision due to the uplift of the Andes (Thouret et al., 2007). In this place, several natural phenomena occur (mass movements) and landslides are one of the most important hazards affecting society (Schuster et al., 2002; Sepúlveda and Petley 2015), generating deaths and economic losses. The causes of these events are related to heavy rainfall, earthquakes, volcanic eruptions, human activity or the combination of these (Wieczorek, 1996; Sepúlveda and Petley (2015)).

The Andes have an intense seismic activity product of subduction, two types of earthquakes can be evidenced: (i) interplate earthquakes with magnitudes that can be >8 Mw (Pisco earthquake 2007, Mw 8 (Lacroix et al., 2013); Iquique earthquake 2014, Mw 8.2 (Candia et al., 2017)) and (ii) cortical earthquakes due to reactivation of active geological faults with magnitudes up to 7 Mw (Parina earthquake 2016, 6.1Mw, Aguirre et al., 2021). These two types of earthquakes generate different processes such as soil liquefaction, tsunamis and landslides.

The Andes behave as a great orographic barrier that controls the climate (Bookhagen and Strecker 2008). In the western flank of the Andes, the northern part has areas of high rainfall due to the high concentration of cloud cover, while the central part has an arid zone without precipitation (Bookhagen and Strecker 2008). Also, these different zones are due to the presence of the Humboldt and El Niño ocean currents (Rossel, 1997; Sanchez et al., 2000; Montes et al., 2011, Sulca et al., 2018). Sepúlveda and Petley (2015) conducted an analysis of non-earthquake-triggered landslides that generated fatalities over a 9-years period (From 2004 to 2013) (Figure 2). Statistical analysis (Figure 3) shows that the main factor controlling the fatal landslide distribution is associated to climatic pulse events like hurricane and heavy rains triggered by El Niño and La Niña phenomena which are warm and cold ENSO events. These phases are believed to arise from ocean-atmosphere interactions in the tropical Pacific Ocean (Wang et al., 1999) and tend to last approximately 1 to 2 years and recur every 3 to 8 years (Okumura and Deser, 2010).

On the other hand, Sepúlveda and Petley (2015) made the relationship with the triggering factors (Figure 3), indicating that more than 85% of the recorded landslides that generated fatalities were caused by extreme weather events (73% torrential rains and 15% by hurricanes or tropical storms) and only 4% of the cases were induced by earthquakes. They also state that human action is causing alterations in the slopes due to excessive irrigation for agriculture or tree felling, which in the future will cause new landslides due to climatic variations.

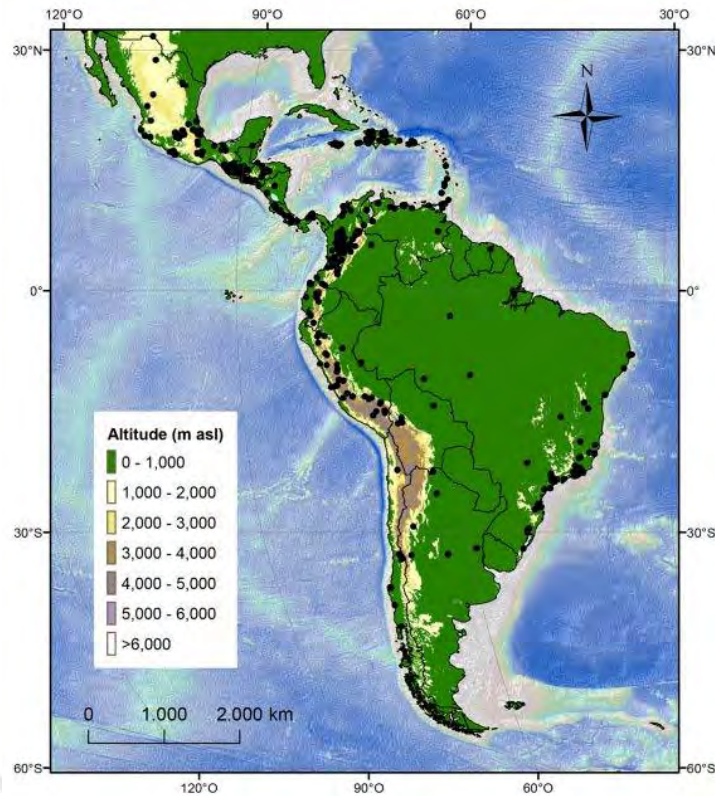


Figure 2. Location of fatal landslides in Latin America and the Caribbean (black dots) in the period 2004–2013 according to the EDFLD. (Sepúlveda and Petley 2015)

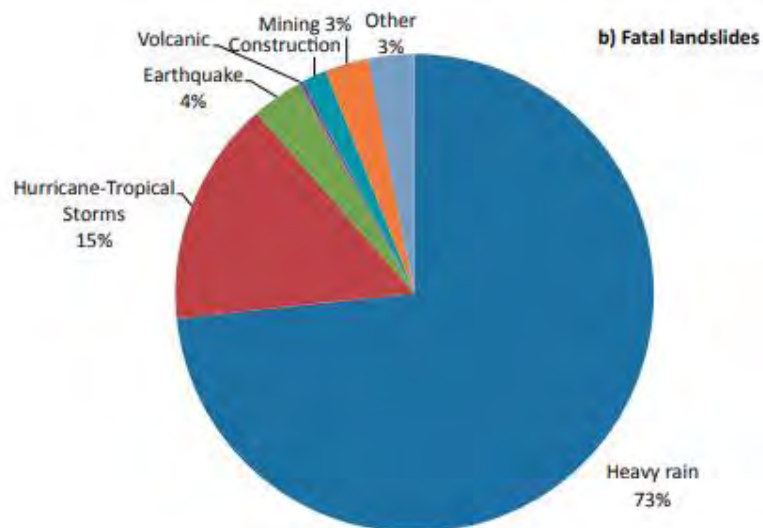


Figure 3. Main triggers of fatal landslides in the period studied (2004-2013). It is observed that the distribution of fatal landslides was mostly triggered by hydraulic controls (torrential rains and by hurricanes or tropical storms). A lower percentage (4%) of landslides were triggered by earthquakes. (Sepúlveda and Petley 2015).

As observed in the works of Hermanns et al., (2012), McPhillips et al., (2014) and Sepúlveda and Petley (2015), the Andes register a large number of landslides, the focus should be on studying large landslides, understanding the processes, because they have a great impact on society.

1.3 Large scale historical failure

Historic chronicals show that landslides are very common in South America (Hermanns et al., 2012). Different types of landslides occur with different sizes from small rockfalls to large landslides that mobilize large volumes of material (millions of m³) and have kilometers of travel length. These large landslides had a great impact on society, causing fatalities and destruction of villages and important infrastructure. One of the extreme events recorded in the Andes is the Huascarán avalanche (Peru) that occurred on May 31, 1970 (Figure 4) after the Chimbote earthquake (7.7 Mw), with epicenter on the Peruvian coast. This earthquake triggered the collapse of the northern summit of Huascarán (Plafker & Ericksen 1978). This part of the mountain was weakened by glacial retreat (Broggi, 1943). Plafker & Ericksen (1978) report that ~22000 people died, burying the towns of Yungay and Ranrahirca (Plafker et al., 1971).



Figure 4. Earthquake-induced debris avalanche on Nevados Huascarán in the 1970th (Peru). Town of Yungay is buried beneath the landslide in middle foreground. The avalanche had a height difference of ~3,500 m from the rupture zone to the Santa. The displacement of the avalanche was 14 km (Plafker et al. 1971) (Photo courtesy of the National Aerophotographic Service of Peru: June 13, 1970).

To the north of the Andes, one of the most important events was the Ruiz avalanche (Mojica et al., 1985; Voight, B. 1990) that destroyed the city of Armero in Colombia (Figure 5), this event occurred on November 13th of 1985, due to the reactivation of the Nevado del Ruiz volcano. This event melted the snow and glaciers on the flanks of the volcano, which triggered lahars. Mojica et al., (1985) indicate that the lahar moved ~ 80 million m^3 generating the death of ~ 25000 people in the valley of Armero and the city of the same name (Figure 5).

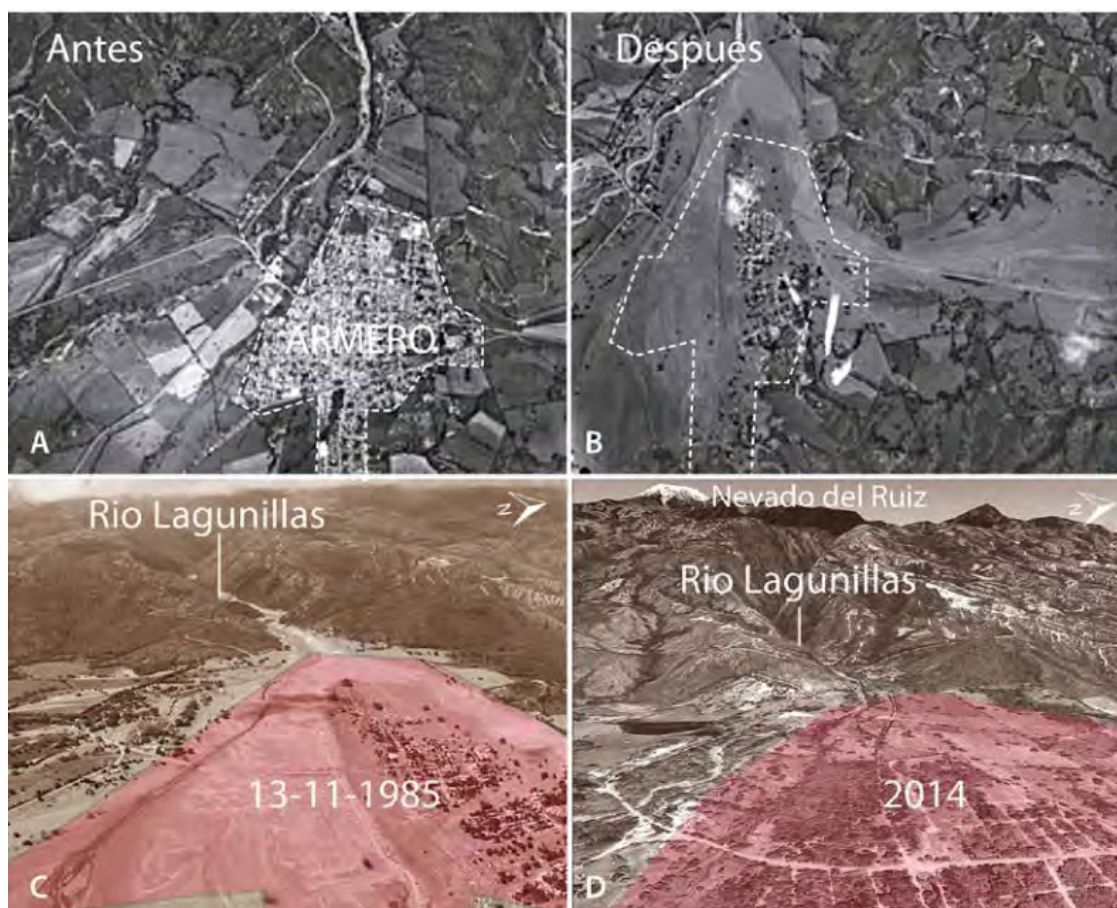


Figure 5. Before (A) and after (B) the lahar of the 1985 eruption of Nevado del Ruiz. The population of Armero (30,000 inhabitants) was almost totally destroyed, causing the loss of some 25,000 people. Situation of the area affected by the lahar just after the eruption (C) and today (D). Since the event the affected land has been used exclusively for agriculture. (Carracedo, J. C. 2015).

Another important landslide that occurred in the Andes was the Mayunmarca landslide in Peru (Figure 6; Galdos, 1975). This event occurred on April 25th of 1974. It displaced ~ 1600 m^3 of material that dammed the Mantaro river (Figure 6; Chang and Alva, 1988) and caused the death of ~ 600 people and the destruction of important infrastructure (houses and roads). The kinematic of the landslide have been characterized by Galdos (1973) that highlights following phenomena such as soil reptation, internal landslides and mudflows before the main triggering of the landslide. The triggering was partly controlled by the poor quality of the rocks, the presence of groundwater and anthropogenic activity due to continuous irrigation for agricultural work (Vilchez, M. 2013).

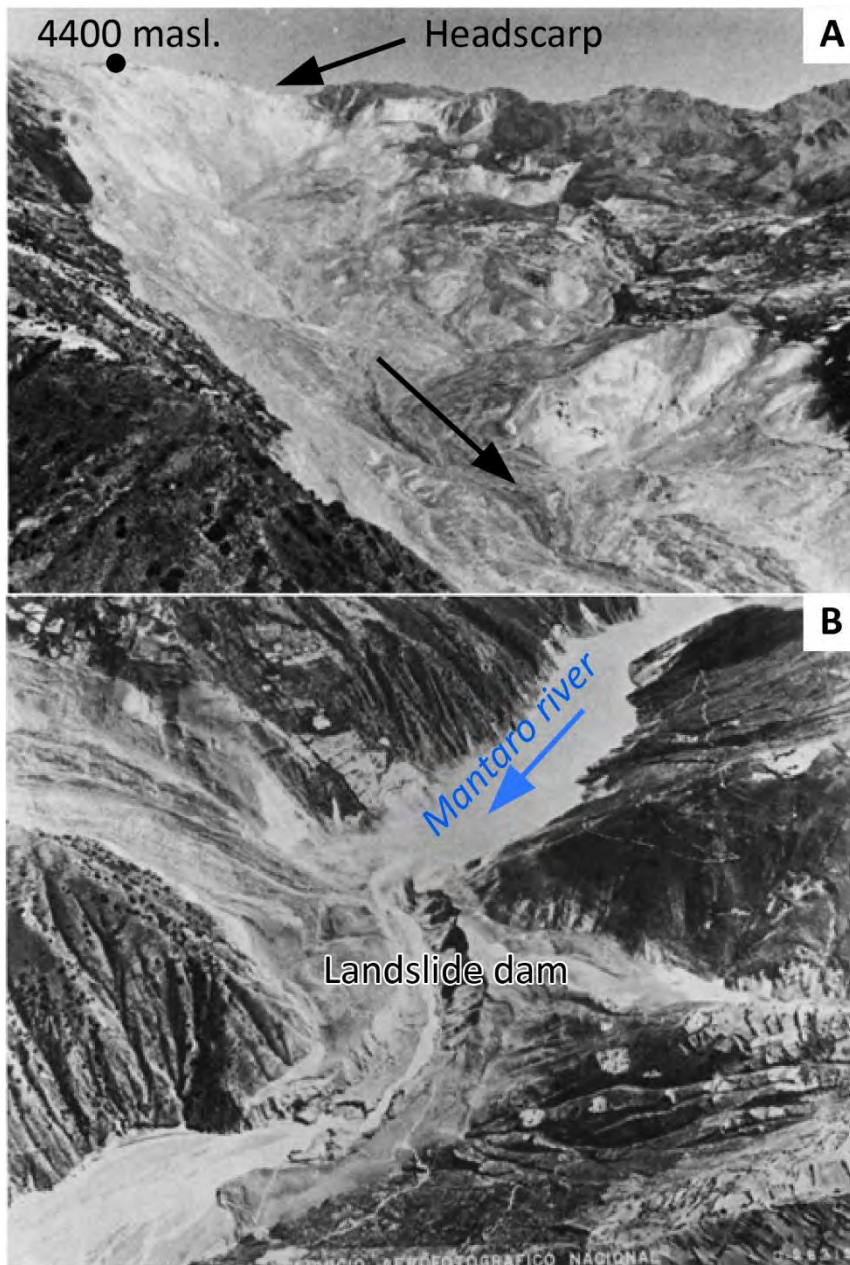


Figure 6. A) Oblique view of slide looking west, showing rockslide source on upper southwest margin, reactivated rotational slides on upper northwest margin, extensive banding in middle reach of debris flow and splatter zone on lower northwest margin (June 1974). B) View of breached landslide dam looking northwest, showing scour zone on right margin of mouth of Quebrada Tinte and associated fall-back ridges (Servicio Aerofotografico Nacional, 9 June 1974). (Modified from Kojan and Hutchinson (1978)).

One of the most recent landslides that occurred this year is the Retamas landslide (Figure 7), located in the town of Retamas (La Libertad-Peru). This landslide occurred in the month of March. The mass of the landslide affected 80 houses, many of these houses were covered by deposits and people were trapped. It has a height difference of 100 m from the main scarp to the foot of the landslide (Figure 7a).



Figure 7. (a) Panoramic view of the landslide that occurred on 15 March this year in the village of Retamas. The white line and the dotted line limit the Retamas landslide (Base Photo Aldair Mejia/PRESIDENCIA PERUANA/ AFP). (b) Image of the precise moment that the landslide begins (Video capture). The white circle is the location of the houses that were covered by the landslide debris and the red polygon are the houses located at the base of the landslide, these houses were affected.

These four examples of catastrophic landslides in the Andes point out the necessity to bring new informations about the comprehension of the large landslides development and triggering for disaster risk management and land-use planning, because they generate great impact on society-

2 Large landslides: state of the art

2.1 Definition

Large landslides mobilize large volumes of rocks and/or soils. They are mainly located in orogenic belts. These areas show strong tectonic activity in relation to relief formation (Korup, 2005; Dortch et al., 2009; Pánek et al., 2019). In these sectors the spatial distribution of landslides is related to regional tectonic activity and local structures (Keefer, 1984; Carlini et al., 2016). The constant and rapid uplift

during prolonged times of the orogenic belts, increases the tilt angle of the orogenic wedge that can reach the stability angle generating landslides that modify the slope and control mountain growth (Whipple et al., 1999; Montgomery, 2001; Montgomery and Brandon, 2002; Larsen and Montgomery, 2012; Roering, 2012; Li et al., 2014). On the other hand, these major instabilities are the product of the interaction of different controlling factors such as lithology, faults, folds, topographic relief, stress state, weather, climate, seismicity and human activity (Agliardi et al., 2012). All of these factors have a major impact on landslide type, location, and frequency of landslide occurrence (Kellogg, 2001; Břežný and Pánek, 2017; Görum, 2019). But, on a short time scale, earthquakes are the main trigger to induce large landslides (Keefer, 1984; Keefer, 1994; Owen et al., 2008) depending on the magnitude of the earthquake and the degree of rock deformation.

According to the literature, different mechanisms of large landslide formation are proposed (Figure 8, Agliardi et al., 2018). Some of these landslides are associated with the development of joints, faults and folds that limit slope stability by reducing the mechanical characteristics of the rock (Figure 8.g, i, j, s). In these cases, the local relief can exceed 1000m. Another characteristic of these landslides they present slip surfaces with variable geometries like curved (Fig. 8 a- g), compound (Figure 8 h-l) or planar (Figure 8 m-r; Sjoberg, 1999; Nichol et al., 2002). Large-scale topplings are common on slopes with deep and persistent discontinuities (Figure 8 u-w, Cruden and Hu, 1994; Kieffer, 1998). In conclusion, the type of landslide depends on the degree of resistance of the rock and the type of discontinuities such as fractures, joints, stratification planes, faults and contact zones between different geological formations (Figure 8).

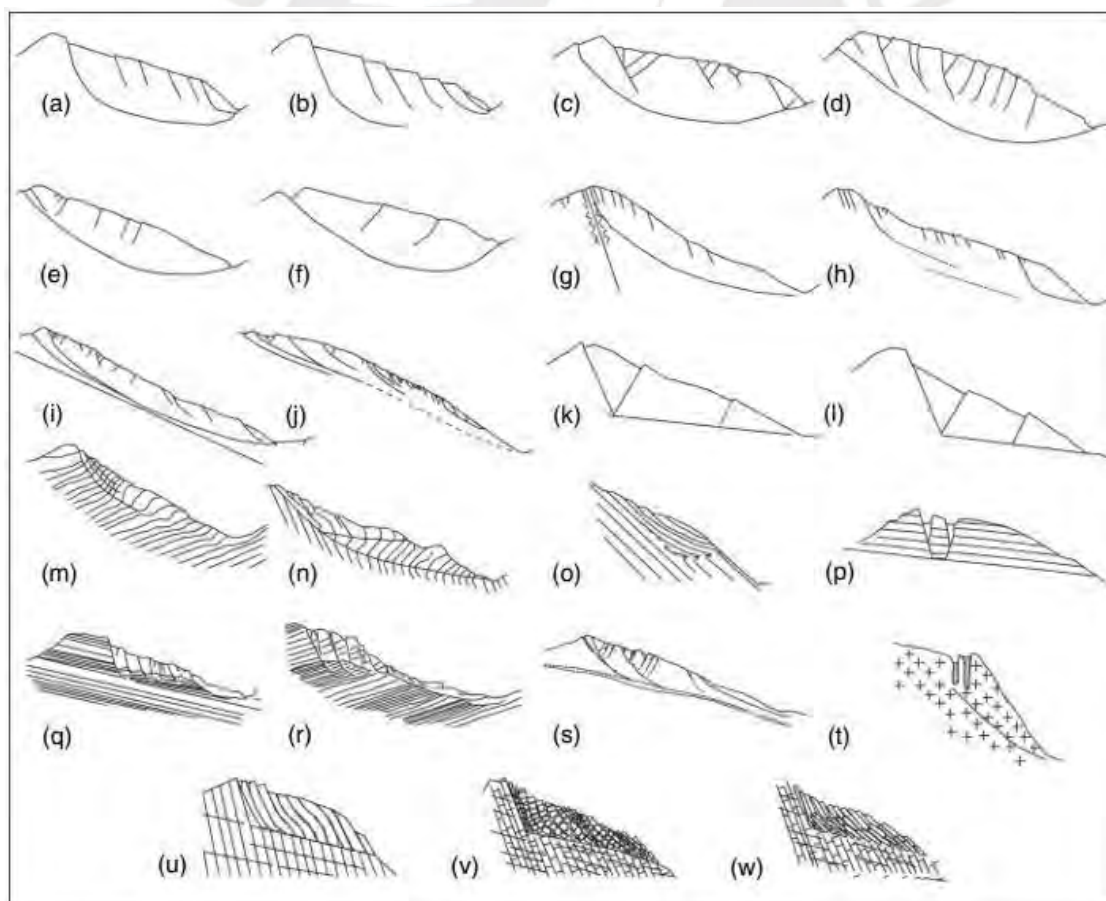


Figure 8. Mechanisms of largescale rock-slope failure proposed in the literature, ordered on the basis of failure geometry and structural controls. (a), (b), (c), (f) Bois et al. (2008); (d) Mahr (1977); (e), (g), (h), (i) Ambrosi and Crosta (2006); (j) Agliardi et al. (2001); (k), (l) Hutchinson (1988); (m), (n) Zischinsky

(1966); (o), (p), (t) Chigira (1992); (q), (r) Nemcok (1972); (s) Agliardi et al. (2009b); (u), (v), (w) Kieffer (1998). (Agliardi et al., 2012).

The scale and timing of landslide depend on the interaction between the behavior of the rock mass and the types and histories of external forces such as weather and earthquakes (Agliardi et al., 2012). The result can produce: (1) small ruptures, (2) frequent landslides (e.g., rock falls), (3) sudden or progressive large-scale landslides (e.g., rock falls and rock avalanches), or (4) slow, non-catastrophic deep-seated slope deformations.

2.2 Geomorphology and type (DSGSD and DSL)

In this part we will focus especially on deep-seated gravitational slope deformation (DSGSD) and deep-seated landslides (DSL), because DSGSD have been documented in many mountain belts around the world (e.g. Pánek et al., 2011). Moreover, DSGSD are places that allow the development of deep-seated landslides (DSL) as indicated by Agliardi et al., (2001) and this fact represents a great risk for cities and people living in the valleys that are located in these mountains.

Deep-seated gravitational slope deformation (DSGSD) are processes that affect the rock mass, generally the slopes of high relief mountains, from valley to ridge, moving and deforming at low rates of movement (mm yr⁻¹) for long periods of time (Varnes et al., 1990; Ambrosi and Crosta, 2006) and moving large volumes (>0.5 km³). DSGSDs reach considerable thicknesses (tens of meters or more) and lateral boundaries are discontinuous and poorly defined (Agliardi et al., 2001; Agliardi et al., 2012; Crosta et al., 2013).

DSGSDs have relatively deep slip surfaces (Agliardi et al., 2001). Although some authors consider that the slip surface is not always clearly observed (Dramis and Sorriso-Valvo, 1994; Soldati, 2013). However, other works suggest the presence of a well-defined slip plane or that most of the time, DSGSDs are controlled by inherited structures (faults, fold axes, stratification planes) (Agliardi et al., 2001; Agliardi et al., 2009b; Pánek et al., 2011; Pánek and Klimeš, 2016).

The formation of DSGSD is generally related to specific geological and structural features, such as stratification, foliation, joints and faults. They depend also of particular topographic situations associated with local slope changes. They are also common in tectonically active areas such as the Alps and the Himalayan Mountain range (Crosta and Zanchi, 2000; Agliardi et al., 2009b; Ambrosi and Crosta, 2011).

The most common indicator of DSGSD is the presence of surface deformation features of gravity origin (Agliardi et al., 2001). Characteristic morphostructures of DSGSD (Figure 9) include double ridges, trenches, tension cracks, counter-scarps, collapsed blocks, buckling folds, toe bulging, rock fracturing, secondary scarps. There are also associations between DSGSDs and mass movements in the middle and lower part (Figure 9, Agliardi et al., 2001).

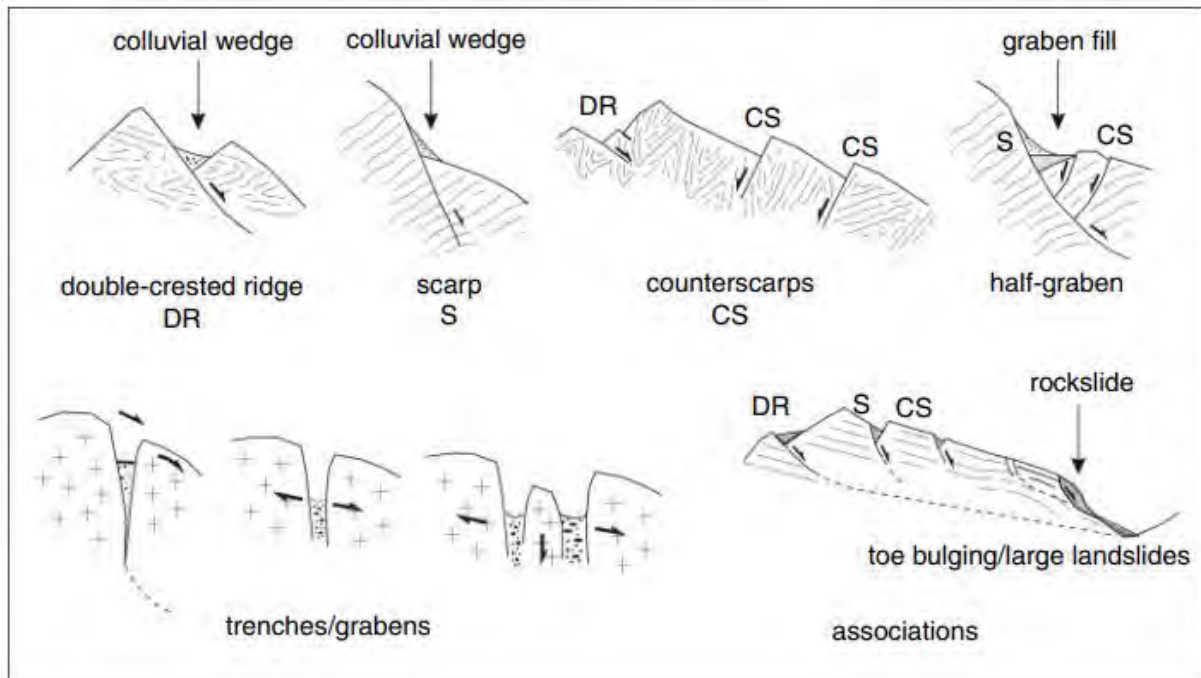


Figure 9. Morpho-structural features diagnostic of deep-seated gravitational slope deformation (DSGSD) phenomena, related kinematic significance, and typical associations (modified after Agliardi et al., 2001). (Agliardi et al., 2012)

Most DSGSDs originate as sackungen (Figure 8, see Zischinsky, 1966; Hutchinson, 1988) in metamorphic, igneous or sedimentary rocks. Sackungen were described by several authors (Zischinsky, 1966; Hutchinson, 1988; Varnes et al., 1989; Crosta, 1996; Agliardi et al., 2001). They form as a result of gravitational deformation of mountains (Radbruch-Hall, 1978), suggest that they are due to a long-term formation process ($>10^3 - 10^4$ years) but with temporary reactivations and/or accelerations (Agliardi et al., 2001; El Bedoui et al., 2009; Hippolyte et al., 2009; Hippolyte et al., 2012; Agliardi et al., 2012; Crosta et al., 2014). Moreover, apart from sackungen there are lateral expansions (Figure 7 p-r; Hutchinson, 1988; Cancelli and Casagli, 1995), these are more common in horizontal or gently sloping areas, where there are sedimentary successions with strongly competing levels (Agliardi et al., 2012).

DSGSD formation depends on stress relief, debuttressing, loss of lateral or frontal support and water pressure in crevasses or diaclases (Pánek et al., 2015), The sackunks are more common in mountainous areas affected by deglaciation processes, rapid river incision, tectonic uplift and seismic events (Agliardi et al., 2001). Sackungen can also occur in non-glacial environments.

Large lateral expansions also form DSGSDs, which can occur in volcanic or compact sedimentary rocks overlying ductile rocks (Dikau et al., 1996). Due to lateral flow of the underlying soft levels or rocks, the more rigid and compact rocks are deformed by the development of tension cracks, trenches and scarps (Pánek and Klimes, 2016), which end up forming surficial topples, rockfalls or landslides. The different structures formed by lateral expansion are similar to those produced by sackungen, which makes it difficult to distinguish them (Pánek and Klimes, 2016).

These processes are globally distributed in mountains that experienced glacial advances. Pánek et al., (2015) performed a compilation of DSGSD in various mountain environments based on studies published since 1990 (Figure 9). The studies used chronological data to differentiate between two types of DSGSD those occurring in glaciated and non-glaciated areas. Those occurring in glaciated areas

experienced advances during the Last Glacial Maximum (LGM, Hughes et al., 2013; Agliardi et al., 2013; Crosta et al., 2013) and DSGSDs at non-glacial sites have paraglacial origins, becoming dated shortly after deglaciation and/or ice retreat (McCalpin and Irvine, 1995; Agliardi et al., 2009a; Hippolyte et al., 2012). Pánek et al., (2015) show that in the case of the Alps there is a high concentration of DSGSD, more than 1000 DSGSD were inventoried (Crosta et al., 2013), only the most significant studies with dating and typical sackung forms were included.

DSLs are landslides with a relatively deep slip surface compared to DSGSDs. These processes have definite characteristics: (i) a generally horseshoe-shaped scarp, (ii) a main body or sliding mass, (iii) have width, length and height relationships, and (iv) high internal deformation (Figure 10, Agliardi et al., 2001). The main triggers are earthquakes, extreme climatic events, groundwater pressure and anthropogenic activity.

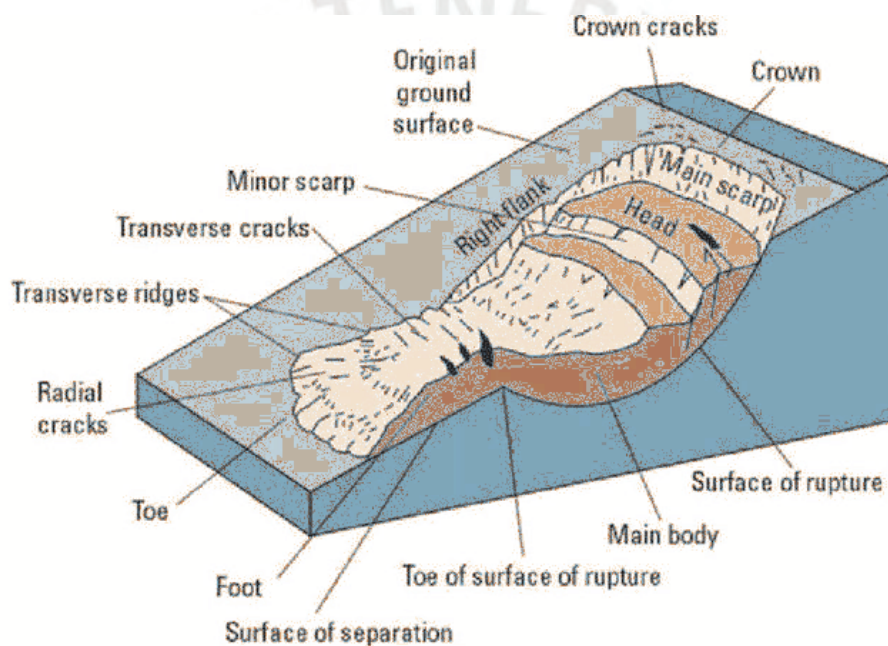


Figure 10. Schematic model of typical deep-seated landslide (Cruden and Varnes 1996; Highland and Bobrowsky 2008).

DSL can be roughly categorized into two typologies: rockslides and rock avalanches. These large events can occur spontaneously or can occur within the mass of a DSGSD.

- Rockslides involve the displacement of material along a slip plane or rupture surface (Figure 10). The slip may be of the translational type with displacement along a planar surface, or it may be rotational due to displacement over a concave rupture surface. Slips of this type move in a single block as a coherent or semi-coherent mass with little internal deformation. The displaced mass may have internal planes that tend to tilt backward (Figure 10). These types of events are the ones that mostly trigger the damming of rivers and valleys (Figure 11; Ermini and Casagli, 2003; Fan et al., 2012; Hermanns et al., 2011).
- Rock avalanches are the result of the rapid fragmentation of large rock masses (>1 Mm³) similar to granular flows; associated with very fast transporting material (Hung et al., 2001), causing

drastic and rapid changes in mountain landscapes. These events as highly mobile flows (Hungre et al., 2001) have an increase in velocity related to the increase in volume (Heim, 1932), based on the H/L ratio (ratio of landslide height to horizontal displacement distance) versus volume (V). These events are also considered one of the most dangerous and costly geological hazards because they damage infrastructure and can cause a large number of deaths (Evans et al., 2006; Hewitt et al., 2008). The destabilization begins with the collapse of a large rock mass, then fragmentation and transport (Strom, 2006). This type of landslide can also generate valley damming (Figure 12; Hermanns et al., 2011). The recurrence of this type of event in the same place can occur after thousands of years (Crosta et al., 2004) or can be within weeks (Eberhardt et al., 2004) depending on the rock consistency.

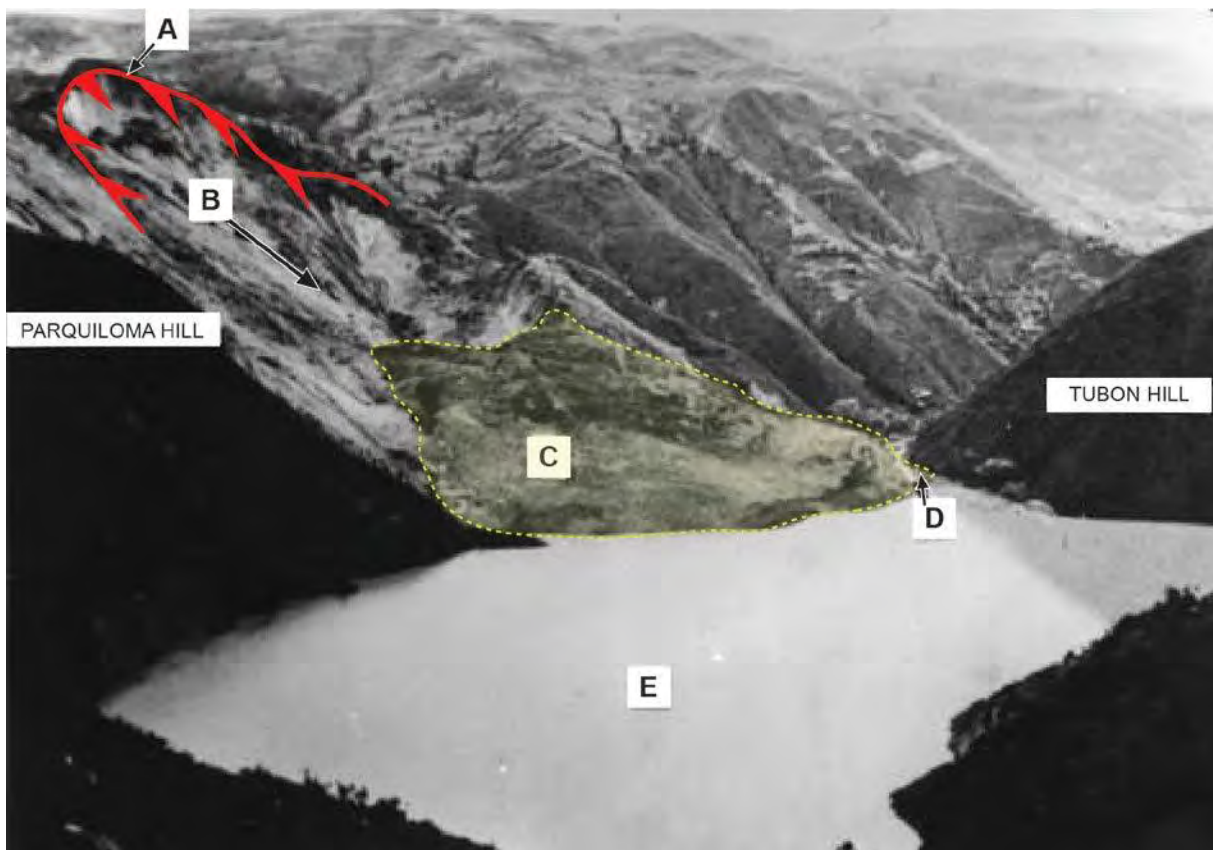


Figure 11. View of the La Josefina landslide that occurred in March 1993 in Ecuador. The landslide of about 20 Mm^3 created a natural dam 100 m high, 300 m wide and 1.1 km long. This landslide filled the Paute river valley. (A) Head scarp, (B) Direction of movement; (C) Partial accumulation of debris, (D) Excavated channel, (E) Dammed lake. (Modified from Plaza et al., 2011).



Figure 12. Oblique view of the rock avalanche deposit that fills the valley of the Melado river. The slide mass forms a large dike and gives rise to Dial Lake, Chile (Modified from Hermanns et al., 2011).

2.3 Long term evolution and controlling factors

2.3.1 Concept of progressive failure: creep to collapse

To estimate the movement or deformation of DSGSD at short-term scales, different methods (Klimes et al., 2012) and tools are used, such as geodetic and remote sensing techniques, global positioning systems, and radar interferograms (Colesanti and Wasowski, 2006). However, landslide monitoring is not relevant for long-term study (>100 years). Geochronological and/or stratigraphic methods (Pánek, 2015) are useful to establish the dynamics of destabilizations over the long-term (>100 year; Walker, 2005). The combination of these recent monitoring data and the use of dating techniques allow reconstructing the evolutionary history of DSGSDs (Hermanns et al., 2013).

One of the procedures performed are the excavations of paleoseismological trenches or trenches (McCalpin, 2009) through gravitational scarps, for which dating methods such as ^{14}C or OSL are used. Cosmogenic nuclides ^{10}Be (Sanchez et al., 2010; Hippolyte et al., 2012) and ^{36}Cl (Zerathe et al., 2013; Zerathe et al., 2014) are also used. The results of exposure dating help to know the evolution of DSGSDs (Hippolyte et al., 2009; Hippolyte et al., 2012), for this purpose, samples are extracted from escarpments or cracks and the time of movement onset can be deduced. For DSLs, the use of cosmogenic nuclides helps us to know when these events occurred (Hippolyte et al., 2012; Gutiérrez et al., 2012).

Dating in DSGSDs demonstrates that these processes have long-term motion, comes to be slow and continuous slip (McCalpin et al., 2011; Hermanns et al., 2013), with discrete episodic motions (Carbonel et al., 2013; Gori et al., 2014, and other researchers). Movements can be steady, accelerated, or decelerated over extended periods of time ($\geq 10^2$ years). Inferred long-term slip rates for DSGSDs range from 0.1 to 5 $\text{mm}\cdot\text{year}^{-1}$ (Gutiérrez et al., 2012b), while for DSLs rates can exceed 15 $\text{mm}\cdot\text{year}^{-1}$ and reach up to 80 $\text{mm}\cdot\text{year}^{-1}$ (El Bedoui et al., 2009).

Creep-type landslides originate from glacial retreat (McCalpin and Irvine, 1995). McCalpin and Irvine, (1995) identified that the movement is not continuous, but rather slowed ($\sim 75\%$) thousands of years after deglaciation began. This long-term deformation is related to the kinematics, the thickness of the rock mass (Hippolyte et al., 2009) and the degree of deformation of the rock. Furthermore, El Bedoui et al., (2009) indicate that post-glacial movements start slow, but during the Holocene they begin to increase the movement, causing the rock to have a progressive decrease in resistance. This fact allows an increase in the rate of deformation that would be the beginning of the rupture and in a short time generate the formation of a rockslide with a movement velocity $>80 \text{ mm.yr}^{-1}$ (Figure 13; El Bedoui et al., 2009). In conclusion, unlike the evolution of DSGSDs, DSLs are processes that may have a shorter evolution process (tens to thousands of years), or may occur instantaneously, and in other cases may be part of the slipped and deformed mass of a DSGSD.

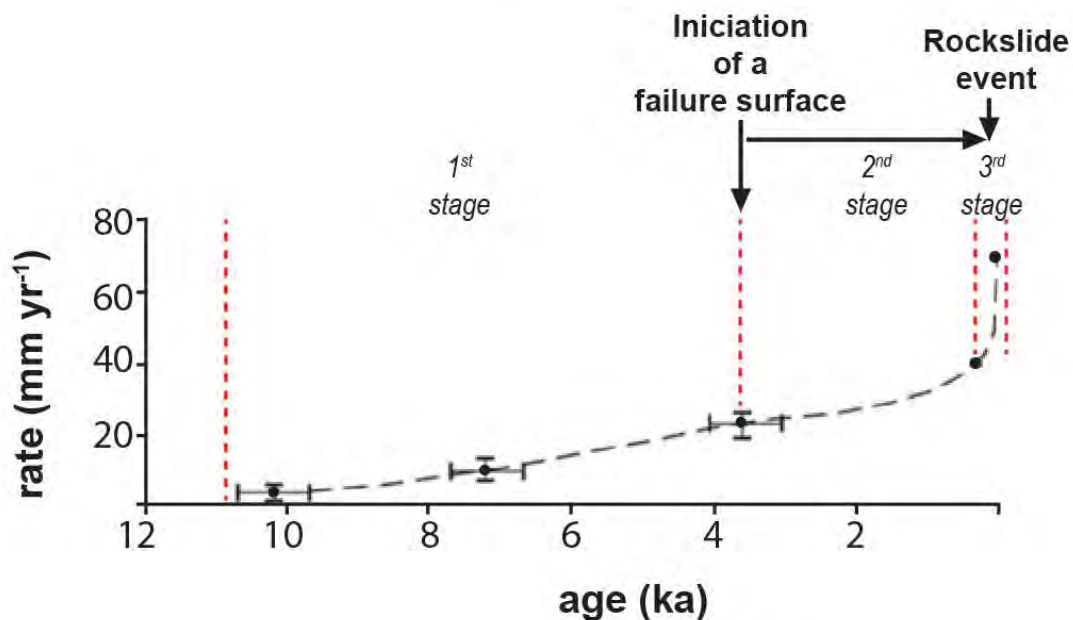


Figure 13. Example of long-lasting horizontal movements and opening of tensile cracks within the La Clapière Sack (French Alps), 3 stages are observed: first a stage of continuous evolution of the landslide that in a second stage (mid-Holocene) transforms into an increase of the deformation rate, finally in the third stage becomes a predominantly vertical and accelerated shearing, which as a result formed a landslide occurred in the last 50 years (Modified from El Bedoui et al., 2009).

2.3.2 Controlling factor (temporal evolution)

The formation of DSGSDs and DSLs is the result of the interaction of different features and controlling processes, including lithology and geological structure such as stratigraphic planes and contacts between geological formations (Agliardi et al., 2001; Ambrosi and Crosta, 2006; Crosta et al., 2013), which are one of the main factors influencing the formation of these processes, but there are also other factors that are: (i) Long-term exhumation controls (Agliardi et al., 2001; Crosta et al., 2013) on active margins such as the Andes where deep valley incision occurs in response to Andes uplift (Thouret et al., 2007), forming steeply sloping hillslopes that can lead to landslides due to rock strength limitation (Schmidt and Montgomery, 1995). (ii) Topographic relief and slope geometry (Ambrosi and Crosta, 2011), influence that above a given slope angle can fail according to rock strength (Schmidt and

Montgomery, 1995; G. K. Li and Moon, 2021). (iii) Tectonic and topographic stresses and their concentration (Ambrosi and Crosta, 2006; Ambrosi and Crosta, 2011; Crosta, 1996; Martel, 2006; Miller and Dunne, 1996; Molnar, 2004; Savage and Swolfs., 1986), result from the interaction between tectonic and topographic stress that influences rock deformation, weakening the rock and exerting a dominant control on landslide formation and landslide size (G. K. Li and Moon, 2021). (iv) Weather and climate (Agliardi et al., 2013; Ballantyne, 2002; Evans and Clague, 1994), precipitation is among the triggers of landslides due to the low mechanical properties of rocks or soils to the saturation of rainfall and changes in the water table (Pánek et al., 2016; Aslan et al., 2021). In the Andes, there are records of landslides correlated with extreme paleoclimatic events recorded in the altiplano (Chuquibamba landslide, Margirier et al., 2015). (v) Glaciation and deglaciation (Augustinus, 1995; Ballantyne, 2002; Cossart et al., 2008; Crosta, 1996; Ustaszewski et al., 2008) are processes that accelerate the development and formation of these processes due to the reduction of glacier ice volume and the recovery of steep valley flanks, leading to landslides and rockfall (Kos et al., 2016). (vi) Seismicity (McCalpin, 1999; Moro et al., 2007; Radbruch-Hall, 1978; Solonenko, 1977), is one of the triggers for landslide formation. Comparisons were made between magnitude and distance, as well as magnitude and area, suggesting that landslides are generated from magnitudes >5 Mw (Keefer, 1984, 1994; Rodriguez et al., 1999). Examples of landslides induced by earthquakes include the Nepal earthquake of magnitude 7.8 MW in 2015, which caused more than 21,000 landslides (Valagussa et al., 2021b). Another example in the Andes is the 2007 Pisco landslide, which had a magnitude of 8.0 MW and generated the formation of more than 800 landslides (Lacroix et al., 2013). (vii) Changes in the groundwater regime (Crosta, 1996) exert pressure on the cracks and/or escarpments increasing the forces that influence instability, increase the weight of the material by saturation and generate changes in the mineralogical composition of the rock (Gonzales de Vallejo et al., 2002). (viii) Rock dissolution and human activity (Heim, 1932; MacFarlane, 2008; Zangerl et al., 2010) due to irrigation for agriculture and indiscriminate logging influence landslide formation and reactivation (Lacroix et al., 2020).

2.4 Synthesis of large landslide dating in the worldwide (landslide dating in mountainous areas)

Determining the age of landslide exposure is an important step in understanding the causes, recurrence and triggers (Corominas and Moya, 2008). Landslide dating is used to correlate with paleoclimatic events (Placzek et al., 2013), paleoseismic events (Aylsworth et al., 2000) or to estimate the erosion rate of a watershed (Antinao and Gosse, 2009).

Different absolute dating techniques are used to date landslides, because they allow to obtain calculated numerical ages (Walker, 2005). Frequently used absolute dating methods comprise radiometric techniques such as radiocarbon (^{14}C), Cosmic Ray Exposure (CRE), Optically Stimulated Luminescence (OSL), Thermoluminescence (TL) and Uranium-series ($^{234}\text{U}/^{230}\text{Th}$) (Figure 14; Pánek, 2015). For recent events or events that occurred in the last few centuries, tree-ring based dendrochronology is used (Figure 15). Radiocarbon dating (^{14}C) allows dating of organic materials (Wood and paleo-soil) mixed or buried by landslide mass; allowing for landslide chronologies (Borgatti and Soldati, 2010). The Cosmic Ray Exposure allows to know the exposure age of landslides by dating the blocks in the landslide mass and the escarpments or landslide plane (Zerathe et al., 2017). OSL, TL and Uranium series techniques have limitations for dating landslides; fine sediments are required for dating (Li et al., 2008; Prager et al., 2008). Dendrochronology is used to date landslides using trees that were damaged by avalanches or rocks in their path, the tree rings allow determining the age of the landslides with precision (López Saez et al., 2012). One of the relative dating methods for landslides is lichenometry (Figure 14), which is related to specific lichens located on landslide blocks that can give a minimum age of the event (Bull, 2003; Lang et al., 1999). Another relative method is tephrochronology

(Figure 15) that can indicate the minimum or maximum age of a landslide depending on the tephra layer that covers or underlies the body of the landslide (Moreiras, 2006; Hermanns and Schellenberger, 2008; Mercier et al., 2013).

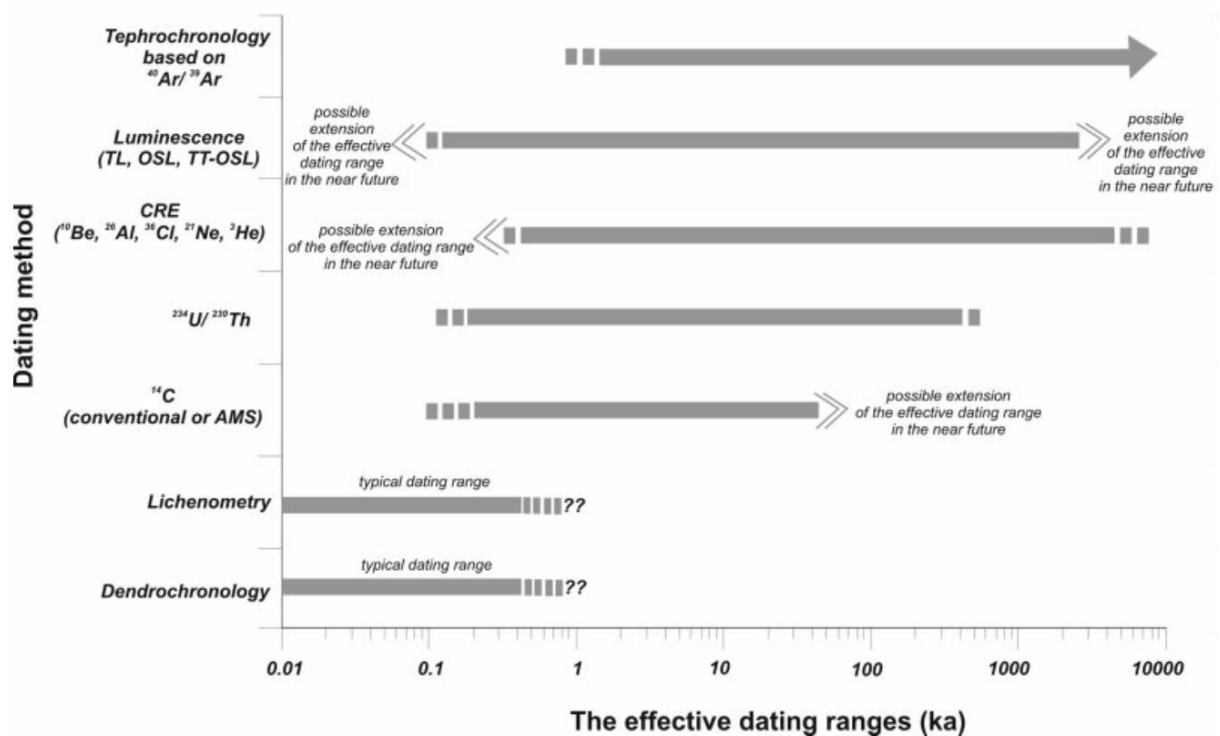


Figure 14. Main dating methods used to date landslides (Modified from Pánek, 2015).

Pánek et al., (2016) conducted a compilation of studies where they used DSGSD and DSL dating methods around the world. They distinguished two groups of events that occurred in glacial and non-glacial environments (Figure 14). The former with ages given between 18 and 10 ka that correspond to deglaciation in mountain belts (e. g. Rocky Mountains, McCalpin and Irvine, 1995; Alaska, McCalpin et al., 2011; Scandinavian Mountains, Hermanns et al., 2013; Alps, Hippolyte et al., 2012; Zerathe et al., 2014; Schwartz et al., 2017; the Pyrenees, Gutiérrez et al., 2008) and the second group that are not related to non-glacial environments, have a longer and more complex evolution, are events prior to the Last Glacial Maximum (Hughes et al., 2013).

Although landslide dating studies have increased worldwide, but regional landslides chronologies are not extensive and are scarce (Figure 15; Pánek, 2015). The glacial advance and retreat, coupled with the presence of intense rainfall in all mountains such as the Alps, the Himalayas, among others, erode and erase the presence of DSGSD and even more the presence of DSL, restricting the study and knowledge of these processes in a short time window (Figure 15). In order to learn more about the behavior, formation and evolution of these large processes, the time window of study must be extended (Figure 15). One of the places in the world that allows the study of these processes is the Western Flank of the Central Andes because it has no rainfall, the surface is preserved and has the presence of large landslides.

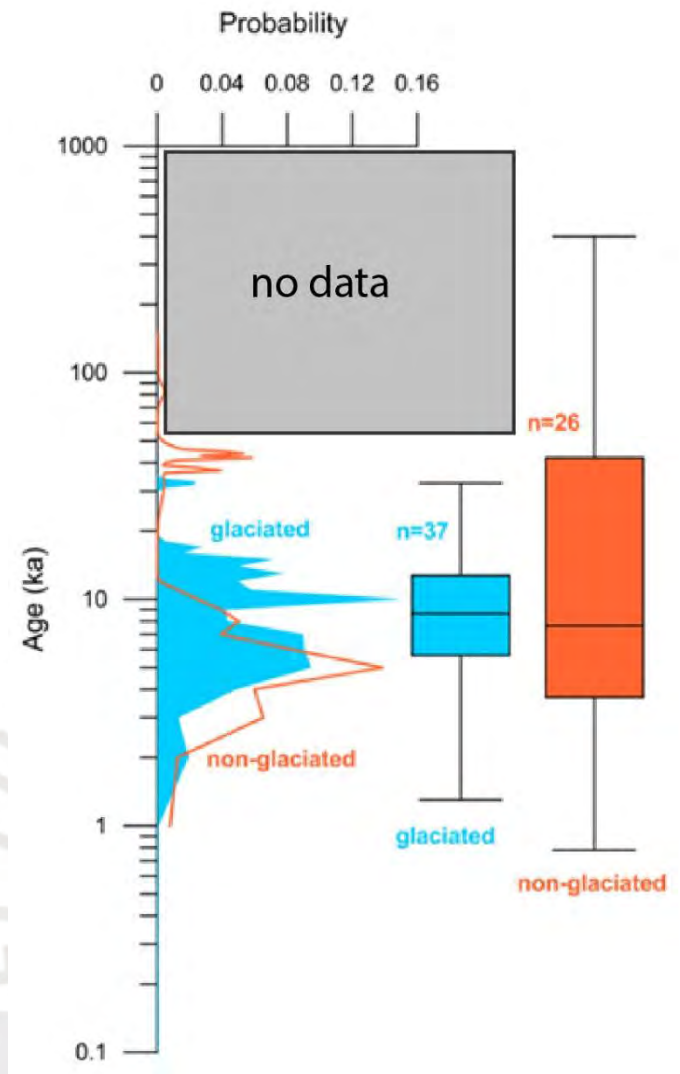


Figure 15. Probability distributions and variability of ages expressed as box-whisker plots for published DSGSDs and DSLs situated in formerly glaciated terrains and in non-glaciated settings. Gray box indicates no data due to lack of landslide studies and dating. (Modified from Pánek and Klimeš (2016)).

3 Western Flank of the Central Andes (WFCA)

3.1 The WFCA a perfect place to study the large landslide activity over 1Ma time window

The Andes is an active mountain belt resulting from combined tectonic and magmatic processes related to the subduction dynamics of the Nazca plate below the South American plate. The main convergence velocity between the two plates reaches 62 mm.yr^{-1} (e.g. Villegas-Lanza et al., 2006). This shortening generates relief construction through long-term processes of surface uplift and volcanism, producing a large orographic barrier at the scale of the South America continent (Bookhagen and Strecker, 2008).

The western flank of the Central Andes (WFCA) presents from east to west different geomorphological zones. a) a coastal mountain range with a maximum elevation of 1000 m asl, b) a coastal plain or central depression, c) the western cordillera range with elevations between 1000 and 4500 m asl, and d) the Altiplano, which reaches an average elevation of 5000 m asl. (Figure 16)

The WFCA is can be considered as a natural laboratory suitable for the study of the large landslides (Figure 16). Indeed the area presents:

(1) High relief that acts as strong orographic barrier. It prevents precipitation from the Amazonian side from crossing to the west (Houston and Hartley, 2003; Bookhagen and Strecker, 2008), thus allowing this place to have a hyper-arid climate and very low erosion rates (<0.5 mm/year, Hall et al., 2008) that allow to preserve the geomorphological markers for millions of years (Kober et al., 2007, Nishiizumi et al., 2005; Dunai et al., 2005), due to the aridity this place is called the Atacama Desert. This place offers the opportunity to trace gravitational processes on an unknown time scale.

(2) The WFCA is carved by deep valleys and canyons that cut through the western cordillera and the central depression and are related to regional uplift (e.g. Thouret et al., 2007), incised and deepened by rivers descending from the altiplano (Evenstar et al., 2017).

(3) The WFCA hosts a large number of fossil mega-slides of plurikilometric cubic volumes as for example Chuquibamba (Margirier et al., 2015), Caquilluco (Zerathe et al., 2017), Lluta (Strasser and Schlunegger, 2005), Miñimiñi and Latagualla landslides (Pinto et al., 2008), El Magnifico landslide (Mather et al., 2014; Crosta et al., 2017). All of these previously studied landslides are located along the western cordillera, with the exception of the El Magnifico landslide, which is located in the coastal cordillera.

(4) In this long term arid climate one of the characteristics of this part of the Andes is the occurrence of intense humid paleoclimatic events in the Atacama Desert (Bartz et al., 2020), producing the formation of temporary paleo lakes (Ritter et al., 2018). Paleo-El Niño events also affect this zone, these were identified by dating debris flows on the Peruvian coastal margin (Wells, 1990; Fontugne et al., 1999; Keefer et al., 2003), suggesting that these events were frequent and severe enough to produce significant erosion and deposition. In the Altiplano shows the occurrence of other recorded paleoclimatic events such as the Tauca phase (18.5 - 14.5 ka) and the Copiasa phase (12.8 - 11 ka) during the Heinrich 1a and Younger Dryas respectively (Placzek et al., 2013) and climatic fluctuations of lake levels and glacial advances during the Tauca phase (Martin et al., 2018) that could have had great impact on landslide formation in this part of the Andes.

(5) The seismicity in this area is due to the convergence between Pacific and the South America plates. This convergence produces uplift related that participate to the construction of the Andes relief. Two types of earthquakes can be distinguished: (i) subduction or crustal earthquakes that generate earthquakes of up to 9 Mw with recurrences every 250 years and (ii) cortical earthquakes due to the reactivation of active geological faults, which generate earthquakes of 7 Mw, these earthquakes are superficial (<30 km deep) and have a recurrence of thousands of years.

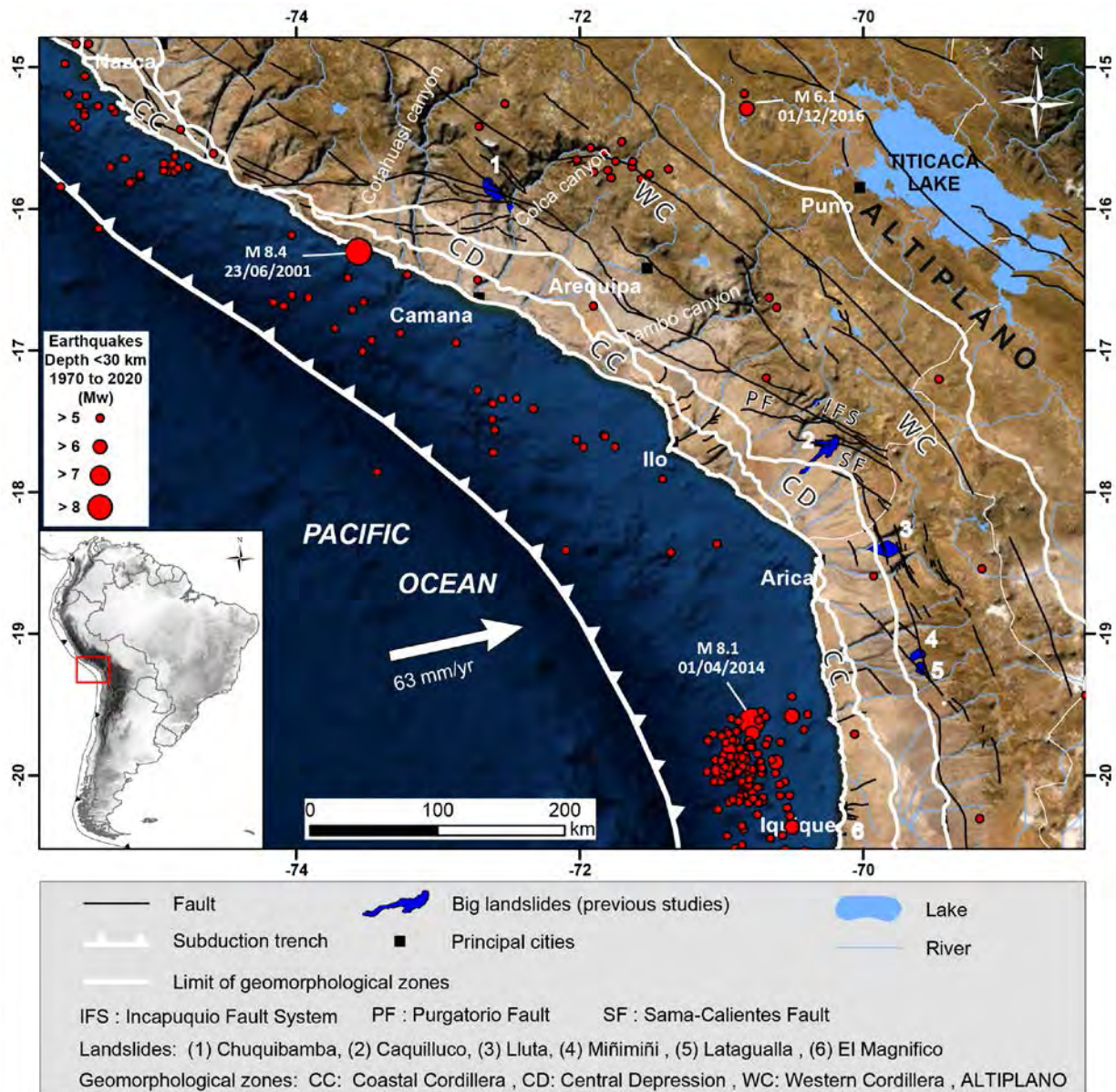


Figure 16. Focus of the Western Flank of the Central Andes divided into geomorphological zones. Large landslides are observed in this part of the Andes: Chuquibamba (Margirier et al., 2015), Caquilluco landslide (Zerathe et al., 2017), Lluta landslide (Wörner et al., 2002; Strasser and Schlunegger, 2005), Miñimiñi and Latagualla landslides (Pinto et al., 2008). There is a rugged topography with mountains, valleys and deep canyons (Cotahuasi, Colca, Tambo). This part has intense seismicity, we consider surface seismicity <30 km (red circle) for subduction and cortical earthquakes (<http://ds.iris.edu/seismon/index.phtml>).

3.2 Geodynamic and tectonic setting

The origin of the Andes is a product of the subduction of the Nazca plate under the South American plate (Pardo-Casas and Molnar, 1987), this process generated the construction of the Andes and gave rise to the formation of successive volcanic arcs. These different arcs were controlled by subduction dip change (Isacks, 1988; Allmendinger et al., 1997; James & Sacks, 1999; Sobolev & Babeyko, 2005; Haschke et al., 2006; Mamani et al., 2008, 2009). These dynamics produced a thickening of the crust,

thus forming the western cordillera. Crustal thickening began in the Upper Cretaceous (Jaillard & Soler, 1996). One of the main volcanic faces corresponds to the so-called Huaylillas arc (24-10 Ma, Quang et al., 2005; Thouret et al., 2007), which produced thick ignimbrite deposits (~300 m thick) on a regional scale. Currently, the western Cordillera is covered by the Huaylillas ignimbrites, being a reference marker. This domain is affected by tectonic shortening, evidencing flexure of the Huaylillas paleosurface and also the presence of crustal fault systems.

The WFCA is deformed and shows important reverse faults due to the crustal shortening and thickening (Armijo et al., 2015) as a result of subduction. In this part of the Andes the tectonic regime is transpressive. Cortical faults generate surface earthquakes with magnitudes up to 7 Mw, the recurrence time of the reactivations of these faults is > 1000 years. One of the last recorded cortical earthquakes was the Parina earthquake with a magnitude of 6.1 MW, which occurred in the Altiplano (Aguirre et al., 2021). In the WFCA the most important structure is the Incapuquio Fault System (IFS), which has a length of more than 200 km with NW-SE direction (Figure 16). This fault system extends along the western cordillera. It is considered as a neotectonic fault because the main surface ruptures have been produced during the Holocene time (Benavente et al., 2021). Another important fault is the Purgatorio Fault (PF), it is a reverse type fault, has an E-W strike and a length ~70 km, this fault shows at least two major ruptures phases that could generate earthquakes up to 7 Mw (Benavente et al., 2017). Another important fault in this part of the Andes is the Sama-Calientes fault (SF), which is considered as a reverse fault. The trace of this fault is located in the central depression with a E-W trending direction and a length of 50 km (Hall et al., 2008).

3.3 Climate and geomorphological setting

The topography of the WFCA results from the competition between erosion processes controlled by climatic conditions and the tectonic context. The western cordillera and the central depression in the WFCA are affected by deep valley incisions and canyons (e.g., Colca Canyon, Cotahuasi Canyon) mainly carved by the regional tectonic uplift (Thouret et al., 2007) related to the formation of the Andes. The estimated uplift rates during the Pleistocene are ranging between 0.2 to 0.4 mm.yr⁻¹ (Hall et al., 2012). This global uplift is due to the shortening and thickening of the continental lithosphere produced by the ongoing subduction of the Nazca plate beneath the South American plate (Isacks, 1988; Horton et al., 2001; Armijo et al., 2015)

Currently, the climate in the WFCA is one of the driest places in the world (Dunai et al., 2005). This place is called the Atacama Desert. This large coastal desert between Peru and Chile has a longitudinal extension of approximately 3500 km and is bounded by the Pacific Ocean to the west and the western cordillera to the east. This narrow topographic zone has a low annual precipitation rate, due to the fact that the Andes Mountain range limits the transfer of precipitation coming from the Atlantic and the Amazon (Bookhagen and Strecker, 2008), and the cold Humboldt current, which is a mass of cold sea water that moves from the South Pacific to the north, covering the coasts of Chile, Peru and Ecuador. It lowers the sea temperature by 5 to 10 degrees, this influences the atmosphere to cool down, limiting evaporation and causing the absence of rainfall, thus creating a strip of sand and coastal desert that becomes the Atacama Desert.

Precipitation during the last decades shows that the main source of moisture for the WFCA comes from the Amazon basin (Figure 17a). Precipitation regime is seasonal with a maximum during the austral summer. Part of this precipitation reaches the upper part of the basins and flows through the rivers to form deep valleys. But the precipitation is restricted to the east (Figure 17 b and c). Thus, the Atacama Desert remains arid, with less than 50 mm/year of precipitation (Strecker et al. 2007).

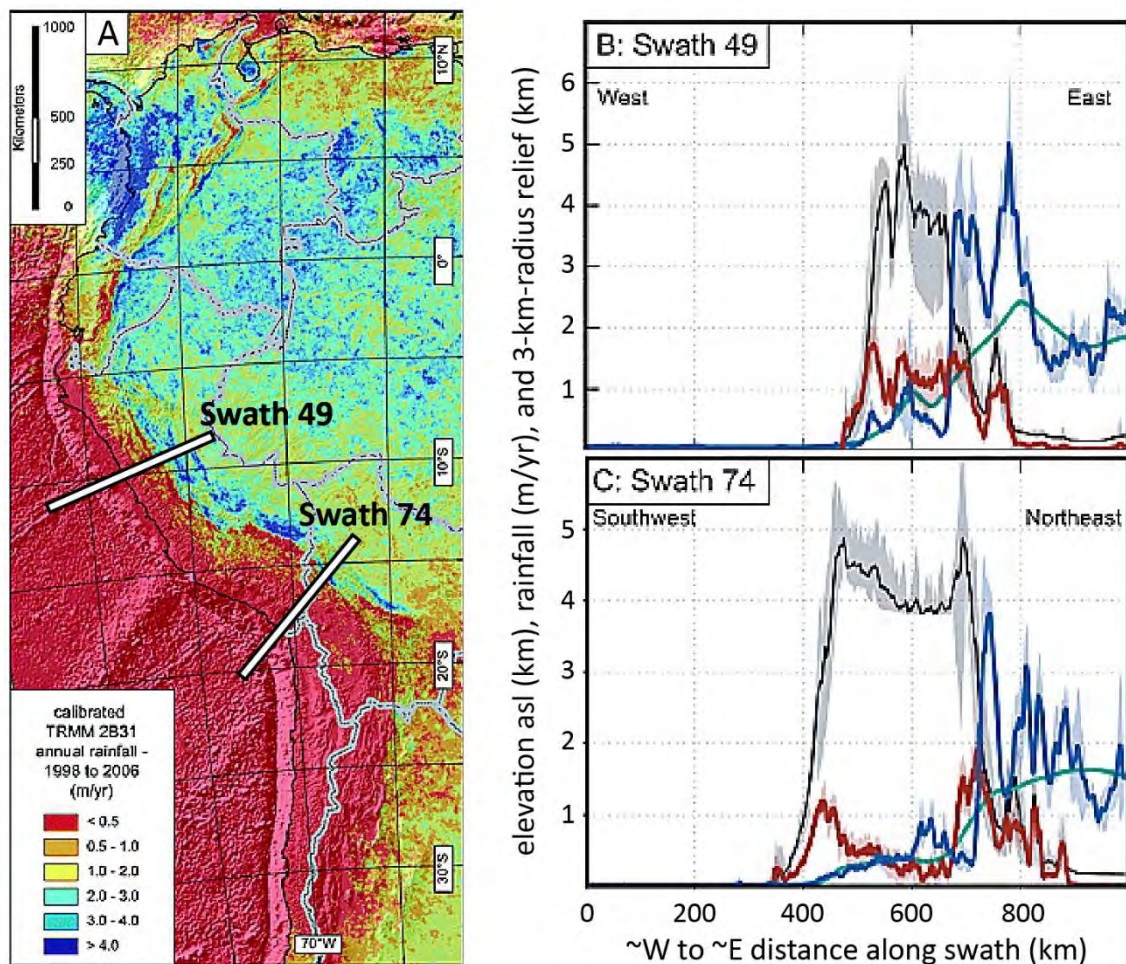


Figure 17. Global precipitation conditions along the Pacific side of the Central Andes. (a) Tropical Rainfall Measuring Mission (TRMM 2B31). The international borders are in grey. The Annual rainfall of the Andes is averaged for the period of 1998 to 2006 (9 years) with a spatial resolution of $\sim 5 \times 5 \text{ km}^2$. We note that the eastern flanks of the Andes represent an important orographic barrier which prevents the overflow of rainfall from the Amazon basin to the west. International borders in gray. (b) and (c) Swath profiles of the Andes, precipitation is in blue (TRMM 2B31) and green (TRMM 3B42); SRTM topography is in black and gray; and 3 km radius relief is in red. (Bookhagen and Strecker, 2008).

The hyperaridity of this site has prevailed for millions of years (Dunai et al., 2005), is responsible for very low denudation rates ($<0.5 \text{ m/Ma}$; e.g. Hall et al., 2008) that allow the preservation of the landscape. Despite aridity, there are studies reporting sparse paleoclimatic records (Bartz et al., 2020) with the presence of paleolakes (Ritter et al., 2017). El Niño phenomenon brings large storms and high amounts of precipitation to the Peruvian coast (Mettier et al., 2009); on the Peruvian coast there is evidence of paleo-floods linked to this phenomenon during the Holocene (Keefer et al., 2003; Lagos et al., 2008; Steffen et al., 2009, 2010), currently these events occur every 2 to 7 years. Paleoclimatic proxies towards the Altiplano are evidenced as periods of higher precipitation recorded in the terraces of the Altiplano paleolake. They show important wet phases between 25 to 11 ka, which is the Tauca Lake period (Baker et al., 2001b; Placzek et al., 2006), as well as this event, there are older events such

as the Ouki cycle (100-120 ka, Placzek et al., 2013) that could also be related to the formation of large landslides (Chuquibamba landslide, Margirier et al., 2015).

3.4 Western Andean large landslides

The WFCA shows the presence of large landslides that imply the gravitational destabilization of large areas greater than 0.1 km². The geomorphological surface of these landslides is well preserved in this part of the Andes due to weak erosion processes controlled by arid climatic conditions over a long period of time (Dunai et al., 2005). Among them the Caquilluco landslide (Figure 18) is a good example. Indeed its main surface is well preserved showing a succession of rock avalanche events with a maximum run out of ~40 km. The main scarp is located at more than 3800 m asl. These types of landslides, due to their large dimensions, disturb the topography, for example the LLuta landslide (Figure 19; Strasser and Schlunegger, 2005), which has a length of ~37 km and it is estimated that the initial collapse mobilized ~26 km³ which modified the topography, filled valleys and changed the course of rivers. This is also observed in the Miñimiñi and Latagualla landslides (Pinto et al., 2008). As well as this landslide there are other landslides where cosmogenic nuclide dating was used to determine the age of exposure (Figure 20); among them the Chuquibamba landslide (100 ka; Margirier et al., 2015; Thouret et al., 2017), Caquilluco landslide (120 - 600 ka; Zerathe et al., 2017; Zerathe et al., 2018), Lluta Landslide (5 - 10 Ma; Wörner et al., 2002; Strasser and Schlunegger, 2005), the Miñimiñi and Latagualla Landslides (8-9 Ma; Pinto et al., 2008). A cluster of avalanches from the El Magnifico landslide was also dated, the avalanches are between 4 - 60 Ka (Mather et al., 2014; Crosta et al., 2017).



Figure 18. Caquilluco landslide (Rock avalanche). It has a drop between the headscarp and the foot of the landslide of ~3250 m and a strike length of ~41 km. Note that the landslide mass is preserved.



Figure 19. 3D view of the Lluta landslide, the 37 km long landslide mass disturbed the topography which was probably like the relief of the right flank of the Lluta valley.

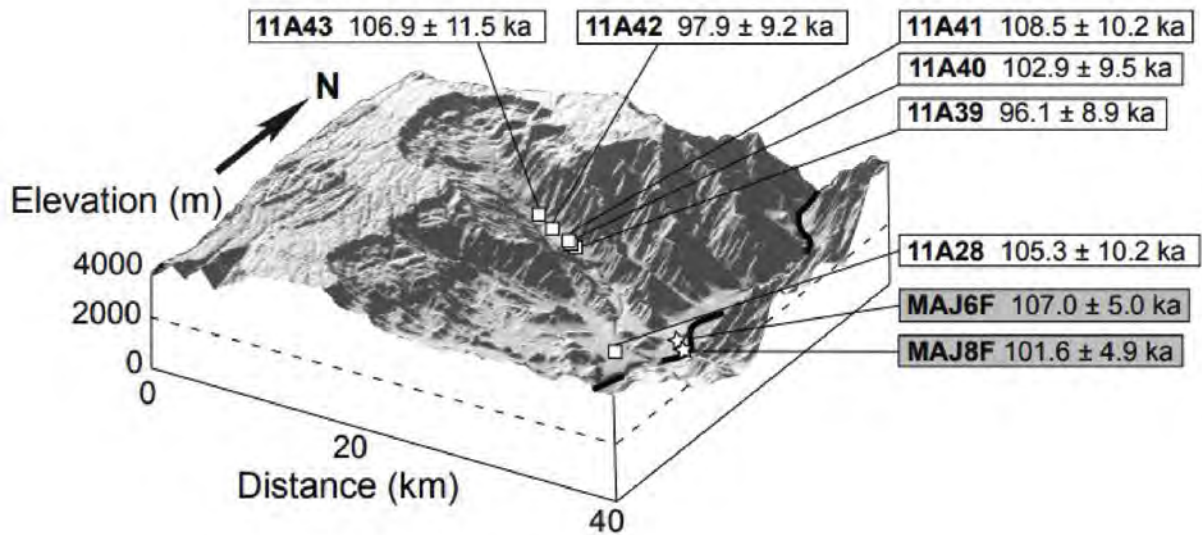


Figure 20. Chuquibamba landslide block diagram (modified Margirier et al., 2015) with digital elevation model (GeoMapApp, SRTM data, 90 m resolution) and the ages obtained by cosmogenic nuclide dating method.

The question of the triggering of these large surface processes is widely debated at present day. McPhillips et al. (2014) suggest that, for this part of the Andes, the seismic activity plays a predominant role in the triggering of landslides, while climatic conditions have a negligible influence. These

conclusions may be valid for landslides of small volume ($<10^4 \text{ m}^3$) and this is reflected in subduction earthquakes, Lacroix et al. (2013) indicate that the last major earthquake in the Pisco area in 2007 (8 Mw) triggered more than 800 landslides, but all were considered small to moderate ($\sim 10^3 \text{ m}^3$).

In contrast, Margirier et al. (2015) propose that the trigger for the Chuquibamba landslide correlates with a $\sim 100 \text{ ka}$ wet climatic pulse (Ouki episode, Placzek et al., 2013). Similarly, results obtained from the Caquilluco mega-slide (Zerathe et al., 2017) suggest a recurrence of triggers higher than the recurrence times of mega-earthquakes. The last Caquilluco landslide episode (100-120 ka) is synchronized with the "Ouki" climatic event marked by heavy precipitation at the altiplano scale (Placzek et al., 2013).

In this part of the Andes there are numerous large avalanches, in some sectors of the WFCA these events were recognized and mapped (Audin and Bechir, 2006; Crosta et al., 2014, 2015) but are not dated, leaving a gap that the use of cosmogenic nuclide dating, applied to escarpments and blocks, could give a better understanding of the formation and triggers of these large events.

4 Main problematics of the PhD and strategy

4.1 Scientific questions

This thesis project focuses on gravity-driven processes, to characterize them by typology, understand their mechanisms and triggers. The Western Flank of the Central Andes provides an opportunity to study these processes and to broaden the knowledge of the conditions and dynamics of these mass movements. It has a high relief with very deep valleys and erosion is very low in this place for millions of years ($<05 \text{ mm/year}$), this allows the landscape to be preserved, but there are also records of extreme climatic events and seismicity in this part of the Andes is recurrent. The main problematic of my PhD work related to the landslide activity in the WFCA rests on the following main questions:

- How to establish an inventory of large landslides at the regional scale?
- How many other landslides exist in the WFCA?
- Does it exist a specific spatial distribution of landslides in this part of the Andes?
- What is the timing of the landslide activity?
- What can be interpreted for the triggering factors?

In order to respond to these main scientific questions, a working strategy has been deployed using satellite image analysis techniques coupled with cosmogenic nuclide dating.

4.2 Strategy methods and data

In order to respond to the main questions, my PhD manuscript is organized around three main parts which are the following chapters:

- ***Inventory of large landslides along the Central Western Andes (ca. 15°–20°S): Landslide distribution patterns and insights on controlling factors (CHAPTER 2)***

This first part will consist of a large-scale survey of the western flank of the central Andes between latitudes 15 and 20° S, identifying and mapping large landslides including previous work, with the objective of providing a complete and updated database of this part of the Andes. The data to be provided will be about the type of landslide, its size and to verify if there is a spatial distribution. A statistical approach will be used in order to identify the conditioning factors associated with the

landslides activity in this part of the Andes. For the development of this first part we will use images from Google Earth, DEM (TanDEM-X (12m), SRTM (30m)) and GIS support (ArcGIS, QGIS).

- ***Giant landslide triggerings and paleoprecipitations in the Central Western Andes: The aricota rockslide dam (South Peru) (CHAPTER 3)***

This second stage will focus on the study of a specific landslide called the Aricota landslide, the mass of which formed a large dam and gave rise to the Aricota lake. The objective for this part is to determine the age of exposure of the landslide and to investigate the triggering factor. For this part, a detailed mapping of the landslide was made and 17 samples were collected in the field from the main escarpment and the landslide mass. The samples were processed following the cosmogenic nuclide methodology (^{10}Be) in quartz mineral. Exposure ages of the samples were obtained using an online calculator (CREEP program, Martin et al., 2017). The obtained results were compared with paleoclimatic and earthquake proxies close to the study area.

- ***Pleistocene chronicles of large landslides triggering on the western flank of the Central Andes revealed by cosmogenic nuclide dating (CHAPTER 4)***

This third stage will focus on a specific place in the western flank of the central Andes with a high concentration of landslides, by carrying out a geochronological study, in order to bring chronological constraints on the landslides activity. The goal is to characterize the patterns of occurrence and/or periodicity of landslide and ultimately to provide new data to investigate their triggering factors (earthquakes or extreme climatic events). For the development of this third part, 8 landslides were chosen, each one was mapped in detail using Pleiades images (2 m resolution), then a sampling strategy was carried out where 52 boulder samples were collected. The samples were processed following the cosmogenic nuclide methodology (^{10}Be) applied on quartz and feldspar minerals. After obtaining the concentrations, using an online calculator (CREP program, Martin et al., 2017) it was possible to obtain the exposure ages, to then compare if there are periodicity patterns and their possible triggers.

References

- Agliardi, F., Crosta, G. B., & Frattini, P. (2012). 18 Slow rock-slope deformation. *Landslides: Types, mechanisms and modeling*, 207.
- Agliardi, F., Crosta, G. B., Frattini, P., & Malusà, M. G. (2013). Giant non-catastrophic landslides and the long-term exhumation of the European Alps. *Earth and Planetary Science Letters*, 365, 263-274.
- Agliardi, F., Crosta, G. B., Zanchi, A. and Ravazzi, C. (2009 b). Onset and timing of deep-seated gravitational slope deformations in the eastern Alps, Italy. *Geomorphology*, 103, 113 –129.
- Agliardi, F., Crosta, G., & Frattini, P. (2012). Slow rock-slope deformation. In J. Clague & D. Stead (Eds.), *Landslides: Types, Mechanisms and Modeling* (pp. 207-221). Cambridge: Cambridge University Press. doi:10.1017/CBO9780511740367.019
- Agliardi, F., Crosta, G., & Zanchi, A. (2001). Structural constraints on deep-seated slope deformation kinematics. *Engineering Geology*, 59(1-2), 83-102.

- Agliardi, F., Zanchi, A. and Crosta, G. B. (2009a). Tectonic vs. gravitational morphostructures in the central Eastern Alps (Italy): Constraints on the recent evolution of the mountain range. *Tectonophysics*, 474, 250–270.
- Aguirre, E., Benavente, C., Audin, L., Wimpenny, S., Baize, S., Rosell, L., Delgado, F., García, B. & Palomino, A. (2021). Earthquake surface ruptures on the altiplano and geomorphological evidence of normal faulting in the December 2016 (Mw 6.1) Parina earthquake, Peru. *Journal of South American Earth Sciences*, 106, 103098.
- Allmendinger, R.W., Jordan, T.E., Kay, S.M. and Isacks, B.L., 1997. The evolution of the Altiplano Puna of the Central Andes. *Annual Reviews Earth Planet. Sci.* 25: 139-174.
- Ambrosi, C. and Crosta, G. B. (2006). Large sackung along major tectonic features in the central Italian Alps. *Engineering Geology*, 83, 183–200.
- Ambrosi, C., & Crosta, G. B. (2011). Valley shape influence on deformation mechanisms of rock slopes. *Geological Society, London, Special Publications*, 351(1), 215-233.
- Antinao, J. L., & Gosse, J. (2009). Large rockslides in the Southern Central Andes of Chile (32–34.5 S): Tectonic control and significance for Quaternary landscape evolution. *Geomorphology*, 104(3-4), 117-133.
- Armijo, R., Lacassin, R., Coudurier-Curveur, A., & Carrizo, D., 2015. Coupled tectonic evolution of Andean orogeny and global climate. *Earth-Science Reviews*, 143, 1-35.
- Aslan, G., De Michele, M., Raucoules, D., Bernardie, S., & Cakir, Z. (2021). Transient motion of the largest landslide on earth, modulated by hydrological forces. *Scientific Reports*, 11(1), 1-12.
- Audin, L., & Bechir, A., 2006. Active tectonics as determinant factor in landslides along the Western Cordillera? Presented at the Congreso Peruano de Geología, 13, Lima, Resúmenes extendidos, Sociedad Geológica del Perú, vol.xxii. October 17–20, 237–239.
- Augustinus, P.C. 1995: Glacial valley cross-profile development: the influence of in situ rock stress and rock mass strength, with examples from the Southern Alps, New Zealand. *Geomorphology* 14, 87–97.
- Aylsworth JM, Lawrence DE, Guertin J (2000) Did two massive earthquakes in the Holocene induce widespread landsliding and near-surface deformation in part of the Ottawa Valley, Canada? *Geology* 28:903–906
- Baker, P. A., G. O. Seltzer, S. C. Fritz, R. B. Dunbar, M. J. Grove, P. M. Tapia, S. L. Cross, H. D. Rowe, and J. P. Broda (2001b), The history of South American tropical precipitation for the past 25,000 years, *Science*, 291(5504), 640–643.
- Ballantyne CK. 2002. Paraglacial geomorphology. *Quaternary Science Reviews* 21: 1935–2017.
- Bartz, M., Duval, M., Brill, D., Zander, A., King, G. E., Rhein, A., ... & Brückner, H. (2020). Testing the potential of K-feldspar pIR-IRSL and quartz ESR for dating coastal alluvial fan complexes in arid environments. *Quaternary International*, 556, 124-143.
- Benavente, C., Wimpenny, S., Rosell, L., Robert, X., Palomino, A., Audin, L., Aguirre, E. & García, B. (2021). Paleoseismic evidence of an Mw 7 pre-hispanic earthquake in the Peruvian forearc. *Tectonics*, 40(6), e2020TC006479.

- Benavente, C., Zerathe, S., Audin, L., Hall, S., Robert, X., Delgado, F., Farber, D.L., ASTER Team., 2017. Active compressional tectonics in the Andean forearc of southern Peru evidenced by direct ¹⁰Be surface exposure dating of an active fault scarp. *Tectonics* 36(9), 1662-1678.
- Bois, S., Bouissou, S. and Guglielmi, Y. (2008). Influence of major inherited faults zones on gravitational slope deformation: A two-dimensional physical modelling of the La Clapière area (southern French Alps). *Earth and Planetary Science Letters*, 272, 709–719.
- Bookhagen, B., & Strecker, M. R. (2008). Orographic barriers, high-resolution TRMM rainfall, and relief variations along the eastern Andes. *Geophysical Research Letters*, 35(6).
- Borgatti L and Soldati M (2010) Landslides as a geomorphological proxy for climate change: A record from the Dolomites (northern Italy). *Geomorphology* 120: 56–64.
- Břežný, M., & Pánek, T. (2017). Deep-seated landslides affecting monoclinical flysch morphostructure: Evaluation of LiDAR-derived topography of the highest range of the Czech Carpathians. *Geomorphology*, 285, 44-57.
- Broggi, J. A. (1943). La desglaciación actual de los Andes del Perú. *Bol. Soc. Geol. Perú*, 14–15, 59–90.
- Bull WB (2003) Lichenometry dating of coseismic changes to a New Zealand landslide complex. *Annals of Geophysics* 46: 1155–1167.
- Cancelli, A. and Casagli, N. (1995). Classificazione e modellazione di fenomeni di instabilità in ammassi rocciosi sovrapposti ad argilliti o argille sovraconsolidate. *Memorie della Società Geologica Italiana*, 50, 83–100.
- Candia, G., Ledezma, C., Montalva, G., & Rollins, K. (2017). Geotechnical observations from the 2014 Iquique earthquake. 16th World Conference on Earthquake, 16WCEE 2017. Paper N° 2163
- Carbonel D, Gutiérrez F, Linares R, et al. (2013) Differentiating between gravitational and tectonic faults by means of geomorphological mapping, trenching and geophysical surveys. The case of the Zenzano Fault (Iberian Chain, N Spain). *Geomorphology* 189: 93–108.
- Carlini, M., Chelli, A., Vescovi, P., Artoni, A., Clemenzi, L., Tellini, C., & Torelli, L. (2016). Tectonic control on the development and distribution of large landslides in the Northern Apennines (Italy). *Geomorphology*, 253, 425-437.
- Carracedo, J. C. (2015). Peligros asociados a megadeslizamientos y lahares. *Enseñanza de las Ciencias de la Tierra*, 23(1), 66-66.
- Chang, L., & Alva, J. (1988) Mapa de distribución de deslizamientos y aluviones en el Perú, en memorias, 7° Congreso Nacional de Ingeniería Civil, Huaraz, Ancash. 51 p.
- Chigira, M. (1992). Long-term gravitational deformation of rock by mass rock creep. *Engineering Geology*, 32, 157–184.
- Colesanti, C., & Wasowski, J. (2006). Investigating landslides with space-borne Synthetic Aperture Radar (SAR) interferometry. *Engineering geology*, 88(3-4), 173-199.
- Collins BD, Jibson RW (2015) Assessment of existing and potential landslide hazards resulting from the April 25, 2015 Gorkha, Nepal earthquake sequence (No. 2015–1142). US Geological Survey
- Corominas, J., & Moya, J. (2008). A review of assessing landslide frequency for hazard zoning purposes. *Engineering geology*, 102(3-4), 193-213.

- Cossart, É, Braucher, R, & Fort, M. (2008) Slope instability in relation to glacial debuttressing in alpine areas (Upper Durance catchment, southeastern France): Evidence from field data and ^{10}Be cosmic ray exposure ages. *Geomorphology* 95: 3–26.
- Crosta, G. (1996). Landslide, spreading, deep-seated gravitational deformation: Analysis, examples, problems and proposals. *Geografia Fisica e Dinamica Quaternaria*, 19, 297 –313.
- Crosta, G. B., Frattini, P., & Agliardi, F. (2013). Deep seated gravitational slope deformations in the European Alps. *Tectonophysics*, 605, 13-33.
- Crosta, G. B., Hermanns, R. L., Dehls, J., Lari, S., & Sepulveda, S., 2017. Rock avalanches clusters along the northern Chile coastal scarp. *Geomorphology*, 289, 27-43.
- Crosta, G., & Zanchi, A. (2000). Deep seated slope deformations: huge, extraordinary, enigmatic phenomena. In *Landslides in Research, Theory and Practice: Proceedings of the 8th International Symposium on Landslides held in Cardiff on 26–30 June 2000* (pp. 1-351). Thomas Telford publishing.
- Crosta, G.B., Utili, S., De Blasio, F.V., & Castellanza, R. (2014). Reassessing rock mass properties and slope instability triggering conditions in Valles Marineris, Mars. *Earth Planetary Science Letters*, 338, 329-343.
- Cruden, D. M. and Hu, X. Q. (1994). Topples on underdip slopes in the Highwood Pass, Alberta, Canada. *Quarterly Journal of Engineering Geology*, 27, 57 –68.
- Cruden, D. M., & Varnes, D. J. (1996). Landslides: investigation and mitigation. Chapter 3-Landslide types and processes. *Transportation research board special report*, (247).
- Dikau, R., Cavallin, A., & Jäger, S. (1996). Databases and GIS for landslide research in Europe. *Geomorphology*, 15(3-4), 227-239.
- Dortch, J., Owen, L.A., Haneberg, W.C., Caffee, M.W., Dietsch, C. & Kamp, D.U. 2009. Nature and timing of large landslides in the Himalaya and Transhimalaya of northern India. *Quaternary Science Reviews*, 28, 1037 –1054.
- Dramis, F., & Sorriso-Valvo, M. (1994). Deep-seated gravitational slope deformations, related landslides and tectonics. *Engineering Geology*, 38(3-4), 231-243.
- Dunai, T.J., Lopez, G.A.G., and Juez-Larre, J., 2005, Oligocene-Miocene age of aridity in the Atacama Desert revealed by exposure dating of erosion-sensitive landforms: *Geology*, v. 33, p. 321–324, doi: 10.1130/G21184.1.
- Eberhardt, E., Stead, D. & Coggan, J.S. 2004. Numerical analysis of initiation and progressive failure in natural rock slopes – the 1991 Randa rockslide. *Int. J. Rock Mech. Min. Sci.* 41(1): 69-87
- El Bedoui, S., Guglielmi, Y., Lebourg, T., & Pérez, J. L. (2009). Deep-seated failure propagation in a fractured rock slope over 10,000 years: the La Clapière slope, the south-eastern French Alps. *Geomorphology*, 105(3-4), 232-238.
- Ermini, L., & Casagli, N. (2003). Prediction of the behaviour of landslide dams using a geomorphological dimensionless index. *Earth Surface Processes and Landforms: The Journal of the British Geomorphological Research Group*, 28(1), 31-47.
- Evans S.G. and Clague J.J. 1994. Recent climate change and catastrophic geomorphic processes in mountain environments. *Geomorphology* 10: 107–128.

- Evans, S. G., Mugnozsa, G. S., Strom, A. L., Hermanns, R. L., Ischuk, A., & Vinnichenko, S. (2006). Landslides from massive rock slope failure and associated phenomena. In *Landslides from massive rock slope failure* (pp. 03-52). Springer, Dordrecht.
- Evenstar, L. A., Mather, A. E., Hartley, A. J., Stuart, F. M., Sparks, R. S. J., & Cooper, F. J., 2017. Geomorphology on geologic timescales: Evolution of the late Cenozoic Pacific paleosurface in Northern Chile and Southern Peru. *Earth-Science Reviews*, 171, 1-27.
- Fan, X., Scaringi, G., Xu, Q., Zhan, W., Dai, L., Li, Y., Pei, X., Yang, Q. & Huang, R. (2018). Coseismic landslides triggered by the 8th August 2017 Ms 7.0 Jiuzhaigou earthquake (Sichuan, China): factors controlling their spatial distribution and implications for the seismogenic blind fault identification. *Landslides*, 15(5), 967-983.
- Fan, X., van Westen, C. J., Xu, Q., Gorum, T., & Dai, F. (2012). Analysis of landslide dams induced by the 2008 Wenchuan earthquake. *Journal of Asian Earth Sciences*, 57, 25-37.
- Fontugne, M., Usselmann, P., Lavallée, D., Julien, M. and Hatté, C. 1999: El Niño variability in the coastal desert of southern Peru during the mid-Holocene. *Quaternary Research* 52, 171-179.
- Froude, M. J., & Petley, D. N. (2018). Global fatal landslide occurrence from 2004 to 2016. *Natural Hazards and Earth System Sciences*, 18(8), 2161-2181.
- Galdos, J., (1973) Estudio geodinámico del área de Mayunmarca, provincia de Acobamba, departamento de Huancavelica, informe técnico. Lima: INGEMMET, 33 p.
- Galdos, J., (1975), Estudio geodinámico del deslizamiento de Mayunmarca (Provincia de Acobamba, departamento de Huancavelica), informe técnico. INGEMMET: Lima, 20 p.
- Gariano, S. L., & Guzzetti, F. (2016). Landslides in a changing climate. *Earth-Science Reviews*, 162, 227-252.
- González de Vallejo, Mercedes Ferrer, Luis Ortuño, Carlos Oteo (2002) INGENIERÍA GEOLÓGICA. PEARSON EDUCACIÓN, Madrid, 2002. BBN: 84-205-3104-9. Materia; Geología, 55. Formato 215 x 270 Páginas: 744
- Gori, S., Falcucci, E., Dramis, F., Galadini, F., Galli, P., Giaccio, B., Pizzi, A., Sposato, A. & Cosentino, D. (2014). Deep-seated gravitational slope deformation, large-scale rock failure, and active normal faulting along Mt. Morrone (Sulmona basin, Central Italy): Geomorphological and paleoseismological analyses. *Geomorphology*, 208, 88-101.
- Görm, T., 2019. Tectonic, topographic and rock-type influences on large landslides at the northern margin of the Anatolian Plateau. *Landslides* 16, 333–346.
- Graber, A., Santi, P., & Meza Arestegui, P. (2021). Constraining the critical groundwater conditions for initiation of large, irrigation-induced landslides, Sigüas River Valley, Peru. *Landslides*, 18(12), 3753-3767.
- Gutiérrez, F., Carbonel, D., Guerrero, J., McCalpin, J. P., Linares, R., Roque, C., & Zarroca, M. (2012). Late Holocene episodic displacement on fault scarps related to interstratal dissolution of evaporites (Teruel Neogene Graben, NE Spain). *Journal of Structural Geology*, 34, 2-19.
- Gutiérrez, F., Linares, R., Roqué, C., Zarroca, M., Rosell, J., Galve, J. P., & Carbonel, D. (2012b). Investigating gravitational grabens related to lateral spreading and evaporite dissolution

- subsidence by means of detailed mapping, trenching, and electrical resistivity tomography (Spanish Pyrenees). *Lithosphere*, 4(4), 331-353.
- Gutiérrez, F., Ortuño, M., Lucha, P., Guerrero, J., Acosta, E., Coratza, P., ... & Soldati, M. (2008). Late Quaternary episodic displacement on a sackung scarp in the central Spanish Pyrenees. Secondary paleoseismic evidence?. *Geodinamica Acta*, 21(4), 187-202.
- Hall, S. R., D. L. Farber, L. Audin, R. C. Finkel, and A. S. Mériaux, 2008. Geochronology of pediment surfaces in southern Peru: Implications for Quaternary deformation of the Andean forearc, *Tectonophysics*, 459(1), 186– 205, doi:10.1016/j.tecto.2007.11.073
- Haschke, M., Günther, A., Melnick, D., Echtler, H., Reutter, K. J., Scheuber, E., & Oncken, O., 2006. Central and southern Andean tectonic evolution inferred from arc magmatism. In *The Andes* (pp. 337-353). Springer, Berlin, Heidelberg.
- Havenith HB, Torgoev I, Meleshko A, Alioshin Y, Torgoev A, Danneels G. 2006. Landslides in the Mailuu-Suu Valley, Kyrgyzstan – hazards and impacts. *Landslides* 3(2): 137–147. <https://doi-org.sid2nomade-2.grenet.fr/10.1007/s10346-006-0035-2>.
- Heim, A. (1932). *Bergsturz und menschenleben* (No. 20). Fretz und Wasmuth, Zurich, p. 218
- Hermanns RL and Schellenberger A (2008) Quaternary tephrochronology helps define conditioning and triggering mechanisms of rock avalanches in Argentina. *Quaternary International* 178: 261–275.
- Hermanns, R. L., Hewitt, K., Strom, A., Evans, S. G., Dunning, S. A., & Scarascia-Mugnozza, G. (2011). The classification of rockslide dams. In *Natural and artificial rockslide dams* (pp. 581-593). Springer, Berlin, Heidelberg.
- Hermanns, R. L., Valderrama Murillo, P. A., Fauqué, L. E., Penna, I. M., Sepúlveda Valenzuela, S. A., Moreiras, S. M., & Zavala Carrión, B. L. (2012). Landslides in the Andes and the need to communicate on an interandean level on landslide mapping and research. 0004-4822.
- Hermanns, R., Oppikofer, T., Dahle, H., Eiken, T., Ivy-Ochs, S., Blikra, L., 2013. Understanding long-term slope deformation for stability assessment of rock slopes: the case of the Oppstadhornet rockslide, Norway. *Ital. J. Eng. Geol. Environ. Book Ser. 6*, 255–264
- Hewitt, K., Clague, J. J., & Orwin, J. F. (2008). Legacies of catastrophic rock slope failures in mountain landscapes. *Earth-Science Reviews*, 87(1-2), 1-38.
- Hewitt, K., Gosse, J., & Clague, J. J. (2011). Rock avalanches and the pace of late Quaternary development of river valleys in the Karakoram Himalaya. *Bulletin*, 123(9-10), 1836-1850.
- Highland LM, & Bobrowsky P (2008) *The landslide handbook: a guide to understanding landslides*. US Geol Survey Circular 1325:129.
- Hippolyte JC, Bourlès D, Braucher R, Carcaillet J, Léanni L, Arnold M, Aumaitre G. 2009. Cosmogenic ¹⁰Be dating of a sackung and its faulted rock glaciers, in the Alps of Savoy (France). *Geomorphology* 108: 312– 320.
- Hippolyte J-C, Bourlès D, Léanni L, Braucher R, Chauvet F, Lebatard AE (2012) ¹⁰Be ages reveal > 12ka of gravitational movement in a major sackung of the Western Alps (France). *Geomorphology* 171:139–153

- Horton, B. K., Hampton, B. A., & Waanders, G. L. (2001). Paleogene synorogenic sedimentation in the Altiplano plateau and implications for initial mountain building in the central Andes. *Geological Society of America Bulletin*, 113, 1387–1400
- Houston, J., & Hartley, A. J. (2003). The central Andean west-slope rainshadow and its potential contribution to the origin of hyper-aridity in the Atacama Desert. *International Journal of Climatology: A Journal of the Royal Meteorological Society*, 23(12), 1453-1464.
- Hughes, P. D., Gibbard, P. L., & Ehlers, J. (2013). Timing of glaciation during the last glacial cycle: evaluating the concept of a global 'Last Glacial Maximum'(LGM). *Earth-Science Reviews*, 125, 171-198.
- Hungr O, Evans SG, Bovis MJ, Hutchinson JN (2001) A review of the classification of landslides of the flow type. *Environ Eng Geosci* 7:221–238
- Hutchinson, J. N. (1988). Morphological and geotechnical parameters of landslides in relation to geology and hydrogeology. In *Proceedings of the 5th International Symposium on Landslides*, Lausanne. Rotterdam: A. A. Balkema, pp. 3–35
- Isacks, B.L., 1988. Uplift of the central Andean plateau and bending of the Bolivian orocline. *Journal of Geophysical Research* 93, 3211–3231.
- Jaillard, E., & Soler, P. (1996). Cretaceous to early Paleogene tectonic evolution of the northern Central Andes (0–18 S) and its relations to geodynamics. *Tectonophysics*, 259(1-3), 41-53.
- James, D. E. & Sacks, I. S., 1999. Cenozoic formation of the Central Andes: A geophysical perspective. In *Geology and Ore Deposits of the Central Andes* (ed. Skinner, B. J.), Society of Economic Geologists, Special Publication 7: 1-25.
- Keefer, D. K. 1984. Landslides caused by earthquakes. *Geological Society of America Bulletin*, 95(4), 406-421.
- Keefer, D. K. 1994. The importance of earthquake-induced landslides to long-term slope erosion and slope-failure hazards in seismically active regions. In *Geomorphology and Natural Hazards* (pp. 265-284). Elsevier.
- Keefer, D. K., Moseley, M. E., & DeFrance, S. D., 2003. A 38 000-year record of floods and debris flows in the Ilo region of southern Peru and its relation to El Niño events and great earthquakes. *Palaeogeography, Palaeoclimatology, Palaeoecology*, 194(1-3), 41-77.
- Kellogg, K. S. (2001). Tectonic controls on a large landslide complex: Williams Fork Mountains near Dillon, Colorado. *Geomorphology*, 41(4), 355-368.
- Kieffer, D. S. (1998). Rock slumping: A compound failure mode of jointed hard rock slopes. Ph.D. thesis, University of California, Berkeley, CA.
- Klimeš, J., Rowberry, M. D., Blahůt, J., Briestenský, M., Hartvich, F., Košťák, B., ... & Štěpančíková, P. (2012). The monitoring of slow-moving landslides and assessment of stabilisation measures using an optical–mechanical crack gauge. *Landslides*, 9(3), 407-415.
- Kober, F., Ivy-Ochs, S., Schlunegger, F., Baur, H., Kubik, P.W., and Wieler, R., 2007, Denudation rates and a topography-driven rainfall threshold in northern Chile: Multiple cosmogenic nuclide data and sediment yield budgets: *Geomorphology*, v. 83, p. 97–120, doi: 10.1016/j.geomorph.2006.06.029.

- Kojan, E., & Hutchinson, J. D. (1978). Mayunmarca rockslide and debris flow, Peru. In *Developments in Geotechnical Engineering* (Vol. 14, pp. 315-353). Elsevier.
- Korup, O. (2005). Geomorphic imprint of landslides on alpine river systems, southwest New Zealand. *Earth Surface Processes and Landforms*, 30(7), 783-800.
- Kos, A., Amann, F., Strozzi, T., Delaloye, R., von Ruetten, J., & Springman, S. (2016). Contemporary glacier retreat triggers a rapid landslide response, Great Aletsch Glacier, Switzerland. *Geophysical Research Letters*, 43(24), 12-466.
- Lacroix, P., Dehecq, A., & Taïpe, E. (2020). Irrigation-triggered landslides in a Peruvian desert caused by modern intensive farming. *Nature Geoscience*, 13(1), 56-60.
- Lacroix, P., Zavala, B., Berthier, E., & Audin, L. (2013). Supervised method of landslide inventory using panchromatic SPOT5 images and application to the earthquake-triggered landslides of Pisco (Peru, 2007, Mw8.0). *Remote Sensing*, 5(6), 2590-2616.
- Lagos, P., Y. Silva, E. Nickl, and K. Mosquera (2008), El Niño-related precipitation variability in Perú, *Adv. Geosci.*, 14, 231– 237.
- Lang, A., Moya, J., Corominas, J., Schrott, L., & Dikau, R. (1999). Classic and new dating methods for assessing the temporal occurrence of mass movements. *Geomorphology*, 30(1-2), 33-52.
- Larsen, I. J., & Montgomery, D. R. (2012). Landslide erosion coupled to tectonics and river incision. *Nature Geoscience*, 5(7), 468-473.
- Li X, Qiulin L, Wang S, et al. (2008) On evaluating the stability of the Baiyian ancient landslide in the Three Gorges Reservoir area, Yangtze River: A geological history analysis. *Environmental Geology* 55: 1699–1711.
- Li, G. K., & Moon, S., 2021. Topographic stress control on bedrock landslide size. *Nature Geoscience*, 14(5), 307-313.
- Li, L., Wang, Y., & Cao, Z. (2014). Probabilistic slope stability analysis by risk aggregation. *Engineering Geology*, 176, 57-65.
- Lopez Saez, J., Corona, C., Stoffel, M., Astrade, L., Berger, F., & Malet, J. P. (2012). Dendrogeomorphic reconstruction of past landslide reactivation with seasonal precision: the Bois Noir landslide, southeast French Alps. *Landslides*, 9(2), 189-203.
- MacFarlane, D. F. (2008). Observations and predictions of the behaviour of large, slow-moving landslides in schist, Clyde Dam reservoir, New Zealand. *Engineering Geology*, 109, 5 –15.
- Mahr, T. (1977). Deep-reaching gravitational deformations of high mountain slopes. *International Association of Engineering Geologists Bulletin*, 16, 121 –127.
- Mamani, M., Tassara, A., & Wörner, G., 2008. Composition and structural control of crustal domains in the central Andes. *Geochemistry, Geophysics, Geosystems*, 9(3).
- Mamani, M., Wörner, G., & Sempere, T., 2009. Geochemical variations in igneous rocks of the Central Andean Orocline (13° to 18°S): Tracing crustal thickening and magma generation through time and space. *Geol. Soc. Amer. Bull.*, 122, 162- 182. doi:10.1130/B26538.1.

- Margirier, A. Audin, L., Carcaillet, J., Schwartz, S., 2015. Tectonic and climatic controls on the Chuquibamba landslide (western Andes, southern Peru). *Earth Surf. Dynam. Discuss.* 2, 1129–1153.
- Martel SJ. 2006. Effect of topographic curvature on near-surface stresses and application to sheeting joints. *Geophysical Research Letters* 33: L01308. DOI: 10.1029/2005GL024710
- Martin, L. C., Blard, P. H., Lavé, J., Condom, T., Prémaillon, M., Jomelli, V., Tibari, B. & ASTER Team., 2018. Lake Tauca highstand (Heinrich Stadial 1a) driven by a southward shift of the Bolivian High. *Science advances*, 4(8), eaar2514.
- Mather, A. E., Hartley, A. J., & Griffiths, J. S., 2014. The giant coastal landslides of Northern Chile: Tectonic and climate interactions on a classic convergent plate margin. *Earth and Planetary Science Letters*, 388, 249-256.
- McCalpin JP, Bruhn RL, Pavlis TL, et al. (2011) Antislope scarps, gravitational spreading, and tectonic faulting in the western Yakutat microplate, south coastal Alaska. *Geosphere* 7: 1143–1158.
- McCalpin, J. P. (1999). Criteria for determining the seismic significance of sackungen and other scarp-like landforms in mountainous regions. *Techniques for Identifying Faults and Determining their Origins*. US Nuclear Regulatory Commission, Washington, 2-55.
- McCalpin, J. P. (2009). *Paleoseismology*. Academic Press.
- McCalpin, J. P. and Irvine, J. R. (1995). Sackungen at the Aspen Highlands ski area, Pitkin County, Colorado. *Environmental and Engineering Geoscience*, 1, 277 –290.
- McPhillips, D., Bierman, P. R., & Rood, D. H. (2014). Millennial-scale record of landslides in the Andes consistent with earthquake trigger. *Nature Geoscience*, 7(12), 925-930.
- Mercier, D., Cossart, E., Decaulne, A., Feuillet, T., Jónsson, H. P., & Sæmundsson, Þ. (2013). The Höfðahólar rock avalanche (sturzström): Chronological constraint of paraglacial landsliding on an Icelandic hillslope. *The Holocene*, 23(3), 432-446.
- Mettier, R., F. Schlunegger, H. Schneider, D. Rieke-Zapp, and M. Schwab (2009), Relationships between landscape morphology, climate and surface erosion in northern Peru at 5°S latitude, *Int. J. Earth Sci.*, 98(8), 2009– 2022.
- Miller D.J. and Dunne T. 1996. Topographic perturbations of regional stresses and consequent bedrock fracturing. *Journal of Geophysical Research* 101(B11): 25,523– 25,536.
- Mojica, J., Colmenares, F., Villarroel, C. Maciac. & Moreno, M. (1985): Características del Flujo de Lodo ocurrido el 13 de noviembre de 1985 en el Valle de Armero (Tolima-Colombia). *Historia y Comentarios de los flujos de 1595 y 1845*. *Geología Colombiana* 14, p.107-140. Bogota
- Molnar P. 2004. Interactions among topographically induced elastic stress, static fatigue, and alley incision. *Journal of Geophysical Research* 109: F02010. DOI: 10.1029/2003JF000097
- Montes, I., Schneider, W., Colas, F., Blanke, B., & Echevin, V. (2011). Subsurface connections in the eastern tropical Pacific during La Niña 1999–2001 and El Niño 2002–2003. *Journal of Geophysical Research: Oceans*, 116(C12).
- Montgomery, D. R., & Brandon, M. T. (2002). Topographic controls on erosion rates in tectonically active mountain ranges. *Earth and Planetary Science Letters*, 201(3-4), 481-489.

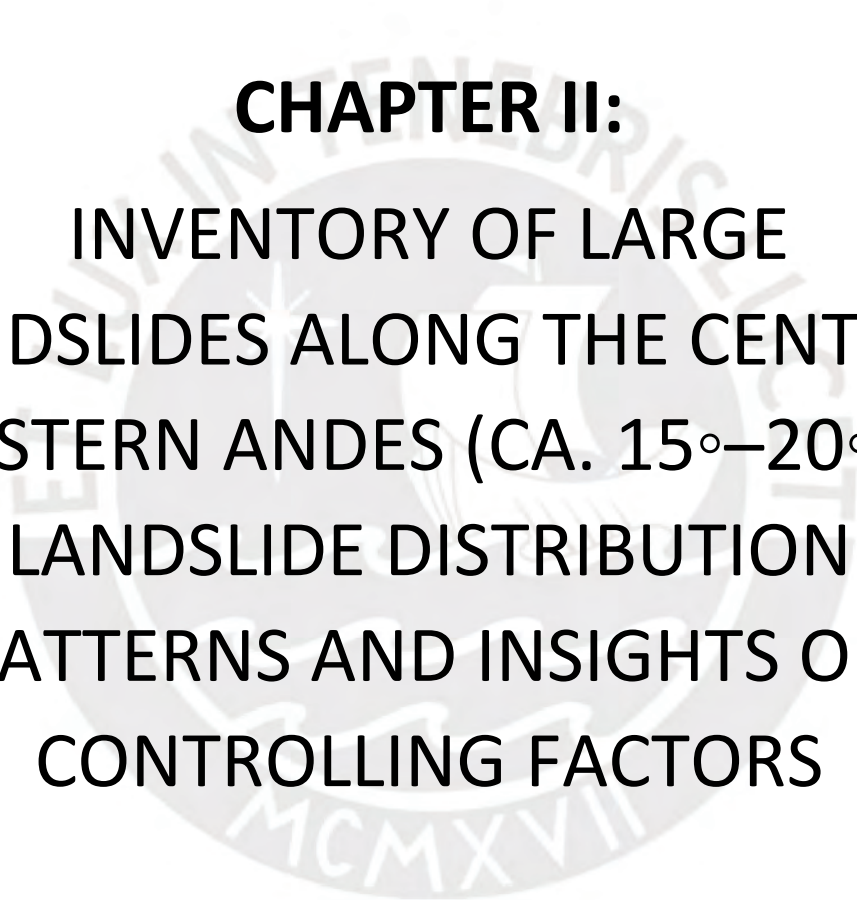
- Montgomery, D. R., 2001. Slope distributions, threshold hillslopes, and steady-state topography. *American Journal of science*, 301(4-5), 432-454.
- Moreiras SM (2006) Chronology of a probable neotectonics Pleistocene rock avalanche, Cordon del Plata (Central Andes), Mendoza, Argentina. *Quaternary International* 148: 138–148.
- Moro, M., Saroli, M., Salvi, S., Stramondo, S. and Doumaz, F. (2007). The relationship between seismic deformation and deep-seated gravitational movements during the 1997 Umbria-Marche (central Italy) earthquakes. *Geomorphology*, 89, 297–307.
- Nemcok, A. (1972). Gravitational slope deformation in high mountains. In *Proceedings of the 24th International Geological Congress, Montreal, PQ*, pp. 132–141.
- Nichol, S. L., Hungr, O. and Evans, S. G. (2002). Large-scale brittle and ductile toppling of rock slopes. *Canadian Geotechnical Journal*, 39, 773–788.
- Nishiizumi, K., Caffee, M.W., Finkel, R.C., Brimhall, G., and Mote, T., 2005, Remnants of a fossil alluvial fan landscape of Miocene age in the Atacama Desert of northern Chile using cosmogenic nuclide exposure age dating: *Earth and Planetary Science Letters*, v. 237, p. 499–507, doi: 10.1016/j.epsl.2005.05.032.
- Okumura, Y. M., & Deser, C. (2010). Asymmetry in the duration of El Niño and La Niña. *Journal of Climate*, 23(21), 5826-5843.
- Owen LA, Kamp U, Khattak G, Harp E, Keefer DK, Bauer M (2008) Landslides triggered by the October 8, 2005, Kashmir earthquake. *Geomorphology* 94:1–9
- Pánek, T. (2015). Recent progress in landslide dating: a global overview. *Progress in Physical Geography*, 39(2), 168-198.
- Pánek, T., & Klimeš, J. (2016). Temporal behavior of deep-seated gravitational slope deformations: A review. *Earth-Science Reviews*, 156, 14-38.
- Pánek, T., Břežný, M., Kapustová, V., Lenart, J., & Chalupa, V. (2019). Large landslides and deep-seated gravitational slope deformations in the Czech Flysch Carpathians: New LiDAR-based inventory. *Geomorphology*, 346, 106852.
- Pánek, T., Korup, O., Minár, J., & Hradecký, J. (2016). Giant landslides and highstands of the Caspian Sea. *Geology*, 44(11), 939-942.
- Pánek, T., Mentlík, P., Ditchburn, B., Zondervan, A., Norton, K., & Hradecký, J. (2015). Are sackungen diagnostic features of (de) glaciated mountains?. *Geomorphology*, 248, 396-410.
- Pánek, T., Tábořík, P., Klimeš, J., Komárková, V., Hradecký, J., & Šťastný, M. (2011). Deep-seated gravitational slope deformations in the highest parts of the Czech Flysch Carpathians: Evolutionary model based on kinematic analysis, electrical imaging and trenching. *Geomorphology*, 129(1-2), 92-112.
- Petley, D. (2012). Global patterns of loss of life from landslides. *Geology*, 40(10), 927-930.
- Pinto, L., Hérial, G., Sepúlveda, S. A., & Krop, P., 2008. A Neogene giant landslide in Tarapacá, northern Chile: A signal of instability of the westernmost Altiplano and palaeoseismicity effects. *Geomorphology*, 102(3-4), 532-541.

- Placzek, C., J. Quade, and P. J. Patchett (2006), Geochronology and stratigraphy of late Pleistocene lake cycles on the southern Bolivian Altiplano: implications for causes of tropical climate change, *Geol. Soc. Am. Bull.*, 118(5–6), 515–532.
- Placzek, C.J., Quade, J., Patchett, P.J., 2013. A 130 ka reconstruction of rainfall on the Bolivian Altiplano. *Earth and Planetary Science Letters*, 363, 97-108
- Plafker, G., & Ericksen, G. E. (1978). Nevados Huascaran avalanches, Peru. In *Developments in Geotechnical Engineering* (Vol. 14, pp. 277-314). Elsevier.
- Plafker, G., Ericksen, G. E., & Fernandez Concha, J. (1971). Geological aspects of the May 31, 1970, Peru earthquake. *Bulletin of the Seismological Society of America*, 61(3), 543-578.
- Plaza, G., Zevallos, O., & Cadier, É. (2011). La Josefina landslide dam and its catastrophic breaching in the Andean region of Ecuador. In *Natural and artificial rockslide dams* (pp. 389-406). Springer, Berlin, Heidelberg.
- Prager, C., Zangerl, C., Patzelt, G., & Brandner, R. (2008). Age distribution of fossil landslides in the Tyrol (Austria) and its surrounding areas. *Natural Hazards and Earth System Sciences*, 8(2), 377-407.
- Qiu H, Regmi AD, Cui P, Cao M, Lee J, Zhu X. 2016. Size distribution of loess slides in relation to local slope height within different slope morphologies. *Catena* 145: 155– 163. <https://doi-org.sid2nomade-2.grenet.fr/10.1016/j.catena.2016.06.005>
- Quang, C. X., Clark, A. H., W. Lee, J. K., & Hawkes, N., 2005. Response of supergene processes to episodic Cenozoic uplift, pediment erosion, and ignimbrite eruption in the porphyry copper province of southern Peru. *Economic Geology*, 100(1), 87-114.
- Radbruch-Hall, D. (1978). Gravitational creep of rock masses on slopes. In *Rockslides and Avalanches; Natural Phenomena*, ed. B. Voight. Amsterdam: Elsevier, pp. 607–657.
- Ritter, B., Binnie, S. A., Stuart, F. M., Wennrich, V., & Dunai, T. J., 2018. Evidence for multiple Plio-Pleistocene lake episodes in the hyperarid Atacama Desert. *Quaternary Geochronology*, 44, 1–12.
- Rodriguez, C. E., Bommer, J. J., & Chandler, R. J. (1999). Earthquake-induced landslides: 1980–1997. *Soil Dynamics and Earthquake Engineering*, 18(5), 325-346.
- Roering, J., 2012. Landslides limit mountain relief. *Nature Geoscience*, 5(7), 446-447.
- Rossel F. 1997. Influencia de El Niño sobre los regimenes hidro-pluviometricos del Ecuador, Tomos I–III. Serie INSEQ (Inundaciones y Sequias) N° 18. Cooperacion Franco-Ecuatoriana, ORSTOM y INAHMI: Quito, Ecuador; 203 pp.
- Rosser N, Kincey M, Oven K, Densmore A, Robinson T, Pujara DS, Dhital MR (2021) Changing significance of landslide Hazard and risk after the 2015 Mw 7.8 Gorkha, Nepal Earthquake. *Progress Disaster Sci* 10:100159
- Sanchez, G., Calienes, R., & Zuta, S. (2000). The 1997-98 El Niño and its effects on the coastal marine ecosystem off Peru. *Reports of California Cooperative Oceanic Fisheries Investigations*, 41(1), 62-86.
- Sanchez, G., Rolland, Y., Corsini, M., Braucher, R., Bourlès, D., Arnold, M., & Aumaître, G. (2010). Relationships between tectonics, slope instability and climate change: cosmic ray exposure dating of active faults, landslides and glacial surfaces in the SW Alps. *Geomorphology*, 117(1-2), 1-13.

- Savage, W. Z., & Swolfs, H. S. (1986). Tectonic and gravitational stress in long symmetric ridges and valleys. *Journal of Geophysical Research: Solid Earth*, 91(B3), 3677-3685.
- Schmidt, K. M., & Montgomery, D. R., 1995. Limits to relief. *Science*, 270(5236), 617-620.
- Schuster RL (1996) Socioeconomic significance of landslides. *Landslides: Investigation and Mitigation* Washington (DC): National Academy Press Transportation Research Board Special Report 247:12–35
- Schuster, R. L., Salcedo, D. A., & Valenzuela, L. (2002). Overview of catastrophic landslides of South America in the twentieth century. *Reviews in Engineering Geology*, 15, 1-34.
- Schwartz, S., Zerathe, S., Jongmans, D., Baillet, L., Carcaillet, J., Audin, L., ... & Lebrouc, V. (2017). Cosmic ray exposure dating on the large landslide of Séchilienne (Western Alps): A synthesis to constrain slope evolution. *Geomorphology*, 278, 329-344.
- Sepúlveda, S. A., & Petley, D. N. (2015). Regional trends and controlling factors of fatal landslides in Latin America and the Caribbean. *Natural Hazards and Earth System Sciences*, 15(8), 1821–1833. <https://doi.org/10.5194/nhess-15-1821-2015>
- Sjoberg, J. (1999). Analysis of large scale rock slopes. Ph.D. thesis, Luleå University of Technology, Luleå, Sweden.
- Sobolev, S. V., & Babeyko, A. Y., 2005. What drives orogeny in the Andes?. *Geology*, 33(8), 617-620.
- Soldati, M. (2013). Deep-seated gravitational slope deformation. In *Encyclopedia of Natural Hazards* (pp. 151-155). Springer Netherlands.
- Solonenko, V. P. (1977). Landslides and collapses in seismic zones and their prediction. *Bulletin of the International Association of Engineering Geology*, 15, 4 –8.
- Steffen, D., F. Schlunegger, and F. Preusser (2009), Drainage basin response to climate change in the Pisco valley, Peru, *Geology*, 37(6), 491– 494.
- Steffen, D., F. Schlunegger, and F. Preusser (2010), Late Pleistocene fans and terraces in the Majes valley, southern Peru, and their relation to climatic variations, *Int. J. Earth Sci.*, 99(8), 1975– 1989.
- Strasser, M., & Schlunegger, F., 2005. Erosional processes, topographic length-scales and geomorphic evolution in arid climatic environments: the ‘Lluta collapse’, northern Chile. *International Journal of Earth Sciences*, 94(3), 433-446.
- Strecker, M. R., Alonso, R. N., Bookhagen, B., Carrapa, B., Hilley, G. E., Sobel, E. R., & Trauth, M. H., 2007. Tectonics and climate of the southern central Andes. *Annu. Rev. Earth Planet. Sci.*, 35, 747-787.
- Strom A. 2013. Geological prerequisites for landslide dams’ disaster assessment and mitigation in Central Asia. In *Progress of Geo-Disaster Mitigation Technology in Asia*, F Wang, M Miyajima, T Li, W Shan, TF Fathani (eds). Springer: Berlin; 17– 53
- Sulca, J., Takahashi, K., Espinoza, J. C., Vuille, M., & Lavado-Casimiro, W. (2018). Impacts of different ENSO flavors and tropical Pacific convection variability (ITCZ, SPCZ) on austral summer rainfall in South America, with a focus on Peru. *International Journal of Climatology*, 38(1), 420-435.

- Thouret, J. C., Gunnell, Y., Jicha, B. R., Paquette, J. L., & Braucher, R., 2017. Canyon incision chronology based on ignimbrite stratigraphy and cut-and-fill sediment sequences in SW Peru documents intermittent uplift of the western Central Andes. *Geomorphology*, 298, 1-19.
- Thouret, J.C.; Wörner, G.; Gunnell, Y.; Singer, B.; Zhang, X.; Souriot, T., 2007. Geochronologic and stratigraphic constrains on canyon incision and Miocene uplift of the Central Andes in Perú. *Earth and Planetary Science Letters* 263: 151-166.
- Ustaszewski, K., Schmid, S. M., FÜGENSCHUH, B., Tischler, M., Kissling, E., & Spakman, W. (2008). A map-view restoration of the Alpine-Carpathian-Dinaridic system for the Early Miocene. *Swiss journal of Geosciences*, 101(1), 273-294.
- Valagussa, A., Frattini, P., Crosta, G., Spizzichino, D., Leoni, G., & Margottini, C. (2021). Multi-risk analysis on European cultural and natural UNESCO heritage sites. *Natural Hazards*, 105(3), 2659-2676.
- Valagussa, A., Frattini, P., Valbuzzi, E., & Crosta, G. B. (2021b). Role of landslides on the volume balance of the Nepal 2015 earthquake sequence. *Scientific reports*, 11(1), 1-12.
- Van der Geest, K. (2018) 'Landslide loss and damage in Sindhupalchok District, Nepal: comparing income groups with implications for compensation and relief'. *International Journal of Disaster Risk Science*. 9(2). pp. 157– 166.
- Varnes, D. J., Radbruch-Hall, D. and Savage, W. Z. (1989). *Topographic and Structural Conditions in Areas of Gravitational Spreading of Ridges in the Western United States*. US Geological Survey, Professional Paper 1496.
- Varnes, D.J., D.H. Radbruch-Hall, K.L. Varnes, W.K. Smith, and W.Z. Savage. 1990. *Measurements of Ridge-Spreading Movements (Sackungen) at Bald Eagle Mountain, Lake County, Colorado, 1975-1989*. U.S. Geological Survey Open File Report 90-543, 13 pp.
- Vílchez, M. (2013) - Redimensionamiento y evaluación del deslizamiento traslacional - flujo de detritos de Mayunmarca y alrededores (Andabamba, Huancavelica). En: *Foro Internacional Peligros Geológicos*, Arequipa, 14-16 octubre 2013, Libro de resúmenes. Arequipa: INGEMMET, pp. 172-176
- Villegas-Lanza, J. C., Chlieh, M., Cavalié, O., Tavera, H., Baby, P., Chire-Chira, J., & Nocquet, J. M., 2016. Active tectonics of Peru: Heterogeneous interseismic coupling along the Nazca megathrust, rigid motion of the Peruvian Sliver, and Subandean shortening accommodation. *Journal of Geophysical Research: Solid Earth*, 121(10), 7371-7394.
- Voight, B. (1990). The 1985 Nevado del Ruiz volcano catastrophe: anatomy and retrospection. *Journal of volcanology and geothermal research*, 42(1-2), 151-188.
- Walker M (2005) *Quaternary dating Methods*. John Willey & Sons Ltd, Chichester
- Wallemacq, P., & House, R., 2018. *Economic losses, poverty & disasters*. Centre for Research on the Epidemiology of Disasters and United Nations Office for Disaster Risk Reduction, Geneva, 1-30.
- Wang, C., Weisberg, R. H., & Virmani, J. I. (1999). Western Pacific interannual variability associated with the El Niño-Southern Oscillation. *Journal of Geophysical Research: Oceans*, 104(C3), 5131-5149.

- Wells, L.E. 1990: Holocene history of the El Niño phenomenon as recorded in flood sediments of northern coastal Peru. *Geology* 18, 1134-1137.
- Whipple, K. X., E. Kirby, and S. H. Brocklehurst (1999), Geomorphic limits to climate-induced increases in topographic relief, *Nature*, 401, 39– 43.
- Wieczorek, G. F. (1996). Landslides: investigation and mitigation. Chapter 4-Landslide triggering mechanisms. Transportation Research Board Special Report, (247).
- Wörner, G., Uhlig, D., Kohler, I., & Seyfried, H. (2002). Evolution of the West Andean Escarpment at 18 S (N. Chile) during the last 25 Ma: uplift, erosion and collapse through time. *Tectonophysics*, 345(1-4), 183-198.
- Wulf, H., Bookhagen, B., & Scherler, D. (2010). Seasonal precipitation gradients and their impact on fluvial sediment flux in the Northwest Himalaya. *Geomorphology*, 118(1-2), 13-21.
- Zangerl, C., Eberhardt, E. and Perzmaier, S. (2010). Kinematic behaviour and velocity characteristics of a complex deep-seated crystalline rockslide system in relation to its interaction with a dam reservoir. *Engineering Geology*, 112, 53 –67.
- Zerathe S., Blard P-H., Audin L., Braucher R., Bourles D., Carcaillet J., Benavente C., Delgado F., AsterTeam., 2017. Toward the feldspar alternative for cosmogenic ¹⁰Be exposure dating. *Quaternary Geochronology* 41, 83-96. <https://doi.org/10.1016/j.quageo.2017.06.004>.
- Zerathe, S., Braucher, R., Lebourg, T., Bourlès, D., Manetti, M., & Léanni, L. (2013). Dating chert (diagenetic silica) using in-situ produced ¹⁰Be: possible complications revealed through a comparison with ³⁶Cl applied to coexisting limestone. *Quaternary Geochronology*, 17, 81-93.
- Zerathe, S., Lebourg, T., Braucher, R., & Bourlès, D. (2014). Mid-Holocene cluster of large-scale landslides revealed in the Southwestern Alps by ³⁶Cl dating. Insight on an Alpine-scale landslide activity. *Quaternary Science Reviews*, 90, 106-127.
- Zerathe, S., Pierre-Henri, B., Régis, B., Didier, B., Laurence, A., Julien, C., ... & Team, A. (2018, April). Toward the feldspar alternative for cosmogenic ¹⁰Be applications. In *EGU General Assembly Conference Abstracts* (p. 14977).
- Zhao, S., Chigira, M., & Wu, X. (2019). Gigantic rockslides induced by fluvial incision in the Diexi area along the eastern margin of the Tibetan Plateau. *Geomorphology*, 338, 27-42.
- Zischinsky, U. (1966). On the deformation of high slopes. In *Proceedings of the First Conference of the International Society for Rock Mechanics*, Vol. 2, pp. 179–185.



CHAPTER II:
INVENTORY OF LARGE
LANDSLIDES ALONG THE CENTRAL
WESTERN ANDES (CA. 15°–20° S):
LANDSLIDE DISTRIBUTION
PATTERNS AND INSIGHTS ON
CONTROLLING FACTORS



Inventory of large landslides along the Central Western Andes (ca. 15°–20° S): Landslide distribution patterns and insights on controlling factors

Fabrizio Delgado^{a,b}, Swann Zerathe^{b,*}, Stéphane Schwartz^b, Bastien Mathieux^b, Carlos Benavente^{a,c}

^a Especialidad Ingeniería Geológica, Facultad de Ciencias e Ingeniería. Pontificia Universidad Católica del Perú, Av. Universitaria 1801, San Miguel, Lima, 15088, Peru

^b Univ. Grenoble Alpes, Univ. Savoie Mont Blanc, CNRS, IRD, IFSTTAR, ISTerre, 38000, Grenoble, France

^c Instituto Geológico, Minero y Metalúrgico INGEMMET, Av. Canadá, 1470, Lima, Peru

ARTICLE INFO

Keywords:

Central Western Andes
Atacama desert
Large landslides
Inventory
Controlling factors

ABSTRACT

The western flank of the Central Andes hosts some of the largest terrestrial landslides ($v > \text{km}^3$), which morphologies are particularly well-preserved due to low erosion rates related to the hyper-arid climate prevailing in this region since the Miocene. First-order questions are pending about the factors controlling the development and the triggering of those large-scale slope failures. Previous studies provided some geomorphological analysis and dating on individual study cases, but a regional-scale vision of landslide processes long the Central Western Andes is missing.

Here we report an original inventory of large landslides (areas from 0.1 to 180 km²) established along the western flank of the Central Andes between latitudes ca. 15 and 20° S, and from the Pacific coast to the Altiplano. Based on manual mapping (using satellite images analysis, Google Earth and DEMs analysis) and a compilation of previous works, we inventoried more than a thousand large landslides in this region. We then statistically explored the database according to the landslides typology, size, abundance and relation to geologic, tectonic and climatic settings of the Central Western Andes in order to provide a first insight on their controlling factors. Landslide size-frequency distribution follows a power-law with an exponent of 2.31 ± 0.16 and a cut-off of $4.0 \pm 1.9 \text{ km}^2$ showing a strong contribution of the largest landslides to the cumulated landslide area. We revealed a dominance of rockslide typology (86%) characterized by in-mass slides, the rest being rock-avalanche type (14%) marked by typical granular-flow morphologies. Combination of specific lithology and great local relief emerge as favorable conditioning factor for large landslide initiation, in particular in the case of river incisions through ignimbrites of the Paleogene-Neogene (Huayllillas Formation), concentrating >30% of the landslides. Moreover, landslide clusters tend to follow crustal faults networks suggesting a long-term control of tectonic activity. Most of the identified landslides are paleo events. We tentatively argue that their triggering could not have been possible in the current hyper-arid conditions of the Atacama Desert and its periphery. Future research providing dating on some of the landslide clusters identified in this study is needed to explore possible temporal correlations between periods of landslide activity and external seismic and/or climatic cycles.

1. Introduction

Landslides are ubiquitous gravity phenomena on Earth, found in any environment with slopes. Their triggering is conditioned by the internal mechanical and hydrological properties of geomaterials (Guzzetti et al., 1996; Stead and Wolter, 2015), and may depend on external factors associated with seismotectonic activity (Fan et al., 2019) or climatic variations (Pánek, 2019). They constitute one of the major sources of

hazard, responsible for thousands of victims and billions of dollars in damages each year (Petley, 2012; Froude and Petley, 2018; Wallemacq and House, 2018). The constant growth of the world population associated with the ongoing climate changes are factors that may severely increase the level of risk and hazard related to landslide activity (Gariano et Gariano and Guzzetti, 2016; Haque et al., 2019). In this context, a better understanding of landslide processes and their causative factors is crucial and those questions have received a growing interest (Wu

* Corresponding author.

E-mail address: swann.zerathe@ird.fr (S. Zerathe).

<https://doi.org/10.1016/j.jsames.2022.103824>

Received 2 November 2021; Received in revised form 9 March 2022; Accepted 19 April 2022

Available online 27 April 2022

0895-9811/© 2022 Elsevier Ltd. All rights reserved.

et al., 2015). On longer timescales, landslides are recognized as the main erosional process in orogenic zones (e.g. Korup et al., 2007). Landslide rate is thought to mirror the long-term trend of tectonic uplift, landslide continuously affecting steep slopes along the valley flanks of incising rivers (Larsen and Montgomery, 2012). Doing so, landslides are the main agent transporting material from hillslopes to rivers and limiting the elevation and the relief construction in mountain ranges (Whipple et al., 1999; Montgomery, 2001; Roering, 2012).

To disentangle hazard issues and to progress toward a better understanding of landslides processes, research strategies based on landslide inventories have shown interesting potential (Malamud et al., 2004; Guzzetti et al., 2012). Numerous landslide inventories have been built after single storm events or strong earthquakes, using remote sensing approaches to detect the triggered landslides (see reviews in Marc et al. (2018) and Tanyaş et al. (2017), for rainfall-induced and earthquake-induced landslide inventories, respectively). Providing statistics on landslide processes, those inventories can highlight specific patterns and reveal generic landslide properties, such as the earthquake-induced landslide size decreasing with distance from the fault trace (Valagussa et al., 2019), the control of relief on landslide size (Medwedeff et al., 2020) or the influence of total rainstorm on the proportion of large landslides (Marc et al., 2018). However, deciphering landslides patterns on a longer time scale (hundreds to thousands of years) and at a large spatial scale is more complex because erosion continuously removes the geomorphological evidence of past events. Furthermore, automatic detection of past landslides in landscapes is not efficient at present-day and establishing paleo landslides inventory requires a manual mapping based on expert vision (e.g. Pánek et al., 2019; Görüm, 2019). Those inventories allow to understand the relations between large landslides and relief properties at an orogenic scale and to unravel the respective effects of long-term seismotectonic activity and Quaternary climate changes on slope instabilities.

In this study, we focus on large landslides along the western flank of the Central Andes between ca. 15° and 20°S, in both south Peru and north Chile, and we aim at establishing a comprehensive inventory of landslides in this area. This region is an atypical place for several aspects. First, it is particularly active geodynamically, related to the long-term convergence between the Nazca and the South America plates (Armijo et al., 2015; Martinod et al., 2020). This global shortening generates relief construction (Martinod et al., 2020) and produces instantaneous deformation (subduction and crustal seismicity; Villegas-Lanza et al., 2016) coupled with long-term processes of surface uplift (Thouret et al., 2017) and volcanism (Mamani et al., 2009). Second, the climate of this region is specific, with some places being one of the driest worldwide: referred to as the Atacama Desert in Northern Chile and Southern Peru (Hartley and Chong, 2002). This desert, where a hyper-arid climate has been maintained for several millions of years (e.g. Hartley and Chong, 2002; Dunai et al., 2005) is often referred to as a Martian proxy (Valdivia-Silva et al., 2011; Irwin et al., 2014). The long-term aridity is responsible for very low erosion and weathering rates (1–10 mm kyr⁻¹; Nishiizumi et al., 2005), allowing for exceptionally long preservation of landscapes and offering a unique time window to study slope instabilities at geological time scales. At the same time, strong storms can episodically occur during El Niño event. Finally, the western flank of the Central Andes hosts some of the largest landslides ever identified on the emerged Earth surface (e.g. Chuquibamba (Margirier et al., 2015), Caquilluco (Crosta et al., 2015), Lluta (Strasser and Schlunegger, 2005), mobilizing volumes of several cubic kilometers, with kilometeric long run-outs, similar to those reported on the Mars surface (Lucas et al., 2014). Some previous studies have been conducted on those individual slope failures, revealing that the instabilities are ancient with ages ranging from tens to hundreds of thousands of years (Zerathe et al., 2017; Crosta et al., 2017; Delgado et al., 2020; Sánchez-Núñez et al., 2020). However, questions remain about the link between those landslides and the conditioning factors along the Central Western Andes and also with the seismicity and the past climate

variations in this region. Other preliminary works have revealed that much more large landslides may exist there (Audin and Bechir, 2006; Mather et al., 2014; Crosta et al., 2014) but a general view of the distribution of the landslide activity at the scale of the Central Western Andes instabilities is missing.

The scope of the paper is to establish a landslide inventory as exhaustive as possible along the northernmost Central Western Andes (ca. 15° - 20°S), our strategy was based on a review of previous works on landslides existing in the literature for this region and on an original mapping of unrecognized large landslides based mainly on satellite images, Google Earth and DEMs analysis. The finalities of this study are: (1) to provide an updated database of large landslides existing between latitudes ca. 15 and 20°S. This database will be open and may be modifiable; (2) to provide a first-order view of their typology, size, abundance and distribution; and (3) to search for statistical patterns between landslide distribution and background settings in order to better understand their conditioning factors.

2. Settings of the western flank of the Central Andes

2.1. Geodynamic and large-scale morphology

The Andean cordillera is located on an active tectonic margin where the subduction of the Nazca plate beneath the South American plate occurs since ~50 Ma (Pardo-Casas and Molnar, 1987) with a convergence rate of ~62 mm. yr⁻¹ (Villegas-Lanza et al., 2016). This process generates the construction of the Andes and leads to the formation of successive volcanic arcs. Their locations varied in time and were controlled by the change of the dip of the subduction slab (Isacks, 1988; Allmendinger et al., 1997; James and Sacks, 1999; Sobolev and Babeyko, 2005; Haschke et al., 2006; Mamani et al., 2008, 2009). This dynamic produced long-term crustal thickening controlled by magmatic underplating and tectonic shortening. The western flank of the Central Andes is classically subdivided into three main areas (Fig. 1) based on different geological and morphological settings inherited from the long-term geodynamics evolution of the Andes.

The first area corresponds to the Coastal Cordillera (CC) which is mainly characterized by Proterozoic craton (so-called the Arequipa massif, Cobbing and Pitcher, 1972) represented by the association of gneisses and migmatites which have been later intruded by Paleozoic plutons (Cobbing and Pitcher, 1972; Cobbing et al., 1977; Mukasa and Henry, 1990). This Coastal Cordillera forms currently a narrow band reaching 50-km-wide and moderate relief and elevation up to 1000 m a.s.l. along the Pacific coastline.

The second area corresponding to the Central Depression (CD) exhibits Tertiary sedimentary series, the so-called Moquegua formation, unconformably resting above the Proterozoic and Paleozoic bedrock. This area corresponds to a flexural depression located in the front of the volcanic arc. This basin collected the erosional products of the Andean relief under construction. Those detrital sedimentary series can be locally more than 1-km thick (Roperch et al., 2006; Thouret et al., 2007; Schildgen et al., 2007; Garzzone et al., 2008). Their lithologies evolve from thin marine sequences at the base toward conglomeratic continental deposits with interstratified ignimbrites levels at their top. At present-day, this area forms a pediment plain, almost flat with mean elevations ranging from 1000 to 1500 m a.s.l., and locally affected by fluvial incision (Thouret et al., 2007; Schildgen et al., 2007; Garzzone et al., 2008).

The third area corresponds to the Western Cordillera (WC) which presents a higher relief from 1000 to 5000 m a.s.l. It is made of Mesozoic marine sequences and Cenozoic, essentially Paleogene-Neogene, volcano-sedimentary series related to the migration of the successive volcanic arcs (Mamani et al., 2010). One of the last main volcanic phases corresponds to the so-called Huaylillas arc (24-10 Ma, Quang et al., 2005; Thouret et al., 2007). It produced thick ignimbrite deposits (up to 300 m of thickness) at a regional scale. Along the Western Cordillera, the

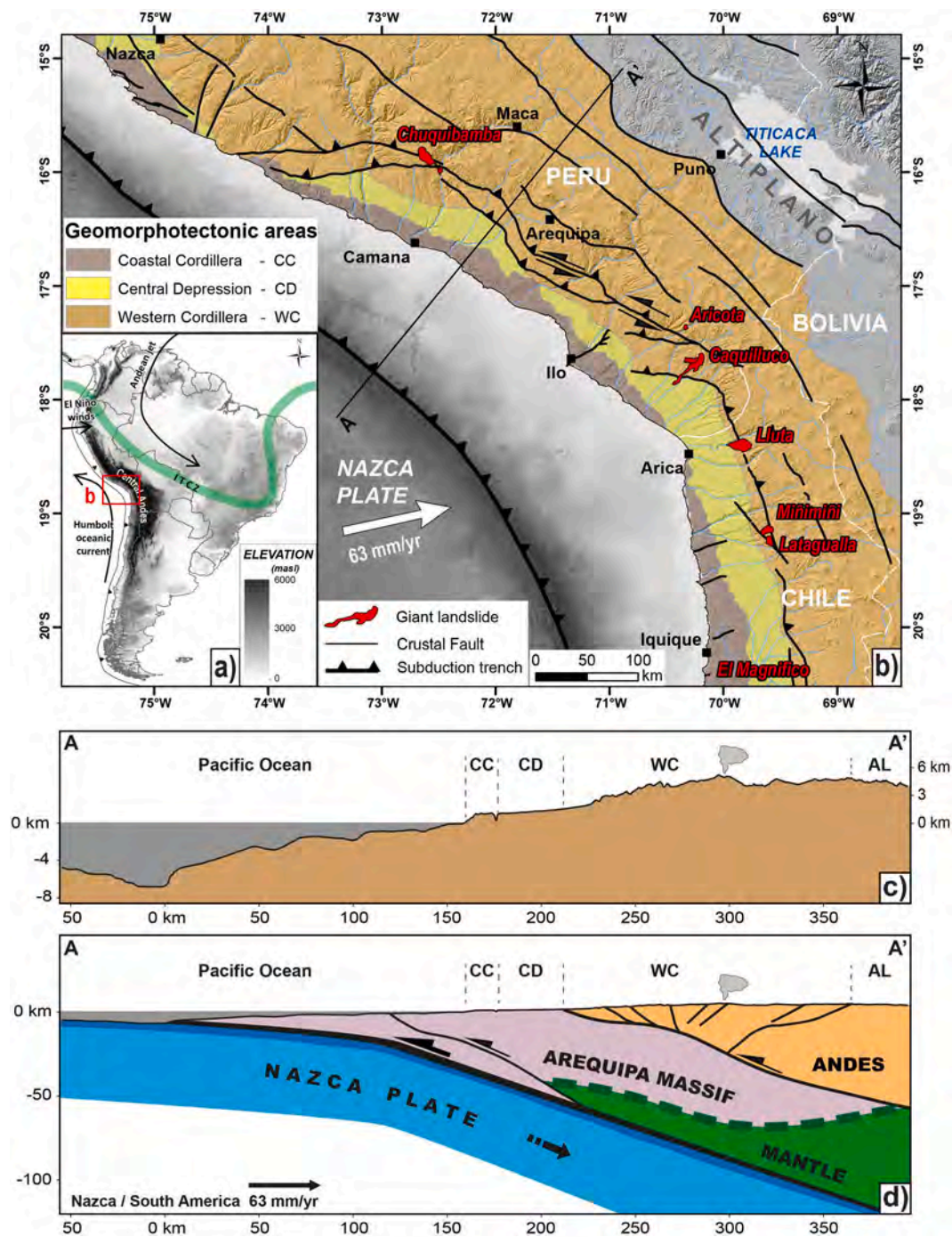


Fig. 1. (a) Study area location and major climatic features of South America showing the Intertropical Convergence Zone (ITCZ), El Niño wings and the Humboldt oceanic current, (b) focus on the study area showing the different geomorphotectonic areas of the Central Western Andes and the location of giant landslides documented in the literature (Chuquibamba landslide - Margirier et al., 2015; Thouret et al., 2017; Aricota landslide - Delgado et al., 2020; Caquilluco landslide - Zerathe et al., 2017; Lluta landslide - Wörner et al., 2002; Strasser and Schlunegger, 2005; Miñimiñi and Latagualla landslides - Pinto et al., 2008; El Magnífico landslide - Mather et al., 2014; Crosta et al., 2017), (c) and (d) AA' topographic profile of the western flank of the Central Andes and its geological interpretation (adapted from Armijo et al., 2015), respectively. CC: Coastal Cordillera, CD: Central Depression, WC: Western Cordillera, AL: Altiplano.

top of the Huaylillas deposits corresponds to a preserved paleosurface used as a reference surface at a regional scale. All this domain is affected by tectonic shortening associated with the development of large-scale anticline geometry, well underline by flexures of the Huaylillas paleosurface, and by pluri-kilometric crustal fault systems.

As previously introduced, among those three sub-areas, the Western Cordillera is the region where some of the largest landslides have been reported in the literature (Chuquibamba landslide - Margirier et al., 2015; Thouret et al., 2017; Aricota landslide - Delgado et al., 2020;

Caquilluco landslide - Zerathe et al., 2017; Lluta landslide - Wörner et al., 2002; Strasser and Schlunegger, 2005; Miñimiñi and Latagualla landslides - Pinto et al., 2008; El Magnífico landslide - Mather et al., 2014; Crosta et al., 2017, Fig. 1). We bring here below further detailed geological and geomorphological descriptions of this key region required to better understand the gravitational destabilization affecting the Central Western Andes.

2.2. Lithostratigraphy

The oldest rocks in the studied area correspond to the Precambrian crystalline basement. It consists of gneiss, migmatites, pegmatites, schists and diorites. This rock assemblage is located between latitudes 15°-18°S, outcropping mainly along the Peruvian Coastal Cordillera along an NW-SE orientation (Fig. 2) and was dated between 1861 ± 32 Ma and 946 Ma by Casquet et al. (2010).

Paleozoic rocks were emplaced in erosional unconformity, their lithostratigraphic units are observed along the Coastal Cordillera (Fig. 2) and are represented by the Marcona (Cambrian), Cabanillas (Devonian), Ambo and Tarma (Carboniferous) formations. These units are mostly made up of limestones, conglomerates, sandstones and shales (Newell, 1945).

The Mesozoic record is characterized by important Jurassic and Cretaceous marine sedimentation, controlled by the tectonic opening of the Arequipa-Tarapacá sedimentary basin (Vicente, 1981). Those deposits outcrop all along the entire western Andean flank and correspond to thick series of limestones (mudstone to grainstone) and marls of the Pelado and Socosani formations (Wilson and García, 1962; Monge and Cervantes, 2000) conformably covered by the Yura Group and the Hualhuani Formation (Wilson and García, 1962; Vicente, 1981) composed of quartz sandstones and black shales interstratified. The top of the Mesozoic series is affected by an erosive discordance, overlain by volcanic and volcano-sedimentary rocks of the Toquepala Group (Bellido Bravo and Guevara, 1963; Bellon and Lefevre, 1916).

The distribution of the Cenozoic lithostratigraphic units is more complex and is related to the formation of the volcanic arc of the Andes, its successive migration and its importance in the creation of forearc, back-arc and intra-arc basins. In the Coastal Depression, deposits of sedimentary sequences accumulated, mainly of marine origin, also from the erosion coming from the proto-Andean under construction, which

generated the almost synchronous creation of the Camaná and Moquegua basins in southern Peru and Azapa in northern Chile. These interstratified sequences of conglomerates with volcanic sequences are called Moquegua Group (Thouret et al., 2007; Schildgen et al., 2007) in Peru while in Chile they correspond to the Azapa Formation (Wörner et al., 2000; Pinto et al., 2007). These sequences, which are up to 800 m thick (Bellido, 1979), are the result of erosion of the Western Cordillera and were deposited from the Oligocene to the late Miocene. From the Eocene onwards, constant volcanic events began and continue to the present day. The Huaylillas formation (Wilson and García, 1962), constitutes a wide surface that extends up to the north of Chile, where it is called Huaylillas surface (Wörner et al., 2000). This formation is a stratigraphic superposition of pyroclastic flows (Wörner et al., 2000; Mamani et al., 2010) developing a thickness between 500 and 600 m (Wilson and García, 1962; Salinas, 1985). This formation is well-preserved due to the hyper-arid climatic conditions and its top surface represents a regional paleosurface. The only forms of erosion are the incision of the valleys produced by the rivers descending from the Altiplano (Evenstar et al., 2017). The northeast is dominated by a large volume of andesites and rhyolites associated with ignimbrites assigned to the Barroso Group (Roperch et al., 2006; Mamani et al., 2010; Acosta et al., 2011), related to the magmatic activity of the Barroso Arc (Mamani et al., 2012). The Quaternary rocks are expressed by Pleistocene lava produced during a recent activity of active volcanoes (e.g. Sabancaya, Ampato, Ubinas) related to the activity of the magmatic arc (e.g. Mariño et al., 2021; Rivera et al., 2020). Quaternary deposits cover a large part of the basement and can reach a few meters thick. These deposits correspond to fluvial and alluvial deposits in the main valley and glacial deposits in high elevation areas that evidence recent climatic fluctuations.

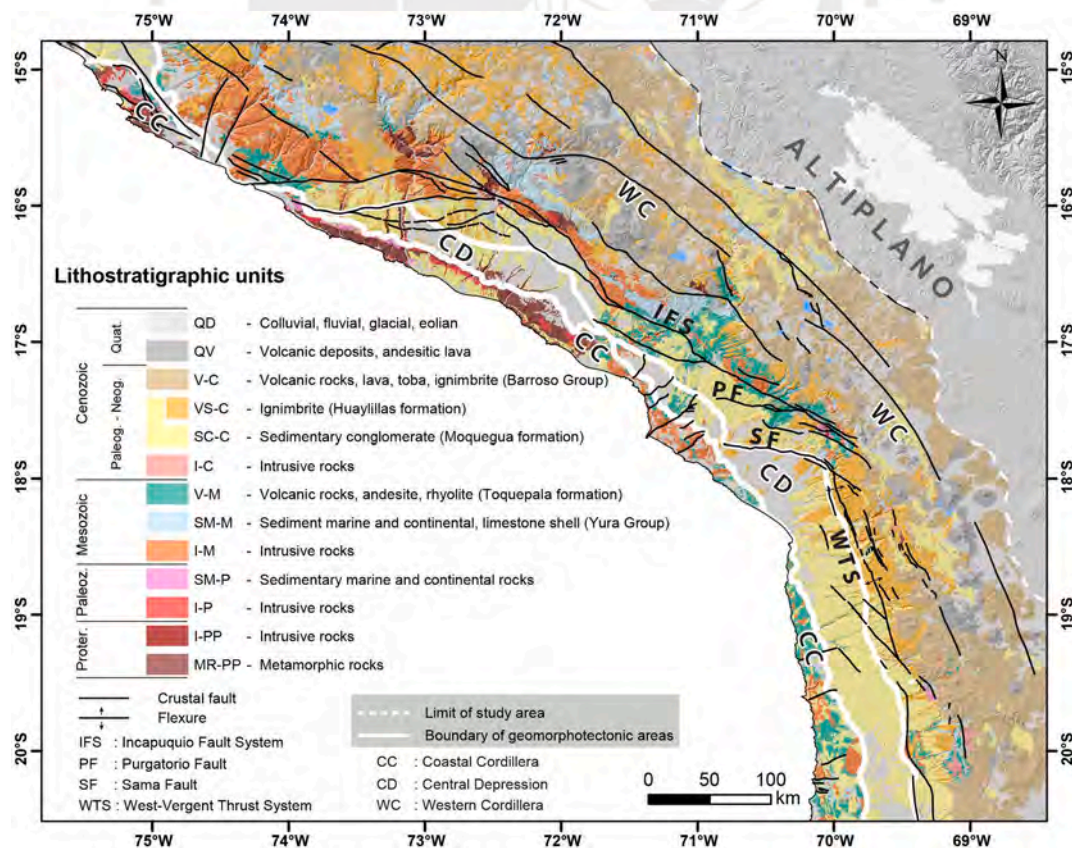


Fig. 2. Lithostratigraphy and main structural features of the Central Western Andes (adapted from <http://geocatmin.ingemmet.gob.pe/geocatmin> for Peru and <https://portalgeominbeta.sernageomin.cl/> for Chile).

2.3. Tectonic setting

Active or neotectonic faults are mostly present along the Western Cordillera area (<http://neotec-opendata.com>; <http://geocatmin.ingemmet.gob.pe/geocatmin>). The width of the Western Cordillera shows important variations being wider in South Peru than along North Chile (Fig. 1). This variation is related to the partitioning of the deformation controlled by the Nazca plate convergence toward a curved shape boundary (Arica bend) of the South American plate (Allmendinger et al., 1997). The Western Cordillera is deformed by intense folding, inverse faults and large overflows due to the shortening and thickening of the crust mainly associated with an increase in the subducted slab angle (Armijo et al., 2015).

In southern Peru, the tectonic regime is transpressive related to the activity of the Incapuquio Fault System (IFS), which extends for more than 200 km along a NW-SE direction (Fig. 2). This crustal-scale fault system displays sinistral displacement affecting mainly the Moquegua Formation and the Toquepala and Yura groups, defining a tectonic contact between them (Jacay et al., 2002). The IFS is considered potentially active as shown by the paleo-seismological studies that

revealed Holocene surface ruptures (Benavente et al., 2021). Other secondary fault systems are connected to the IFS such as: (i) the Purgatorio fault (PF), located between the Pampa Purgatorio and the village of Mirave, striking E-W along 70 km (Benavente et al., 2017b) or (ii) the Sama-Calientes fault (SF), striking E-W along ~50 km (Hall et al., 2008). Both are mainly reverse faults with a slight dextral component and have registered Holocene reactivations and surface failures (Benavente and Audin, 2009; Benavente et al., 2017b).

To the south of the Arica bend (in North of Chile) the tectonic regime becomes compressive and correlated with an important increase in the plate convergence during the last 30-20 Myr (Pardo-Casas and Molnar, 1987; Somoza, 1998). The most important structure corresponds to the West-Vergent Thrust System (WTS) located in the Western Cordillera (Fig. 2) with an N-S trending direction and extending over 450 km in northern Chile (García et al., 2004, 2013; Blanco and Tomlinson, 2013; Valenzuela et al., 2014; Morandé et al., 2015; Tomlinson et al., 2015). This main regional tectonic structure presents W-dipping high angle segments associated with the development of large folds with monoclinical geometry described as regional flexures. These structures present slight variations in the magnitude of displacement along the course

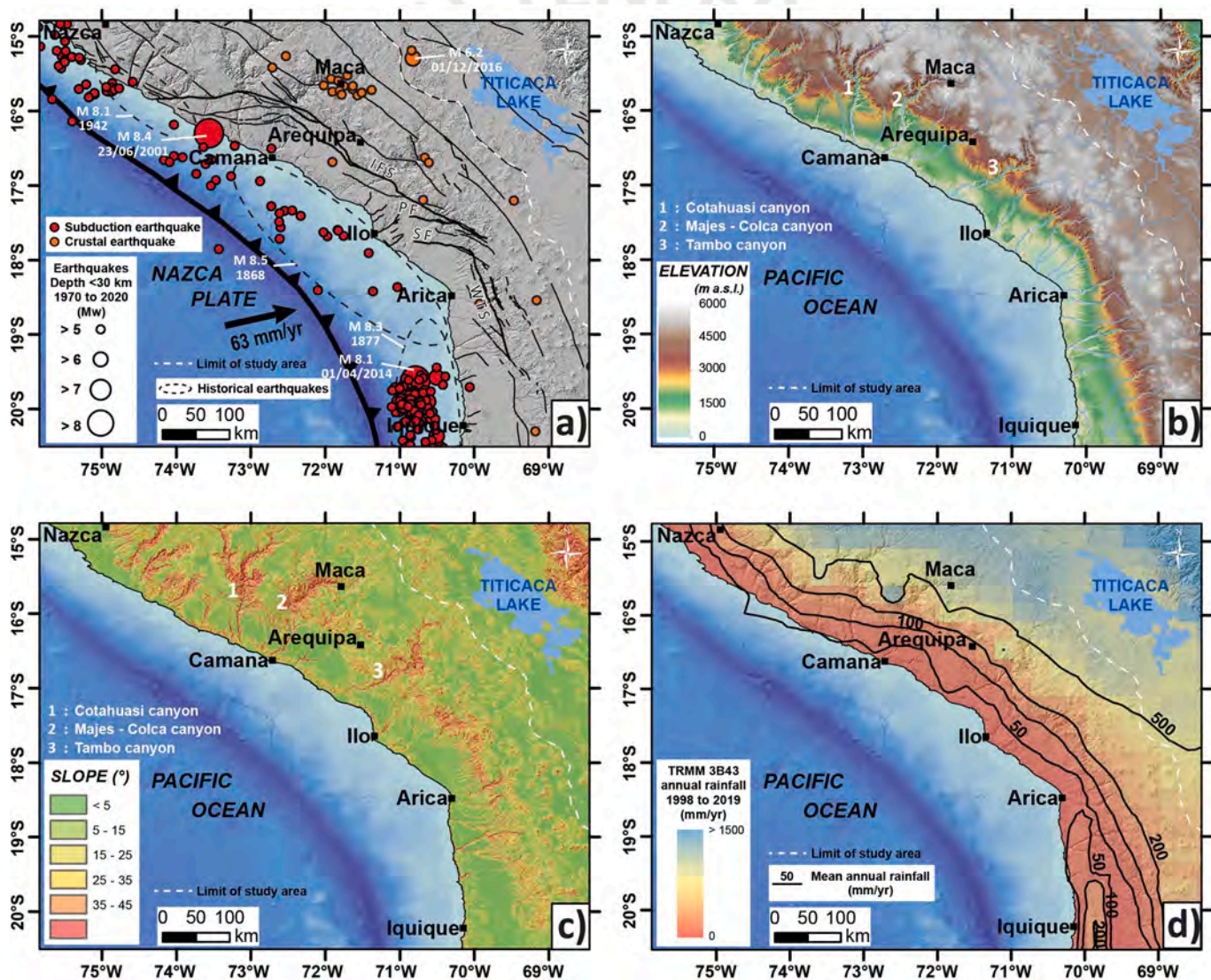


Fig. 3. Settings of the western flank of the Central Andes. (a) fault and seismicity (faults database: <http://neotec-opendata.com> and <http://geocatmin.ingemmet.gob.pe/geocatmin>; instrumental earthquakes from <http://ds.iris.edu/seismon/index.phtml> and historical earthquakes from Villegas-Lanza et al., 2016). (b) and (c) topography and slope, respectively (both derived from SRTM DEM of 30 m of resolution), (d) mean annual rainfall (TRMM 3B43 annual rainfall of the Andes averaged for the period of 1998–2019). The white dashed line marks the eastern limit of our study area.

(Pinto et al., 2004; Farfás et al., 2005) and affect rocks of the Moquegua Group and the Huaylillas formation (ignimbrites).

2.4. Seismicity

The western flank of the Central Andes is affected by two types of seismic activity (Fig. 3a). The first one is related to the subduction dynamics that produce earthquakes with magnitudes that could be higher than 8, with slab ruptures of several hundreds of kilometers along the subduction zone (Villegas-Lanza et al., 2016). Recent strong subduction earthquakes include the 2007 Pisco earthquake (Mw 8.0, depth 18 km, ~100 km north to the study area), the 2001 Arequipa earthquake (Mw8.4; depth 30 km) and the 2014 Iquique earthquake (Mw8.1, depth 20 km) (Fig. 3d). Those earthquakes were also associated with swarms of seismicity and aftershocks of moderate to high magnitudes (Fig. 3a). Several historical mega earthquakes are also documented in this area (see Fig. 3a). A recurrence time between 100 and 300 years is proposed for those events for the same slab portion (Kelleher, 1972; Dorbath et al., 1990; Chlieh et al., 2011).

The second one is related to the crustal faults network. The Coastal Cordillera, Central Depression and the Western Cordillera are affected by several major faults (Figs. 2 and 3a) that experienced recent seismotectonic activity (Lavenue et al., 2000; Jacay et al., 2002; Audin et al., 2003, 2006; Barrientos et al., 2004; Lavenue, 2005; PMA, 2009; Leyton et al., 2010; Benavente et al., 2017a, 2017b). The seismic record in the study area is mainly focused on the subduction dynamics because it produces the strongest earthquakes. In contrast, the western cordillera does not benefit from a seismic network allowing the location of earthquakes at crustal-scale depth in relation to the major faults distribution (Figs. 2 and 3d). However, some seismic records over the last 50 years apart from the region of Maca (upper Colca) (Fig. 3a) have been reported that indicate moderate seismicity up to Mw5. Paleoseismological studies show that some of these faults have produced recurrent shallow seismicity during the Holocene. The analyses of the offsets along the rupture surfaces are consistent with earthquake magnitudes up to Mw7.5 (e.g. Benavente et al., 2017a; Santibáñez et al., 2019). These are some examples: the Incapuquio fault (Audin et al., 2008; Benavente et al., 2021), the Purgatorio fault (Benavente et al., 2017b), the Sama-Calientes fault (Audin et al., 2006) and the Bajo Molle fault (González et al., 2015). The length of fault failure is smaller compared to subduction earthquakes, but the energy and the ground acceleration generated by the shallow ruptures along those faults can be very strong (Benavente et al., 2017a). The recurrence period for this type of crustal seismicity is commonly assumed to be about thousand years (Leyton et al., 2010; Benavente et al., 2017b).

2.5. Topography

As shown by Fig. 3b and c, the western flank of the Central Andes is characterized by two main types of topography. First, a large wavelength topography that is directly related to the orogen formation and its evolution. This topography, with elevation ranges between 1500 and 4500 m a.s.l. forms the Western Andean flank itself, striking NW-SE in Peru and NNW-SSE in Chile, roughly parallel to the subduction trench (Fig. 3b). Steep slopes (20–30°) are found at the southern extremity of the Western Cordillera, along the main reverse faults and anticlinal-flexure growth (Fig. 3a). This large-scale wave-length topography is also revealed by a major paleosurface developed above the Huaylillas ignimbrite. This major geomorphological feature exists all along the western flank of the Central Andes (Fig. 2), characterized by a regular primitive drainage network forming a large striped surface. Its mean slope varies between 5° and 20° (mainly toward the South) depending on the local amplitude of the structural flexure and fault-propagation folds (Wilson and García, 1962). Second, a more local but stronger topography corresponds to the deep canyons that dissect the Western Cordillera. They are up to several kilometers deep in some places in

southern Peru (Cotahuasi, Majes, Tambo, see Fig. 3b and c), generating strong local relief and very steep slopes (>30°) along their flanks (Fig. 3c). The formation of those canyons started during the late Miocene and is related to the regional uplift and the specific climate of this region (Thouret et al., 2007; Schildgen et al., 2009, 2010; Gunnell et al., 2010).

2.6. Current and past climate

The Central Western Andes of southern Peru and northern Chile are part of the Atacama Desert, known as one of the driest places worldwide. Several factors are often proposed to explain this extreme lack of precipitation: (1) the mid-latitude of the region (~20°S) located along the sinking branch of the Hadley Circulation generating high pressure of dry air; (2) the oceanic Humboldt Current, characterized by upwelling of cold water along the South American Pacific coast, which cools the air near the surface and prevent moisture evaporation from the Pacific ocean (La Niña-like conditions); (3) the rain shadow effect of the Andes limiting the transfer of moisture coming from the Atlantic and the Amazonia (Houston and Hartley, 2003).

The main source of moisture is coming from the northeast, from the Atlantic Ocean and the Amazonian basin as depicted by a north-south rainfall gradient (Fig. 3d). Precipitations can reach ~1000 mm/yr in the northeastern boundary of our study area (at latitude ~15°S) and along the western boundary of the Central Altiplano (Fig. 3d). Those precipitations are seasonal, occurring mostly during the austral summer, associated with the South American monsoon regime and the seasonal southward shift of the Intertropical convergence zone above the Altiplano. Despite a little of this moisture can reach the upper part of the Pacific watersheds, the Western Cordillera, as part of the Atacama Desert, remains arid receiving less than 200 mm/yr of rain, while the coast and coastal depression receive less than 50 mm/yr of rain (New et al., 2002; Strecker et al., 2007). The hyper-aridity of the Atacama Desert, and such climatic setting, are thought to prevail since at least 10 Ma (Rech et al., 2019 and references therein), responsible for very low denudation rates over the long term (erosion <0.5 m/Ma; e.g. Hall et al., 2008; Placzek et al., 2013) and long-term preservation of landscapes. On the other hand, as the upper of the watersheds received precipitations from Amazonian moisture, the main rivers have strong erosional capacity which produced deep canyon incisions (Cotahuasi, Majes, Tambo; Fig. 3b and c) through the arid Western Cordillera.

The current meteorological conditions can be episodically modulated by El Niño Southern Oscillation (ENSO) which results in a warming of the Pacific Ocean surface related to the Trade winds carrying warm water from the eastern equatorial Pacific towards the South American coast. This can lead to very strong storms such as in March 2015, when up to 40 mm of 1-day accumulated precipitation fed the Atacama region (Bozkurt et al., 2016), triggering strong flash floods and debris flows (Aguilar et al., 2020). Despite paleoclimate records covering the Late Quaternary in the Atacama region being rare and often discontinuous (e.g. Bartz et al., 2020), some evidences of past humid phases has been also reported. They included widespread pluvial stages termed the Central Andean Pluvial Event (CAPE, e.g. Quade et al., 2008; Gayo et al., 2012) recorded as lake extensions and glacier advances in the Central Atacama of Northern Chile. Records of flash floods and debris flows linked to paleo-El Niño events have been reported during the late Pleistocene in Southern Peru (e.g. Keefer et al., 2003). Then evidences of more persistent humid conditions related to ENSO-like climate configuration during the last interglacial periods are recorded as paleolakes extensions (e.g. Ritter et al., 2018; Placzek et al., 2013) and fluvial terraces aggradation in the valleys (Steffen et al., 2010; Litty et al., 2016). Those humid events are thought to have persisted over millennial to pluri-millennial periods (i.e. the Ouki Event (100–120 ka), Placzek et al., 2013; Ritter et al., 2019).

3. Methods

3.1. Landslide mapping strategy

Our main objective was to establish an inventory as exhaustive as possible of large landslides (areas >0.1 km²) along the Central Western Andes in a region bounded to the north and south by the exact latitudes 14.8 and 20.5°S, and to the west and east by the Pacific coast and the western limit of the Altiplano, respectively (Fig. 1b). As detailed here below, our landslide inventory was based on: (1) a review of previous works and mapping of landslides existing in the literature for this region and (2) a manual mapping of newly recognized large landslides based on specific geomorphologic criteria combing GIS analysis (using Google Earth and DEMs (30 m TanDEM-X and 2 m Pleiades). This mapping using remote tools was made possible by the collective expertise of our team acquired during several past field works dedicated to landslide-geomorphology-tectonic in this region for a dozen years. About 10% of the landslides inventoried in this study were visited in the field, several of those being mapped in detail as already published in previous works involving our team (e.g. Zavala et al., 2013; Margirier et al., 2015; Zerathe et al., 2016, 2017; Delgado et al., 2020).

Indeed, the reviews of previous studies included individual landslide case studies (e.g. Strasser and Schlunegger, 2005; Pinto et al., 2008; Hermanns et al., 2012; Zavala et al., 2013; Margirier et al., 2015; Zerathe et al., 2016, 2017; Bontemps et al., 2018; Lacroix et al., 2015, 2019, 2020; Thouret et al., 2017; Delgado et al., 2020; Gaidzik et al., 2020; Sánchez-Núñez et al., 2020). We also revised a few studies including some local landslide databases such as (Audin and Bechir, 2006 and Crosta et al., 2014 for South Peru and Mather et al., 2014 and Crosta et al., 2014 for North Chile). Following this review, we note that two main types of landslide dominate in this region (Fig. 4): (i) coherent landslides for which the slipped mass moved in only one or few packets, typically corresponding to rockslide typology, and (ii) disrupted landslides which evolve as a granular flow of rock and boulders, typically corresponding to rock avalanche typology. In order to decipher if those two landslide types may have different controlling factors, we kept this binary classification for our mapping.

Fig. 4 illustrates the specific geomorphologic criteria that we used for

mapping and classification for both cases. Importantly, a landslide phenomenon was ascribed to a site only if the formal identification of a headscarp associated to a slipped mass was possible. To the contrary, morphologies such as large erosional amphitheatres or slope-break were not mapped as a landslide if a slipped mass was not clearly identified at the scarp base. Finally, we attempted to define a qualitative state of activity for our mapped landslides, trying to distinguish between two main types (Fig. 4). First the recent or active landslides, that are known to affect human infrastructures (agricultural land, road, village, etc.), showing fresh morphologies (fresh scarp, recent river dam, etc.) and/or which are monitored and referred in published papers. Additionally, we attempted to revise each mapped landslide on the Google Earth time-lapse tools, to visually check if some surface large-scale displacements (>100 m) might occur in the last 37-years. The oldest images (from 1985 to ~2005) being of rather poor quality, only displacements of >100 m might have been detectable. Second, the ancient or paleo landslides, being typically characterized by smooth and weathered surface morphologies, partially covered by eolian sand, laharcic flows or which have been significantly re-eroded or re-incised by rivers (see also Hermanns et al., 2012).

In order to carry out the recognition and mapping of landslides as much as possible in an orderly and reproducible way, we gridded our study area (cells of 0.5 × 1°) and we explored and mapped analyzing cell by cell. The grid used is provided in the supplementary data. For each identified landslide, a polygon including the headscarp and the slipped mass was drawn (Fig. 5).

3.2. Dimensional and geological landslide parameters

Understanding the occurrence of landslides requires a thorough knowledge of their initial failure conditions. It thus requires data on the terrain morphology (elevation, slope, local relief) on which landslides has developed, on the lithology and on the morphometric characteristics of the landslide itself. For each mapped landslide, we compiled this data in a database described in detail below (Supplement, Table 1). This database was further used for statistical analysis of landslides patterns. All calculations were made using ArcGIS software and using the SRTM DEM of 30 m of resolution (SRTM, DOI:/10.5066/F7K072R7). The

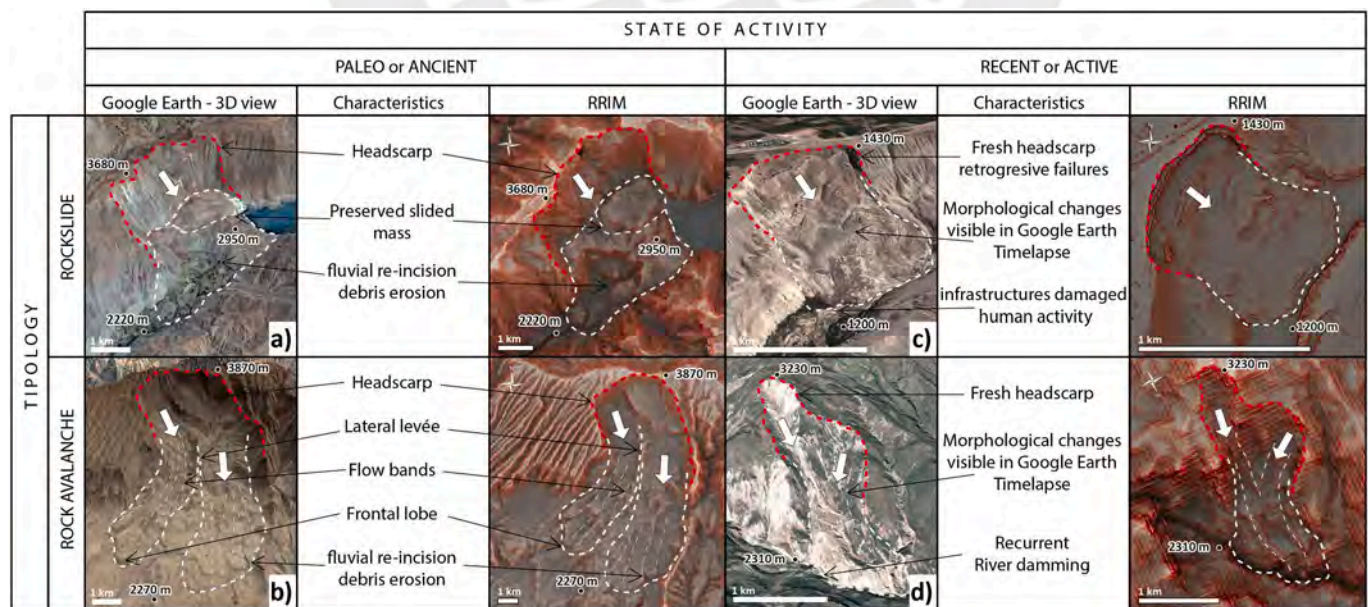


Fig. 4. Morphological criteria used for landslide recognition and mapping along the Central Western Andes. We classified the landslides according to two main typologies (rockslide and rock avalanche) and also attempted to ascribe a qualitative state of activity (paleo or recent) to each identified case (see text for details). Illustrated examples are from (a) the Aricota paleo rockslide (Delgado et al., 2020) (b) the Caquilluco paleo rock avalanche (Zerathe et al., 2017), (c) the Siguas active landslide (Lacroix et al., 2019) and (d) an active landslide from this study (landslide n° 109. RRIM: Red Relief Image Map).

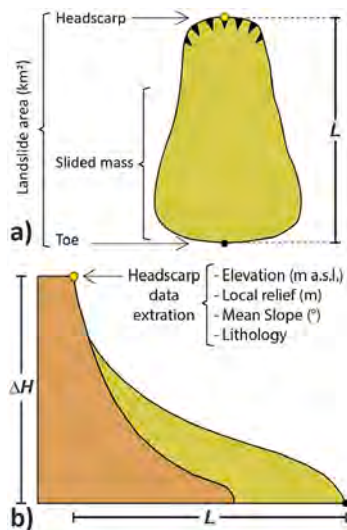


Fig. 5. Landslide sketch illustrating data collection procedure. (a) plan view and b cross-section. The green polygon delimits the whole landslide area (headscarp and slided mass). The yellow dot locates the centroid of the headscarp, considered as the origin of the landslide where several data are extracted (see text for details).

Spatial Analyst tool of ArcGIS toolbox was used to compute slope and local relief map, both calculated considering cells of 2×2 km.

For each landslide, we extracted the area (km^2) of the polygon. Then, two points were set: one located at the center of the headscarp and another one located at the landslide toe, in order to indicate the origin of the landslide and its lower limit, respectively (Fig. 5). At the location of the headscarp point, as recommended by Yilmaz and Ercanoglu (2019), we extracted the lithology in which the landslide developed following the lithostratigraphic layers defined in Fig. 2. We also extracted at this location the characteristic of the topography: the elevation (m a.s.l.), the slope ($^\circ$) and the local relief (m). Finally, using the headscarp point and the toe point, we calculated the landslide length (L in km) and the landslide height (ΔH in km).

All of these morphometric parameters are necessary to perform basic statistical analyses (histograms) of landslide properties in order to better understand their controlling factors. This involves exploring relationships that exist between landslides, topography and lithology through analyzing the frequency distribution of landslides as a function of their area, elevation above sea level, slope and lithology. Through analyzing the relationships ΔH vs L and L vs A , according to the different landslide type, we also explored the mobility of landslide masses and their dimensional properties.

3.3. Landslide spatial density analysis

The activity of landslides is conditioned by different factors among which are for instance the local relief, the slope, the geology of the site (lithology, faults, structures, etc.). In some areas, the interplay of those factors may generate higher landslide susceptibility and thus landslide clustering. In order to identify if the landslide location responds to a clustering in the western flank of the Central Andes, we applied the Ripley's K Function (Ripley, 1977). This function allows determining statistically if the phenomenon appears to be spatially dispersed, clustered, or randomly distributed throughout the study area. It has been often used to explore the spatial pattern of landslides in previous studies (Tonini et al., 2014; Görüm, 2019; Pánek et al., 2019).

Computations were done with the R software (R Core Team, 2019), using the package 'spatstat' (Baddeley et al., 2020). As recommended by Tonini et al. (2014), we applied the "Kinhom" function (Baddeley and Turner, 2005), which is a modification of the original Ripley's

K-function for inhomogeneous point distribution. This variant "Kinhom (r)" allows taking into account the non-stationarity of the studied process due to spatial variability of the geological and topographical characteristics over the studied area (Tonini et al., 2014). The Kinhom(r) function can be defined as (Marcon et Puech, 2009):

$$\hat{K}_{inhom}(r) = \frac{1}{A} \sum_{i=1}^N \sum_{j=1, i \neq j}^N \frac{c(i,j,r)}{\lambda(i)\lambda(j)} \quad (1)$$

where r is the radius in m, A is the studied area in m^2 , the indicator $C(i,j,r)$ is the average number of neighbors, being equal to 1 if the distance between points i and j equals at most r , or equals 0 otherwise, and $\lambda(i)$ $\lambda(j)$ are the process density at points i and j , respectively. Theoretically, when $\text{Kinhom}(r) = \pi r^2$, the analyzed points are distributed independently (or randomly) from each other. When $\text{Kinhom}(r) > \pi r^2$, the probability to find a neighboring point at the distance r is greater than the probability to find a point in the same area at any other place, i.e. the points are aggregated. When $\text{Kinhom}(r) < \pi r^2$, the points are dispersed. Final results were plotted as the Linhom function (Besag and Diggle, 1977), which is a normalization of the Kinhom(r) function to get a benchmark at zero and to facilitate visualization:

$$L(r) = \sqrt{\frac{\hat{K}(r)}{\pi}} - r \quad (2)$$

We used the centroid of the landslide headscarps (Fig. 5) as point input for the Kinhom analysis as recommended by Yilmaz and Ercanoglu (2019) and references therein. In the case of large destabilized areas ($>0.1 \text{ km}^2$), with debris that can have long run-out, the landslide headscarp centroids can provide a better assessment of the geological and topographical conditions of the landslide initiation than any other point located along the debris path or at the landslide toe for instance (Yilmaz and Ercanoglu, 2019). Finally, we used the range of radius obtained from this analysis, to calculate a kernel density of landslides over the studied area and to image the point of the higher frequency distribution of landslides.

3.4. Frequency-area relationships

We first explore the distribution of the mapped landslides according to their area using non-cumulated histograms. Then we compute frequency-area distributions (FAD), which is commonly used to explore the statistical properties of landslide inventories, to compare it with sub-datasets of the same region or with other inventories previously published (e.g. Valagussa et al., 2019). Frequency-area distributions are plotted considering landslide-area bins versus their corresponding non-cumulative frequency-density values. It has been defined by Malamud et al. (2004) as:

$$f(A_L) = \delta N_L / \delta A_L \quad (3)$$

where δN_L is the number of landslides with areas between A_L and $A_L + \delta A_L$, A_L being the area of landslide and δA_L is the width of a given landslide area class (bin). The obtained distributions are often plotted in a doubly logarithmic plot (Tebbens, 2020 and references therein). Classically applied to landslides inventoried after strong earthquakes or storms, this analysis revealed that the frequency of landslide-sizes displays a nonlinear pattern through landslide scales (see recent review in Tanyaş et al., 2019). For large to medium landslide ranges, the frequency strongly increases with the decreasing landslide areas, mimicking a negative power-law and suggesting fractal scaling. Then at a certain range of medium landslide area, the frequency area distribution generally shows an inflexion and the power-law no longer applies. Finally, a rollover is sometimes observed for the smallest landslide ranges for which the frequency decreases (Tanyaş et al., 2019).

Two main strategies and derivative interpretations of those distributions exist. Malamud et al. (2004) considered the inflexion and the rollover to represent the natural landslide distribution and proposed a fit

of the complete distribution with a three-parameter inverse gamma distribution. A second strategy (e.g. Pánek et al., 2019; Görüm, 2019) is to fit solely the tail of the distribution for medium to large landslides using a power-law above a certain cut-off value of landslide size. For landslide sizes smaller than this cut-off, the inventory is considered as incomplete. Here we applied the second strategy because we chose to map landslides starting from areas of 0.1 km² that biases the distribution for small landslide ranges. Moreover, as our inventory stack a large period of time, it is very probable that some of the smallest landslides were eroded.

First, we applied the method of Clauset et al. (2009) focusing on landslide areas only (non-binned). Using the maximum likelihood estimate, it provides the best fit of a power-law, and its exponent labelled alpha, for the landslide-areas higher than a certain cut-off value. To obtain the power-law fit of a frequency-area distribution, the exponent value is converted using the relation beta = alpha + 1 (Guzzetti et al., 2002; Clauset et al., 2009). We computed the FAD using equation (3) and applied log-spaced bins that respect two conditions: (1) a low number of bins according to the scale-range of the database and (2) to avoid empty bins.

The power-law exponent generally varies between 1.5 and 3.5 (Tanyaş et al., 2019). It reveals how much large landslides contribute to the inventory. A lower value of β value means a more important contribution of large landslides to the total inventory (Van Den Eckhaut et al., 2007).

4. Results

4.1. Landslide inventory, typology and morphology

The landslide inventory obtained in this study is presented in Fig. 6 according to the two typologies and state of activity previously defined. The complete landslide database, including all landslide properties and a kmz file of the landslide polygons, are provided in supplementary data. In total, we have identified and mapped more than a thousand landslides distributed between ca. 15 and 20°S along the Western Central Andes, covering a total area of 3782 km² (Table 1).

Our results show that gravitational destabilizations along the Western Central Andes are dominated by rockslide typology, representing ~86% of the identified landslides while the rest corresponds to rock avalanche type (Fig. 6a). Importantly, we also show that a great majority of landslides (more than 90%) are paleo landslides. The few active

landslides that we identified are located in specific regions such as the upper Colca valley or the Sihuas region (Fig. 6b).

The landslides distribution over the three main geomorphotectonic units of the western Andean flank is summarized in Table 1. The highest percentage of landslides is found along the Western Cordillera and the Central Depression, each holding 76% and 21% of all the mapped landslides, respectively. Regarding the typologies, the Central Depression is strictly dominated by rockslide type (~99%), while the relative amount of rockslide/rock avalanche type is about 20%/80% for both the Coastal Cordillera and the Western Cordillera. We found that the Western Cordillera and the Central Depression present both about 2% of destabilized areas while the Coastal Cordillera have only 0.3% of its areas affected by large landslides.

4.2. Landslide spatial distributions

Results of the Ripley's K Function applied to our landslide database are plotted on Fig. 7 as the Linhom(r) trend for the whole landslide database (n = 1006), the rockslides (n = 866) and the rock avalanches (n = 140) group. Compared to the theoretical Linhom(r) trend for random data, those results indicate that the landslides are not randomly

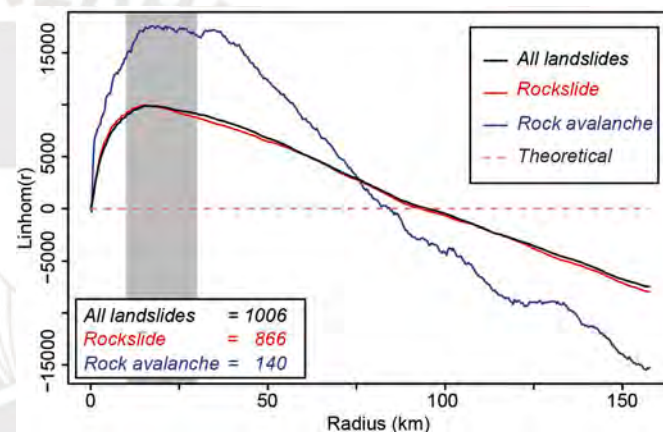


Fig. 7. Results of the Ripley's L-function for our landslide inventory. Grey bar is the range of maximum distribution frequency and is similar for the whole dataset and the two different typologies.

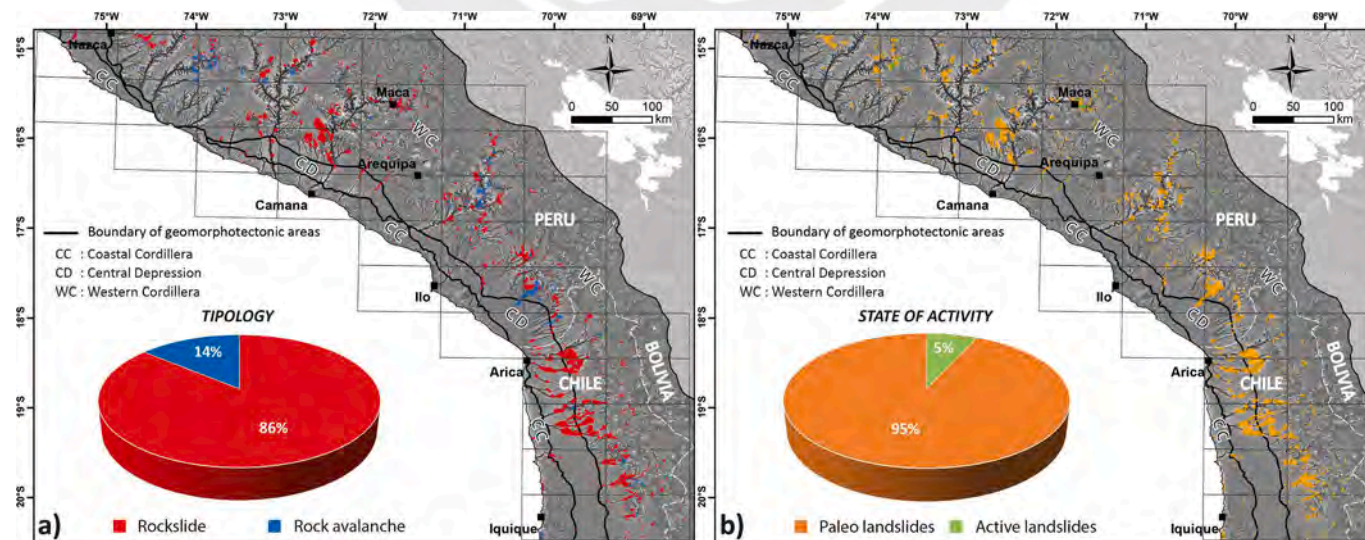


Fig. 6. Landslides inventory along the Western Central Andes between ca. 15 and 20°S. A) Distribution of landslides by typology: rockslide and rock avalanche. B) Landslides distribution according to their state of activity: recent (or active) and paleo. CC: Coastal Cordillera, CD: Central Depression, WC: Western Cordillera. The black grid corresponds to cells of 50 × 100 km that were explored one by one for the landslide mapping (see text for details).

distributed along the western Andean flank, but instead that they display some spatial clustering, with cluster radius up to ca. 100 km. The shape Linhom(r) curves are roughly the same for both the whole dataset and for each individual typology, indicating a similar spatial pattern. The maximum distribution frequency for the different datasets is reached between 10 and 30 km (Fig. 7). This range of radius corresponds to the mean radius of the aggregates of events where the highest number of landslides is found (Goreaud, 2000).

Kernel density maps of landslides were produced using a mean and conservative radius of 20 km (Fig. 8). As expected from the Ripley's K Function analysis, the spatial distribution of large landslides is not homogeneous along the Western Andean flank. Considering the whole landslide database (Fig. 8a), several clusters are revealed, the most significant ones being along the Western Cordillera zone. In particular, we note an important landslide cluster in North Chile at ca. 20°S – 69.5°W between Iquique and Arica latitudes. Three other clusters are located in southernmost Peru, 50 km northeast from Ilo at ca. 17.5°S – 70.5°W, and are aligned along a strike NW-SE. Another cluster is identified 100 km north from Arequipa at ca. 16°S – 71.5°W. This zone corresponds to the upper Colca Valley where numerous landslides have been already reported and studied (e.g. Lacroix et al., 2015). Finally, two smaller clusters are detected at ca. 15°S – 74°W and 15°S – 74.5°W, 50 km east from Nazca (Fig. 8a).

The kernel density distribution of rockslide (Fig. 8b) is similar to the one obtained for the whole database (Fig. 8a) consistently with the fact that rockslide is the dominant typology in this inventory. All the clusters previously listed also exist in the rockslide kernel density map (Fig. 8b).

Then, kernel density of rock avalanche also displays also a clustering mainly located along the Western Cordillera (Fig. 8c). The main clusters of rock avalanches coincide with some of the general clusters at ca. 20°S – 69.5°W, ca. 17.5°S – 70.5°W, and ca. 15°S – 74°W (Fig. 8c). On the other hand, several other clusters identified for the rockslide type do not appear on the kernel density map of rock avalanches. This suggests some specificities of the factors controlling the rock avalanche processes, that may be different from those controlling rockslide occurrences.

4.3. Landslide size distribution

According to the minimal landslide area considered for this inventory (>0.1 km²) all the mapped landslides fall in the category “large landslide”. The histogram of landslide areas (Fig. 9) shows a strong asymmetrical distribution with a decrease of the number of landslides function to the destabilized surface areas. About 93% of the landslides show areas between 0.1 and 10 km² (Fig. 9a). In detail (Fig. 9b), in this range, we still observe this asymmetric trend, the landslide sizes being more represented are the range 0.1–2 km², cumulating 67% of landslides. Fig. 9a evidences the absence of landslides for areas ranging between 80 and 170 km². Beyond 170 km², three giant landslides are recorded (i.e. Chuquibamba, Caquilluco and Lluta). Looking at the cumulative areas, the landslides of the range above 10 km² represent more than 50% of the total landslide area although being less represented (<7%). The 3 largest landslides are contributing alone to 10% of the total cumulative area. In Fig. 9c, it can be observed that the clusters along the Western Cordillera are dominated by landslides with individual areas smaller than 10 km² and located in the headwaters of the main basins and sub-basins. Interestingly, the three largest giant landslides previously mentioned do not belong to the previously described clusters (Fig. 8). Instead, they locate in areas with relatively low to moderate density of landslides. This might suggest that the factors controlling very large landslides are different from those triggering smaller features.

The obtained p-values of the frequency area density distribution of landslides are about ~0.5 (Fig. 10), indicating a good consistency between a power-law model and the tail of our distributions (Clauset et al., 2009). For the whole landslide dataset (ALL), a power-law can be fitted over 2 to 3 orders of magnitude of landslide areas, displaying an

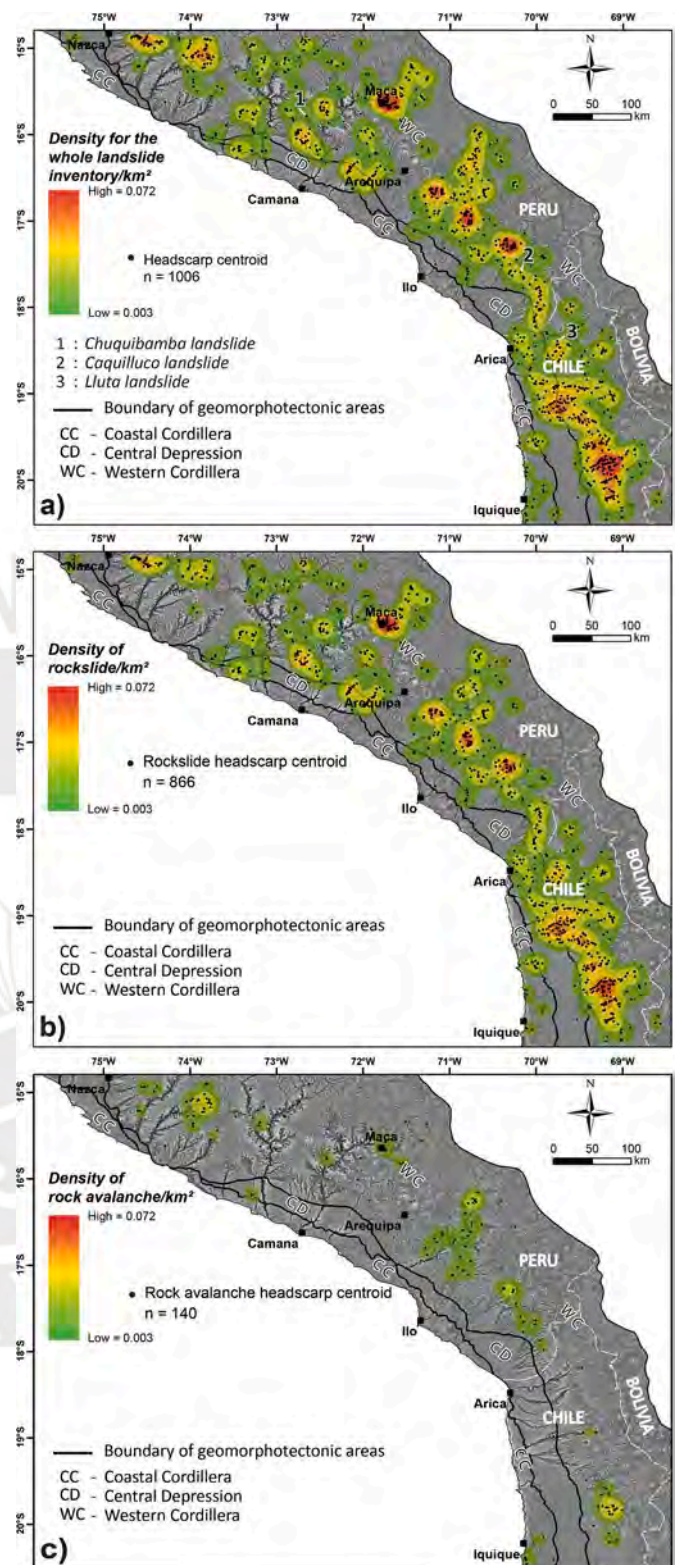


Fig. 8. Spatial distribution analysis of landslides along the western flank of the Central Andes computed through kernel density analysis using a searching radius 20 km for (a) the whole inventory, (b) the rockslide type and (c) the rock avalanche type.

exponent (beta) of 2.31 ± 0.16 and a cut-off value of $4.0 \pm 1.9 \times 10^6$ m². Considering their respective uncertainties, the best-fit parameters of the rockslide and rock avalanche sub datasets remain both almost undifferentiated with those of the whole dataset. We note that the rock

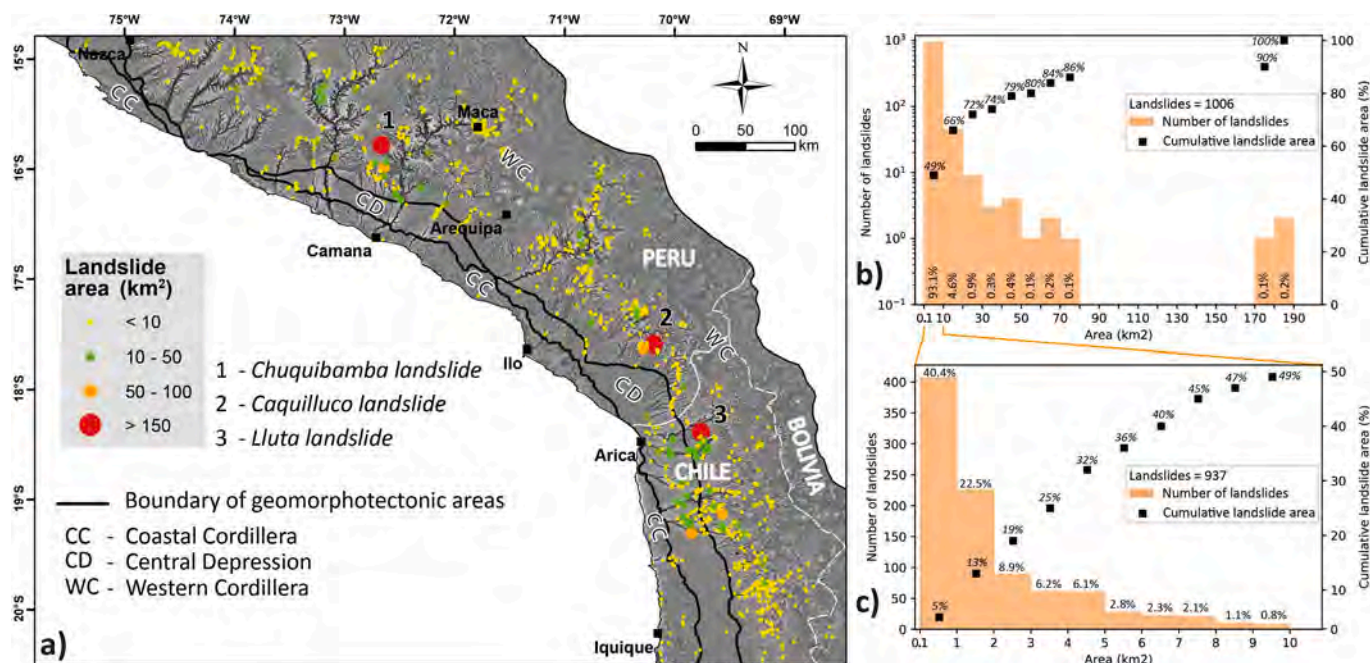


Fig. 9. (a) Spatial distribution of landslides according to their size. Histograms showing the frequency of landslide areas and corresponding cumulative areas in percentage, (b) for the whole dataset using a 10 km² bin width and (c) for the sub-range 0.1–10 km² using a bin of 1 km². CC: Coastal Cordillera, CD: Central Depression, WC: Western Cordillera.

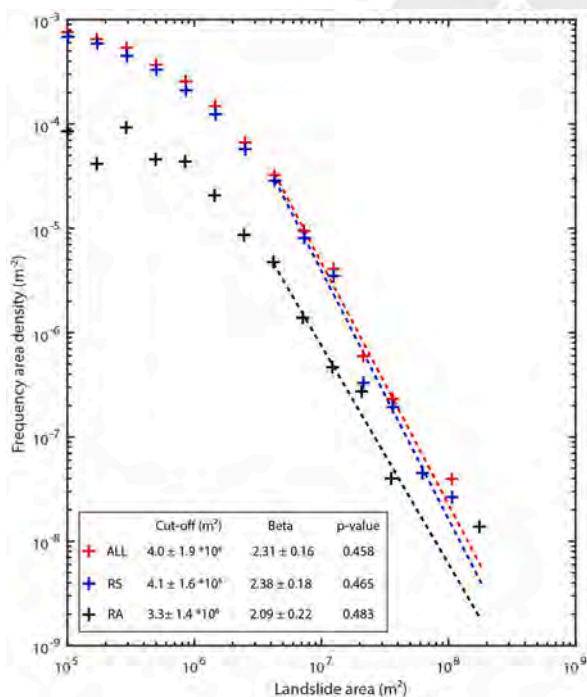


Fig. 10. Frequency area density distributions of landslides in the Central Western Andes given for the whole dataset (ALL) and the sub datasets rockslide (RS) and rock avalanche (RA). The best parameters and associated uncertainties for the power-law fit of the distribution tails are given from the method of Clauset et al. (2009).

avalanche group provides a slight lower power-law exponent (2.09 ± 0.22) which may reflect a dominance of larger landslide features in this typology.

4.4. Landslide morphometry

The analysis of morphometric parameters (ΔH , L and A) associated with the two landslide typologies (rockslide and rock avalanche) provide first order view of the respective landslide dimensions and it highlights some trends (Fig. 11). A correlation ($r = \sim 0.7$) is obtained between landslide height (ΔH) versus landslide run-out (L), for both rockslides and rock avalanches, indicating that higher is the landslide height, longer is the run-out of debris (Fig. 11a). The behavior is similar for both typologies as most of the points overlap. The maximum run-out ~ 41.3 km is obtained for a rock avalanche showing a height of ~ 3.3 km. However, medians reveal the greater size of rock avalanches, which are about two times higher in length and height than the rockslides (Fig. 11a). A good correlation ($r = \sim 0.9$) is also obtained between the landslide run-out (L) and landslide area (A) showing that larger areas are mainly explained by greater landslide lengths (Fig. 11b). Rock avalanches have median areas that are slightly lower than rockslides. Rock avalanches distribution indicates that for the same area than rockslide, rock avalanche debris can reach greater run-out, which is consistent with the highest mobility of granular flows.

5. Interpretation and discussion

5.1. Study limitations

The main limitations of this landslide inventory are the following. 1) Due to the large extension of the study area, it is likely that despite our effort some landslides have been missed during the mapping. We attached a database in .xml format and a file in .kmz format that will serve for future researchers and Peruvian and or Chilean institutions who eventually wish to complete and expand this database. 2) Due to the variability of resolution of the Google Earth images, and sometimes the difficulty leading to the identification of landslide boundaries, we consider that an uncertainty of ca. 100 m applies for the boundary of landslide polygons. This also applies to all the results derived from landslide polygons (landslide area, height, length). 3) In this study, we classified the landslides inventoried into two main categories, rockslide

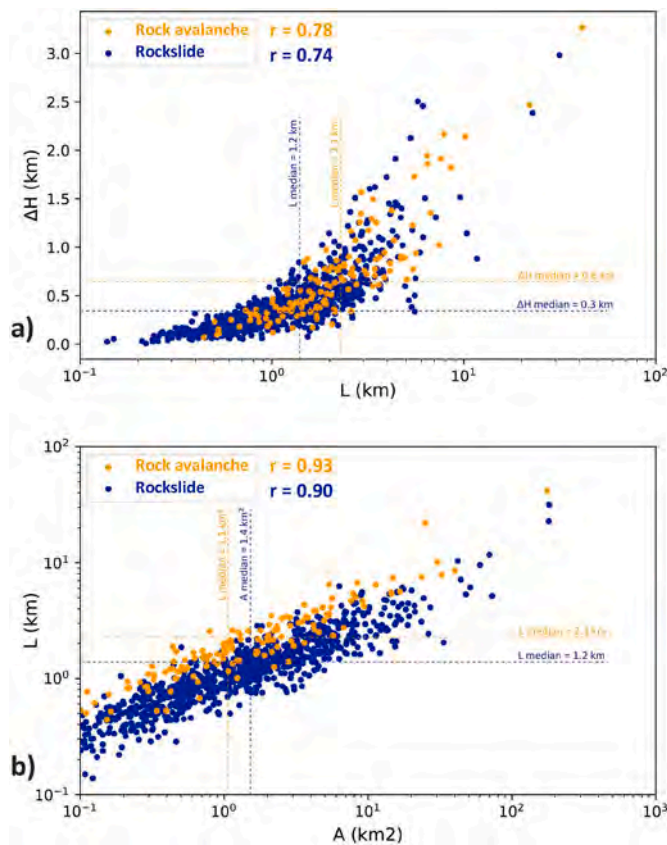


Fig. 11. Morphometric parameters of the landslides for each typology. Relationship between (a) landslide height (ΔH) versus landslide length (L) and (b) landslide length (L) versus landslide area (A). r is the coefficient of correlation of Pearson.

and rock avalanche, as identified by the literature in this region. More details about each landslide feature could be added during future studies, such as to distinguish between planar or rotational failure modes of rockslides to identify their dominant processes. 4) The state of activity of landslides was tentatively defined here according to morphological indices and criteria to differentiate between currently active (or recent) landslides and ancient (or paleo) events. However, the absolute ages of the great majority of the ancient landslides remain unknown and this should be completed with dating methods in future studies. Tracking quantitatively the activity of ongoing landslide failures also would be also very interesting but it requires a dedicated research applying remote sensing methods (e.g. InSAR), applied at a large-scale, which is far beyond the scope of the present study aiming primarily at establishing for the first time a comprehensive inventory of large landslides in the Central Western Andes.

5.2. Landslide controlling factors

In this section we discuss the primary factors that may control or influence landslide susceptibility along the western flank of the Central Andes. We perform comparisons between the landslide frequency distribution and the main settings of this area including the stratigraphy, the relief, the seismotectonic activity and the precipitation patterns.

5.2.1. Landslides versus lithostratigraphy

The type of material (e.g. rock, mud, soil, etc.) is recognized for several decades as one of the first parameters controlling landslide type and their spatial distribution (Varnes, 1978). Several authors further explored the relations between landslides susceptibility and lithology (Hansen, 1984; Guzzetti et al., 1996, 1999; Henriques et al., 2015;

Kumar et al., 2019; Kumar and Gupta, 2021) showing that landslides may vary in typology, dimension and movement rate according to the geomechanical, structural and hydrogeological properties of the material involved (Pradhan and Lee, 2010; Guzzetti et al., 1996). Identifying a specific lithostratigraphic layer prone to landslides can be also useful in terms of hazard management.

Crossing the landslide database with the unified lithostratigraphic map, we explored the relationships between landslides and lithology along the Central Western Andes. In the first order, the results show consistency between the dominant lithologies of the study area and their respective high proportion of landslides (Fig. 12 and Table 2). It concerns mainly: the Quaternary rocks, covering ~27% of the total area and cumulating ~10% of the landslides; the Paleogene-Neogene layers,

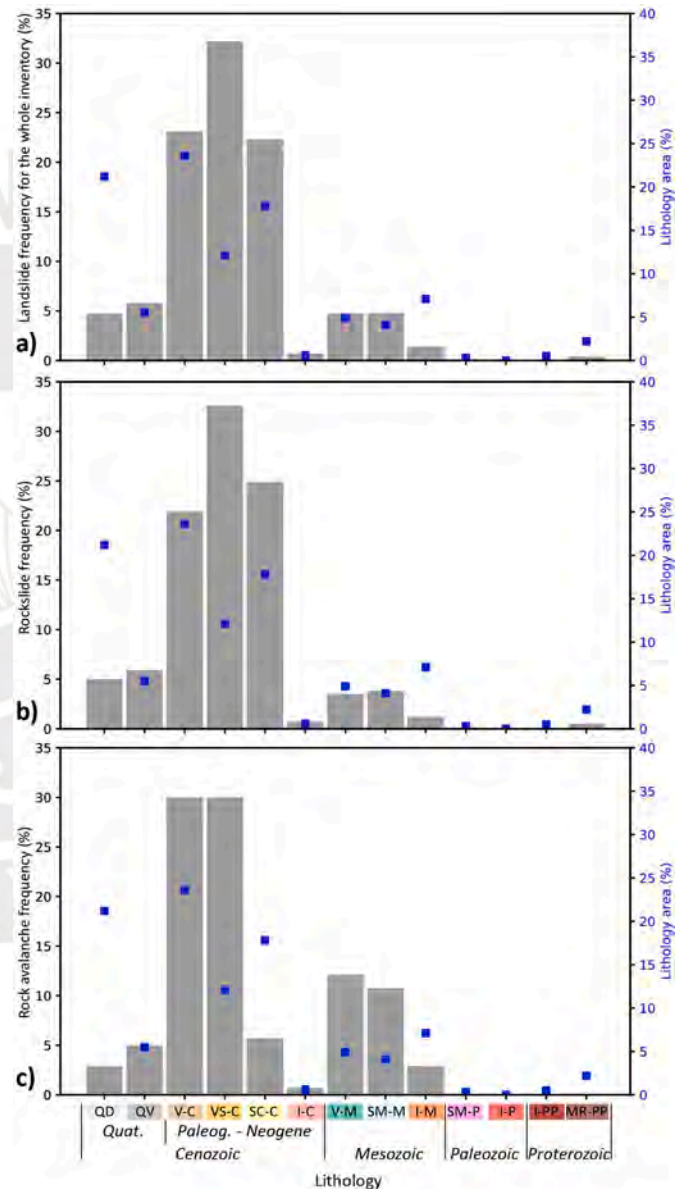


Fig. 12. a) Landslides frequency (in percent) for each lithological unit considering: (a) the whole landslide inventory; (b) the rockslide type and (c) the rock avalanche type. QD: Quaternary deposits (colluvial, fluvial, glacial, eolian); QV: Quaternary volcanic (andesitic lava, volcanic deposits); V-C: Volcanic rock (lava, toba, ignimbrite); SC-C: Sedimentary conglomerate; VS-C: Volcano-Sedimentary (ignimbrite, toba); I-C: Intrusive rocks (granite); V-M: Volcanic rocks (andesite, rhyolite); SM-M: Sedimentary Marine (limestone and shells); I-M: Intrusive (granite); SM-P: Sedimentary marine; I-P: Intrusive (granite); MR-PP: Metamorphic rocks.

Table 1
Main statistics of the landslide inventory.

Geomorphotectonic areas	Surface of Geomorphotectonic area (km ²)	Number of landslides	% of landslides	Type of landslides (Number of landslides = Percentage)	Type of landslides (State of activity = Number of landslides = Percentage)		Total landslide area (km ²)	Percentage covered by landslides (% of total area)
					Rockslide (RS)	Rock avalanche (RA)		
Coastal Cordillera (CC)	15620	26	3%	RS (20 = 77%), RA (6 = 23%)	R = 0 = 0%/P = 20 = 100%	R = 0 = 0%/P = 6 = 100%	52	0.3%
Central Depression (CD)	23198	118	21%	RS (210 = 97%), RA (3 = 3%)	R = 17 = 8%/P = 193 = 92%	R = 0 = 0%/P = 3 = 100%	564	2.4%
Western Cordillera (WC)	136033	862	76%	RS (636 = 85%), RA (131 = 15%)	R = 14 = 11%/P = 117 = 89%	R = 14 = 11%/P = 117 = 89%	3166	2.3%
Total	174851	1006	-	-	-	-	3782	2.2%

State of activity: R: Recent or active, P: Paleo.

Table 2
Statistic of landslides versus lithology.

	Lithology Code	Lithostratigraphic	Study area		Landslides statistic							
			Area km ²	%	All landslides	%	Rockslide	%	Rock avalanche	%		
<i>Cenozoic</i>	Quaternary	QD	Quaternary Deposits: colluvial, fluvial, glacial, eolian	37036	21.2%	47	4.7%	43	5.0%	4	2.9%	
		QV	Quaternary Volcanic: andesitic lava, volcanic deposits	9560	5.5%	58	5.8%	51	5.9%	7	5.0%	
	Paleogene-Neogene	Cumulative			46596	26.7%	105	10.5%	94	10.9%	11	7.9%
		V-C	Volcanic: lava, toba, ignimbrite (Barroso Group)	41126	23.6%	232	23.1%	190	21.9%	42	30.0%	
		SC-C	Sedimentary Conglomerate (Moquegua Formation)	30950	17.8%	224	22.3%	216	24.9%	8	5.7%	
		VS-C	Volcano-Sedimentary: ignimbrite, toba (Huaylillas formation)	21100	12.1%	324	32.2%	282	32.6%	42	30.0%	
<i>Mesozoic</i>	I-C	Intrusive rocks: granite	997	0.6%	7	0.7%	6	0.7%	1	0.7%		
		Cumulative	94173	54.1%	787	78.3%	694	80.1%	93	66.4%		
	V-M	Volcanic: andesite, rhyolite (Toquepala formation)	8583	4.9%	47	4.7%	30	3.5%	17	12.1%		
	SM-M	Sediment Marine: limestone and shells (Yura Group)	7232	4.1%	48	4.8%	33	3.8%	15	10.7%		
	I-M	Intrusive: granite	12350	7.1%	14	1.4%	10	1.2%	4	2.9%		
	Cumulative	28165	16.1%	109	10.9%	73	8.5%	36	25.7%			
<i>Paleozoic</i>	SM-P	Sedimentary Marine	576	0.3%	1	0.1%	1	0.1%	-	-		
	I-P	Intrusive: granite	10	>0.1%	-	-	-	-	-	-		
<i>Proterozoic</i>	Cumulative			586	0.3%	1	0.1%	1	0.1%	-	-	
	I-PP	Intrusive: granite	947	0.5%	-	-	-	-	-	-		
	MR-PP	Metamorphic Rocks	3886	2.2%	4	0.4%	4	0.5%	-	-		
Cumulative			4833	2.7%	4	0.4%	4	0.5%	-	-		

covering ~54% of the total area and cumulating ~78% of the landslides; the Mesozoic rocks, covering ~16% of the total area, are cumulating ~11% of the landslides. For the Paleogene-Neogene layers (Table 2), that are dominant in the region, we found that ~23% of landslides are located in volcanic rocks (V-C) corresponding to undifferentiated lava; ~20% of landslides located in the Sedimentary conglomerate (SC-C) corresponding to the Moquegua Formation (Fig. 12); ~32% of landslides originated in the volcanic sedimentary rocks (VS-C) corresponding to ignimbrites layers. These results logically indicate that the common occurrence of the different lithology in the study area is roughly representative of the landslide distribution. Nevertheless, a higher general susceptibility for Paleogene-Neogene volcano-sedimentary rocks (VS-C; Huaylillas formation) is shown (Fig. 12a). Those ignimbrites cumulate >30% of the inventoried landslides whereas they only represent ~12% of the study area.

Then some particularities emerge when looking at the landslide type distribution in detail. While the rockslides follow the same pattern as previously described (Fig. 12b), we observe that the rock avalanches are

more frequent in the volcanic series (Fig. 12c). The lava, toba and ignimbrite sequences of the Quaternary (QV), Paleogene-Neogene (V-C and VS-C) and Mesozoic (V-M) cumulate more >75% of the rock avalanches (Table 2). This finding can be useful for future studies dedicated to rock avalanche hazard management and call for geotechnical works to better understand why those volcanic sequences are much more prone to rock avalanches. Several previous studies reported, through field observations and data, the strong anisotropy of rock strength of the Paleogene-Neogene volcanic sequences (e.g. García et al., 2004; Strasser and Schlunegger, 2005; Pinto et al., 2008; Irwin et al., 2014) that can be a conditioning factor for landsliding. Indeed, those volcanic sequences are made of weak layers (e.g. unwelded pumice, toba, tuff, volcanic ash, epiclastic layers) alternating with much stronger ones (e.g. lava, pyroclastic flow deposits, ignimbrite) that can have a compressive strength that can be multiple times higher (Irwin et al., 2014). This anisotropy affects also the hydrogeological properties of the material, the weaker layers being much more permeable than the stronger layers (Strasser and Schlunegger, 2005). Three main hypotheses, possibly acting at the

same time, were proposed to explain the slope instabilities in this context: groundwater sapping, flood erosion of strong-over-weak stratigraphy, and the toppling of vertically jointed rock (Irwin et al., 2014).

To the contrary, rock avalanche is almost absent (<5%) from the conglomerates of the Moquegua Formation (Table 2), that is rather affected by rockslides (~25%) (Table 2). This may be due to the fact that this formation has fairly similar overall rock strength, as reported by Graber et al. (2020), in addition to being porous and permeable that can favor the development of listric failure planes and subsequent rockslides

such as the Siguas landslide (Lacroix et al., 2019, 2020).

Finally, we note that the intrusive granite and the metamorphic rocks show particularly low susceptibility to large-scale landslides cumulating only <3% of the total landslide database (Table 2).

5.2.2. Landslides versus relief

In order to explore the link between landslides and relief along the western flank of the Central Andes, we analyzed the relationship between the landslides database and elevation, local relief, mean slope and

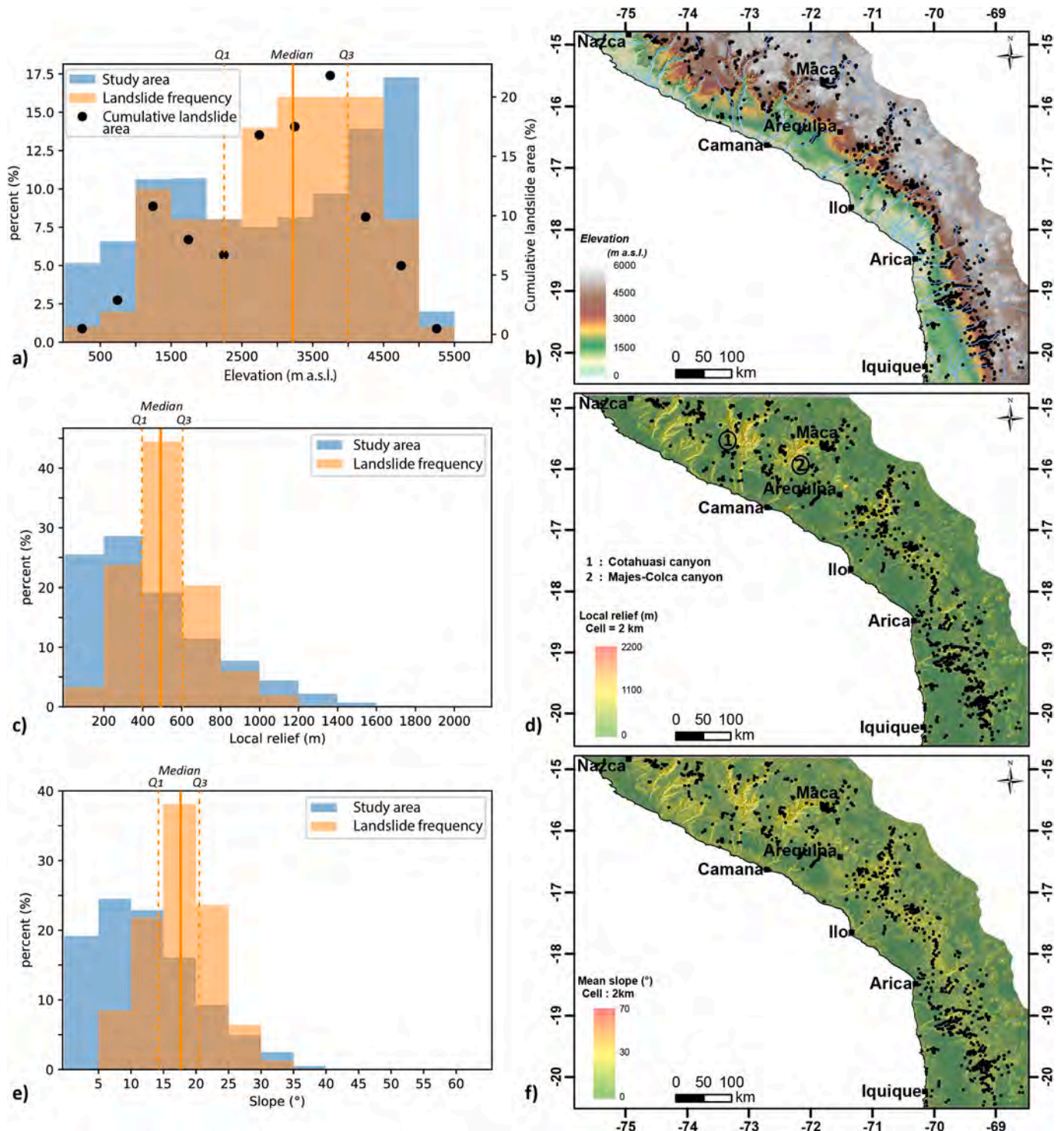


Fig. 13. Landslide statistics versus topography considering (a) and (b) landslide frequency versus elevation, (c) and (d) landslide frequency versus local relief (calculated with cells of 2 × 2 km), (e) and (f) landslide frequency versus slope (calculated with a cell of 2 × 2 km).

river locations. Most of the mapped landslides (~62%) originate in the elevation range between 2500 and 4500 m a.s.l. (Fig. 13a; Fig. 13b) corresponding to the Western Cordillera zone (Fig. 6). Another important range of concentration is between 1000 and 1500 m a.s.l., which corresponds to the Central Depression zone (Fig. 6). Analyzing the cumulative landslide area versus elevation (Fig. 13a; Fig. 13b), we found that >50% of the cumulative landslide areas are between 2500 and 4000 m. a.s.l. (Fig. 13a). This means that landslides are both more frequent and larger in this range of elevation, thus contributing more to the erosion budget. The higher landslide frequency in this elevation range may also be explained by a co-correlation with the lithology of the Western Cordillera unit, that is dominated by volcanic Paleogene-Neogene rocks, that are highly prone to destabilizations as we have previously seen (Fig. 12).

The comparison between landslides and local relief show a unimodal distribution (Fig. 12c). Very few landslides (<5%) are recorded below 200 m of local relief (Fig. 13c). More than 90% of the landslides originate between the local relief ranging from 200 to 800 m (Fig. 13c; Fig. 13d), with the highest frequency peak between 400 and 600 m corresponding to ~50% of the landslides (quartiles Q1 and Q3, Fig. 13c). Then, the frequency of landslides is lower for the greater local relief, <10% of landslides being located in range 800–1000 m. Finally, almost no landslide (<1%) are recorded for the highest local relief ranging from 1000 to 1600 m, despite that they are sharing ~8% of the total study area (Fig. 13c). Those strong reliefs (1000–1600 m) mainly correspond to the deepest and central parts of the Cotahuasi and Majes-Colca canyons, that are almost landslide-free (Fig. 13d). Looking at the mean slope of the study area, the general pattern of landslides distribution previously described is similar, ~80% of the landslides occurring between the range of 10° and 25°, with 50% of those originating on slopes between 14 and 21° (Q1 and Q3 respectively). From slopes >30°, the occurrence of landslides is minimal (<2%).

Those results slightly differ from what is commonly reported from others large landslides inventories, where an asymmetric landslide frequency versus relief (or slope) is often obtained: the highest landslide frequency being concentrated in the highest local relief (e.g. Görüm, 2019; Pánek et al., 2019; Junquera-Torrado et al., 2019). The worldwide compilation of large landslides provided by Korup et al. (2007) also shows this tendency, half of giant landslides occurring in the steepest 15% of mountainous terrain. The higher frequency of landslides in the steepest relief has been related to the threshold hillslope concept (Korup et al., 2007), predicting that above a certain hillslope-angle, or local relief, mountain flanks may fail readily because of the limitation of landscape-scale rock strength (e.g. Schmidt and Montgomery, 1995; Larsen and Montgomery, 2012; Roering, 2012).

In our study area, we interpret the almost absence of large landslides in the areas of extreme relief (1000–1600 m) as due to a lithological effect. Indeed, the deepest sections of the Cotahuasi and Majes-Colca canyons are incised through strong lithologies such as intrusive granite, metamorphic rocks and/or limestone (Fig. 2). Those lithologies having great strength, it is probable that those canyon incisions could reach such depth without occurrence of large to very large landslides. The valley flank erosion in those contexts might be dominated by debris flows, scree, which mobilize smaller volumes of rock that are not documented in this inventory. On the other hand, looking at the general spatial distribution of large landslides at the scale of the study area (Fig. 3d) and excepting the cases the central Cotahuasi and Majes-Colca canyons, we note that the landslides distribution mainly follows the river network and their incisions, where most of the local relief locates (Fig. 3c and d). This suggests that the lithological control on large landslide susceptibility might dominate, whereas the relief would come as secondary.

5.2.3. Landslides versus seismicity and active faults

The link between landslide and seismicity has been well documented by the literature in the Central Western Andes, either for earthquake-

induced landslides activity (e.g. Keefer and Moseley, 2004; Lacroix et al., 2013; Lacroix et al., 2015) or to tentatively link paleo landslide records with the seismogenic context of the Andes (e.g. Mc Phillips et al., 2014; Crosta et al., 2017; Junquera-Torrado et al., 2021). In Fig. 14, we confront the landslide density from this study to the seismicity recorded and the main active faults. To what concern the seismicity related to the subduction, there is no evidence of an increase of landslide density closer to the subduction (Fig. 14). This may be explained by the fact that landslides eventually triggered by subduction earthquakes remain relatively small (e.g. Lacroix et al., 2013). Indeed, the inventory from Lacroix et al. (2013) indicates that the ~866 landslides were triggered during the Pisco mega-earthquake (Mw8.0) were (1) relatively small, with areas ranging between 10^{-4} to 10^{-1} km²; and (2) they mostly corresponded to rockfalls and superficial topples along roads. To explain the fact that a rather low number of landslides were triggered by this Mw8.0 earthquake, while around 10^5 triggered landslides would be predicted for such magnitude (Keefer, 2002), the authors evoked (1) the attenuation of the waves due to the depth of the seismic source and its distance with the relief (>80 km), (2) the climate setting of the region, which long term aridity does not favor soil development and strongly limits the bedrock weathering and the groundwater saturation. Observations were similar for the other historical or recent mega earthquakes of subduction such as the Arequipa Mw8.4 (2001) in southern Peru or the Iquique Mw8.1 (2014) in northern Chile (Fig. 14), for which no observation of triggering, nor reactivation of large landslides (>1 km²) were ever reported (see Borrero 2002; Stirling et al., 2002; Candia et al., 2017). At the plurimillennial-scale, Mc Phillips et al. (2014) suggest a link between landslide triggering and subduction earthquakes in the Pisco region but again it concerns relatively small landslide sizes from 10^{-3} to 10^{-1} km². Those different examples strongly contrast with our mapping showing a thousand of large to giant landslides (areas up to 180 km²) that are well-preserved along the arid Central Western Andes. In summary, given the previous statements, we suggest that while the subduction seismicity can indeed trigger small to moderate superficial landslides and rockfalls, it probably plays a negligible role in forcing large-scale and deep-seated landslides in the arid conditions of the Western Cordillera. On the other hand, frequent and recurrent subduction earthquakes (Mw8 has a recurrence of 100–300 yrs; Chlieh et al., 2011) can contribute to the long-term weathering and rock damage as reported by Keefer and Moseley (2004) observing pervasive coseismic ground cracking and microfracturing of hillslope during the 2001 Arequipa earthquake.

The other source of seismicity along the Central Western Andes is produced by crustal faults activity. In Fig. 14, we confront the landslide density to the neotectonic fault network as well as to the crustal seismicity. As previously stated (62.4), no crustal shallow earthquake of Mw > 6 occurred in this region during the last fifty years. One exception is the region of Maca (Fig. 14) where a seismic swarm (Mw~5) clearly correlates with a landslide cluster. In this region landslides are very specific, developing in lacustrine sediments of a paleolake (Zerathe et al., 2016), where several studies (Lacroix et al., 2015; Lacroix et al., 2019; Bontemps et al., 2018; Gaidzik et al., 2020) already pointed the effect of frequent local earthquakes linked to the volcanic activity.

Another interesting point is the well-marked spatial correlation at large-scale between the landslide clusters and the neotectonics fault pattern (Fig. 14). This correlation can be observed (1) in Peru where several landslides clusters are aligned, from Arequipa to Tacna, with the Incapuquio Fault System (IFS); and (2) in Chile where the West-Vergent Thrust System (WTS) overlaps the main landslide clusters (Fig. 14). Several interpretations can be raised. First, those faults play an important role in the relief building (e.g. Hall et al., 2008), thus the landslide-fault correlation might be indirect, these landslide clusters being rather linked to the relief. Second, those faults are associated with thick damage zones of kilometer width, where the rock strength is decreased and the deep-water circulation along fractures is enhanced. Third, there might be a link between paleoseismicity and paleo landslide

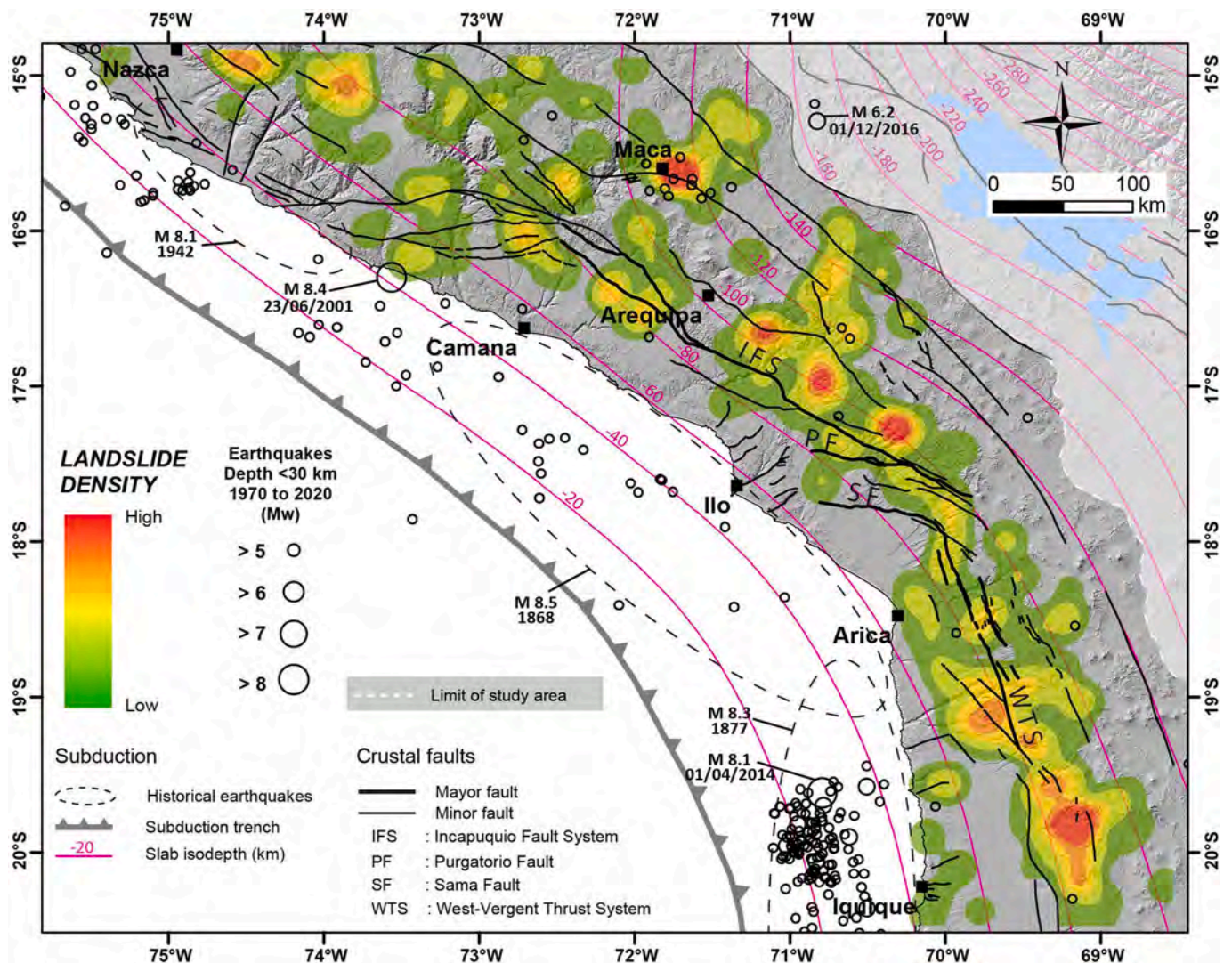


Fig. 14. Landslides density (from Fig. 8a) along the Central Western Andes confronted to the instrumental seismic catalogues for the last 50 years from USGS (earthquakes >Mw5 and depth <30 km), the available historical seismicity and to the main neotectonics crustal faults (see references on the caption of Fig. 3).

triggering. This discussion is speculative because the timing of paleo-earthquakes and paleo landslides remain largely undocumented. However, Benavente et al. (2017b) revealed that tectonic activity occurred along the Purgatorio fault in the last thousand years, showing two ruptures of ~3 and ~2 m of vertical surface offset, equivalent to seismic events of ~Mw7. Evidence of tectonic activities have been also revealed along the ~400 km long IFS (Benavente et al., 2021), where paleo-seismic trenching shows at least 2–3 m of net slip in the last 500 years interpreted as single Mw7.4–7.7 earthquake. Basically, the susceptibility that a bedrock landslide could be triggered or reactivated by an earthquake (Fan et al., 2019) depends on several parameters: (1) the local rock mass properties (linked to the lithology, frequency of fractures and joint discontinuities, etc.) and the level of hillslope stability, and (2) the local ground motion produced by the earthquake that is modulated by the distance from the source and local site effect of wave amplification (topography, lithological contrast, etc.). For crustal earthquakes, relationships between landslide size and ground motion, with larger and deeper landslides associated with higher ground motion, have been reported (Valagussa et al., 2019). Case studies of earthquake-induced landslides inventories after an event of Mw7 and beyond showed that the larger landslides (>0.1 km²) are found generally in areas where the peak ground acceleration exceed 0.5 g, in the close field of the fault (at 10–20 km of the fault) (Valagussa et al., 2019; Junquera-Torrado et al.,

2021). Therefore, it is likely that some of the inventoried large landslides in the western central Andes near the major IFS and WTS faults were triggered by past earthquakes along these faults. There is a need for more research carried out on the timing of both crustal faults and paleo landslides in this part of the Andes.

5.2.4. Landslides versus rainfall

Rainfall is the most frequent forcing and triggering factor of mass movements in mountainous areas. Physical processes related to the addition of water on or below the earth’s surface and their effects on slope instabilities are well described by hydro-mechanical models (e.g., critical soil-state mechanics and rate-and-state friction) developed from numerical theory (Iverson et al., 2000; Baum et al., 2010) coupled to laboratory experiments and confronted to in-situ landslide monitoring and statistics (Glade et al., 2000; Dai and Lee, 2001). The influence of rainfall on landslides differs substantially upon landslide type (typology, dimension, depth), the material involved (mechanical and hydrological properties) and the characteristic of the rainfall (intensity and duration). Groundwater recharge acts as a key factor for slope failures by decreasing the resistance of materials due to pore water pressure variations (Iverson et al., 2000). While shallow landslides (1–2 m depth) are usually triggered a few hours or days after the rainfall onset, depending on the time required for water infiltration and critical pore pressure

increase (Iverson et al., 2000; Baum et al., 2010), larger and deeper landslides (depth >10 m), which are the case of study in this inventory, are more likely to respond to a much longer rainfall duration (months to years). Deep-seated landslides are often in subcritical stability state and subject to long term creep deformation (Lacroix and Amitrano, 2013). These slow movements progressively increase the rock damage and the permeability, reducing the whole landslide strength, until the strain localizes along basal shear failure surfaces (Eberhardt et al., 2004) and a catastrophic collapse can ultimately occur. As shown by recent studies (Handwerger et al., 2019; Agliardi et al., 2020), the conditions for the collapse triggering are often: (1) the presence of a long-term water table water-saturating the basal shear zone; and (2) short-term pore-pressure increase linked to rapid water recharges.

Active landslides are mainly located in the northern part of the study area, where the mean annual rainfall is the highest (Fig. 15a). About 70% of the active landslides are found in areas receiving more than 400 mm/year of rainfall (Fig. 15b). This is consistent with the threshold of 500 mm/yr that have been previously documented for the triggering of the Colca landslides (Zerathe et al., 2016; Bontemps et al., 2018). On the other hand, no active landslides were identified in the desertic south-western part of the study area (Fig. 15). One exception is a group of active anthropic landslides located ~50 km west of Arequipa (Fig. 15; Lacroix et al., 2020; Graber et al., 2021) which develop along the flanks of the Siguas and the Vitor valleys (Fig. 16). They correspond actually to paleo landslides that have been re-activated for ~40 years due to irrigation water input for agricultural lands located just uphill the destabilized valley flanks (Hermann et al., 2012; Araujo et al., 2017; Lacroix et al., 2020). Recently, Graber et al. (2021) demonstrated the critical role played by the anthropic groundwater table rise for those landslide reactivations. Moreover, several other large ancient landslides of the same type are located on the opposite valley flanks and they remain inactive in the absence of irrigation on those sides (Fig. 16). This suggests that the past activation of those ancient landslides could have been linked to climatic conditions that were not the same as nowadays, much more humid, allowing local rainfall and long-term natural recharge of the water table.

At large-scale over the whole study area, the distribution of paleo landslides is not consistent with the current rainfall pattern. They

display an inverse relation with rainfall, drier being the region, higher being the paleo landslide frequency (Fig. 15c). About 70% of the paleo landslides are located in areas that currently receive less than 300 mm/yr of rainfall (Fig. 15c). This distribution might be explained by the fact that drier conditions favor long-term preservation of the paleo-landslide forms. If more humid, younger failures and erosion would have erased those relicts. However, considering the hydro-mechanical conditions required for the triggering of deep-seated landslides, it is on the other hand very improbable that those collapses occurred in such arid conditions. As shown with many examples in the literature (Odin et al., 2018) and the cases of Siguas-Vitor valleys (Graber et al., 2021), the triggering of those large landslides requires a significant recharge of water tables, that are only allowed by perennial rainfall over several months to years. Despite producing very strong storms, the intense rainfalls linked to only few days long El Niño events are very unlikely to feed such groundwater recharge. The rock-hard ground and the lack of vegetation does not allow water absorption and only lead to surficial erosion and flashfloods (Aguilar et al., 2020). On the other hand, ongoing researches on paleoclimate reconstructions in the region show that the Atacama Desert and the Central Western Andes could have experienced more long-term (years to millennial) climate variability during the Pleistocene, as recorded in alluvial fan progradation (Ritter et al., 2019, 2020), paleolake development (Ritter et al., 2019), alluvial terraces sequences (Steffen et al., 2010) and groundwater discharge deposits (Saez et al., 2016). The few giant paleo landslides that were dated have failure ages that are consistent with those events (e.g. Aricota rockslide, ~18 ka with Henrich Stadial (Delgado et al., 2020); the Chuquibamba (~100 ka) and the Caquilluco rock avalanches (100–120 ka) with the Ouki event (Margirier et al., 2015; Zerathe et al., 2017). It is probable that such persistent humid periods have produced sufficient aquifer recharge promoting the triggering of those large landslides. More dating of landslides coupled with local paleo climatic studies are required to disentangle those questions.

6. Conclusion

We report in this paper an original inventory of large landslides (>0.1 km²) along the hyper arid Central Western Andes (latitudes ca.

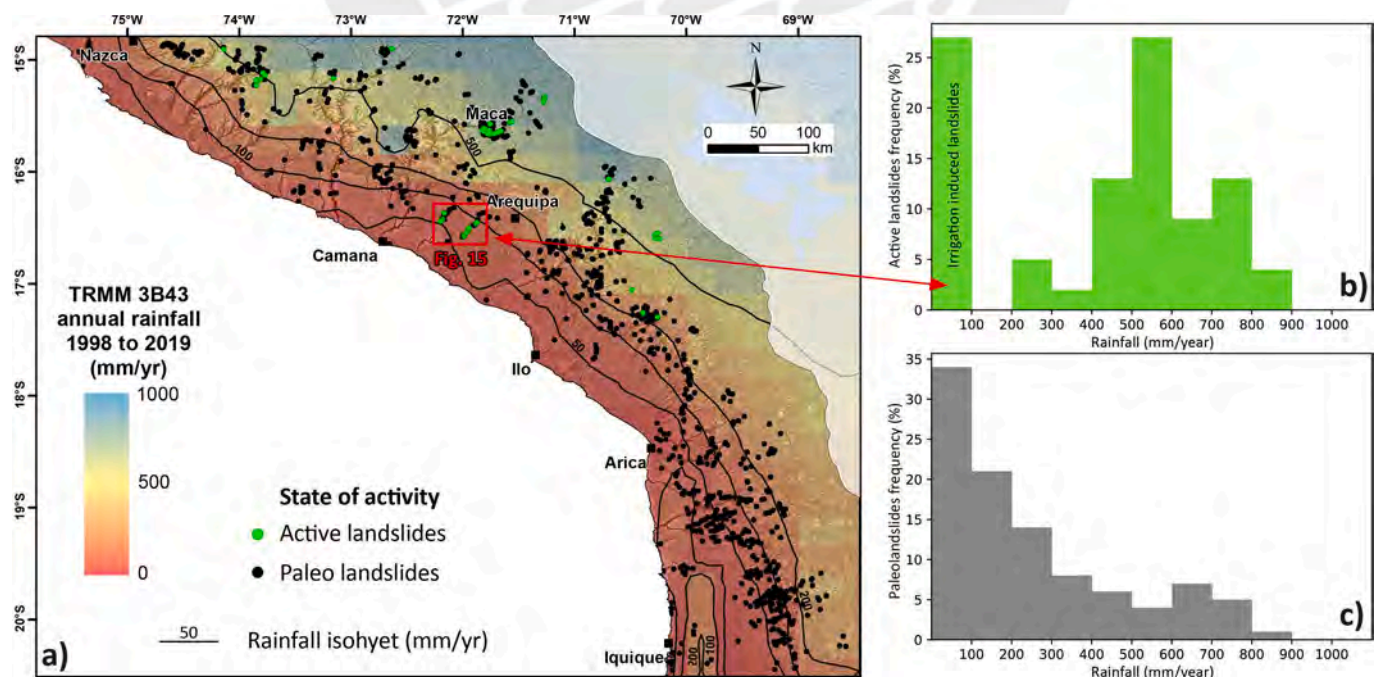


Fig. 15. a) Landslide inventory along the Central Western Andes compared to the mean rainfall of the last two decades; b) and c) Frequency of recent and ancient landslides, respectively, versus rainfall patterns.

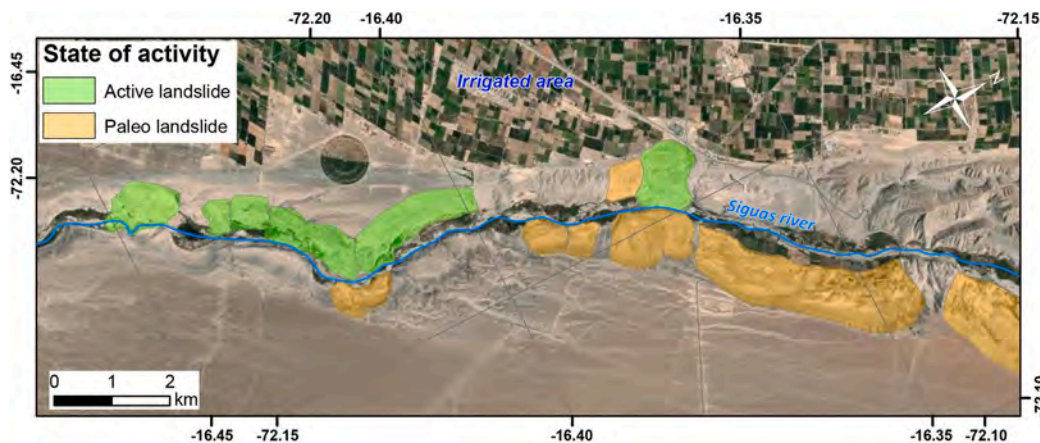


Fig. 16. Anthropogenic reactivation of paleo landslides induced by irrigation for agriculture along (a) the Sigüas valley modified from Graber et al. (2021). See location on Fig. 13. a. The Identification of the landslides reactivated by irrigation comes from Lacroix et al. (2020) while the location of the paleo landslides is from this study. Of importance is the fact that the re-activation of those paleo landslides has need more than 40 years of constant irrigation to increase sufficiently the groundwater level, suggesting that a very different climate must have been acting there at past to produce similar conditions.

15° to 20°S). A systematic mapping of newly identified landslides by satellite images, Google Earth and DEMs analysis, added to the compilation of previous works, allows the inventory of more than a thousand large slope failures. The destabilized area covers ~3782 km² and represents about 2% of the whole study area. Landslide size distribution follows a power-law with an exponent of 2.31 ± 0.16 and a cut-off of 4.0 ± 1.9 km², the largest landslides being up to 180 km² in size. According to the landslide typologies, the rockslides (or coherent landslides) are the dominant failure mode representing 86% of the inventory while the rock avalanches (granular landslides) represent 14%. The statistical analysis of this landslide inventory confronted to topographical, geological constraints of this region provides first-order understanding about the main conditioning factors of slope failures in the Central Western Andes. We identified a combination of a lithological and relief effects on landslide distribution. Ignimbrites of the Paleogene-Neogene (Hualyilllas Formation) concentrate about 30% of the inventoried landslides. The majority of landslides has developed along the flanks of valleys incising through the Western Cordillera. Nevertheless, the deepest areas of two major canyons (Majes-Colca and Cotahuasi) appear less prone to large landslide failure, possibly because they are incising through granite. Finally, we identified a control of fracturing and weathering related to the long-term fault activity suggested by the spatial correlation between landslide clustering and the regional crustal faults network.

This new landslide inventory provides perspectives on the respective roles of climatic and seismotectonic forcing's on the landslide activity in the Central Western Andes. Our dataset suggests that subduction seismicity play a negligible role in forcing those large landslides, while the clustered landslide distribution suggests a more efficient role of crustal seismicity. The majority of the mapped landslides corresponds to paleo landslides (more than 90%), mainly located in the driest areas (rainfall <300 mm/yr). On the other hand, the sole active landslides either anthropic, controlled by water infiltration due to irrigation, or either located in the northern part of the study area receiving rainfall from the Amazonian monsoon (>400 mm/year). We suggest that the triggering of those paleo landslides could not have been possible in the dry conditions of the Central Western Andes, even during strong earthquakes. Alternatively, the period of activity of those paleo landslides may have been related to long-term (years to millennial) climate shift toward more humid conditions during the Pleistocene, and possibly coupled to seismic effect. Next challenging researches will be to add chronological constraints on this landslide inventory to explore possible temporal correlations between periods of landslide activity and external seismic and/or climatic cycles.

CRedit authorship contribution statement

Fabrizio Delgado: Writing – original draft, Methodology,

Investigation, Formal analysis, Conceptualization. **Swann Zerathe:** Writing – review & editing, Validation, Supervision, Project administration, Methodology, Investigation, Funding acquisition, Formal analysis, Conceptualization. **Stéphane Schwartz:** Writing – review & editing, Validation, Supervision, Project administration, Investigation, Funding acquisition. **Bastien Mathieux:** Investigation, Formal analysis. **Carlos Benavente:** Supervision, Project administration.

Declaration of competing interest

The authors declare that they have no known competing financial interests or personal relationships that could have appeared to influence the work reported in this paper.

Acknowledgments

All the data used to perform this study are available in the paper and in the supplemental material. This research is part of the PhD project of Fabrizio Delgado, and also belong to agreement between IRD and INGEMMET. This work was supported by the PhD fellowship program of the EDFPCIG, by the TelluS and Alea Programs of CNRS/INSU and by the CONCYTEC/FONDECYT in the framework of the call Movilizaciones con ECOS Nord-Perú 2019–01 008–2020. We acknowledge the German Aerospace Centre (DLR) for providing the TANDEM-X DEM. We sincerely acknowledge the anonymous Reviewer and German Aguilar, who provided detailed comments that significantly helped to clarify our interpretations and a previous version of this manuscript.

Appendix A. Supplementary data

Supplementary data associated with this article can be found, in the online version, at <https://doi.org/10.1016/j.jsames.2022.103824>.

References

- Acosta, H., Alván, A., Mamani, M., Oviedo, M., Rodríguez, J., 2011. Mapa Geológico del cuadrángulo de La Yarada (37-u), Hoja 37-u-IV. Dirección de Geología Regional (INGEMMET), Lima, Perú. Serie (A), 1 mapa.
- Allmendinger, R.W., Jordan, T.E., Kay, S.M., Isacks, B.L., 1997. The evolution of the Altiplano puna of the central Andes. *Annu. Rev. Earth Planet Sci.* 25, 139–174.
- Armijo, R., Lacassin, R., Coudurier-Curveur, A., Carrizo, D., 2015. Coupled tectonic evolution of Andean orogeny and global climate. *Earth Sci. Rev.* 143, 1–35.
- Audin, L., Bechir, A., 2006. Active tectonics as determinant factor in landslides along the western cordillera? Presented at the congreso peruano de Geología, 13. Lima. Resúmenes extendidos, Sociedad Geológica del Perú xxii, 237–239. October 17–20.
- Audin, L., Hérail, G., Riquelme, R., Darrozes, J., Martinod, J., Font, E., 2003. Geomorphological markers of faulting and neotectonic activity along the western Andean margin, northern Chile. *J. Quat. Sci.* 18 (8), 681–694.
- Audin, L., David, C., Hall, S., Farber, D., Hérail, G., 2006. Geomorphic evidences of recent tectonic activity in the forearc, southern Peru. *Rev. Asoc. Geol. Argent.* 61 (4), 545–554.

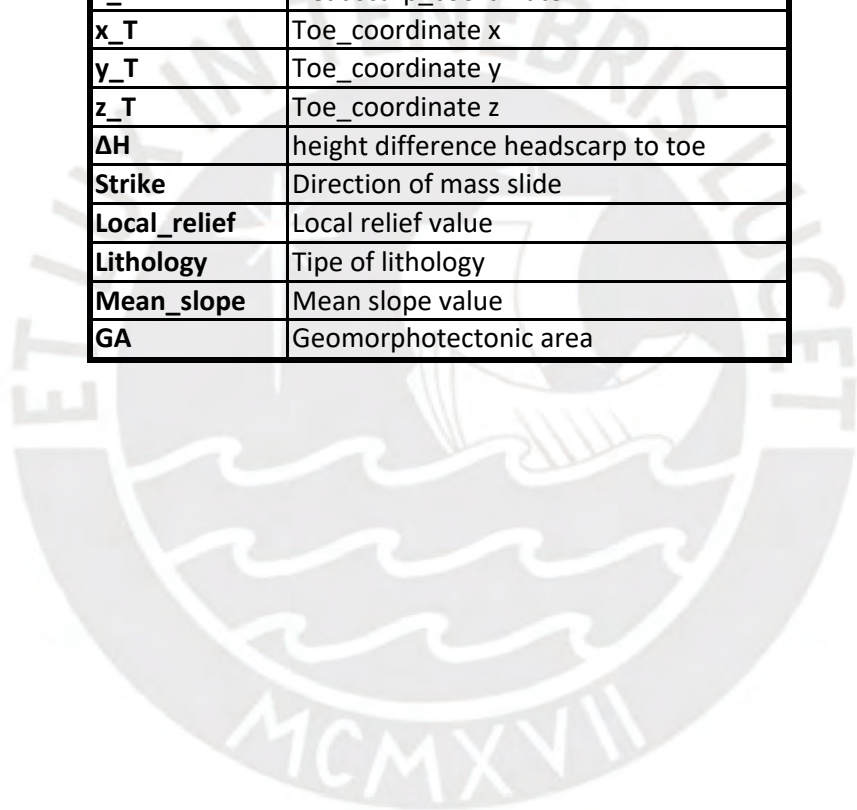
- Audin, L., Lacan, P., Tavera, H., Bondoux, F., 2008. Upper plate deformation and seismic barrier in front of Nazca subduction zone: the Chololo Fault System and active tectonics along the Coastal Cordillera, southern Peru. *Tectonophysics* 459, 174–185.
- Baddeley, A., Turner, R., 2005. spatstat: an R package for analyzing spatial point patterns. *J. Stat. Software* 12 (6), 1–42.
- Baddeley, A.D., Hitch, G.J., Allen, R.J., 2020. A Multicomponent Model of Working Memory. Oxford University Press, Oxford.
- Barrientos, S., Vera, E., Alvarado, P., Monfret, T., 2004. Crustal seismicity in Central Chile. *J. South Am. Earth Sci.* 16, 759–768.
- Bellido, E., 1979. Geología del cuadrángulo de Moquegua. INGEMMET, Boletín, Serie A: Carta Geológica Nacional 15, 78.
- Bellido Bravo, E., Guevara, C., 1963. Geología de los cuadrángulos de Punta de Bonbon y Clemei. Com. Carta Geol. Nacional., Lima bol. no 5.
- Bellon, H., Lefevre, Cl, 1916. Données géochronométriques sur le volcanisme andin dans le Sud du Pérou. Implications volcano-tectoniques. *C. R. Acad. Sci.* 283, 1–4.
- Benavente, C., Audin, L., 2009. Geometría, morfología y peligro sísmico de la falla Purgatorio Mirave - antearco del sur del Perú. *Bol. Soc. Geol. Peru* 103 (15), 15–26.
- Benavente, C., Delgado, G., García, B., Aguirre, E., Audin, L., 2017a. Neotectónica, evolución del relieve y peligro sísmico en la región Arequipa. INGEMMET, Boletín Serie C: Geodin. Ing. Geol. 64, 370.
- Benavente, C., Zerathe, S., Audin, L., Hall, S., Robert, X., Delgado, F., Farber, D.L., ASTER Team., 2017b. Active compressional tectonics in the Andean forearc of southern Peru evidenced by direct ¹⁰Be surface exposure dating of an active fault scarp. *Tectonics* 36 (9), 1662–1678.
- Benavente, C., Rosell, L., García, B., Palomino, A., Aguirre, E., Taibe, E., Robert, X., 2021. Neotectónica de la región Tacna. INGEMMET, Boletín, Serie C: Geodin. Ing. Geol. 84, 171 pp., 1 mapa.
- Besag, J., Diggle, P.J., 1977. Simple Monte Carlo tests for spatial pattern. *J. Roy. Stat. Soc. C-App.* 26, 327–333.
- Blanco, N., Tomlinson, A., 2013. Carta Guatacondo, Región de Tarapacá. Servicio Nacional de Geología y Minería, Carta Geológica de Chile. Serie Geología Básica 156, 1 mapa escala 1:100.000. Santiago.
- Bontemps, N., Lacroix, P., Doin, M.P., 2018. Inversion of deformation fields time-series from optical images, and application to the long term kinematics of slow-moving landslides in Peru. *Rem. Sens. Environ.* 210, 144–158.
- Candia, G., De Pascale, G.P., Montalva, G., Ledezma, C., 2017. Geotechnical aspects of the 2015 Mw 8.3 Illapel megathrust earthquake sequence in Chile. *Earthq. Spectra* 33 (2), 709–728.
- Casquet, C., Fanning, C.M., Galindo, C., Pankhurst, R.J., Rapela, C.W., Torres, P., 2010. The Arequipa massif of Peru: new SHRIMP and isotope constraints on a paleoproterozoic inlier in the grevillian orogen. *J. S. Am. Earth Sci.* 29 (1), 128–142.
- Chlieh, M., Perfettini, H., Tavera, H., Avouac, J.P., Remy, D., Nocquet, J.M., Rolandone, F., Bondoux, F., Gabalda, G., Bonvalot, S., 2011. Interseismic coupling and seismic potential along the Central Andes subduction zone. *J. Geophys. Res. Solid Earth* 116 (B12). <https://doi.org/10.1029/2010JB008166>.
- Clauset, A., Shalizi, C.R., Newman, M.E., 2009. Power-law distributions in empirical data. *SIAM Rev.* 51, 661–703.
- Cobbing, E.J., Pitcher, W.S., 1972. The coastal batholith of central Peru. *J. Geol. Soc.* 128 (5), 421–454.
- Cobbing, E.J., Ozard, J.M., Snelling, N.J., 1977. Reconnaissance geochronology of the crystalline basement rocks of the Coastal Cordillera of southern Peru. *Geol. Soc. Am. Bull.* 88 (2), 241–246.
- Crosta, G.B., Hermanns, R.L., Frattini, P., Valbuzzi, E., Valagussa, A., 2014. Large slope instabilities in northern Chile: inventory, characterisation and possible triggers. In: *Proceedings of the 3rd World Landslide Forum*, 2–6 June 2014, p. 6. https://doi.org/10.1007/978-3-319-04996-0_28. Beijing.
- Crosta, G.B., Paolo, F., Elena, V., Hermanns, R.L., 2015. The Cerro Caquilluco–Cerrillos Negros Giant Rock Avalanches (Tacna, Peru). *IAEG*, p. N159. Torino 2014.
- Crosta, G.B., Hermanns, R.L., Dehls, J., Lari, S., Sepulveda, S., 2017. Rock avalanches clusters along the northern Chile coastal scarp. *Geomorphology* 289, 27–43.
- Delgado, F., Zerathe, S., Audin, L., Schwartz, S., Benavente, C., Carcaillet, J., Bourles, D. L., ASTER Team, 2020. Giant landslide triggerings and paleoprecipitations in the Central Western Andes: the aricota rockslide dam (South Peru). *Geomorphology* 350. <https://doi.org/10.1016/j.geomorph.2019.106932>.
- Dorbath, L., Cisternas, A., Dorbath, C., 1990. Assessment of the size of large and great historical earthquakes in Peru. *Bull. Seismol. Soc. Am.* 80 (3), 551–576.
- Dunai, T.J., Gonzalez López, G.A., Juez-Larré, J., 2005. Oligocene–Miocene age of aridity in the Atacama desert revealed by exposure dating of erosion-sensitive landforms. *Geology* 33 (4), 321–324.
- Eberhardt, E., Stead, D., Coggan, J.S., 2004. Numerical analysis of initiation and progressive failure in natural rock slopes—the 1991 Randa rockslide. *Int. J. Rock Mech. Min. Sci.* 41, 69–87. [https://doi.org/10.1016/S1365-1609\(03\)00076-5](https://doi.org/10.1016/S1365-1609(03)00076-5).
- Evenstar, L.A., Mather, A.E., Hartley, A.J., Stuart, F.M., Sparks, R.S.J., Cooper, F.J., 2017. Geomorphology on geologic timescales: evolution of the late cenozoic pacific paleosurface in northern Chile and southern Peru. *Earth Sci. Rev.* 171, 1–27.
- Fariás, M., Charrier, R., Comte, D., Martinod, J., Hérail, G., 2005. Late Cenozoic deformation and uplift of the western flank of the Altiplano: evidence from the depositional, tectonic, and geomorphologic evolution and shallow seismic activity (northern Chile at 19°30'S). *Tectonics* 24, 1–27.
- Froude, M.J., Petley, D.N., 2018. Global fatal landslide occurrence from 2004 to 2016. *Nat. Hazards Earth Syst. Sci.* 18 (8), 2161–2181.
- Gaidzik, K., Zaba, J., Ciesielczuk, J., 2020. Tectonic control on slow-moving andean landslides in the Colca valley, Peru. *J. Mt. Sci.* 17 (8), 1807–1825.
- García, M., Gardeweg, M., Clavero, J., Hérail, G., 2004. Hoja Arica, Región de Tarapacá. Servicio Nacional de Geología y Minería, Carta Geológica de Chile. Serie Geología Básica 84, 150, 1 mapa escala 1:250.000.
- García, M., Fuentes, G., Riquelme, F., 2013. Carta Miñimi, Regiones de Arica y Parinacota y de Tarapacá. Servicio Nacional de Geología y Minería, Carta Geológica de Chile. Serie Geología Básica 157, 49 pp., 1 mapa escala 1:100.000.
- Gariano, S.L., Guzzetti, F., 2016. Landslides in a changing climate. *Earth Sci. Rev.* 162, 227–252.
- Garzone, C.N., Hoke, G.D., Libarkin, J.C., Withers, S., MacFadden, B., Eiler, J., Ghosh, P., Mulch, A., 2008. Rise of the Andes. *Science* 320, 1304–1307.
- Gayo, E.M., Latorre, C., Jordan, T.E., Nester, P.L., Estay, S.A., Ojeda, K.F., Santoro, C.M., 2012. Late Quaternary hydrological and ecological changes in the hyperarid core of the northern Atacama Desert (~ 21 S). *Earth Sci. Rev.* 113 (3–4), 120–140.
- González, G., Salazar, P., Loveless, J.P., Allmendinger, R.W., Aron, F., Shrivastava, M., 2015. Upper plate reverse fault reactivation and the unclamping of the megathrust during the 2014 northern Chile earthquake sequence. *Geology* 43 (8), 671–674.
- Goreaud, F., 2000. Apports de l'analyse de la structure spatiale en forêt tempérée à l'étude et la modélisation des peuplements complexes. Ph.D. thesis. Ecole Nationale du Génie Rural, des Eaux et des Forêts, France.
- Görüm, T., 2019. Tectonic, topographic and rock-type influences on large landslides at the northern margin of the Anatolian Plateau. *Landslides* 16, 333–346.
- Gunnell, Y., Thouret, J.C., Bricau, S., Carter, A., Gallagher, K., 2010. Low-temperature thermochronology in the Peruvian Central Andes: implications for long-term continental denudation, timing of plateau uplift, canyon incision and lithosphere dynamics. *J. Geol. Soc.* 167 (4), 803–815.
- Guzzetti, F., Cardinali, M., Reichenbach, P., 1996. The influence of structural setting and lithology on landslide type and pattern. *Environ. Eng. Geosci.* 2 (4), 531–555.
- Guzzetti, F., Carrara, A., Cardinali, M., Reichenbach, P., 1999. Landslide hazard evaluation: a review of current techniques and their application in a multi-scale study, Central Italy. *Geomorphology* 31 (1–4), 181–216.
- Guzzetti, F., Malamud, B.D., Turcotte, D.L., Reichenbach, P., 2002. Power-law correlations of landslide areas in central Italy. *Earth Planet Sci. Lett.* 195, 169–183.
- Guzzetti, F., Mondini, A.C., Cardinali, M., Fiorucci, F., Santangelo, M., Chang, K.T., 2012. Landslide inventory maps: new tools for an old problem. *Earth Sci. Rev.* 112, 42–66.
- Hall, S.R., Farber, D.L., Audin, L., Finkel, R.C., Mériaux, A.S., 2008. Geochronology of pediment surfaces in southern Peru: implications for Quaternary deformation of the Andean forearc. *Tectonophysics* 459 (1), 186–205. <https://doi.org/10.1016/j.tecto.2007.11.073>.
- Hansen, A., 1984. Engineering geomorphology: the application of an evolutionary model of Hong Kong's terrain. *Z. Geomorphol.* 51, 39–50.
- Haque, U., Da Silva, P.F., Devoli, G., Pilz, J., Zhao, B., Khaloua, A., Glass, G.E., 2019. The human cost of global warming: deadly landslides and their triggers (1995–2014). *Sci. Total Environ.* 682, 673–684.
- Hartley, A.J., Chong, G., 2002. Late pliocene age for the Atacama Desert: implications for the desertification of western south America. *Geology* 30 (1), 43–46.
- Haschke, M., Günther, A., Melnick, D., Echlter, H., Reutter, K.J., Scheuber, E., Oncken, O., 2006. Central and southern Andean tectonic evolution inferred from arc magmatism. In: *The Andes*. Springer, Berlin, Heidelberg, pp. 337–353.
- Henriques, C., Zézere, J.L., Marques, F., 2015. The role of the lithological setting on the landslide pattern and distribution. *Eng. Geol.* 189, 17–31.
- Houston, J., Hartley, A.J., 2003. The Central Andean west-slope rainshadow and its potential contribution to the origin of hyper-aridity in the Atacama Desert. *Int. J. Climatol.* 23, 1453–1464.
- Irwin III, R.P., Tooth, S., Craddock, R.A., Howard, A.D., de Latour, A.B., 2014. Origin and development of theater-headed valleys in the Atacama Desert, northern Chile: morphological analogs to martian valley networks. *Icarus* 243, 296–310.
- Isacks, B.L., 1988. Uplift of the central Andean plateau and bending of the Bolivian orocline. *J. Geophys. Res.* 93, 3211–3231.
- Jacay, J., Sempere, T., Husson, L., Pino, A., 2002. Structural characteristics of the Incapucuy fault system, southern Peru. In: *V International Symposium on Andean Geodynamics ISAG*, Extended Abstracts, pp. 319–321. Toulouse, France.
- James, D.E., Sacks, I.S., 1999. Cenozoic formation of the Central Andes: a geophysical perspective. In: Skinner, B.J. (Ed.), *Geology and Ore Deposits of the Central Andes*, vol. 7. Society of Economic Geologists, Special Publication, pp. 1–25.
- Junquera-Torrado, S., Moreiras, S.M., Sepúlveda, S.A., 2019. Distribution of landslides along the Andean active orogenic front (Argentinean Precordillera 31°–33° S). *Quat. Int.* 512, 18–34.
- Junquera-Torrado, S., Moreiras, S.M., Rodríguez-Peces, M.J., Sepúlveda, S.A., 2021. Linking earthquake-triggered paleolandslides to their seismic source and to the possible seismic event that originated them in a portion of the Argentine Precordillera (31°–33° S). *Nat. Hazards* 106, 43–78. <https://doi.org/10.1007/s11069-020-04447-1>.
- Keefer, D.K., 2002. Investigating landslides caused by earthquakes—a historical review. *Surv. Geophys.* 23 (6), 473–510.
- Keefer, D.K., Moseley, M.E., 2004. Southern Peru desert shattered by the great 2001 earthquake: implications for paleoseismic and paleo-El Niño–Southern Oscillation records. *Proc. Natl. Acad. Sci. Unit. States Am.* 101 (30), 10878–10883.
- Keefer, D.K., Moseley, M.E., DeFrance, S.D., 2003. A 38 000-year record of floods and debris flows in the Ilo region of southern Peru and its relation to El Niño events and great earthquakes. *Palaeogeogr. Palaeoclimatol. Palaeoecol.* 194 (1–3), 41–77.
- Kelleher, J.A., 1972. Rupture zones of large South American earthquakes and some predictions. *J. Geophys. Res.* 77 (11), 2087–2103.
- Korup, O., Clague, J.J., Hermanns, R.L., Hewitt, K., Strom, A.L., Weidinger, J.T., 2007. Giant landslides topography and erosion. *Earth Planet Sci. Lett.* 261, 578–589.

- Kumar, S., Gupta, V., 2021. Evaluation of spatial probability of landslides using bivariate and multivariate approaches in the Goriganga valley, Kumaun Himalaya, India. *Nat. Hazards* 1–28.
- Kumar, V., Gupta, V., Jamir, I., Chatteraj, S.L., 2019. Evaluation of potential landslide damming: case study of Urni landslide, Kinnaur, Satluj valley, India. *Geosci. Front.* 10 (2), 753–767.
- Lacroix, P., Amtrano, D., 2013. Long-term dynamics of rockslides and damage propagation inferred from mechanical modeling. *J. Geophys. Res.: Earth Surf.* 118 (4), 2292–2307.
- Lacroix, P., Zavala, B., Berthier, E., Audin, L., 2013. Supervised method of landslide inventory using panchromatic SPOT5 images and application to the earthquake-triggered landslides of Pisco (Peru, 2007, Mw8.0). *Rem. Sens.* 5 (6), 2590–2616.
- Lacroix, P., Berthier, E., Taïpe, E., 2015. Earthquake-driven acceleration of slow-moving landslides in the Colca valley, Peru, detected from Pleiades images. *Rem. Sens. Environ.* 165, 148–158. <https://doi.org/10.1016/j.rse.2015.05.010>.
- Lacroix, P., Araujo, G., Hollingsworth, J., Taïpe, E., 2019. Self-entrainment motion of a slow-moving landslide inferred from landsat-8 time series. *J. Geophys. Res.: Earth Surf.* 124 (5), 1201–1216.
- Lacroix, P., Dehecq, A., Taïpe, E., 2020. Irrigation-triggered landslides in a Peruvian desert caused by modern intensive farming. *Nat. Geosci.* 13 (1), 56–60.
- Larsen, I.J., Montgomery, D.R., 2012. Landslide erosion coupled to tectonics and river incision. *Nat. Geosci.* 5 (7), 468–473.
- Lavenu, A., 2005. Fallas Cuaternarias de Chile, vol. 62. Servicio Nacional de Geología y Minería, Boletín, Santiago, p. 71.
- Lavenu, A., Thiele, R., Mächette, M., Dart, R., Bradley, L., Haller, K., 2000. Maps and Database of Quaternary Faults in Bolivia and Chile, p. 50. U.S. Geological Survey Open-File Report 00-283.
- Leyton, F., Ruiz, S., Sepúlveda, S., 2010. Reevaluación del peligro sísmico probabilístico en Chile Central. *Andean Geol.* 37 (2), 455–472. <https://doi.org/10.5027/andgeoV37n2-a11>.
- Litty, C., Duller, R., Schlunegger, F., 2016. Paleohydraulic reconstruction of a 40 ka-old terrace sequence implies that water discharge was larger than today. *Earth Surf. Process. Landforms* 41 (7), 884–898.
- Malamud, B.D., Turcotte, D.L., Guzzetti, F., Reichenbach, P., 2004. Landslides, earthquakes, and erosion. *Earth Planet Sci. Lett.* 229 (1–2), 45–59.
- Mamani, M., Tassara, A., Wörner, G., 2008. Composition and structural control of crustal domains in the central Andes. *G-cubed* 9 (3). <https://doi.org/10.1029/2007GC001925>.
- Mamani, M., Wörner, G., Sempere, T., 2009. Geochemical variations in igneous rocks of the Central Andean Orocline (13° to 18°S): tracing crustal thickening and magma generation through time and space. *Geol. Soc. Am. Bull.* 122, 162–182. <https://doi.org/10.1130/B26538.1>.
- Mamani, M., Navarro, P., Carlotto, V., Acosta, H., Rodríguez, J., Jaimes, F., Santos, A., Rodríguez, R., Chavez, L., Cueva, E., Cereceda, C., 2010. Arcos magmáticos meso-cenozoicos del Perú. In: XV Congreso Peruano de Geología, Cusco. Sociedad Geológica del Perú, Resúmenes Extendidos, pp. 563–566.
- Mamani, M., Rodríguez, R., Acosta, H., Jaimes, F., Navarro, P., Carlotto, V., 2012. Características litológicas y geoquímicas más resaltantes de los arcos magmáticos del Perú desde el Ordovícico. XVI Congreso Peruano de Geología, p. 5 resúmenes extendidos.
- Marc, O., Stumpf, A., Malet, J.P., Gosset, M., Uchida, T., Chiang, S.H., 2018. Towards a global database of rainfall-induced landslide inventories: first insights from past and new events. *Earth Surf. Dyn. Discuss.* <https://doi.org/10.5194/esurf-2018-20>.
- Margirier, A., Audin, L., Carcaillet, J., Schwartz, S., 2015. Tectonic and climatic controls on the Chuquibamba landslide (western Andes, southern Peru). *Earth Surf. Dynam. Discuss.* 2, 1129–1153.
- Mariño, J., Samaniego, P., Manrique, N., Valderrama, P., Roche, O., de Vries, B.V.W., Liorzou, C., 2021. The Tutupaca volcanic complex (Southern Peru): eruptive chronology and successive destabilization of a dacitic dome complex. *J. S. Am. Earth Sci.* 109, 103227.
- Martinod, J., Gérault, M., Husson, L., Regard, V., 2020. Widening of the Andes: an interplay between subduction dynamics and crustal wedge tectonics. *Earth Sci. Rev.* 204, 103170.
- Mather, A.E., Hartley, A.J., Griffiths, J.S., 2014. The giant coastal landslides of Northern Chile: tectonic and climate interactions on a classic convergent plate margin. *Earth Planet Sci. Lett.* 388, 249–256.
- Medwedeff, W.G., Clark, M.K., Zekkos, D., West, A.J., 2020. Characteristic landslide distributions: an investigation of landscape controls on landslide size. *Earth Planet Sci. Lett.* 539, 116203.
- Monge, R., Cervantes, J., 2000. Memoria explicativa de la geología del cuadrángulo de Pachía (36v) y Palca (36x). Dirección de Geología Regional del INGEMMET, Lima, Perú, p. 11.
- Montgomery, D.R., 2001. Slope distributions, threshold hillslopes, and steady-state topography. *Am. J. Sci.* 301 (4–5), 432–454.
- Morandé, F., Gallardo, F., Farías, M., 2015. Carta Guaviña, Región de Tarapacá. Servicio Nacional de Geología y Minería, Carta Geológica de Chile. Serie Geología Básica 177, 1 mapa escala 1:100.000.
- Mukasa, S.B., Henry, D.J., 1990. The San Nicolas batholith of coastal Peru: early Palaeozoic continental arc or continental rift magmatism? *J. Geol. Soc.* 147 (1), 27–39.
- New, M., Lister, D., Hulme, M., Makin, I., 2002. A high-resolution data set of surface climate over global land areas. *Clim. Res.* 21 (1), 1–25.
- Newell, N.D., 1945. Investigaciones geológicas en las zonas circunvecinas al lago Titicaca. Boletín Sociedad Geológica del Perú 18, 44–68.
- Pánek, T., 2019. Landslides and Quaternary climate changes—the state of the art. *Earth Sci. Rev.* 196, 102871.
- Pánek, T., Brežný, M., Kapustová, V., Lenart, J., Chalupa, V., 2019. Large landslides and deep-seated gravitational slope deformations in the Czech Flysch Carpathians: new LiDAR-based inventory. *Geomorphology* 346, 106852.
- Pardo-Casas, F., Molnar, P., 1987. Relative motion of the Nazca (farallon) and south-American plates since late cretaceous time. *Tectonics* 6, 233–248.
- Petley, D., 2012. Global patterns of loss of life from landslides. *Geology* 40 (10), 927–930.
- Pinto, L., Hérail, G., Charrier, R., 2004. Sedimentación sintectónica asociada a las estructuras Neógenas en la Precordillera de la zona de Moquella (19°15'S, norte de Chile). *Rev. Geol. Chile* 31 (1), 19–44. <https://doi.org/10.5027/andgeoV31n1-a02>.
- Pinto, L., Hérail, G., Fontan, F., de Parseval, 2007. Neogene erosion and uplift of the western edge of the Andean Plateau as determined by detrital heavy mineral analysis. *Sediment. Geol.* 195, 217–237.
- Pinto, L., Hérail, G., Sepúlveda, S.A., Krop, P., 2008. A Neogene giant landslide in Tarapacá, northern Chile: a signal of instability of the westernmost Altiplano and palaeoseismicity effects. *Geomorphology* 102 (3–4), 532–541.
- Placzek, C.J., Quade, J., Patchett, P.J., 2013. A 130 ka reconstruction of rainfall on the Bolivian Altiplano. *Earth Planet Sci. Lett.* 363, 97–108.
- Pradhan, B., Lee, S., 2010. Landslide susceptibility assessment and factor effect analysis: backpropagation artificial neural networks and their comparison with frequency ratio and bivariate logistic regression modelling. *Environ. Model. Software* 25 (6), 747–759.
- Proyecto Multinacional Andino, P.M.A.G., 2009. Geociencia para las Comunidades Andinas. Atlas de deformaciones cuaternarias de los Andes. Servicio Nacional de Geología y Minería, Publicación Geológica Multinacional 7, 320 pp., 1 mapa en CD. Santiago.
- Quade, J., Rech, J.A., Betancourt, J.L., Latorre, C., Quade, B., Rylander, K.A., Fisher, T., 2008. Paleowetlands and regional climate change in the central Atacama Desert, northern Chile. *Quat. Res.* 69 (3), 343–360.
- Quang, C.X., Clark, A.H., Lee, J.K., Hawkes, N., 2005. Response of superege processes to episodic Cenozoic uplift, pediment erosion, and ignimbrite eruption in the porphyry copper province of southern Peru. *Econ. Geol.* 100 (1), 87–114.
- R Core Team, 2019. R: A Language and Environment for Statistical Computing. R Foundation for Statistical Computing, Vienna, Austria. <https://www.R-project.org/>.
- Ripley, B.D., 1977. Modelling spatial patterns. *J. Roy. Stat. Soc. B* 39 (2), 172–212.
- Ritter, B., Binnie, S.A., Stuart, F.M., Wennrich, V., Dunai, T.J., 2018. Evidence for multiple Plio-Pleistocene lake episodes in the hyperarid Atacama Desert. *Quat. Geochronol.* 44, 1–12.
- Ritter, B., Wennrich, V., Medialdea, A., Brill, D., King, G., Schneiderwind, S., Niemann, K., Fernández-Galego, E., Diederich, J., Rolf, C., Bao, R., Melles, M., Dunai, T.J., 2019. Climatic fluctuations in the hyperarid core of the Atacama Desert during the past 215 ka. *Sci. Rep.* 9 (1), 1–13.
- Rivera, M., Samaniego, P., Vela, J., Le Penec, J.L., Guillou, H., Paquette, J.L., Liorzou, C., 2020. The eruptive chronology of the Yucamane-Calientes compound volcano: a potentially active edifice of the Central Andes (southern Peru). *J. Volcanol. Geoth. Res.* 393, 106787.
- Roering, J., 2012. Landslides limit mountain relief. *Nat. Geosci.* 5 (7), 446–447.
- Roperch, P., Sempere, T., Macedo, O., Arriagada, C., Fornari, M., Tapia, C., García, M., Laj, C., 2006. Counterclockwise rotation of late Eocene-Oligocene fore-arc deposits in southern Peru and its significance for oroclinal bending in the central Andes. *Tectonics* 25 (3), 1–29. <https://doi.org/10.1029/2005TC001882>.
- Salinas, E., 1985. Evolución paleogeográfica del Sur del Perú a la luz de los métodos de análisis sedimentológico de las series del Departamento de Tacna. Tesis de grado. UNSA, Arequipa.
- Sánchez-Núñez, J.M., Gómez, J.C., Macías, J.L., Arce, J.L., 2020. Pleistocene rock avalanche, damming, and secondary debris flow along the Cotahuasi river, Peru. *J. S. Am. Earth Sci.* 104, 102901.
- Santibáñez, I., Cembrano, J., García, T., Costa, C., Yañez, G., Marquardt, C., Arancibia, G., González, G., 2019. Crustal faults in the Chilean Andes: geological constraints and seismic potential. *Andean Geol.* 46, 32–65.
- Schildgen, T.F., Hodges, K.V., Whipple, K.X., Reiners, P.W., Pringle, M.S., 2007. Uplift of the western margin of the Andean plateau revealed from canyon incision history, southern Peru. *Geology* 35, 523–526.
- Schildgen, T.F., Hodges, K.V., Whipple, K.X., Pringle, M.S., van Soest, M., Cornell, K., 2009. Late Cenozoic structural and tectonic development of the western margin of the central Andean Plateau in southwest Peru. *Tectonics* 28, TC4007. <https://doi.org/10.1029/2008TC002403>.
- Schildgen, T.F., Balco, G., Schuster, G., 2010. Canyon incision and knickpoint propagation recorded by apatite ⁴He/³He thermochronometry. *Earth Planet Sci. Lett.* 293, 377–387.
- Schmidt, K.M., Montgomery, D.R., 1995. Limits to relief. *Science* 270 (5236), 617–620.
- Sobolev, S.V., Babeyko, A.Y., 2005. What drives orogeny in the Andes? *Geology* 33 (8), 617–620.
- Somoza, R., 1998. Updated Nazca (Farallon) - south America relative motions during the last 40 My: implications for mountain building in the central Andean region. *J. S. Am. Earth Sci.* 11, 211–215.
- Stead, D., Wolter, A., 2015. A critical review of rock slope failure mechanisms: the importance of structural geology. *J. Struct. Geol.* 74, 1–23.
- Steffen, D., Schlunegger, F., Preusser, F., 2010. Late Pleistocene fans and terraces in the Majes valley, southern Peru, and their relation to climatic variations. *Int. J. Earth Sci.* 99 (8), 1975–1989.
- Stirling, M.W., Langridge, R., Benites, R., Aleman, H., 2002. The Magnitude 8.3 June 23 2001 Southern Peru Earthquake and Tsunami: Reconnaissance Team Report. Institute of Geological & Nuclear Sciences.

- Strasser, M., Schlunegger, F., 2005. Erosional processes, topographic length-scales and geomorphic evolution in arid climatic environments: the 'Lluta collapse', northern Chile. *Int. J. Earth Sci.* 94 (3), 433–446.
- Strecker, M.R., Alonso, R.N., Bookhagen, B., Carrapa, B., Hillel, G.E., Sobel, E.R., Trauth, M.H., 2007. Tectonics and climate of the southern central Andes. *Annu. Rev. Earth Planet Sci.* 35, 747–787.
- Tanyaş, H., Van Westen, C.J., Allstadt, K.E., Anna Nowicki Jessee, M., Görüm, T., Jibson, R.W., Hovius, N., 2017. Presentation and analysis of a worldwide database of earthquake-induced landslide inventories. *J. Geophys. Res.: Earth Surf.* 122 (10), 1991–2015.
- Tanyaş, H., van Westen, C.J., Allstadt, K.E., Jibson, R.W., 2019. Factors controlling landslide frequency–area distributions. *Earth Surf. Process. Landforms* 44 (4), 900–917.
- Tebbens, S.F., 2020. Landslide scaling: a review. *Earth Space Sci.* 7 (1), e2019EA000662.
- Thouret, J.C., Wörner, G., Gunnell, Y., Singer, B., Zhang, X., Souriot, T., 2007. Geochronologic and stratigraphic constrains on canyon incision and Miocene uplift of the Central Andes in Perú. *Earth Planet Sci. Lett.* 263, 151–166.
- Thouret, J.C., Gunnell, Y., Jicha, B.R., Paquette, J.L., Braucher, R., 2017. Canyon incision chronology based on ignimbrite stratigraphy and cut-and-fill sediment sequences in SW Peru documents intermittent uplift of the western Central Andes. *Geomorphology* 298, 1–19.
- Tomlinson, A., Blanco, N., Ladino, M., 2015. Carta Mamiña, Región de Tarapacá. Servicio Nacional de Geología y Minería, Carta Geológica de Chile. Serie Geología Básica 174, 1 mapa escala 1:100.000. Santiago.
- Tonini, M., Pedrazzini, A., Penna, I., Jaboyedoff, M., 2014. Spatial pattern of landslides in Swiss rhone valley. *Nat. Hazards* 73, 97–110.
- Valagussa, A., Marc, O., Frattini, P., Crosta, G.B., 2019. Seismic and geological controls on earthquake-induced landslide size. *Earth Planet Sci. Lett.* 506, 268–281.
- Valdivia-Silva, J.E., Navarro-González, R., Ortega-Gutierrez, F., Fletcher, L.E., Perez-Montano, S., Condori-Apaza, R., McKay, C.P., 2011. Multidisciplinary approach of the hyperarid desert of Pampas de La Joya in southern Peru as a new Mars-like soil analog. *Geochem. Cosmochim. Acta* 75 (7), 1975–1991.
- Valenzuela, J.I., Herrera, S., Pinto, L., Del Real, I., 2014. Carta Camiña, regiones de Arica-Parinacota y Tarapacá. Servicio Nacional de Geología y Minería, Carta Geológica de Chile. Serie Geología Básica 170, 97 pp., 1 mapa escala 1:100.000.
- Van Den Eeckhaut, M., Poesen, J., Govers, G., Verstraeten, G., Demoulin, A., 2007. Characteristics of the size distribution of recent and historical landslides in a populated hilly region. *Earth Planet Sci. Lett.* 256, 588–603.
- Varnes, D.J., 1978. Slope movement types and processes. *Sp. Rep.* 176, 11–33.
- Vicente, J.C., 1981. Elementos de la estratigrafía Mesozoica sur Peruana. In: Volkheimer, Musacchio (Eds.), Comité Sudamericano del Jurásico y Cretácico: Cuencas sedimentarias del Jurásico y Cretácico de América del sur, vol. 1, pp. 319–351.
- Villegas-Lanza, J.C., Chlieh, M., Cavalie, O., Tavera, H., Baby, P., Chire-Chira, J., Nocquet, J.M., 2016. Active tectonics of Peru: heterogeneous interseismic coupling along the Nazca megathrust, rigid motion of the Peruvian Sliver, and Subandean shortening accommodation. *J. Geophys. Res. Solid Earth* 121 (10), 7371–7394.
- Wallemacq, P., House, R., 2018. Economic Losses, Poverty & Disasters. Centre for Research on the Epidemiology of Disasters and United Nations Office for Disaster Risk Reduction, Geneva, pp. 1–30.
- Whipple, K.X., Kirby, E., Brocklehurst, S.H., 1999. Geomorphic limits to climate-induced increases in topographic relief. *Nature* 401 (6748), 39–43.
- Wilson, J., García, W., 1962. Geología de los Cuadrángulos de Pachia y Palca. Comisión de la Carta Geológica Nacional 2 (4), 1–81.
- Wörner, G., Hammerschmidt, K., Henjes-Kunst, F., Lezaun, J., Wilke, H., 2000. Geochronology (40Ar/39Ar, K-Ar and He-exposure ages) of Cenozoic magmatic rocks from northern Chile (18–22° S): implications for magmatism and tectonic evolution of the central Andes. *Rev. Geol. Chile* 27, 205–240.
- Wörner, G., Uhlir, D., Kohler, I., Seyfried, H., 2002. Evolution of the West Andean Escarpment at 18 S (N. Chile) during the last 25 Ma: uplift, erosion and collapse through time. *Tectonophysics* 345 (1–4), 183–198.
- Wu, X., Chen, X., Zhan, F.B., Hong, S., 2015. Global research trends in landslides during 1991–2014: a bibliometric analysis. *Landslides* 12, 1215–1226.
- Yilmaz, I., Ercanoglu, M., 2019. Landslide inventory, sampling and effect of sampling strategies on landslide susceptibility/hazard modelling at a glance. In: *Natural Hazards GIS-Based Spatial Modeling Using Data Mining Techniques*. Springer, Cham, pp. 205–224.
- Zavala, B., Mariño, J., Lacroix, P., Taipe, E., Tatard, L., Benavente, C., Pari, W., Macedo, L., Peña, E., Paxi, R., Delgado, F., Fidel, L., Vilchez, M., Gomez, J.C., 2013. Evaluación de la seguridad física del distrito de Maca, Estudio geológicos, geofísicos y monitoreo de movimientos en masa. INGEMMET-IRD-IGP Publications, Lima. Informe Técnico No. A6628.
- Zerathe, S., Lacroix, P., Jongmans, D., Marino, J., Taipe, E., Wathelet, M., Pari, W., Fidel, L., Norabuena, E., Guillier, B., Tatard, L., 2016. Morphology, structure and kinematics of a rainfall controlled slow-moving Andean landslide, Peru. *Earth Surf. Process. Landforms* 41 (11), 1477–1493.
- Zerathe, S., Blard, P.H., Audin, L., Braucher, R., Bourles, D., Carcaillet, J., Benavente, C., Delgado, F., AsterTeam, 2017. Toward the feldspar alternative for cosmogenic 10Be exposure dating. *Quat. Geochronol.* 41, 83–96.

Supplementary data: Landslides database

Codigo	Code
Type	Type
SA	State os activity
Area_km2	Area
x_H	Headscarp_coordinate x
y_H	Headscarp_coordinate y
z_H	Headscarp_coordinate z
x_T	Toe_coordinate x
y_T	Toe_coordinate y
z_T	Toe_coordinate z
ΔH	height difference headscarp to toe
Strike	Direction of mass slide
Local_relief	Local relief value
Lithology	Tipe of lithology
Mean_slope	Mean slope value
GA	Geomorphotectonic area



Codigo	Type	SA	Area_km2	x_H	y_H	z_H	x_T	y_T	z_T	ΔH	Strike	Local_relief	Lithology	Mean_slope	GA
1	RS	P	1.201296	-105434	8350418	2740.324	-106153	8350646	2467.094	273.230452	287.583450	564	VS-PN	20.59090	CO
2	RS	P	4.703028	-92870	8349827	3290.625	-94857.1	8350884	2725.168	565.457348	298.012103	447	VS-PN	17.81130	CO
3	RA	F	0.109949	-110563	8349551	2560.864	-111565	8350012	2232.066	230.987820	287.619191	458	V-PN	20.55450	CO
4	RS	P	0.630977	-107846	8350256	2615.257	-107389	8348658	2183.408	328.797645	294.700774	459	VS-PN	16.22330	CO
5	RS	P	1.869201	100388.9	8349730	4878.624	102280	8348869	4217.6	431.849715	164.050719	543	VS-PN	19.00840	CO
6	RS	P	1.757089	-102750	8348990	2822.003	-103811	8349328	2478.53	661.024561	114.462381	762	VS-PN	26.02950	CO
7	RS	P	1.696769	-183036	8349175	614.9903	-185368	8349593	114.0972	343.473011	287.630690	480	VS-PN	16.26890	CO
8	RS	P	11.425178	-105223	8349041	2644.242	-106322	8349158	2293.825	500.893102	280.150826	369	SC-PN	9.69144	PC
9	RS	P	0.960470	-53253.5	8348261	3424.91	-52665.6	8349617	2818.224	350.417809	276.091358	584	VS-PN	20.79770	CO
10	RS	P	1.554977	104232.7	8348964	4445.826	104143.4	8348460	4253.868	606.685904	23.429555	700	VS-PN	24.30400	CO
11	RS	P	0.511419	-108843	8349278	2583.006	-107887	8347991	2105.56	191.957793	190.058830	600	VS-PN	19.58700	CO
12	RS	P	1.526656	-93978	8347696	3152.885	-96255.3	8348952	2556.169	477.445524	143.383023	559	VS-PN	19.55550	CO
13	RS	P	4.877448	-112503	8347800	2384.249	-112015	8346893	2110.278	596.715867	298.870208	467	VS-PN	18.02110	CO
14	RS	P	0.581463	-103216	8347095	2677.652	-103631	8347202	2553.44	273.970567	151.705960	438	VS-PN	17.60760	CO
15	RA	P	0.212824	-17284.5	8347568	3933.527	-17220.8	8346764	3781.708	185.997312	161.735416	377	V-C	14.85550	CO
16	RS	P	0.289313	105225.6	8346162	4912.061	100038	8348255	4234.998	124.211911	284.454796	453	VS-PN	17.34010	CO
17	RS	P	0.429168	-100646	8347924	2872.533	-98706.6	8345840	2231.553	151.819060	175.474769	379	V-C	12.06770	CO
18	RS	P	15.918502	-20751.1	8348005	4060.594	-21553.3	8345168	3421.654	677.063146	291.968173	591	V-PN	19.14910	CO
19	RS	P	11.584197	-102509	8346483	2780.404	-102996	8346716	2594.493	640.979490	137.067614	469	VS-PN	16.56340	CO
20	RS	P	2.878701	-52690.8	8346267	3617.681	-52146.1	8347030	3425.479	638.939687	195.788052	578	V-PN	16.71040	CO
21	RS	P	0.233890	174767.5	8345691	4665.368	174041.7	8346577	4387.068	185.911568	295.625616	441	VS-PN	17.30190	CO
22	RS	F	0.278018	-14058.8	8346652	4302.686	-17792.1	8345484	3635.529	192.201763	35.524537	335	VS-PN	11.52930	CO
23	RA	P	0.448064	-95133.5	8345573	2994.174	-97929.4	8346705	2295.956	412.271182	162.482705	486	V-C	19.44190	CO
24	RS	P	0.532963	99194.27	8346527	4342.57	100138.1	8345697	3796.322	278.300281	320.654477	360	V-PN	11.61980	CO
25	RS	P	8.548672	-184191	8345376	674.7746	-186136	8345431	60.45589	667.156453	252.639972	579	V-C	17.15960	CO
26	RS	P	6.579523	173922.5	8344861	4667.896	173329.2	8345434	4399.758	698.218516	292.048555	428	VS-PN	16.15410	CO
27	RS	P	1.814730	-38943.8	8345014	3875.259	-40176.6	8344473	3570.655	546.247720	131.347029	883	VS-PN	22.53510	CO
28	RA	P	0.283544	-97003.2	8343514	2861.385	-99432.5	8345120	2183.503	286.147619	315.254037	363	V-PN	13.30580	CO
29	RS	P	4.590097	102941.1	8343410	4796.305	99342.12	8343670	3695.742	614.318731	271.605429	389	SC-PN	10.80650	PC
30	RS	P	0.421719	-74199.6	8343257	3582.524	-75003.3	8343248	3372.818	268.137996	314.016057	369	V-PN	12.75560	CO
31	RS	P	1.195016	-75652.4	8343304	3534.238	-74896.6	8342762	3341.275	304.603659	246.273818	415	V-C	13.53570	CO
32	RS	P	7.946723	41209.32	8341644	4552.276	40792.64	8343092	4201.515	677.882266	303.468068	513	VS-PN	16.42520	CO
33	RS	P	6.837753	37931.32	8342573	4136.428	38194.26	8342082	3881.087	1100.562490	274.127155	660	VS-PN	20.05000	CO
34	RS	P	0.585715	-76412.7	8342466	3456.428	-75891.1	8341727	3214.014	209.705915	269.319914	343	VS-PN	16.83580	CO
35	RS	P	1.464418	-81386.9	8343038	3323.447	-81810.4	8340782	2778.517	192.963271	125.628835	338	VS-PN	13.55460	CO
36	RS	P	1.469938	39347.88	8341553	4411.998	37910.9	8341824	3833.771	350.761242	343.941498	624	VS-PN	14.76990	CO
37	RA	P	1.234087	-38741.9	8341499	3600.824	-39178.4	8341605	3408.934	120.994209	176.653904	464	VS-PN	18.13380	CO
38	RS	P	0.152773	-78029.7	8341323	3399.776	-79023.8	8341010	3025.663	255.340102	151.831801	556	VS-PN	22.50620	CO
39	RS	P	0.988084	-94371.1	8341643	2897.619	-96283.8	8340067	2453.305	242.413706	144.804159	365	VS-PN	15.47590	CO
40	RA	P	0.675927	-19233.4	8341201	3425.576	-19619.5	8339863	3234.121	180.880983	288.383951	436	VS-PN	17.56020	CO
41	RS	P	1.927005	-77660.8	8340186	3179.213	-78106.8	8339519	2873.67	544.929855	190.628959	523	VS-PN	20.43610	CO
42	RS	P	1.591029	-91788.5	8340935	2968.256	-93684.6	8338835	2487.674	578.227089	280.704592	661	VS-PN	19.12940	CO
43	RA	P	1.901947	-193166	8339989	351.5	-191693	8339248	32.69329	333.546310	297.819328	432	VS-PN	14.67300	CO
44	RS	P	0.275794	-88023.7	8339716	3072.75	-87528.7	8338670	2711.033	191.889915	283.722544	328	V-C	17.68890	CO
45	RS	P	1.723757	35483.33	8338799	3809.406	34832.92	8339290	3350.617	374.113177	252.504981	509	VS-PN	19.71410	CO
46	RS	P	4.009498	-18296.4	8339217	3282.481	-18582.3	8338890	3122.429	444.314432	230.524562	452	VS-PN	19.07200	CO
47	RA	P	0.537406	-40146.6	8338101	3527.96	-40897.6	8338217	3308.748	356.394575	151.830166	659	VS-PN	24.03390	CO
48	RS	P	2.357189	-89369.5	8338984	3091.234	-88692.4	8337296	2565.15	191.455792	196.100493	216	D-C	8.71222	CO

49	RS	P	0.294629	-96439.4	8338446	2715.082	-96201.2	8337286	2395.672	305.542792	213.762523	624	VS-PN	19.64150	CO
50	RS	P	6.214856	-91129.4	8338586	2871.391	-92650.1	8336914	2361.472	480.581045	222.073561	465	VS-PN	18.38910	CO
51	RS	P	4.195012	-40789.1	8336779	3535.221	-41371	8337137	3284.092	318.806737	116.744957	339	D-C	9.82940	PC
52	RS	P	1.737263	-90916.7	8337486	2827.069	-90313.7	8335228	2336.257	361.716470	154.674199	490	VS-PN	16.32060	CO
53	RS	P	0.290536	-41474.6	8335846	3457.102	-41984.7	8336186	3263.466	458.788599	307.027465	950	V-PN	25.42890	CO
54	RS	P	0.152763	103242.7	8336117	4663.223	100696.8	8335896	3298.66	160.051989	221.220278	436	V-PN	16.51960	CO
55	RS	P	0.397730	120541.8	8335328	4846.813	121025.3	8336162	4504.327	219.211839	278.758209	348	V-C	17.86900	CO
56	RS	P	2.252191	-19048.6	8335680	3080.602	-18162.5	8335961	2756.59	526.083514	158.135881	525	VS-PN	14.50310	CO
57	RS	P	0.752040	-20085.7	8335956	3209.918	-20162.4	8335577	3126.786	319.410291	168.392111	408	VS-PN	18.93910	CO
58	RS	P	3.788848	-20859.7	8335129	3386.975	-20625.3	8335663	3226.979	509.918890	222.288858	642	VS-PN	18.32460	CO
59	RS	P	0.251582	116370	8331740	4799.266	114615	8333614	4175.651	251.129236	301.599281	293	V-C	17.29270	CO
60	RS	P	6.123272	-29103.8	8331769	3973.987	-27919.3	8330518	3388.046	490.811877	165.045798	591	VS-PN	19.60290	CO
61	RS	P	0.343832	-31794.3	8329787	3240.763	-33057.6	8328762	2752.483	193.635873	303.657582	303	V-C	15.93510	CO
62	RS	P	5.427351	-23700.7	8326821	2826.638	-23283.6	8327029	2619.841	1364.562878	265.023119	805	VS-PN	19.46830	CO
63	RS	P	0.595449	-47515.6	8327132	3221.258	-47189.1	8326696	2985.197	342.485703	30.096273	436	VS-PN	15.56420	CO
64	RS	P	1.293033	-47015.1	8326022	3245.85	-47516	8326493	2968.686	324.012292	72.425882	577	V-PN	19.73540	CO
65	RS	P	0.271421	54658.42	8326629	4459.324	51939.36	8325111	3830.916	83.131831	191.406464	584	V-PN	16.09040	CO
66	RS	P	0.274859	-16947.6	8324978	2667.678	-17666.3	8326375	2123.871	159.995990	23.698783	500	V-PN	15.76410	CO
67	RA	P	0.298415	-189121	8325549	435.3064	-190193	8325018	10.56368	351.841382	285.171083	681	I-M	18.92740	CO
68	RA	P	5.338033	-35591.2	8325628	2824.955	-35702.3	8324813	2523.919	875.237555	99.293354	356	V-PN	13.56760	CO
69	RS	P	4.329647	79641.79	8325104	4057.071	81723.49	8324975	3284.092	623.614407	316.872790	418	VS-PN	13.85120	CO
70	RS	P	1.219831	-10180.7	8325358	3254.567	-10526.9	8324373	3050.628	585.940912	136.562754	619	V-PN	19.17910	CO
71	RS	P	1.472479	50368.72	8324699	4154.914	51331.25	8323573	3653.025	488.280077	230.937483	955	V-PN	20.35380	CO
72	RA	P	1.023405	-35200.1	8324050	2427.242	-34863.1	8323256	2157.091	756.904863	90.556488	615	V-PN	20.02680	CO
73	RA	P	5.719666	54287.59	8323205	4565	51419.47	8323707	3663.141	659.511241	84.625719	653	V-PN	16.11210	CO
74	RA	P	2.879746	-35901.5	8323204	2313.989	-35408.5	8323377	2196.494	1258.532780	338.676859	1076	VS-PN	27.50310	CO
75	RS	P	0.147130	84683.27	8322878	4274.286	81914.52	8323483	3019.93	206.796809	63.456349	656	SC-PN	24.80330	CO
76	RS	P	0.787344	79782.39	8322795	3350.76	80309.75	8323030	3074.626	236.061632	143.217034	343	VS-PN	14.31500	CO
77	RA	P	0.437889	138189.2	8322536	4487.72	138798	8322522	4190.213	575.261949	101.565680	854	V-PN	22.45310	CO
78	RA	P	0.534941	53519.21	8321758	4291.43	51485.77	8321675	3800.626	310.461068	128.791209	531	VS-PN	20.69050	CO
79	RS	P	0.240093	132651.5	8321032	4596.888	133504.6	8321636	4228.552	277.163923	313.285766	340	SMC-M	15.37380	CO
80	RS	P	6.042449	152690.2	8320247	4628.58	152947.5	8319124	4180.985	628.408432	240.819148	634	VS-PN	17.30530	CO
81	RS	P	1.644078	137251.3	8320182	4375.564	138002.3	8319146	4024.331	543.806467	332.768290	850	V-PN	25.30150	CO
82	RS	P	1.913511	236075.4	8319489	4307.962	235359.8	8319251	4176.779	424.742710	243.675876	612	M-PP	16.76290	CC
83	RS	P	0.359775	151989.9	8319499	4482.877	152049.5	8318753	4162.087	301.036171	187.759323	765	V-PN	22.99770	CO
84	RA	P	2.128280	78815.59	8318572	3444.545	80361.97	8316707	2554.209	1254.200971	251.120813	825	V-PN	26.21650	CO
85	RS	P	2.302908	237339.1	8317396	4271.774	236938.1	8316687	4080.994	772.978252	93.541523	1154	VS-PN	34.37200	CO
86	RS	P	1.768823	69180.36	8317672	4176.204	69127.01	8315560	3119.514	203.939183	199.383577	436	D-C	11.82950	CO
87	RA	P	1.133113	98437.23	8315755	4927.018	97866.37	8318317	3804.683	521.727289	136.110151	805	D-C	19.65460	CO
88	RA	F	0.853998	236513.6	8316222	4301.528	236909	8316723	4081.251	551.073070	29.592419	952	V-PN	24.39920	CO
89	RS	P	4.972716	-17024.8	8316931	3180.179	-18838.8	8316027	2600.226	501.888889	139.480427	601	VS-PN	15.20940	CO
90	RS	P	0.365912	144380.2	8317014	4413.931	144940.4	8315291	3901.269	1270.150671	156.993349	621	V-PN	23.31640	CO
91	RA	P	14.890956	237240	8315748	4286.542	237760.7	8316500	4058.903	1020.515041	96.253083	245	VS-PN	6.55234	CO
92	RS	P	4.587543	238856.2	8315233	4197.544	238160.8	8315411	4033.264	901.858780	279.932176	650	D-C	17.94810	CO
93	RS	P	0.316050	83675.62	8310590	4075.645	83637.26	8312819	3064.106	117.494406	70.659303	551	V-PN	22.27210	CO
94	RA	P	2.528482	51518.22	8310391	4494.695	46954.77	8309145	3095.67	1293.105701	276.799686	760	V-PN	23.91090	CO
95	RS	P	6.429615	234251.5	8309269	4208.66	235463.2	8308677	3935.123	1254.355954	282.315352	726	VS-PN	25.37030	CO
96	RS	P	0.422667	245368	8309170	4184.964	245120.5	8308683	4000.622	276.134003	65.983420	982	D-C	28.54710	CO
97	RS	P	0.915713	243978.4	8308222	4332.01	244674	8309305	3988.877	297.506840	91.357573	410	VS-PN	15.29040	CO

98	RA	F	1.664729	46276.07	8306460	4021.608	40203.6	8307154	1564.256	296.335585	22.910921	568	D-C	15.63640	CO
99	RS	P	4.447670	183977.2	8306069	4772.677	181821.6	8306083	4390.207	490.803903	267.681379	704	VS-PN	21.64030	CO
100	RS	P	1.024526	180649.7	8305622	4545.914	180959.8	8305007	4367.429	368.335985	54.729974	592	V-PN	16.43560	CO
101	RA	F	0.324492	45495.75	8303772	4001.519	39770.06	8303153	1496.824	216.421832	341.641408	568	VS-PN	20.96850	CO
102	RS	P	1.275324	256814	8303239	4493.254	257056.6	8302952	4438.262	447.595564	167.098541	520	V-PN	18.68920	CO
103	RS	P	1.605374	257725.2	8303386	4545.771	257206.3	8303205	4462.75	351.233099	144.080375	453	VS-PN	12.56410	CO
104	RS	P	0.563256	256592.1	8302629	4455.393	256875.4	8302670	4414.684	131.183005	251.637852	248	V-PN	12.23680	CO
105	RS	P	0.318068	230355.4	8302273	4377.871	231011.6	8302028	4106.154	320.789862	175.427392	545	V-PN	20.41730	CO
106	RA	P	14.590193	256939.5	8301819	4402.161	256570.8	8301923	4355.581	1224.661235	302.733386	524	V-PN	20.64610	CO
107	RS	P	5.884034	256067.2	8300497	4285.329	256249.5	8300344	4236.337	890.336090	140.330960	1533	VS-PN	34.18480	CO
108	RS	P	0.799611	234063.9	8299689	4385.329	234631.1	8300949	3946.334	190.780251	209.491697	371	V-PN	13.99830	CO
109	RA	F	2.195741	233850.1	8299602	4330.593	232678.2	8299712	3890.852	863.288565	14.369131	829	V-PN	23.67480	CO
110	RS	P	4.979148	31142.43	8298626	3836.137	33026.92	8298162	2930.219	1056.689733	181.446940	735	VS-PN	20.11030	CO
111	RS	P	4.542669	187305.6	829851	5150.694	186830.6	8292381	4758.051	1122.335523	347.438880	598	V-PN	19.10830	CO
112	RS	P	0.574943	93738.09	8289521	4271.971	93989.48	8289793	4174.151	220.276440	38.276427	263	V-PN	12.85590	CO
113	RS	F	3.192477	223405.7	8289939	4654.311	222970.5	8289318	4456.832	579.952186	243.492906	621	V-PN	17.50990	CO
114	RS	P	3.788818	94342.98	8288830	4278.327	94799.58	8288771	3989.784	512.661656	161.993772	489	V-PN	13.93950	CO
115	RS	P	0.562611	145820.8	8289585	4360.84	146003.8	8287585	3500.505	227.639063	34.691301	306	V-PN	15.84960	CO
116	RA	F	0.389799	224460.5	8289192	4541.496	224698.7	8287778	4235.078	287.468285	92.655800	771	V-PN	23.19600	CO
117	RS	P	0.386933	243437.5	8288100	4466.234	242591.7	8288039	4209.595	164.280332	284.340352	443	V-PN	15.62540	CO
118	RA	F	8.232869	226259.8	8288515	4500.828	226317.2	8286756	4099.721	668.173886	20.453063	427	V-PN	11.97180	CO
119	RA	P	7.882050	148635	8287557	4306.552	146238.1	8287814	3563.895	776.390733	0.934192	293	VS-PN	8.57162	CO
120	RS	P	4.522505	92705.1	8287918	4309.232	93535.71	8286748	3762.939	1011.538431	359.013889	697	VS-PN	20.58100	CO
121	RA	P	1.147956	-33647.4	8286538	3108.723	-34634.5	8286836	2652.777	714.142676	121.894191	419	VS-PN	10.79000	CO
122	RA	P	2.346211	2160.089	8285140	3728.236	521.4614	8286217	3333.492	456.009433	215.145021	338	VS-PN	10.66610	CO
123	RS	P	13.491721	147014.9	8285713	3982.679	146310.5	8283401	3068.707	1399.025109	254.732673	800	V-PN	21.17130	CO
124	RS	P	1.105002	223769.7	8282573	4361.222	226490.7	8281919	3876.174	273.536309	116.011258	440	V-PN	18.56550	CO
125	RA	P	30.377200	-28809.5	8281258	3556.97	-30208.9	8280823	2991.282	2144.660333	317.259972	717	SMC-M	18.27480	CO
126	RA	P	8.410461	248928.6	8279805	4178.335	249237.2	8280112	4062.699	1350.972381	351.018197	637	V-PN	17.29630	CO
127	RS	P	0.222267	226303.2	8279684	3887.753	225868.1	8279733	3720.103	184.341999	206.912321	413	V-PN	18.45760	CO
128	RA	P	23.725368	224927	8278970	3769.13	225142.9	8278620	3695.705	1910.315692	313.785284	856	VS-PN	23.22430	CO
129	RS	P	1.032415	224292.4	8278594	3743.898	224435.1	8278239	3688.362	343.132818	32.720190	527	V-PN	19.71040	CO
130	RA	P	5.369880	196990.2	8278710	4434.897	195804.2	8277704	3734.008	1858.938075	350.826435	481	SMC-M	18.39720	CO
131	RS	P	17.263940	207789.5	8278440	4834.211	208930.7	8277573	4440.815	2457.351753	276.524798	789	V-PN	23.47990	CO
132	RS	P	2.959800	250914.3	8276967	4348.145	251661.5	8277397	4153.472	382.470000	270.359128	247	V-PN	8.53190	CO
133	RS	P	0.352467	207469.2	8277517	4722.362	208515.1	8276028	4277.711	178.484589	153.229796	250	V-PN	13.63370	CO
134	RS	P	20.076121	171325.2	8278960	4177.765	175136.1	8275318	2051.692	2504.695448	263.827144	972	VS-PN	24.08870	CO
135	RS	F	0.161073	206950.1	8276391	4561.015	207793.3	8276480	4377.509	54.992571	139.813244	256	SC-PN	9.44049	CO
136	RS	F	0.380182	197224	8276739	4058.145	197628.3	8276038	3580.181	83.020918	250.824723	262	D-C	8.63545	CO
137	RS	P	0.100766	218977.6	8277422	4357.352	219742.7	8275167	3843.588	40.709151	81.885480	259	SC-PN	9.19819	CO
138	RA	P	0.787781	203400.3	8275258	4449.26	201923.3	8275616	3880.381	726.310491	124.894574	673	V-PN	19.05600	CO
139	RS	P	0.147043	180531.1	8275954	3740.992	177245.7	8274938	2120.841	271.717142	110.475135	671	SC-PN	18.72800	CO
140	RS	F	0.235271	253287.2	8274569	4423.379	254193.6	8275105	4223.336	46.579997	285.758522	301	D-C	9.49061	CO
141	RS	P	0.143810	196706.3	8274675	3601.083	197023.8	8273983	3176.081	48.992405	130.035061	235	SC-PN	9.38184	CO
142	RS	P	1.470295	208208.9	8274615	4310.582	209157.1	8273421	3988.717	438.994745	24.237126	518	V-PN	19.35550	CO
143	RA	F	0.100093	196507.9	8273461	3142.912	195926	8273362	3075.481	112.593786	275.321572	243	SC-PN	9.81333	CO
144	RS	P	0.604462	207771.3	8272629	4231.749	208826.5	8272774	3844.572	439.740420	275.336013	599	V-PN	20.30490	CO
145	RA	P	11.349585	205778.7	8272890	4130.131	206527.5	8271600	3794.227	1945.842333	263.682220	723	V-PN	20.58410	CO
146	RS	P	3.967520	198539	8272168	3273.099	197569.2	8271321	3063.227	905.917558	54.655353	720	V-C	17.67320	CO

147	RA	P	14.502745	217972.9	8271470	4053.696	217026.1	8271336	3629.954	1728.941448	281.119148	928	V-PN	23.39420	CO
148	RA	P	9.145784	207375.8	8270957	4084.584	206335.2	8271352	3732.378	878.460536	267.479823	606	SMC-M	19.70360	CO
149	RS	P	0.303164	103953.8	8271043	4692.159	103214	8271202	4466.995	392.643163	225.305801	557	V-PN	21.94100	CO
150	RA	P	0.466853	197593.3	8270278	3392.715	197615.3	8271250	3057.011	469.970000	224.782308	522	V-PN	21.41680	CO
151	RA	P	3.043534	200946.2	8271674	3377.398	200739.3	8269592	3136.561	412.579918	218.855035	530	SMC-M	18.42510	CO
152	RS	P	0.107082	207582	8270765	4091.158	209056.7	8270289	3595.464	97.820587	42.730120	354	VS-PN	10.85060	CO
153	RS	P	0.837944	202770.7	8270473	3320.824	202750.1	8269403	3176.41	197.478513	215.052408	350	SC-PN	11.06810	CO
154	RS	P	0.461724	204640.8	8270459	3507.902	204530	8269387	3203.533	288.543755	97.382362	441	V-PN	19.59920	CO
155	RS	P	2.923815	199608.8	8269490	3356.316	199823.5	8270059	3108.574	860.334443	174.774812	646	V-PN	16.72890	CO
156	RS	P	1.919721	127405	8269939	3674.19	127539.6	8269203	3301.685	306.417872	170.438620	406	SC-PN	12.31490	CO
157	RS	P	0.521562	215889.8	8269862	3493.675	215814.6	8269177	3355.252	256.638262	265.833917	743	V-PN	21.83520	CO
158	RS	P	1.255203	132978.9	8269446	4243.968	133007.2	8268625	3883.807	401.107054	178.131927	401	SC-PN	14.59460	CO
159	RS	P	3.361962	131699.9	8269251	4123.218	131642.4	8268178	3598.46	742.657807	276.112290	823	SMC-M	26.69110	CO
160	RS	P	1.540374	203303.1	8266902	3500.037	203541.4	8269491	3191.258	546.292923	144.606870	502	V-PN	9.89745	CO
161	RS	P	0.794731	205988.3	8267735	3422.26	206079.7	8268818	3220.307	455.946056	286.802017	583	VS-PN	24.07600	CO
162	RA	P	3.294254	125476.5	8268700	3397.477	125629.7	8267614	2773.81	758.378942	180.732399	447	SMC-M	14.88250	CO
163	RS	P	2.032731	212975.8	8268485	3571.419	212749.1	8267474	3401.106	394.744209	303.335546	344	I-PN	15.59210	CO
164	RS	P	3.380186	242327.8	8268137	4567.259	240714.7	8267856	4154.146	913.972373	196.942742	702	SMC-M	20.09120	CO
165	RS	P	4.954393	210068.7	8267145	3392.073	209936.1	8267464	3276.687	485.048164	103.522169	509	V-C	14.08000	CO
166	RS	P	0.746547	209130.5	8266766	3364.352	209094	8267296	3274.258	565.688910	252.712582	832	I-M	25.24950	CO
167	RS	P	0.285262	198762.4	8266474	4459.024	200186.8	8266328	3875.386	115.636457	45.147537	234	VS-PN	11.81650	CO
168	RS	F	0.134840	200711	8265656	4421.277	200292.6	8266529	3834.122	167.649791	276.382732	604	V-PN	22.73270	CO
169	RS	F	0.314312	49168.38	8266494	3661.735	49793.54	8265053	3057.25	73.425069	148.318364	731	D-C	18.60540	CO
170	RS	F	0.197779	221844.4	8265104	4096.665	221030.2	8265409	3931.737	55.536766	158.109339	705	D-C	20.74940	CO
171	RA	P	1.050777	217165.8	8265330	4124.785	216408.4	8265031	3799.323	204.864030	246.968607	281	VS-PN	13.06580	CO
172	RS	P	1.538873	220582.6	8264463	4338.992	220540.5	8265809	3846.908	700.889700	229.689459	832	V-C	27.49300	CO
173	RS	P	1.557630	208519.7	8264996	3925.952	209108.1	8264622	3716.198	393.396256	127.211040	528	V-C	18.81450	CO
174	RS	P	0.483463	209744	8264208	3919.802	209250.5	8264725	3709.047	194.673276	60.086840	275	VS-PN	10.82530	CO
175	RA	P	1.853172	212056.1	8264308	3806.22	211534.6	8264531	3634.183	792.857736	230.186713	743	V-PN	22.03070	CO
176	RA	F	1.123680	218193.8	8264655	4387.264	217707	8264287	4167.804	436.260225	280.514270	416	V-C	15.59160	CO
177	RS	P	1.650162	219761.3	8263439	4555.22	219888.6	8265448	3870.69	444.650599	144.922671	520	V-C	18.54580	CO
178	RS	P	8.938608	124531.1	8263973	2897.189	125769.7	8264119	2342.455	2126.072868	133.704897	736	VS-PN	26.99730	CO
179	RS	P	0.600674	211944.4	8263693	3884.32	211554.7	8264007	3695.478	183.506324	83.966338	518	V-C	14.48760	CO
180	RS	P	0.316372	208852.1	8262224	4254.495	208370.5	8263914	3871.044	477.963888	150.050507	942	V-PN	29.03600	CO
181	RS	P	3.128746	124641.4	8262493	2748.076	126026.2	8262517	2182.25	513.764234	161.253480	659	V-C	16.44230	CO
182	RS	P	2.159490	128968.6	8262688	3380.383	126089.7	8261405	2104.371	568.878847	283.639671	611	V-C	19.26710	CO
183	RA	P	1.788396	124209.3	8261685	2713.862	123131.1	8260832	2129.179	758.032078	71.858534	641	I-M	29.88970	CO
184	RS	P	4.465404	81299.49	8259914	3825.994	79703.8	8257734	3035.992	1620.150738	252.818015	1271	V-PN	37.28790	CO
185	RS	P	0.783836	128912.4	8259538	2572.519	128296.1	8258689	2012.443	200.043402	59.377495	287	VS-PN	10.16290	CO
186	RS	P	0.272616	125512.2	8259131	2286.192	125046.5	8258859	2054.283	425.001481	155.344243	835	V-PN	29.02100	CO
187	RS	P	1.627275	133251	8258364	3137.775	130327.3	8258760	2235.086	321.865143	141.549405	452	V-C	13.77480	CO
188	RS	P	0.129157	88089.47	8258332	3793.621	87281.78	8258657	3613.469	67.431040	260.323727	449	V-C	19.09050	CO
189	RS	P	1.029503	83151.55	8259502	3939.78	81188.72	8256832	3018.081	387.177721	82.179941	484	V-C	19.74760	CO
190	RS	P	4.204162	27128.64	8257594	2524.596	27932.78	8257836	2079.433	335.903178	149.850321	495	V-C	18.20080	CO
191	RS	F	2.877949	28996.55	8257851	2626.412	27985.24	8257238	2008.972	209.872043	228.871944	434	D-C	11.70420	CO
192	RS	P	1.420015	134479.6	8257678	3318.079	132816.6	8256611	2661.812	423.741254	261.983556	533	V-C	14.47220	CO
193	RS	P	2.484586	83690.39	8257504	3647.954	84680.82	8255829	3271.44	352.206566	290.773359	384	V-C	18.26830	CO
194	RS	P	0.683460	45335.72	8256915	2881.693	46770.81	8255608	2289.946	225.163569	282.180053	411	V-C	11.15060	CO
195	RS	F	0.506992	33468.64	8256448	2533.852	31791.85	8256317	2008.024	335.704257	1.292082	866	D-C	24.91660	CO

196	RS	F	5.162874	25059.37	8255988	2608.907	25375.85	8256227	2294.303	240.836586	185.673285	445	D-C	13.76630	CO
197	RS	P	2.013873	25482.35	8255570	2573.695	26198.03	8255991	2126.67	495.694401	107.910388	430	V-C	18.71290	CO
198	RS	F	1.038225	40734.83	8254654	2580.051	38882.44	8251334	1843.245	144.414141	181.105415	362	D-C	9.77930	CO
199	RS	F	1.226169	43818.51	8253513	2703.711	49374.1	8251528	1757.646	304.369428	185.899756	652	D-C	20.84500	CO
200	RS	F	0.434412	25792.5	8253016	2561.05	28531.99	8251482	1902.067	247.742181	20.687180	1127	SMC-M	29.44700	CO
201	RS	P	0.447786	42159.22	8251894	2590.965	40635.92	8252369	2135.748	372.505294	169.642672	784	V-C	28.02940	CO
202	RS	F	0.562492	24664.16	8249257	2569.595	27364.83	8249355	2018.088	138.423038	186.261077	537	D-C	15.27730	CO
203	RS	P	0.979345	90427.86	8248406	3496.313	87841.53	8248422	2959.987	360.160850	178.029301	1200	D-C	28.52080	CO
204	RS	P	1.413607	225001.1	8246548	4418.642	223992.8	8246543	4200.775	524.757833	183.066720	1192	SMC-M	25.18450	CO
205	RS	F	7.766861	41292.8	8246473	2324.801	39150.09	8245437	1667.689	308.778927	5.258170	952	D-C	22.93000	CO
206	RS	F	1.697080	91217.61	8245642	3588.666	89682.56	8245602	3242.908	201.952911	4.823330	494	V-PN	14.50340	CO
207	RS	P	0.649935	153544.7	8245309	3708.528	150487.5	8242632	2256.742	623.666904	171.964832	1004	V-C	33.15260	CO
208	RS	F	0.603841	135000.2	8242678	1607.129	135037.7	8244018	947.7973	170.313186	192.642223	539	D-C	14.90870	CO
209	RS	P	3.004586	225415.6	8242803	4755.873	223800.6	8243272	4063.924	413.113602	260.136247	334	V-PN	9.43726	CO
210	RA	P	2.333267	107014.3	8251371	3684.882	128227.8	8228113	701.9663	784.738894	164.234667	492	VS-PN	13.16610	CO
211	RS	F	0.245642	62213.96	8237910	1537.007	58153.48	8237582	496.2423	115.386342	337.439365	465	D-C	16.12420	CO
212	RS	F	0.377749	8184.637	8237496	1748.566	7605.538	8236770	1389.975	90.094374	356.060545	592	V-PN	19.23600	CO
213	RA	F	0.325715	183552	8236340	3908.754	183095.3	8236191	3727.512	239.825265	68.599458	666	V-PN	19.58330	CO
214	RS	P	1.954241	317146.5	8236171	4167.799	316244.6	8235374	4020.841	583.637559	95.855494	661	V-C	22.60890	CO
215	RS	P	1.239988	315729.6	8234475	4247.97	316369.7	8235018	4005.837	587.154301	334.387183	797	V-C	21.27800	CO
216	RS	P	1.260850	41439.52	8234729	1890.786	39873.44	8233528	1454.179	604.484368	156.543119	566	VS-PN	16.62170	CO
217	RA	P	0.556024	180239.3	8234311	3781.31	181278.4	8233674	3382.766	425.264827	66.857476	666	V-C	19.54710	CO
218	RS	P	0.340667	111975.1	8234842	2960.317	115495.8	8232672	1621.048	164.927983	290.545088	510	V-PN	17.82970	CO
219	RS	P	1.036903	175887.6	8233671	3429.346	175006.6	8233312	3111.274	325.462575	248.485198	666	V-PN	21.27340	CO
220	RS	P	1.003471	324510.1	8233729	4195.119	325403.6	8233137	3902.003	492.083514	358.206672	707	V-PN	20.18710	CO
221	RA	P	5.383979	97818.3	8233549	2979.778	96187.43	8232528	2571.269	895.437319	180.232883	546	VS-M	21.98900	CO
222	RS	P	0.581298	181427.1	8231843	3775.066	180612.8	8232564	3265.75	209.753736	122.450635	419	V-C	15.62220	CO
223	RS	P	0.403534	41087.84	8231510	1759.104	41553.04	8232607	1447.134	210.755614	316.348278	551	V-PN	15.46400	CO
224	RS	P	0.160631	322353.1	8231990	4220.538	323649.7	8231465	3922.745	172.037280	293.135334	510	V-PN	16.84200	CO
225	RS	P	0.477314	97570.62	8230841	2856.99	96345.69	8230712	2359.031	219.460475	232.918293	586	V-PN	20.28370	CO
226	RS	P	1.687077	189241.4	8230457	3765.151	188307	8231018	3287.651	684.529983	3.623671	516	V-PN	15.44170	CO
227	RS	P	1.535831	42300.6	8230017	1680.9	42993.04	8230270	1408.946	554.733241	83.311193	675	V-C	20.04790	CO
228	RS	P	0.139209	94807.89	8230147	2580.312	96306.57	8229443	2278.396	188.841699	308.836326	521	V-PN	19.23450	CO
229	RS	P	2.752800	321341	8230304	4154.257	321524.2	8228931	3881.559	383.451544	344.089505	418	V-PN	13.45720	CO
230	RS	P	2.283081	42573.3	8228691	1643.673	43527.03	8228649	1367.411	565.825839	89.018241	624	V-C	22.39830	CO
231	RS	P	6.952133	97725.34	8228955	2667.509	96821.31	8228502	2268.581	1276.011674	245.979002	1007	SMC-M	29.19300	CO
232	RS	P	4.360339	100713.5	8233554	2959.75	101675.4	8223240	1817.601	584.683787	231.656176	685	V-C	22.99560	CO
233	RS	P	3.297037	110494.4	8228973	2514.743	119789	8226745	998.4555	790.002471	216.201726	631	VS-PN	17.06630	CO
234	RS	P	1.555910	191001	8228014	3791.687	191719.9	8226946	3166.971	560.075911	215.979364	1141	SMC-M	27.28670	CO
235	RS	P	0.236862	94914.37	8227299	2581.061	96835.45	8227842	2229.832	231.909575	239.712548	770	V-C	31.20330	CO
236	RS	P	6.358148	-4360.83	8227028	1833.684	-5076.58	8227014	1721.459	902.689093	277.707052	830	SMC-M	20.87980	CO
237	RS	P	1.296917	322649.1	8227324	4236.525	321988	8226503	3848.471	180.151240	291.929089	355	V-C	12.88060	CO
238	RS	P	4.661324	318677.5	8225011	4389.387	318678.6	8227505	3973.954	921.699222	216.320286	536	VS-PN	16.45150	CO
239	RS	P	0.425234	106775.4	8225486	2412.444	105815.8	8225237	2067.774	445.162412	73.231270	577	VS-PN	19.64070	CO
240	RS	P	3.211734	360230.3	8224444	4910.263	361075.5	8225139	4616.017	617.440156	238.768890	707	V-PN	17.19640	CO
241	RS	P	3.631490	-4547.18	8224837	1750.826	-6248.33	8224936	1581.891	656.267043	237.311908	849	SMC-M	19.30380	CO
242	RS	P	3.366916	186788	8224678	3435.156	187919.8	8223905	2742.353	376.514682	149.406393	483	V-C	16.51180	CO
243	RS	P	3.708303	319583	8223531	4349.718	322383.9	8224266	3799.571	591.747236	132.329390	569	VS-PN	16.05670	CO
244	RS	P	1.459442	57700.2	8223173	1960.528	54486.19	8223489	358.9448	525.827156	265.510498	494	VS-PN	13.88960	CO

245	RS	P	0.251482	95455.65	8222860	2375.705	96066.49	8223391	1965.569	314.603683	53.030541	499	VS-PN	20.91650	CO
246	RS	P	0.456667	344200.6	8223182	4850.629	345204.9	8222657	4472.545	447.025084	59.540862	590	VS-PN	25.24200	CO
247	RA	P	2.859533	-8676.69	8221951	1437.506	-9047.56	8221949	1309.709	1494.372737	220.936629	837	SMC-M	28.95310	CO
248	RA	P	7.634905	100433.2	8220943	1990.991	99593.69	8220456	1720.069	902.681493	237.509901	536	V-C	20.55990	CO
249	RA	P	0.439930	109882.5	8220556	2227.549	107944.3	8219744	1627.486	778.606500	259.842236	969	SMC-M	25.84070	CO
250	RS	P	6.906192	102526.5	8218619	2181.444	100678.3	8218593	1662.386	736.806130	209.158759	502	VS-PN	14.36190	CO
251	RS	P	17.658000	107022.5	8219375	2012.472	106201.8	8218850	1772.526	946.064821	109.662599	446	VS-PN	14.34660	CO
252	RS	P	5.464190	107133	8219139	1917.828	107958.9	8218702	1577.088	658.982774	119.251871	413	SC-PN	15.36750	CO
253	RS	P	2.309465	335264.7	8218521	4463.563	336095.4	8218825	4127.931	455.216906	287.318110	545	VS-PN	14.36220	CO
254	RA	P	2.930059	106233.6	8218136	1724.184	105785.4	8217823	1583.533	358.035099	36.920874	393	V-PN	14.70210	CO
255	RS	P	4.872140	182688.4	8218074	2874.032	182946.1	8217643	2680.277	551.506684	87.922757	409	VS-PN	12.19790	CO
256	RA	P	0.425117	183308.8	8217188	2811.343	182683	8217262	2619.771	245.824569	264.117332	320	V-PN	12.88000	CO
257	RS	P	3.089071	105495.9	8216861	1846.42	106217.4	8217151	1542.682	536.325269	270.372589	438	SC-PN	16.04330	CO
258	RS	P	0.709028	103034	8216826	2069.735	102296	8216759	1775.713	217.866854	269.713954	438	V-PN	14.67230	CO
259	RS	P	3.778628	119778.3	8214233	1783.752	120847.1	8214222	1526.905	657.112619	244.212162	642	VS-PN	16.71350	CO
260	RS	P	2.537621	251206.8	8214161	4124.136	252292.9	8213475	3797.756	345.758737	268.527984	413	VS-PN	15.60530	CO
261	RS	P	10.225997	317772.5	8212184	4308.016	317267.3	8211559	3984.392	1451.786052	228.796254	746	SMC-M	26.43990	CO
262	RS	P	1.124474	112604.2	8211400	1920.13	111277.2	8211476	1551.098	659.331316	1.605958	1195	I-M	29.56140	CO
263	RS	P	1.379977	24399.62	8211550	1340.19	23970.11	8211708	1238.376	691.948705	286.200364	704	V-PN	22.65750	CO
264	RS	P	182.024611	145623.2	8209349	1577.273	145647.8	8212824	1102.98	2982.915991	137.631838	656	VS-PN	16.32760	CO
265	RS	P	13.025304	259172.1	8211730	4190.897	258557.9	8211013	3859.403	1040.764755	265.380161	702	SC-PN	21.92100	CO
266	RS	F	1.119229	26221.68	8211194	1436.344	25472.89	8211415	1347.098	358.591383	218.568299	426	VS-PN	20.01800	CO
267	RS	P	0.222837	258550.4	8210185	4128.913	259101.3	8210498	3871.783	181.241639	251.914920	393	SC-PN	15.38030	CO
268	RS	P	1.758140	259760.4	8209464	4240.493	260035.4	8210331	3893.677	146.957839	228.514580	293	SC-PN	12.01980	CO
269	RS	P	1.658298	317411.8	8209602	4359.94	318892.8	8210129	3686.428	242.132702	49.707042	507	V-PN	13.14050	CO
270	RS	P	7.075590	125067.9	8209141	1393.599	127019	8209968	542.762	436.607142	232.502573	441	VS-PN	15.66210	CO
271	RS	P	1.495477	322046.1	8209500	3916.478	321472.5	8208754	3678.29	398.544712	121.510740	669	V-C	16.27230	CO
272	RS	P	10.158382	120786.8	8208520	1698.822	121972.3	8209063	1221.078	1339.269242	121.643864	445	VS-PN	15.47240	CO
273	RS	P	0.843227	24430.52	8208715	1356.967	23991.91	8208570	1275.779	318.071269	247.802218	501	SC-PN	19.24010	CO
274	RS	P	1.587303	18554.48	8207559	1094.625	17954.32	8207532	875.7036	293.116826	123.553304	414	SC-PN	13.04300	CO
275	RS	P	5.663155	121509.6	8206810	1635.159	123548.9	8207701	1041.735	408.508910	237.938929	490	D-C	14.70770	CO
276	RS	P	1.146767	39534.64	8206639	1546.087	39325.27	8206625	1513.514	509.316147	311.536302	801	VS-PN	19.84340	CO
277	RS	P	2.006379	17465.87	8206210	1068.201	18069.35	8206002	782.3244	311.970120	22.970670	398	SM-PN	13.02430	CO
278	RS	P	2.261804	26649.05	8206119	1275.647	26890.89	8205700	1214.321	297.793332	112.033312	326	SC-PN	10.18310	CO
279	RS	P	1.727129	193362.9	8205888	2858.192	192908.3	8206004	2733.26	497.958748	263.966659	524	SM-PN	16.25880	CO
280	RS	P	0.953332	58310.56	8205941	1407.806	55900.74	8205324	188.4165	477.499934	300.976602	617	VS-PN	23.31390	CO
281	RS	P	1.090705	25616.54	8205857	1291.024	25888.63	8205261	1190.029	271.953801	69.941394	417	VS-PN	12.77640	CO
282	RS	P	1.546880	24647.52	8205207	1256.933	24095.18	8205248	1155.719	301.916324	115.165536	422	SC-PN	19.11570	CO
283	RS	P	1.237710	194571.9	8205252	2906.372	194442.4	8204814	2726.01	272.698018	172.397857	367	SC-PN	14.43350	CO
284	RS	P	1.385820	53102.1	8204989	1369.176	55084.33	8205025	227.5153	276.261892	92.523441	422	VS-PN	15.41430	CO
285	RS	P	0.798252	343376.8	8205223	4487.144	343102.7	8204475	4279.884	398.928043	243.358287	555	SM-PN	18.68430	CO
286	RS	P	42.082869	211278.2	8204132	2576.851	211076.7	8204300	2470.839	1142.149010	174.671698	444	VS-PN	14.51740	CO
287	RS	P	60.067641	194499.4	8204260	2870.517	194269.2	8203677	2637.85	1516.287106	103.479995	539	VS-PN	16.07730	CO
288	RS	P	1.379796	170648.4	8203324	1921.595	171708.4	8202820	1573.807	624.715511	146.065588	678	V-PN	20.30560	CO
289	RS	P	7.065077	122486.1	8202432	1513.421	126470.4	8203463	665.8484	351.228331	74.221898	440	VS-PN	18.84090	CO
290	RS	P	0.575854	311098.8	8198957	3865.797	312535.1	8199242	3340.792	112.225055	268.889439	190	SC-PN	10.84200	CO
291	RS	P	0.679728	126903.6	8196641	1190.654	128580.9	8199225	412.1989	388.054778	218.832972	484	SC-PN	20.51350	CO
292	RA	P	0.468669	348993.8	8197642	4556.841	348811.1	8197152	4419.313	356.059967	156.914333	501	SMC-M	21.61750	CO
293	RS	P	4.937982	348465.8	8197422	4470.139	348295.1	8196884	4358.895	415.433628	0.024292	280	V-PN	8.18621	CO

294	RS	P	2.008805	350248.8	8196233	4606.504	348581.3	8196947	4383.093	344.670045	255.410408	545	VS-PN	14.44520	CO
295	RS	P	1.535051	22388.33	8196543	504.5239	21862.38	8196292	199.1816	294.245731	50.586573	432	V-PN	16.32810	CO
296	RS	P	5.539941	317697.9	8194360	4187.507	317408.6	8194663	4034.863	168.935172	273.322994	236	SC-PN	11.87370	CO
297	RS	P	0.987154	171570.9	8193306	1656.378	169236.5	8194498	1385.419	692.802927	124.307153	728	V-PN	22.70970	CO
298	RS	F	12.483615	316348.6	8194116	4054.682	314025.7	8193884	3205.558	550.147433	75.283483	276	V-PN	8.35333	CO
299	RS	P	7.967539	111205.6	8193666	1237.256	110298.2	8193035	983.9854	1601.582997	275.611845	820	SC-PN	24.58650	PC
300	RS	P	2.665360	132503.8	8191902	1222.249	130658.5	8192636	334.5792	410.136046	49.018927	526	VS-PN	14.99420	CO
301	RS	P	1.004613	167830.5	8191088	1552.748	167073	8191938	1311.706	378.083784	117.598442	484	V-PN	16.67340	CO
302	RS	P	0.115289	303640.1	8190309	4083.654	302926.7	8190597	3738.338	127.796989	269.660685	279	SC-PN	12.67910	CO
303	RS	P	1.412246	316029.6	8190213	4111.776	313739.1	8190254	3287.362	270.922085	239.898838	473	SC-PN	25.05700	CO
304	RS	P	14.775536	166047.6	8188787	1480.936	165310	8189223	1252.206	600.062649	247.251979	551	VS-PN	17.63970	CO
305	RS	P	6.137640	199872	8188786	1854.494	200470	8187633	1463.404	519.058297	269.164812	512	VS-PN	15.60370	CO
306	RS	P	1.639006	299818.3	8188656	3882.009	300335.3	8187297	3383.032	239.946135	237.410880	492	SC-PN	20.54030	CO
307	RS	P	1.385820	162378.7	8187905	1424.005	163281.7	8187204	1208.576	340.740245	117.857567	504	SC-PN	20.43960	CO
308	RS	P	0.587002	162337.3	8187024	1403.392	162867.2	8186725	1193.096	335.632460	69.906824	460	SC-PN	21.08380	CO
309	RS	P	0.326598	164042.4	8186570	1392.427	163205.7	8186969	1206.486	140.651396	235.116159	413	SC-PN	19.82950	CO
310	RS	P	0.220277	196001.2	8186785	1648.655	196463.5	8186597	1484.003	193.755474	149.119646	341	M-PP	17.30410	CO
311	RS	P	0.468742	296936	8185525	4659.389	301311	8186593	3227.386	191.571645	276.768862	586	V-PN	21.71190	CO
312	RS	P	1.453614	163406.2	8185569	1371.356	162931.7	8185870	1178.067	303.738155	68.075598	435	SC-PN	23.50980	CO
313	RS	P	0.787707	318649	8186015	4159.359	318416	8185337	3923.583	294.022113	264.818398	509	VS-PN	20.12870	CO
314	RS	P	1.353268	319884.1	8186038	4217.647	320728.1	8184958	3985.546	256.846862	90.593697	446	SC-PN	20.88040	CO
315	RS	P	1.567440	163112.9	8185073	1308.27	162581.4	8185275	1158.981	326.379801	122.285903	435	VS-PN	10.74830	CO
316	RA	P	1.712701	205775.6	8184251	1846.297	206250.5	8184204	1729.549	778.835148	102.737321	793	SMC-M	25.15740	CO
317	RS	P	0.454576	296988.3	8183100	4586.029	301533.4	8184244	3280.525	323.623972	218.956653	685	SMC-M	24.91210	CO
318	RS	P	1.629834	213470.8	8183390	2020.7	213244	8183155	1930.893	369.032169	273.252148	443	VS-PN	20.74590	CO
319	RS	P	0.184523	161298	8183220	1319.337	161883.1	8183180	1122.1	101.813886	290.177562	216	VS-PN	9.00185	PC
320	RS	P	15.982592	300848.2	8181461	4166.748	303208.5	8183226	3007.788	474.292438	0.406754	409	SC-PN	12.86710	CO
321	RS	P	0.503456	194626.2	8181759	1558.034	193769.6	8182063	1301.213	331.493680	220.600198	447	V-C	16.62160	CO
322	RS	P	0.375825	162686.6	8181673	1300.835	162235.7	8181865	1104.581	89.246200	286.420899	131	SC-PN	7.25298	PC
323	RS	P	0.198312	161009.6	8181743	1272.569	161319.9	8181362	1080.71	257.129113	60.429820	388	V-C	14.58050	CO
324	RS	P	0.745007	320696.3	8181216	3922.723	320123.5	8181340	3694.02	346.816571	17.610232	459	V-PN	17.45320	CO
325	RS	P	1.346422	160098.7	8180919	1283.144	160565.3	8180656	1066.227	673.512426	70.438217	656	SMC-M	19.65620	CO
326	RS	P	3.817028	159924.4	8180371	1266.573	160429.3	8180137	1053.941	850.836848	67.031183	643	SC-PN	21.29570	CO
327	RS	P	1.501713	159117.8	8179380	1260.683	159809.4	8178908	1053.872	238.188253	217.557493	769	SMC-M	26.26470	CO
328	RS	P	1.276576	303942.2	8179564	3363.147	305037	8178056	2565.338	477.744459	65.405655	556	VS-PN	17.51960	CO
329	RS	P	0.166623	193850.4	8178574	1495.161	193351.2	8178683	1311.934	81.188681	251.720324	205	SC-PN	7.57358	PC
330	RS	P	0.201396	299084.6	8178824	4294.878	302738.3	8177998	3327.789	218.921732	267.434193	396	SC-P	21.81600	CC
331	RS	P	3.879844	303063.6	8178803	3418.663	303860.8	8177759	2771.548	593.423345	66.395826	534	VS-PN	15.43520	CO
332	RS	P	0.131016	193206.2	8177439	1476.562	192418.5	8177797	1230.049	32.572453	266.175721	150	SC-PN	8.57111	PC
333	RA	P	0.153262	190271.5	8175995	1346.974	190516.8	8176399	1210.13	71.872565	245.527262	164	SC-PN	8.93548	PC
334	RS	P	0.229795	191524.6	8175928	1396.263	191368.2	8176445	1243.308	285.876363	109.008666	432	VS-PN	17.28930	CC
335	RS	P	0.104224	276442	8174737	4732.587	274316	8173798	4371.059	61.325659	149.992374	142	SM-PN	5.17396	PC
336	RS	P	0.136289	186663.8	8173130	1347.123	186148	8173430	1114.787	124.932582	284.291657	509	SMC-M	22.06480	CO
337	RS	P	4.997151	186197.3	8172342	1327.15	185598.7	8172643	1100.641	1219.389947	255.628637	831	M-PP	20.83100	PC
338	RS	P	0.518061	334401.5	8172346	4681.17	334878.6	8171678	4331.919	100.995379	155.453816	144	SM-PN	6.72730	PC
339	RA	P	0.163592	185619.3	8170828	1310.665	184556.3	8171263	1082.724	97.596874	214.602210	173	SC-PN	7.85414	PC
340	RS	P	0.172216	183976	8168902	1158.551	183680.1	8169085	1064.512	101.214145	274.315930	184	SC-PN	8.24371	PC
341	RS	P	0.588303	365533	8169488	4727.936	365745	8168513	4562.007	180.361635	196.470002	562	SMC-M	22.60460	CO
342	RS	P	2.743339	183851.3	8168411	1207.946	183306.8	8168578	1057.499	1141.661158	88.957532	832	SC-PN	19.53490	PC

343	RA	P	0.794652	364237.8	8168391	4658.193	364831.2	8167819	4503.498	681.552731	122.374689	760	VS-PN	24.64060	CO
344	RS	P	0.488349	182869.4	8166715	1195.766	182622.8	8166971	1039.166	207.259288	200.119906	328	SC-PN	13.63790	CO
345	RS	P	0.119009	181947.8	8165548	1158.842	181516.9	8165577	1027.05	106.012233	309.886126	310	V-C	16.49750	CO
346	RA	P	1.119024	180469.8	8165689	1116.655	180646.6	8165098	1022.049	636.248743	272.390793	707	V-PN	18.69050	CO
347	RS	P	0.713572	181588.3	8164819	1164.165	181316.6	8165052	1020.876	232.667019	201.528829	444	SMC-M	22.06160	CO
348	RS	P	1.438522	364607.8	8165067	4620.93	364201.3	8164210	4477.253	347.787340	115.462646	429	SC-PN	12.84110	CO
349	RA	P	1.305368	180329.4	8164390	1126.352	179908.5	8164802	1012.574	760.331078	276.069409	694	V-PN	17.67360	CO
350	RS	P	27.100675	368887.2	8164547	5023.556	369483.7	8162736	4659.684	847.572574	75.496217	540	VS-PN	18.69420	CO
351	RA	P	1.668536	263306.9	8161675	3443.328	263995	8161409	3196.129	170.926478	177.823096	322	V-PN	10.41330	CO
352	RA	P	0.291649	333383.6	8161306	5085.64	332164.4	8161552	4739.209	231.164592	244.071896	486	I-M	16.90000	CO
353	RA	P	3.807330	269371.3	8161262	3600.486	267773.4	8161297	3057.365	599.840203	225.064644	534	V-PN	14.46740	CO
354	RA	P	0.125725	262406	8161268	3333.104	262180.3	8160316	2987.236	251.464469	95.033583	759	VS-PN	21.33040	CO
355	RS	P	1.026408	328141.1	8160259	4728.254	328090.7	8161173	4475.329	525.005147	78.743163	1073	SC-PN	25.35580	CO
356	RA	P	0.211839	264258.8	8160317	3327.156	263700.6	8160276	3121.225	311.703146	83.760453	848	VS-PN	21.01840	CO
357	RA	P	1.086566	270234.4	8161387	3621.04	270802	8158604	3020.397	612.490541	173.606028	702	V-PN	24.90490	CO
358	RS	P	10.948844	261945.4	8159967	3224.685	262296.3	8160265	2970.426	778.454824	32.980252	617	SC-PN	16.40090	CO
359	RS	P	0.241315	330119.7	8160082	4862.427	329253.1	8159649	4612.654	137.527510	200.450457	434	V-PN	12.05200	CO
360	RS	P	0.243321	263994.4	8159552	3293.846	263689.2	8159783	3061.4	111.244210	197.622313	310	SC-PN	10.16190	CO
361	RS	P	1.434392	327333.7	8159301	4729.773	326020.1	8159332	4511.976	223.410571	293.181582	296	V-PN	11.89590	CO
362	RS	P	0.561932	166134	8159569	1036.763	166349.2	8158961	702.617	305.342323	244.460004	605	M-PP	23.47050	CC
363	RS	P	0.136045	261172.4	8159471	3423.44	262675.9	8158896	2858.273	152.644025	316.338043	469	SC-PN	15.75000	CO
364	RS	P	13.792424	269318.2	8158841	3260.402	270383.2	8157872	2873.785	270.959229	297.036222	232	SC-PN	6.78573	CO
365	RS	P	3.483097	275598.5	8158368	3463.265	276228.8	8157725	3067.139	849.123182	264.297408	598	SC-PN	20.73570	CO
366	RS	P	2.941049	327517.4	8157841	4874.092	326245.1	8158081	4421.963	253.270979	235.203224	492	SC-PN	16.64880	PC
367	RS	P	4.861252	276770.6	8157508	3298.362	277755.9	8157085	2988.892	887.669674	291.688178	595	SC-PN	12.75280	PC
368	RS	P	1.850738	269027.5	8156507	2867.965	269704.2	8155849	2629.947	241.041539	318.288918	293	SC-PN	8.68034	CO
369	RS	P	0.598590	328387.7	8156110	4961.153	325467	8155782	4246.394	345.316676	291.951712	1097	VS-PN	29.58240	CO
370	RS	P	2.019510	291364.8	8155323	2690.889	290618.1	8155936	2285.592	824.413544	271.015884	904	SC-PN	24.48700	CO
371	RS	P	3.475697	276194.4	8155794	2808.729	275425.2	8155704	2565.596	228.729320	300.546359	291	SC-PN	8.22303	PC
372	RS	P	0.795506	110425.9	8156352	257.3439	110225.4	8154978	8.93034	391.089228	152.575715	532	I-M	21.52400	CO
373	RS	P	0.635963	263206	8156068	3179.153	261882.7	8154679	2471.467	498.976932	159.171695	957	V-C	25.69450	CO
374	RS	F	0.907323	264399.3	8155256	3011.405	265432.6	8155081	2779.419	215.429158	127.807447	269	D-C	7.46436	PC
375	RS	P	0.338374	278766	8154335	3079.063	277686.6	8154944	2554.265	210.295912	119.468893	265	D-C	9.41936	PC
376	RS	P	1.155305	328694.3	8155064	4838.244	327519.2	8153895	4309.355	185.940959	295.450946	271	SC-PN	9.02725	PC
377	RS	P	0.196496	276180.3	8154077	2527.015	275707.5	8153886	2313.393	164.651817	112.096036	339	SC-PN	12.27910	CO
378	RA	P	4.177426	264647.2	8154028	2821.041	265535.4	8153832	2534.027	1343.440782	257.737439	1017	VS-PN	31.45680	CO
379	RS	P	8.280703	299578.2	8153913	3120.748	299574.7	8152866	2656.679	1432.003721	76.280307	817	VS-PN	22.24030	CO
380	RS	F	0.258316	255047.3	8152257	2925.103	253882.6	8152199	2534.223	193.288981	302.366218	278	SC-PN	10.30800	PC
381	RS	P	0.607704	328664.9	8152745	4898.879	325794	8151244	4028.064	235.776351	198.976967	449	SC-PN	16.08020	CO
382	RS	P	0.587399	254323.3	8150513	2834.171	253582.6	8150939	2473.542	232.100832	142.011545	353	SC-PN	13.90650	CO
383	RS	P	0.370694	330670.2	8150709	5130.927	327648.3	8150113	4330.874	149.289092	290.816752	279	SC-PN	11.59980	PC
384	RS	P	0.161383	322068	8149914	3673.901	321238.7	8150065	3242.767	116.747239	95.678410	311	I-M	17.43280	CO
385	RS	P	7.904405	264135.7	8150178	2717.809	264363	8148938	2377.267	1305.503894	75.876089	680	VS-PN	17.64590	CO
386	RS	P	0.143699	242898.6	8148909	2463.696	242751	8148885	2409.428	89.807366	223.999083	220	VS-PN	11.02070	CO
387	RS	P	1.275570	287673.7	8149416	1896.584	287580.3	8148526	1634.047	197.236749	93.867087	255	SC-PN	9.13418	PC
388	RS	P	7.213409	242579.6	8147830	2425.374	242396.8	8148026	2298.767	1158.960045	53.220333	956	V-PN	22.35520	CO
389	RS	P	0.366705	314064.8	8147690	2585.463	314099.9	8146782	2130.639	256.821256	289.558274	318	D-C	10.64520	CO
390	RS	F	0.475184	313041	8147497	2441.169	313334.4	8146649	2085.422	196.254382	293.142252	264	D-C	9.29250	PC
391	RS	F	0.923043	304656.4	8143986	2465.224	304618	8145775	1639.294	191.859051	140.803190	258	SC-PN	12.26490	PC

392	RS	P	0.185942	294819.8	8146808	2361.021	295435.8	8143194	1794.645	228.702631	282.214028	619	SC-PN	19.43070	CO
393	RS	F	0.350303	281211.1	8142798	2397.501	278454.9	8144243	1149.955	216.917401	119.375129	257	SC-PN	10.80540	PC
394	RS	F	0.228020	282449.1	8142319	2743.897	280453.9	8140991	1760.313	212.632213	114.898771	262	SC-PN	12.19510	PC
395	RS	F	0.792660	312877.6	8135581	4273.015	307728.5	8137138	3097.812	206.810874	124.324073	259	D-C	11.45390	PC
396	RS	P	0.504707	273239.4	8132329	2071.258	270360	8132735	949.7993	797.808470	143.953365	964	VS-M	26.50300	CO
397	RS	F	0.437687	306765.4	8132647	3790.3	306692	8132104	3515.738	183.226823	282.367390	296	D-C	10.58900	CO
398	RS	P	3.236168	309327.1	8131518	4101.25	307830	8132585	3715.569	967.089322	102.737245	674	V-PN	17.41480	CO
399	RS	P	0.446298	268060.5	8131992	1722.851	270048.7	8131376	923.7248	647.114565	142.629178	1083	VS-M	25.77190	CO
400	RS	F	0.787059	307117.4	8130556	3948.906	306349.4	8132067	3460.628	246.512337	294.430212	294	D-C	12.72720	CO
401	RS	P	0.223738	305026.1	8129801	3774.812	304253.8	8131527	3180.165	136.844088	31.294153	290	SC-PN	12.76320	CO
402	RS	P	0.513199	242268	8129629	1533.979	241768.7	8129755	1247.385	152.954387	343.153712	285	SC-PN	13.02030	CO
403	RA	P	9.391628	272130.1	8129026	2433.069	269663.6	8130150	923.2989	1378.775272	70.795215	818	VS-PN	23.20270	CO
404	RS	F	1.983795	267068	8128440	1612.487	265222.9	8129001	856.5968	361.528215	246.177938	430	V-PN	13.75610	CO
405	RS	F	0.447605	304489.4	8128902	3547.248	304743.3	8128410	3388.6	232.335655	300.129355	290	D-C	10.74340	PC
406	RS	F	0.722332	306269.3	8129259	3846.131	304429.6	8128051	3302.001	226.509049	296.713923	282	SC-PN	8.66631	PC
407	RS	P	0.536732	303769	8128616	3488.061	303833.6	8127868	3253.846	349.251117	144.471017	488	V-PN	19.49940	CO
408	RA	P	4.345416	304546.5	8126826	3634.727	303901.9	8127872	3256.802	945.353158	70.903191	728	VS-PN	24.47100	CO
409	RS	F	2.094548	313223.8	8127863	4091.654	313663.4	8126029	3718.309	227.941026	292.256073	261	D-C	7.81025	PC
410	RA	P	3.507698	307042.8	8126964	3813.683	307168.4	8125965	3472.184	720.986201	202.033778	528	V-PN	19.09040	CO
411	RA	F	0.754620	311466.2	8126922	3971.011	311721	8125824	3562.604	166.659494	199.936778	238	D-C	7.55519	CO
412	RS	F	0.136200	261744.2	8124216	1768.172	261366.1	8127221	790.6008	94.039223	301.743113	247	SC-PN	9.96109	PC
413	RS	F	1.398366	304582.4	8126219	3617.625	303819.9	8125758	3319.729	165.928988	167.733171	226	D-C	8.06773	CO
414	RS	F	0.354130	335362	8122504	4797.833	335121.4	8122294	4683.036	150.446895	287.034276	247	SC-PN	9.29650	PC
415	RS	F	0.939714	327992.1	8121854	4219.608	328256.3	8121468	3994.334	154.695530	133.974130	256	D-C	9.94057	CO
416	RS	F	0.226053	310186.6	8121206	3674.633	309648.8	8120652	3327.402	156.599730	316.164275	227	SC-PN	10.06280	PC
417	RS	F	0.162192	313546.3	8120607	3809.19	313769.3	8120126	3572.002	131.791810	273.930336	227	SC-PN	10.94820	PC
418	RS	P	0.326263	312516.7	8120132	3729.471	312803.2	8119501	3492.394	94.605865	163.354071	222	SC-PN	11.28960	PC
419	RS	F	0.282082	299663.8	8120596	3258.508	301443.4	8117398	2646.658	143.288835	310.579342	217	SC-PN	10.13790	PC
420	RS	F	0.853761	278627.7	8119103	2370.644	278786.8	8117261	2054.61	143.676759	205.387336	306	V-PN	10.04550	CO
421	RS	P	0.273999	313222.3	8118774	3685.85	312903.5	8117723	3331.326	113.777648	314.395902	221	SC-PN	11.68100	PC
422	RA	P	40.006834	309652.2	8118136	3514.215	309860.6	8117139	3086.459	1821.792771	93.860695	1021	V-C	24.21130	CO
423	RS	F	3.554964	311304.2	8116591	3511.868	310960	8117404	3176.612	363.872135	161.762477	352	V-PN	14.07810	CO
424	RA	P	2.225878	308708.2	8115642	3360.699	307974.3	8116936	2942.788	1165.469312	203.242256	1228	I-M	33.11010	CO
425	RA	P	2.303410	312891.6	8116514	3595.642	312982.9	8115583	3136.052	1074.282152	69.279703	862	V-PN	24.50170	CO
426	RS	P	0.800658	310090.3	8115266	3403.275	310696	8114046	2969.22	247.198303	111.136044	463	V-PN	19.37720	CO
427	RS	P	1.291134	302797	8113590	2706.818	302279.6	8113063	2410.318	346.430898	281.405925	670	V-PN	23.07840	CO
428	RS	P	1.413657	342368.9	8113610	5153.555	341476.4	8112933	4719.905	543.120894	271.246190	624	V-PN	17.13810	CO
429	RS	P	1.763821	260489.9	8111504	1670.203	260530.8	8111217	1561.127	345.868120	193.332734	549	V-PN	21.12680	CO
430	RS	P	0.537869	261099.9	8111438	1679.443	261068.2	8111136	1575.468	252.925224	356.849248	335	V-PN	13.62190	CO
431	RS	P	0.357366	276237.1	8109444	2046.557	276865.7	8108887	1834.306	205.931059	265.833074	466	V-PN	22.92660	CO
432	RS	P	4.359673	321332.7	8109363	3549.855	321196.8	8108837	3253.182	600.642608	168.471969	584	V-PN	17.37890	CO
433	RS	P	0.133532	295254.9	8108285	2236.397	295006.6	8108945	1872.168	254.259276	49.685337	594	V-PN	22.13760	CO
434	RS	P	1.481186	304635.4	8108328	2368.731	304715.5	8107598	2168.039	249.772540	243.421836	454	V-PN	16.67100	CO
435	RS	P	0.103420	243741.1	8106831	1048.592	243870.6	8106532	979.7783	232.445650	307.089580	504	V-PN	21.84910	CO
436	RS	P	2.732825	243380.8	8106623	1040.647	243515.1	8106258	964.9254	217.797681	271.384915	430	V-PN	12.47850	CO
437	RS	P	0.266673	242102.7	8105612	1003.891	242289.7	8105204	936.8475	334.145515	160.516515	455	SC-PN	21.01210	PC
438	RS	P	1.649543	292446.9	8105252	2327.771	294365.2	8104262	1742.423	565.166974	110.948356	516	V-PN	19.59710	CO
439	RS	P	1.637606	378865.5	8104481	4585.59	377203.5	8104318	4267.067	386.617066	132.283062	503	SC-PN	19.00580	CO
440	RA	P	0.656978	328891.5	8102570	3900.392	328126.8	8101684	3532.115	323.536891	175.137144	639	V-PN	20.81630	CO

441	RS	P	0.508665	204163.1	8101922	187.0789	203879.2	8102115	36.6079	396.126317	135.601908	711	V-PN	23.87340	CO
442	RS	P	0.643251	306150.1	8098096	2434.554	305679.5	8098594	2280.586	452.129155	280.708467	542	V-PN	16.87810	CO
443	RS	P	0.855970	356135.4	8097763	3940.711	356647	8097169	3578.754	309.469909	113.263638	672	V-PN	22.18770	CO
444	RA	P	2.058224	357376.1	8096738	3948.624	356709.8	8097156	3568.591	1568.213193	107.990106	862	VS-M	29.05650	CO
445	RS	P	1.032672	355551.5	8096695	3879.387	356287.6	8096272	3511.653	238.017622	134.200134	605	SMC-M	21.45550	CO
446	RS	P	8.388572	347309.8	8096472	4031.59	346874.6	8096306	3876.269	714.759250	263.585532	530	V-PN	14.04190	CO
447	RS	F	0.703134	354524	8096220	3909.875	355802	8095381	3432.508	405.297744	309.404494	512	SMC-M	22.02390	CO
448	RS	P	0.823152	357171.1	8095025	3917.783	355706.8	8095090	3395.434	243.133553	263.349072	689	SMC-M	23.32530	CO
449	RS	P	4.092493	354528.5	8094837	3854.84	355133.5	8094700	3647.511	248.413558	188.303449	293	SM-PN	12.11130	CC
450	RS	F	2.611590	343588.1	8094469	4072.791	342585.1	8093995	3714.758	707.686017	223.615586	710	SC-PN	24.10950	CO
451	RS	P	1.079954	299445.8	8093193	1993.967	298660.6	8094248	1646.747	231.985926	99.626797	829	I-M	22.51960	CO
452	RS	P	1.089652	365898.3	8091698	3676.121	367923.8	8091592	3235.602	524.797932	299.424579	655	SMC-M	23.60140	CO
453	RS	P	1.587032	357641.9	8091249	3816.02	355908	8091945	3091.556	528.888422	225.157540	688	V-PN	18.25910	CO
454	RS	P	0.235982	374199.3	8091301	3572.071	373450.4	8090962	3298.389	213.622086	247.957111	558	D-C	23.51100	CO
455	RS	P	0.696193	343839.2	8089106	3716.952	343096.5	8089488	3373.816	287.013861	102.465193	735	D-C	24.61480	CO
456	RS	P	1.117496	349124.1	8089219	3644.879	347713.6	8088910	3193.98	464.068309	180.193011	673	V-C	20.14260	CO
457	RA	P	0.707243	362874.4	8088915	3781.203	362345.5	8088996	3597.518	648.597653	218.257426	644	SC-PN	20.00760	CO
458	RA	P	1.471417	361403	8089017	3868.372	362066.3	8088371	3532.753	340.917338	285.415316	972	V-C	30.05640	CO
459	RS	P	1.028385	366648.2	8088443	3603.551	369378.2	8088404	2985.211	390.880143	267.142744	460	V-PN	14.92120	CO
460	RS	P	6.790279	362933.1	8087989	3883.334	361980.3	8088112	3491.354	870.815106	242.399479	603	V-PN	22.93090	CO
461	RS	P	0.733662	357154.4	8087295	3857.381	353388	8089044	2841.259	360.629643	299.895611	555	SMC-M	21.77200	CO
462	RS	P	5.879711	362018.4	8086035	3841.895	361027.3	8086511	3364.604	800.052605	258.846502	595	V-PN	17.80790	CO
463	RS	P	0.266914	312118.9	8086411	2195.344	312326.6	8086019	2087.885	431.133876	280.319679	741	D-C	21.48230	CO
464	RS	P	0.749863	367457.2	8086600	3493.613	369626	8085660	2890.097	340.542061	169.612035	578	SMC-M	22.62420	CO
465	RA	P	32.695208	357904.3	8087216	3841.157	358614	8084724	3128.263	2165.226246	180.542936	878	VS-PN	31.91540	CO
466	RS	P	0.108176	352478.2	8084682	3548.452	349475.9	8085960	2500.588	54.268252	260.649446	451	V-PN	18.84640	CO
467	RS	P	0.796046	367474.2	8085892	3425.059	367217	8084705	3084.177	262.536892	185.997278	511	SMC-M	21.36790	CO
468	RS	P	0.107588	360906.9	8083638	3783.595	359070.7	8085040	3167.665	126.607452	316.996306	388	SMC-M	17.93990	CO
469	RA	P	0.613340	280328.4	8084422	1566.652	280699.2	8084135	1365.262	762.060788	240.026268	1051	SMC-M	31.68170	CO
470	RS	P	0.372522	317842.8	8084149	2161.116	317424.4	8084105	2046.52	454.823503	177.784336	782	V-C	27.53540	CO
471	RA	P	4.232011	383211.3	8083266	4048.594	381853.8	8083668	3470.915	703.778284	224.818244	449	V-PN	16.21800	CO
472	RS	P	0.956152	314302.5	8083520	2069.548	314467.4	8083086	1949.365	355.746675	160.930844	599	V-C	25.55020	CO
473	RS	P	1.427830	362834.5	8084019	3872.252	364549.9	8081641	2742.819	825.930017	358.772711	799	SMC-M	24.72520	CO
474	RA	P	2.033600	322392.2	8081783	2150.202	321924.7	8081438	2024.725	826.832857	20.807578	982	SMC-M	24.59390	CO
475	RS	P	9.220560	346777.1	8080711	2942.546	345025.1	8081217	1918.054	566.376017	170.326206	951	VS-M	31.14900	CO
476	RS	P	3.805173	357611.1	8081923	3640.694	359831.1	8077981	2741.764	1247.545881	297.659454	1030	SMC-M	28.50270	CO
477	RS	P	2.117710	333435	8078984	2537.115	332856.5	8079523	2203.221	983.583246	236.352225	812	VS-M	27.67660	CO
478	RA	P	0.730202	322545.2	8078538	1976.645	322959.1	8078113	1834.173	545.284773	211.115793	515	SMC-M	18.50240	CO
479	RS	P	14.113514	321842.4	8076219	1766.225	321257.9	8076128	1690.586	1175.202773	286.822676	495	VS-PN	19.52150	CO
480	RS	P	4.705842	328793.1	8075537	1999.289	327914.1	8076228	1703.042	1121.458416	278.029707	631	SMC-M	25.03690	CO
481	RS	P	0.293722	322891.8	8075869	1894.989	322086.3	8075824	1673.174	274.562179	187.699006	574	VS-M	20.35780	CO
482	RS	P	2.344606	401137.3	8076152	4689.031	400495.9	8075157	4400.902	385.681090	305.483702	422	VS-PN	14.52810	CO
483	RA	P	0.992656	399301.1	8074731	4436.452	398822.2	8074097	4132.218	378.305513	162.990724	536	VS-M	18.87650	CO
484	RS	P	6.128452	353715.7	8073463	2405.698	353082	8074973	1856.84	799.126699	107.216972	981	VS-M	27.77570	CO
485	RS	P	2.761789	313123.5	8075052	1688.424	311112.8	8069881	1185.883	488.277642	333.047294	513	VS-PN	17.32360	CO
486	RS	P	5.051281	404513.5	8073418	4889.174	404518.7	8072420	4513.201	594.646737	335.889897	617	VS-PN	19.49970	CO
487	RA	P	0.970967	402161.4	8073033	4717.544	401669.8	8071995	4294.633	472.448763	244.385843	651	VS-M	25.98460	CO
488	RS	P	0.190197	325847.9	8070874	1818.529	325107.8	8071299	1483.251	286.594308	284.177124	414	I-M	24.42080	CO
489	RS	P	4.714921	345550.4	8069612	2222.711	344998.3	8071044	1647.125	1509.769844	294.499373	984	I-PN	32.01390	CO

490	RS	P	2.272690	327042.8	8069316	1757.192	326656.5	8069409	1618.394	755.890446	286.897765	907	VS-M	29.66730	CO
491	RS	P	0.533547	361137	8064651	2169.726	360504.3	8065989	1591.41	158.647233	152.685684	528	VS-PN	18.21180	CO
492	RS	P	1.691403	269553.4	8063523	827.9564	268574.5	8064045	438.2282	544.130316	236.705694	438	VS-PN	17.44170	CO
493	RS	P	0.496644	386946.9	8063775	3210.789	386380.4	8062693	2751.789	234.215218	175.068175	534	VS-PN	18.71650	CO
494	RS	P	2.345237	351298.9	8063407	2037.165	352320.4	8061476	1229.06	377.924699	328.363333	506	VS-PN	16.70530	CO
495	RS	P	3.351561	308677.6	8058753	1101.405	308076.4	8059148	836.6887	373.345061	166.526881	388	VS-PN	14.42260	CO
496	RS	P	0.765619	362249.5	8056304	2765.147	360728.4	8057154	2127.156	341.498697	172.832114	509	VS-PN	17.62510	CO
497	RS	P	1.735036	367424.3	8055693	3425.156	368361.7	8057723	2690.842	408.407085	166.940424	517	VS-PN	19.45560	CO
498	RS	P	7.875639	309711.1	8055010	1093.667	308052.9	8055739	674.7643	977.571411	352.829570	850	VS-M	26.22660	CO
499	RS	P	0.580166	360727.8	8054680	2550.704	359229.7	8055345	2084.506	297.895360	238.867001	431	VS-PN	16.83500	CO
500	RA	P	1.151793	359782.3	8052566	2309.102	358492.8	8052748	1880.111	288.529711	168.542417	415	VS-PN	17.35760	CO
501	RS	P	0.207137	309419.8	8051824	946.1927	310931.3	8050039	539.0551	114.796882	229.066099	398	V-PN	13.88050	CO
502	RS	P	0.219442	377436.3	8048939	3308.689	376103.8	8047770	2784.514	225.274144	145.611943	572	VS-PN	18.81960	CO
503	RS	P	0.803575	364003.4	8050379	2549.478	361227.5	8044916	1447.298	347.230850	224.124400	565	VS-PN	20.32290	CO
504	RS	P	0.156935	308003.6	8046654	604.5866	307431.7	8046908	462.3089	237.188000	155.159056	381	VS-PN	16.37570	CO
505	RS	P	1.056419	377708.2	8046101	2953.947	375741.1	8046087	2535.122	237.076956	155.584222	482	VS-PN	15.73880	CO
506	RS	P	7.959334	306841.2	8044882	561.3563	306447.2	8045155	432.2943	611.849996	150.908081	468	VS-PN	17.55490	CO
507	RS	P	2.797709	403801.7	8042439	4355.211	403289.6	8043897	3608.472	316.034027	175.064061	293	VS-M	13.27910	CO
508	RS	P	1.182487	385660.7	8039195	2859.564	386866.5	8038879	2440.702	354.523652	196.884796	561	VS-PN	20.58330	CO
509	RS	P	1.729771	395708.7	8035368	3276.476	392390.7	8036493	2497.181	427.755886	168.196810	599	VS-PN	16.26750	CO
510	RS	P	2.330805	396902.9	8035425	3451.848	397851.6	8033733	2872.432	335.255806	337.047503	467	VS-PN	19.15640	CO
511	RA	P	3.620567	393100.8	8033001	2868.869	391210.7	8033486	2401.235	510.419335	184.979421	415	VS-PN	15.69750	CO
512	RS	F	2.296353	394166.1	8033922	3209.268	393279.8	8031998	2561.591	417.910441	330.437139	481	VS-PN	13.14340	CO
513	RS	F	0.504092	356607.3	8032980	1184.115	356314.4	8032482	1018.428	459.590114	174.405550	605	VS-PN	23.48050	CO
514	RS	F	2.597191	397912.9	8031276	3354.336	395917	8030446	2681.477	434.055199	153.591314	524	VS-PN	15.34340	CO
515	RS	P	0.309058	399217.2	8030075	3437.799	399137.9	8029259	3081.513	296.499166	224.446528	451	SC-PN	19.44450	CO
516	RS	F	1.305823	397832.4	8027747	3364.642	396748.9	8029067	2720.809	433.650139	232.831253	954	V-PN	25.12950	CO
517	RA	P	1.710990	399449	8025086	3358.568	398599	8026029	2679.415	386.698810	201.506248	602	VS-M	18.08790	CO
518	RS	P	0.107456	398785.8	8020023	3179.644	396381.8	8018477	2168.613	109.076458	171.896039	223	D-C	12.37650	CO
519	RS	P	0.122785	395036	8015531	2502.836	395054.3	8013246	1695.236	103.975033	185.982878	217	D-C	12.71110	CO
520	RS	P	0.438095	434751.2	8014102	3911.207	435068.1	8012488	3670.985	212.251202	131.500081	314	SC-PN	13.11380	CO
521	RS	P	0.159661	435814.3	8011503	3887.354	435143.7	8012470	3683.996	296.672455	194.468153	716	VS-M	23.53190	CO
522	RS	P	0.456688	393475.4	8010642	2006.44	392500.9	8012452	1601.645	364.228577	339.373729	574	VS-M	27.33380	CO
523	RS	P	0.297289	438802.5	8011432	3934.722	433395.2	8010176	3598.895	200.692317	173.727786	492	VS-M	21.11590	CO
524	RA	P	1.135433	398309.8	8007883	2471.67	398247.8	8007017	2099.665	972.586984	212.642727	796	VS-PN	20.91700	CO
525	RA	P	0.316117	430419	8007800	3851.192	432168.9	8006935	3548.857	392.646097	303.259804	544	VS-M	24.59470	CO
526	RS	P	0.107976	399462.7	8007063	2513.459	398891	8007584	2213.065	68.813307	156.560955	156	D-C	6.62573	PC
527	RS	P	0.127446	397084.9	8007412	2292.992	397326.5	8006678	1974.452	75.721140	159.834081	142	D-C	6.46950	PC
528	RS	P	0.163595	430610.6	8006754	3792.362	431811.9	8005765	3526.464	67.043915	155.369734	165	D-C	6.98551	PC
529	RA	P	3.714197	397319.7	8005923	2065.352	397235.9	8005281	1849.506	777.374840	218.740450	581	VS-M	24.56730	CO
530	RS	P	1.956103	436892.9	8003717	4052.664	436665.4	8003373	3991.008	585.347764	117.301828	725	VS-M	25.58840	CO
531	RS	P	2.153554	393624.1	7999846	1625.335	393977.7	7999136	1267.843	318.522855	264.428934	444	V-PN	14.94740	CO
532	RS	P	1.587760	391766.2	7997170	1335.676	391037.9	7997686	992.2701	368.276466	220.808774	526	VS-PN	19.19370	CO
533	RS	P	0.386928	391142.2	7996047	1349.007	390322	7996414	929.116	150.471024	304.283099	200	D-C	7.47886	CC
534	RS	P	0.519211	391290.8	7993046	1220.003	391642.3	7992182	992.3618	153.968287	316.630989	341	SC-PN	14.18200	CO
535	RS	P	0.466637	392222.7	7991615	1195.831	392328.7	7991188	997.5533	361.956579	139.264742	488	VS-PN	15.41340	CO
536	RS	P	0.304051	390942.4	7991436	1103.523	390992.2	7990592	935.1031	380.032572	302.109187	475	VS-PN	16.67350	CO
537	RS	P	0.611182	392861	7985526	1377.089	393093.3	7985238	1266.828	367.734500	119.862284	524	VS-PN	17.69180	CO
538	RS	P	0.286652	393070	7984664	1378.844	392802.3	7984953	1258.067	155.321527	249.081918	316	VS-PN	16.25540	CO

539	RS	P	1.389149	444729.4	7984379	4415.628	441897.3	7984439	3641.264	477.366206	123.269665	448	VS-PN	14.95960	CO
540	RS	P	2.913573	440086.7	7983800	3517.607	439487.2	7983707	3256.801	522.349435	272.549409	504	VS-PN	17.55830	CO
541	RS	P	0.588809	439454	7982051	3788.828	438977.9	7983845	3213.682	207.328712	102.828326	601	VS-PN	17.79410	CO
542	RS	P	0.612017	367732.1	7982273	518.0536	368229.9	7980533	243.5218	358.032434	244.692671	513	VS-PN	16.42950	CO
543	RS	P	2.676355	439642.3	7981504	3876.634	438459.8	7980363	3231.181	347.220300	323.326093	428	SC-PN	11.85430	CO
544	RS	P	7.894533	474018.5	7981162	5068.764	472901.7	7979956	4712.95	440.518788	92.980334	358	VS-PN	11.75300	CO
545	RS	P	6.318200	406096.7	7977852	2329.539	405607.2	7978158	2125.907	724.463341	291.879361	579	VS-PN	13.73420	CO
546	RS	P	1.085740	407413.3	7976102	2366.726	407653.7	7975411	2114.059	273.681834	245.614210	613	VS-PA	22.67940	CO
547	RA	F	0.418631	371112.6	7974900	496.6129	371411.7	7973719	337.9648	517.451885	146.302612	888	VS-PN	22.41410	CO
548	RA	F	0.297991	392470.6	7973236	1204.523	392458.3	7974244	993.7699	301.335043	149.115819	853	VS-M	24.71640	CO
549	RA	F	0.490119	378824.8	7971270	741.0258	377739.5	7972736	485.6181	568.203581	128.871496	1008	VS-PN	24.77530	CO
550	RA	P	5.524171	484826	7971913	4804.843	484084.7	7971770	4633.484	835.532046	86.189693	414	VS-PN	12.08480	CO
551	RS	P	0.891883	374533.1	7971159	516.798	373912.9	7971970	355.0086	343.135808	297.221073	536	VS-M	19.31330	CO
552	RS	P	1.784126	367473.4	7966657	328.8192	367459.2	7966210	152.0894	450.899095	257.630366	619	VS-PN	23.38470	CO
553	RS	F	0.179018	376412.5	7965787	558.7281	376427.5	7964679	290.4954	183.684864	278.686995	444	VS-PN	15.63890	CO
554	RS	P	1.139419	419879.4	7966858	3268.016	397156.3	7964969	882.2766	335.618950	134.209973	441	VS-PN	14.98290	CO
555	RS	F	4.189966	370913.1	7964868	434.9157	370986.5	7964103	212.3423	618.339147	90.810859	575	VS-PN	15.91700	CO
556	RS	P	0.861108	432582.7	7962591	3133.13	433879.5	7962041	2558.767	391.979892	277.358244	445	VS-PN	14.96060	CO
557	RS	P	16.208025	469212	7961593	4303.214	469335.9	7961943	4246.543	1016.121170	294.899285	364	VS-PN	14.13100	CO
558	RS	F	1.377728	420201.7	7962459	3287.646	420617.7	7960655	2614.409	477.290483	295.644346	530	VS-PN	17.85890	CO
559	RS	P	0.334906	432162.3	7962163	3157.923	432469.3	7960923	2392.877	107.459038	152.073635	243	SC-PN	16.10680	CO
560	RS	F	4.778727	434470.7	7960461	2995.192	434519.9	7961589	2530.212	603.516395	113.437119	480	VS-M	17.69690	CO
561	RS	P	13.419785	418578	7961606	3179.638	419569	7960314	2532.197	712.893703	164.100040	395	VS-PN	14.19030	CO
562	RA	P	3.611233	392832	7959442	1361.058	389174.3	7960373	598.0123	1073.166317	140.763182	556	VS-PN	16.08000	CO
563	RS	P	3.169944	384755.5	7957458	1036.99	385354.7	7959537	518.7319	1047.864168	293.061141	607	VS-PN	17.14720	CO
564	RS	F	0.848551	422387.5	7958280	3415.428	419489.2	7959068	2543.447	340.881854	192.222704	535	VS-M	17.39190	CO
565	RA	P	0.623576	475826.1	7956580	4400.024	474411.1	7957258	4146.678	442.586615	111.073968	707	VS-M	18.01690	CO
566	RA	P	1.294331	423050.2	7958112	3374.975	426306.9	7955372	1966.718	809.484261	120.654363	476	VS-PN	14.40650	CO
567	RS	P	3.190040	418454.1	7954065	3302.55	412151.3	7957432	1994.773	615.929275	307.360819	476	VS-PN	16.17890	CO
568	RS	P	0.182361	479231.9	7955226	4252.978	479087.8	7955015	4176.397	201.389930	127.733217	434	SC-PN	20.13560	CO
569	RS	P	0.109765	475868.8	7955407	4284.748	474436.7	7954737	4118.251	114.596187	263.964982	296	SC-PN	14.71530	CO
570	RS	P	1.367502	370532.8	7954675	445.8391	370197.6	7953942	176.3932	577.678436	286.507441	712	V-PN	23.72190	CO
571	RS	P	0.331967	474528.3	7953453	4218.531	474713.1	7953944	4119.038	120.183472	159.203252	292	SC-PN	17.58170	CO
572	RS	P	7.654203	453061.5	7953537	4710.693	452732.2	7952800	4376.23	1129.432666	144.185123	454	VS-PN	15.29150	CO
573	RS	P	0.189364	477717.1	7953004	4265.94	476991.7	7952806	4110.246	125.476537	233.555547	394	SC-PN	17.37120	CO
574	RS	P	2.160274	473558.1	7952524	4269.487	473548.8	7952183	4168.372	1024.491992	286.116425	1052	VS-PA	28.49420	CO
575	RS	P	14.956786	426983	7951047	3546.716	423908.6	7953526	1825.016	898.929996	150.611575	774	VS-PA	28.25070	CO
576	RS	P	0.349902	418080.9	7953784	3163.578	418534.6	7949557	1994.328	333.894154	312.995069	443	VS-M	21.43680	CO
577	RS	P	0.576669	473677.4	7951327	4271.9	473979.1	7951864	4160.211	142.471506	135.737516	333	SC-PN	17.37780	CO
578	RS	P	0.844028	416515	7952753	2984.272	417632.2	7946591	1477.658	75.639741	261.134359	365	SC-PN	18.58390	CO
579	RS	P	1.387080	382578.7	7949662	740.9842	381719	7948561	405.6166	296.246913	308.191118	550	SC-PN	19.63130	CO
580	RS	P	0.549627	424405	7947827	3508.683	420377.3	7949590	1596.482	221.815279	266.777547	397	SC-PN	19.31800	CO
581	RS	P	1.120672	463800.5	7948576	4890.124	465295.5	7947836	4529.859	288.128457	212.808446	359	V-PN	13.28800	CO
582	RS	P	1.672060	379184.2	7946431	782.167	380015.5	7948361	368.9368	304.233873	217.074274	591	VS-PN	24.00230	CO
583	RS	P	2.060409	389259.4	7948573	1134.922	388288.2	7946099	632.4362	548.857886	337.234622	726	VS-M	31.41840	CO
584	RS	P	15.990278	449563.7	7947164	3564.46	449301.8	7946957	3400.696	502.540257	201.247483	457	SC-PN	17.58610	CO
585	RS	P	0.567880	414144.4	7948392	2262.031	415339.2	7945121	1299.19	375.972254	179.703236	436	V-PN	15.72400	CO
586	RS	P	0.746472	408306.1	7948097	1862.403	407560.4	7945095	1056.762	422.910067	205.323483	572	V-PN	20.23240	CO
587	RS	P	0.562598	390712.1	7942703	1209.063	390772.9	7944744	609.3516	335.277970	299.881743	478	SC-PN	21.31040	CO

588	RA	P	0.459535	407077.7	7943173	1749.609	407082.2	7944853	1029.588	429.769966	284.235728	515	VS-PA	27.14020	CO
589	RS	P	1.303546	409733.5	7943031	1819.219	410061.7	7944634	1105.263	575.585743	338.917508	1021	VS-M	31.41140	CO
590	RS	P	0.104693	422263.3	7942888	3150.349	418506	7945169	1687.925	138.797727	283.540308	351	SC-PN	20.18960	CO
591	RS	P	2.333277	415518.7	7941744	2113.317	414505.6	7944633	1393.242	578.316460	334.688238	697	VS-M	25.55980	CO
592	RS	P	0.769970	447225.8	7941683	3506.572	446677.2	7941734	3329.14	389.728216	298.052517	586	VS-M	24.22110	PC
593	RS	P	1.156337	421120.2	7940248	2839.049	421489.1	7939689	2523.467	459.000865	207.637504	627	VS-M	26.43870	CO
594	RS	P	4.112707	456993.9	7939454	3935.64	456416.7	7939047	3686.795	808.105800	152.116698	714	VS-M	25.75020	CO
595	RS	P	0.363209	372373.4	7936930	662.3227	374132.2	7938129	352.4463	264.716435	303.327164	413	SC-PN	14.81530	CO
596	RS	P	3.054464	452329.3	7937612	3834.878	452183.9	7937111	3683.256	637.990821	299.171778	835	VS-PN	24.51610	CO
597	RS	P	4.841104	387292.8	7932336	1044.542	386567.3	7931216	676.8176	734.314646	24.784063	601	VS-PN	21.84230	CO
598	RS	P	4.187619	385989	7929907	1040.307	386586	7931105	668.6103	418.902255	293.732637	388	SC-PN	15.08470	CO
599	RS	P	4.309330	475419.9	7928865	4612.017	474642.8	7927775	4334.073	466.197614	293.933707	650	VS-PN	23.19980	CO
600	RS	P	0.754910	453345	7924534	3824.985	453529.2	7924040	3647.855	428.990463	278.053021	577	VS-PN	26.38400	CO
601	RS	P	5.403037	453646.2	7923733	3805.684	453421.3	7923952	3637.632	407.137617	139.735391	398	SC-PN	13.61980	CO
602	RA	P	0.989401	386682.5	7922104	1047.496	386043.3	7920705	738.2395	596.646465	270.664536	518	VS-M	23.18310	CO
603	RS	P	1.939391	389279.5	7918281	1130.21	389568.3	7919907	811.7245	524.174323	228.740499	718	VS-PN	23.61570	CO
604	RS	P	51.266341	456152.5	7917347	3759.11	455737.5	7916149	3431.878	1102.180030	206.938896	583	VS-PN	24.54610	CO
605	RS	P	0.871847	407117.8	7914894	1571.322	406446.4	7915582	1202.715	142.277657	293.943890	212	D-C	8.13010	PC
606	RS	P	3.533365	471686.8	7915381	4005.493	470794.4	7915097	3787.353	418.824711	269.591081	688	VS-PN	24.23390	CO
607	RS	P	0.290852	402559.3	7916070	1534.475	403011.2	7913497	1062.279	129.061993	304.682090	204	D-C	7.01175	PC
608	RA	P	2.329532	472643.1	7914432	3982.799	471613	7914175	3762.713	862.950436	165.080162	802	VS-M	23.14080	CO
609	RS	P	2.347741	474777.3	7914232	4028.75	473646.8	7914242	3786.344	746.739070	340.647834	867	SMC-M	23.06080	CO
610	RA	P	175.299335	393721.2	7914852	1229.101	393424.4	7913235	734.4908	3270.163624	221.500980	529	VS-PN	22.88010	CO
611	RS	P	1.116752	427532	7913066	2324.716	427082.9	7913281	2143.422	418.862075	104.663022	544	VS-PN	21.90720	CO
612	RS	P	9.329752	399924.3	7912223	1409.906	399875.2	7913754	955.4332	779.294894	288.742811	630	VS-PN	18.93880	CO
613	RS	P	2.713573	391595.6	7911837	1239.887	391436.7	7913963	661.2516	579.415810	150.719920	437	VS-PN	20.02890	CO
614	RS	P	1.722086	398682.4	7912146	1305.661	397765.9	7913342	894.1992	467.634099	284.394401	660	VS-PN	21.00700	CO
615	RS	P	1.224022	426970.2	7912553	2301.879	426604.2	7912853	2085.069	647.677007	204.735658	538	VS-PN	23.38340	CO
616	RA	P	6.775901	402431.6	7911608	1543.854	402119.9	7913811	1021.74	615.626630	232.865723	528	VS-PN	21.05350	CO
617	RS	P	0.245518	393121.5	7911385	1233.184	393467.5	7913212	731.0251	165.686907	210.452079	325	VS-PN	15.13780	CO
618	RS	P	1.473863	421157.8	7909739	1976.551	420865.5	7909944	1816.951	672.859290	247.418089	659	VS-PN	20.96140	CO
619	RS	P	0.760509	417640.3	7909713	1827.182	417821.1	7908669	1366.255	356.285917	185.550862	694	VS-PN	19.72050	CO
620	RS	P	2.705431	436448.2	7909060	2700.331	436255.2	7907991	2045.164	643.833207	320.624883	548	VS-PN	20.92190	CO
621	RS	P	2.761022	420010.1	7908041	1944.117	419040.8	7908790	1515.738	679.153671	317.955243	823	VS-PN	21.84680	CO
622	RA	P	0.708918	434904.5	7908794	2557.412	435129.1	7907062	1983.711	884.826557	325.461774	877	VS-PN	27.44170	CO
623	RS	P	1.696921	418998.6	7907084	1867.723	416393.5	7907876	1261	1011.031095	237.260768	728	VS-PN	23.62060	CO
624	RS	P	5.522049	415117.3	7907523	1493.418	415215.2	7906500	1141.518	807.599453	179.540418	749	VS-PN	28.60360	CO
625	RS	P	4.587500	441375.4	7908659	2765.971	440734.5	7904990	1838.076	240.222030	168.893477	221	V-PN	7.24832	CO
626	RS	P	4.956596	432753.4	7908677	2536.405	433266.1	7904954	1457.005	203.358678	325.288073	260	V-PN	12.10750	CO
627	RS	P	5.541105	469181.3	7906797	3784.338	469008	7906144	3547.444	404.795651	331.693815	723	VS-PN	22.40960	CO
628	RS	P	9.102732	446335.5	7907591	3170.7	445147.5	7905498	2216.12	335.826947	256.922321	234	V-PN	10.80530	CO
629	RA	P	24.934448	454631.1	7906582	3481.326	454481.1	7905328	2757.536	2468.303098	244.299987	650	VS-PN	19.72930	CO
630	RS	P	0.647529	416135	7905248	1767.604	415402.8	7906559	1157.154	372.004833	184.095636	653	VS-PN	26.29840	CO
631	RS	P	1.319009	429262.4	7907885	2466.364	431009.4	7903773	1360.041	302.334906	116.297722	248	V-PN	6.41523	CO
632	RS	P	0.630720	450157.4	7906412	3258.66	450117.1	7905033	2415.27	300.394464	312.370543	662	VS-PN	27.51400	CO
633	RS	P	0.665450	456740.2	7906115	3601.785	456310.3	7904974	2969.076	318.539417	161.778292	691	VS-PN	26.03050	CO
634	RS	P	1.782417	448443	7906594	3180.467	447758.6	7904597	2238.799	265.898052	129.458263	306	SC-PN	9.12124	CO
635	RS	P	0.685874	453059.8	7903875	3413.949	452809.8	7905336	2615.226	215.845442	187.446928	605	VS-PN	22.11610	CO
636	RS	P	0.226455	445118.6	7902418	3044.336	444553.4	7905058	2063.378	61.655135	213.455827	300	V-C	9.85064	CO

637	RS	P	0.830324	483648.8	7902222	4708.054	483140.9	7901273	4323.11	357.491555	153.515201	544	VS-PN	18.39330	CO
638	RS	P	1.065479	406188.1	7902360	1568.519	408559.1	7899651	836.9583	343.405426	305.355503	525	VS-PN	20.30760	CO
639	RS	P	0.481252	461905.4	7900112	3649.13	462210.6	7900264	3477.706	419.891097	294.146103	537	VS-PN	18.60010	CO
640	RS	P	1.155423	484226.9	7898676	4478.758	485092.6	7897889	4192.074	227.641169	157.877819	505	SC-PN	25.57950	PC
641	RS	P	0.465523	485996.8	7897579	4374.485	485480.1	7897526	4266.614	198.278082	166.070049	512	SC-PN	24.68700	PC
642	RS	P	0.853937	424476.8	7896304	2257.483	423898.6	7897636	1697.229	168.419819	176.622514	452	SC-PN	24.57320	PC
643	RA	P	5.148483	489236.4	7897131	4946.665	488138.4	7896404	4511.749	612.020890	283.174399	338	V-PN	15.56100	CO
644	RS	P	0.203003	477854.1	7895783	4118.006	476787.2	7896141	3903.273	110.260948	141.186948	197	VS-PN	11.36290	PC
645	RS	P	0.202191	396298.1	7896969	1339.45	397424.9	7894472	497.3056	120.777328	317.168132	202	VS-PN	10.87020	PC
646	RS	P	1.829494	432414.7	7896354	2619.81	432576.2	7894639	2288.355	774.364238	271.206124	597	VS-PN	23.80220	CO
647	RS	P	0.321206	403369.2	7893335	1343.748	402233.9	7896599	565.4105	260.806141	261.231659	599	VS-PN	22.01750	CO
648	RS	P	1.135638	487572.7	7894715	4490.577	487613.9	7893961	4300.723	575.145415	345.139490	620	VS-PN	24.29330	CO
649	RS	P	10.738298	474296.5	7893660	3768.07	474548.5	7893113	3709.103	274.531881	164.033794	245	SC-PN	7.47343	PC
650	RS	P	0.925247	441604.1	7893866	2902.823	441557.4	7892972	2648.248	645.452489	226.004804	565	VS-PN	24.78840	CO
651	RS	P	1.933872	487373.8	7892679	4423.788	486705.1	7893579	4221.375	355.814159	222.787942	564	V-PN	21.59020	CO
652	RS	P	0.302481	398192.7	7892047	1265.03	397291.8	7893850	473.1881	203.632303	301.994112	474	VS-PN	18.19050	CO
653	RS	P	0.686670	437019.4	7893301	2748.169	436927.2	7892740	2524.247	252.666893	160.824414	457	VS-PN	16.18350	CO
654	RS	P	2.033119	470871.4	7893156	3729.845	470673	7892481	3675.295	158.648100	165.785644	250	VS-PN	7.65600	PC
655	RS	P	2.216961	439291.6	7893069	2888.552	439518.3	7891847	2500.818	210.753439	359.301287	344	SC-PN	11.62340	PC
656	RS	P	5.126552	432632.1	7892850	2429.295	433090.1	7891250	2179.191	255.407735	323.493858	319	SC-PN	8.82159	PC
657	RS	P	0.530421	423317.3	7892246	2019.994	424089.6	7890759	1764.302	171.358323	259.083807	290	VS-PN	11.32090	CO
658	RS	P	1.428990	437384.5	7890615	2740.877	437203.4	7891609	2453.528	161.789421	322.597372	295	VS-PN	9.66633	PC
659	RS	P	0.525669	488188	7890797	4530.364	488718.6	7889897	4207.797	176.729840	181.819312	292	SC-PN	11.96400	PC
660	RS	P	2.645632	420265.9	7889272	1701.342	419506.3	7889683	1416.46	268.232650	179.224697	398	VS-PN	10.45840	PC
661	RS	P	180.624400	428584	7890203	2296.612	429679.6	7888872	1872.544	2385.739148	265.246320	698	VS-PN	20.24180	CO
662	RS	P	0.598005	416084.1	7888927	1650.523	417575.5	7887867	1298.466	222.573430	174.525795	331	SC-PN	11.11290	PC
663	RS	P	1.458476	430213.4	7887796	2240.808	429253.1	7888725	1854.553	574.362789	112.981263	615	V-PN	17.92610	CO
664	RS	P	0.228798	422757.4	7887759	1977.623	422309.7	7886100	1580.115	56.671350	19.474116	79	SC-PN	5.16076	CO
665	RS	P	3.019913	433433.3	7887289	2476.395	434524.5	7886337	2193.625	673.236604	167.016763	618	VS-PN	24.06380	CO
666	RS	P	1.007677	459354.9	7886683	3747.131	459934.3	7886187	3493.856	765.045362	166.094736	824	V-PN	22.07200	CO
667	RS	P	1.341493	425573.8	7887348	1953.736	425802.3	7885614	1661.098	464.979978	2.498415	690	VS-PN	23.23470	CO
668	RS	P	2.604894	413950.4	7886997	1531.603	414963.9	7885830	1124.226	647.441334	142.515278	701	VS-PN	27.53590	CO
669	RS	P	21.214725	411738.1	7885963	1427.32	412012.8	7884772	983.9849	763.045430	284.282188	458	VS-PN	17.94920	PC
670	RS	P	5.629820	410276.5	7884954	1380.087	410934.5	7883969	930.4415	518.258134	16.072890	329	VS-PN	11.56160	PC
671	RS	P	4.119321	420683.7	7883474	1489.737	420684.3	7882896	1343.355	871.980852	285.220886	617	VS-PN	23.67050	CO
672	RS	P	2.453518	440742.2	7884650	2805.47	429710.1	7880680	1923.461	253.345936	295.592981	265	V-PN	10.72230	CO
673	RS	P	21.045524	418979.5	7882584	1417.142	419239.5	7881878	1207.042	1408.256842	130.068654	775	VS-PN	23.27220	CO
674	RS	P	44.157701	407445.9	7882371	1249.93	408890.2	7880495	791.076	1307.776754	298.106531	631	VS-PN	19.42800	CO
675	RS	P	0.194585	415138.4	7880231	1291.315	415019.4	7881270	1011.306	76.581285	214.324394	210	V-PN	9.06351	CO
676	RS	P	3.489546	403244.5	7881660	1156.864	403419.9	7879781	635.284	166.496734	244.925801	319	V-PN	10.71950	CO
677	RS	P	1.507148	427765.9	7880990	2018.58	428720	7879906	1678.199	269.445926	204.581543	341	SC-PN	9.64136	PC
678	RS	P	0.316961	429659.8	7878583	2037.221	428484.1	7879252	1634.626	99.492547	20.617843	184	SC-PN	9.19875	CO
679	RS	P	0.353105	397930.4	7879615	1069.172	398434.1	7878018	484.6397	334.463071	204.078846	599	VS-PN	20.97480	CO
680	RS	P	1.840932	481493	7878897	4044.819	480938.8	7878061	3810.308	155.693562	254.744671	258	SC-PN	9.32343	CO
681	RS	P	0.204574	423729.4	7879166	1759.542	424474.9	7877706	1378.022	101.115007	181.555637	158	SC-PN	9.92474	CO
682	RS	P	18.348427	426480.8	7877313	1850.095	426351.9	7878390	1508.73	1721.699718	308.881136	884	VS-PN	22.99260	CO
683	RS	P	6.537257	404977.6	7875540	1202.241	402568.6	7879853	603.692	1169.250425	173.873035	683	VS-PN	17.84330	CO
684	RS	P	0.926512	409089.4	7876076	1269.182	409426.8	7878989	818.2725	111.688712	29.331618	165	SC-PN	7.90534	CO
685	RS	P	6.309795	425318.7	7876570	1756.968	424412.9	7877530	1384.998	1506.613754	169.723368	491	VS-PN	18.02840	CO

686	RS	P	1.950408	401805.6	7875669	1104.531	399167.6	7878124	506.5477	335.367657	218.001988	513	SC-PN	13.43760	PC
687	RS	P	17.164784	451632.4	7876792	3240.938	452207.6	7876127	2927.139	1912.200815	293.636428	790	VS-PN	21.10510	CO
688	RS	P	1.276596	419064.4	7875523	1546.85	418927.4	7876405	1149.375	360.265371	116.327280	354	V-PN	13.81590	CO
689	RS	P	15.740926	422319.5	7875068	1669.537	422060.2	7876710	1261.672	413.230192	23.302678	328	SC-PN	9.28089	PC
690	RS	P	13.526973	452601.7	7876023	3104.31	453089.5	7875440	2838.38	502.485918	201.430571	499	SC-PN	14.22210	PC
691	RS	P	0.172288	454831.2	7874462	3266.617	453088.4	7875325	2830.611	163.764055	231.568131	425	VS-PN	17.70200	CO
692	RS	P	14.253422	476822.8	7874750	3986.449	476360.8	7874325	3843.009	962.840815	159.933855	655	VS-PN	16.58720	CO
693	RS	P	23.527610	449137.8	7872961	3007.488	449508.1	7872176	2735.494	805.640440	193.948286	605	VS-PN	16.92890	PC
694	RS	P	33.611745	410098	7873944	1293.633	409531.4	7871100	771.3505	599.711489	1.705573	442	SC-PN	17.82280	PC
695	RS	P	4.407410	440044.5	7872588	2551.263	434752.2	7871908	2170.573	720.020691	0.152645	615	SC-PN	16.40190	PC
696	RS	P	4.588804	420383.3	7869230	1456.805	419565.8	7870720	1049.341	713.955458	11.567943	675	VS-PN	18.30320	PC
697	RS	P	7.964345	445427.6	7869803	2731.94	445696.2	7869015	2417.046	1462.423978	301.265288	779	VS-PN	22.15770	CO
698	RS	P	15.648857	484717.6	7869177	4217.737	484369.6	7868753	4051.219	720.075247	340.674626	493	VS-PN	14.89510	CO
699	RS	P	0.527238	434511.2	7868512	1939.831	433290.4	7869320	1511.52	177.431378	275.376277	328	V-PN	15.69320	CO
700	RS	P	0.686707	411313.6	7865302	1296.195	411799.5	7870444	843.3988	315.582155	146.544461	575	VS-PN	23.09390	CO
701	RS	P	0.243896	445633.3	7867527	2706.742	444527.7	7868522	2292.368	248.844630	234.859232	399	SC-PN	21.63470	CO
702	RS	P	7.152746	423149.2	7868782	1475.16	423091.9	7867096	1134.996	309.876460	55.727321	258	D-C	6.86634	PC
703	RS	P	0.375653	441583.9	7868692	2547.046	441990.8	7866391	1787.582	151.621767	196.199987	266	V-PN	11.98470	CO
704	RS	P	2.360665	426636.6	7865147	1777.132	425762.5	7867254	1307.323	367.724575	212.928239	420	SC-PN	10.17110	PC
705	RS	P	3.299561	447344.2	7866483	2825.306	447111.5	7865658	2418.235	371.697157	26.483712	390	SC-PN	10.44770	PC
706	RS	P	1.446725	437860.7	7867289	2066.425	437029.8	7864710	1559.945	277.943966	215.489491	326	V-PN	12.93820	CO
707	RS	P	0.329612	423431.6	7864764	1618.626	422783.3	7866466	1255.98	177.130358	159.581103	378	VS-PN	16.28130	CO
708	RS	P	0.349042	457450.6	7866848	3060.103	458189.8	7864543	2486.041	168.051923	314.223920	287	VS-PN	13.14980	CO
709	RS	P	3.650585	447118.1	7865173	2529.376	446709.8	7865539	2356.087	309.256613	204.560975	326	SC-PN	10.51120	PC
710	RS	P	4.210484	462334.8	7865005	3186.704	459113.9	7864873	2564.73	318.485158	10.076180	260	SC-PN	7.63017	PC
711	RS	P	1.076725	453583.9	7865652	2945.899	454019	7863445	2489.931	327.231984	199.106289	648	V-PN	19.63410	CO
712	RS	P	0.781507	464134.5	7863855	3292.895	463924.3	7862288	2856.143	368.607618	315.709952	495	SC-PN	19.43680	PC
713	RS	P	0.566559	450688.7	7863296	2482.789	450990.4	7862672	2161.149	218.139973	252.351445	304	V-PN	14.03130	CO
714	RS	P	12.233624	458430.1	7863198	2720.732	457872.2	7861602	2421.749	472.195841	170.039704	369	SC-PN	12.07280	PC
715	RS	P	1.093065	466475.9	7862813	3464.364	466055	7861600	3070.738	220.086160	256.028500	294	V-PN	13.42230	CO
716	RS	P	1.874666	446751.5	7863443	2662.982	447350.2	7860869	2003.131	242.405467	270.536122	449	V-PN	13.22480	CO
717	RS	P	2.991764	450787.9	7861716	2437.466	450425.2	7862401	2137.251	494.610371	190.406265	423	SC-PN	12.10450	PC
718	RS	P	0.244203	371883.5	7861914	1065.631	369407.1	7860286	63.52971	181.294372	295.592630	376	VS-PN	18.49760	CO
719	RS	P	1.720458	455810.8	7859444	2885.421	455662.1	7858547	2587.171	454.473183	358.163120	434	SC-PN	17.33290	PC
720	RS	P	3.703828	469264.7	7851354	3603.623	466382	7852007	3082.123	578.635387	355.725140	434	SC-PN	10.72740	PC
721	RS	P	2.966619	459073.5	7850894	3018.062	459967.7	7850000	2628.617	411.462141	322.529526	485	SC-PN	20.11770	PC
722	RS	P	0.388699	458775.3	7850227	2876.875	459507.2	7849534	2592.944	216.810321	309.314003	361	VS-PN	18.16280	CO
723	RS	P	7.315726	462425	7847142	3064.677	463670.5	7845906	2637.008	522.114043	351.946392	388	SC-PN	15.80870	PC
724	RS	P	3.256862	478538.8	7845367	3514.328	477280	7847678	3111.456	502.158565	10.728034	437	SC-PN	14.08110	PC
725	RS	P	0.193437	471644.8	7846094	3025.98	470529.4	7844892	2561.65	159.599635	305.048852	366	VS-PN	15.90800	CO
726	RS	P	3.898884	475254.9	7841839	2976.48	475211.2	7841033	2768.99	460.926801	170.176583	723	VS-PN	19.35130	PC
727	RS	P	1.012929	482857.1	7841600	3768.689	481176.4	7840325	3290.117	655.166952	190.226936	742	VS-PN	23.46250	CO
728	RS	P	1.929968	393982.3	7841144	1003.955	393284	7839819	763.9959	428.378731	307.696003	543	VS-PN	14.59470	CO
729	RS	P	3.406609	390543.7	7839498	1028.653	391495.4	7841102	726.0647	573.700599	172.613719	577	VS-PN	18.32430	CO
730	RS	P	5.285874	481400.1	7838510	3818.609	481772	7839866	3351.031	606.722994	286.900585	548	VS-PN	17.73470	PC
731	RS	P	1.079948	480192.2	7837146	3792.832	476276.5	7839899	2774.096	351.900195	174.532296	752	SC-PN	20.29110	PC
732	RS	P	9.971080	473536.8	7838436	2827.487	472847.8	7838450	2632.36	927.894921	189.908127	610	VS-PN	20.05970	CO
733	RS	P	7.042680	397333	7838382	1053.342	396986.3	7838068	920.5727	1079.399381	172.160948	512	VS-PN	17.29080	CO
734	RS	P	0.381708	396714.2	7837523	1097.075	397105.2	7837883	924.0294	236.894811	194.863818	434	V-PN	15.79410	CO

735	RS	P	7.625544	402523.9	7837935	1141.333	402407.5	7837450	1060.795	954.579324	209.578163	643	VS-PN	20.93500	CO
736	RS	P	1.487435	384512.7	7837402	961.9895	384461.4	7837899	855.8061	723.789827	186.822353	780	VS-PN	21.13760	CO
737	RS	P	2.874101	462238.8	7836806	2335.278	461552.9	7836801	2086.146	610.450026	330.820169	770	VS-PN	23.76660	PC
738	RS	P	19.044596	374524.3	7835706	411.3525	373608.5	7835689	41.29883	1106.323141	156.983142	533	SC-PN	19.70880	CO
739	RA	P	0.982490	393175.4	7834710	1145.069	393687.4	7834827	1068.533	846.458508	173.567583	783	VS-PN	23.04330	CO
740	RA	P	0.757260	471222.6	7835439	3233.412	470073.4	7834342	2767.429	401.217403	171.394835	467	V-PN	15.35720	CO
741	RS	P	2.146912	473074.7	7835529	3223.834	473059.8	7833905	2760.176	843.389799	181.671750	775	VS-PN	23.64080	CO
742	RS	P	1.408454	465763.8	7834038	2612.641	466505.2	7834924	2270.525	632.708529	200.646346	689	VS-PN	25.08450	CO
743	RS	P	3.224555	457269.1	7835536	2390.137	457507.6	7833057	1914.549	941.667679	198.918489	712	VS-PN	20.95520	CO
744	RS	P	6.295475	463540.9	7833392	2556.05	462091.5	7834685	2014.933	798.722721	350.284512	940	VS-PN	23.75630	CO
745	RS	P	4.556616	522697.8	7833946	4255.184	524208.4	7833692	4179.523	980.958247	347.913162	703	VS-PN	21.14690	CO
746	RS	P	0.588112	453351.5	7834360	2281.874	453785.5	7832107	1778.11	384.944231	208.169423	573	V-C	18.62530	CO
747	RS	P	12.442778	458773.8	7832044	2280.999	458233.4	7833084	1911.277	731.561077	138.798350	455	SC-PN	12.00930	PC
748	RS	P	0.157288	456026.8	7832274	2057.258	455749.6	7832918	1823.127	171.424646	63.531412	263	V-PN	13.05680	CO
749	RA	P	4.951813	394440.7	7832474	1127.959	394661.3	7832657	1083.551	1173.844207	143.822437	606	SC-PN	19.91840	PC
750	RS	P	0.511591	395439	7832117	1117.209	395447.1	7832355	1090.318	286.683651	132.242007	413	V-C	15.32360	CO
751	RS	P	0.234828	458363.6	7831838	2247.593	458338.8	7830739	1962.326	107.870764	264.162315	563	V-C	18.35170	CO
752	RS	P	1.590482	452115.7	7830190	2096.573	452690.9	7831339	1761.876	560.253740	336.543770	665	SC-PN	16.94880	CO
753	RS	P	0.876906	465923.6	7831500	2709.218	466025	7830143	2294.12	434.915856	236.469530	610	V-C	20.72160	CO
754	RS	P	1.441772	464724.4	7831106	2671.836	464363.3	7829904	2214.828	214.732469	288.544167	497	V-C	16.48540	CO
755	RS	P	13.377124	455820.4	7829032	2323.836	455564.2	7830628	1856.656	842.144356	155.714977	648	SC-PN	15.46020	PC
756	RS	P	3.194013	463091	7828951	2657.679	463525.6	7830530	2211.639	331.454856	174.623930	315	SC-PN	14.71180	CO
757	RS	P	19.307382	514542.9	7828145	4743.663	514085.8	7826734	4571.043	778.337292	340.819485	466	SC-PN	12.89470	PC
758	RS	P	0.519088	513738.7	7827598	4687.115	513665.6	7826715	4626.163	189.854455	176.878485	568	V-C	20.60010	CO
759	RS	P	0.571899	505929.3	7825830	4265.436	505570.9	7826193	4069.798	58.966677	155.251633	193	V-PN	7.30470	CO
760	RS	P	0.834397	505337.1	7825390	4229.162	504607.1	7825710	3952.552	254.575189	182.990892	410	SC-PN	21.06390	CO
761	RS	P	1.367819	448178.8	7823425	1976	448123.5	7823552	1951.072	202.412527	323.400036	408	V-C	12.83110	CO
762	RS	P	4.705251	503848.5	7822169	4088.631	503528.2	7822536	3889.104	791.841854	333.447964	618	SC-PN	13.75830	PC
763	RS	P	0.566203	503200.3	7821385	4081.214	502665.5	7821758	3864.36	223.922398	189.330355	464	SC-PN	18.78930	CO
764	RS	P	0.276036	514882.9	7821366	4740.598	514777.7	7820724	4433.925	54.550083	196.377413	87	V-PN	5.28131	CO
765	RS	P	2.096761	478606.7	7819680	3241.414	478018.7	7819448	3051.208	387.733651	169.492040	500	SC-PN	18.66660	CO
766	RS	P	12.088369	498191.4	7818142	3917.148	498571.7	7817685	3617.293	250.103666	164.019449	419	SC-PN	19.07080	CO
767	RS	P	4.380650	494991.5	7817799	3983.836	495177.9	7817401	3782.562	255.692363	152.560229	383	SC-PN	18.65040	CO
768	RS	P	2.899474	457681.6	7817209	2193.736	456941.9	7817502	2045.772	287.348944	349.674918	404	SC-PN	20.28380	CO
769	RS	P	0.528037	499039.6	7817106	3865.275	498219.3	7817465	3599.551	322.566966	149.475758	347	V-C	12.52990	CO
770	RS	P	0.690122	484259.9	7817459	3991.242	485103.3	7816120	3511.101	284.881899	298.403447	492	VS-PN	22.42100	CO
771	RS	P	4.706743	490413.5	7815917	3955.39	489578.5	7816966	3639.73	424.067686	140.556743	381	SC-PN	14.36640	CO
772	RS	P	6.462532	497862.5	7815533	3813.543	497000.9	7815728	3545.203	352.057349	125.413971	374	SC-PN	12.54840	PC
773	RS	P	1.515410	474210.6	7816216	2980.986	474718.2	7815089	2497.76	386.255601	314.037971	508	SC-PN	21.46960	CO
774	RS	P	4.075120	477137.3	7814377	2965.198	474624.1	7814924	2486.144	397.507994	195.095522	467	SC-PN	18.88650	CO
775	RS	P	3.359974	477853.4	7815467	3121.354	478351.9	7814802	2973.114	282.769566	131.080341	343	SC-PN	18.57160	CO
776	RS	P	0.891440	488580.2	7814931	3635.565	488190.4	7815224	3453.005	253.275776	130.600319	368	V-PN	16.24360	CO
777	RS	P	5.594107	486008.4	7815829	3862.814	486645.9	7814467	3193.82	292.637768	172.489679	397	SC-PN	18.20960	CO
778	RS	P	3.523316	472585.4	7814606	2862.344	473508.8	7813696	2376.163	407.377348	139.029652	413	SC-PN	12.09930	PC
779	RS	P	2.352539	455948.7	7813546	2060.597	455696	7814080	1939.832	443.334895	167.015186	511	SC-PN	11.91230	PC
780	RS	P	1.101850	480709.5	7815264	3315.808	480719.6	7811842	2623.19	449.645251	146.236107	505	SC-PN	12.43070	PC
781	RS	P	0.459524	471244.6	7812864	2763.035	472551.2	7812121	2299.373	146.381804	179.937815	415	SC-PN	18.99780	CO
782	RS	P	69.736973	483671.7	7810786	3418.7	483395.4	7812912	2767.31	882.008921	250.208197	558	V-PN	17.58570	CO
783	RS	P	1.537585	488031	7811782	3705.414	487668	7811360	3473.385	210.100867	159.769117	380	SC-PN	15.49170	PC

784	RS	P	3.911808	527767.6	7811505	4671.663	526969.9	7811076	4426.458	458.853847	142.403664	437	SC-PN	13.08480	PC
785	RS	P	1.728402	484648.5	7810438	3437.201	485658.4	7811838	2906.831	280.009552	353.468830	490	SC-PN	20.91740	PC
786	RS	P	15.422940	470343.8	7811409	2740.782	471312.9	7810442	2201.891	521.580347	174.667636	458	SC-PN	12.29390	PC
787	RS	P	4.076626	489060.2	7811592	3698.291	489469.4	7810375	3272.059	340.381407	138.661783	361	SC-PN	14.34720	CO
788	RS	P	3.531828	477895.1	7809150	3002.517	476628	7811256	2378.06	402.594863	299.653082	487	SC-PN	17.85590	CO
789	RS	P	3.385989	442032.4	7809741	1579.464	441554.9	7810222	1513.582	584.532150	162.493358	527	SC-PN	22.78460	PC
790	RS	P	1.334145	474828.3	7808993	2898.35	474504.2	7810636	2289.352	234.511294	213.518403	330	V-PN	14.31960	CO
791	RS	P	7.126459	519717	7809243	4576.075	517951.2	7809327	4300.853	381.519590	152.944814	437	SC-PN	17.17560	CO
792	RS	P	0.975681	468495.2	7809357	2571.229	469311.9	7807904	2274.389	341.365610	353.169842	534	SC-PN	20.22270	CO
793	RS	P	24.371492	521093	7806799	4467.308	520763.2	7807164	4387.081	598.549047	330.816478	339	SC-PN	10.05660	PC
794	RS	P	15.373712	465947.7	7807224	2400.646	466695.2	7805953	1984.676	450.909561	6.607732	304	SC-PN	10.12820	PC
795	RS	P	2.830667	476158.7	7808044	2936.465	474903.9	7805955	2415.535	371.969832	316.651240	520	SC-PN	18.63840	CO
796	RS	P	6.937321	470782.9	7805230	2502.918	470105.2	7806392	2175.954	597.982981	312.943430	417	SC-PN	11.15840	PC
797	RS	P	1.401086	483974.3	7806039	3386.572	484092.6	7805617	3247.423	313.798847	139.167550	398	V-PN	16.40690	CO
798	RS	P	1.014180	482997.7	7805629	3318.54	483029.8	7805298	3168.896	397.474855	351.176212	485	SC-PN	15.53430	PC
799	RS	P	5.311770	475298.2	7804703	2884.215	475841.9	7805826	2419.327	407.865015	351.029741	374	SC-PN	12.97830	PC
800	RS	P	2.722007	463613.6	7806336	2345.572	464837.9	7804415	1840.979	265.929764	140.097489	465	SC-PN	19.81740	CO
801	RS	P	10.374661	461075.8	7804858	2210.4	461315.9	7803703	1757.367	436.006529	296.339826	450	V-PN	14.81130	CO
802	RS	P	0.520301	452687.9	7804282	1857.261	453132.1	7803106	1575.136	143.440662	227.434993	355	V-PN	13.98040	CO
803	RS	P	1.743799	468987.1	7803116	2521.443	468486.2	7803887	2178.826	271.994499	154.738862	410	V-PN	15.50350	CO
804	RS	P	18.893319	477108.8	7802864	2943.97	477861.8	7803802	2598.51	522.282835	191.267897	406	SC-PN	10.71560	PC
805	RS	P	47.878537	464303.2	7802399	2315.308	463857.4	7803890	1891.104	380.689945	262.682003	472	V-PN	16.04850	CO
806	RS	P	4.349011	382881.7	7804203	883.8886	380694.4	7803510	1.90163	407.464032	331.257342	458	SC-PN	19.69360	PC
807	RS	P	1.078865	505128.3	7802538	4150.478	505737.6	7801991	3955.667	314.893459	161.182398	530	V-PN	17.82990	CO
808	RS	P	0.490019	456550.3	7800751	1953.399	456862.6	7801583	1757.063	166.518149	219.348078	403	V-PN	15.31540	CO
809	RS	P	1.480576	475508.5	7800928	2885.445	475374.4	7800726	2800.015	428.311359	303.499887	493	SC-PN	19.72890	CO
810	RS	P	72.987749	484516.9	7801198	3363.601	484370	7800465	3201.491	452.796357	5.398338	290	SC-PN	8.71355	PC
811	RS	P	5.370944	462660.3	7800704	2269.672	462647	7800271	2089.281	414.373820	311.975157	578	V-PN	18.80540	CO
812	RS	P	6.905324	382869.4	7798448	781.7721	380569	7797982	5.329585	340.164599	181.946190	458	SC-PN	15.43300	PC
813	RS	P	11.331291	521947.5	7797568	4245.978	519755.4	7797823	4050.5	759.464138	169.971369	542	V-PN	15.14100	CO
814	RS	P	7.870304	480714.9	7797215	3148.251	480583.6	7796724	2955.385	469.809184	337.475257	475	V-PN	16.52790	PC
815	RS	P	0.440886	476511.5	7796736	2878.453	476451.9	7796446	2756.904	407.070803	195.747183	601	V-PN	17.84150	CO
816	RS	P	6.226438	484946.4	7795769	3394.898	484572.9	7795062	3126.091	506.480391	197.863466	556	SC-PN	19.90290	CO
817	RS	P	2.845312	491562.6	7793418	3954.217	490141.9	7793797	3551.043	362.645429	339.142948	428	SC-PN	12.28240	PC
818	RS	P	4.247405	382320.8	7793412	597.5982	380852.7	7793213	3.885506	574.061194	162.215754	572	SC-PN	18.99960	CO
819	RS	P	0.326258	489581.7	7792140	3784.501	488509	7793242	3497.786	173.289685	311.808009	614	SC-PN	20.82240	CO
820	RS	P	17.002598	510401.7	7792409	4501.31	508199.1	7791450	4099.523	621.974166	267.656700	409	V-PN	14.98080	CO
821	RS	P	4.068552	492674.6	7790742	3783.186	492287.5	7789809	3489.334	455.967872	168.848499	646	SC-PN	16.04980	CO
822	RS	P	1.279518	485789.4	7790690	3531.265	486321.3	7789457	3114.87	436.751392	187.642294	480	V-PN	15.43090	CO
823	RS	P	0.422553	483504.8	7789272	3281.048	483749	7788327	2906.353	321.639829	154.185761	776	VS-PN	24.10450	CO
824	RS	P	1.359224	479652.7	7788393	3015.462	479543.9	7787345	2675.151	298.983084	199.264490	392	SC-PN	15.83840	CO
825	RS	P	4.540534	478684.4	7788187	2963.11	478849.9	7787150	2641.521	393.625747	199.134891	540	V-PN	15.25790	CO
826	RS	P	3.542567	496613	7786666	4032.107	496315.3	7787978	3827.12	659.851423	166.908743	591	V-PN	19.13880	CO
827	RS	P	0.830735	494223.2	7786131	4167.456	495642.9	7786924	3864.38	300.215418	332.096257	416	VS-PN	24.47040	CO
828	RS	P	3.131667	480055.7	7786348	3000.666	478327.2	7786544	2620.729	1002.101727	236.675744	709	SC-M	17.79720	CC
829	RS	P	0.787065	476385.7	7786525	2842.112	476615.6	7785699	2526.402	298.249461	189.415657	483	V-PN	22.80880	CO
830	RS	P	9.575917	478139	7784866	2920.382	477713.9	7785970	2564.819	521.499620	282.769020	534	V-PN	23.02270	CO
831	RS	P	0.797675	474089.7	7785530	2666.768	474105.4	7785089	2469.057	389.445223	134.986397	522	VS-PN	21.94550	CO
832	RS	P	0.452675	457618.6	7784719	1837.588	457248.4	7784704	1691.72	283.930838	133.451103	469	VS-PN	20.25570	CO

833	RS	P	2.390769	459218.6	7783339	1875.745	459017	7782921	1758.85	427.669000	134.781160	558	V-PN	21.23540	CO
834	RS	P	5.016064	495828.2	7783003	4430.107	495086.3	7782196	4006.197	402.872150	331.421321	687	V-PN	17.36620	CO
835	RS	P	1.243191	404173.2	7781669	1396.87	403904.7	7781636	1286.572	464.330341	222.864950	643	V-PN	18.75300	CO
836	RS	P	0.260186	461033.4	7781588	1942.163	461064.5	7781230	1777.386	207.490061	183.101197	716	V-PN	24.48800	CO
837	RS	P	2.184371	478379.3	7778669	2820.316	478372	7778058	2609.143	478.572007	232.812761	557	V-PN	17.27480	CO
838	RS	P	4.961884	476621.8	7777596	2671.142	476769.4	7777104	2503.911	239.959600	207.796615	300	SC-PN	7.91653	PC
839	RS	P	8.459011	403172.7	7775887	1210.925	402782.7	7775980	1109.51	302.588462	30.690470	253	SC-PN	8.03813	PC
840	RS	P	2.242924	487538.2	7774284	3731.626	486427.5	7773937	3345.158	467.578017	15.338291	540	V-PN	17.98600	CO
841	RS	P	12.956893	486008.6	7774522	3677.699	484602.7	7773046	3220.296	1018.735418	305.106792	562	V-PN	15.19470	CO
842	RS	P	0.407976	488408	7772915	3786.806	487940.3	7771663	3387.553	195.127254	271.095354	354	V-PN	16.05970	CO
843	RS	P	0.268372	543478.1	7771078	4302.943	542343.6	7772163	4169.58	132.769642	227.782554	220	SC-PN	12.14810	PC
844	RS	P	0.173467	488429.9	7768533	3493.111	488851.6	7767446	3003.353	173.045439	47.354017	252	SC-PN	11.34900	PC
845	RS	P	1.101626	486560.1	7767677	3273.384	486901.8	7766549	2815.453	80.538534	193.515573	121	SC-PN	6.42379	PC
846	RS	P	0.348318	485080.6	7766637	3118.421	485497.7	7765704	2701.902	106.183409	354.110519	196	SC-PN	8.56389	CC
847	RA	P	2.730249	444898.2	7766045	1114.495	444790.5	7765853	1107.987	709.147511	307.069355	601	V-PN	18.77000	CO
848	RS	P	0.791321	483133.5	7766091	2926.518	483195.7	7765259	2672.163	249.131165	269.535167	402	VS-PN	21.17530	CO
849	RS	P	1.005936	478799.8	7765674	2635.793	478707.8	7764825	2286.628	370.053652	268.913963	506	SC-PN	15.01040	CC
850	RS	P	0.754887	481274.9	7765647	2741.167	481220.9	7764657	2437.458	76.535337	77.204270	178	SC-PN	6.52907	CC
851	RS	P	1.373239	488707.2	7764129	3429.919	488318.4	7765332	3010.32	465.983396	226.317363	533	V-PN	22.38650	CO
852	RS	P	1.716671	479796.6	7763118	2673.219	479350.4	7762299	2358.577	463.657699	180.526721	460	V-PN	21.95730	CO
853	RS	P	1.977826	480590.2	7762229	2673.521	479916.7	7761739	2412.276	342.115415	39.931276	579	VS-PN	19.43220	CO
854	RS	P	8.040531	539988.1	7761599	4472.13	539593.6	7761534	4342.244	475.588437	174.505196	499	VS-PN	18.75590	CO
855	RS	P	4.537322	494358.2	7760562	4138.718	494978.2	7760613	4024.533	541.117317	311.744813	695	SC-PN	22.62630	CO
856	RA	P	16.715523	545853	7760988	4221.884	545909.3	7760036	4006.104	941.502608	271.641077	479	V-PN	15.61850	CO
857	RS	P	3.870345	509269.9	7755746	4054.911	510751.1	7754888	3825.326	75.661063	99.561491	178	V-PN	7.07945	CO
858	RS	P	8.538020	383641.7	7754871	481.3419	383215.9	7755276	178.3118	503.763820	169.094422	394	VS-PN	17.50360	CO
859	RS	P	4.242569	390358.3	7753882	876.1342	390244.7	7753558	739.3735	369.721922	332.548503	610	VS-PN	18.56220	CO
860	RS	P	0.757584	498097.7	7753734	4225.426	498563	7753511	4155.618	234.131255	336.723269	410	VS-PN	17.67150	CO
861	RS	P	0.309097	497984.9	7749106	4039.586	498081.8	7748870	4007.13	44.407341	50.303000	151	SC-PN	5.79064	CC
862	RS	P	0.122404	420160.8	7747833	1163.5	420784.7	7747579	1011.845	26.891034	1.936500	84	SC-PN	4.46972	CC
863	RS	P	3.624862	481296.3	7745138	2589.793	481964.6	7744561	2487.622	285.267192	181.292105	448	VS-PN	17.75120	CO
864	RS	P	2.049642	499196.9	7740857	4057.43	499375.6	7740634	3989.532	334.697375	26.603005	460	VS-PN	17.10330	CO
865	RS	P	1.772806	497858.5	7739812	3964.984	498081.4	7739609	3899.003	415.098104	175.730368	451	VS-PN	24.13510	CO
866	RS	P	1.656969	479323.3	7738162	2365.137	478609.1	7738485	2103.889	457.007416	196.723289	588	VS-PN	25.38680	CO
867	RS	P	8.839273	-80017	8342896	3312.788	-79958	8341889	3191.794	467.179644	350.878762	344	SC-PN	12.65060	CO
868	RS	P	8.046715	-96486.4	8341844	2809.325	-97127.7	8342057	2628.444	446.040509	15.387743	515	SC-PN	15.08950	CO
869	RS	P	1.164463	-99522.4	8341232	2548.041	-100923	8341971	2214.495	172.619838	197.953224	196	V-PN	7.73743	CO
870	RS	P	0.298346	-20812.2	8333684	3396.128	-17377.6	8333122	2520.89	60.951936	184.731294	255	V-PN	8.75476	CO
871	RA	P	1.071004	-35124.8	8327518	3044.798	-32779.8	8327739	2385.286	363.845197	243.762966	476	SC-PN	16.78030	CO
872	RA	P	1.256047	-43174	8323670	3264.778	-35802	8322862	2244.263	565.371716	164.161085	533	V-PN	18.16290	CO
873	RS	P	0.162646	-12442.3	8321400	3172.403	-11776.7	8322974	2876.068	195.638157	315.325761	469	V-PN	15.22220	CO
874	RS	P	0.359430	-101811	8310954	2042.503	-99590.1	8309572	1328.361	276.610088	293.641069	415	V-PN	15.62790	CO
875	RS	P	0.122211	-103700	8310598	1986.074	-104783	8309059	1530.065	24.928455	336.416900	156	SC-PN	7.34800	CO
876	RS	P	0.311716	256254.4	8299784	4317.508	255727.7	8299833	4204.914	199.527359	318.868376	283	V-PN	14.53380	CO
877	RS	P	0.362010	-33936.8	8292005	3541.288	-35134.9	8290518	3128.708	216.853588	304.882747	380	V-PN	13.75930	CO
878	RS	P	0.289007	-68436.8	8266090	1997.276	-68451.5	8262459	1101.838	306.673462	189.304433	520	V-PN	19.54680	CO
879	RS	P	0.615210	270743.2	8148449	2966.6	268875.6	8146570	2262.822	190.205962	248.432051	536	V-PN	22.03900	CO
880	RS	P	0.465937	296998.7	8117562	3095.121	296822.1	8115535	2584.702	299.855364	140.252267	423	V-PN	16.89530	CO
881	RS	P	0.176124	377486	8034132	2386.763	375294.6	8032473	1771.136	201.273906	154.923023	434	V-PN	15.51020	CO

882	RS	P	0.483877	403041.7	8012164	3239.819	383199.5	8002615	771.5163	147.964614	291.600560	308	SC-PN	18.16850	CO
883	RS	P	1.301454	450209.5	7988781	4780.829	446703.5	7989601	4168.808	265.723586	293.646911	420	V-PN	15.36520	CO
884	RS	P	1.314615	479163.8	7833976	3746.455	473534.5	7834137	2804.952	480.141194	147.791642	687	V-PN	26.47510	CO
885	RS	P	1.293264	474564.2	7826762	3299.89	473526.5	7826250	2936.045	315.659168	321.491370	503	V-PN	16.82680	CO
886	RS	P	0.471220	487575.8	7812865	3672.789	485532.2	7811905	2873.599	268.339743	282.785794	359	V-PN	15.08630	CO
887	RS	P	3.304245	475312.7	7812747	2741.401	475057.9	7811339	2428.273	483.226607	155.744392	603	SC-PN	20.58730	CO
888	RS	P	10.393510	488502.2	7811486	3702.275	488554.1	7810443	3316.992	479.053901	282.284734	524	V-PN	18.31100	CO
889	RS	P	1.037872	481544.8	7810319	3302.173	480962.9	7811915	2639.475	148.239938	143.153917	447	V-PN	17.05700	CO
890	RS	P	0.148106	479891.3	7810097	3185.096	479100.7	7811657	2546.727	182.560510	306.915532	534	V-PN	16.86700	CO
891	RS	P	3.622555	483094.7	7804977	3269.083	482917.3	7803727	2927.812	668.993728	154.908120	676	V-PN	21.78970	CO
892	RS	P	1.737306	483953	7801795	3304.686	483778.5	7803180	2858.015	486.181034	134.560704	647	SC-PN	20.78240	CO
893	RS	P	0.489791	487331.4	7801355	3543.365	487277.8	7802690	3111.69	120.765282	334.677959	303	VS-PN	13.28570	CO
894	RS	P	16.216723	464886.8	7786858	2412.078	464434	7786592	2258.243	692.618116	179.831415	613	V-PN	18.35170	CO
895	RA	P	1.996969	483126.2	7777183	3238.643	481661.1	7776343	2872.463	799.190243	244.821190	486	V-PN	15.81360	CO
896	RS	P	4.034471	403681.5	7772690	1140.137	403266.8	7772367	1032.095	463.662200	119.626789	539	SC-PN	17.64550	CO
897	RA	P	1.233699	416186.4	7743976	1469.411	417176.3	7742951	1087.915	313.128002	190.259501	466	V-PN	17.76240	CO
898	RS	P	4.677925	109118.8	8349837	4825.825	108640.4	8349989	4594.837	651.390652	352.593402	535	V-PN	15.13370	CO
899	RS	P	0.234215	-17957.5	8347617	3950.922	-17661.1	8346719	3764.924	232.028766	220.729563	727	V-PN	20.09820	CO
900	RS	P	1.395443	-19689.2	8346896	3929.37	-19267.3	8345559	3517.099	245.204861	241.750335	689	V-PN	18.08050	CO
901	RS	P	1.769835	174282.1	8345307	4685.349	173685.1	8345909	4399.201	530.369860	35.817377	514	V-PN	14.87090	CO
902	RA	P	0.613504	36469.49	8341443	4000.558	37030.73	8340395	3644.163	385.283277	177.151226	675	V-PN	19.03490	CO
903	RS	P	1.379959	-83422	8335183	2609.982	-84479.4	8335470	2258.141	538.891282	134.927876	582	SC-PN	19.46830	CO
904	RS	P	1.106910	-17934.4	8328486	3045.212	-15958.9	8328467	2288.307	426.231941	161.422986	538	V-PN	16.34470	CO
905	RA	P	2.147006	97981.23	8326337	4133.801	96939.73	8329005	2875.269	662.698601	339.967419	637	SC-PN	18.39560	CO
906	RA	P	1.023376	-28032.8	8326700	3181.983	-26843.5	8326457	2606.721	638.368838	333.119575	624	V-PN	21.21610	CO
907	RS	P	5.783311	-14389.1	8326991	2943.741	-13255.8	8326080	2633.28	624.457276	328.964538	508	V-PN	16.96700	CO
908	RA	P	1.137849	-28860.8	8325529	3188.509	-32168.5	8324398	1934.308	539.716156	133.962644	563	SC-PN	19.54830	CO
909	RS	P	0.855131	-37186.8	8325241	2845.817	-35849.6	8323851	2324.089	65.881972	315.191941	120	SC-PN	4.23784	PC
910	RS	P	2.351883	-14522.5	8323471	3038.262	-13830.7	8324689	2487.189	608.998670	348.844722	566	V-PN	22.48820	CO
911	RS	P	0.979770	-16258.1	8323053	3278.686	-19538.6	8323444	1985.58	275.222096	272.712638	336	V-PN	12.10210	CO
912	RA	P	2.008311	53500.85	8319372	4192.306	53193.35	8320299	3975.885	334.877210	216.799517	448	VS-M	18.00150	CO
913	RS	P	5.015375	-12737.2	8316862	3904.638	-17278.7	8319781	2679.977	296.840609	150.671101	526	SC-PN	17.11780	CO
914	RA	P	0.260747	-21009.8	8315884	3055.393	-20473	8317980	2192.105	266.398926	140.539153	374	V-PN	15.60790	CO
915	RS	P	0.266934	-20568.2	8315533	3076.957	-19436	8315480	2789.488	80.227562	317.962822	430	V-PN	12.51520	CO
916	RA	P	0.112005	-20616.7	8311236	3270.563	-18855	8315960	2602.389	320.590010	168.435441	444	V-PN	16.41610	CO
917	RA	P	0.219507	-22892.1	8310923	3435.043	-22803.6	8316354	2658.652	356.740833	162.341827	435	V-PN	17.29170	CO
918	RS	P	2.580203	-34347.3	8305825	3647.996	-41244.2	8313288	1503.335	415.970460	149.546256	511	SC-PN	17.51550	CO
919	RA	P	0.158150	18558.52	8305726	4361.994	17510.22	8312359	3011.022	348.330834	146.905419	484	V-PN	19.18430	CO
920	RS	P	26.307838	80212.15	8307143	4167.442	74755.68	8312372	2257.127	520.930264	210.989931	488	V-PN	18.70990	CO
921	RS	P	1.905302	-41421	8305461	3358.395	-42453.5	8311854	1499.457	326.964289	329.736116	587	VS-PN	22.94550	CO
922	RS	P	0.430837	230266.9	8302891	4627.523	232368.4	8301426	3901.212	139.149078	164.340321	303	V-PN	14.77890	CO
923	RA	P	4.200677	48942.28	8299041	4240.031	42542.76	8298332	2294.188	688.361871	217.758759	605	V-PN	18.69190	CO
924	RS	P	0.113727	48014.93	8295094	3665.474	42614.37	8296156	1936.532	149.644645	174.468007	350	V-PN	15.11820	CO
925	RS	P	1.934408	-34389.4	8295753	3834.802	-39080.2	8295547	2956.341	464.887923	25.848114	531	SC-PN	17.87460	CO
926	RS	P	5.713398	187801.1	8292758	5245.699	187090.5	8292042	4775.729	504.593527	147.497646	452	VS-PN	16.38930	CO
927	RA	P	2.228211	-3887.61	8287914	4033.212	-3926.35	8284883	3274.833	341.270462	188.080010	488	SM-M	18.81320	CO
928	RS	P	0.743256	249913.5	8278775	4282.456	248022.1	8277971	4077.592	453.032709	168.253638	488	VS-PN	17.71490	CO
929	RS	P	2.599300	199296.1	8277936	4528.022	197726.3	8276627	3735.164	282.125366	159.307313	341	SC-PN	12.53770	CO
930	RS	P	0.492973	205567.6	8276842	4811.278	203743.7	8277181	4375.017	342.616422	326.962018	587	SC-PN	17.90350	CO

931	RS	P	4.442289	-11773.5	8274849	3163.239	-9299.02	8275659	2405.207	345.459635	38.736494	466	VS-PN	13.74110	CO
932	RS	P	2.740263	50166.05	8268286	3841.109	50878.51	8265763	3056.37	424.204036	343.356791	480	SC-PN	16.66730	CO
933	RS	P	9.642806	205371.9	8266395	3700.825	206374.5	8266787	3461	881.986970	252.418654	690	VS-M	18.09810	CC
934	RA	P	2.808776	204947.4	8265351	4045.426	206087.8	8265838	3620.161	446.671241	352.819251	481	VS-PN	18.02520	CO
935	RS	P	0.342956	131927.5	8256008	3239.094	129729.7	8253474	1744.721	194.810845	131.937779	315	V-PN	13.30160	CO
936	RA	P	0.901678	174512	8255588	4761.158	170556.8	8253069	3858.477	431.675137	357.703249	383	VS-M	17.59340	CO
937	RS	P	0.789770	133141.8	8253474	3048.741	131285.8	8253141	2270.135	196.335664	20.583382	372	V-M	17.98460	CO
938	RS	P	0.101279	227828.7	8249867	4871.87	229093	8251550	4513.835	85.429167	213.630947	298	VS-PN	14.33250	CO
939	RS	P	1.658617	223891.9	8249067	4589.596	223127.6	8248988	4343.772	162.110891	191.330032	353	VS-PN	18.42190	CO
940	RS	P	0.398159	171703	8227387	3637.085	172158.5	8226319	3281.026	180.391030	181.751429	326	VS-PN	15.43440	CO
941	RS	P	7.404931	319939.8	8212995	4379.929	322070.3	8212514	3601.094	776.442495	258.546628	533	VS-M	14.91090	CC
942	RS	P	7.485607	40794.42	8206230	1510.99	40392.85	8206048	1439.117	195.477638	276.633003	175	V-PN	10.08610	CO
943	RS	P	0.909322	40803.77	8205438	1491.293	40509.86	8205012	1393.697	192.865952	194.968073	278	VS-PN	18.13160	CO
944	RS	P	0.255396	313841.5	8205283	4145.962	315183.4	8204432	3464.409	121.549806	191.619759	287	VS-PN	15.97160	CO
945	RS	P	3.066733	317190.2	8203933	4089.044	315064	8204022	3452.796	268.806922	207.852739	394	VS-PN	18.77160	CO
946	RS	P	2.480788	317087.7	8202801	4216.627	314915	8203032	3456.296	403.174723	284.945606	421	SC-M	19.36340	CO
947	RS	P	3.135038	348567.8	8202331	4587.776	348629.6	8200706	4416.85	593.712684	262.280549	687	VS-M	19.54340	CC
948	RS	P	1.430061	186380.9	8201577	2248.604	185611.7	8201203	2017.439	286.714920	315.767854	457	SC-M	20.76030	CO
949	RS	P	7.893993	318649.2	8200694	4422.037	316279.1	8198329	3822.197	401.787374	246.470047	316	V-PN	13.82410	CO
950	RS	P	1.967775	309130.5	8199242	4189.558	309740.7	8199189	3938.094	293.851510	202.520246	409	V-PN	17.43230	CO
951	RS	P	3.086797	308872	8198915	4304.471	309688	8199004	3992.768	416.394502	156.668432	527	VS-PN	16.00730	CO
952	RS	P	3.411185	314537.2	8199677	4180.376	314752.2	8197758	3567.885	374.694893	165.512000	518	VS-PN	17.02010	CO
953	RS	P	1.035178	306416.5	8186643	4361.848	303573.8	8186025	3018.407	340.310616	185.924303	454	VS-PN	16.26750	CO
954	RS	P	0.191717	313287.7	8173973	4880.261	317257.9	8175355	3501.486	321.589326	170.932517	411	SC-PN	14.97030	CO
955	RS	P	0.765513	313313.8	8170619	4952.831	316952.1	8171878	4007.478	204.987262	347.214508	599	SC-M	16.55270	CO
956	RA	P	0.396477	325801.9	8172214	4342.989	324636.3	8169334	3622.002	153.835340	239.537924	242	V-M	12.88430	CO
957	RS	P	2.395761	367017.5	8169813	4774.528	366581	8168609	4607.869	303.075899	60.812896	571	V-PN	21.87440	CO
958	RS	P	1.575661	302022.5	8164204	4556.043	310554.4	8163629	2734.251	379.937388	276.477443	421	SC-PN	18.34840	CO
959	RS	P	2.530281	312344.9	8162799	3199.186	311327.4	8160430	2033.716	315.710046	164.450543	443	VS-PN	15.72280	CO
960	RS	P	4.220614	276010.8	8161120	3949.45	278558.8	8162084	2875.168	355.562679	338.930771	465	VS-PN	13.16940	CO
961	RS	P	0.422067	277520.7	8158536	3433.144	277600.2	8157602	3109.607	197.711326	177.968613	454	V-M	16.63840	CO
962	RS	P	0.321047	308370.5	8157416	3459.091	311143.1	8156516	1890.877	145.868002	267.597818	279	VS-PN	14.29100	CO
963	RS	P	0.409149	266826.9	8153357	2785.348	265746.4	8151987	2136.75	116.894998	205.773333	295	I-M	11.43670	CO
964	RS	P	1.133571	292378.5	8152409	2369.622	289891.8	8153094	2028.704	423.910381	222.577442	513	V-PN	21.37880	CO
965	RS	P	0.143683	303993	8153727	3791.345	303918.6	8145876	1626.119	110.298494	263.013160	405	I-M	14.32740	CC
966	RS	P	0.315502	290950.6	8148287	2628.039	289493.9	8147447	1865.978	164.776936	175.031833	296	V-M	14.09770	CO
967	RS	P	0.506715	305387.8	8143728	2511.138	306228.8	8145941	1684.305	211.173297	180.682070	376	VS-M	16.23870	CO
968	RS	P	0.208697	256511.4	8141359	2810.236	255704.2	8140022	2264.951	167.231438	163.313524	330	VS-PN	16.33940	CO
969	RA	P	1.033932	258756.1	8132509	2337.759	259275.5	8130811	1959.453	366.179836	240.160830	710	I-PN	22.64920	CO
970	RS	P	0.208570	300423.5	8130439	3241.182	298979.3	8129746	2768.733	101.415018	283.443330	278	I-M	10.21000	CC
971	RS	P	0.746862	313091.2	8125177	3778.137	313359.4	8123853	3489.607	386.468373	252.670963	813	I-PN	24.76840	CO
972	RS	P	3.030139	304011.6	8112773	2593.457	303385.7	8111185	2206.758	457.403403	223.618434	747	I-PN	22.73790	CO
973	RA	P	0.340349	310368.8	8107965	3249.433	309335.3	8106352	2276.846	108.041939	232.114788	234	V-M	9.27206	CC
974	RS	P	1.315779	289742.2	8106833	2402.44	288673.1	8107534	2009.794	399.252447	200.486469	676	I-PN	24.14670	CO
975	RS	P	1.943312	289783.1	8106503	2440.561	287631.4	8103821	1663.186	133.363152	313.702494	207	V-PN	10.70810	CO
976	RA	P	0.896736	353605.3	8090884	3458.016	354272.5	8089883	2940.564	514.963419	336.038985	561	V-PN	18.73440	CO
977	RS	P	1.561439	353629.6	8090268	3230.985	354028	8089602	2929.65	489.758051	158.790322	650	I-PN	24.16470	CO
978	RS	P	1.617499	352849.8	8090033	3441.604	353744	8089312	2873.4	457.930688	163.155294	556	VS-PN	19.86650	CO
979	RS	P	1.653453	365072.8	8089352	3912.055	369193.1	8089627	3076.523	416.519142	155.897824	530	VS-PN	19.15600	CO

980	RS	P	0.186491	364971.4	8087181	3927.593	367702	8083838	2854.426	6.507883	209.278410	77	SC-PN	2.85617	PC
981	RS	P	1.214089	364622.8	8085455	3639.908	366021.3	8084917	3197.322	254.355707	175.724653	458	VS-PN	15.18970	CO
982	RA	P	0.507181	363896.3	8085310	3839.97	365947.7	8084094	3030.486	380.802589	172.229536	483	VS-PN	16.47520	CO
983	RS	P	3.050761	368475.4	8070677	2845.639	367506.5	8070922	2415.869	349.164423	186.183038	491	VS-PN	17.45100	CO
984	RS	P	1.187275	392775.1	8049817	4117.551	390769.4	8049841	3520.904	303.708992	183.119553	512	VS-PN	16.66670	CO
985	RS	P	1.752042	392672.1	8044812	3347.621	393399	8042084	2484.67	419.599620	342.083391	652	V-PN	19.82560	CO
986	RA	P	0.465126	374354.3	8054611	3841.64	346963.2	8023652	571.476	260.402015	281.908139	323	SC-M	14.60390	CC
987	RS	P	0.754941	397069	8023656	3204.573	396202.1	8024915	2319.746	314.641652	208.569121	427	SC-PN	18.22240	CO
988	RS	P	1.434132	451229.4	7906481	3357.003	451394	7905021	2510.544	261.244490	233.932539	418	VS-PN	17.61880	CO
989	RS	P	0.267631	467248.8	7906578	3895.67	467462.2	7905168	3494.452	129.886132	260.696421	450	V-PN	14.17820	CO
990	RS	P	0.625127	415543.6	7900833	2081.878	417417.1	7898271	908.0338	114.185040	85.327356	158	V-PN	9.62663	CO
991	RS	P	0.611190	475655.6	7835968	3395.637	472913.1	7838040	2686.489	215.780456	176.615429	513	V-PN	12.93210	CO
992	RS	P	4.419042	482402.4	7827575	4126.814	483083.8	7825173	3561.442	229.584844	120.093836	292	V-PN	8.50536	CO
993	RS	P	0.277703	469801.4	7810730	2679.154	471092.5	7809484	2139.438	303.030085	313.631322	507	SC-PN	11.15170	CC
994	RS	P	0.158309	492729.5	7809069	3865.067	491452.7	7807362	3530.19	136.760768	199.329689	270	SC-M	12.20440	CC
995	RS	P	0.282092	490440.8	7807812	3777.807	491030.6	7807095	3511.408	69.807409	115.563748	133	V-PN	7.30600	CO
996	RS	P	0.110342	489634.7	7807130	3735.21	489788.4	7806379	3414.62	32.455882	157.623300	164	V-PN	7.62596	CO
997	RS	P	0.485729	489293.2	7807021	3756.582	489543.9	7806234	3399.841	151.654438	112.152904	270	I-M	11.01260	CC
998	RA	P	4.564294	488891.4	7806747	3729.16	489290	7806135	3380.829	901.009794	241.692639	771	D-C	17.86700	CC
999	RS	P	1.737343	499694.4	7806877	4370.386	497340.4	7803838	3682.024	102.171679	130.770719	230	SC-PN	7.74422	CO
1000	RA	P	1.274710	493348.2	7767934	3961.694	492684.2	7769428	3446.731	381.496142	136.005143	470	SC-M	20.12570	CC
1001	RA	P	5.635952	484039.6	7766167	2998.719	484211.3	7764909	2617.917	893.081260	250.235526	708	VS-M	15.95620	CC
1002	RS	P	0.464744	392157.1	7764104	1123.213	390484.7	7764457	862.811	67.897507	141.281215	213	V-PN	7.05174	CO
1003	RS	P	0.119602	381941.5	7745585	993.0911	379729.2	7744394	92.08126	65.980508	132.322086	232	V-PN	8.29323	CO
1004	RS	P	1.109321	383117	7743055	908.0904	378479.5	7741389	15.00916	261.247981	294.375064	428	SC-PN	11.59440	CO
1005	RA	P	4.828010	383882.2	7736968	815.9595	379835.3	7737719	60.14639	755.813152	280.503242	662	VS-M	17.08420	CC
1006	RA	P	2.488527	378110.8	8047726	3140.836	379492.9	8045891	2455.907	684.929317	143.022318	730	VS-PN	27.04540	CO



CHAPTER III:
GIANT LANDSLIDE TRIGGERINGS
AND PALEOPRECIPITATIONS IN
THE CENTRAL WESTERN ANDES:
THE ARICOTA ROCKSLIDE DAM
(SOUTH PERU)



Giant landslide triggerings and paleoprecipitations in the Central Western Andes: The aricota rockslide dam (South Peru)

Fabrizio Delgado^{a,b,c}, Swann Zerathe^{b,*}, Laurence Audin^b, Stéphane Schwartz^b, Carlos Benavente^c, Julien Carcaillet^b, Didier L. Bourlès^d, Aster Team^{d,1}

^a Especialidad Ingeniería Geológica, Facultad de Ciencias e Ingeniería, Pontificia Universidad Católica del Perú, Av. Universitaria 1801, San Miguel, Lima 15088, Perú

^b Univ. Grenoble Alpes, Univ. Savoie Mont Blanc, CNRS, IRD, IFSTTAR, ISTERre, 38000 Grenoble, France

^c Instituto Geológico, Minero y Metalúrgico INGEMMET, Av. Canadá 1470, Lima, Perú

^d Aix-Marseille Univ., CNRS, IRD, Coll. France, UM 34 CEREGE, Technopôle de l'Environnement Arbois-Méditerranée, BP80, 13545 Aix-en-Provence, France



ARTICLE INFO

Article history:

Received 5 February 2019

Received in revised form 15 October 2019

Accepted 30 October 2019

Available online 2 November 2019

Keywords:

Giant landslide dam

Central Western Andes

¹⁰Be dating

Triggering factors

ABSTRACT

The central part of the Western Andes holds an exceptional concentration of giant paleolandslides involving very large volumes of rock material ($v > \text{km}^3$). While those gravitational slope failures are interpreted consensually as an erosional response to the geodynamic activity of the Andes (relief formation and tectonic activity), the question of their triggering mechanisms remains enigmatic. To clarify the respective roles of climatic versus seismic forcing on the Andean landslides, new temporal constraints on paleo movements are essential. Here, we focus on one of those giant slope failures, the Aricota giant rockslide that dammed the Locumba valley in southern Peru. We conducted fieldwork, high-resolution DEM analysis and cosmogenic nuclide dating to decipher its development history and failure mechanisms. Our results point to the occurrence of two successive events. A giant failure mobilizing a rock volume of ca. 2 km^3 first produced a dam at $17.9 \pm 0.7 \text{ ka}$. Considering its height of ca. 600 m, the Aricota rockslide dam is one of the three largest landslide dams worldwide. At $12.1 \pm 0.2 \text{ ka}$, a second event produced ca. 0.2 km^3 of material, and the rock-avalanche debris spread out over the dam. As the chronology of those two events is pointing to the two main paleoclimatic pluvial periods in this region (Heinrich Stadial 1a and Younger Dryas), we favor the interpretation of a climatic forcing. At a regional scale, the concomitant aggradation of alluvial terraces and fan systems along the nearby valleys highlights higher regional erosion, sediments supply and mass-wasting events during those paleoprecipitation events and strengthens this conclusion.

© 2019 Elsevier B.V. All rights reserved.

1. Introduction

The Western flank of the Central Andes (south Peru - north Chile) holds one of the most exceptional concentrations of giant landslides worldwide (Crosta et al., 2014). Those gravitational instabilities mobilize large volume of rock material ($> 10^9 \text{ m}^3$), with debris propagation over long distance ($> 10^3 \text{ m}$) affecting the Western Cordillera from elevations between 4500 m to sea level (e.g. Wörner et al., 2002; Strasser and Schlunegger, 2005; Pinto et al., 2008; Crosta et al., 2014). This Andean area is particularly active geodynamically, related to the long-term convergence between the Nazca and the South America plates. The global shortening is associated

with the relief construction, producing instantaneous deformation (crustal seismicity) coupled with long-term processes of surface uplift and volcanism (Thouret et al., 2017; Benavente et al., 2017). In this region, the large-scale landsliding is suspected to be an efficient relief erosion mechanism at regional scale (Mather et al., 2014).

Additionally, the Western Andean flank presents a climatic setting marked by a dominant hyper-aridity persisting at least since 20 million years (e.g. Dunai et al., 2005). This particular climate environment, with very low denudation rates (typically $1\text{--}10 \text{ mm.kyr}^{-1}$; Nishiizumi et al., 2005; Madella et al., 2018), allows the local preservation of landscape over hundreds of thousands years (e.g. Zerathe et al., 2017). This offers a unique opportunity to track gravitational slope processes over a temporal scale currently unknown, close to the timing of the orogen evolution (Hermanns et al., 2001).

* Corresponding author.

E-mail address: swann.zerathe@ird.fr (S. Zerathe).

¹ Georges Aumaître and Karim Keddadouche.

On the other hand, the development of such giant landslides in a desert environment raise the question of their triggering conditions and failure mechanisms. In the literature, this question is largely debated with two main opposite views implying seismicity versus climatic controls (Moreiras and Sepúlveda, 2015). For examples, McPhillips et al. (2014) suggest that at a millennial-scale, the record of landslides activity in the Andes is mainly consistent with earthquake trigger, whereas Margirier et al. (2015) identified a correlation between the activity phases of a giant paleolandslide (Chuquibamba, south Peru) and wet climatic events on the Altiplano. As pointed by Moreiras and Sepúlveda (2015), in order to push away the limit of this debate and to decipher the respective role of each forcing, new temporal constraints on giant Andean paleolandslides are required. Indeed, while numerous giant landslides have been identified along the western Andean flank (Audin and Bechir, 2006; Crosta et al., 2014), the great majority of them have not been dated yet. In this context, the cosmogenic nuclide dating, applied to either landslide scarps or boulders, is specifically pertinent to constrain the timing of slope evolution (Zerathe et al., 2017; Crosta et al., 2017).

In this paper, we combined geomorphological analysis based on high resolution Pléiades DEMs and geochronological dating using ^{10}Be produced within quartz minerals (in situ-produced ^{10}Be) in order to document the chronology and to determine the context in which the Aricota giant rockslide dam (Central Western Andes, South Peru) occurred.

2. Geological context and landslide setting

The study area is located in the South Peru at $\sim 17^\circ\text{S}$ latitude, along the Western flank of the Central Andean Cordillera (Fig. 1), where ongoing subduction of the Nazca Plate occurs with a convergence velocity of about $62\text{ mm}\cdot\text{yr}^{-1}$ (e.g. Villegas-Lanza et al., 2016). The geomorphology of this region is contrasted and shows from West to East: (1) a coastal cordillera with a maximum elevation of 1000 m a.s.l. , (2) the Western Cordillera with elevations comprised between 1000 and 4500 m a.s.l. , and (3) the Altiplano plateau reaching 5000 m a.s.l. This western flank of the Andes is carved by deep valleys and canyons related to a regional uplift (e.g. Thouret et al., 2007; Schildgen et al., 2009; Gunnell et al., 2010 and references therein). The Western Cordillera is affected by westward major thrusts (Fig. 1) oriented parallel to the subduction trench (Hall et al., 2012; Benavente et al., 2017). The timing and the processes involved in the creation of the Andean relief in this region are still debated. Sempere et al. (2008) propose a rapid uplift of about 2.5 km since the Late Miocene (11 to 6 Ma) in response to a large-scale mantle delamination. Armijo et al. (2015) propose that the topography was controlled by crustal thickening during the Paleogene (50 to 30 Ma) in response to the tectonic shortening of the Central Andes. This process is responsible for aridity increase of the Atacama Desert during the Neogene (Evenstar et al., 2015). Recently, Thouret et al. (2017) provide a compilation of $^{40}\text{Ar}/^{39}\text{Ar}$ and U/Pb dating of ignimbrite deposit covering this region, which helped to decipher the canyon incision chronology. Their dataset suggest that uplift was gradual over the past 25 Ma and accelerated after 9 Ma . The valley incisions start around 11 – 9 Ma and accelerate between 5 and 4 Ma . Pleistocene uplift rates of 0.2 to $0.4\text{ mm}\cdot\text{yr}^{-1}$ have been derived from cosmogenic dating (Hall et al., 2012), and interpreted as a combination of tectonic shortening along steep westvergent faults of the western flank and isostatic responses to fluvial erosion associated with large scale landslide processes. The same conclusion is reached by Viveen and Schlunegger (2018) showing uplift at the Quaternary time scale in the Moquegua region. However, at the scale of the Peruvian forearc, their conclusions open other perspectives showing possible alter-

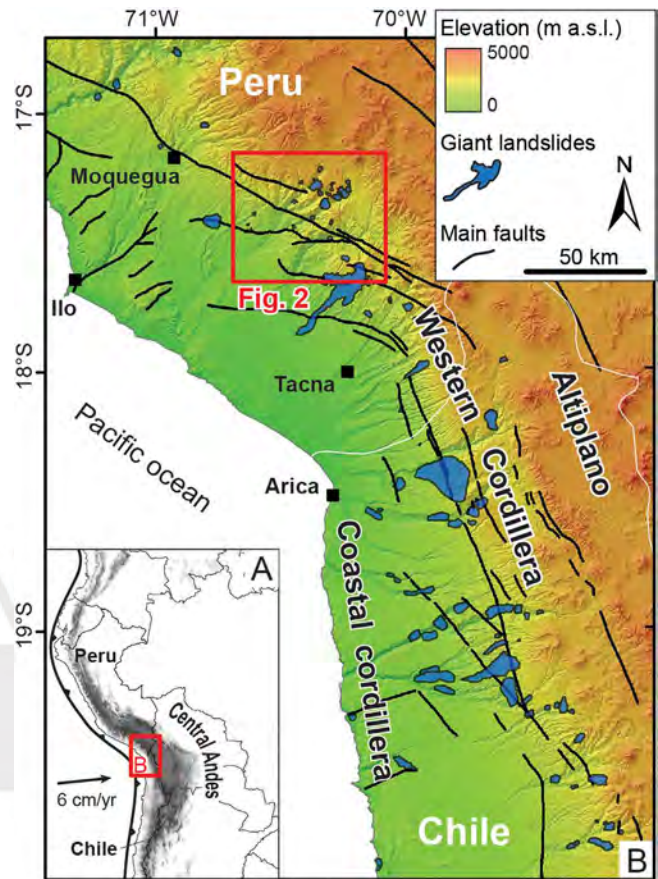


Fig. 1. Morpho-tectonic context of the Central Western Andes and location of the study area. Hillshade and elevation are produced using the ASTER DEM (resolution 30 m). Main faults are reported from Hall et al. (2012); Armijo et al. (2015) and Benavente et al. (2017). The database of giant landslides is compiled from Audin and Bechir (2006); Crosta et al. (2014); Mather et al. (2014); Zerathe et al. (2017) and adding personal mapping from this study.

nating phases of compressional and transtensional tectonics during the Cenozoic.

The progressive Cenozoic onset of the Andean relief acted as an important topographic barrier impeding the cross of cloud currents and precipitation from the Amazonian basin (Houston and Hartley, 2003). As a result, hyper-arid conditions have developed and still currently prevail in the so-called Atacama Desert, along the Western Central Andes, allowing for long-term preservation of landscapes (up to several millions of years, e.g. Dunai et al., 2005). As contrasting with this long-term dry climate, the flank of Western Central Andes, between latitudes 17°S and 20°S , holds an exceptional concentration of some of the largest landslides identified at the Earth surface (Fig. 1). The imprint of those giant landslides have been progressively identified and mapped since a decade (e.g. Audin and Bechir, 2006; Crosta et al., 2014). From North to South, some impressive examples among others are: the Chuquibamba landslide - 40 km^3 (Margirier et al., 2015; Thouret et al., 2017), the Caquilluco landslide - 15 km^3 (Zerathe et al., 2017), the Lluta landslide - 26 km^3 (Wörner et al., 2002; Strasser and Schlunegger, 2005), the Minimini landslide - $>5\text{ km}^3$, the Latagualla landslide - 5.4 km^3 (Pinto et al., 2008) or the Magnifico landslide - 0.2 km^3 (Mather et al., 2014; Crosta et al., 2017). Only few of those giant landslides have been precisely dated (e.g. Zerathe et al., 2017; Crosta et al., 2017). Paleo-climatic variations and/or active tectonic and seismicity are considered both as possible factors of forcing. However, mainly because of the lack precise of chronological constraints on

these events, there is no consensus to date about the reason of their triggerings (McPhillips et al., 2014; Margirier et al., 2015).

In this paper, we focus on one of those giant landslides, the Aricota rockslide dam. It developed in the middle of the Locumba valley whose basin extends across the whole Western Cordillera, from the Altiplano down to Pacific Ocean. The Aricota rockslide generated a large dam in the Locumba valley, forming a 6 km-long lake. The lithology observed around the valley is dominated by volcano-sedimentary rocks (Fig. 2). The Aricota rockslide affects geological series that are almost horizontal. From the valley bottom to the plateau, we observe the following stratigraphic cross section: Cretaceous andesite and rhyolite of the Quellaveco formation, Paleogene silt and shales of the Tarata formation and Neogene ignimbrite of the Huaylillas formation unconformably covering the former (Fig. 2). The Cretaceous layers are cut by intrusive granite at the north-east of the Aricota rockslide zone. Neotectonic faults activities have been described recently south-west of the Aricota rockslide, mainly along the Incapuquio fault system and the Purgatorio fault (Hall et al., 2012; Benavente et al., 2017). The Incapuquio fault system is a sub-vertical lineament of ~400 km in length with a northwest-southeast trending direction and accommodates left lateral transpressive displacement. The Purgatorio fault accommodates right lateral transpressive displacement which has produced at least two ruptures during the last thousands years with superficial offsets of several meters (Benavente et al., 2017).

On the Aricota rockslide dam site, two hydroelectric plants, Áricota I and II (35 MW) were built in 1967. The continuous pumping of water caused a drop of the lake level of ~100 m in the last 50 years, which allow studying paleo shorelines revealed by diatomite deposits (Placzek et al., 2001). Placzek et al. (2001) obtained radiocarbon calibrated ages ranging between ca. 300 and 7000 yr B.P., pointing to high lake levels around 6100 yr B.P. and 1700–1300 yr B.P. and giving a minimum age of ca. 7 ka for the rockslide-dam emplacement. They identified in the morphology the existence of two successive failure events. However, the precise chronology of this rockslide, the failure and triggering mechanisms remain unknown yet.

3. Methods

3.1. Pléiades DEM elaboration and mapping

To identify and map the structures and deposits associated to the Aricota giant rockslide activity, we combine geomorphic and tectonic observations based on field data, analyses of high-resolution Digital Elevation Model (DEM) and Google Earth images. A high-resolution DEM was derived from two stereo images acquired by the Pléiades satellites on October 2015. The full resolution of these optical images is 0.7 m and their orientation was assessed using the Rational Polynomial Coefficient (RPC) provided in their ancillary data. We generated the DEM using the open source software Ames Stereo Pipeline (ASP) developed by NASA (Broxton and Edwards, 2008) and followed the three-step procedure. First, each image was map-projected using the low-resolution (30 m) SRTM DEM. Then the two images were bundle-adjusted based on automatically extracted tie points, before finding the disparities. The third step involved finding the intersection of all the rays coming from the homologous points of the image pair. This step leads to a point cloud of the surface topography, which is then converted onto a 2-m resolution grid (Fig. 3A). Field campaigns were conducted in 2014 and 2015 to (1) validate the observations/interpretations made about the different deposits and related events within the rockslide mass, and (2) to sample boulders and scarps for cosmogenic nuclide surface exposure dating.

3.2. Cosmogenic nuclide surface exposure dating

In order to determine the ages of the different events that occurred on the Aricota rockslide area, a sampling strategy was designed according to our geomorphological mapping. Seventeen samples were selected (Fig. 3B). In order to constrain an accurate long-term and local denudation rate, one sample (AR1) was taken on the eroding surface (presumed at steady state) that is located on the plateau above the rockslide scarp at ca. 3700 m a.s.l. Three samples (AR3, AR4 and AR5) were extracted from the free-face of two preserved sub vertical scarps (bedrock). Thirteen samples were extracted from boulders distributed all over the rockslide mass, including six samples (AR14 to AR21) from the main dam and seven others (AR6 to AR12, and AR27 to AR29) from a rock-avalanche deposit located on top of the dam (Fig. 3B). A last boulder, AR29, has been taken tentatively to estimate past variations of the Aricota lake level (Fig. 3B). Indeed, despite belonging morphologically to the rock-avalanche deposit, this boulder stands at an elevation that is of about 40 m below the pre-1967 lake level (date of artificial lake lowering by pumping). In other words, before 1967, tens of meters of water, sufficient to protect quasi-completely the AR29 boulder from cosmic ray primary and secondary particles, were covering it. Thus, any concentration measured in this sample might represent periods of past lake level drop that would be large enough to allow exposing the AR29 boulder to cosmic ray particles (at ten meters depth, the cosmogenic nuclide production rates are less than 0.2% that at the surface, Gosse and Phillips, 2001).

In general, we paid special attention to select boulders whose height and length were higher than 2 m and with no trace of post-deposition toppling, nor large desquamations. Elevation, latitude and longitude were recorded with a handle GPS. Pictures of the boulders are provided in the supplementary material.

Sample preparation and ^{10}Be chemical extraction were achieved following routine procedure, which is detailed in the supplementary information, at the GTC Plateform, ISTERRE laboratory (Grenoble, France). $^{10}\text{Be}/^9\text{Be}$ measurements were performed at the French AMS National Facility, located at CEREGE in Aix-en-Provence (Arnold et al., 2013). $^{10}\text{Be}/^9\text{Be}$ ratios were calibrated against the in-house standard STD-11, using an assigned $^{10}\text{Be}/^9\text{Be}$ ratio of $(1.191 \pm 0.013) \times 10^{-11}$ (Braucher et al., 2015). Uncertainties on ^{10}Be concentrations (reported as 1σ) are calculated according to the standard error propagation method using the quadratic sum of the relative errors and include a conservative 0.5% external machine uncertainty (Arnold et al., 2010), a 1.08% uncertainty on the certified standard ratio, a 1σ uncertainty associated to the mean of the standard ratio measurements during the measurement cycles, a 1σ statistical error on counted events and the uncertainty associated with the chemical and analytical blank correction.

Denudation rates and exposure durations were both calculated using the MATLAB®-based CRONUScalc program, developed by Marrero et al. (2016). We applied a globally calibrated ^{10}Be spallation production rate of $4.09 \pm 0.35 \text{ at.gr}^{-1}.\text{yr}^{-1}$ (sea level and high latitude; Borchers et al., 2016) which was scaled at the geographical and altitudinal location of each sampling site using the LSD scaling scheme (SF; Lifton et al., 2014; see details in the supplementary information).

We initially calculated long-term denudation rates for this area. As this will be detailed in the following results, in addition to the dedicated sample AR1, two other samples (AR14 and AR15) were considered for denudation rates calculation.

Finally, exposure duration calculations were performed considering this locally constrained denudation rate. Both analytical and total uncertainties (1σ) are reported. Analytical age uncertainties (i.e. internal) include uncertainties of the measured ^{10}Be concentrations (Table 1, supplementary data), pressure ($\pm 5 \text{ hPa}$), sample thickness ($\pm 1 \text{ cm}$), shielding factor (± 0.01), denudation

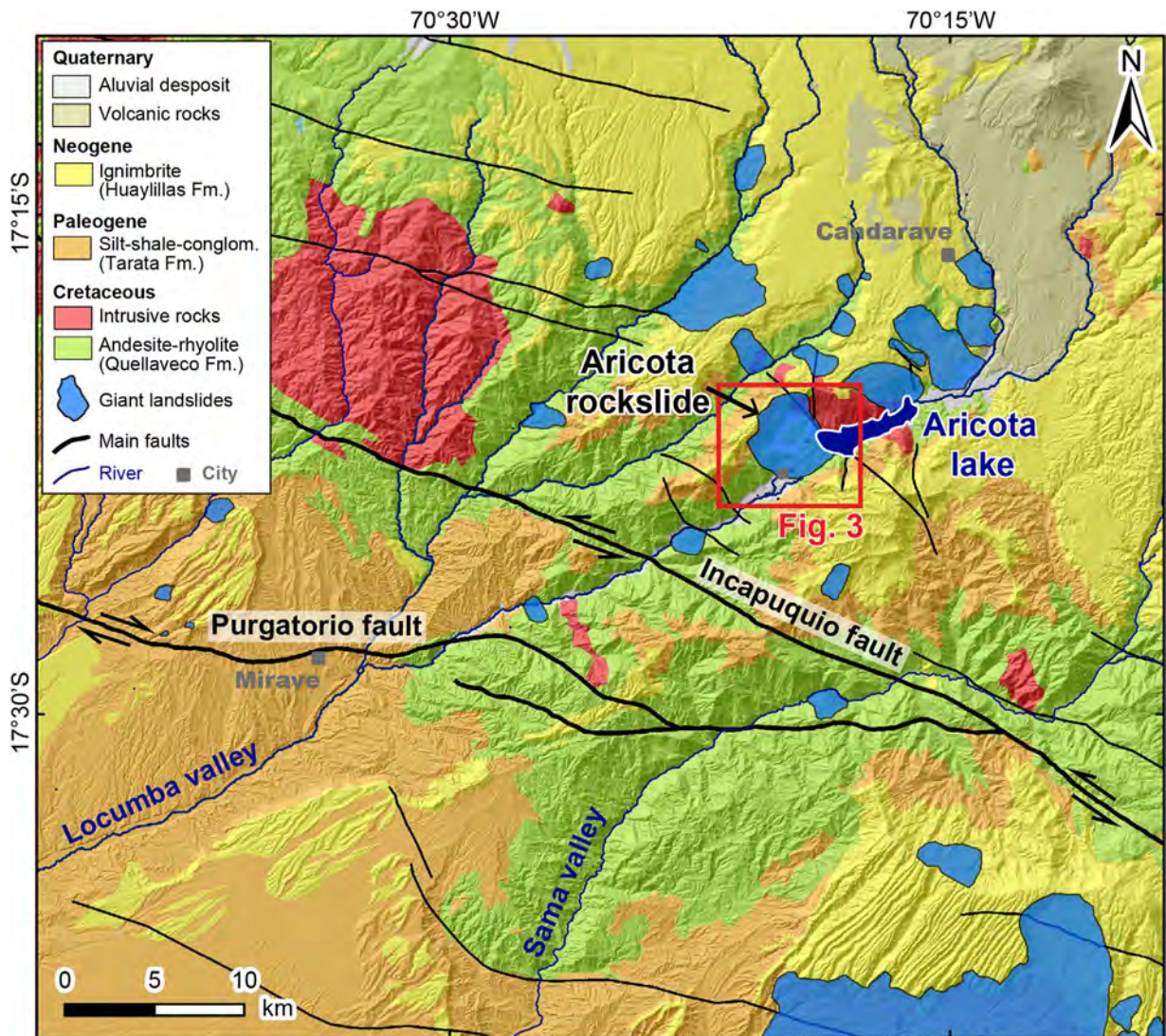


Fig. 2. Geological settings around the Aricota rockslide (see frame location on Fig. 1). The geological map is adapted from INGEMMET (2011) and draped above hillshade produced using the TanDEM-X DEM (resolution 12 m). Quaternary crustal faults are reported (e.g. Incapuquio-Purgatorio fault system; Hall et al., 2012; Benavente et al., 2017). Giant landslides reported were mapped during this study.

rate ($\pm 0.4 \text{ mm.ka}^{-1}$) and attenuation length ($\pm 10 \text{ g. cm}^{-2}$). Total age uncertainties (i.e. external) include contributions from the analytical method and production rate uncertainty (Marrero et al., 2016). All results are presented in Table 1 (supplementary data).

4. Results and interpretations

4.1. Rockslide morphology

The failure of the Aricota giant rockslide has left a spectacular morphological imprint in the Locumba valley and has deeply modified the surrounding landscapes (Figs. 3–4A). It generated a natural dam of about 600 m of height impounding a lake of $\sim 0.8 \text{ km}^3$ with a length of $\sim 6 \text{ km}$ (Aricota lake) and produced a large scar of about 4 km of width along the northern flank of the valley (Fig. 3A). As it is visible on the Fig. 3A, the main scarp intercepts a plateau, corresponding to a paleo ignimbrite surface (Huayllilas formation, Fig. 2), at an elevation of ca. 3700 m a.s.l. According to the geomorphological description proposed by Placzek et al. (2001), two successive deposits can be distinguished in the rockslide mass. The dam itself and a subsequent rock-avalanche deposit overlying

its northern part. The whole destabilized area extends over $\sim 3 \text{ km}$ of length towards the south until the opposite valley slope.

We observe in the central part of the dam a continuous lithological succession, locally fractured, composed from bottom to top by the Huayllilas ignimbrites (Fig. 5A), overlying the metasediment (silts-shales) and pyroclastics of the Tarata formation. This lithological succession is comparable with the one outcropping along the stable valley slopes (Figs. 3B and 4). On southern extremity of the dam (i.e. the most distal part), we observe a dominance of andesite from the Quellaveco formation (Fig. 3B), derived from the lowermost layer of the original slope, with a high degree of destruction, also mixing all the other lithologies (Fig. 4B). According to those observations, the dam was likely produced during a first large and “in mass” rockslide failure that have affected the whole valley flank.

The western side of the dam (downstream side) shows a large amphitheater (Fig. 3A), affected by gullies and landslides with scarps of several hundred meters in length (Fig. 6A). Water seeping is also observable at the base of the dam (see location of current and paleo springs on Fig. 3B). We interpret this morphology as regressive erosion processes affecting the dam due to its steep topography and to the high level of rock fracturing produced during the rock-

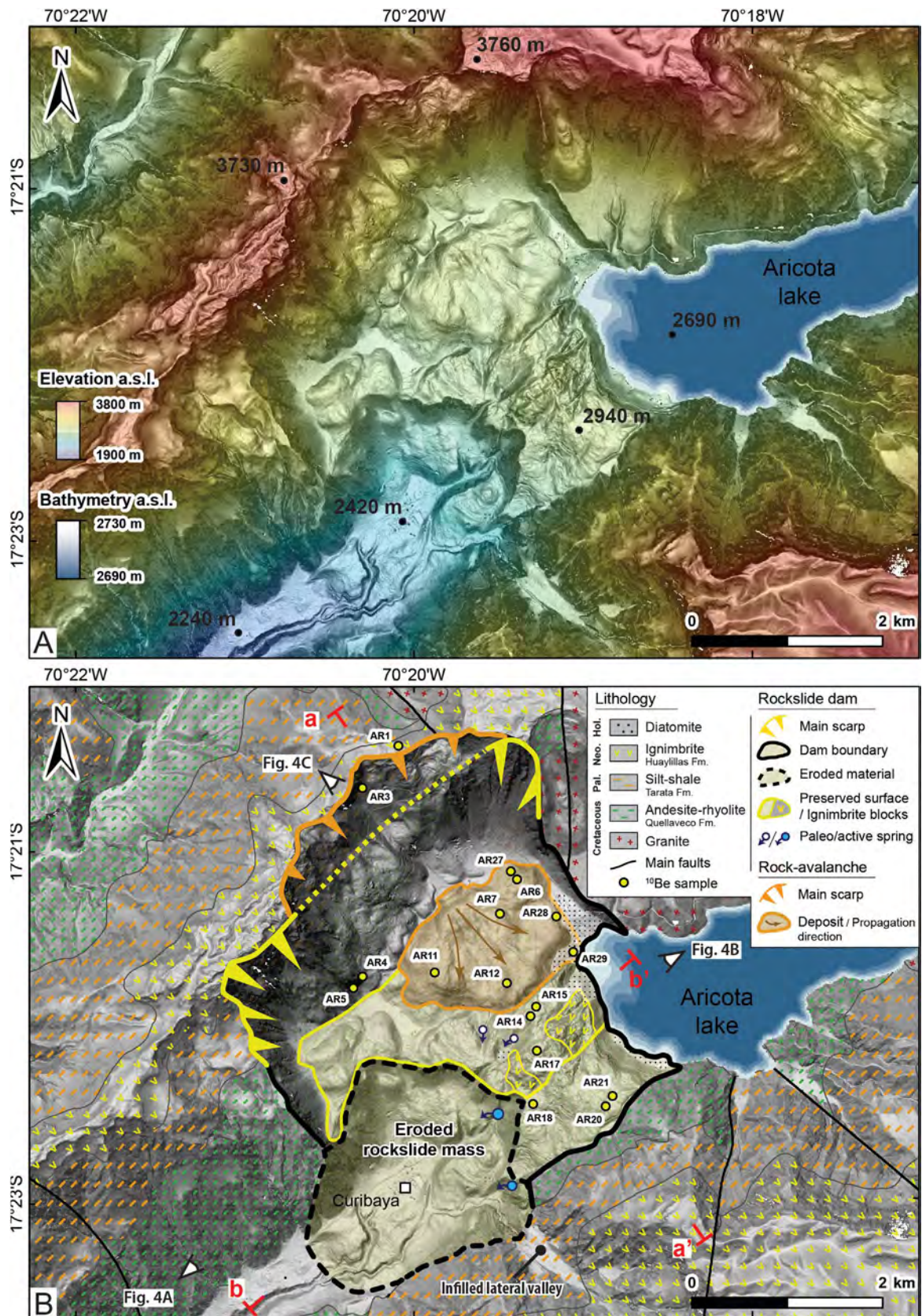


Fig. 3. The Aricota giant rockslide (see frame location on Fig. 2). (A) Raw hillshade and elevation image derived from high resolution (2 m) Pléiades DEM (see text for details). The bathymetry of the Aricota lake (resolution 1 m) has been provided by the company EGESUR. (B) Geomorphological map of the Aricota rockslide showing the two failure events. The first and main event that generated the dam in the valley is mapped in yellow. Note the regressive erosion affecting southwestern part of the slipped mass and the infill of the secondary valley located at the southern center of the map. The second event, a rock-avalanche that have affected the main scarp of the first event, is depicted in orange. Yellow points correspond to samples extracted for ^{10}Be cosmic ray exposure dating (1 above the rockslide scarp, 3 on the free face of the rockslide scarp and 13 on boulders distributed over the landslide mass). Outside of the rockslide area, the geology is the same as Fig. 3.

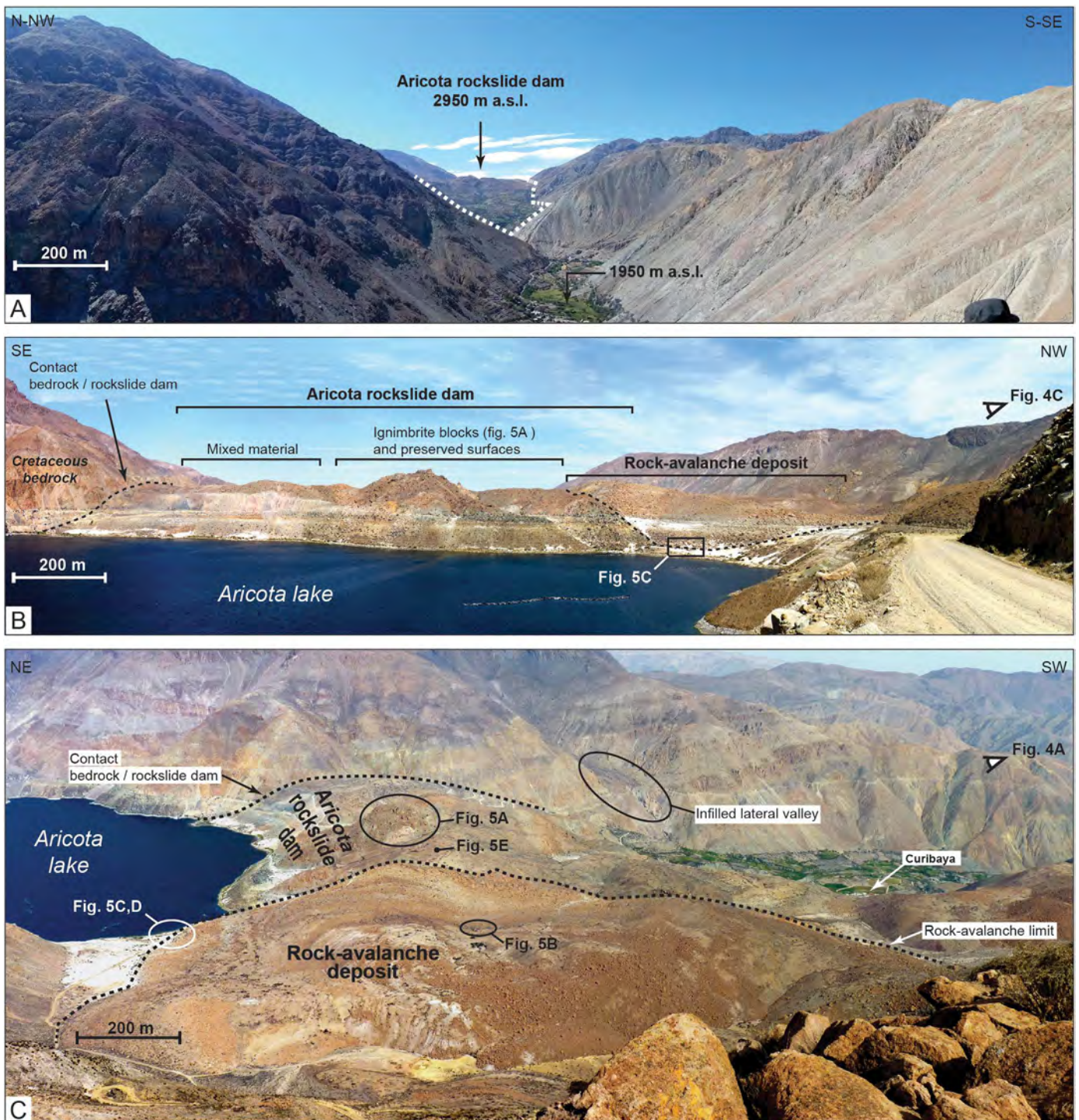


Fig. 4. Panoramic views illustrating the main structures of the Aricota giant rockslide area. (A) Panoramic view from the downstream part of the Locumba valley (see location on Fig. 4C). Note the general V-shape of the valley and the contact between the giant Aricota rockslide and the flank underlined by a dotted white line. (B) Westward view taken from the road along the lake (see location on Fig. 3B) and showing the dam generated by the first giant event. Along the dam, two bodies can be discriminated. On the central part, pre-rockslide topographic surfaces and large ignimbrite blocks are preserved (see also Fig. 5A). On the south-eastern part, mixed and highly deformed material are outcropping. Rock-avalanche deposits overly the top the rockslide dam. (C) Southward view of the whole rockslide area taken from the top of the scarp (see location on Fig. 4B). Note on the opposite Locumba valley flank, the lateral valley infilled by accumulation of deposits reflecting its obstruction by the main Aricota rockslide dam.

slide propagation. On the opposite Locumba valley flank (southern flank), our DEM (Fig. 3A) highlights a flat and perched surface, at the same elevation than the Aricota dam (ca. 2700–2800 m a.s.l.), infilling a small lateral valley (Fig. 4C). This morphology suggests that the former dam reached this area before being eroded.

Postulating that before the rockslide triggering, the valley had a typical v-shaped morphology (Fig. 4A) we reconstructed a pre-

failure topography. Then taking into account the strike and dip of the main scarp, we estimate a volume of ca. $2 \pm 0.3 \text{ km}^3$ for the Aricota rockslide dam, which includes an estimation of the volume eroded since it emplaced.

On its northern part, the dam is covered by a secondary rock-avalanche deposit constituting a circular lobe of debris of 800 m of radius (Fig. 3A). The contact between the dam and this rock-



Fig. 5. Detailed morphologies of the Aricota rockslide. (A) Preserved large ignimbrite boulders outcropping in the central part of the rockslide dam. (B) Large boulders from the Tarata formation (bedded silt and shales) aligned in the rock-avalanche deposit. (C) Boulders of the rock-avalanche partially covered by diatomite. This zone was immersed before the hydroelectric lake drop. (D) Boulder (AR29) sampled to tentatively track the paleo-lake level variations. (E) Boulder of sample AR15. (F) Ignimbrite surface located on the plateau at the top of rockslide scarp and sampled to estimate the long-term local denudation rate (see location on Fig. 3B). On all pictures, see the persons for scale and their location on Fig. 4.

avalanche deposit is delineated on the DEM by a slope break (Fig. 3). On the field, it corresponds to a clear contact between a chaotic deposit of blocs of thickness of 60 to 100 m overlying the oldest dam surface. Taking into account the area covered by the rock-avalanche and its mean thickness; we estimated a volume $\sim 0.2 \text{ km}^3$ for this

second event. Above this rock-avalanche deposit, we observe a high cliff of more than 200 m of elevation, cutting through the intercalations of silts and shales from the Tarata formation (Fig. 6C). This cliff crosscuts morphologically the main scarp left by the first fail-

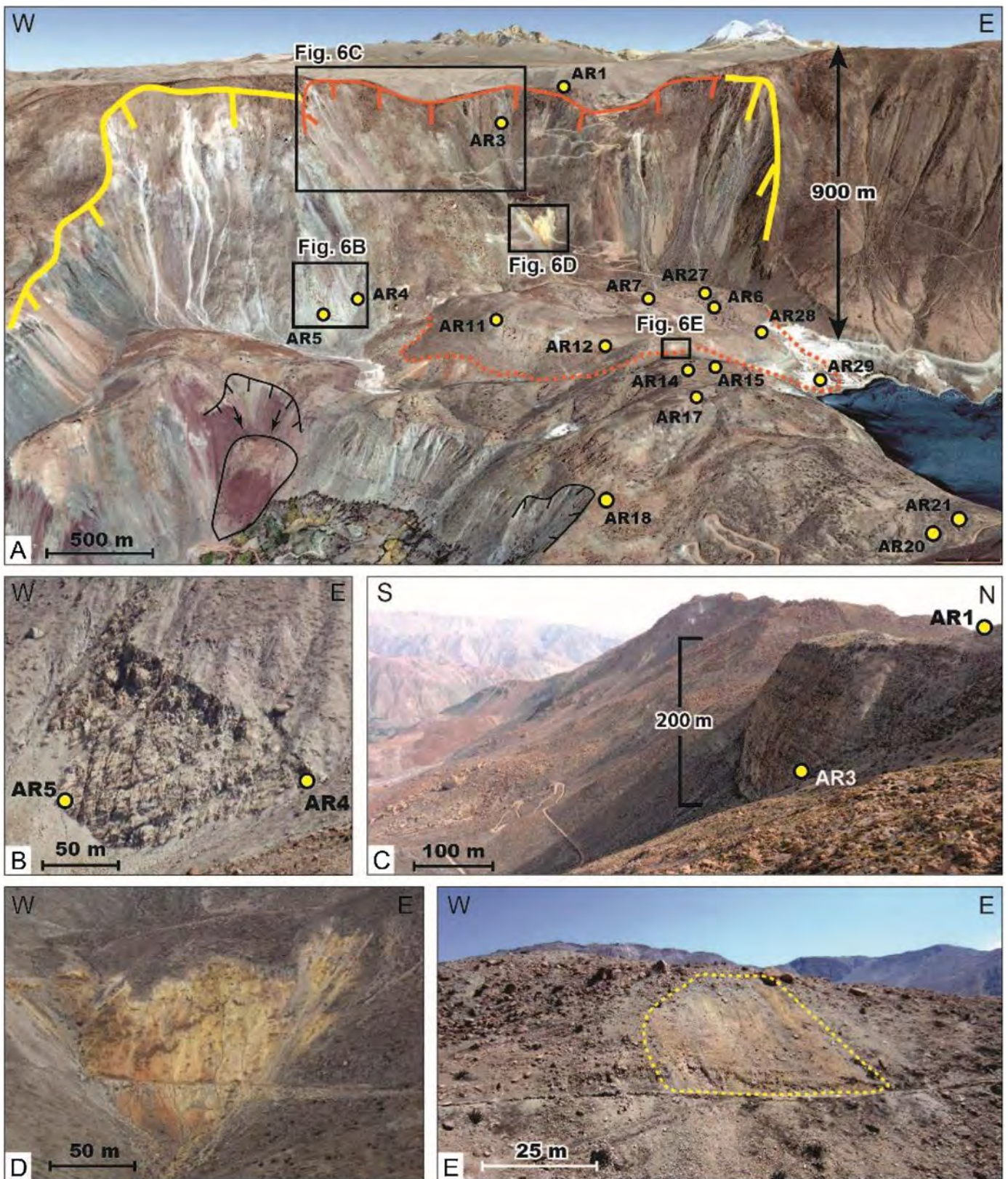


Fig. 6. Main scarp morphologies of the Aricota rockslide. (A) 3D view of the Aricota rockslide area (Google Earth). The scarp of the rockslide dam (first event) is depicted in yellow while the rock-avalanche scarp (second event) is in orange. Dashed orange line highlights the boundary of the rock-avalanche deposit. Small landslides (in black) affect the southwestern slope of the rockslide dam. (B) Preserved scarp surface of the first failure event and location of samples AR4 and AR5. (C) Vertical scarp generated by the second failure event and cutting through alternating silts and black shales of the Tarata formation. Sample AR3 was extracted from the scarp toe. See also location of the sample AR1 at the top of the slope, dedicated to constrain long-term denudation rate. (D) Layer corresponding to a regional paleo weathering profile interbedded in Cretaceous series. (E) Same weathered material (yellow) reworked and transported by the rock-avalanche.

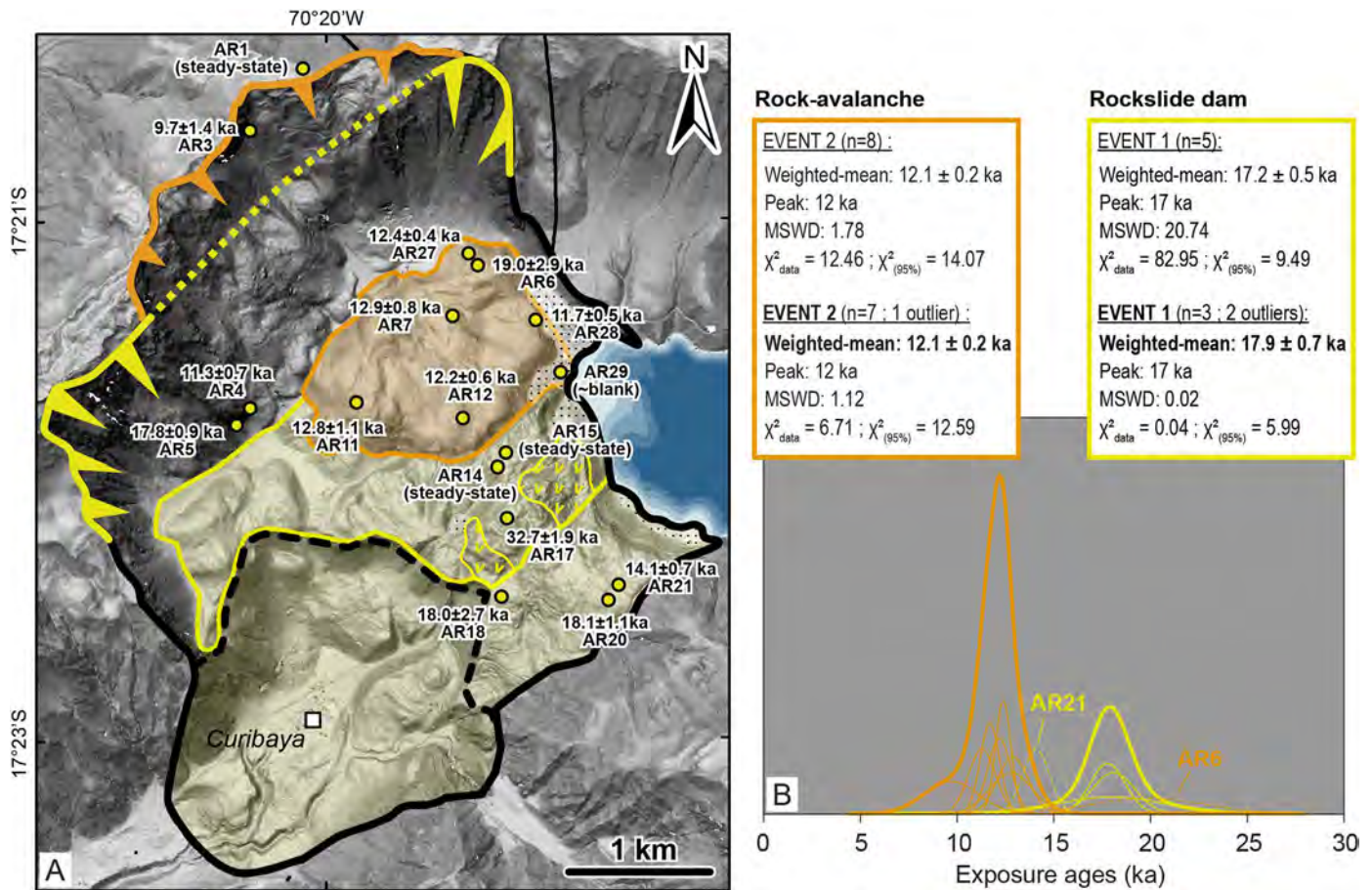


Fig. 7. Exposure durations results on the Aricota giant rockslide. (A) Rockslide map and sample ages (1σ internal uncertainty, Table 1, supplementary data). Legend is the same as Fig. 3B. (B) Probability density plot and statistics over exposure durations (1σ internal uncertainty, Table 1, supplementary data). Yellow curves and orange curves correspond to the rockslide dam (event 1) and the rock-avalanche (event 2), respectively. Thin lines correspond to individual exposure durations. Dashed lines refer to exposure durations interpreted as outliers (see text for details). Exposure duration from sample AR17 (32.7 ± 1.9 ka) is considered as an outlier (out of frame). Thick curves refer to the summed probability density function for each event (excluding outliers).

ure over a width of ~ 3 km (Figs. 3B and 6 A) inducing a regression toward the north of about 600–700 m.

Two types of structures can be distinguished in the rock-avalanche deposit. The firsts ones correspond to radial structures in the morphology (Fig. 3A), which directions point mainly toward the southeast. They are interpreted as an indication of the main direction of debris propagation toward the southeast. The second types of structures are concentric and are revealed by several bands of colors (black, brown and white) that are alternating in the deposit (Fig. 4C and Fig. 6A). Those colors correspond to different lithology of boulders. Indeed, from the northern to the southern part of the deposit, we can recognize boulders of ignimbrite and weathered material from the Huayllilas formation, followed by alignment of black silt-shale boulders from the Tarata formation (e.g. Fig. 5B) and finally very large boulders (up to 25 m in length) of andesitic breccia from the Quellaveco formation. The eastern side of the rock-avalanche deposit is composed of granitic boulders such as they outcrop above and along the top of the scarp (Fig. 3B). At the front of the rock-avalanche deposit (Fig. 6A), we observed an outcrop of weathered yellow material that originates from the middle part of the upper slope (Fig. 6D).

As a whole, those morphologies and such spatial distribution of boulders indicate that the former lithological succession of the slope was not mixed during the rock-avalanche and debris transport. The failure mode probably follows a translational failure allowing the bottom part of the slope to be projected in the distal part of the deposit.

4.2. Denudation rate and exposure duration results

Denudation rate and exposure durations derived from ^{10}Be data are reported in Table 1 (supplementary data). As previously mentioned, our first objective was to constrain the local denudation rate of the Aricota rockslide area in order to derive accurate exposure durations. The sample AR1, extracted on the ignimbritic plateau for this purpose, provided a high concentration of $38.00 \pm 1.36 \times 10^5$ at. g^{-1} . This indicates a saturation of ^{10}Be , i.e. a steady state, which is reached after an exposure duration greater than 1 Ma (Gosse and Phillips, 2001) at this latitude and elevation (17°S and ca. 3700 m a.s.l.) and corresponds to a denudation rate of 3.1 ± 0.6 $\text{mm} \cdot \text{ka}^{-1}$. Unexpectedly two other samples, AR14 and AR15, taken at the top of the Aricota rockslide dam also provided steady-state concentrations of $43.78 \pm 1.42 \times 10^5$ and $50.49 \pm 1.47 \times 10^5$ at. g^{-1} , corresponding respectively to denudation rates of 2.6 ± 0.5 and 2.2 ± 0.4 $\text{mm} \cdot \text{ka}^{-1}$. The presence of those steady-state surfaces in the main rockslide body suggests that a part of the original topography of the plateau was preserved during the mass movement. The implications of that result for the understanding of the failure typology will be more specifically discussed hereafter. All agreeing within uncertainties, those three denudation rates success a chi-2 test (1.39/5.99 (95%)) and belong to the same population whose weighted mean is 2.6 ± 0.4 $\text{mm} \cdot \text{ka}^{-1}$ (uncertainty attached is 1 sigma weighted standard deviation).

Exposure durations were then calculated using this mean denudation rate. In general, as shown on the Fig. 7B, exposure dura-

tions obtained are in good agreement with the geomorphological settings and they allow discriminating the two successive events that occurred on the Aricota rockslide. In the following, the exposure durations are reported with one sigma internal uncertainty.

The youngest exposure durations correspond to boulders of the rock-avalanche deposits, corresponding to the second event. Five exposure durations over six (samples AR7, AR11, AR12, AR27 and AR28) range between 11.7 ± 0.5 and 12.8 ± 1.1 ka (Table 1 (supplementary data) and Fig. 7B). The sample AR6 (19.0 ± 2.9 ka) is the only one age of this lobe of deposit falling out of this range, and for which we suspect likely inheritance. Comparing with exposure durations of ca. 12–13 ka, the excess of ^{10}Be concentration in this sample would be about 1×10^5 at g^{-1} . Along a depth profile that is theoretically at the equilibrium, and considering the denudation and the production rate conditions of the plateau (mean denudation rate of $2.6 \pm 0.4 \text{ mm} \cdot \text{ka}^{-1}$, “infinite” time, and production scaling of sample AR1), this concentration would be achieved at depth of 4 to 6 m. It is thus probable that the boulder AR19 comes from this pre-failure depth location and then was deposited in the debris with non-zero initial ^{10}Be concentration, giving an apparent older exposure duration. The sample AR3, picked at the foot of the vertical scarp located directly above the debris lobe (Fig. 6A and C), provided an exposure duration of 9.7 ± 1.4 ka, not significantly different from the previous ones considering the uncertainties. It confirms the relation between this secondary scarp and the rock-avalanche deposits.

Finally, the sample AR4, that was extracted from the northern part of the scarp presented on Fig. 6B (see also location on Fig. 3B), provided an exposure duration of 11.3 ± 0.7 ka that also agree with the one's previously listed. It is likely that the rock-avalanche failure has rejuvenated this side of the main scarp during its propagation. A probability density plot including all those samples (Fig. 7B) highlights a unimodal distribution (chi-2 test (95%): 6.71/12.59), the weighted mean of which is 12.1 ± 0.7 ka (uncertainty attached is 1 sigma weighted standard deviation). Considered or not, the AR4 and AR6 samples do not affect the result (Fig. 7B).

Exposure durations obtained from the five samples picked on the dam area (AR5, AR17, AR18, AR20, AR21), and its corresponding scarp, are significantly older. They range between 14.1 ± 0.7 and 32.7 ± 1.9 ka (Table 1, supplementary data). The probability density distribution provided on Fig. 7B shows that three of those ages (AR5, AR18 and AR20) agree within uncertainties (chi-2 test (95%): 0.04/5.99) and point to a weighted mean of 17.9 ± 0.7 ka. Inheritance is inferred in the sample AR17 (32.7 ± 1.9 ka) leading to a significantly older apparent exposure duration than the mean duration. This is fairly concordant with the fact that (1) the sample AR17 was extracted on boulders close to the samples AR14 and AR15 at steady state, and (2) all those samples are all standing in an area of preserved surface (Figs. 3B and 7) representing pre-rockslide topography.

The ^{10}Be concentration of sample AR21 (14.1 ± 0.7 ka) leads to a significantly younger apparent exposure duration. We interpret this younger apparent age as the consequence of a desquamation process of the boulder surface following the typical onion-skin weathering of the Atacama desert.

We measured in the sample AR29 (Fig. 5C and D) a $^{10}\text{Be}/^9\text{Be}$ ratio of $0.56 \pm 0.08 \times 10^{-14}$ that is equivalent to the corresponding blank value for this run ($0.52 \pm 0.23 \times 10^{-14}$, Table 1, supplementary data). This means that the ^{10}Be concentration in this sample is close to the detection limit, implying an exposure duration close to zero. The Fig. 8 shows the morphological context of the boulder AR29. It stands at an elevation of 2760 m, while the pre-1967 level was at 2790 m and the highest level deduced from diatomite deposit (Placzek et al., 2001) was estimated at ca. 2830 m (Fig. 8B). As this boulder belongs morphologically to the second event (mean age of deposition is 12.1 ± 0.7 ka), its very low ^{10}Be concentra-

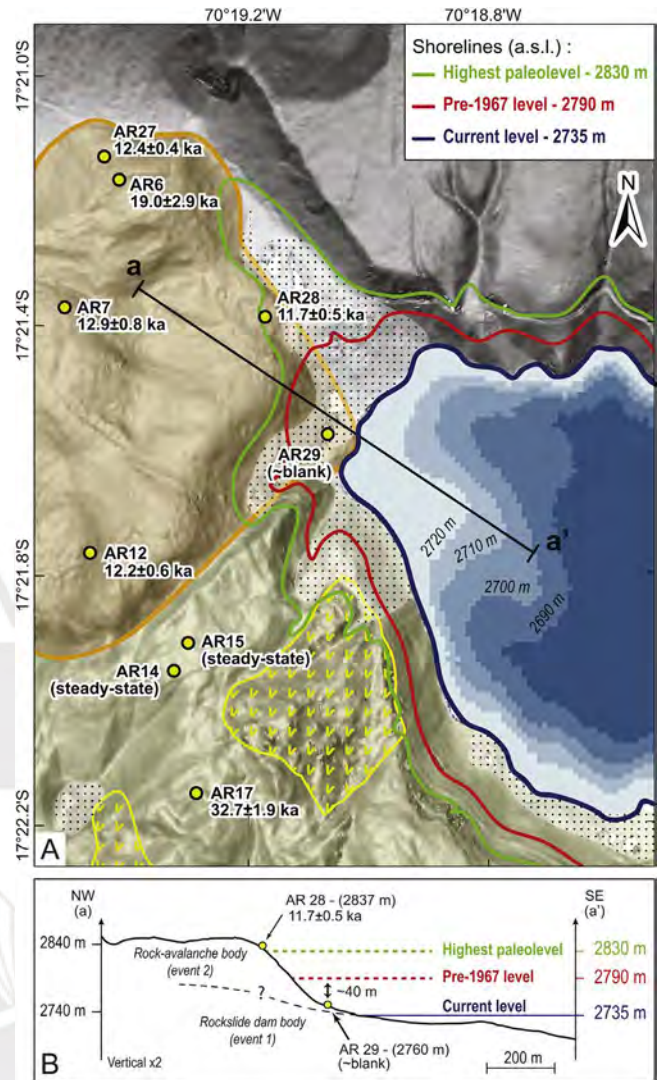


Fig. 8. Morphological context around the sample AR29. (A) Geomorphological map of the north-eastern part of the Aricota dam showing the location of the sample AR29 and the main variations of the Aricota lake shorelines (the probable highest paleo-lake level was reconstructed according to diatomite deposits (Placzek et al., 2001)). (B) Topographic profile extracted from the Pléiades DEM (see location on Fig. 8B). The legend of the rockslide morphologies is the same as Fig. 3B.

tion suggests that during the rock-avalanche, the boulder likely fell directly in deep water, thus shielded from the incident cosmic ray particles up to now.

5. Discussion

Most of the large landslides identified in the Central Western Andes, including the Aricota rockslide, have developed along the flank of deeply incised canyons (Fig. 1; e.g. Crosta et al., 2014; Thouret et al., 2017). In those canyons, the incision can locally exceed 1500 m (Thouret et al., 2017) suggesting that the topography is probably the first preconditioning factor for those giant gravitational failures. The same conclusions were made by Strasser and Schlunegger (2005), and Wörner et al. (2002) regarding the Lluta landslide. The deep incision of those canyons is the result of the peculiar conditions prevailing along the Central Western Andes since several millions of years (Schlunegger et al., 2006; García et al., 2011; Gunnell et al., 2010; Bissig and Riquelme, 2010; Jeffery et al., 2013). It is first related to the uplift of the region since the Cenozoic (e.g. Schildgen et al., 2009; Thouret et al., 2007). Second, it is related

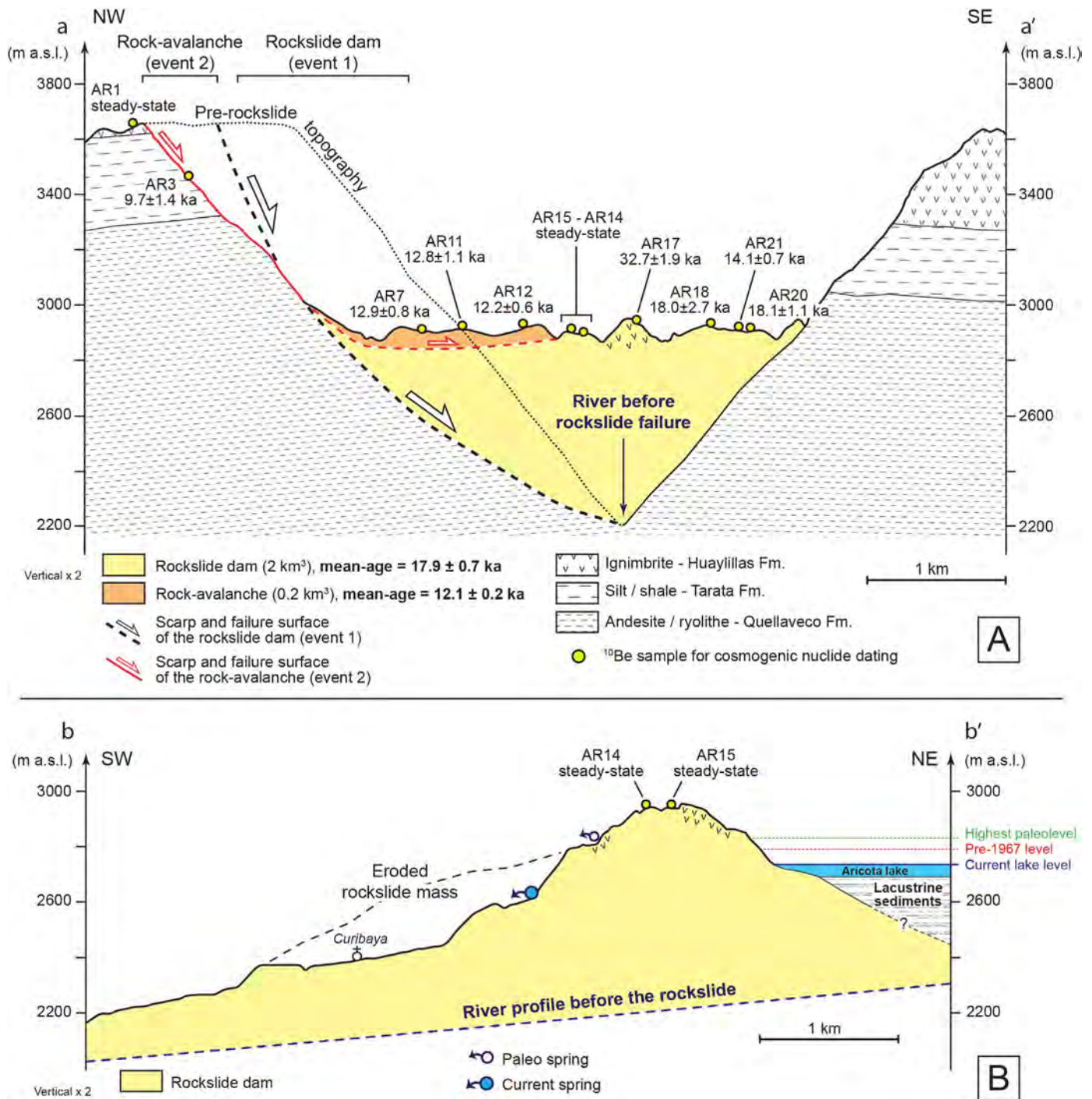


Fig. 9. Interpretative cross-sections of the Aricota giant rockslide. See locations on Fig. 3B. (A) Perpendicular to the Locumba valley. The pre-rockslide topography, before the first event, is reconstructed considering the volume estimation of the rockslide dam and interpolating the slope of the valley flanks (Delgado et al., 2018). Samples for ¹⁰Be cosmic ray exposure dating are projected on the cross-section. (B) Parallel to the Locumba valley. The pre-rockslide dam river profile is indicated from Delgado et al. (2018).

to the specific climate condition marked by a long lasting hyper-aridity affecting all the Central Western Andean flank (Atacama desert) until elevations of about 3000 m a.s.l., and, on the other hand, precipitations from the easterlies that reached the upper part of the western watersheds (Altiplano and Western Cordillera). Indeed, after Huffman et al. (2007), while current mean precipitation are ~0 mm/yr along the coast and the Western Cordillera, about 800 mm/yr of precipitation in average are recorded on the Altiplano. This rain shadow effect started possibly at 12/10 Ma (e.g. Ehlers and Poulsen, 2009; Insel et al., 2012; Rech et al., 2019). This

way, while the western flank of the Andes remains hyper-arid, the upper catchments collect a significant amount of water, flowing then throughout the Cordillera toward the Pacific (Litty et al., 2017). This discharge has maintained a constant incision in the valleys thus contributing to maintain very steep canyon flanks and critical topographic wedges highly prone to large-scale landslide failure (Thouret et al., 2017). As it was globally reported by Korup et al. (2007), and locally by Wörner et al. (2002) in the Lluta valley, this suggests that the critical relief (see also Blöthe et al., 2015) that can be close, or even beyond, to its proposed upper strength limit may

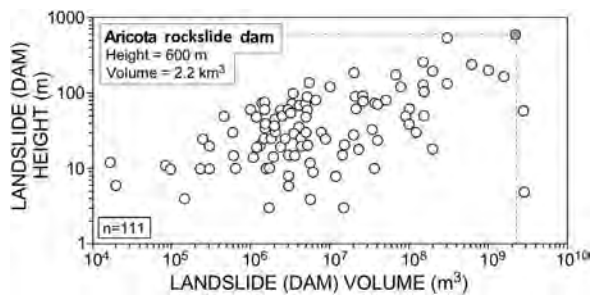


Fig. 10. Worldwide compilation of landslide dams modified from Korup et al. (2004) showing the relations between the landslide volumes and heights (n is the number of landslides of the database). The Aricota rockslide (grey circle) stands within the 3 largest landslide dams and the highest height reported worldwide.

be one of the primary factor controlling the development of large landslides in the Andean canyons.

In the Locumba valley, the gravitational failure of the canyon flank was deep and large enough to produce a massive dam generating upstream a lake more than 6 km long. As shown by our morphological analysis, two successive failure events occurred at the Aricota site (Fig. 3 and Fig. 9). A first main event, of rockslide typology, created the dam and then a second event occurred, of rock-avalanche typology, which deposits spread out on top of the first ones, reinforcing the initial dam. Taking into account the height of the dam (~ 600 m), its volume (2 ± 0.3 km³) and the pre-rockslide valley morphology, we propose that the first event (rockslide dam) has affected the ignimbritic plateau over a maximal width of 400–500 m (Fig. 9A). The failure allowed the collapse of a part of this plateau originally located at ca. 3650 m a.s.l. Ignimbritic rock volume outcrops at the present-day at the top of the rockslide dam at ca. 2900 m a.s.l. (Fig. 9A). Translational movements probably dominated the failure type as the vertical distribution of the stratigraphy is preserved in the dam. This morphological characteristic has been already described in various study cases of large slope destabilizations (Shreve, 1968; Strom, 2006; Humair et al., 2013). According to the classification of Hermanns et al. (2011), the distribution of the Aricota rockslide deposits in the Locumba valley corresponds to a type “IV a” in plan view. Indeed, the run-out of the debris was long enough (~ 3 km) to reach the opposite valley flank and to dam a small tributary valley (Fig. 3). As shown on the geological cross-section Fig. 9A, along a cross-valley profile, the deposit profile is roughly flat and symmetric to the original valley profile. This would correspond to a type “i” of cross-valley profile in the classification of Hermanns et al. (2011). The cross-section of the rockslide deposit, parallel to the valley (Fig. 9B), highlights the large thickness of the dam (600 m) and shows similarities with the type “2” of the along-valley profile classification of rockslide dams that is associated with a large lake (Hermanns et al., 2011). The great depth of the failure surface and the confined setting of the original Locumba valley may explain the high thickness of the deposit (Fig. 9B).

As shown on Fig. 10, comparing with the compilation of landslide dams established by Korup (2004), the Aricota rockslide dam stands among the largest worldwide. To explore the geotechnical stability of this dam, we compiled the two indexes developed by Casagli and Ermini (1999). They are based on geomorphometric parameters of the site: (1) the Blockage Index $I_b = \log(V_D * A_C^{-1})$ and (2) the Impoundment Index $I_i = \log(V_D * V_L^{-1})$, where V_D and V_L are the volumes of the rockslide dam and the lake [in m³], respectively, and A_C is catchment area upstream of the blockage [in km²]. The values obtained for the Aricota rockslide dam are $I_b = 6$ and $I_i = 3.4$ (taking $V_D = 2 * 10^9$ m³, $A_C = 1600$ km² and $V_L = 8 * 10^5$ m³ (Placzek et al., 2001)) indicating the stability of the site. Indeed Korup et al. (2004) shown that below $I_b = 2$ no landslide-dammed lakes formed,

whereas unstable lakes form at $I_b < 4$ and that impoundments with $I_b > 7$ have remained stable. Similarly, sites where $I_i > 1$ have all retained existing lakes, whereas locations with $I_i < 1$ comprise both stable and unstable landslide dams. Since the dam emplacement, the progressive infilling of the lake by lacustrine sediments (Fig. 9B) have also decreased the water volume and therefore reduced the pressure imposed to the dam. More generally, megatsunami is another hazard potentially linked to mountain lakes (either natural, landslide dam or artificial lakes) that can be triggered by slope failures around the lake (Hermanns et al., 2004). Taking into account the steep slope around the Aricota lake, this hazard cannot be excluded and deserve to be studied.

In the case of large landslide processes, Glade and Crozier (2005), or Hermanns et al. (2006) introduce that both preparatory factors (static and dynamic) and triggering factors are often interdependent and play crucial role in the slope failure evolution. In our study the geomorphological observations combined with cosmogenic nuclide dating obtained on the Aricota rockslide area show clearly two stages of destabilization at 17.9 ± 0.7 ka and 12.1 ± 0.2 ka, corresponding to the main rockslide dam event and to the secondary rock-avalanche, respectively (Fig. 9A). This timing of events provides a frame to discuss the nature of forcings that may have triggered the two slope failures. However, we do not have any constraints to discuss the preparatory phases and their related factors, thus the following discussion focuses on triggering factors only.

According to the literature, most of the contemporaneous, or historical landslide dams, have been triggered by earthquakes. Some of the most impressive cases are the Usoy landslide (volume = 2.4 km³, impounding a lake of a 17 km³), triggered in 1911 by an earthquake of Mw7.7 (Ambraseys and Bilham, 2012), the Tortum landslide (0.18 km³) in Turkey (Duman, 2009), or the numerous landslide dams in southeastern Italy which triggered by earthquakes of intensity VII to X during the 17th (Nicoletti and Parise, 2002). In the Andes, mostly in the NW Argentina, numerous paleo-landslide dams were reported and attributed also to past earthquakes (Wayne, 1999; Hermanns and Schellenberger, 2008; Moreiras et al., 2015).

Considering that the Aricota rockslide is located in a tectonically active region, with two large crustal fault systems (Incapuquio and Purgatorio faults) located from 10 to 20 km south of the rockslide (Fig. 2), a coseismic triggering of the Aricota slope failures is probable. Indeed, Benavente et al. (2017) revealed Holocene seismotectonic activity of the Purgatorio fault, showing at least two ruptures of ~ 3 and ~ 2 m of vertical offset at the surface, equivalent to $> M_w 7$ shallow seismic events. However, even if those faults represent high seismogenic potential in the close field of the rockslide, it does not exist for the moment any paleoseismic records as old as the Aricota slope failures that would corroborate a coseismic trigger. Another observation is that several landslides, including the Aricota ones, seem to cluster spatially on the hanging wall of the Incapuquio fault (transpressive senestral, Fig. 2). Similarly to what was reported by Gorum et al. (2011) in the Sichuan after the 2008 Wenchuan earthquake, such a landslide distribution could reflect a coseismic “hanging wall” effect. Indeed, Gorum et al. (2011) noticed that most of the landslides triggered during the Wenchuan earthquake occurred on the hanging wall block of the Wenchuan-Maowen fault. This massive landslide triggering was interpreted as a site effect and a probable amplification of ground motion in this area (Chiou and Youngs, 2014). Over the long-term, a higher concentration of slope failures on the hanging wall of the Incapuquio fault (Fig. 2) can be interpreted also as the effect of the river incision into the uplifting block, which may have increased and steepened the relief there.

On the other hand, several studies reported that in northwestern Argentinian Andes many landslide producing dammed lakes may have formed during wet periods (e.g. Trauth et al., 2003). Moreiras

and Sepúlveda (2015) provide an up-to-date inventory of mega paleolandslides in the Central Andes at 32–34°S and discuss traditional hypotheses used to explain landslide occurrences. Whereas earthquakes have been widely proposed as the main triggering mechanism of the Chilean slope failures, paleoclimatic conditions are considered as the main cause of mega-landslides in Argentina. However, Moreiras and Sepúlveda (2015) also insist on the fact that local evidences and geological records of those wetter periods are often lacking. On our study area at 17°S, it is striking to note the synchronicity between the chronic of failures of the Aricota rockslide and the two latest humid periods recorded at the scale of the Central Altiplano since 20 ka, pointing to a potential climatic control on the Aricota rockslide triggering. Those humid periods, documented since the 80 S' (e.g. Blodgett et al., 1997), are characterized mainly by two major expansions of the Altiplano lakes: the Tauca (18.5–14.5 ka) and the Coipasa (12.8–11 ka) phases (Placzek et al., 2013), during the Heinrich Stadial 1a and the Younger Dryas, respectively. Recently Martin et al. (2018) explored in details the past climate conditions during the Tauca phase by simultaneously reconstructing the fluctuations of lake levels and glacier advances in the Altiplano region. They found that during this period, on the northwestern edge of the Altiplano and the upper Locumba basin, the paleoprecipitations were amplified by 2–3 times compared to the present day precipitation. At a regional scale, the occurrence of such drastic increases of the paleoprecipitation is corroborated also by the concomitant aggradation of alluvial terraces and fan systems on valley floors along the western Peruvian margin. For instance, in the Majes river, located at about 300 km northwest to the Locumba valley, Steffen et al. (2010) pointed to the occurrence of major periods of aggradation at ca. 20 ka and between 12–8 ka. In the Moquegua valley (50 km northwest to Aricota), Keefer et al. (2003) reported the existence of extensive flood and debris flow deposits dated between 12 and 8.4 ka, and at least ten severe events that took place between 38 and 13 ka. At a larger scale along the western margin of the Andes in Peru, Litty et al. (2017) highlighted changes in precipitations patterns during the last 100 ka through shifts of the sediment provenance. In the Pisco valley, 700 km northwest to the Locumba valley, Steffen et al. (2010) and Bekaddour et al. (2014) conclude that phases of sediment aggradation and accumulation were triggered by shifts toward a more humid climate conditions during the Tauca paleolakes maximal expansions.

As a summary, several lines of evidences point toward significant increase of paleoprecipitation regime along the Central Western Andes during the periods 18.5–14.5 ka and 12.8–11 ka (Placzek et al., 2013). Given the correlation between those wet events and the timing of the Aricota rockslide (17.9 ± 0.7 ka and 12.1 ± 0.2 ka, Fig. 7); we tentatively propose that the generation of catastrophic mass movements in the Locumba valley was firstly climatically driven. Prolonged periods of increased precipitation may have reduced thresholds for slope instabilities by increasing water content in the unstable masses, decreasing the effective friction over the sliding planes, and eroding slope foots because of higher river discharge.

6. Conclusions

In this paper, we provide a geomorphological analysis and dating of the Aricota giant rockslide, located in the Central Western Cordillera of southern Peru (17°S). Our results indicate the occurrence of two successive events. A giant failure producing a rockslide dam occurred first at 17.9 ± 0.7 ka. This first destabilization event mobilized a rock volume of ca. 2 km³ and affected the northern flank of the Locumba valley. As shown by the presence of large preserved ignimbrite blocks overlying mixed and fragmented material in the dam, this first failure event was “in mass”. It gener-

ated an impressive dam in the main valley with a height of about 600 m, impounding a lake of approximately 6 km long upstream that remains until today. At 12.1 ± 0.2 ka, a second event of destabilization cross-cutting the initial scarp produced a rock-avalanche of ca. 0.2 km³ which debris spread out at the top of the northern part of the dam formed by the first event. The chronology of those two events of destabilization is compatible with the main paleoclimatic events of this region during the Heinrich Stadial 1a and the Younger Dryas, both characterized by paleoprecipitation increases. Furthermore, aggradation of alluvial terraces and fan systems are concomitant along the valley floors of the western Peruvian margin highlighting higher regional erosion, sediments supply and mass-wasting events during those two periods. This temporal correlation suggests that the climate has played a preponderant role on the triggering of the Aricota rockslide. However, additional and/or concomitant effect of crustal earthquakes on the rockslide initiation cannot be ruled out considering the seismotectonic setting of this Andean region. Future studies related to paleoseismicity would help to clarify this debated question. At the scale of the Central Andes, although numerous giant paleolandslides are recognized on its western arid flank, their understanding still suffers of a lack of time constraints, either in term of climatic events or in term of their individual geomorphic description.

Declaration of Competing Interest

The authors declare that they have no known competing financial interests or personal relationships that could have appeared to influence the work reported in this paper.

Acknowledgments

All the data used to perform this study are available in the paper and in the supplemental material. This research is part of the agreement between IRD and INGEMMET. It was financially supported by IRD and INGEMMET (Neotectonics program), a grant from Labex OSUG@2020, the French National Research Agency in the framework of the “Investissements d’avenir” program (ANR-15-IDEX-02 and ANR10 LABX56) and the CNES through the program TOSCA. The Astrium and the ISIS/CNES program provided the Pléiades images. The authors acknowledge Pascal Lacroix for his support during the Pléiades images processing. The company EGESUR is thank for having sharing the bathymetry data of the Aricota lake. The sample processing and chemical extraction of the ¹⁰Be were performed at the GTC plateform (ISTerre, Grenoble). We gratefully thank Francis Coeur for the sample processing. The ¹⁰Be measurements were performed at the ASTER AMS national facility (CEREGE, Aix en Provence) which is supported by the INSU/CNRS, the ANR through the Projets thématiques d’excellence program for the Équipements d’excellence ASTER-CEREGE action and IRD. Pr Fritz Schlunegger and an Anonymous Reviewer are acknowledged for their very constructive comments, which strongly helped to improve the manuscript.

Appendix A. Supplementary data

Supplementary material related to this article can be found, in the online version, at doi:<https://doi.org/10.1016/j.geomorph.2019.106932>.

References

- Ambraseys, N., Bilham, R., 2012. The Sarez-Pamir earthquake and landslide of 18 February 1911. *Seismol. Res. Lett.* 83 (2), 294–314.
- Armijo, R., Lacassin, R., Coudurier-Curveur, A., Carrizo, D., 2015. Coupled tectonic evolution of Andean orogeny and global climate. *Earth Science Reviews* 143, 1–35.
- Arnold, M., Merchel, S., Bourlès, D.L., Braucher, R., Benedetti, L., Finkel, R.C., Aumaître, G., Gottang, A., Klein, M., 2010. The French accelerator mass spectrometry facil-

- ity ASTER: improved performance and developments. *Nucl. Instrum. Methods Phys. Res. B Beam Interactions with Materials and Atoms* 268, 1954–1959.
- Arnold, M., Aumaître, G., Bourlès, D.L., Keddaddouche, K., Braucher, R., Finkel, R.C., Nottoli, E., Benedetti, L., Merchel, S., 2013. The French accelerator mass spectrometry facility ASTER after 4 years: Status and recent developments on 36Cl and 129I. *Nucl. Instrum. Methods Phys. Res. B* 294, 24–28.
- Audin, L., Behir, A., vol.xxii 2006. Active Tectonics As Determinant Factor in Landslides Along the Western Cordillera? Congreso Peruano De Geologia 13, Extended Abstract of the Sociedad Geologica Del Peru., pp. 237–239.
- Benavente, C., Zerathe, S., Audin, L., Hall, S.R., Robert, X., Delgado, F., Carcaillet, J., Team, A.S.T.E.R., 2017. Active transpressional tectonics in the Andean forearc of southern Peru quantified by ¹⁰Be surface exposure dating of an active fault scarp. *Tectonics* 36 (9), 1662–1678.
- Bekaddour, T., Schlunegger, F., Vogel, H., Delunel, R., Norton, K.P., Akçar, N., Kubik, P., 2014. Paleo erosion rates and climate shifts recorded by Quaternary cut-and-fill sequences in the Pisco valley, central Peru. *Earth Planet. Sci. Lett.* 390, 103–115.
- Bissig, T., Riquelme, R., 2010. Andean uplift and climate evolution in the southern Atacama desert deduced from geomorphology and supergene alunite-group minerals. *Earth Planet. Sci. Lett.* 299, 447–457.
- Blodgett, T.A., Isacks, B.L., Lenters, J.D., 1997. Constraints on the origin of paleolake expansions in the central Andes. *Earth Interact.* 1 (1), 1–28.
- Blöthe, J.H., Korup, O., Schwanghart, W., 2015. Large landslides lie low: excess topography in the Himalaya-Karakoram ranges. *Geology* 43 (6), 523–526.
- Borchers, B., Marrero, S., Balco, G., Caffee, M., Goehring, B., Lifton, N., Stone, J., 2016. Geological calibration of spallation production rates in the CRONUS-Earth project. *Quat. Geochronol.* 31, 188–198.
- Braucher, F., Guillou, V., Bourlès, D.L., Arnold, M., Aumaître, G., Keddaddouche, K., Nottoli, E., 2015. Preparation of ASTER in-house ¹⁰Be/⁹Be standard solutions. *Nucl. Instrum. Methods Phys. Res. B Beam Interactions with Materials and Atoms* 361, 335–340.
- Broxton, M.J., Edwards, L.J., 2008. Lunar and Planetary Science Conference The Ames stereo pipeline: automated 3D surface reconstruction from orbital imagery, vol 39, abstract 2419.
- Casagli, N., Ermini, L., 1999. Geomorphic analysis of landslide dams in the northern Apennine. *Transaction of the Japanese Geomorphologic Union* 20, 219–249.
- Chiou, B.S.J., Youngs, R.R., 2014. Update of the Chiou and Youngs NGA model for the average horizontal component of peak ground motion and response spectra. *Earthq. Spectra* 30 (3), 1117–1153.
- Crosta, G.B., Hermanns, R.L., Dehls, J., Lari, S., Sepúlveda, S., 2017. Rock avalanches clusters along the northern Chile coastal scarp. *Geomorphology* 289, 27–43.
- Crosta, G.B., Hermanns, R.L., Frattini, P., Valbuzzi, E., Valagussa, A., 2014. Large slope instabilities in Northern Chile: inventory, characterisation and possible triggers. In: Proceedings of the 3rd World Landslide Forum, 2–6 June 2014, Beijing, http://dx.doi.org/10.1007/978-3-319-04996-0_28, p 6.
- Delgado, F., Zerathe, S., Audin, L., Robert, X., Litty, C., Benavente, C., Carcaillet, J., Team, A., 2018. Quantifying basin-average denudation rates over the past 20 ka from landslide-dammed lake sediments in the South Western Peruvian Andes. *EGU General Assembly Conference Abstracts* (Vol. 20, p. 16124).
- Duman, T.Y., 2009. The largest landslide dam in Turkey: tortum landslide. *Eng. Geol.* 104 (1–2), 66–79.
- Dunai, T.J., Gonzalez López, G.A., Juez-Larré, J., 2005. Oligocene–Miocene age of aridity in the Atacama desert revealed by exposure dating of erosion-sensitive landforms. *Geology* 33 (4), 321–324.
- Evenstar, L., Stuart, F.M., Hartley, A.J., Tattich, B., 2015. Slow Cenozoic uplift of the western Andean Cordillera indicated by cosmogenic ³He in alluvial boulders from the Pacific Planation Surface. *Geophys. Res. Lett.* 82, 8448–8455.
- Ehlers, T.A., Poulsen, C.J., 2009. Influence of Andean uplift on climate and paleoaltimetry estimates. *Earth Planet. Sci. Lett.* 281, 238–248.
- García, M., Riquelme, R., Farías, M., Hérial, G., Charrier, R., 2011. Late Miocene–holocene canyon incision in the western Altiplano, northern Chile: tectonic or climatic forcing? *J. Geol. Soc.* 168, 1047–1060.
- Glade, T., Crozier, M.J., 2005. The nature of landslide hazard impact. In: *Landslide Hazard and Risk*, pp. 43–74.
- Gorum, T., Fan, X., van Westen, C.J., Huang, R.Q., Xu, Q., Tang, C., Wang, G., 2011. Distribution pattern of earthquake-induced landslides triggered by the 12 May 2008 Wenchuan earthquake. *Geomorphology* 133 (3–4), 152–167.
- Gosse, J.C., Phillips, F.M., 2001. Terrestrial in situ cosmogenic nuclides: theory and application. *Quat. Sci. Rev.* 20 (14), 1475–1560, [http://dx.doi.org/10.1016/S0277-3791\(00\)00171-2](http://dx.doi.org/10.1016/S0277-3791(00)00171-2).
- Gunnell, Y., Thouret, J.C., Bricchau, S., Carter, A., Gallagher, K., 2010. Low-temperature thermochronology in the Peruvian Central Andes: implications for long-term continental denudation, timing of plateau uplift, canyon incision and lithosphere dynamics. *J. Geol. Soc.* 167 (4), 803–815.
- Hall, S.R., Farber, D.L., Audin, L., Finkel, R.C., 2012. Recently active contractile deformation in the forearc of southern Peru. *Earth Planet. Sci. Lett.* 337, 85–92.
- Hermanns, R.L., Niedermann, S., Villanueva García, A., Sosa Gomez, J., Strecker, M.R., 2001. Neotectonics and catastrophic failure of mountain fronts in the southern intra-Andean Puna plateau, Argentina. *Geology* 29 (7), 619–623.
- Hermanns, R., Niedermann, S., Kubik, P., 2004. Rock avalanching into a landslide-dammed lake causing multiple dam failure in Las Conchas valley (NW Argentina) — evidence from surface exposure dating and stratigraphic analyses. *Landslides* 1, 113–122.
- Hermanns, R., Niedermann, S., Villanueva García, A., Schellenberger, A., 2006. Rock avalanching in the NW Argentine Andes as a result of complex interactions of lithologic, structural and topographic boundary conditions, climate change and active tectonics: landslides from massive rock slope failure. *NATO Science Series IV* 49, 539–569.
- Hermanns, R.L., Schellenberger, A., 2008. Quaternary tephrochronology helps define conditioning factors and triggering mechanisms of rock avalanches in NW Argentina. *Quat. Int.* 178 (1), 261–275.
- Hermanns, R.L., Hewitt, K., Strom, A., Evans, S.G., Dunning, S.A., Scarascia-Mugnozza, G., 2011. The classification of rockslide dams. In: *Natural and Artificial Rockslide Dams*. Springer, Berlin, Heidelberg, pp. 581–593.
- Houston, J., Hartley, A.J., 2003. The central Andean west-slope rainshadow and its potential contribution to the origin of hyper-aridity in the Atacama desert. *Int. J. Climatol.* 23 (12), 1453–1464.
- Huffman, G.J., Bolvin, D.T., Nelkin, E.J., Wolff, D.B., Adler, R.F., Gu, G., Stocker, E.F., 2007. The TRMM multisatellite precipitation analysis (TMPA): quasi-global, multiyear, combined-sensor precipitation estimates at fine scales. *J. Hydrometeorol.* 8 (1), 38–55.
- Humair, F., Pedrazzini, A., Epard, J.-L., Froese, C.R., Jaboyedoff, M., 2013. Structural characterization of Turtle Mountain anticline (Alberta, Canada) and impact on rock slope failure. *Tectonophysics* 605, 133–148.
- Insel, N., Poulsen, C.J., Ehlers, T.A., Sturm, C., 2012. Response of meteoric $\delta^{18}O$ to surface uplift—Implications for Cenozoic Andean Plateau growth. *Earth and Planetary Science Letters* *Earth Planet. Sci. Lett.* 317, 262–272.
- Jeffery, M.L., Ehlers, T.A., Yanites, B.J., Poulsen, C.J., 2013. Quantifying the role of paleoclimate and Andean Plateau uplift on river incision. *J. Geophys. Res. Earth Surf.* 118, 852–871.
- Keefer, D.K., Moseley, M.E., deFrance, S.D., 2003. A 38,000-year record of floods and debris flows in the ilo region of southern peru and its relation to el niño events and great earthquakes. *Palaeogeogr. Palaeoclimatol. Palaeoecol.* 194, 41–77.
- Korup, O., 2004. Geomorphometric characteristics of New Zealand landslide dams. *Eng. Geol.* 73 (1–2), 13–35.
- Korup, O., Clague, J.J., Hermanns, R.L., Hewitt, K., Strom, A.L., Weidinger, J.T., 2007. Giant landslides, topography, and erosion. *Earth Planet. Sci. Lett.* 261 (3–4), 578–589.
- Lifton, N., Sato, T., Dunai, T.J., 2014. Scaling in situ cosmogenic nuclide production rates using analytical approximations to atmospheric cosmic-ray fluxes. *Earth Planet. Sci. Lett.* 386, 149–160, <http://dx.doi.org/10.1016/j.epsl.2013.10.052>.
- Litty, C., Lanari, P., Burn, M., Schlunegger, F., 2017. Climate-controlled shifts in sediment provenance inferred from detrital zircon ages, western Peruvian Andes. *Geology* 45 (1), 59–62.
- Madella, A., Delunel, R., Akçar, N., Schlunegger, F., Christl, M., 2018. 10 Be-inferred paleo-denudation rates imply that the mid-Miocene western central Andes eroded as slowly as today. *Sci. Rep.* 8 (1), 2299.
- Margirier, A., Audin, L., Carcaillet, J., Schwartz, S., 2015. Tectonic and climatic controls on the Chuquiabamba landslide (western Andes, southern Peru). *Earth Surf. Dyn. Discuss.* 2, 1129–1153.
- Marrero, S.M., Phillips, F.M., Borchers, B., Lifton, N., Aumer, R., Balco, G., 2016. Cosmogenic nuclide systematics and the CRONUScal program. *Quat. Geochronol.* 31, 160–187, <http://dx.doi.org/10.1016/j.quageo.2015.09.005>.
- Martin, L.C., Blard, P.H., Lavé, J., Condom, T., Prémaillon, M., Jomelli, V., Tibari, B., 2018. Lake Tauca highstand (Heinrich Stadial 1a) driven by a southward shift of the Bolivian High. *Sci. Adv.* 4 (8), eaar2514.
- Mather, A.E., Hartley, A.J., Griffiths, J.S., 2014. The giant coastal landslides of Northern Chile: tectonic and climate interactions on a classic convergent plate margin. *Earth Planet. Sci. Lett.* 388, 249–256.
- McPhillips, D., Bierman, P.R., Rood, D.H., 2014. Millennial-scale record of landslides in the Andes consistent with earthquake trigger. *Nat. Geosci.* 7, 925–930.
- Moreiras, S.M., Sepúlveda, S.A., 2015. Megalandslides in the Andes of central Chile and Argentina (32°–34° S) and potential hazards. *Geol. Soc. London Spec.* 399 (1), 329–344.
- Moreiras, S.M., Hermanns, R.L., Fauqué, L., 2015. Cosmogenic dating of rock avalanches constraining Quaternary stratigraphy and regional neotectonics in the Argentine Central Andes (32 S). *Quat. Sci. Rev.* 112, 45–58.
- Nicoletti, P.G., Parise, M., 2002. Seven landslide dams of old seismic origin in south-eastern Sicily (Italy). *Geomorphology* 46 (3–4), 203–222.
- Nishiizumi, K., Caffee, M.W., Finkel, R.C., Brimhall, G., Mote, T., 2005. Remnants of a fossil alluvial fan landscape of Miocene age in the Atacama desert of northern Chile using cosmogenic nuclide exposure age dating. *Earth Planet. Sci. Lett.* 237, 499–507.
- Pinto, L., Hérial, G., Sepúlveda, S.A., Krop, P., 2008. A Neogene giant landslide in Tarapacá, northern Chile: a signal of instability of the westernmost Altiplano and palaeoseismicity effects. *Geomorphology* 102 (3–4), 532–541.
- Placzek, C., Quade, J., Betancourt, J.L., 2001. Holocene lake-level fluctuations of Lake Aricota, southern Peru. *Quat. Res.* 56 (2), 181–190.
- Placzek, C.J., Quade, J., Patchett, P.J., 2013. A 130 ka reconstruction of rainfall on the Bolivian Altiplano. *Earth Planet. Sci. Lett.* 363, 97–108.
- Rech, J.A., Currie, B.S., Jordan, T.E., Riquelme, R., Lehmann, S.B., Kirk-Lawlor, N.E., Li, S., Gooley, J.T., 2019. Massive middle Miocene gypsic paleosols in the Atacama desert and the formation of the Central Andean rain-shadow. *Earth Planet. Sci. Lett.* 506, 184–194.
- Schildgen, T.F., Ehlers, T.A., Whipple, K.X., Whipple, D.M., van Soest, M.C., Hodges, K.V., 2009. Quantifying canyon incision and Andean Plateau surface uplift, southwest Peru: a thermochronometer and numerical modeling approach. *J. Geophys. Res. Earth Surf.* 114, F04014.
- Schlunegger, F., Zeilinger, G., Kounov, A., Kober, F., Hüsser, B., 2006. Scale of relief growth in the forearc of the Andes of Northern Chile (Arica latitude, 18 S). *Terra Nova* 18, 217–223.

- Sempere, T., Folguera, A., Gerbault, M., 2008. *Tectonophysics New Insights into the Andean Evolution: an Introduction to Contributions from the 6th IASAG Symposium* (Barcelona, 2005), vol. 459, pp. 1–13.
- Shreve, R.L., 1968. The blachhawk landslide: geological society of america. *Special Paper* 108, 4–47.
- Steffen, D., Schlunegger, F., Preusser, F., 2010. Late Pleistocene fans and terraces in the Majes valley, southern Peru, and their relation to climatic variations. *Int. J. Earth Sci.* 99 (8), 1975–1989.
- Strom, A.L., 2006. Morphology and internal structure of rockslides and rock avalanches: grounds and constraints for their modelling. In: Evans, S.G., Scarascia Mugnozza, G., Strom, A.L., Hermanns, R.L. (Eds.), *Landslides from Massive Rock Slope Failures* 49: Dordrecht. Springer.
- Strasser, M., Schlunegger, F., 2005. Erosional processes, topographic length-scales and geomorphic evolution in arid climatic environments: the ‘Lluta collapse’, northern Chile. *Int. J. Earth Sci.* 94 (3), 433–446.
- Thouret, J.C., Gunnell, Y., Jicha, B.R., Paquette, J.L., Braucher, R., 2017. Canyon incision chronology based on ignimbrite stratigraphy and cut-and-fill sediment sequences in SW Peru documents intermittent uplift of the western Central Andes. *Geomorphology* 298, 1–19.
- Thouret, J.C., Wörner, G., Gunnell, Y., Singer, B., Zhang, X., Souriot, T., 2007. Geochronologic and stratigraphic constraints on canyon incision and Miocene uplift of the Central Andes in Peru. *Earth Planet. Sci. Lett.* 263 (3–4), 151–166.
- Trauth, M.H., Bookhagen, B., Marwan, N., Strecker, M.R., 2003. Multiple landslide clusters record Quaternary climate changes in the northwestern Argentine Andes. *Palaeogeogr. Palaeoclimatol. Palaeoecol.* 194 (1–3), 109–121.
- Villegas-Lanza, J.C., Chlieh, M., Cavalié, O., Tavera, H., Baby, P., Chire-Chira, J., Nocquet, J.-M., 2016. Active tectonics of Peru: Heterogeneous interseismic coupling along the Nazca megathrust, rigid motion of the Peruvian Sliver, and Subandean shortening accommodation. *J. Geophys. Res. Solid Earth* 121, 7371–7394, <http://dx.doi.org/10.1002/2016JB013080>.
- Viveen, W., Schlunegger, F., 2018. Prolonged extension and subsidence of the Peruvian forearc during the Cenozoic. *Tectonophysics* 730, 48–62.
- Wayne, W.J., 1999. The Alemania rockfall dam: a record of a mid-holocene earthquake and catastrophic flood in northwestern Argentina. *Geomorphology* 27 (3–4), 295–306.
- Wörner, G., Uhlig, D., Kohler, I., Seyfried, H., 2002. Evolution of the West Andean Escarpment at 18 S (N. Chile) during the last 25 Ma: uplift, erosion and collapse through time. *Tectonophysics* 345 (1–4), 183–198.
- Zerathe, S., Blard, P.H., Braucher, R., Bourlès, D., Audin, L., Carcaillet, J., Delgado, F., Benavente, C., Keddadouche, K., 2017. Toward the feldspar alternative for cosmogenic ¹⁰Be applications. *Quat. Geochronol.* 41, 83–96.



2 **Sample preparation**

3 Sample preparation and ^{10}Be chemical extraction were achieved following routine procedure at the
4 GTC Platform, ISTerre laboratory (Grenoble, France). The samples were crushed and sieved to obtain
5 a grain-size of 0.2–0.8 mm. Then pure quartz was obtained by successive magnetic separations using
6 a Frantz magnetic separator and subsequent leaching in a mixture (1:2) of hydrochloric and
7 hexafluorosilicic acids. After atmospheric ^{10}Be decontamination (by 3 sequential HF leaching), ^9Be
8 carrier solution (1000 mg.l^{-1} , Scharlab Be batch 14569501) was added and the sample was then
9 dissolved in 40% HF. Beryllium was isolated using anion and cation exchange columns followed by
10 selective pH precipitation techniques (Brown et al., 1991). The beryllium hydroxides were precipitated,
11 dried, and calcined at 850 °C to BeO . $^{10}\text{Be}/^9\text{Be}$ measurements were performed at the French AMS
12 National Facility, located at CEREGE in Aix-en-Provence (Arnold et al., 2013). $^{10}\text{Be}/^9\text{Be}$ ratios were
13 calibrated against the in-house standard STD-11, using an assigned $^{10}\text{Be}/^9\text{Be}$ ratio of (1.191 ± 0.013)
14 $\times 10^{-11}$ (Braucher et al., 2015). Uncertainties on ^{10}Be concentrations (reported as 1σ) are calculated
15 according to the standard error propagation method using the quadratic sum of the relative errors and
16 include a conservative 0.5% external machine uncertainty (Arnold et al., 2010), a 1.08% uncertainty on
17 the certified standard ratio, a 1σ uncertainty associated to the mean of the standard ratio
18 measurements during the measurement cycles, a 1σ statistical error on counted events and the
19 uncertainty associated with the chemical and analytical blank correction. The $^{10}\text{Be}/^9\text{Be}$ blank correction
20 values were $5.21 \pm 2.30 \times 10^{-15}$ for the run of samples AR27, AR28 and AR29, and $2.77 \pm 0.47 \times 10^{-15}$ for the
21 other samples (Table 1).

22 Denudation rates and exposure durations were both calculated using the MATLAB[®]-based CRONUScalc
23 program, developed by Marrero et al. (2016). This production rate was scaled at the geographical and
24 altitudinal location of each sampling site using the LSD scaling scheme (SF) of Lifton et al. (2014) which
25 is a time-dependent model based on equations from a nuclear physics model and incorporating dipole

26 and non-dipole magnetic field fluctuations and solar modulation (Marrero et al., 2016). Atmospheric
27 pressure at the sampling site was derived from the ERA-40 atmosphere model (Uppala et al., 2005).
28 We applied a density estimate of 2.6 g.cm^{-3} for the ignimbrite and an attenuation length of 160 g.cm^{-2}
29 for the neutron component (Dunne et al., 1999). For the muons scheme, we kept the default
30 parameters of CRONUScalc program (Marrero et al., 2016). Snowfall almost never occurred in this
31 semi-arid area, thus this correction was neglected. Data templates including all the parameter
32 previously listed are provided in the supplementary data for any recalculation.



33 Table 1: Samples parameters, cosmogenic ^{10}Be data and results. Z is the sample thickness, S is the topographic shielding factor, Pn and P μ are the
 34 contemporary depth average production rate outputs from the CRONUS Earth Web Calculators (version 2.0; Marrero et al., 2016) for the neutrons and
 35 slow/fast muons, respectively. All the uncertainties reported are 1 sigma.

Morphology	Sample	Latitude (S°)	Longitude (W°)	Elevation (m a.s.l.)	Z (cm)	S	Mass (g)	^9Be carrier (10^{19} atoms)	$^{10}\text{Be}/^9\text{Be}$ (10^{-14})	$^{10}\text{Be}^a$ (10^5 at.g^{-1})	Pn ($\text{at.g}^{-1}.\text{yr}^{-1}$)	P μ ($\text{at.g}^{-1}.\text{yr}^{-1}$)	Exposure ^b ages (ka)	Denudation rates (mm/ka)
Scarps	AR3	17.34418	70.33860	3488	6.0	0.494	1.73	2.04	1.21 ± 0.09	1.10 ± 0.12	11.95	0.09	9.7 ± 1.4 (1.7)	
	AR4	17.36217	70.33842	2870	5.5	0.792	4.87	2.04	3.64 ± 0.17	1.41 ± 0.08	13.50	0.11	11.3 ± 0.7 (1.3)	
	AR5	17.36312	70.33930	2856	1.5	0.591	5.45	2.04	4.82 ± 0.22	1.70 ± 0.08	10.32	0.08	17.8 ± 0.9 (1.7)	
Boulders	AR6	17.35278	70.32345	2933	3.0	0.976	6.34	2.03	9.99 ± 1.74	3.11 ± 0.56	17.62	0.14	19.0 ± 2.9 (3.2)	
	AR7	17.35618	70.32500	2918	4.0	0.971	4.46	2.03	4.79 ± 0.25	2.05 ± 0.12	17.24	0.14	12.9 ± 0.8 (1.4)	
	AR11	17.36170	70.33145	2935	5.5	0.984	2.76	2.03	3.07 ± 0.21	2.05 ± 0.16	17.44	0.14	12.8 ± 1.1 (1.6)	
	AR12	17.36274	70.32433	2907	5.0	0.925	5.12	2.02	4.90 ± 0.22	1.82 ± 0.09	16.18	0.13	12.2 ± 0.6 (1.2)	
	AR17	17.36917	70.32143	2928	3.5	0.995	1.08	2.05	3.35 ± 0.18	5.83 ± 0.36	17.84	0.14	32.7 ± 1.9 (3.2)	
	AR18	17.37422	70.32235	2822	2.5	0.992	0.45	2.09	0.90 ± 0.09	2.89 ± 0.47	16.84	0.14	18.0 ± 2.7 (3.0)	
	AR20	17.37403	70.31420	2909	5.5	0.981	8.10	2.06	11.55 ± 0.75	2.87 ± 0.19	17.12	0.14	18.1 ± 1.1 (1.8)	
	AR21	17.37372	70.31408	2907	5.0	0.987	5.07	2.06	5.76 ± 0.28	2.23 ± 0.11	17.27	0.14	14.1 ± 0.7 (1.4)	
	AR27	17.35217	70.32387	2925	3.0	0.964	8.58	4.10	4.58 ± 0.15	1.98 ± 0.06	17.32	0.14	12.4 ± 0.4 (1.2)	
	AR28	17.35647	70.31943	2837	3.8	0.980	8.70	3.42	5.06 ± 0.22	1.79 ± 0.07	16.61	0.14	11.7 ± 0.5 (1.2)	
	AR29	17.35985	70.31778	2750	3.5	0.969	3.12	3.39	0.56 ± 0.08	-	-	-	-	
Boulders	AR1	17.34085	70.33488	3674	2.0	1	3.07	2.03	57.81 ± 2.05	38.00 ± 1.36	24.93	0.19	3.1 ± 0.6	
	AR14	17.36590	70.32203	2923	4.0	1	0.75	2.08	16.12 ± 0.51	43.78 ± 1.42	24.93	0.19	2.6 ± 0.5	
	AR15	17.36515	70.32163	2910	3.0	1	5.59	2.04	138.70 ± 4.04	50.49 ± 1.47	24.93	0.19	2.2 ± 0.4	
	BI1 ^c	-	-	-	-	-	-	2.03	0.28 ± 0.47	-	-	-	-	
	BI2 ^d	-	-	-	-	-	-	3.37	0.52 ± 0.23	-	-	-	-	

^a Uncertainties reported include the counting statistics, the machine stability ($\sim 0.5\%$) and the blank correction.

^b Exposure ages are reported with analytical and total uncertainties (the total uncertainty is in parentheses), that both include the propagation of uncertainties of each parameters by partial derivatives such as described in Marrero et al. (2016). Exposure ages were calculated with a locally estimated mean denudation rate of $2.6 \pm 0.5 \text{ mm.k}^{-1}$ (see text for explanations).

^c This sample was extracted from the top of a boulder that morphologically belongs to the deposit of the secondary rock-avalanche event, but which was located below the lake surface before 1967 (see text for details). As the concentration measured in this sample is equivalent to the blank value measured during this run (BI2), we did not calculate a corresponding exposure age.

^d This blank corresponds to the first run of measurements done in 2014 and its correction was applied to samples: AR1, AR3, AR4, AR5, AR6, AR7, AR11, AR12, AR14, AR15, AR17, AR18, AR20 and AR21.

^e This blank corresponds to the second run of measurements done in 2018 and its correction was applied to samples: AR27, AR28 and AR29.

37 **References**

- 38 Arnold, M., Aumaître, G., Bourlès, D.L., Keddaddouche, K., Braucher, R., Finkel, R.C., Nottoli, E.,
39 Benedetti, L., Merchel, S., 2013. The French accelerator mass spectrometry facility ASTER after 4
40 years: Status and recent developments on ^{36}Cl and ^{129}I . Nuclear Instruments and Methods in
41 Physics Research Section B: Beam Interactions with Materials and Atoms 294, 24-28.
- 42 Arnold, M., Merchel, S., Bourlès, D.L., Braucher, R., Benedetti, L., Finkel, R.C., Aumaître, G., Gott dang,
43 A., Klein, M., 2010. The French accelerator mass spectrometry facility ASTER: Improved
44 performance and developments. Nuclear Instruments and Methods in Physics Research Section B:
45 Beam Interactions with Materials and Atoms 268, 1954-1959.
- 46 Brown, E.T., Edmond, J.M., Raisbeck, G.M., Yiou, F., Kurz, M.D., Brook, E.J., 1991. Examination of
47 surface exposure ages of moraines in Arena Valley, Antarctica using in situ produced ^{10}Be and ^{26}Al .
48 Geochimica et Cosmochimica Acta 55, 2269-2283.
- 49 Chmeleff, J., von Blanckenburg, F., Kossert, K., Jakob, D., 2010. Determination of the ^{10}Be half-life by
50 multicollector ICP-MS and liquid scintillation counting. Nuclear Instruments and Methods in
51 Physics Research Section B: Beam Interactions with Materials and Atoms 268, 192-199.
- 52 Dunne, A., Elmore, D., Muzicar, P., 1999. Scaling of cosmogenic nuclide production rates for geometric
53 shielding and attenuation at depth on sloped surfaces. Geomorphology 27, 3–11.
- 54 Korschinek, G., Bergmaier, A., Faestermann, T., Gerstmann, U. C., Knie, K., Rugel, G., Kossert, K., 2010.
55 A new value for the half-life of ^{10}Be by heavy-ion elastic recoil detection and liquid scintillation
56 counting. Nuclear Instruments and Methods in Physics Research Section B: Beam Interactions with
57 Materials and Atoms 268, 187-191.
- 58 Lifton, N., Sato, T., Dunai, T. J., 2014. Scaling in situ cosmogenic nuclide production rates using
59 analytical approximations to atmospheric cosmic-ray fluxes. Earth and Planetary Science Letters
60 386, 149-160, doi:10.1016/j.epsl.2013.10.052.

61 Nishiizumi, K., Imamura, M., Caffee, M.W., Southon, J.R., Finkel, R.C., McAninch, J., 2007. Absolute
62 calibration of ^{10}Be AMS standards. Nuclear Instruments and Methods in Physics Research Section
63 B: Beam Interactions with Materials and Atoms 258, 403-413.

64 Uppala, S. M., Kållberg, P.W., Simmons, A.J., Andrae, U., Bechtold, V.D., Fiorino, M., Li, X., 2005. The
65 ERA-40 re-analysis. Quarterly Journal of the Royal Meteorological Society 131(612), 2961-3012,
66 doi:10.1256/qj.04.176.



CHAPTER IV:
PLEISTOCENE CHRONICLES OF
LARGE LANDSLIDES TRIGGERING
ON THE WESTERN FLANK OF THE
CENTRAL ANDES REVEALED BY
COSMOGENIC NUCLIDE DATING

Pleistocene chronicles of large landslides triggering on the western flank of the Central Andes revealed by cosmogenic nuclide dating

Delgado, F^{1,2}, Zerathe, S², Schwartz, S², Gaidzik, K³, Robert, X², Carcaillet, J², Benavente, C⁴, & Aster TEAM^{5,#}

¹ *Especialidad Ingeniería Geológica, Facultad de Ciencias e Ingeniería. Pontificia Universidad Católica del Perú, Av. Universitaria 1801, San Miguel, Lima 15088, Perú.*

² *Univ. Grenoble Alpes, Univ. Savoie Mont Blanc, CNRS, IRD, IFSTTAR, ISTERRE, 38000 Grenoble, France*

³ *Institute of Earth Sciences, University of Silesia, Będzińska 60, 41-200, Sosnowiec, Poland*

⁴ *Instituto Geológico, Minero y Metalúrgico INGEMMET, Av. Canadá 1470, Lima, Perú*

⁵ *Aix-Marseille Univ., CNRS, IRD, Coll. France, UM 34 CEREGE, Technopôle de l'Environnement Arbois-Méditerranée, BP80, 13545 Aix-en-Provence, France*

[#] *Georges Aumaître and Karim Keddadouche*

Abstract

The Western flank of the Central Andes presents a high concentration of giant paleo-landslides that are well preserved due to the long-term aridity of the region. Based on an exhaustive inventory established at the scale of the Western Cordillera in South Peru and North Chile, a previous study indicates that the formation of those giant paleo-landslides was favored by coupled conditioning factors including lithology and strong local relief generated by the incision of deep canyons. In particular, spatial clustering was highlighted by the presence of dozens of large landslides spatially concentrated within a few kilometers. In this part of the Andes, the strong seismic activity linked to the ruptures of crustal faults and past climatic changes could have played a major role in the triggering of these large gravity instabilities. However, the precise timing of most of these landslides remains unknown, hampering our understanding of their frequency of occurrence. Thus, additional data are required to further investigate the question of their factor of trigger through time.

To shed new light on those questions, we focus in this study on one of those previously identified clusters: the “Locumba cluster”. The largest landslide in this area corresponds to the Aricota rockslide dam. A previous study shows that two failure events occurred at the Aricota site, a rockslide dam of $\sim 2 \text{ km}^3$ at ca. 18 ka and then a secondary rock-avalanche of $\sim 0.2 \text{ km}^3$ at ca. 12 ka, the timing of which suggests a correlation with humid episodes in the high central Andes. Our aim here was to date several other large landslides, located near and around the Aricota rockslide, to explore their possible correlation in time. We selected 8 paleo-landslides, including paleo-rockslide’s dams and rock-avalanches, distributed all along the Locumba river and its neighboring valleys: the Huanara and the Ilabaya rivers. On each site, we conducted a detailed mapping of the landslide’s morphologies using a high-resolution DEM (TanDEM-X and Pléiades), Google Earth images, and fieldworks to define a geological and geomorphological model of the landslides and to identify, when this applies, their successive internal failure events. Then, based on those frameworks, we used cosmogenic nuclide exposure dating to constrain their timing of failure, sampling 52 boulders in total. We used alternatively $^{10}\text{Be}/\text{quartz}$ or $^{10}\text{Be}/\text{feldspar}$ depending on the lithology available.

For half of the landslides, the exposure ages that we obtained show a strong scattering, including very old apparent ages up to ~1 Ma, which does not allow to determine the precise date of their triggering. For those cases, probable time ranges of landslide occurrence could be proposed only. We discuss and attribute this age-scattering mainly due to the inheritance problem. Indeed, inheritance is expected to be very strong in these arid regions where most of the slopes are slowly eroding, likely at steady-state equilibrium, and thus with a very high cosmogenic nuclide concentration at surface and at shallow depth (first 20 m). Nevertheless, we obtained good constraints for four of the landslides. All occurred during the Pleistocene with mean ages of ca. 16 ka, 18 ka, 114 ka, and 205 ka. So far, despite the spatial clustering of those landslides, their chronological constraints suggest that their triggering was related to various events, that spread through time. When comparing this to the previous dating in the region and other climatic proxies, the time ranges of 16-18 ka and 100-120 ka correspond to two well-defined humid periods, known as the Henrich stadial 1a and the Ouki event (during MIS5), respectively. These results suggest that past climate changes corresponding to the shift from hyper-arid to prolonged wetter conditions played a primary role in large landslide activity.

Keywords: Central Western Andes, Peru, Large paleo-landslides, Locumba cluster, Cosmogenic nuclides dating, Triggering factors.

1. Introduction

Landslides are gravitational phenomena that can be observed worldwide in various environments, from areas with strong topographic gradients such as orogenic and/or volcanic zones to oceanic slopes. In the continental domain they constitute one of the most important hazards generating loss of human lives and infrastructure (Petley, 2012; Froude and Petley, 2018; Wallemacq and House, 2018). On a longer time scale, large landslides are recognized as an efficient mechanism of regional-scale relief erosion in orogenic zones (e.g. Korup et al., 2007). The rate of landsliding is thought to reflect the long-term trend of tectonic uplift, with mass movements continuously affecting steep slopes along the flanks of incised river valleys (e.g. Larsen and Montgomery, 2012). Thus, landslides are the primary agent of material transport from hillslopes to rivers, limiting the relief construction in mountain ranges (Whipple et al., 1999; Montgomery, 2001; Roering, 2012).

During the last decades, studies of landslides on long-time scales (eg., hundreds to thousands of years), through the use of various dating approaches, have increased in different mountain ranges around the world (e.g., Dortch et al., 2009; Hermanns et al., 2013; Zerathe et al., 2014; Pánek, T., 2015; Schwartz et al., 2017) with the purpose of investigating potential relations between landslides activity and past climate oscillations or with long-term seismotectonic forcing. For instance, those results documented possible correlations between paleo-earthquake and landslide (e.g. Lebourg et al., 2014; Oswald et al., 2021), between last glacier retreats, permafrost melting, and slope debuttressing although with possible time-lags (e.g. Bigot-Cormier et al., 2005; Sanchez et al., 2010; Cossart et al., 2013; Lebrouc et al., 2014; Grämiger et al., 2017), and also between enhanced landslide activity and humid periods (e.g. Zerathe et al., 2014; Pánek, 2019). Nevertheless, as shown by a recent review from Pánek et al. (2017) and Pánek (2019), most of those landslide dating is restricted to the Holocene, very rarely to the Late Pleistocene. Our ability to document older landslide sequences is strongly hampered by the fact that landslide morphologies older than the last maximum glacial advance were not

preserved in the high mountains because of glacial and then fluvial erosion. Thus, up to now, very little is known about the effect of Quaternary climate oscillations on landsliding rates.

The Central Western Andes shows an interesting potential to study landslide chronicles on such long and undocumented time scales. Indeed, the Western flank of the Central Andes presents a high concentration of giant paleo-landslides (Figure. 1; Crosta et al., 2014; Delgado et al., 2022), and these large instabilities show exceptionally good states of preservation due to the low erosion and weathering related to the hyper-arid climate of the Atacama Desert since the Miocene (Dunai et al., 2005). As such, pioneered studies in this region were able to document landslide ages up to hundred thousand years (e.g. Margirier et al., 2015; Thouret et al., 2017; Crosta et al., 2017) or more (e.g. Pinto et al., 2008; Zerathe et al., 2017). However, first-order questions regarding the triggering of these large landslides remain pending. In particular, the respective roles of the strong and frequent seismicity along the Andean plate margin (either from subduction or crustal faults), as well as the effect of variations in precipitation patterns associated with past climate change, are debated.

Based on a landslide inventory elaborated in South Peru and North Chile, Delgado et al. (2022) documented about a thousand large landslides along the western flank of the central Andes. They made the correlation between favorable conditioning factors for the slope failures including lithology and strong local relief related to the incision of deep canyons. They also highlight spatial clustering of landslides, with several clusters grouping dozens of large landslides over radiuses of a few kilometers (Figure 1). Since most of these landslides remain undated, the main questions to be addressed now concern the temporal evolution setting of these landslide clusters. Do these clusters form during a single and strong triggering event, as in the case of a major earthquake (e.g. Valagussa et al., 2019; Junquera-Torrado et al., 2021)? Or do these clusters correspond to the accumulation of several slope failures spread over a long period of time interrupted by periods of quiescence?

In this study, we focus on one of these clusters, the Locumba cluster (Figure 1 and Figure 2) located in southern Peru. At the center of this cluster, the large Aricota rockslide was previously dated revealing two major slope failures, at about 18 ka and 12 ka (Delgado et al., 2020), possibly synchronous with wetter climate phases in the high central Andes (Martin et al., 2018). Our aim here was to constrain the ages of more landslides of the Locumba cluster around the Aricota rockslide, to explore their possible correlation in time. From perspective, we selected 8 paleo-landslides, including paleo-rockslide's dams and rock-avalanches, distributed all along the Locumba river and its neighboring valleys, the Huanara, and the Ilabaya rivers. Our detailed objectives were: (1) to perform a detailed mapping of those landslides and their internal events; (2) to constrain their age; (3) to look for patterns of occurrence and/or periodicity; (4) to explore the question of climatic or seismic triggering under the light of those new chronological constraints.

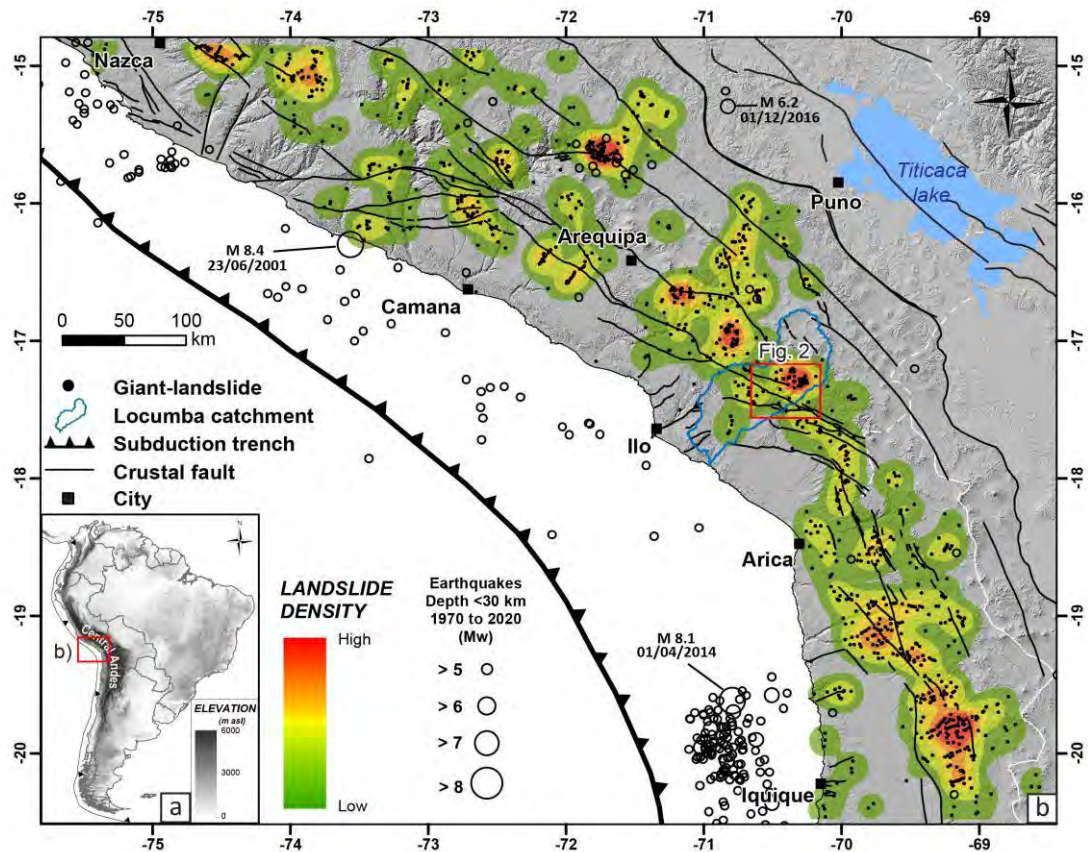


Figure 1. a) Location of the study area in the Central Andes. b) Density of large landslides along the Western flank of the Central Andes compared with the seismic catalog of the last 50 years by USGS (earthquakes > 5 Mw and depth < 30 km) and the main active crustal faults (from Delgado et al., 2022). The study area, located in the central part of the Locumba catchment (blue outline) is indicated by a red box.

2. Settings

2.1. Geological context

The orogenic zone of the Andes is located on an active tectonic margin, where the Nazca plate subducts below the South American plate with a convergence rate of $\sim 62 \text{ mm}\cdot\text{yr}^{-1}$ (Villegas-Lanza et al., 2016) producing long-term crustal thickening and uplift of the Andes range. The western flank is carved by deep valleys and canyons related to regional uplift (Thouret et al., 2007; Schildgen et al., 2009; Gunnell et al., 2010), it is also affected by important fault system oriented parallel to the subduction trench (Hall et al., 2012; Benavente et al., 2017, 2021). The study area is located on the Western Flank of the Central Andes, in the central part of the Locumba catchment at $\sim 17.5^\circ \text{ S}$ latitude (Figure 1).

In the study area, the lithology corresponds to a thick sequence of Mesozoic to Cenozoic volcano-sedimentary rocks (Figure 2). The Mesozoic sedimentation was controlled by the tectonic opening of the Arequipa-Tarapacá sedimentary basin (Vicente, 1982; Armijo et al., 2015). This tectonic context allows the sedimentation of thick series of limestones (mudstone to grainstone) and marls of the Pelado and Socosani formations (Wilson and García, 1962; Monge and Cervantes, 2000) along the entire Western Flank of the Andes. This formation is conformably covered by the Yura Group and the Hualhuani Formation (Wilson and García, 1962;

Vicente, 1982) composed of quartz sandstones and interstratified black shales; small outcrops are observed in south part of the study area. The top of the Mesozoic series is affected by an erosional unconformity, overlain by volcanic and volcano-sedimentary rocks of the Toquepala Group (Bellido and Guevara, 1963; Bellón and Lefèvre 1976), which outcrop in the central part.

The distribution of the Cenozoic lithostratigraphic units is divided into Paleogene, Neogene rocks, and Quaternary deposits. These rocks are related to the migration of the active Andean volcanic arc controlled by the variation of the dip of the Nazca subducting slab (Mamani et al., 2008). The migration of the volcanic arc controls the location of forearc, back-arc, and intra-arc basins. In the Coastal Depression, deposits of sedimentary sequences accumulated, mainly of marine origin, and the erosion of the proto-Andean under construction, which generated the almost synchronous creation of the Moquegua basin. These interstratified sequences of conglomerates with volcanic sequences are called the Moquegua Group (Thouret et al., 2007; Schildgen et al., 2007). These Oligocene to the late Miocene sequences, up to 800 m thick (Bellido, 1979), are the result of erosion of the Western Cordillera. From the Eocene onwards, constant volcanic events began and continue to the present day. The Huaylillas formation (Wilson and García 1962), constitutes a wide ~600 m thick ignimbrites succession (Wilson and García, 1962; Salinas, 1985). It is a stratigraphic superposition of pyroclastic flows (Wörner et al., 2000; Mamani et al., 2010). This formation is well preserved due to hyper-arid conditions and its upper surface represents a regional paleosurface. The only forms of erosion are valley incision produced by rivers descending from the Altiplano (Evenstar et al., 2017). This sector is also dominated by a large volume of andesites and rhyolites associated with ignimbrites assigned to the Barroso Group (Roperch et al., 2006; Mamani et al., 2010; Acosta et al., 2011), related to the magmatic activity of the Barroso Arc (Mamani et al., 2012). The rocks from the Quaternary correspond to the large volume of lava flows produced during the Pleistocene in relation with the active volcanoes (e.g., Yucamane; Rivera et al., 2020). These volcanic rocks are associated with fluvial and alluvial deposits in the main valley and glacial deposits in the higher areas such as the headwaters of the Locumba catchment. These deposits cover a large part of the basement and can reach a few meters thick in response to recent climatic fluctuations (Keefer et al., 2003, Engel et al., 2014; Bookhagen and Strecker, 2008). Regarding the landslides of the Locumba cluster, these have their starting zone or headscarp in the Huaylillas ignimbrites (Delgado et al., 2022). This suggests that the lithology is an important factor in the formation of these large events, however, the age of occurrence of these processes is still unknown.

In the study area, the structural framework is marked by the presence of major fault systems where the neotectonic fault activities have been described mainly along the Incapuquio and the Purgatorio fault system (Figure 2; Hall et al., 2012; Benavente et al., 2017; 2021). The Incapuquio fault system is a ~400 km long subvertical lineament with a NW-trending direction and hosts left-lateral transpressional displacement. Recent study by Benavente et al, (2021) evidences a last reactivation during the XV century that generated an earthquake of magnitude >7. The Purgatorio fault hosts a right-lateral transpressional displacement that has produced at least two ruptures during the last few thousand years with surface displacements of several meters (Benavente et al., 2017).

More than 30 large landslides of the Locumba cluster occur close to these faults. Thus, it is not excluded that the probable trigger of these landslides is due to the reactivation of one of these faults. To define the probable triggering factor, it is necessary to date the landslides and correlate them with climatic or tectonic events.

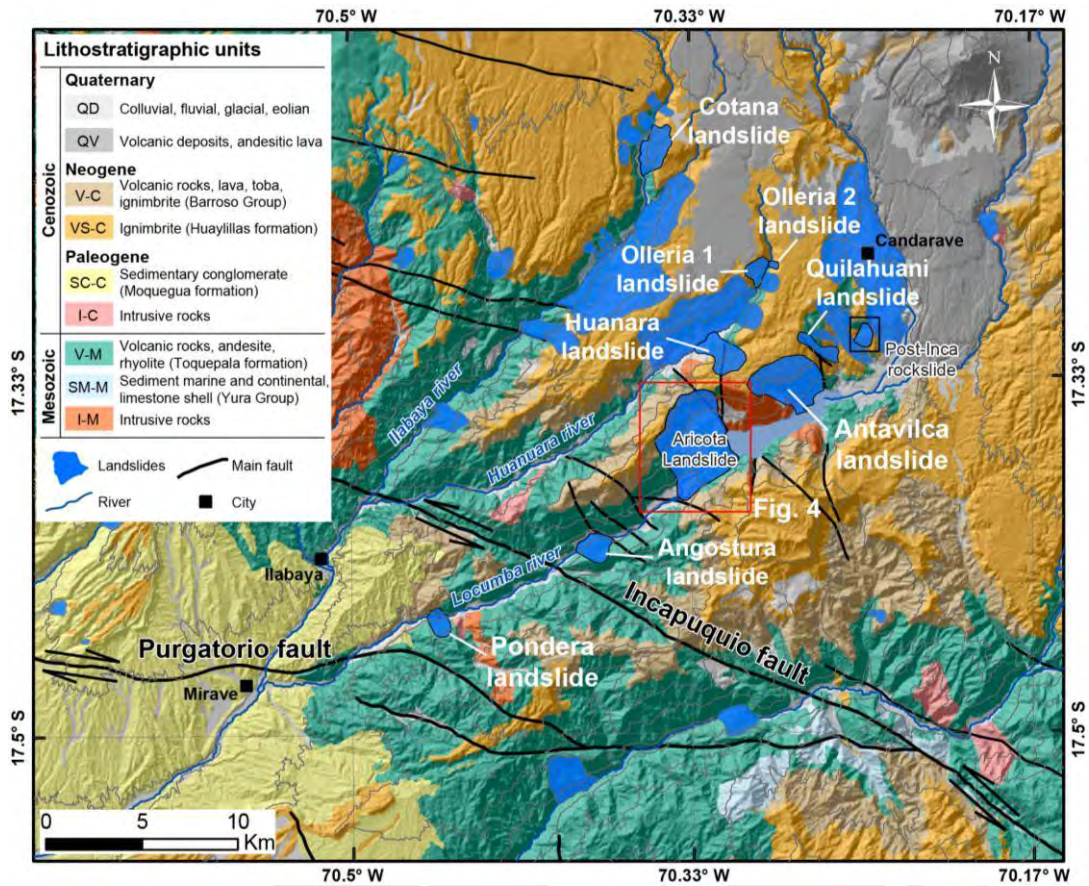


Figure 2. Lithostratigraphic map of the study area, where the Locumba cluster is located, with more than 30 landslides inventoried (Delgado et al., 2022). Eight landslides (Pondera, Angostura, Antavilca, Quilahuani, Huanara, Olleria 1, Olleria 2 and Cotana) were chosen for study. The red box marks the Aricota landslide (Delgado et al., 2020) and the other Black box shows the post-Inca rockslide.

2.2. Geomorphology and landslides of the Locumba region

The highest point of the Locumba catchment is at 5700 m asl. and the lowest point is at the confluence of the Locumba river and the Pacific Ocean. The main river is the Locumba river. The catchment is characterized by deep valleys with steep slopes due to the incision caused by the Locumba river that transports the water coming from the precipitation in the Altiplano. Several giant landslides were identified in this catchment (Delgado et al., 2022). Knickpoints observed on the swath profile of the Locumba river (Figure 3A, 3B; Mathieux, B. 2021) correspond to the location of landslides mapped by Delgado et al. (2022) (Figure 3B). In addition, landslides identified by Delgado et al. (2022) coincide also with areas of higher incisions (Figure 3c).

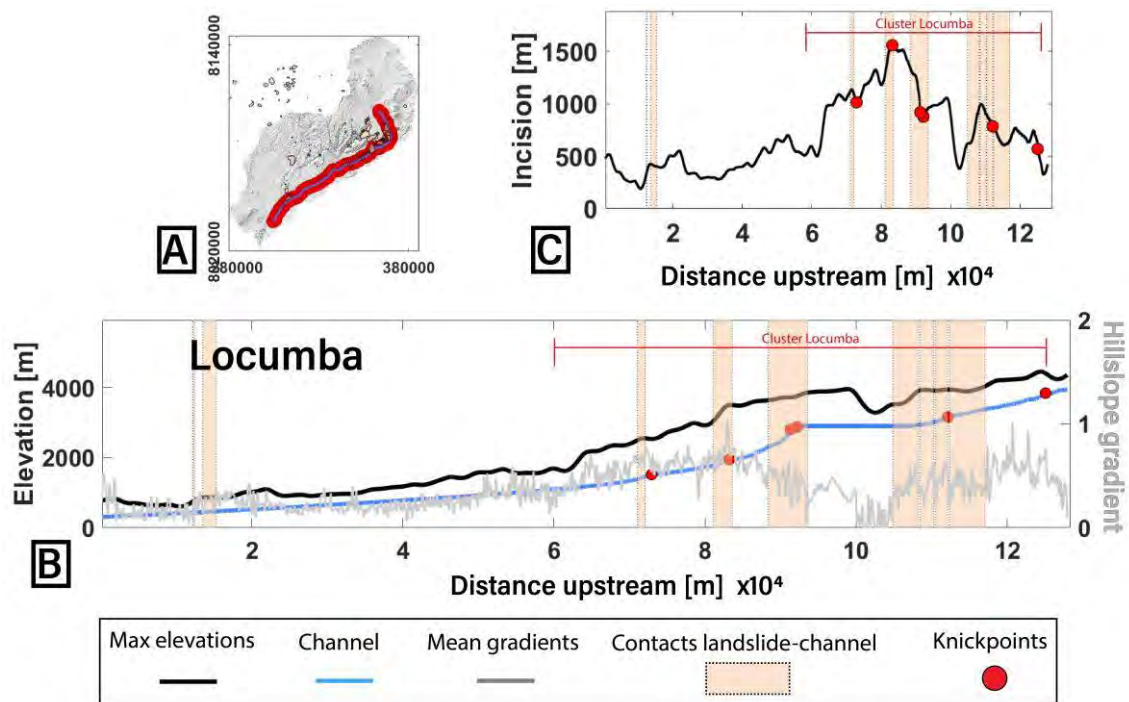


Figure 3. (A) Locumba catchment, the red stripe is the swath profile box. (B) Swath profile of the Locumba river, showing the correlation between knickpoints and landslides. (C) Relationship between landslide location and valley incision. (modified from Mathieux, B. 2021)

Delgado et al., (2020) conducted a geochronological study of the Aricota rockslide (part of the Locumba cluster) by cosmogenic ^{10}Be dating (Figure 2, Figure 4). This landslide mobilized $\sim 2.2 \text{ km}^3$, formed a large dam that blocked the Locumba river valley, and gave rise to the Aricota lake. The landslide occurred in two major events of destabilization (Figure 4), the first was a rockslide ($17.9 \pm 0.7 \text{ ka}$) that dammed the Locumba river valley and formed a dam, and the second event was a rock avalanche ($12.1 \pm 0.2 \text{ ka}$) that was deposited on top of the first event. Based on the obtained exposure ages, these events may be related to climatic changes associated with maximum expansions of Altiplano lakes during the Heinrich Stadial 1a and Younger Dryas, respectively (Placzek et al., 2013; Martin et al., 2018). The Aricota rockslide is a first advance to define/recognize the age of deformation and the triggering factor in the Locumba cluster. Still, a larger area must be analyzed, and more landslides must be studied to identify patterns in the age of formation, the triggering factor and whether these landslides occur simultaneously. The study of landslide clustering based on a detailed study of the Locumba cluster will help to answer these main questions. For that, eight landslides were chosen that show the following characteristics: 1) the origin of the landslides is located in similar lithologies, and 2) the main escarpment is located between 2000 and $\sim 4000 \text{ m asl}$. All selected landslides are distributed along the Locumba, Huanuara, and Ilabaya rivers. This division will help to identify if there are any patterns of their formation in each valley.



Figure 4. 3D Google Earth view of the Aricota rockslide (modified from Delgado et al., 2020). It is observed that the first event (17.9 ± 0.7 ka) filled the valley and formed a big dam and the second event (12.1 ± 0.2 ka) was deposited on top of the first event.

3. Methodology

3.1. Mapping of landslides

Detailed mapping of the selected landslides (headscarps, sliding-mass, and debris deposits boundary, etc.) in the Locumba watershed is based on geomorphological and structural observations (headscarps and tension cracks) from high-resolution Digital Elevation Model (DEM) analysis, Google Earth images and fieldwork. This geomorphological characterization is essential in the case of landslides presenting multiple events of mass mobilization because it facilitates the interpretation of cosmogenic ages in terms of destabilization dynamics. In order to have a high-resolution DEM of the Locumba cluster, eleven stereoscopic images covering the study area were obtained. These images were acquired by the Pléiades satellites in June 2020. The full resolution of these optical images is 0.7 m. We generated the DEM using the open-source Ames Stereo Pipeline (ASP) software developed by NASA (Broxton and Edwards, 2008) and followed the recommended three-step procedure: i) each image was projected onto the map using the low-resolution (30 m) SRTM DEM, ii) the two images were adjusted based on the automatically extracted tie points before finding disparities, iii) finding the intersection of all the rays coming from the homologous points of the image pair. This step leads to a point cloud of the surface topography, which is then converted to a 2 m resolution grid.

Fieldwork was conducted in 2019, in order to (1) validate the Google Earth and DEM observations/interpretations previously made on each site, and (2) sample boulders for cosmogenic nuclides dating.

3.2. Cosmogenic nuclide surface exposure dating

To determine the ages of the eight landslides selected in the Locumba cluster, a sampling strategy was designed according to the detailed geomorphological mapping of each landslide. When sampling, special attention was paid to selected reliable boulders, having heights and lengths both larger than ~2 m and, as far as possible, with traces of post-depositional movements, weathering, or desquamation. Elevation, latitude, and longitude data were recorded with a handheld GPS. In total, 52 samples were collected and processed (Table 1), with at least three samples collected per landslide.

Sample preparation and ^{10}Be chemical extraction were performed at the GTC Platform laboratory, ISTERre (Grenoble, France), following the ^{10}Be /quartz (Corbett et al., 2016) and ^{10}Be /feldspar (Zerathe et al., 2017) procedures depending on the mineralogical composition of the sample. The $^{10}\text{Be}/^9\text{Be}$ measurements were performed at the French national accelerator ASTER, located at CEREGE in Aix-en-Provence (Arnold et al., 2013). The $^{10}\text{Be}/^9\text{Be}$ ratios were calibrated against the internal standard STD-11, using an assigned $^{10}\text{Be}/^9\text{Be}$ ratio of $(1.191 \pm 0.013) \times 10^{-11}$ (Braucher et al., 2015). Uncertainties in the ^{10}Be concentrations (reported as 1σ) are calculated according to the standard error propagation method using the quadratic sum of the relative errors and include a conservative 0.5 % external uncertainty in the machine (Arnold et al., 2010), a 1.08% uncertainty in the certified standard ratio, a 1σ uncertainty associated with the mean of the standard ratio measurements over measurement cycles, a 1σ statistical error in the counted events, and the uncertainty associated with the chemical and analytical correction of the blank.

Exposure ages were calculated using the CREP online calculator developed by Martin et al. (2017). For the quartz targets, we applied a globally calibrated ^{10}Be spallation production rate of $4.09 \pm 0.35 \text{ at.gr}^{-1}.\text{yr}^{-1}$ (sea level and high latitude; Borchers et al., 2016) that was scaled to the geographic and altitudinal location of each sampling site using the LSD scaling scheme (SF; Lifton et al., 2014). For feldspar targets, we applied a calibrated ^{10}Be spallation production rate of $3.57 \pm 0.21 \text{ at.gr}^{-1}.\text{yr}^{-1}$ (Zerathe et al., 2017).

The CREP program assumes that denudation is constant over exposure time (Martin et al., 2017), but for this site, we used a denudation rate of $2 \times 10^{-5} \text{ cm.yr}^{-1}$ (Delgado et al., 2020). Analytical age uncertainties (i.e., internal) include uncertainties on the measured ^{10}Be concentrations. Total age uncertainties (i.e., external) include the production rate uncertainty. All data are presented in Table 1.

4. Results and interpretations

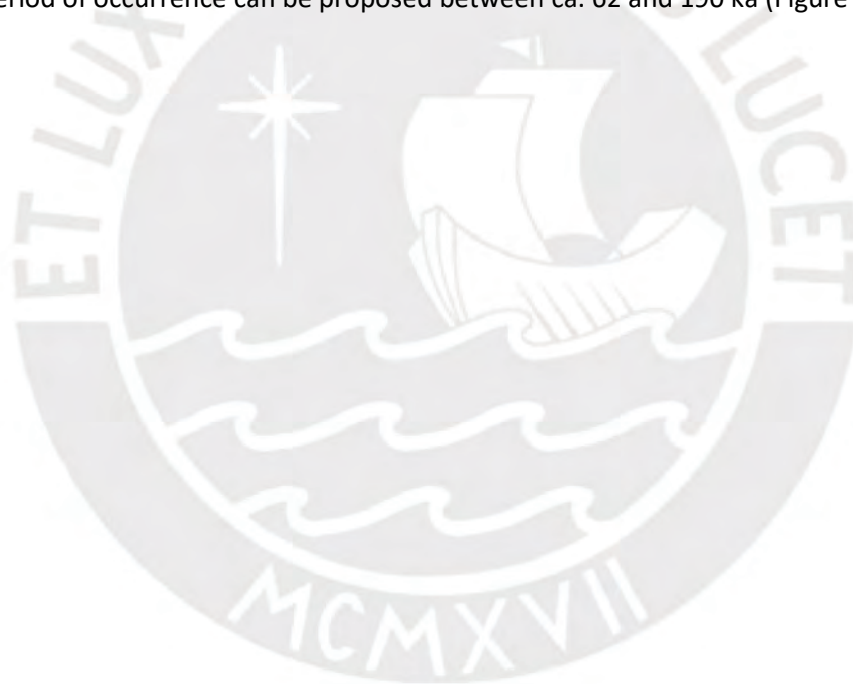
4.1. Locumba river

4.1.1. Pondera landslide

The Pondera landslide is a rockslide with headscarp located on the left flank of the Locumba River (Figure 5a) at 17.45° S latitude, at an elevation of $>2220 \text{ m asl}$. It has an escarpment of ~1 km wide. The headscarp developed in Mesozoic volcanic rocks (Figure 2, Figure 5b). According to our geomorphological analysis, only one event occurred, that filled the valley forming a dam ~200 m high and ~0.9 km long to the north. The dam has been re-incised and largely eroded by the Locumba river (Figure 5a, 5b, Figure 6a). Only relicts of the deposit remain visible on both

flanks of the valley (Figure 5a). The profile of the eroded dam shows very large rock blocks (Figure 5a, Figure 6a). These dam blocks correspond to andesites which is the lithology observed on the valley flanks in this part. Northeast of the dam, DEM highlights a flat surface that is at the same elevation as the dam (between 1580-1640 m asl; Figure 5a, Figure 6a). This surface corresponds to a tributary valley dammed by the rockslide and subsequently filled by lacustrine deposits (Figure 5a, Figure 6c). On the right flank of the Locumba River, ~2 km east of the landslide, other thick lacustrine deposits were mapped. These correspond to lacustrine deposits that were deposited in the Locumba river. These deposits show some folds and deformations that are interpreted as slumps (Figure 5a, Figure 6d). The top of these deposits stands at ~1700 m asl (Figure 5a, Figure 5b).

Three blocks (PO-01, PO-02, PO-03) were sampled on the top of the dam relic to determine their surface exposure ages (Figure 5a, Figure 7). They yielded exposure ages of 100 ± 6 Ka, 68 ± 6 ka, and 180 ± 10 ka (Table 1). Whereas a single age should be obtained as the geomorphology indicates only one failure event, the ages obtained are scattered, which does not permit to point to a weighted-mean age for this failure (Figure 7). Both strong differential erosion between the boulders, or variable amount of ^{10}Be inheritance, can explain this scattering. This will be discussed in the discussion part. Without any additional age on the Pondera rockslide, only a probable period of occurrence can be proposed between ca. 62 and 190 ka (Figure 7).



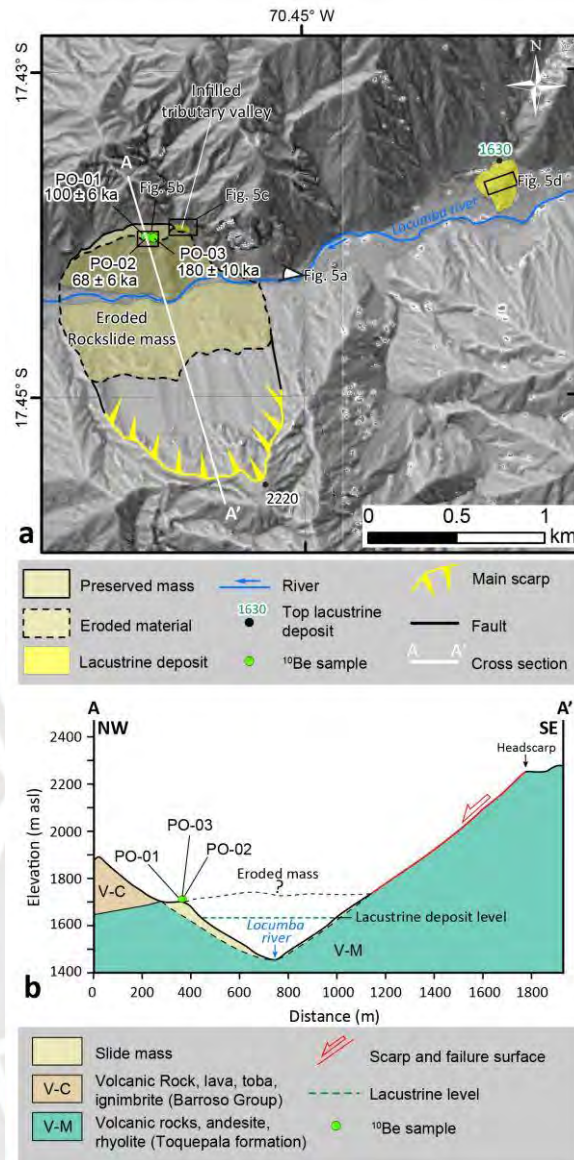


Figure 5. (a) Geomorphological map of the Pondera rockslide that filled the valley and formed a large dam. This is currently eroded. (b) Cross section of Pondera rockslide.

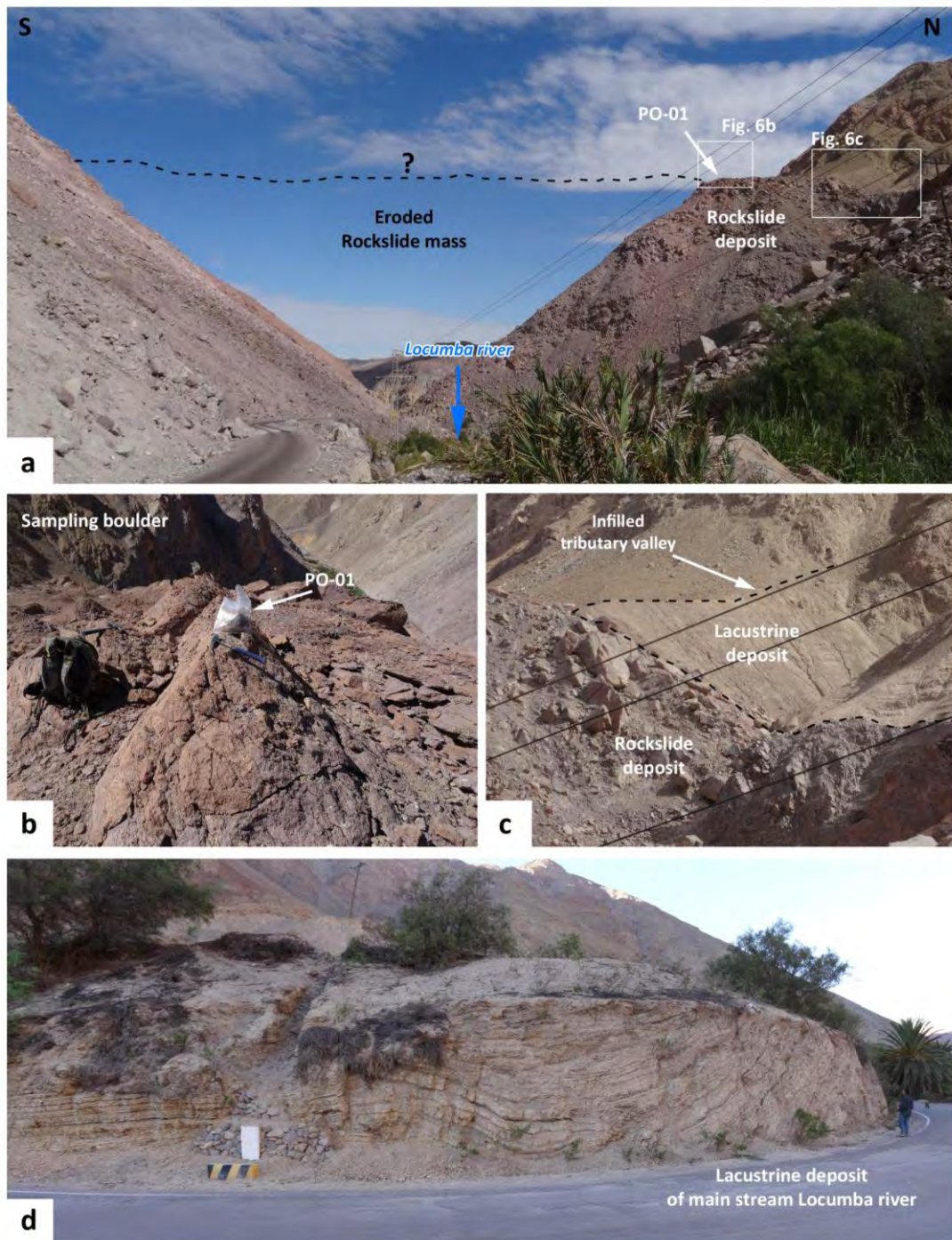


Figure 6. a) Panoramic view of the eroded dam of the Pondera rockslide. Note to the north, the perched lacustrine deposits that are outcropping along a tributary dammed by the rockslide deposit, (b) Samples collection for cosmogenic nuclide dating (^{10}Be), (c) Close up on the perched lacustrine deposits, (d) Thick lacustrine deposits located along the main stream, ~2 km upstream to the dam along the Locumba valley.

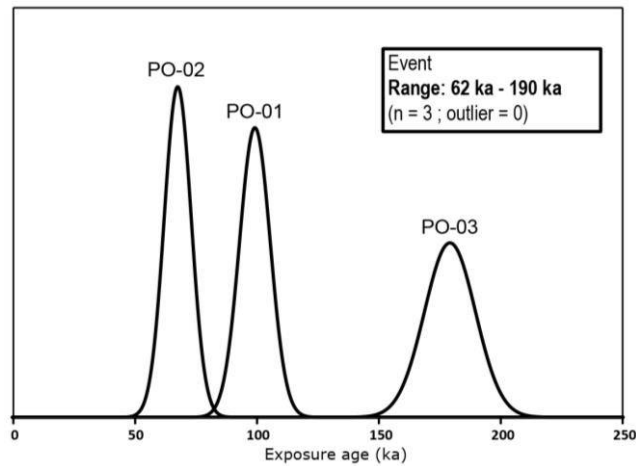


Figure 7. Probability density plot of the exposure ages obtained on boulders on top of the Pondera rockslide deposits.

4.1.2. Angostura landslide

The Angostura landslide is of a rockslide typology. It is located on the left flank of the Locumba River (Figure 8a) at 17.42° S latitude, at an elevation of ~2450 m asl (headscarp). It has an escarpment of ~1.5 km wide. The headscarp originates in Mesozoic volcanic rocks (Figure 2, 8b). Geomorphological mapping shows a single event that filled the Locumba valley forming a dam ~400 m high and ~2 km long to the north (opposite slope). Part of the dam is eroded and re-incised by the Locumba river activity (Figure 8a, Figure 9a). The incision profile in the dam shows that it is formed by blocks of Mesozoic volcanic rock corresponding to the rocks that outcrop on the stable slope of the valley (Figure 8b). On the right flank of the Locumba River, next to the dam and upstream (~ 2km), lacustrine and fluvial deposits are observed that correspond to the lake formed by the dam (Figure 8a, Figure 9b, 9d). The top of these deposits culminates at an altitude of ~2130 m asl (Figure 8a, 8b).

Seven boulders were sampled at the top of the Angostura slided mass (AA-01, AA-02, AA-03, AA-04, AA-05, AA-06, AA-07) (Figure 10). Four exposure ages (AA-02, AA-03, AA-04, AA-06) range from 178 ± 15 ka to 238 ± 17 ka (Table 1), which are compatible with a unique event (chi-2 test (95%): 7.07/7.81) and point to a weighted mean of 205 ± 9 ka (Figure 10). Three others exposure ages are significantly older: AR-01 (318 ± 39 Ka), AR-05 (330 ± 23 ka), and AR-07 (703 ± 51 ka). They are likely attributed to inheritance. See discussion hereafter.

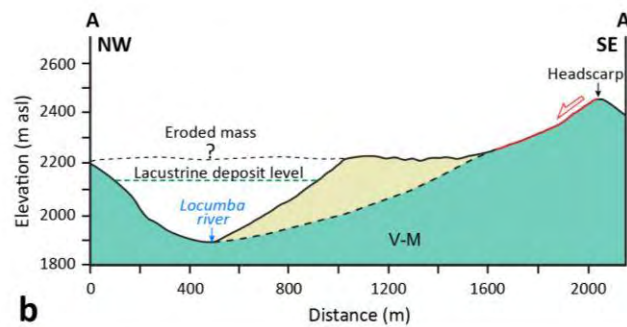
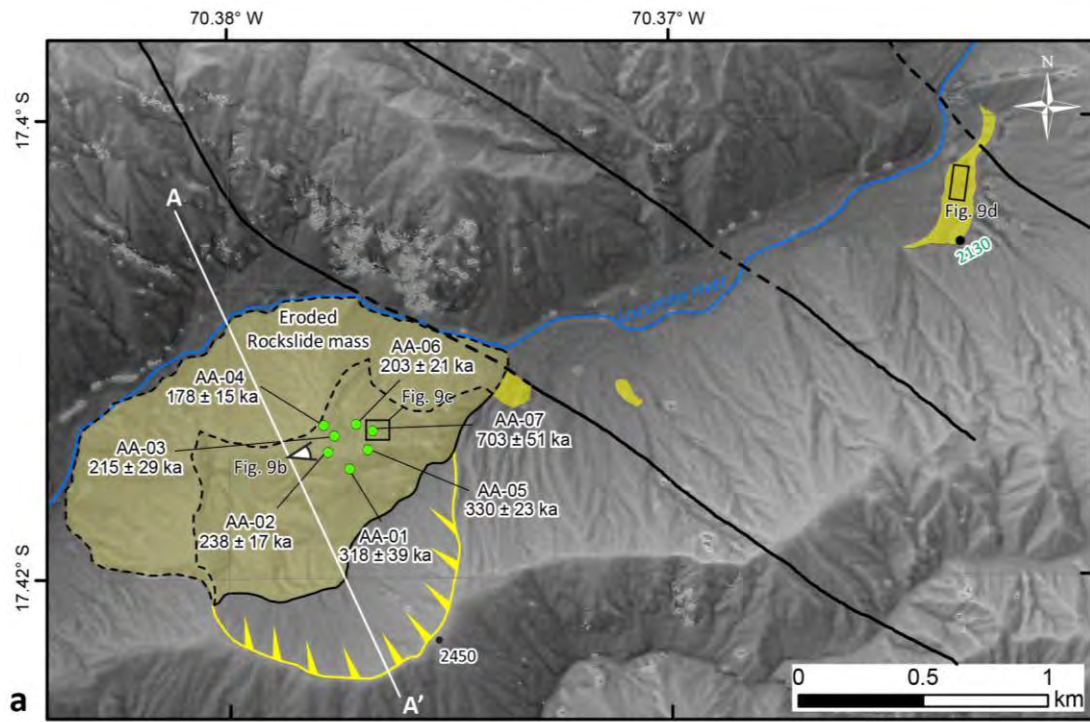


Figure 8. (a) Geomorphological map of the Angostura rockslide that filled the valley and formed a large dam. Part of this rockslide dam is currently eroded. (b) Cross section of the Angostura rockslide.

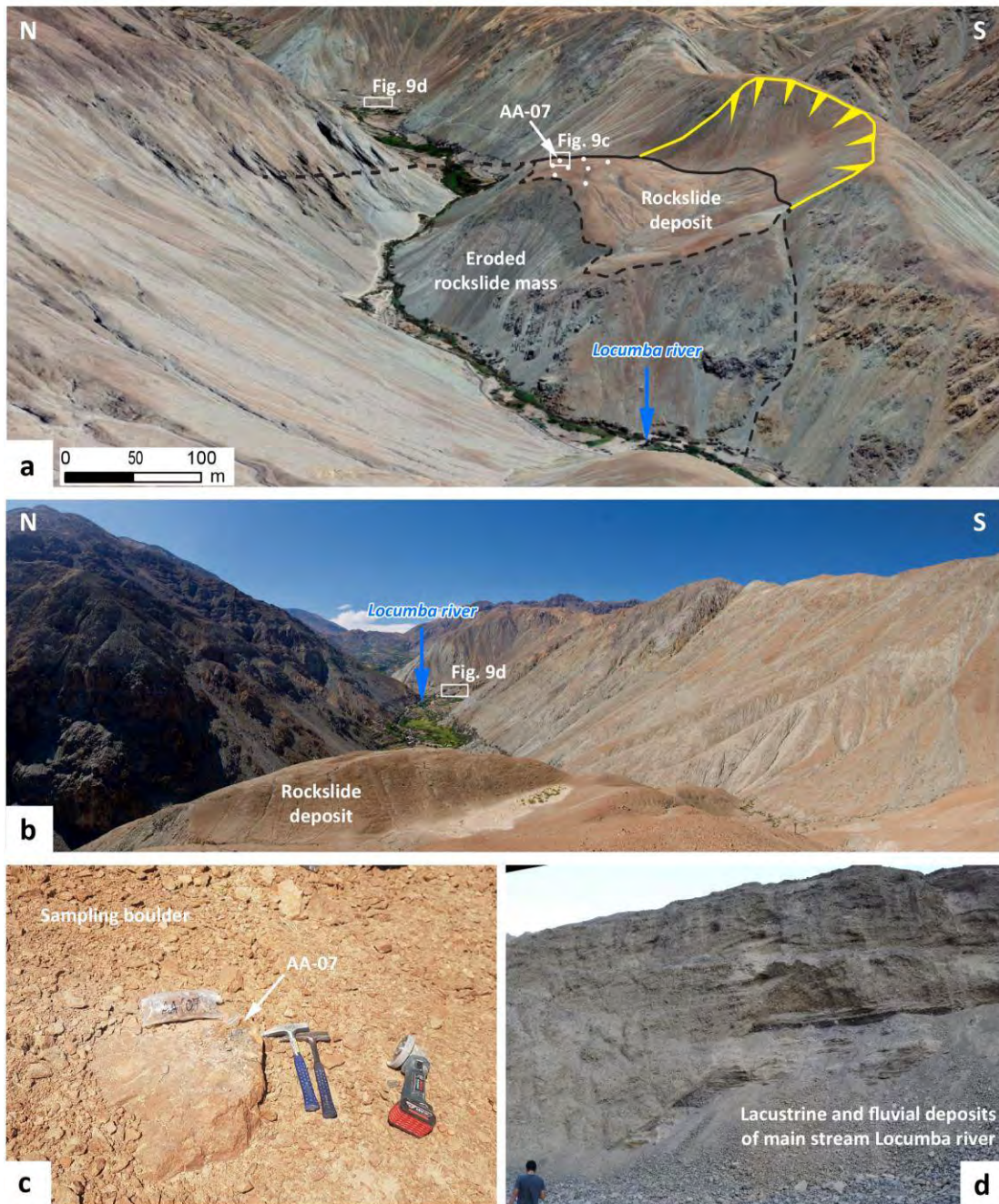


Figure 9. (a) Google Earth 3D image, showing the Angostura rockslide, the preserved deposit, and the eroded mass by the Locumba river, (b) Panoramic view to the northeast, upstream of the dam, location of lacustrine deposits ~2km away, (c) Samples collection for cosmogenic nuclide dating (^{10}Be), (d) Thick lacustrine and fluvial deposits located along the main stream, ~2km upstream to the dam along the Locumba valley.

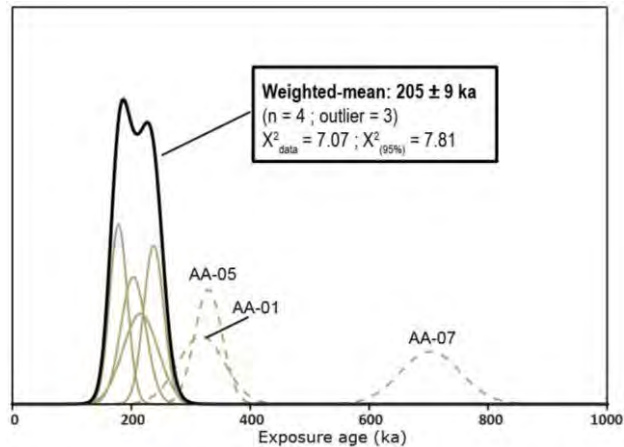


Figure 10. Probability density plot of the exposure-ages obtained on boulders on top of the Angostura rockslide deposit.

4.1.3. Antavilca landslide

The Antavilca landslide is located on the right flank of the Aricota lake (Figure 11a) at 17. 33° S latitude, at an altitude of ~3890 m asl. (headscarp), the base of this landslide is at 2750 m asl (Aricota lake level). A sequence of scarps in this landslide may indicate a progressive failure that took place over a prolonged period of time. In addition, numerous tension cracks above the main scarp and other cracks in the landslide mass are observed. These cracks indicate a movement of the landslide mass toward the south (Figure 11a, Figure 12a). All these characteristics suggest that it is a deep-seated gravitational slope deformation (DSGSD). On the southern side of this large DSGSD, some sliding mass converted into two rock-avalanches that reached the Aricota lake (Figure 11a, 11b, Figure 12a). The first event is an avalanche that mobilized a large part of the body of the Antavilca landslide (Figure 12a, 12b), the avalanche deposits reached the Aricota lake (travel length of >3km) (Figure 11b). The second event is an internal avalanche that mobilized part of the avalanche deposits of the first event (Figure 11a, 11b).

We focus on the second avalanche because it is the last event to occur. The avalanche surface has large boulders (boulders >2m, Figure 12c, 12d) that allow us to perform characteristic sampling and then determine the age of exposure using cosmogenic nuclides ¹⁰Be (Figure 12c, 12d). Six samples (AN-06, AN-07, AN-08, AN-09, AN-10, AN-11) were collected from boulders found on the avalanche surface (Figure 11a). Four exposure ages (AN-07, AN-08, AN-10, AN-11) range from 16 ± 1 ka to 17 ± 1 ka (Table 1). Samples AN-06 (19 ± 1 Ka) and AN-09 (6.1 ± 0.2 Ka) can be called outliers because these ages are outside the range. We suspect that sample AN-06 has an inheritance from the first event, while sample AN-09 may be a block displaced after the emplacement.

The ages obtained from four samples (AN-07, AN-08, AN-10, AN-11) of the rock avalanche deposit are tightly grouped (Figure 13), pointing to a weighted-mean age of 16.3 ± 0.3 ka (chi-2 test (95%): 3.44 / 7.81).

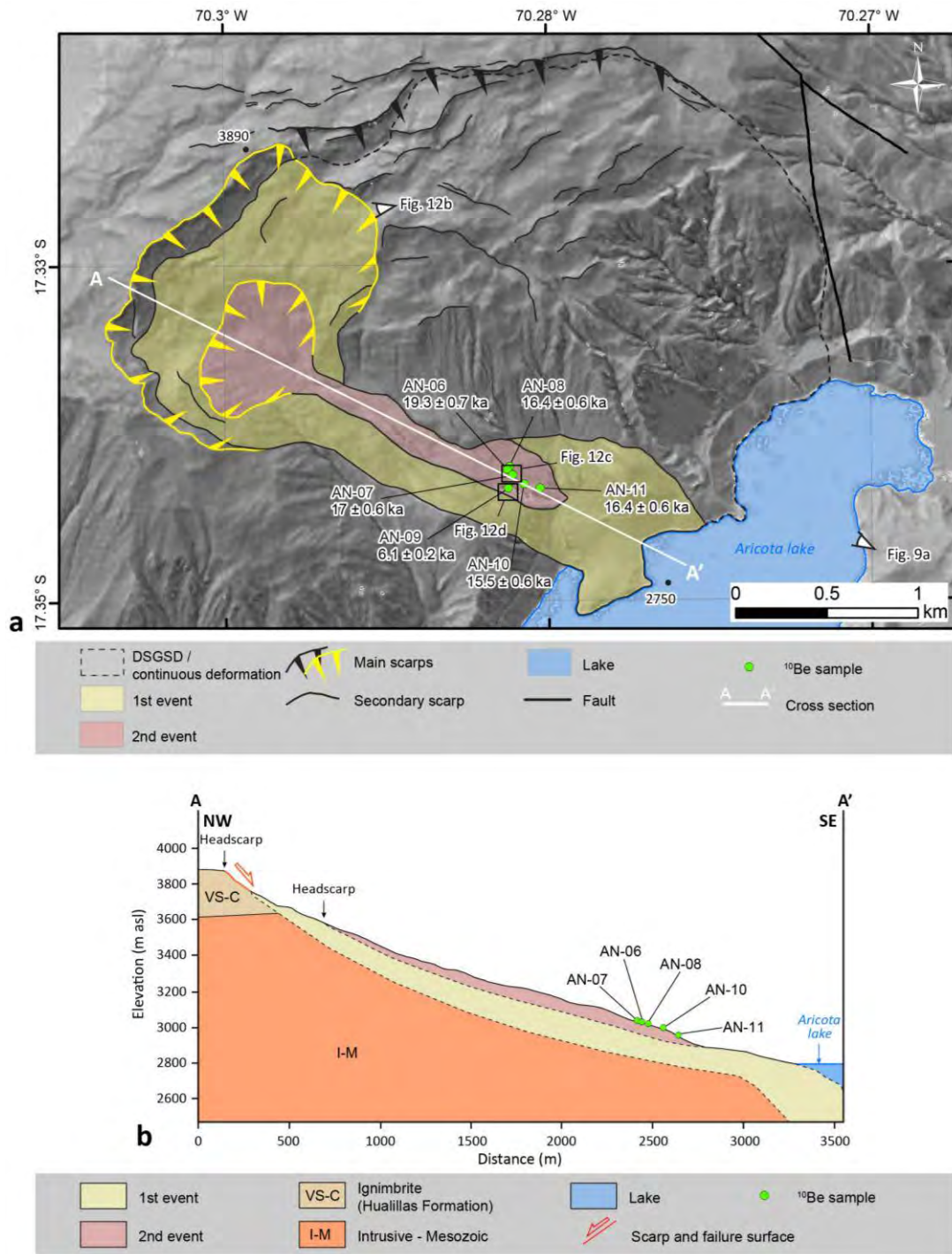


Figure 11. (a) Geomorphological map of the Antavilca landslide showing the typical morphology of DSGSD, as well as the two rock avalanches that have developed at the southern extremity of the landslide. (b) Cross section of the Antavilca landslide, showing the first and second rock-avalanche.

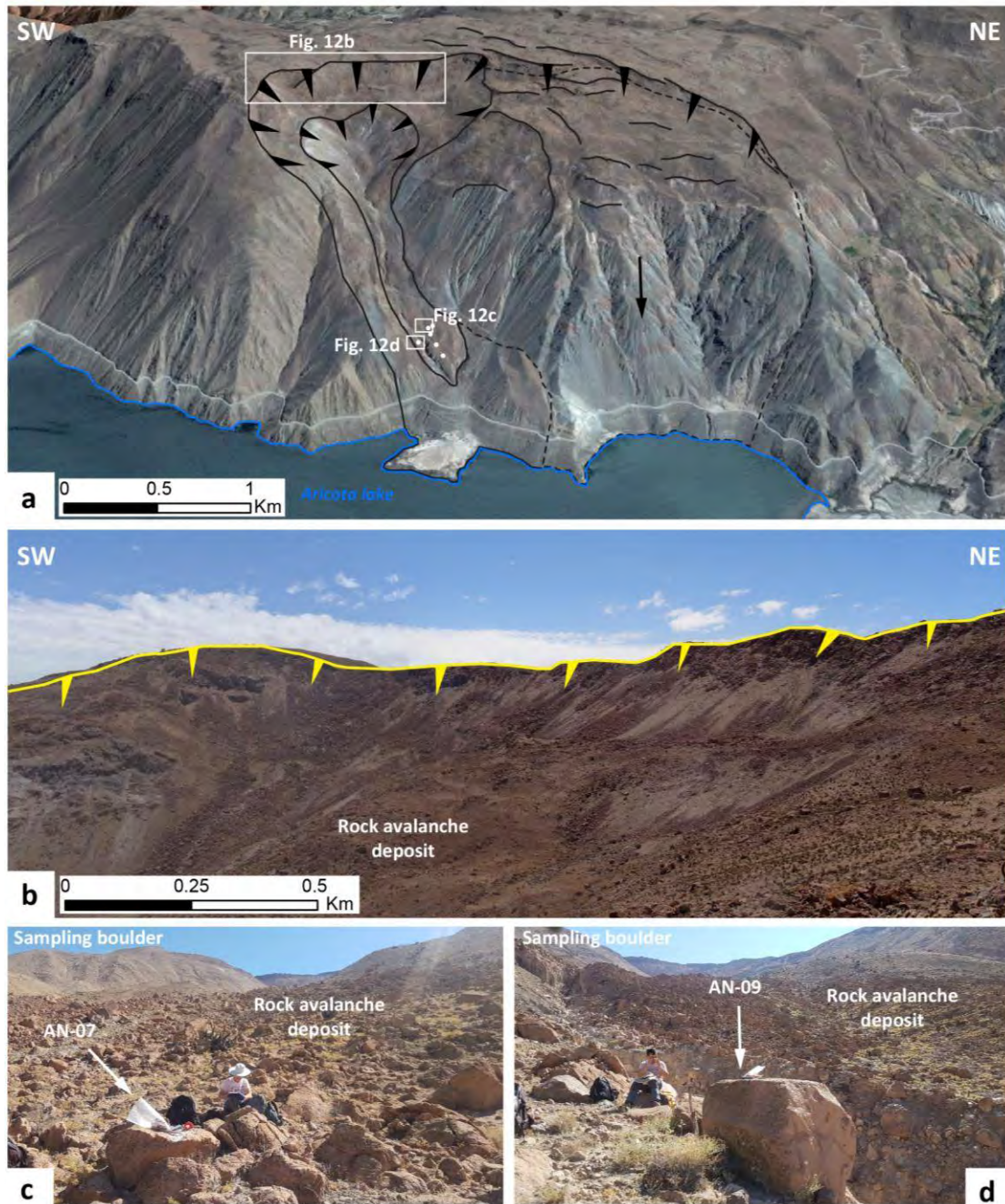


Figure 12. (a) Google Earth 3D image, showing the Antavilca landslide (DSGSD), and two rock avalanches located to the south of the landslide, (b) view of the headscarp of the first event and the deposit of the first avalanche. (c) and (d) Samples collection for cosmogenic nuclide dating (^{10}Be).

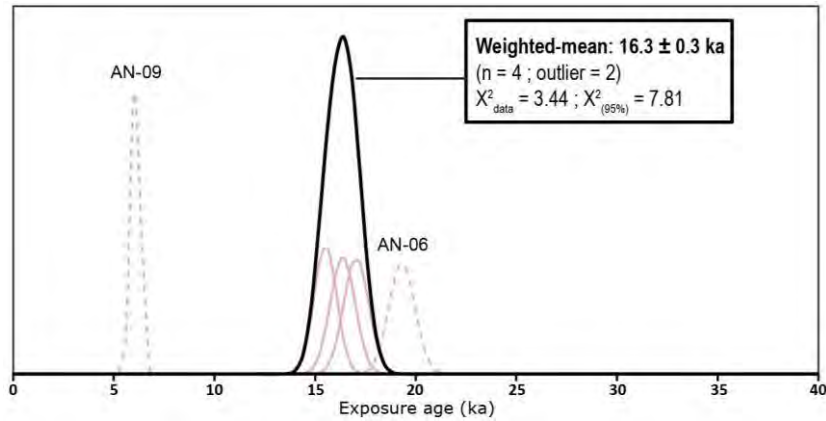


Figure 13: Probability density plot of the exposure ages obtained on boulders on top of the second rock avalanche deposit.

4.1.4. Quilahuani landslide

The Quilahuani landslide is a rock avalanche located on the right flank of the Quilahuani river (Figure 14a), i.e., a tributary of the Aricota lake, at 17.32° S latitude, at an altitude of 3870 m asl. (headscarp). It has an escarpment of ~0.5 km wide, and the toe of the avalanche deposits stands at ca. 3000 m asl. The headscarp developed within ignimbrites of the Huaylillas formation (Figure 2, figure 14b). There is an event with a length of ~2 km towards the southeast (Figure 14a), there are lateral and frontal levees that channel and limit the avalanche path (Figure 14a, figure 15b). The avalanche boulders correspond to the ignimbrites of the Huaylillas formation (Figure 14b, figure 15a). The deposit is currently eroded and re-incised at the foot of the avalanche (Figure 14a).

Ten boulders distributed all along the avalanche deposit were sampled to determine the timing of the failure (Figure 14a). Five exposure ages (QL-02, QL-04, QL-07, QL-09, QL-10) range from 109 ± 4 ka to 120 ± 4 ka (Table 1). Those ages show a single gaussian distribution (chi-2 test (95%): 5.72/9.49), pointing to a weighted-mean age of 114 ± 2 ka (Figure 16). Five other ages are more scattered, corresponding either to younger (QL-01A: 65 ± 2 Ka; QL-05: 70 ± 4 ka; QL-08: 60 ± 2 ka), or older ages (QL-03: 170 ± 4 ka; QL-06: 192 ± 5 ka). As only one main rock-avalanche event can be observed in the morphology, we favor the interpretation of a failure event at 114 ± 2 ka (Figure 16). Younger and older scattered ages are likely attributed to post-depositional erosion of the boulders and to inheritance, respectively.

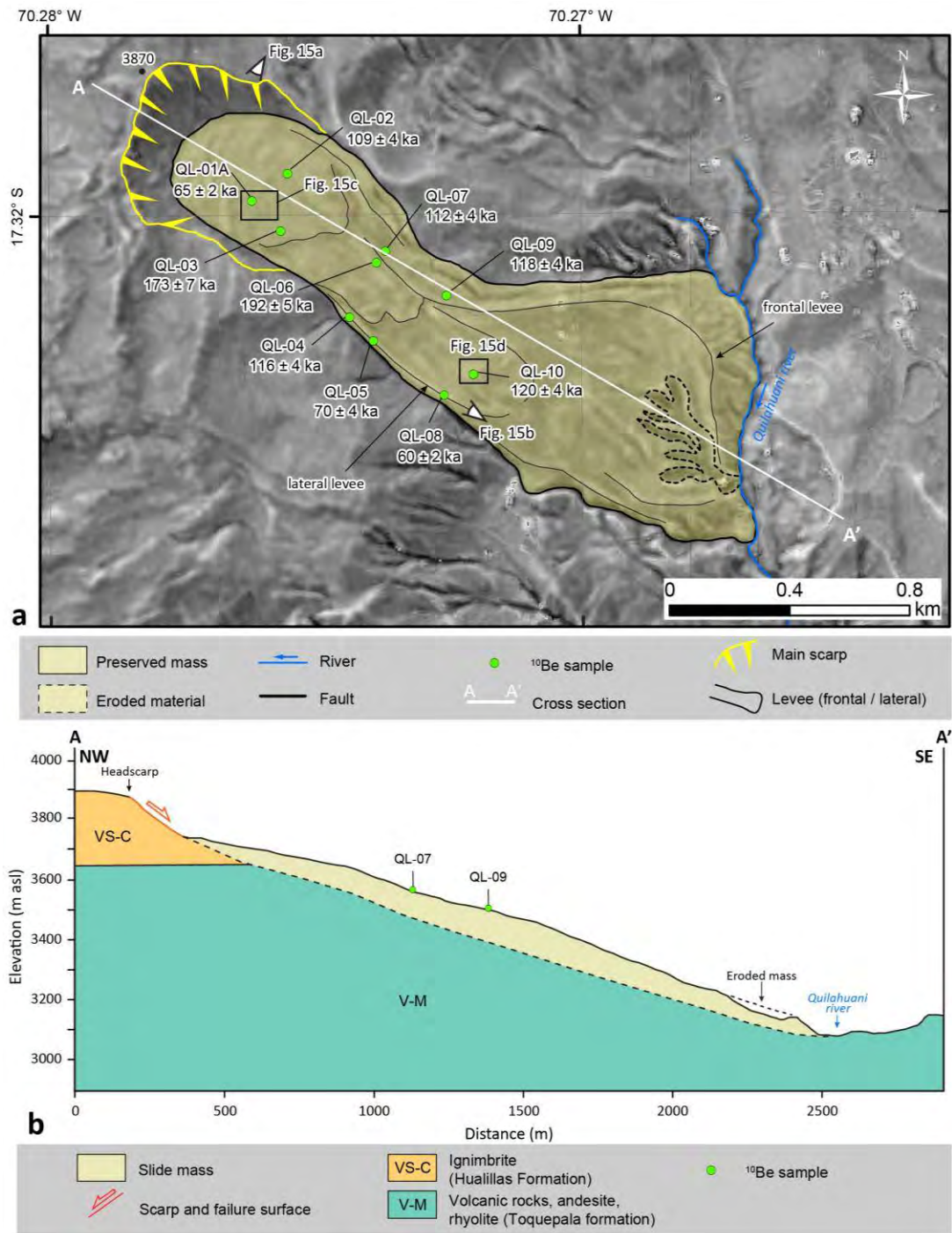


Figure 14. (a) Geomorphological map of the Quilahuani rock avalanche. We observed levees (frontal and lateral) and an erosional process at the foot of the avalanche. (b) Cross section of the Quilahuani rock avalanche.

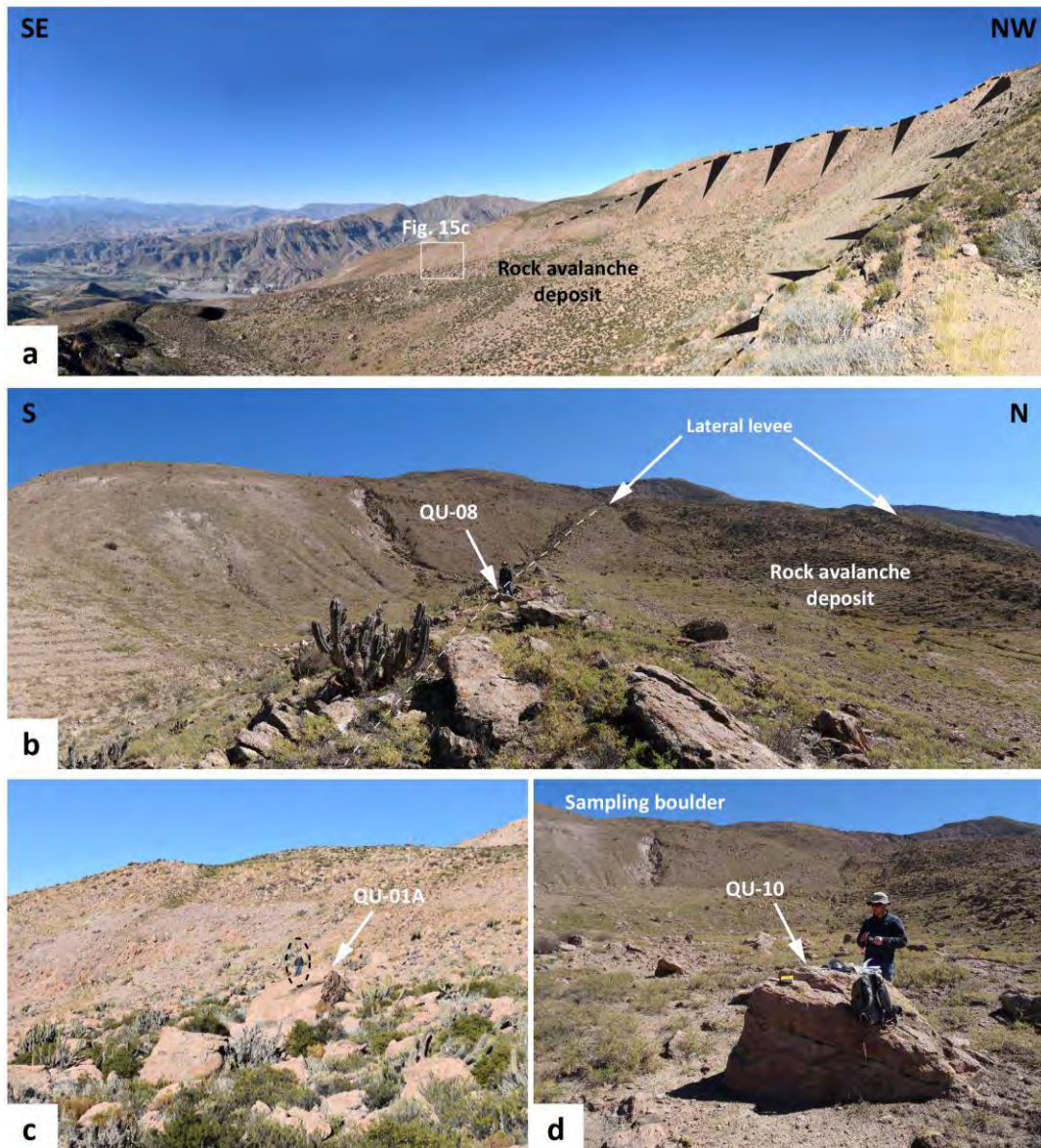


Figure 15. (a) Panoramic view of the Quilahuani rock avalanche main scarp and the avalanche deposit, (b) Lateral levees channeling the rock avalanche deposit, (c) Detail of the size of ignimbrite blocks, (d) Boulder sampled for cosmogenic nuclide dating (^{10}Be).

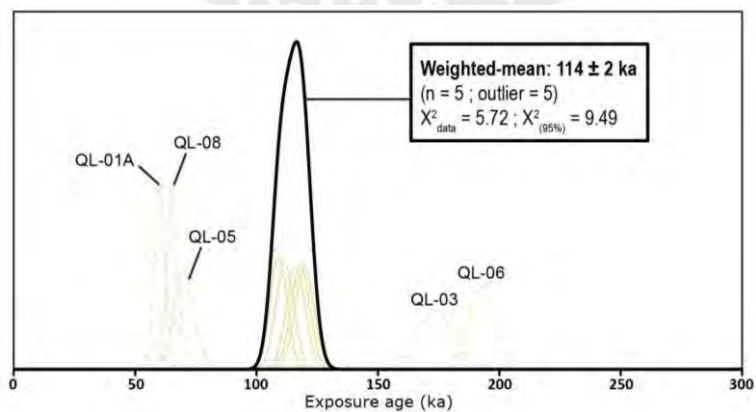


Figure 16. Probability density plot of the exposure ages obtained on boulders on top of the Quilahuani rock avalanche deposit.

4.2. Huanuara river

4.2.1. Huanara landslide

The Huanara landslide has a rock avalanche typology. It is located on the left flank of the Huanara River (Figure 17a) at 17.33° S latitude, at an elevation of 3780 m asl. (headscarp). It has an escarpment of ~2 km wide, and the foot of the avalanche is at 3150 m asl. This landslide presents several internal events (Figure 17a), the first event corresponds to an old avalanche that deposits reached the Huanara river. The avalanche deposit is strongly eroded, part of the avalanche has been reactivated and is cut by river (Figure 17a, figure 18a). On the left flank of this landslide, there is a sequence of events subsequent to the main event (Figure 17a) and this sector is the area of greatest interest because it presents recent events. A second avalanche was identified (Figure 17a, 17b) that originated in the headscarp and has a length of ~2.2 km; it is a retrogressive process that also mobilized part of the avalanche deposit of the first event. The headscarp originates in Mesozoic intrusive rocks (Figure 2, 17b). Levees can be observed as a product of the avalanche path (Figure 17a, figure 18a, 18c). Also the deposit is eroded. A third event occurred in the avalanche deposit of the second event (Figure 17a, 17b, figure 18b). This event corresponds to an internal avalanche and has a travel length of ~0.7 km. Finally, a fourth event was identified that corresponds to an avalanche, the headscarp is located at ~3730 m asl., the deposits of this avalanche cover part of the second and third event and show a travel length of ~0.7 km (Figure 17a). The boulders of these avalanches correspond to intrusive rocks and ignimbrites of the Huaylillas formation.

After the identification of internal events, a systematic sampling was carried out and 12 boulder samples (>2m, Figure 18d, 18e) were collected. These samples are equitably distributed in each deposit (Figure 17a). Five samples (HU-08, HU-09, HU-10, HU-11, and HU-12) were collected from the second avalanche, of which four exposure ages range from 682 ± 50 ka to 1261 ± 75 ka (Table 1). The exposure age of sample HU-08 (318 ± 22 Ka) we qualify as an outlier because it is outside the range. This sample is probably a block moved later at the site. From the third avalanche, three samples were collected (HU-01, HU-06, and HU-07), and the exposure ages are between 369 ± 28 ka and 499 ± 31 ka (Table 1). For the fourth avalanche, four samples were collected (HU-02, HU-03, HU-04, and HU-05), and the exposure ages of these samples are between 177 ± 5 ka and 325 ± 28 ka (table 1). The ages obtained in the three deposits are scattered and a weighted mean age could not be obtained (Figure 19), but a range of occurrence could be determined by taking into account the ages and their uncertainties. For this reason, we argue that: i) the second avalanche occurred in the range between 632 ka and 1336 ka, ii) the third avalanche occurred between 341 ka and 530 ka, iii) the fourth avalanche is the most recent event occurred in the range between 172 ka and 353 ka (Figure. 19).

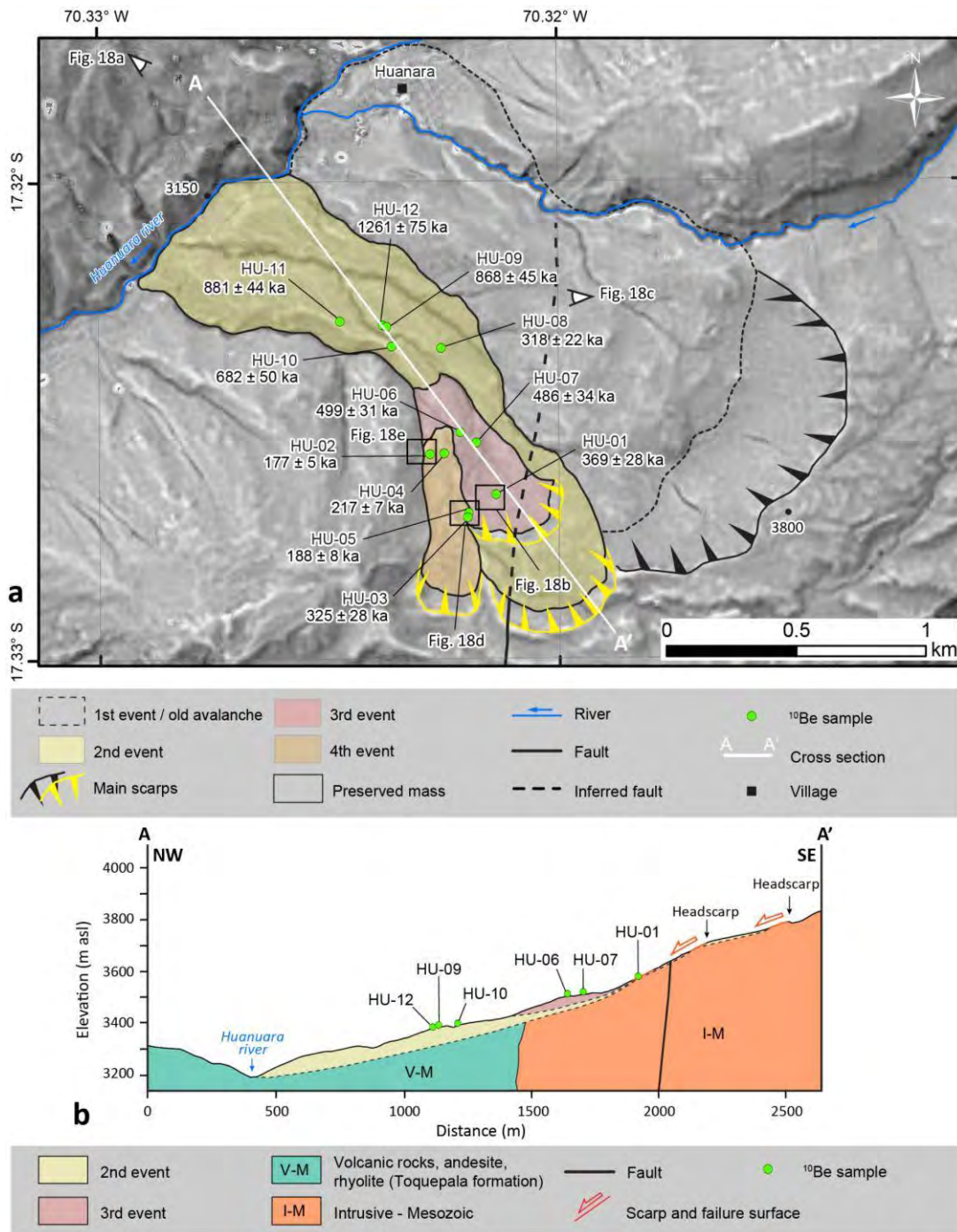


Figure 17. (a) Geomorphological map of the Huanara landslide, four internal events were identified as rock-avalanche. (b) Cross section of the internal avalanches (second and third event) of the Huanara landslide.



Figure 18. (a) Panoramic view of Huanara landslide, showing the deposits of the successive rock-avalanche generations, (b) Headscarp and slide surface of the third event, (c) Lateral levee channeling the deposits from the second rock-avalanche, (d) and (e) Sampling on top of boulders for cosmogenic nuclide dating (^{10}Be).

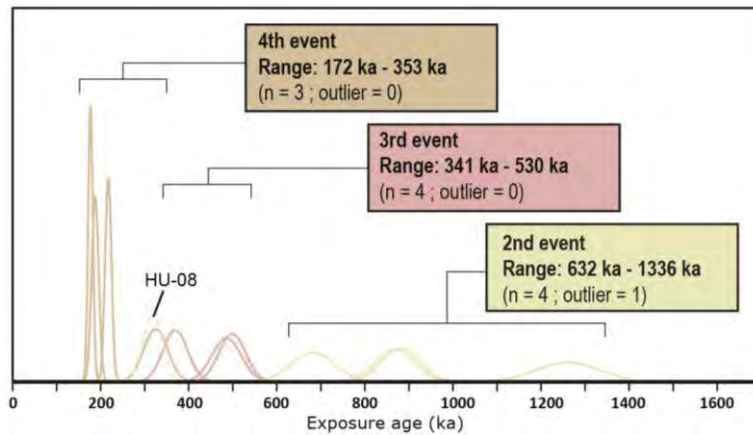


Figure 19. Probability density plot of the exposure-ages obtained on boulders from rock avalanche deposits.

4.2.2. Olleria 1 landslide

Olleria 1 landslide is a rockslide located on the right flank of the Huanuara River (Figure 20a) at 17.28° S latitude and an elevation of ~3890 m asl (headscarp). It has a ~1 km wide headscarp and the foot of the landslide is at 3450 m asl. In the detailed mapping of the landslide, we were able to identify three internal events (Figure 20a). The first event corresponds to the main event. This is a rockslide which deposits reached the Huanuara river. The headscarp originates in the ignimbrites of the Huaylillas formation (Figure 2, figure 20b). The second event corresponds to a rockslide. It is a reactivation of the rockslide deposits of the first event. This rockslide is small but fills and obstructs the Huanuara river (Figure 20a, figure 21a). This filling generated an epigenetic wedging of the river, modifying the normal course, causing the river to generate a rapid erosion and incision of the bedrock (Figure 21d). A third event was identified that corresponds to a rock avalanche, that originated in the headscarp and the deposits were accumulated on the mass of the first event (Figure 20a, figure 21a, 21b). The boulders visible on the surface of these events correspond to ignimbrites of the Huaylillas Formation.

After identifying all the internal events, a sampling was carried out to determine the exposure ages of the first and second events. Five samples (EP-01, EP-02, EP-03, EP-04, EP-05) were collected on large boulders (boulders >2m, Figure 21b, 21c) to determine the exposure age using cosmogenic nuclides ¹⁰Be. For the first event three samples were collected (EP-03, EP-04, EP-05), the exposure ages of these samples are between 295 ± 8 ka and 840 ± 22 ka (table 1). For the second event, two samples were collected (EP-01, and EP-02) that yielded ages between 52 ± 3 ka and 64 ± 2 ka (table 1). The ages obtained are scattered and a weighted mean age could not be obtained (figure 22), but a range of occurrence could be determined by taking into account the ages and their uncertainties. The first event, called the main event, occurred between 295 ka and 840 ka. The second event, which corresponds to the recent landslide that modified the course of the Huanuara river, occurred between 49 ka and 66 ka (Figure 22). Although the age scattering, the relative age of the event is in agreement with the mapping, i.e., the deposits with older ages, being overlaid by the deposit with the younger ages.

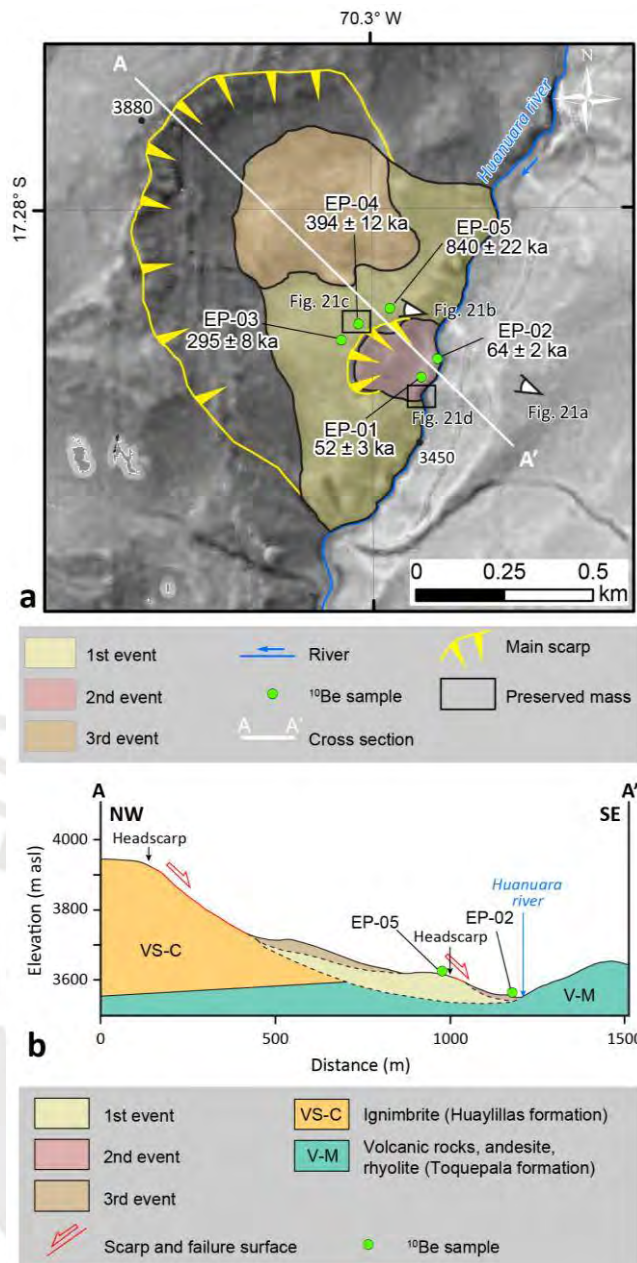


Figure 20. (a) Geomorphologic map of the Olleria 1 landslide, three internal events were observed, the first and second event are rockslides and the third event corresponds to a rock avalanche deposited on top of the first event. (b) Cross section of the internal events.

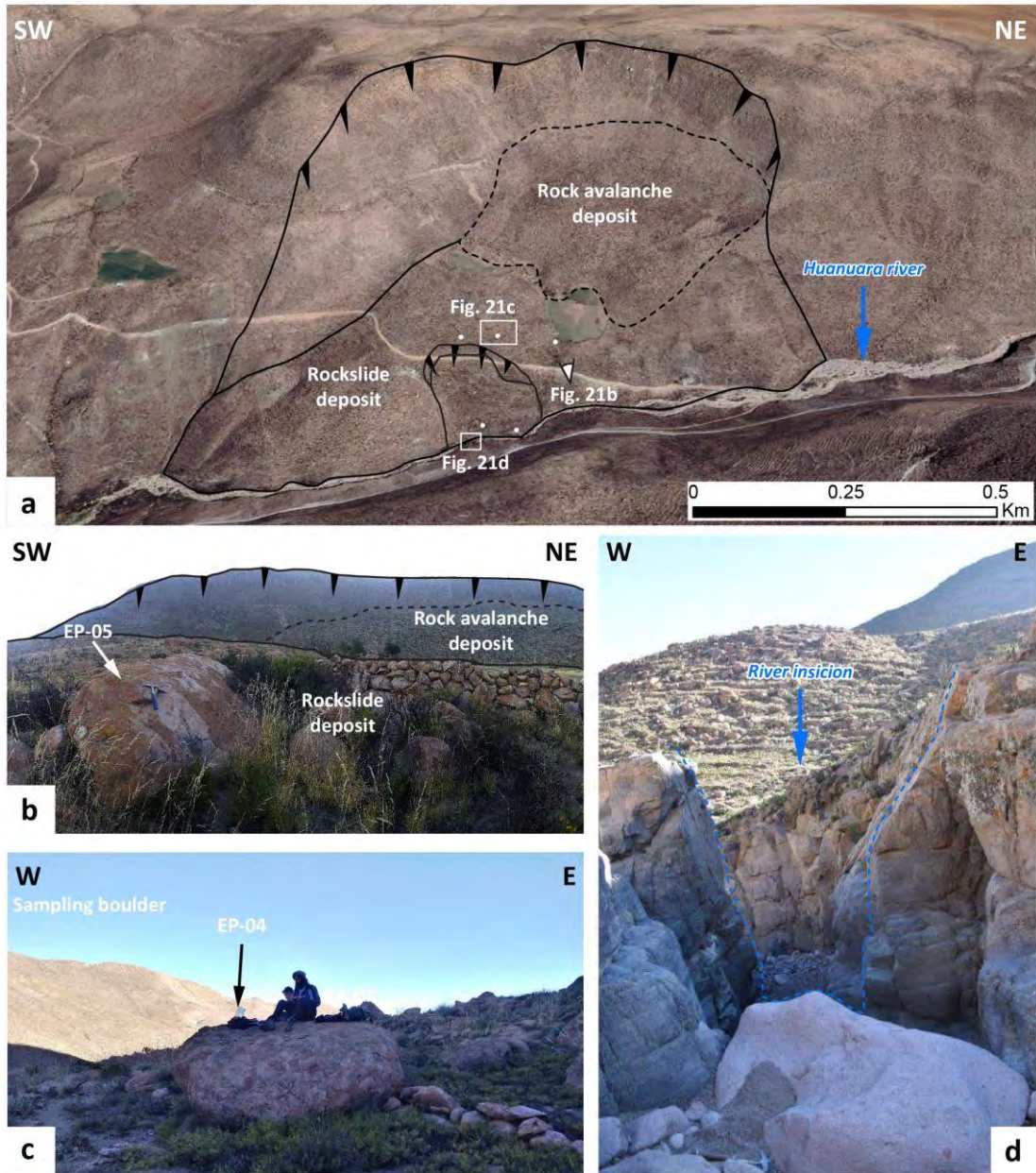


Figure 21. (a) Google Earth 3D image of the Olleria 1 landslide where the three internal events are observed, (b) view of the headscarp of the Olleria 1 landslide. The deposits of the first event (rockslide) and the third event (avalanche rock) can be observed (Figure. 15a). (c) sample collection for cosmogenic nuclide (^{10}Be) dating. (d) Epigenetic process and river incision of bedrock due to blockage of the main channel of the Huanuara river.

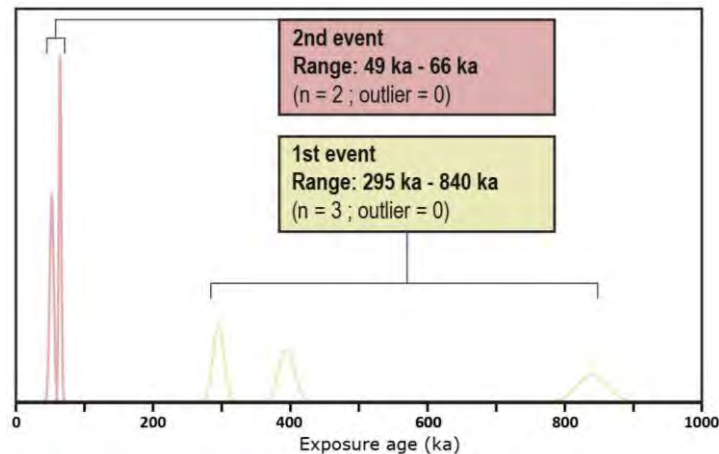


Figure 22. Probability density plot of the exposure ages obtained on boulders from rockslide deposits.

4.2.3. Ollería 2 landslide

The Ollería 2 landslide is a rockslide located on the left flank of the Huanuara river (Figure 23a) at 17.28° S latitude and at an elevation of ~3800 m asl (head scarp). It has an escarpment ~0.45 km wide. The headscarp originates from ignimbrites of the Huaylillas formation (Figure 2, Figure 23b). We performed detailed mapping and identified a unique event that formed a small dam blocking the Huanuara river. The height of the dam is ~10 m and it has a length of ~0.6 km towards the northwest (opposite slope).

Currently, part of the dam is incised and eroded by the activity of the Huanuara river (Figure 23a, Figure 24a, 24c). The profile of the eroded dam shows that the slipped mass is formed by ignimbrite blocks corresponding to the rocks that outcrop on the slopes of this part of the valley (Figure 23b). Also, attached to the eroded dam are lacustrine deposits corresponding to the lake formed by the landslide (Figure 23a, Figure 24d), this lake was small ~0.3 km long. The upper part of these deposits is at an altitude of ~3700 m asl (Figure 23b).

Large boulders (>2m, Figure 23a, Figure 24b) were selected for TCNs dating. Six samples (KS-01, KS-02, KS-03, KS-04, KS-05, KS-06) were collected (Figure 23a). The age shows a strong scatter and a weighted average age cannot be obtained (Figure 25). The exposure ages of these samples are between 56 ± 2 Ka and 682 ± 21 Ka. This landslide has a height difference of 200 m from the headscarp to the Ilabaya river, it is likely that the landslide mass was not modified at the time of the event. We believe that some of the boulder ages are inherited (Figure 23a). From the results obtained it is not possible to define an average age, only that the Ollería 2 landslide occurred between the range 52 ka and 703 ka (Figure 25).

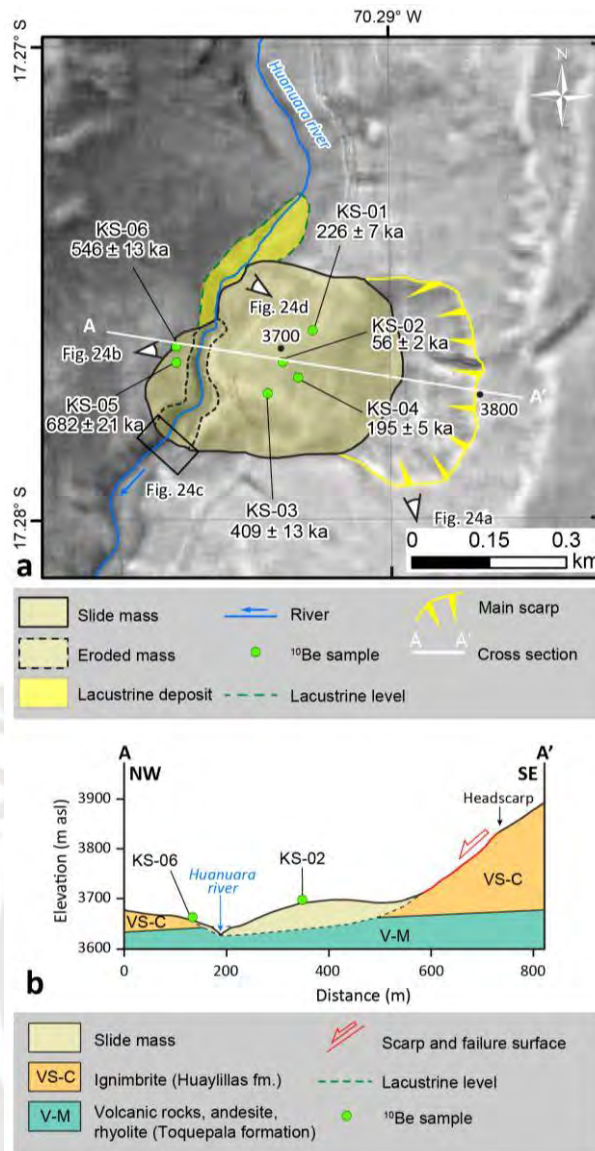


Figure 23. (a) Geomorphological map of the Olleria 2 rockslide. The rockslide deposit that filled the valley and formed a dam are observed, also the lacustrine deposits of the formed palaeolake are observed, (b) Cross section of Olleria 2 rockslide.

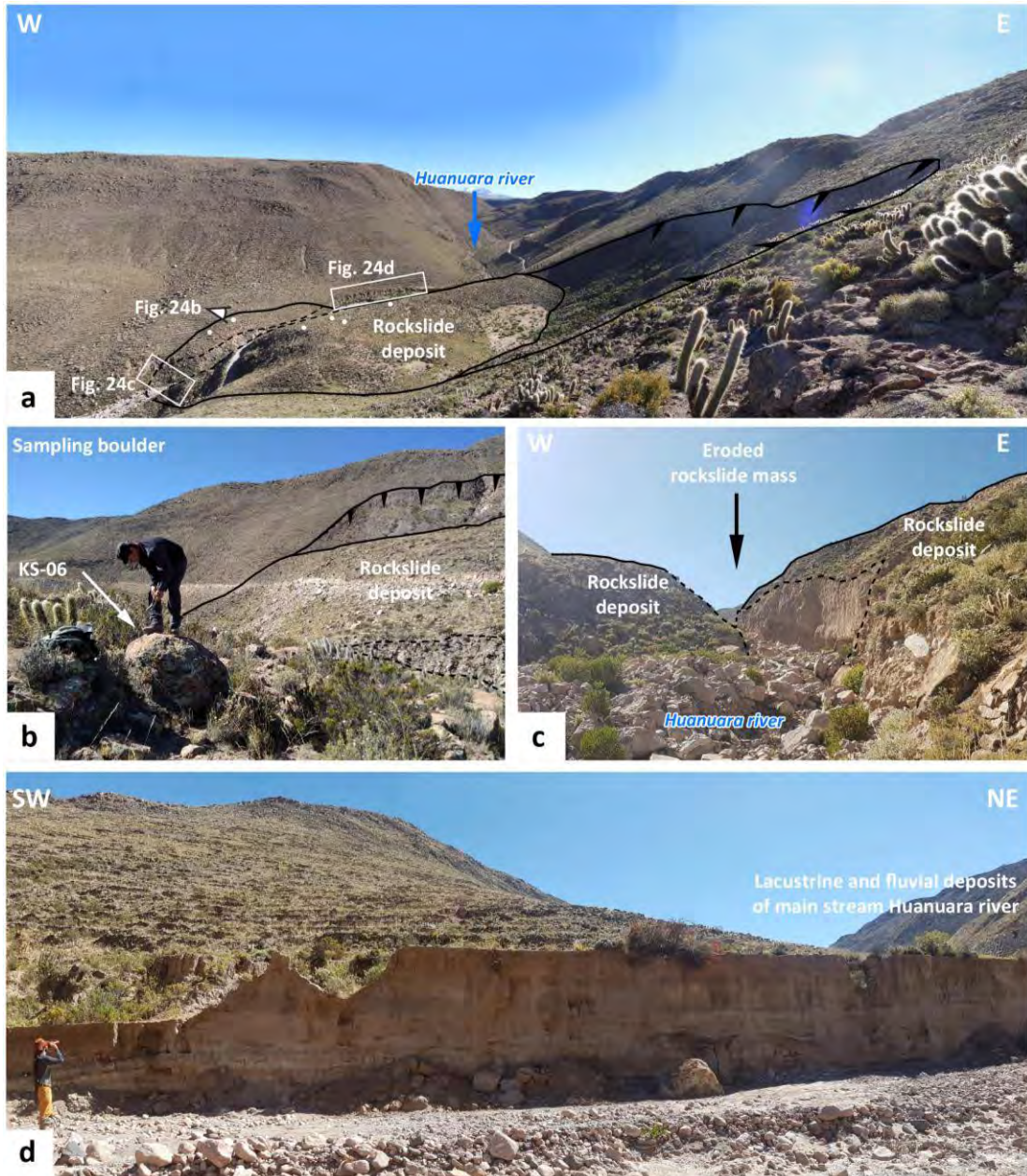


Figure 24. (a) Panoramic view to the north of the Olleria 2 rockslide, showing the landslide mass. The deposits are observed on the opposite flank of the river and the dam is eroded, (b) sample collection for cosmogenic nuclide dating (^{10}Be) dating. (c) Detail of the rockslide dam incised and eroded by the Huanuara river, (d) lacustrine deposits located along the main stream. The lake is formed by the Olleria 2 rockslide.

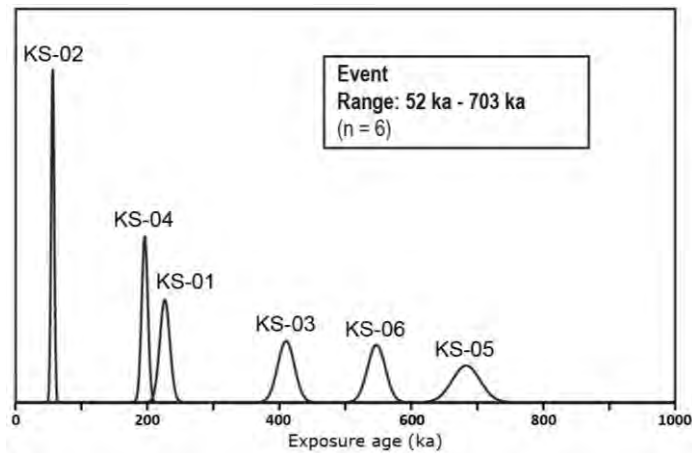


Figure 25. Probability density plot of the exposure ages obtained on boulders on top of the Olleria 2 rockslide deposit.

4.3. Ilabaya river

4.3.1. Cotana landslide

The Cotana landslide has several internal events. This large landslide is located on the left flank of the Ilabaya River (Figure 26a) between latitudes 17.22° S and 17.23° S. This landslide has a headscarp >2 km wide (Figure 26a). The landslide mass modified the channel and direction of the Ilabaya River. Four events could be identified by detailed mapping (Figure 26a, Figure 27a): The first event is a rockfall, the deposits reached the Ilabaya river. The escarpment originated in the ignimbrites of the Huaylillas formation (figure 2, figure 27b). The second event is a rock avalanche deposited on top of the first event (Figure 26a, Figure 27a). The third event is a rock avalanche affecting both previous events (Figure 26a, Figure 27a, 27c). This avalanche has a length of ~1.3 km. The fourth event is also a rock avalanche that originates from the avalanche deposits of the second event (Figure 26a). All boulders observed at the surface of these processes correspond to ignimbrites of the Huaylillas Formation (Figure 26b).

Of these four events, we choose to preliminary determine the exposure age of the second event for accessibility reasons on the field. Three samples were collected from boulders on top of the rock-avalanche (Figure. 19d). The samples yielded the following ages AB-02: 19 ± 1 ka, AB-03: 17 ± 1 ka, AB-04: 42 ± 1 ka (Table 1). The first two ages are compatible within uncertainties, corresponding to a mean age of 18 ± 0.4 ka (Figure 28). The third and older age is likely attributed to inheritance.

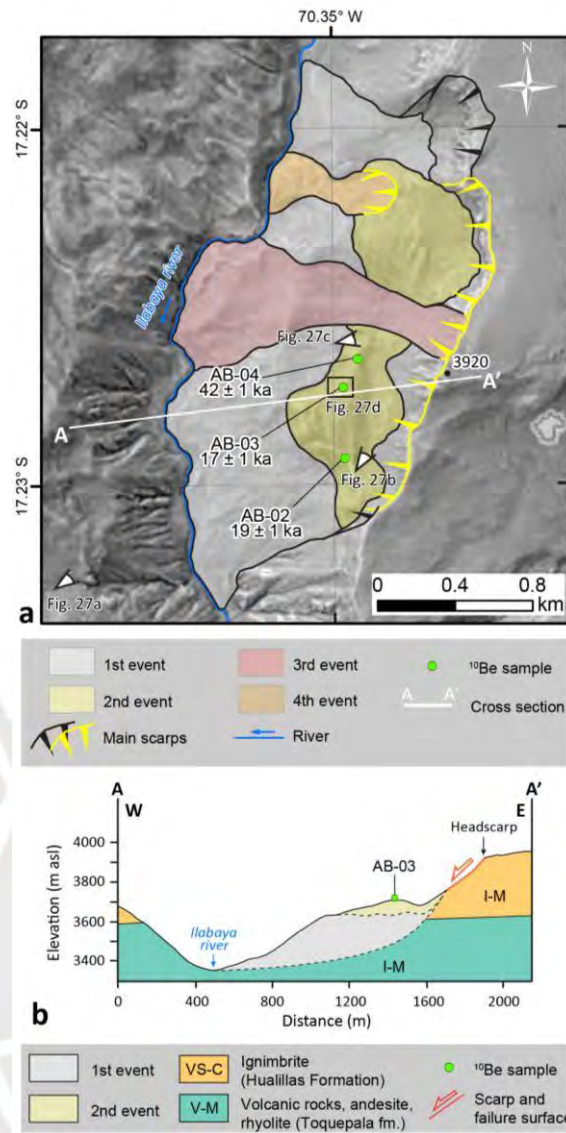


Figure 26. (a) Geomorphological map of the Cotana landslide, up to four events are observed: the first event corresponds to a rockslide and the other three events are rock avalanches, (b) Cross section showing the first (rockslide) and second event (rock avalanche).

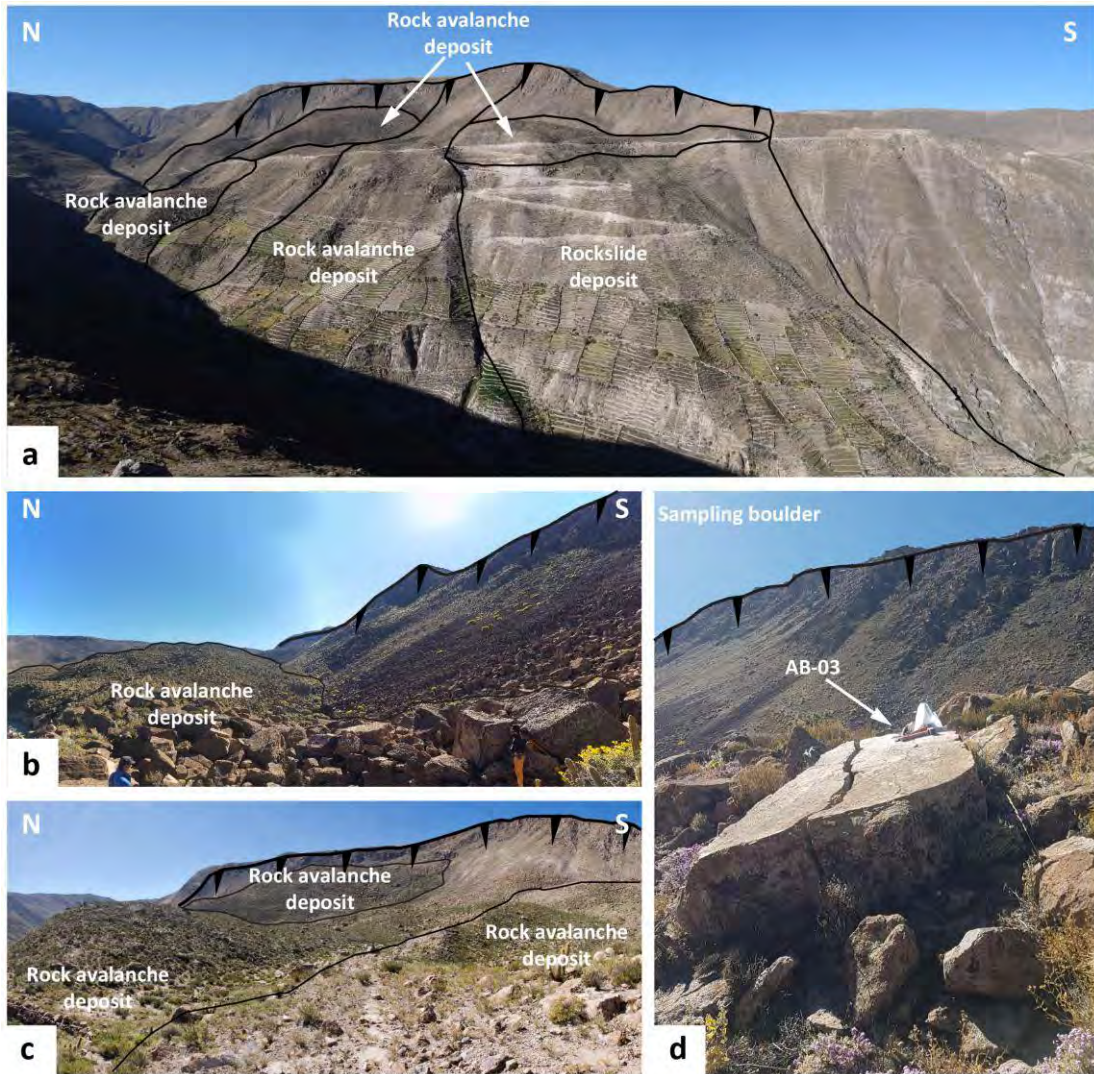


Figure 27. (a) Panoramic view to the Cotana landslide, this landslide has several internal events, the main event is a rockslide and the others are rock avalanches, (b) Detail of the headscarp and rock avalanche deposit of the second event, (c) Detail of the avalanches of the second and third events (Figure 18a), (d) sample collection for cosmogenic nuclide dating (^{10}Be).

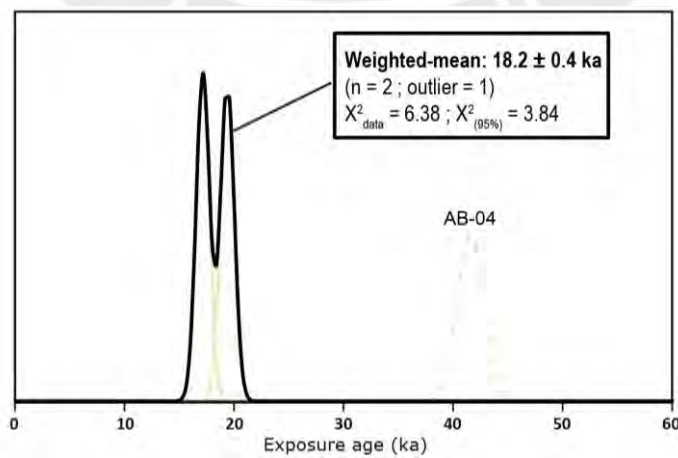


Figure 28. Probability density plot of the exposure ages obtained on boulders on top of the second event (rock avalanche).

Table 1: Samples parameters, cosmogenic ^{10}Be data and results. Z is the sample thickness, St is the topographic shielding factor. All the uncertainties reported are 1 sigma (σ).

Landslide	Sample	Latitude (S°)	Longitude (W°)	Elevation (m a.s.l.)	Z (cm)	St (%)	Mass (g)	^9Be carrier (10^{19} atoms)	$^{10}\text{Be}/^9\text{Be}$ (10^{-14})	^{10}Be (10^5 at.g $^{-1}$)	Age (ka)	1 σ (ka)	1 σ without PR error (ka)
Locumba river													
Pondera	PO-01	17.44175	70.45839	1836	1.0	0.979	5.18	3.47	12.62 ± 0.66	8.04 ± 0.42	100	6	4
	PO-02	17.44182	70.45827	1836	3.0	0.979	5.23	3.39	8.98 ± 0.60	5.41 ± 0.33	68	6	4
	PO-03	17.44183	70.45795	1835	4.0	0.973	5.21	3.48	21.61 ± 0.81	13.99 ± 0.50	180	10	5
Angostura	AA-01	17.41267	70.37878	2235	2	0.988	2.16	3.45	21.14 ± 2.24	32.27 ± 3.47	318	39	34
	AA-02	17.41207	70.3796	2235	3	0.990	4.07	3.44	30.27 ± 1.00	25.10 ± 0.77	238	17	8
	AA-03	17.41148	70.37935	2228	3.5	0.988	2.42	3.46	16.60 ± 2.17	22.90 ± 2.99	215	29	27
	AA-04	17.41108	70.37975	2214	3	0.987	1.91	3.43	10.89 ± 0.85	18.40 ± 1.43	178	15	12
	AA-05	17.41199	70.37809	2244	3	0.988	1.73	3.45	17.51 ± 0.56	33.70 ± 1.06	330	23	11
	AA-06	17.41106	70.37853	2204	3	0.983	2.67	3.45	17.08 ± 1.89	21.30 ± 2.20	203	201	18
	AA-07	17.41130	70.37789	2225	3	0.976	3.75	3.47	62.62 ± 1.96	57.30 ± 1.74	703	51	22
Antavilca	AN-06	17.34334	70.28532	3008	3	0.955	5.58	3.43	6.53 ± 0.21	3.59 ± 0.11	19.3	0.7	0.5
	AN-07	17.34349	70.28542	3007	3.5	0.955	5.21	3.42	5.40 ± 0.18	3.10 ± 0.09	17.0	0.6	0.5
	AN-08	17.34375	70.28516	2972	3	0.974	6.02	3.43	5.91 ± 0.19	2.98 ± 0.09	16.4	0.6	0.5
	AN-09	17.34441	70.28538	2971	2	0.984	7.18	3.42	2.80 ± 0.13	1.01 ± 0.04	6.1	0.2	0.2
	AN-10	17.34421	70.28457	2964	2	0.984	7.37	3.43	6.79 ± 0.21	2.85 ± 0.09	15.5	0.6	0.4
	AN-11	17.34441	70.28376	2935	2	0.975	5.31	3.43	5.23 ± 0.18	2.94 ± 0.09	16.4	0.6	0.5
Quilahuani	QL-01A	17.31622	70.27694	3649	3.5	0.986	8.04	3.41	46.38 ± 1.53	19.46 ± 0.59	65	2	2
	QL-02	17.31540	70.27582	3642	1.5	0.958	8.12	3.43	77.29 ± 2.45	32.47 ± 0.99	109	4	3
	QL-03	17.31714	70.27605	3626	2	0.988	8.08	3.43	121.74 ± 3.97	51.41 ± 1.54	173	7	5
	QL-04	17.31974	70.27391	3544	4.5	0.985	8.25	3.45	79.80 ± 2.60	33.14 ± 1.00	116	4	3
	QL-05	17.32046	70.27317	3515	3.5	0.979	8.16	3.39	46.85 ± 2.82	19.24 ± 0.92	70	4	4
	QL-06	17.31776	70.27277	3505	3.5	0.992	7.87	3.44	124.99 ± 5.56	54.38 ± 1.63	192	5	4
	QL-07	17.31810	70.27304	3510	3.5	0.990	7.86	3.43	72.65 ± 2.54	31.52 ± 1.01	112	4	3
	QL-08	17.32210	70.27096	3454	2	0.989	8.13	3.43	37.98 ± 1.29	15.83 ± 0.51	60	2	2
	QL-09	17.31910	70.27087	3468	2.5	0.996	8.13	3.43	79.29 ± 3.12	33.20 ± 1.01	118	4	3
	QL-10	17.32148	70.27004	3445	3	0.986	7.94	3.44	76.39 ± 2.50	32.88 ± 1.00	120	4	3

Huanuara river													
Huanara	HU-01	17.32761	70.31892	3524	2	0.969	5.56	3.43	128.48 ± 4.48	78.93 ± 2.38	369	28	14
	HU-02	17.32619	70.32131	3480	2.5	0.988	3.52	3.44	50.03 ± 1.02	48.12 ± 0.92	177	5	3
	HU-03	17.32840	70.31995	3548	5	0.970	4.33	3.45	90.18 ± 6.43	71.48 ± 3.98	325	28	19
	HU-04	17.32616	70.32079	3486	2	0.985	2.97	3.43	53.54 ± 1.15	61.08 ± 1.18	217	7	4
	HU-05	17.32824	70.31991	3546	3.5	0.970	4.36	3.45	55.37 ± 1.81	43.29 ± 1.30	188	8	3
	HU-06	17.32544	70.32020	3465	2.3	0.985	5.31	3.46	148.77 ± 4.45	96.54 ± 2.33	499	31	11
	HU-07	17.32580	70.31962	3471	4	0.972	4.22	3.45	113.47 ± 4.08	92.19 ± 3.14	486	34	17
	HU-08	17.32249	70.32088	3386	4.5	0.971	5.68	3.43	107.22 ± 4.62	64.44 ± 2.46	318	22	12
	HU-09	17.32243	70.32268	3348	4.5	0.977	4.41	3.46	169.06 ± 3.54	132.06 ± 2.45	868	45	11
	HU-10	17.32169	70.32300	3356	4	0.992	5.51	3.44	182.44 ± 5.67	113.46 ± 3.38	682	50	21
	HU-11	17.32154	70.32456	3315	4	0.977	4.51	3.45	173.05 ± 3.64	131.78 ± 2.61	881	44	14
	HU-12	17.32173	70.32287	3343	1	0.992	4.30	3.46	218.24 ± 7.83	174.86 ± 5.30	1,261	75	36
Olleria 1	EP-01	17.28764	70.29868	3514	4.5	0.982	5.79	3.43	24.65 ± 0.80	14.19 ± 0.41	52	3	2
	EP-02	17.28718	70.29824	3519	3	0.954	5.09	3.42	26.30 ± 0.78	17.21 ± 0.47	64	2	1
	EP-03	17.28668	70.30079	3589	1	0.970	4.96	3.42	122.19 ± 2.08	83.87 ± 1.30	295	8	4
	EP-04	17.28627	70.30033	3583	3	0.973	5.19	3.42	156.86 ± 2.54	102.91 ± 1.50	394	12	6
	EP-05	17.28588	70.2995	3578	2	0.979	5.47	3.43	289.40 ± 4.22	180.86 ± 2.20	840	22	10
Olleria 2	KS-01	17.28000	70.29306	3688	3	0.961	7.85	3.43	156.67 ± 2.69	68.27 ± 0.91	226	7	3
	KS-02	17.28056	70.29361	3678	4	0.968	8.68	3.44	41.22 ± 1.00	16.13 ± 0.36	56	2	1
	KS-03	17.28111	70.29389	3680	1	0.964	8.53	3.44	279.81 ± 4.74	112.82 ± 1.54	409	13	6
	KS-04	17.28083	70.29333	3684	3	0.961	7.84	3.45	136.07 ± 3.49	59.67 ± 1.12	195	5	2
	KS-05	17.28056	70.29556	3638	2	0.974	9.95	3.41	466.13 ± 6.84	159.78 ± 1.85	682	21	8
	KS-06	17.28028	70.29556	3643	2	0.967	8.82	3.44	352.26 ± 5.75	137.09 ± 1.78	546	13	6
Ilabaya river													
Cotana	AB-02	17.23211	70.34943	3626	3	0.977	5.28	3.43	8.75 ± 0.28	5.24 ± 0.16	19	1	0.5
	AB-03	17.22879	70.34951	3652	2.5	0.991	5.15	3.44	7.71 ± 0.24	4.70 ± 0.14	17	1	0.5
	AB-04	17.22746	70.3488	3658	2	0.974	5.74	3.44	22.39 ± 0.68	13.03 ± 0.39	42	1	0.9
	BI1												
	BI2	-	-	-	-	-	-				-	-	-
	BI3	-	-	-	-	-	-				-	-	-

5. Discussion

5.1. Exposure ages scattering

In summary, we were able to reach robust dating constraints in agreement with the geomorphological mappings, for four over eight of the landslides sampled for cosmogenic nuclide dating. For half of the landslides, the obtained exposure ages show a strong dispersion, including very old apparent ages up to ~ 1 Ma, which are incompatible with their failure scenarios (one or more successive events) deduced from the morphology analysis.

One of the most outstanding examples is the Olleria 2 rockslide (Figure 23 and Figure 24). At this site, we obtained six ages ranging from 52 to 703 ka (Table 1), being all incompatible with each other's (Figure 25), while the geomorphology of the rockslide favors the interpretation of a single and simple failure event (Figure 23).

The scattering, or the incompatibility, of cosmogenic nuclide exposure ages with scenarios inferred from geomorphological observations, or other independent dating constraints, has been frequently reported in the literature. It concerns various topics such as the dating of terraces and alluvial deposits (e.g. Litty et al., 2019), the dating of glacier retreat and moraine abandonment (e.g. Heyman et al., 2011; Larsen et al., 2021), the dating of rock-glacier (e.g. Çiner et al., 2017), the dating of fluvial gorge incision (e.g. Cardinal et al., 2021); the dating of landslides, either sampling boulders (e.g. Ivy-ochs et al., 2009) or headscarps (e.g. Le Roux et al., 2009; Zerathe et al., 2014; Böhme et al., 2019). Too young or too old ages (Heyman et al., 2011) have been respectively related to two main factors: (i) incomplete exposure, yielding exposure ages that are too young, either due to post-depositional boulder rotation, shielding by shallow soil or moraine deposits, scarp rejuvenation; and (ii) inheritance, or prior exposure, yielding exposure ages that are too old (see references listed above). All of this is related to the main specificity of the cosmogenic nuclide dating tool: the exponential attenuation of incident cosmic ray particles when they cross the matter (Lal, 1991; Gosse and Phillips, 2001).

Hilger et al. (2019) explored recently the question of the significance of the inheritance when dating landslide boulders with terrestrial cosmogenic nuclide dating (TCN). According to this study the probability of sampling a boulder that may contain a non-negligible amount of inherited TCN concentration (Figure 29a and 29b) depends on two main parameters: (1) the amount of inherited TCN in the pre-failure hillslope and (2) the ability of the landslide in mixing and disintegrating the rock mass, further exposing boulders that were previously either deeply buried, or located at shallow depth below the pre-failure hillslope. Of course, the situation can be even more unfavorable if the dated landslide is young ($< \text{few ka}$, Hilger et al., 2019), implying a lower ratio between the concentration acquired by direct exposure, and the inherited component one's (Zerathe et al., 2014).

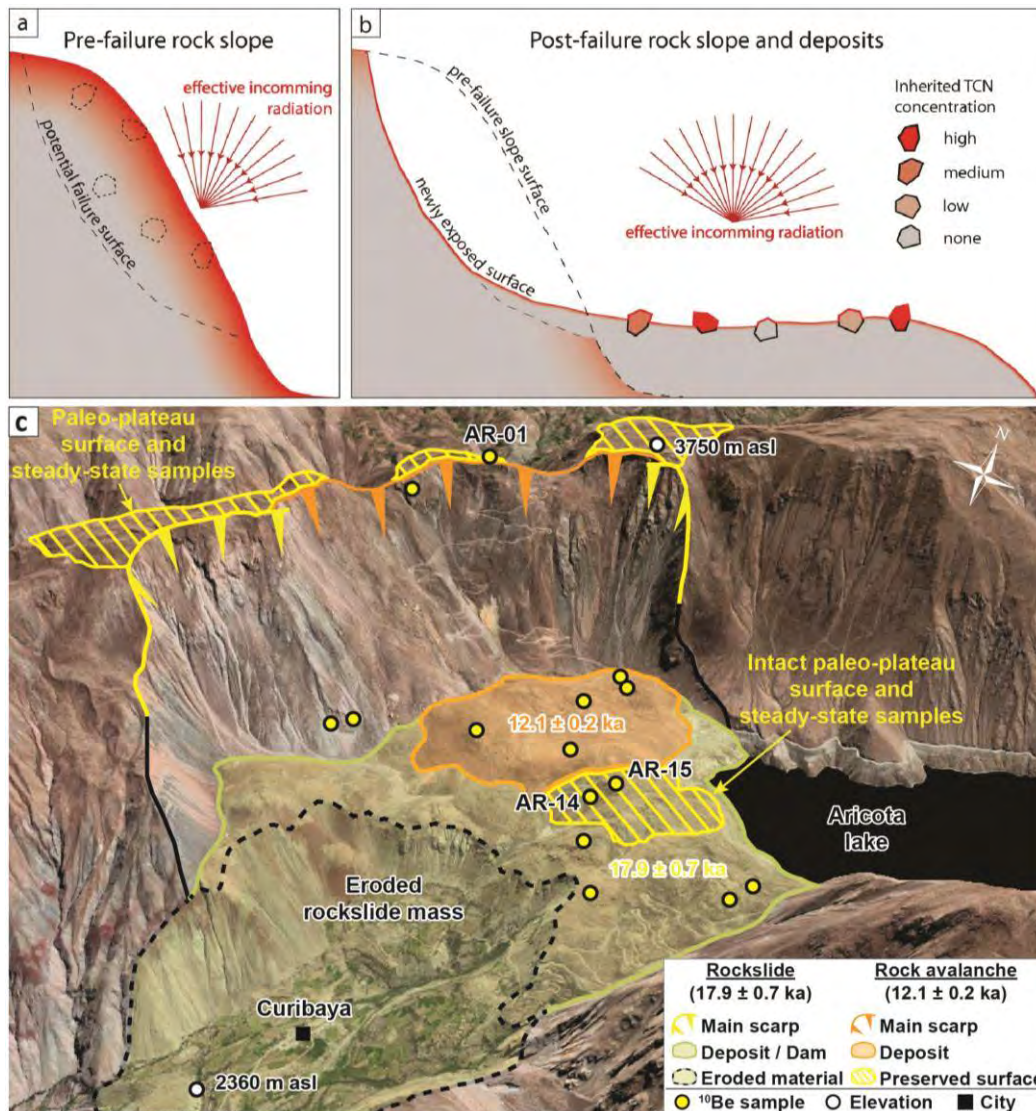


Figure 29. (a) and (b) Setting the inheritance problem from Hilger et al. (2019), (c) the Aricota rockslide dam (modified from Delgado et al., 2020) where steady-state concentration was measured on the plateau at the landslide top (AR1) and where an intact relict of this paleo-plateau was mapped in the slided-mass and on which sampled boulders (AR14 and AR15) provided steady-state similar concentrations.

To what concerns the first parameter, arid hillslopes of the Central Andes offer a strongly unfavorable context in comparison to high latitude mountains that were glaciated during the Last Glacial Maximum (LGM). Indeed, in the domains covered by ice during LGM, hillslopes were ice-shielded for a long time and completely rejuvenated by glacier erosion. Thus, in these contexts, the inheritance calculation has to be integrated over ca. 20 ka only (Schwartz et al., 2017; Hilger et al., 2019). As shown in Figure 30, this implies inherited TCN concentrations ranging from 10^3 to 10^5 at.g⁻¹, corresponding to apparent exposure ages ranging from 1 to 20 ka in the first 2 meters, which then become negligible at greater depth. On the other hand, in the arid Central Andes, Quaternary glaciers only affected the higher elevations (>5000 m asl) and the hillslopes below have been shaped by a very low erosion for millions of years, with surfaces being most of the time at steady-state equilibrium (e.g. Placzek et al., 2009). An example is the

Aricota rockslide, where we measured concentrations of more than 10^7 at.g⁻¹ along the pre-failure slope, at the top of the landslide plateau (Figure 29; sample AAR1; Delgado et al., 2020). In this context, an “infinite time” must be considered when calculating the profile of inherited TCN concentrations, which strongly increases the concentrations of TCN produced and also generates significant content of TCN at great depths, down to 20 m. As shown in Figure 30, this implies TCN concentrations from 10^5 to 10^7 in the first 20 meters of depth, corresponding to apparent exposure ages between 20 ka to 1 Ma. In this context, if one samples a landslide boulder that was previously located in the first 20 meters below the pre-failure hillslope, the inferred exposure age may be erroneously overestimated by 1 to 3 orders of magnitude.

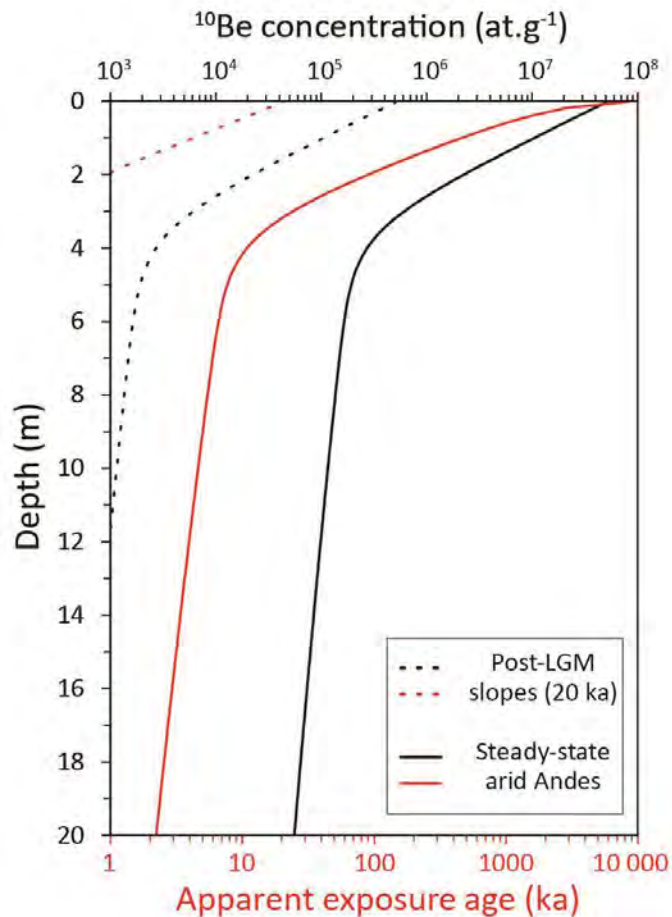


Figure 30. Theoretical depth profiles and related apparent exposure ages (adapted from Hilger et al., 2019) calculated for two different configurations: i) hillslopes after LGM glacier retreat, considering an exposure duration of ~ 20 ka; ii) the steady-state arid Andes, considering an « infinite time ». ^{10}Be concentrations and exposure ages were calculated following equations described in Martin et al. (2017), parametrization described in Delgado et al. (2020), using production rate scaled at the elevations and latitude of the Locumba cluster and accounting for the muogenic productions.

Regarding the ability of the landslide to mix the rock mass, this parameter depends on the slope failure mechanisms and landslide typology, which play a major role in exposing boulders that were previously either deeply buried or located at shallow depth below the pre-failure hillslope (Hilger et al., 2019). The situation can be critical for “in-mass” rockslides, as shown in the Aricota

rockslide case (Delgado et al, 2020), where almost intact relict surfaces of the pre-failure plateau were mapped and sampled on the slid-mass (Figure 29c). As another example, for a post-Inca rockslide near Candarave (Figure 31A), several field evidences indicate almost complete preservation of the pre-failure slope in the slid-mass. Indeed, tilted Inca terraces were found in the landslide, despite having moved for ~300 meters downward (Figure 31C). We can expect a similar effect on the Olleria 2 rockslide (Figure 31B), where suspiciously old, and strongly scattered, exposure ages can be attributed to the preservation of the steady-state pre-failure hillslope. In the case of rock-avalanche type, because the movement is typically a granular-flow, and as the run out of material is often longer, at higher level a mass-destructuration can be expected.

In summary, strong caution should be taken when sampling landslide boulders for TCNs dating in regard of mentioned inheritance problems, especially in arid environments. Boulder selection should be based on careful evaluation of the degree of preservation of the pre-failure hillslope. We also recommend to multiple the dating, sampling the headscarp if possible, using multiple dating techniques to ensure to reach robust conclusions.

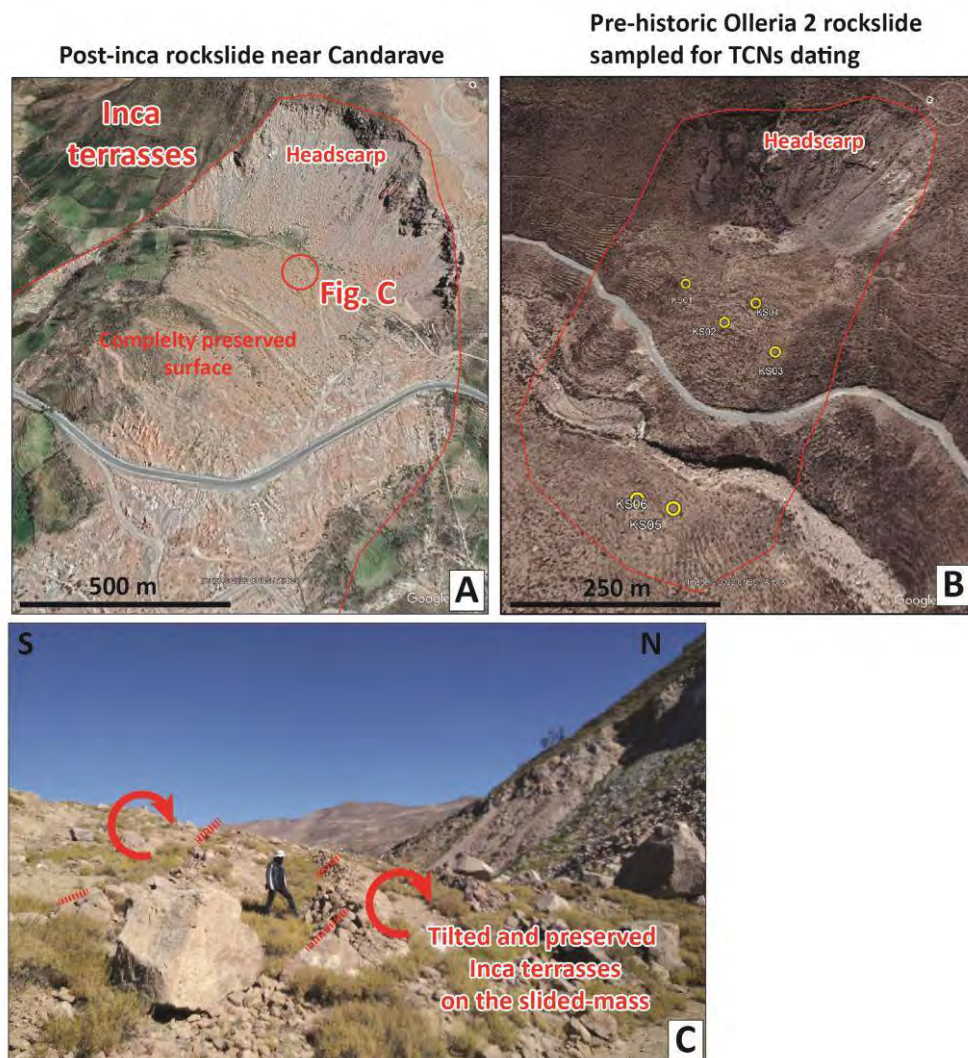


Figure 31. Morphological similitudes between (A) a post-Inca rockslide mapped near Candarave (see location in Figure 2) and (B) the Olleria 2 paleo-rockslide sampled for TCN dating. (C) Tilted, but preserved, Inca terraces as evidences of preserved pre-failure hillslope in the slid-mass.

5.2. Implication of landslide timings for the triggering factors

One of the main purposes of applying the cosmogenic nuclide dating was to constrain the age of failure of a significant amount of the paleo-landslides composing the Locumba cluster in order to investigate their possible triggering factor. Of the eight landslides sampled, robust mean ages could be obtained for four landslides only (Angostura (205 ± 9 ka), Antavilca (16.3 ± 0.3 ka), Quilahuani (114 ± 2 ka), Cotana (18 ± 0.7 ka), Figure 32). For the rest of the landslides, because of age scattering, as mentioned above, only the potential range of time of occurrence was documented.

The map Figure 32 shows a synthesis of the dating at the scale of the Locumba cluster. On the basis of our data, we can say that the spatial distribution of landslide ages does not reveal any specific pattern. For instance, large landslides with different time ranges (ca. 12-18 ka; 100 and 200 ka) co-exist along the Locumba river. We do not observe any signal of upward knickpoint propagation in the valley, young and old landslides dam being located indifferently at the upper and the lower part of the catchment.

Figure 32 allows also to discuss the possible co-seismic triggering of those landslides. Two active crustal faults are bounding the Locumba cluster to the south: 1) the Incapuquio fault, dominated by sinistral transpression, and 2) the Purgatorio fault, a dextral reverse fault. Recent paleoseismological studies were carried out along those faults indicating: (i) at least two earthquakes of ca. Mw 7 along the Purgatorio fault during thousand years, with very shallow epicenters as they implied surface ruptures with offset of several meters (Benavente et al., 2017 and 2021); and (ii) at least one earthquake of Mw 7.4–7.8 for the Incapuquio fault during the last five hundred years, related to kilometers long surface ruptures and scarps offset of 2-4 meters (Benavente et al., 2021). Those results support that the triggering of landslides by past earthquakes is probable in the Locumba area because most of the investigated landslides are located in the close-field (< 20 km) of those active fault segments. Some of the landslides affecting Inca terraces, such as the example illustrated in Figure 31A, may have been directly related to those historical earthquakes. On the other hand, in the absence of older paleoseismic records, no definitive conclusions can be reached on the link between Pleistocene giant landslides and earthquakes. We can nevertheless notice that those large landslides seem to have a relatively lower frequency of occurrence (ca. 10 to 100 ka) than the crustal seismicity in this region (ca 100 to 1000 years).

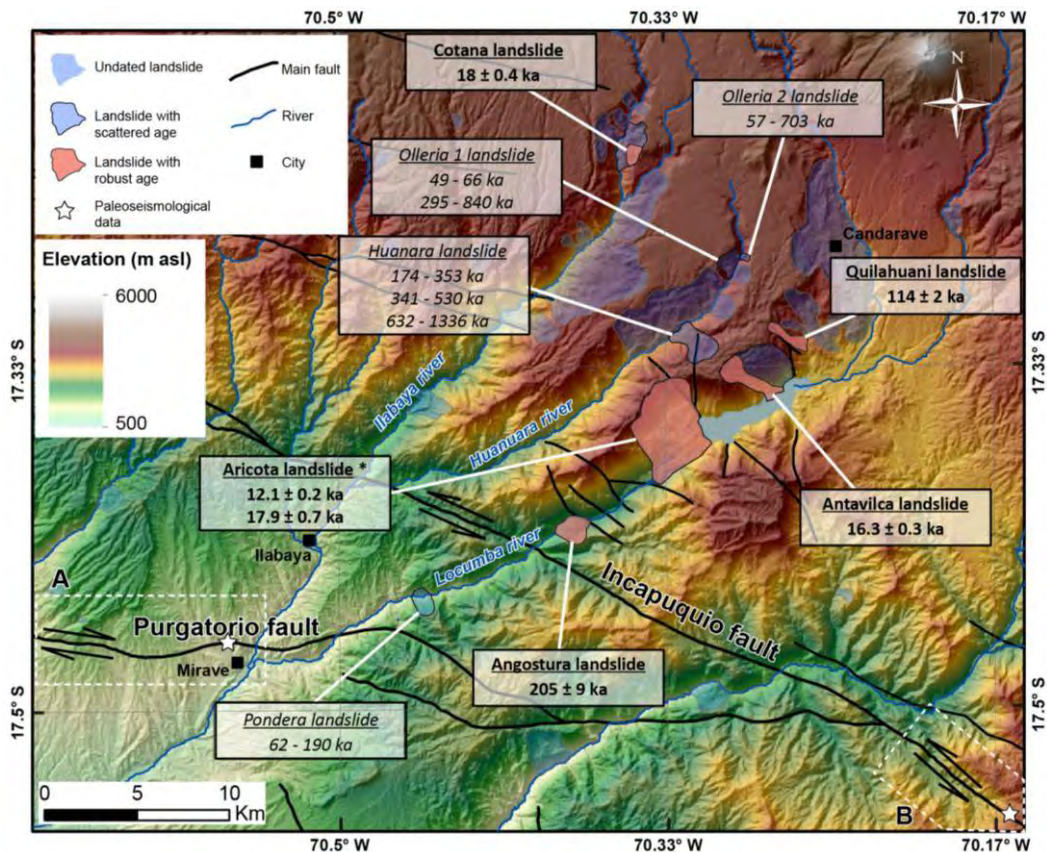


Figure 32: Summary map of landslide dating in the Locumba cluster. Paleoseismological studies (Benavente et al. 2017; 2021) with (A) Purgatorio fault and (B) Incapuquio fault. (*) Previous study (Delgado et al., 2020).

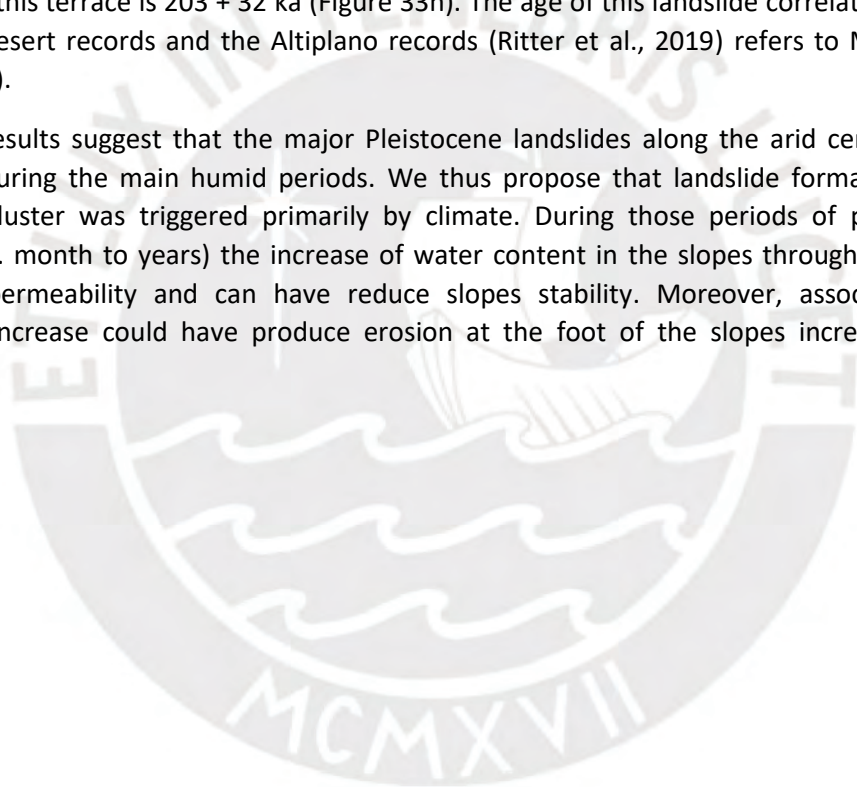
In Figure 33, we propose a compilation of dated landslides along the Central Western Andes. The four landslides dated in this study are compared with previous studies on landslides in this part of the Andes such as the Chuquibamba landslide (Margirier et al., 2015), the Caquilluco landslide (Zerathe et al., 2017, 2018), and the Aricota landslide (Delgado et al., 2020). Those landslide chronicles are then compared to local climate reconstructions and other climatic proxies such as alluvial terraces aggradation or paleolakes records.

The Western Flank of the Central Andes has a hyper-arid climate (Dunai et al., 2005), but there is evidence of past humid phases recorded during the Pleistocene as lake extensions and glacial advances (Quade et al., 2008; Gayo et al., 2012; Placzek et al., 2013; Martin et al., 2018, 2020; Bromley et al., 2016; Ritter et al., 2018). Also, towards the coast, records of alluvial terraces have been reported (Hall et al., 2008 and 2012; Steffen et al., 2010; McPhillips et al., 2013; Litty et al., 2018) and debris flows corresponding to Paleo-El Niño events have been dated (Keefer et al., 2003). Even, deposits from a blocked endorheic basin correlated with extreme climatic events (Ritter et al., 2019).

Starting with the youngest event, the Aricota rock avalanche (12.1 ± 0.2 ka). This landslide correlates with a lacustrine expansion in the Altiplano called the Copiasa phase (Bloggett et al., 1997) during the Younger Dryas (Placzek et al., 2013). It also correlates with dated terraces in the Majes valley (Steffen et al., 2010) and the Pisco river (McPhillips et al., 2013). Then there are three events, the Antavilca rock avalanche (16.3 ± 0.3 ka), the Pondera rock avalanche ($18.2 \pm$

0.4 ka), and the Aricota rockslide (17.9 ± 0.7 ka). These events correlate with a large lacustrine expansion in the Altiplano known as the Tauca phase or Heinrich Stadial 1a (Placzek et al., 2013; Martin et al., 2018) that occurred between 14.5 - 18.5 ka (Figure 33e, 33f). Moreover, these landslides also correlate with 16-24 ka terraces on the Pisco river (Steffen et al., 2009; McPhillips et al., 2013) (Figure 33j). Correlating with climatic fluctuations in the Atacama Desert (Ritter et al., 2019), it can be seen that at the time of the Antavilca and Pondera landslides, there is a decrease in aridity (Figure 33k). The Quilahuani rock avalanche (114 ± 2 ka) can be correlated with the Ouki phase identified in the Altiplano (80-120 ka) (Placzek et al., 2013) (Figure 33b). The age of this landslide can also be correlated to one of the terraces dated by Hall et al., (2008) in Mirave in Tacna (129 ± 24 ka; Figure 33h), and terrace in the Majes river (approx. 100 - 110 ka; Figure 33i) dated by Steffen et al., (2010). In terms of climatic fluctuations in the Atacama Desert (Ritter et al., 2019), the age of the Quilahuani landslide correspond with changes in the Pacific Ocean marine record, and decreasing aridity (Figure 33k). Older feature, i.e., Angostura rockslide (205 ± 9 ka), can be correlated with one of the terraces dated by Ritter et al., (2018) in the Atacama Desert (Figure 33e) and with other terraces dated by Hall et al., (2008) in Palpa (Nazca). The age of this terrace is 203 ± 32 ka (Figure 33h). The age of this landslide correlated with the Atacama Desert records and the Altiplano records (Ritter et al., 2019) refers to MIS Stage 7 (Figure 33k).

All these results suggest that the major Pleistocene landslides along the arid central Andes occurred during the main humid periods. We thus propose that landslide formation in the Locumba cluster was triggered primarily by climate. During those periods of prolonged rainfalls (ie. month to years) the increase of water content in the slopes through cracks and fractures permeability and can have reduce slopes stability. Moreover, associated river discharge increase could have produce erosion at the foot of the slopes increasing slope instability.



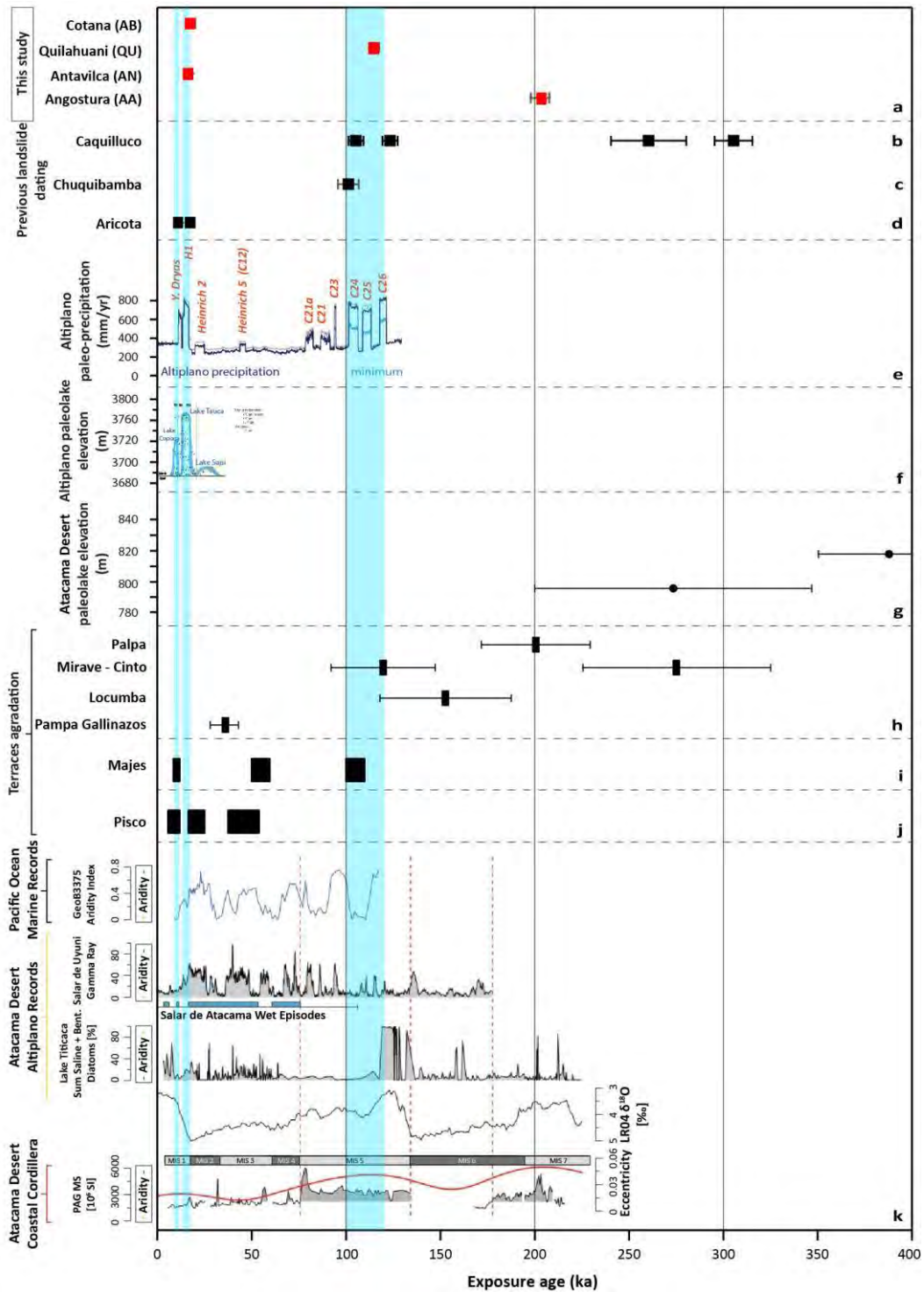


Figure 33. Compilation of landslide exposure ages for the Locumba cluster and comparison with climatic proxies. (a) Exposure ages of the present study. (b, c, d) Previous landslide studies (Caquilluco landslide - Zerathe et al., 2017, 2018; Chuquibamba Landslide - Margirier et al., 2015; Aricota landslide - Delgado et al., 2020). (e) Paleoclimatic study in the Altiplano (Placzek et al., 2013). (f) Paleoclimatic study in lakes in the Altiplano (Martin et al., 2018, 2020). (g) Paleoclimatic study in the Atacama Desert (Ritter et al., 2018). (h, i, j) dated terraces on the western flank of the Andes (Hall et al., 2008; Steffen et al., 2010; McPhillips et al., 2013). (k) climatic fluctuations in the Atacama Desert (Ritter et al., 2019).

6. Conclusion

In this study, we focused on a spatial cluster of large paleo-landslides located along the Western Flank of the Central Andes, in the Locumba catchment, southern Peru. Selecting eight large landslides, distributed all around the giant Aricota rockslide (Delgado et al., 2020), we conducted field mapping and applied cosmogenic nuclide exposure dating on each site in order to reconstruct their failure history. Both rockslides and rock-avalanches were identified and the detailed geomorphological reconstructions of failure events were used as a basis for the sampling strategy and for the subsequent interpretation of exposure ages. Reliable timing of the triggering could be obtained for half of the studied landslides, while for the others, incompatibilities between dating and geomorphology as well as age scattering were attributed to inheritance problems. The landslides occurred during the Pleistocene with mean ages of ca. 16 ka for the Cotana rockslide, ca. 18 ka for the Antavilca rock-avalanche, ca. 114 ka for the Quilahuani rock-avalanche, and ca. 205 ka for the Angostura rockslide. Despite the fact that all those landslides are spatially clustered in a radius of less than 10 km, their chronological constraints highlight that they were triggered at different periods of time, with time lags up to several tens of thousands of years between each event. A seismic trigger is a possible interpretation for those collapses as the Locumba landslide cluster is bounded by two active crustal faults, that produced surface ruptures equivalent to several earthquakes of $M_w \sim 7$ during the last thousand years. However, the frequency of earthquake recurrence (hundreds to thousand years) differs from the timing of the landslides documented in this study. When comparing the chronicle of landslide episodes in the Locumba cluster, with the other mass movements previously dated in the Central Western Andes, as well as with Quaternary paleoclimate reconstructions and climatic proxies, some correlations emerge. Three periods characterized by mass movements activities synchronous with wet events or periods of enhanced precipitations are identified: the younger Dryas (ca. 12 ka), the Henrich stadial 1a (ca. 16-18 ka), and the MIS5, locally named "Ouki event" (100-120 ka). These results suggest that past climate changes corresponding to the shift from hyper-arid to prolonged wetter conditions played a primary role in large landslide activity in the Central Western Andes.

7. Acknowledgments

All the data used to perform this study are available in the paper and in the supplemental material. This research is part of the PhD project of Fabrizio Delgado, and also belong to agreement between IRD and INGEMMET. This work was supported by the PhD fellowship program of the EDFPCIG, by the TelluS and Alea Programs of CNRS/INSU, by the CONCYTEC/FONDECYT in the framework of the call "Movilizaciones con ECOS Nord-Perú 2019-01" 008-2020. We acknowledge the German Aerospace Centre (DLR) for providing the TANDEM-X DEM. The Astrium and the ISIS/CNES program provided the Pléiades images. The sample processing and chemical extraction of the ^{10}Be were performed at the GTC platform (ISTerre, Grenoble). We gratefully thank Francis Coeur for the sample processing. The ^{10}Be measurements were performed at the ASTER AMS national facility (CEREGE, Aix en Provence) which is supported by the INSU/CNRS, the ANR through the "Projets thématiques d'excellence" program for the "Equipements d'excellence" ASTER-CEREGE action and IRD.

8. References

- Acosta, H., Alván, A., Mamani, M., Oviedo, M., Rodríguez, J., 2011. Mapa Geológico del cuadrángulo de La Yarada (37-u), Hoja 37-u-IV. Dirección de Geología Regional (INGEMMET), Lima, Perú. Serie (A), 1 mapa.
- Armijo, R., Lacassin, R., Coudurier-Curveur, A., Carrizo, D., 2015. Coupled tectonic evolution of Andean orogeny and global climate. *Earth Science Reviews* 143, 1–35.
- Arnold, M., Aumaître, G., Bourlès, D.L., Keddaddouche, K., Braucher, R., Finkel, R.C., Nottoli, E., Benedetti, L., Merchel, S., 2013. The French accelerator mass spectrometry facility ASTER after 4 years: Status and recent developments on ^{36}Cl and ^{129}I . *Nucl. Instrum. Methods Phys. Res. B* 294, 24–28.
- Arnold, M., Merchel, S., Bourlès, D.L., Braucher, R., Benedetti, L., Finkel, R.C., Aumaître, G., Gottdang, A., Klein, M., 2010. The French accelerator mass spectrometry facility ASTER: improved performance and developments. *Nucl. Instrum. Methods Phys. Res. B Beam Interactions with Materials and Atoms* 268, 1954–1959.
- Bellido, E. & Guevara, C. (1963) - Geología de los cuadrángulos de Punta de Bombón y Cledesí. Comisión Carta Geológica Nacional, 5, 92 p.
- Bellido, E., 1979. Geología del cuadrángulo de Moquegua. INGEMMET, Boletín, Serie A: Carta Geológica Nacional 15, 78.
- Bellon, H., Lefevre, Cl, 1916. Données géochronométriques sur le volcanisme andin dans le Sud du Pérou. Implications volcano-tectoniques. *C. R. Acad. Sci.* 283, 1–4.
- Benavente, C., Wimpenny, S., Rosell, L., Robert, X., Palomino, A., Audin, L., ... & García, B. (2021). Paleoseismic Evidence of an Mw 7 Pre-Hispanic Earthquake in the Peruvian Forearc. *Tectonics*, 40(6), e2020TC006479.
- Benavente, C., Zerathe, S., Audin, L., Hall, S., Robert, X., Delgado, F., Farber, D.L., ASTER Team., 2017. Active compressional tectonics in the Andean forearc of southern Peru evidenced by direct ^{10}Be surface exposure dating of an active fault scarp. *Tectonics* 36 (9), 1662–1678.
- Bigot-Cormier, F., Braucher, R., Bourlès, D., Guglielmi, Y., Dubar, M., & Stéphan, J. F. (2005). Chronological constraints on processes leading to large active landslides. *Earth and Planetary Science Letters*, 235(1-2), 141-150.
- Blodgett, T.A., Isacks, B.L., Lenters, J.D., 1997. Constraints on the origin of paleolake expansions in the central Andes. *Earth Interact.* 1 (1), 1–28.
- Böhme, M., Hermanns, RL, Gosse, J., Hilger, P., Eiken, T., Lauknes, TR y Dehls, JF (2019). Comparación de los datos de monitoreo con las tasas de paleo-deslizamiento: la datación por nucleidos cosmogénicos detecta la aceleración de un deslizamiento de rocas. *Geología*, 47 (4), 339-342.
- Bookhagen, B., & Strecker, M. R. (2008). Orographic barriers, high-resolution TRMM rainfall, and relief variations along the eastern Andes. *Geophysical Research Letters*, 35(6).
- Borchers, B., Marrero, S., Balco, G., Caffee, M., Goehring, B., Lifton, N., Stone, J., 2016. Geological calibration of spallation production rates in the CRONUS-Earth project. *Quat. Geochronol.* 31, 188–198.

- Braucher, R., Guillou, V., Bourlès, D.L., Arnold, M., Aumaître, G., Keddadouche, K., Nottoli, E., 2015. Preparation of ASTER in-house $^{10}\text{Be}/^{9}\text{Be}$ standard solutions. *Nucl. Instrum. Methods Phys. Res. B Beam Interactions with Materials and Atoms* 361, 335–340.
- Bromley, G. R., Schaefer, J. M., Hall, B. L., Rademaker, K. M., Putnam, A. E., Todd, C. E., ... & Strand, P. D. (2016). A cosmogenic ^{10}Be chronology for the local last glacial maximum and termination in the Cordillera Oriental, southern Peruvian Andes: Implications for the tropical role in global climate. *Quaternary Science Reviews*, 148, 54-67.
- Broxton, M.J., Edwards, L.J., 2008. Lunar and Planetary Science Conference The Ames stereo pipeline: automated 3D surface reconstruction from orbital imagery, vol 39, abstract 2419.
- Cardinal, T., Audin, L., Rolland, Y., Schwartz, S., Petit, C., Zerathe, S., ... & Guillou, V. (2021). Interplay of fluvial incision and rockfalls in shaping periglacial mountain gorges. *Geomorphology*, 381, 107665.
- Çiner, A., Sarıkaya, M. A., & Yıldırım, C. (2017). Misleading old age on a young landform? The dilemma of cosmogenic inheritance in surface exposure dating: moraines vs. rock glaciers. *Quaternary Geochronology*, 42, 76-88.
- Corbett, L. B., Bierman, P. R., & Rood, D. H. (2016). An approach for optimizing in situ cosmogenic ^{10}Be sample preparation. *Quaternary Geochronology*, 33, 24-34.
- Cossart, E., Mercier, D., Decaulne, A., & Feuillet, T. (2013). An overview of the consequences of paraglacial landsliding on deglaciated mountain slopes: typology, timing and contribution to cascading fluxes. *Quaternaire. Revue de l'Association française pour l'étude du Quaternaire*, 24(1), 13-24.
- Crosta, G. B., Hermanns, R. L., Dehls, J., Lari, S., & Sepulveda, S., 2017. Rock avalanches clusters along the northern Chile coastal scarp. *Geomorphology*, 289, 27-43.
- Crosta, G.B., Utili, S., De Blasio, F.V., & Castellanza, R. (2014). Reassessing rock mass properties and slope instability triggering conditions in Valles Marineris, Mars. *Earth Planetary Science Letters*, 338, 329-343.
- Delgado, F., Zerathe, S., Audin, L., Schwartz, S., Benavente, C., Carcaillet, J., Bourles, D. L., ASTER Team, 2020. Giant landslide triggerings and paleoprecipitations in the Central Western Andes: the aricota rockslide dam (South Peru). *Geomorphology* 350. <https://doi.org/10.1016/j.geomorph.2019.106932>.
- Delgado, F., Zerathe, S., Schwartz, S., Mathieux, B., & Benavente, C. (2022). Inventory of large landslides along the Central Western Andes (ca. 15°–20° S): Landslide distribution patterns and insights on controlling factors. *Journal of South American Earth Sciences*, 116, 103824.
- Dortch, J., Owen, L.A., Haneberg, W.C., Caffee, M.W., Dietsch, C. & Kamp, D.U. 2009. Nature and timing of large landslides in the Himalaya and Transhimalaya of northern India. *Quaternary Science Reviews*, 28, 1037 –1054.
- Dunai, T.J., Lopez, G.A.G., and Juez-Larre, J., 2005, Oligocene-Miocene age of aridity in the Atacama Desert revealed by exposure dating of erosion-sensitive landforms: *Geology*, v. 33, p. 321–324, doi: 10.1130/G21184.1.

- Engel, Z., Skrzypek, G., Chuman, T., Šefrna, L., & Mihaljevič, M. (2014). Climate in the Western Cordillera of the Central Andes over the last 4300 years. *Quaternary Science Reviews*, 99, 60-77.
- Evenstar, L.A., Mather, A.E., Hartley, A.J., Stuart, F.M., Sparks, R.S.J., Cooper, F.J., 2017. Geomorphology on geologic timescales: evolution of the late cenozoic pacific paleosurface in northern Chile and southern Peru. *Earth Sci. Rev.* 171, 1–27.
- Froude, M. J., & Petley, D. N. (2018). Global fatal landslide occurrence from 2004 to 2016. *Natural Hazards and Earth System Sciences*, 18(8), 2161-2181.
- Gayo, E. M., Latorre, C., Jordan, T. E., Nester, P. L., Estay, S. A., Ojeda, K. F., & Santoro, C. M. (2012). Late Quaternary hydrological and ecological changes in the hyperarid core of the northern Atacama Desert (~ 21 S). *Earth-Science Reviews*, 113(3-4), 120-140.
- Gosse, J.C., Phillips, F.M., 2001. Terrestrial in situ cosmogenic nuclides: theory and application. *Quat. Sci. Rev.* 20 (14), 1475–1560, [http://dx.doi.org/10.1016/S0277-3791\(00\)00171-2](http://dx.doi.org/10.1016/S0277-3791(00)00171-2).
- Grämiger, L. M., Moore, J. R., Gischig, V. S., Ivy-Ochs, S., & Loew, S. (2017). Beyond debutting: Mechanics of paraglacial rock slope damage during repeat glacial cycles. *Journal of Geophysical Research: Earth Surface*, 122(4), 1004-1036.
- Gunnell, Y., Thouret, J.C., Bricchau, S., Carter, A., Gallagher, K., 2010. Low-temperature thermochronology in the Peruvian Central Andes: implications for long-term continental denudation, timing of plateau uplift, canyon incision and lithosphere dynamics. *J. Geol. Soc.* 167 (4), 803–815.
- Hall, S. R., D. L. Farber, L. Audin, R. C. Finkel, and A. S. Mériaux, 2008. Geochronology of pediment surfaces in southern Peru: Implications for Quaternary deformation of the Andean forearc, *Tectonophysics*, 459(1), 186– 205, doi:10.1016/j.tecto.2007.11.073
- Hall, S.R., Farber, D.L., Audin, L., Finkel, R.C., 2012. Recently active contractile deformation in the forearc of southern Peru. *Earth Planet. Sci. Lett.* 337, 85-92.
- Hermanns, R., Oppikofer, T., Dahle, H., Eiken, T., Ivy-Ochs, S., Blikra, L., 2013. Understanding long-term slope deformation for stability assessment of rock slopes: the case of the Oppstadhornet rockslide, Norway. *Ital. J. Eng. Geol. Environ. Book Ser.* 6, 255–264
- Heyman, J., Stroeve, A. P., Harbor, J. M., & Caffee, M. W. (2011). Too young or too old: evaluating cosmogenic exposure dating based on an analysis of compiled boulder exposure ages. *Earth and Planetary Science Letters*, 302(1-2), 71-80.
- Hilger, P., Gosse, J. C., & Hermanns, R. L. (2019). How significant is inheritance when dating rockslide boulders with terrestrial cosmogenic nuclide dating? - a case study of an historic event. *Landslides*, 16(4), 729-738.
- Ivy-Ochs, S., Poschinger, A. V., Synal, H. A., & Maisch, M. (2009). Surface exposure dating of the Flims landslide, Graubünden, Switzerland. *Geomorphology*, 103(1), 104-112.
- Junquera-Torrado, S., Moreiras, S.M., Sepúlveda, S.A., 2019. Distribution of landslides along the Andean active orogenic front (Argentinean Precordillera 31–33° S). *Quat. Int.* 512, 18–34.

- Keefer, D. K., Moseley, M. E., & DeFrance, S. D., 2003. A 38 000-year record of floods and debris flows in the Ilo region of southern Peru and its relation to El Niño events and great earthquakes. *Palaeogeography, Palaeoclimatology, Palaeoecology*, 194(1-3), 41-77.
- Korup, O., Clague, J.J., Hermanns, R.L., Hewitt, K., Strom, A.L., Weidinger, J.T., 2007. Giant landslides topography and erosion. *Earth Planet Sci. Lett.* 261, 578–589.
- Lal, D. (1991). Cosmic ray labeling of erosion surfaces: in situ nuclide production rates and erosion models. *Earth and Planetary Science Letters*, 104(2-4), 424-439.
- Larsen, I. J., & Montgomery, D. R. (2012). Landslide erosion coupled to tectonics and river incision. *Nature Geoscience*, 5(7), 468-473.
- Larsen, N. K., Søndergaard, A. S., Levy, L. B., Laursen, C. H., Bjørk, A. A., Kjeldsen, K. K., ... & Kjær, K. H. (2021). Cosmogenic nuclide inheritance in Little Ice Age moraines-A case study from Greenland. *Quaternary Geochronology*, 65, 101200.
- Le Roux, O., Jongmans, D., Kasperski, J., Schwartz, S., Potherat, P., Lebrouc, V., ... & Meric, O. (2011). Deep geophysical investigation of the large Séchilienne landslide (Western Alps, France) and calibration with geological data. *Engineering Geology*, 120(1-4), 18-31.
- Lebourg, T., Zerathe, S., Fabre, R., Giuliano, J., & Vidal, M. (2014). A Late Holocene deep-seated landslide in the northern French Pyrenees. *Geomorphology*, 208, 1-10.
- Lifton, N., Sato, T., Dunai, T.J., 2014. Scaling in situ cosmogenic nuclide production rates using analytical approximations to atmospheric cosmic-ray fluxes. *Earth Planet. Sci. Lett.* 386, 149–160, <http://dx.doi.org/10.1016/j.epsl.2013.10.052>.
- Litty, C., Schlunegger, F., Akçar, N., Delunel, R., Christl, M., & Vockenhuber, C. (2018). Chronology of alluvial terrace sediment accumulation and incision in the Pativilca Valley, western Peruvian Andes. *Geomorphology*, 315, 45-56.
- Litty, C., Schlunegger, F., Akçar, N., Lanari, P., Christl, M., & Vockenhuber, C. (2019). Possible climatic controls on the accumulation of Peru's most prominent alluvial fan: The Lima Conglomerate. *Earth surface processes and landforms*, 44(5), 991-1003.
- Mamani, M., Navarro, P., Carlotto, V., Acosta, H., Rodríguez, J., Jaimes, F., Santos, A., Rodríguez, R., Chavez, L., Cueva, E., Cereceda, C., 2010. Arcos magmáticos meso-cenozoicos del Perú. In: XV Congreso Peruano de Geología, Cusco. Sociedad Geológica del Perú, Resúmenes Extendidos, pp. 563–566.
- Mamani, M., Rodríguez, R., Acosta, H., Jaimes, F., Navarro, P., Carlotto, V., 2012. Características litológicas y geoquímicas más resaltantes de los arcos magmáticos del Peru desde el Ordovícico. XVI Congreso Peruano de Geología, p. 5 resúmenes extendidos.
- Mamani, M., Tassara, A., & Wörner, G., 2008. Composition and structural control of crustal domains in the central Andes. *Geochemistry, Geophysics, Geosystems*, 9(3).
- Margirier, A. Audin, L., Carcaillet, J., Schwartz, S., 2015. Tectonic and climatic controls on the Chuquibamba landslide (western Andes, southern Peru). *Earth Surf. Dynam. Discuss.* 2, 1129–1153.
- Martin, L. C. P., Blard, P. H., Balco, G., Lavé, J., Delunel, R., Lifton, N., & Laurent, V. (2017). The CREP program and the ICE-D production rate calibration database: A fully parameterizable

and updated online tool to compute cosmic-ray exposure ages. *Quaternary geochronology*, 38, 25-49.

Martin, L. C., Blard, P. H., Lavé, J., Condom, T., Prémaillon, M., Jomelli, V., Tibari, B. & ASTER Team., 2018. Lake Tauca highstand (Heinrich Stadial 1a) driven by a southward shift of the Bolivian High. *Science advances*, 4(8), eaar2514.

Martin, L. C., Blard, P. H., Lavé, J., Jomelli, V., Charreau, J., Condom, T., ... & Keddadouche, K. (2020). Antarctic-like temperature variations in the Tropical Andes recorded by glaciers and lakes during the last deglaciation. *Quaternary Science Reviews*, 247, 106542.

Mathieux, B. 2021. Comparative analysis between fluvial network characteristics and giant paleo-landslide processes along the Central Western Andes. Master's thesis, Geodynamics-UGA.

McPhillips, D., Bierman, P. R., Crocker, T., & Rood, D. H. (2013). Landscape response to Pleistocene-Holocene precipitation change in the Western Cordillera, Peru: ^{10}Be concentrations in modern sediments and terrace fills. *Journal of Geophysical Research: Earth Surface*, 118(4), 2488-2499.

Monge, R., Cervantes, J., 2000. Memoria explicativa de la geología del cuadrángulo de Pachía (36v) y Palca (36x). Dirección de Geología Regional del INGEMMET, Lima, Perú, p. 11.

Montgomery, D. R., 2001. Slope distributions, threshold hillslopes, and steady-state topography. *American Journal of science*, 301(4-5), 432-454.

Oswald, P., Strasser, M., Hammerl, C., & Moernaut, J. (2021). Seismic control of large prehistoric rockslides in the Eastern Alps. *Nature communications*, 12(1), 1-8.

Pánek, T. (2015). Recent progress in landslide dating: a global overview. *Progress in Physical Geography*, 39(2), 168-198.

Pánek, T., 2019. Landslides and Quaternary climate changes—the state of the art. *Earth Sci. Rev.* 196, 102871.

Pánek, T., Mentlík, P., Engel, Z., Braucher, R., Zondervan, A., & Team, A. (2017). Late Quaternary sackungen in the highest mountains of the Carpathians. *Quaternary Science Reviews*, 159, 47-62.

Petley, D. (2012). Global patterns of loss of life from landslides. *Geology*, 40(10), 927-930.

Pinto, L., Hérail, G., Sepúlveda, S. A., & Krop, P., 2008. A Neogene giant landslide in Tarapacá, northern Chile: A signal of instability of the westernmost Altiplano and palaeoseismicity effects. *Geomorphology*, 102(3-4), 532-541.

Placzek, C., Quade, J., Betancourt, J. L., Patchett, P. J., Rech, J. A., Latorre, C., ... & English, N. B. (2009). Climate in the dry central Andes over geologic, millennial, and interannual timescales. *Annals of the Missouri Botanical Garden*, 96(3), 386-397.

Placzek, C.J., Quade, J., Patchett, P.J., 2013. A 130 ka reconstruction of rainfall on the Bolivian Altiplano. *Earth and Planetary Science Letters*, 363, 97-108

Quade, J., Rech, J. A., Betancourt, J. L., Latorre, C., Quade, B., Rylander, K. A., & Fisher, T. (2008). Paleowetlands and regional climate change in the central Atacama Desert, northern Chile. *Quaternary Research*, 69(3), 343-360.

- Ritter, B., Binnie, S. A., Stuart, F. M., Wennrich, V., & Dunai, T. J. (2018). Evidence for multiple Plio-Pleistocene lake episodes in the hyperarid Atacama Desert. *Quaternary Geochronology*, 44, 1-12.
- Ritter, B., Wennrich, V., Medialdea, A., Brill, D., King, G., Schneiderwind, S., ... & Dunai, T. J. (2019). Climatic fluctuations in the hyperarid core of the Atacama Desert during the past 215 ka. *Scientific reports*, 9(1), 1-13.
- Rivera, M., Samaniego, P., Vela, J., Le Pennec, J.L., Guillou, H., Paquette, J.L., Liorzou, C., 2020. The eruptive chronology of the Yucamane-Calientes compound volcano: a potentially active edifice of the Central Andes (southern Peru). *J. Volcanol. Geoth. Res.* 393, 106787.
- Roering, J., 2012. Landslides limit mountain relief. *Nature Geoscience*, 5(7), 446-447.
- Roperch, P., Sempere, T., Macedo, O., Arriagada, C., Fornari, M., Tapia, C., García, M., Laj, C., 2006. Counterclockwise rotation of late Eocene-Oligocene fore-arc deposits in southern Perú and its significance for oroclinal bending in the central Andes. *Tectonics* 25 (3), 1–29. <https://doi.org/10.1029/2005TC001882>.
- Salinas, E., 1985. Evolución paleogeográfica del Sur del Perú a la luz de los métodos de análisis sedimentológico de las series del Departamento de Tacna. Tesis de grado. UNSA, Arequipa.
- Sanchez, G., Rolland, Y., Corsini, M., Braucher, R., Bourlès, D., Arnold, M., & Aumaître, G. (2010). Relationships between tectonics, slope instability and climate change: cosmic ray exposure dating of active faults, landslides and glacial surfaces in the SW Alps. *Geomorphology*, 117(1-2), 1-13.
- Schildgen, T.F., Hodges, K.V., Whipple, K.X., Pringle, M.S., van Soest, M., Cornell, K., 2009. Late Cenozoic structural and tectonic development of the western margin of the central Andean Plateau in southwest Peru. *Tectonics* 28, TC4007. <https://doi.org/10.1029/2008TC002403>.
- Schildgen, T.F., Hodges, K.V., Whipple, K.X., Reiners, P.W., Pringle, M.S., 2007. Uplift of the western margin of the Andean plateau revealed from canyon incision history, southern Peru. *Geology* 35, 523–526.
- Schwartz, S., Zerathe, S., Jongmans, D., Baillet, L., Carcaillet, J., Audin, L., ... & Lebrouc, V. (2017). Cosmic ray exposure dating on the large landslide of Séchilienne (Western Alps): A synthesis to constrain slope evolution. *Geomorphology*, 278, 329-344.
- Steffen, D., F. Schlunegger, and F. Preusser (2010), Late Pleistocene fans and terraces in the Majes valley, southern Peru, and their relation to climatic variations, *Int. J. Earth Sci.*, 99(8), 1975– 1989.
- Steffen, D., Schlunegger, F., & Preusser, F. (2009). Drainage basin response to climate change in the Pisco valley, Peru. *Geology*, 37(6), 491-494.
- Thouret, J. C., Gunnell, Y., Jicha, B. R., Paquette, J. L., & Braucher, R., 2017. Canyon incision chronology based on ignimbrite stratigraphy and cut-and-fill sediment sequences in SW Peru documents intermittent uplift of the western Central Andes. *Geomorphology*, 298, 1-19.
- Thouret, J.C.; Wörner, G.; Gunnell, Y.; Singer, B.; Zhang, X.; Souriot, T., 2007. Geochronologic and stratigraphic constrains on canyon incision and Miocene uplift of the Central Andes in Perú. *Earth and Planetary Science Letters* 263: 151-166.

- Valagussa, A., Marc, O., Frattini, P., Crosta, G.B., 2019. Seismic and geological controls on earthquake-induced landslide size. *Earth Planet Sci. Lett.* 506, 268–281.
- Vicente, J.C.; Beaudoin, B.; Chávez, A. & León, I., (1982) – La cuenca de Arequipa (Sur Perú) durante el Jurásico-Cretácico inferior. En: Congreso Latinoamericano de Geología, 5, Buenos Aires, 1982. Actas. Buenos Aires: Servicio Geológico Nacional, t. 1, p. 121-153.
- Villegas-Lanza, J. C., Chlieh, M., Cavalié, O., Tavera, H., Baby, P., Chire-Chira, J., & Nocquet, J. M., 2016. Active tectonics of Peru: Heterogeneous interseismic coupling along the Nazca megathrust, rigid motion of the Peruvian Sliver, and Subandean shortening accommodation. *Journal of Geophysical Research: Solid Earth*, 121(10), 7371-7394.
- Wallemacq, P., & House, R., 2018. Economic losses, poverty & disasters. Centre for Research on the Epidemiology of Disasters and United Nations Office for Disaster Risk Reduction, Geneva, 1-30.
- Whipple, K. X., E. Kirby, and S. H. Brocklehurst (1999), Geomorphic limits to climate-induced increases in topographic relief, *Nature*, 401, 39– 43.
- Wilson, J., García, W., 1962. Geología de los Cuadrángulos de Pachia y Palca. Comisión de la Carta Geológica Nacional 2 (4), 1–81.
- Wörner, G., Hammerschmidt, K., Henjes-Kunst, F., Lezaun, J., Wilke, H., 2000. Geochronology ($^{40}\text{Ar}/^{39}\text{Ar}$, K-Ar and He-exposure ages) of Cenozoic magmatic rocks from northern Chile ($18\text{-}22^\circ\text{ S}$): implications for magmatism and tectonic evolution of the central Andes. *Rev. Geol. Chile* 27, 205–240.
- Zerathe S., Blard P-H., Audin L., Braucher R., Bourles D., Carcaillet J., Benavente C., Delgado F., AsterTeam., 2017. Toward the feldspar alternative for cosmogenic ^{10}Be exposure dating. *Quaternary Geochronology* 41, 83-96. <https://doi.org/10.1016/j.quageo.2017.06.004>.
- Zerathe, S., Lebourg, T., Braucher, R., & Bourlès, D. (2014). Mid-Holocene cluster of large-scale landslides revealed in the Southwestern Alps by ^{36}Cl dating. Insight on an Alpine-scale landslide activity. *Quaternary Science Reviews*, 90, 106-127.
- Zerathe, S., Pierre-Henri, B., Régis, B., Didier, B., Laurence, A., Julien, C., ... & Team, A. (2018, April). Toward the feldspar alternative for cosmogenic ^{10}Be applications. In EGU General Assembly Conference Abstracts (p. 14977).

CHAPTER V:
CONCLUSIONS AND PERSPECTIVES



CHAPTER 5: CONCLUSIONS AND PERSPECTIVES

1. Conclusions

Landslides are gravitational phenomena that affect society, in many cases resulting in economic loss and people death. These processes can be triggered by climatic, tectonic or anthropogenic events. Some of the largest landslides, and that are among the most destructive, occur mostly on mountain fronts such as the Andes, Himalayas, Alps (and others) because these places cumulate strong reliefs, steep slopes, active tectonics and frequently strong seasonal precipitations. The main reasons that motivated a focus on the Central Western Andes during this PhD thesis include the facts that (1) since now, those processes were only poorly studied and misunderstood in this region despite a strong level of hazard ; (2) that, due to its low erosion and dominant aridity, the Central Andes offers an interesting case of study to improve our knowledge on landslides evolution and triggering on long time-scales (i.e. beyond the Holocene) In this context, first order questions have guided our research during this PhD project : What are the characteristics of the large landslides (type, size, abundance, spatial, distribution, etc.) along the Western flank of the Central Andes? What can we learn from those characteristics about the factors that conditioned their developments? What is the chronology of these landslides and what can be deduced from this chronology to better understand their factors of triggering?

To answer those questions, our research was based on a pluridisciplinary approach which included (1) geomorphological studies combining field mapping and analyses, study of satellite images and digital elevation models, and (2) geochronological studies based on cosmogenic nuclide dating.

Our strategy was based on three scales of study: i) a regional-scale though the inventory of large landslides along the south Peru and the north Chile, ii) a local-scale (slope-scale) with a detailed analysis and dating of an emblematic large landslide of the southern Peru and iii) an intermediate-scale with the dating of several landslides in an area of high concentration of landslide. The results were presented through three main chapters based on two published papers (Delgado et al., 2020 and Delgado et al., 2022) and a third one currently ready for submission (Delgado et al., in prep).

In the first part, our regional-scale study focused on mapping and inventorying all major landslides along the western flank of the Central Andes between latitudes 15 and 20° S (Delgado et al., 2022). The main objective was to search for control patterns for landslide formation. The mapping was carried out using satellite imagery, Google Earth, DEM and field verifications. We inventoried more than a thousand large landslides $> 0,1 \text{ km}^2$, identifying two main types of mass movements: rockslides (86% of the inventory) and rock-avalanches (14% of the inventory). Most of the mass movements mapped were identified as paleo slope-failures (>90 %). Crossing this landslide database with geological background settings, a combination of primary conditioning factors including lithology and local relief produced by the main valleys was identified, revealing in particular a strong susceptibility of the ignimbrites of the Paleogene-Neogene (Huayllillas Formation) to generate large-scale slope failures. Analyzing the spatial distribution of landslides at the regional scale, we highlighted several landslide clusters, grouping dozens of large slope failures in radiuses of $\sim 20 \text{ km}$. According to this landslide distribution and its spatial concordance with the main crustal faults of the Western Cordillera, we discussed the possible role played by those tectonic structures for the initiation of landslides (relief construction, long term rock weathering, seismic trigger). Finally, comparing the location paleo-landslides, that are dominant along the arid Western Cordillera, with the location of active landslides, that are more frequent in the northern regions receiving seasonal rainfall, we suggested that the triggering of paleo-

landslides was unlikely to occur in such very arid conditions, calling for more absolute dating of landslide to explore the question of their possible link with past climate variations.

In the second part, we focus on one of the largest landslide of the southern Peru: the Aricota rockslide dam, located in the Locumba valley (Delgado et al., 2020). Detailed geomorphological mapping was combined with cosmogenic nuclide dating to document the timing of those failures and to provide the necessary temporal frame for discussing the context their triggers. The results indicate the occurrence of two events. The first was a rockslide, dated at 17.9 ± 0.7 ka, that filled the Locumba valley and formed a dam with a height of ~ 600 m, generating a lake reservoir of ~ 6 km long. The second event was a rock avalanche, dated at 12.1 ± 0.2 ka, which debris were deposited on top of the rockslide dam of the first event. The chronology of these successive slope failures coincides with paleoclimatic events recorded on the Altiplano: the Heinrich Stadial 1a and the Younger Dryas. Both events were characterized by increased precipitation, leading to glacier advances and Altiplano lakes water level increase. This correlation suggested that climate may have played an important role in the triggering of the Aricota landslide, however, the effect of concomitant earthquake could not be ruled out.

In the third part, making use of the expertise and the knowledge acquired on the Aricota rockslide, we expanded our dating approach to several others large landslides identified all around the Aricota site that we named the "Locumba landslide cluster". Eight landslides of different typologies (rockslides and rock-avalanches) were selected. The main objective of this study was to test whether the landslides forming the Locumba spatial cluster occurred synchronously or not, further exploring the condition of landslide triggering in this valley. On each site, we performed geomorphological reconstructions, with mapping of the successive internal events, completed by cosmogenic nuclide exposure dating. A reliable chronology could be obtained for half of the studied landslides, while for the others the results showed an overdispersion of ages interpreted as problems related to cosmogenic nuclide inheritance. The dated landslides occurred all during the Pleistocene: the Cotana rock avalanche at ca. 16 ka, the Antavilca rock-avalanche at ca. 18 ka, the Quilahuani rock-avalanche at ca. 114 ka and the Angostura rockslide at ca. 205 ka. Consequently, although being spatially clustered, the chronology of these landslides indicates different periods of occurrence of slope failures revealing a long history of triggering. It could be argued that a seismic trigger could have been the cause of these events, since these landslides are located close to two neotectonics crustal faults that produced $M_w \sim 7$ earthquakes in the last thousand years. On the other hand, comparing the landslide chronology of this PhD together with other, previously published, landslide dating, with Quaternary paleoclimate reconstructions and with climate proxies, more systematic correlations were observed. Once again, compatible timing was found between the Heinrich 1a stadial (ca. 16-18 ka) and the occurrence of two additional large landslides in the Locumba valley. Moreover, we found a synchronicity between another older wet event during the MIS 5, called the "Ouki event" (100-120 ka), and the triggering of the Quilahuani rock-avalanche (ca. 114 ka), the Chuquibamba landslide (ca. 102 ka; Margirier et al., 2015) and the latest events of the Caquilluco rock-avalanche complex (ca. 100-120 ka; Zerathe et al., 2017). Altogether, those results favor a vision where temporary, but strong, environmental and climatic changes, from arid to more humid weather, were responsible for the triggering of large landslides, erosion pulses and significant landscape perturbations in the Central Western Andes during the Quaternary.

2. Perspectives

We propose here below some perspectives in the continuity of the research developed during this PhD.

- **The potential of Artificial Intelligence for automatic recognition and mapping of large landslides**

Recent studies have reported the use of Artificial Intelligence (AI) and deep learning systems to automatically map landslides. For example, Prasad et al., (2021) used AI to prepare landslide susceptibility maps in India. They divided the mapped landslides into two groups, the first was for training purposes for the program and the second group of landslides was for validation of the results. They conclude that this new methodology is effective and promising for landslide susceptibility assessment. Schönfeldt et al. (2022) trained two Convolutional Neural Networks (CNNs, AlexNet and U-Net) to detect large landslides in Patagonia. They used optical data (Sentinel-2) and topographic data (TanDEM-X) on elevation, surface roughness and curvature to train the program. Confronting results to field evidences they conclude that CNNs can be a good and powerful tool for detecting large landslides at regional-scales although visual inspection should be still recommended for validation and to correctly delimit landslides.

The use such automated AI systems could be very interesting in the case the arid Central Western Andes. According to the previous attempts cited here above, we can expect that this methodology would be particularly efficient on our study area because the morphologies are very well preserved (almost intact) due to the aridity and the absence of vegetation. Using the landslide database that we built, we could train the CNNs and then run it again on our study area to detect more landslides. Then, once the systems trained, this would also allow to extend the landslide mapping to north and to the south of the study area of this PhD. Such an automatic mapping could strongly reduce the mapping time in comparison to manual mapping only. Additionally, the deep learning based on our database of landslides, acquired in arid environments such as the western flank of the Central Andes, could be a useful base for landslide recognition in other arid environments of the World and even on other telluric planets such as Mars.

- **Criteria and improvement for landslide dating**

During the application of the Cosmogenic Nuclide (CN) dating tool to constrain the timing of landslides, we encountered some problems with the inherited content of CN at shallow depth. As previously discussed, the strong presence of inheritance in our cases seems to be specific to the areas that experienced long-term aridity, such as the Central Andes, because it strongly limits erosion and because Quaternary glaciations almost never reach elevations below 5000 m there. Thus, on one hand such regions offer a strong potential to study long term evolution of landscape, but on the other hand inheritance problem with the CN can arise, limiting its use. In order to get around this problem, we would recommend to (i) combine CN sampling with Schmidt hammer that allow to test the relative age of the boulders according to its state of erosion; (ii) to combine boulders and scarp samples if possible; (iii) to combine multiple dating techniques (Pánek, T., 2015) such as OSL when some lacustrine deposits are trapped behind the slided mass. In this way, one will be able to improve the methodology by cross-checking information and it will ensure a more complete history of the landslide.

- **Progressive landslide failure and link with ultimate collapse triggering**

In chapters 3 and 4, the dated landslides were mass movements that have already collapsed. It would be interesting to investigate and to date landslides that have not yet collapsed, but that are in the process of formation, affected by progressive failure. The landslide to be studied could be the Antavilca rockslide. This landslide has the same dimensions as the Aricota rockslide (width and height). In a first stage of this PhD, we were thinking to included this case in our dating strategy. Thus this rockslide was sampled but, because of covid crisis and lack of time, we were not able to process the samples. Sampling profiles were made along the main escarpments of the landslide (Figure 1), with the aim of finding out when the landslide began to form, estimating the speed of its movement and identifying the stages in which the movement of the landslide accelerated. This could be another interesting contribution to better understand the evolution and triggering of large landslides in the Central Andes.

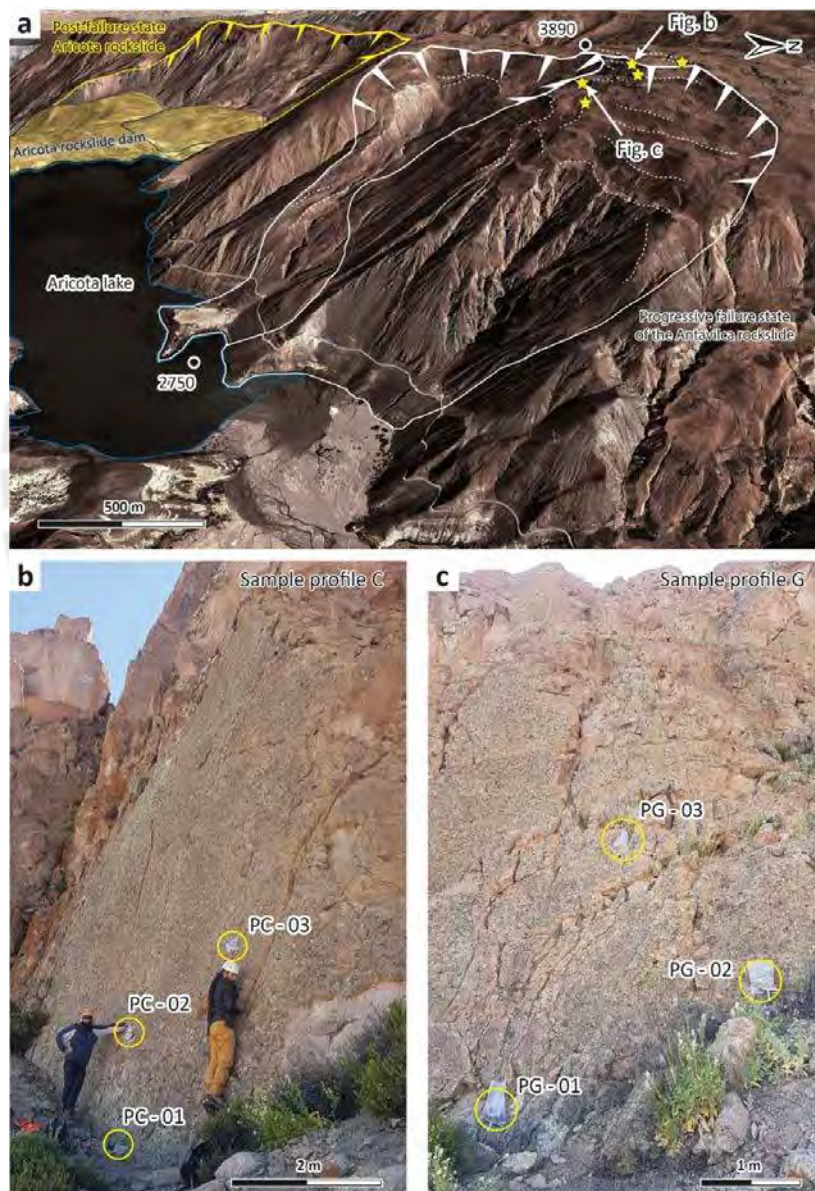


Figure 1. (a) Google Earth perspective view of the Antavilca rockslide, the dotted lines are main scarp though the mass affected by progressive failure. The yellow stars are the locations where sampling profiles were performed. (b) and (c) examples of sample collection along the scarps of the Antavilca rockslide.

- **Toward a better mitigation of landslide hazard in Peru**

In order to contribute to landslide risk management plans in Peru, the inventory and database of landslides on the western flank of the Peruvian Andes could be expanded. The first part of the landslide inventory for the western flank of the Central Andes should be used in the work of INGEMMET, the Peruvian Geological Survey. In addition, it could be proposed to implement a paleo-landslide inventory layer in the GEOCATMIN - INGEMMET viewer, as these are potential instability zones for the future. Our regional-scale landslide mapping also reveals an increased susceptibility of some lithological layers which should now be considered in the hazard maps.

Another complementary approach could be the use of InSAR (Interferometric Synthetic Aperture Radar) to detect active landslides. The InSAR methodology is based on the phase difference measurement between two or more SAR images of the same location, but from different time periods of acquisition. It allows to detect very small surface displacements (few mm/yr) whereas larger displacements can be revealed by InSAR decorrelation. Currently, a great opportunity is offered by the products provided by the ForM@Ter Large-scale Sentinel-1 Multi-Temporal Interface Sentinel-1 (FLATSIM) service which processed a massive quantity of multi-temporal Sentinel-1 data (Thollard et al., 2021). In particular, they covered most of the Central Andes of Peru and Chile, providing a map of surface displacement cumulated over the period 2014-2021 (see example on Figure 2A). Those data look very promising as we can see on this displacement map the signal from large-scale plate convergence, the continuous uplift of some volcanos, the impact of anthropogenic projects such as open mining extraction, the surface ruptures of some faults associated to the last earthquakes and also several landslides (Figure 2A and 2B). First steps that could be conducted about landslides could be : (1) to compare this displacement map with our landslide database to check the state of activity of the landslides inventoried, (2) to verify our classification of active and paleo-landslides; (3) to explore whether other slopes could have been affected by slow deformations missed during our mapping. Additionally to the cumulated surface displacement, each pixel contains time-series of displacement covering the 6 years of study (Thollard et al., 2021) and which could allow to study the response of landslides to specific forcing such as contemporaneous earthquakes or strong rainfall.

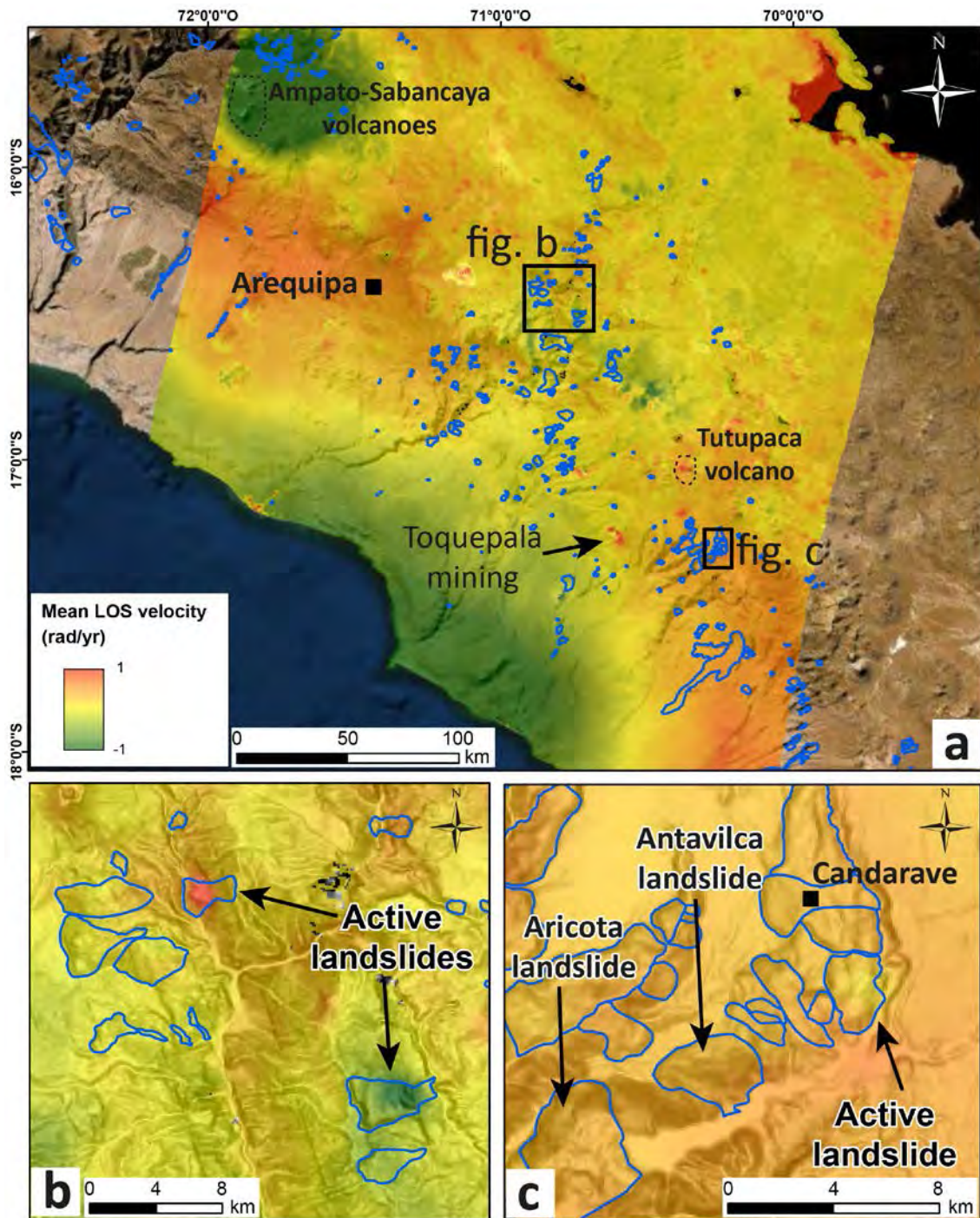


Figure 2. (a) Example of surface displacement map produced by FLATSIM by the massive processing of multi-temporal Sentinel-1 data (positive displacements are away from the satellite). Landslide polygons (in blue) are reported for comparison from Delgado et al. (2022). (b) Close up view on some large landslides where InSAR results indicate some active cases. (c) Close up view on the Locumba landslide cluster where a large landslide below orrelation of landslide mapping with deformation areas recorded in the InSAR model.

References:

- Delgado, F., Zerathe, S., Audin, L., Schwartz, S., Benavente, C., Carcaillet, J., Bourles, D. L., ASTER Team, 2020. Giant landslide triggerings and paleoprecipitations in the Central Western Andes: the aricota rockslide dam (South Peru). *Geomorphology* 350. <https://doi.org/10.1016/j.geomorph.2019.106932>.
- Delgado, F., Zerathe, S., Schwartz, S., Mathieux, B., & Benavente, C. (2022). Inventory of large landslides along the Central Western Andes (ca. 15°–20° S): Landslide distribution patterns and insights on controlling factors. *Journal of South American Earth Sciences*, 116, 103824.
- Margirier, A., Audin, L., Carcaillet, J., Schwartz, S., 2015. Tectonic and climatic controls on the Chuquibamba landslide (western Andes, southern Peru). *Earth Surf. Dynam. Discuss.* 2, 1129–1153.
- Pánek, T. (2015). Recent progress in landslide dating: a global overview. *Progress in Physical Geography*, 39(2), 168-198.
- Prasad, P., Loveson, V. J., Das, S., & Chandra, P. (2021). Artificial intelligence approaches for spatial prediction of landslides in mountainous regions of western India. *Environmental Earth Sciences*, 80(21), 1-20.
- Schönfeldt, E., Winocur, D., Pánek, T., & Korup, O. (2022). Deep learning reveals one of Earth's largest landslide terrain in Patagonia. *Earth and Planetary Science Letters*, 593, 117642.
- Thollard, F., Clesse, D., Doin, M. P., Donadieu, J., Durand, P., Grandin, R., ... & Specht, B. (2021). FLATSIM: The ForM@ Ter LARge-Scale Multi-Temporal Sentinel-1 InterferoMetry Service. *Remote Sensing*, 13(18), 3734.
- Zerathe, S., Blard, P.H., Audin, L., Braucher, R., Bourles, D., Carcaillet, J., Benavente, C., Delgado, F., AsterTeam, 2017. Toward the feldspar alternative for cosmogenic ¹⁰Be exposure dating. *Quat. Geochronol.* 41, 83–96.

ANNEXES

Participation in conferences:

Delgado, F., Zerathe, S., Schwartz, S., Benavente, C., Robert, X., Gaidzik, K., ... & Team, A. (2021, April). 10Be dating reveal a one-million-years records of landslide activities in the Central Western Andes. In EGU General Assembly Conference Abstracts (pp. EGU21-13580).

Fabrizio, D., Swann, Z., Stéphane, S., & Carlos, B. (2020). Large landslides database along the Central Western Andes (15°-20° S): constraints on mass-movement development and implications on relief evolution (No. EGU2020-10169). Copernicus Meetings.

Delgado Madera, G. F., Zerathe, S., Schwartz, S., Benavente Escobar, C. L., Audin, L., Carcaillet, J., & Team, A. (2019). What are the main factors that trigger the giant-landslides in the Peruvian western Andes? The Aricota giant-landslide case study. 8th International Symposium on Andean Geodynamics (ISAG).

Gérard, B., Robert, X., Audin, L., Gautheron, C., Bernet, M., Benavente Escobar, C. L., & Delgado Madera, G. F. (2019). Differential exhumation driven by Tectonic processes in the Abancay deflection (Peruvian Andes). 8th International Symposium on Andean Geodynamics (ISAG).

EGU21-13580

<https://doi.org/10.5194/egusphere-egu21-13580>

EGU General Assembly 2021

© Author(s) 2022. This work is distributed under the Creative Commons Attribution 4.0 License.



¹⁰Be dating reveal a one-million-years records of landslide activities in the Central Western Andes

Fabrizio Delgado^{1,2}, Swann Zerathe², Stephane Schwartz², Carlos Benavente³, Xavier Robert², Krzysztof Gaidzik⁴, Julien Carcaillet², and Aster Team⁵

¹Especialidad Ingeniería Geológica, Facultad de Ciencias e Ingeniería. Pontificia Universidad Católica del Perú, Av.

Universitaria 1801, San Miguel, Lima 15088, Perú (delgado.f@pucp.edu.pe)

²Univ. Grenoble Alpes, Univ. Savoie Mont Blanc, CNRS, IRD, IFSTTAR, ISTerre, 38000 Grenoble, France (swann.zerathe@ird.fr / stephane.schwartz@univ-grenoble-alpes.fr / xavier.robert@univ-grenoble-alpes.fr / julien.carcaillet@univ-grenoble-alpes.fr)

³Instituto Geológico, Minero y Metalúrgico INGEMMET, Av. Canadá 1470, Lima, Perú. (cbenavente@ingemmet.gob.pe)

⁴Institute of Earth Sciences, University of Silesia, Będzińska 60, 41-200 Sosnowiec, Poland (k.gaidzik@gmail.com)

⁵Aix-Marseille Univ., CNRS, IRD, Coll. France, UM 34 CEREGE, Technopôle de l'Environnement Arbois-Méditerranée, BP80, 13545 Aix-en-Provence, France

The western flank of the Central Andes shows a high concentration of giant landslides (Strasser and Schlunegger, 2005; Audin & Bechir 2006; Pinto et al., 2008; Matther et al., 2014; Crosta et al., 2014, Margirier et al., 2015; Zerathe et al., 2017; Delgado et al., 2020) related to specific characteristics such as a strong local relief (canyons, structural-flexures, etc.), strong and recurrent seismo-tectonic activities, and atypical climate combining long-term hyper-aridity and punctual extreme precipitation events. In this context, ongoing studies inventorying more than one-thousand giant paleo-landslides in this region underline their spatial clustering that is controlled by coupled conditioning factors including high topographical gradients and specific lithology (Delgado et al., 2020).

The purpose of this study is to constrain now the kinematics of landsliding and ultimately to get time-frequency law of the gravitational slope destabilizations of this Andean region. For this, we focus on the Locumba valley (south Peru) where more than 30 giant landslides are clustered and distributed in two main typologies (rockslide and rock-avalanche). We applied cosmogenic nuclide dating to 8 paleo-landslides, sampling 52 boulders. We used alternatively ¹⁰Be/quartz or ¹⁰Be/feldspar depending on the available lithology.

Our dataset opens an unprecedented opportunity for paleolandslides studies and reconstructions. Indeed, the exposure-ages obtained range from the Holocene to the Pleistocene, the oldest ages reaching one-million years. This new temporal-scale allows to address and discuss triggering processes in the context of seismo-tectonic activities and Quaternary climate changes. Exposure-ages distribution shows several time-frequency peaks suggesting that gravitational destabilizations are episodic phenomena with time recurrence on the range of ~100 ka. Additionally, our time-constraints indicate that most of the current landscapes along this Western

Andean flank are older than one-million years. Especially, fluvial incision and valley deepening processes are currently very low as testified by relicts of landslide dams and associated lacustrine sediments of hundred's thousand years old that are preserved along the main canyons and still not fully re-incised.



EGU2020-10169, updated on 31 Aug 2022
<https://doi.org/10.5194/egusphere-egu2020-10169>
EGU General Assembly 2020
© Author(s) 2022. This work is distributed under
the Creative Commons Attribution 4.0 License.



Large landslides database along the Central Western Andes (15° - 20° S): constraints on mass-movement development and implications on relief evolution

Delgado Fabrizio^{1,2}, Zerathe Swann², Schwartz Stéphane², and Benavente Carlos³

¹Especialidad Ingeniería Geológica, Facultad de Ciencias e Ingeniería. Pontificia Universidad Católica del Perú, Av. Universitaria 1801, San Miguel, Lima 15088, Perú (delgado.f@pucp.edu.pe)

²Univ. Grenoble Alpes, Univ. Savoie Mont Blanc, CNRS, IRD, IFSTTAR, ISTERRE, 38000 Grenoble, France (swann.zerathe@ird.fr / stephane.schwartz@univ-grenoble-alpes.fr)

³Instituto Geológico, Minero y Metalúrgico INGEMMET, Av. Canadá 1470, Lima, Perú. (cbenavente@ingemmet.gob.pe)

The western flank of the central Andes presents an exceptional concentration of large paleo-landslides ($v > 100 \times 10^6 \text{ m}^3$), most of which being well-preserved morphologies due to low erosion and weathering related to the hyper-arid climate of the Atacama Desert since the Miocene. First order questions are pending about the triggering of those mass-movements, their dynamics, their locations and their roles on the Andean relief evolution. Previous studies included geomorphological analysis and few dating on individual landslides (e.g. in Peru: Margirier et al., 2015; Crosta et al., 2014; Zerathe et al., 2017; Delgado et al., 2020; e.g. in Chile: Strasser and Schlunegger, 2005; Pinto et al., 2008; Crosta et al., 2017). Preliminary regional mapping have been attempted in Peru (Geocatmin-INGEMMET and Audin & Bechir 2006) and in Chile (Matther et al., 2014 and Crosta et al., 2014).

Here we proposed a new and exhaustive mapping of large landslides of the Western Andes updating and homogenizing the previous works. The considered area locates between latitude 15° and 20°S, from the coast to the mean elevation of the Altiplano (~5000 m a.s.l). The landslide mapping was done by using Google Earth and DEMs (TanDEM-X and Pléiades). We mapped polygons (surface area $> 0.1 \text{ km}^2$) corresponding to destructured areas and strictly including the evidence of major landslide scarps (cliffs, unusual slope-breaks, etc.) and its sliding mass (offset lithology, boulders fields, etc.).

We identified more than 700 landslides, distributed into three main typologies: (1) deep-seated rockslide (DSR) showing “in-mass” displacement; (2) rock-avalanche (RA) with typical granular-flow morphologies (e.g. levees, boulders fields) and (3) destabilizations associated with both dynamics. This GIS database allows statistical analysis and interpretations crossing the landslide distribution and typologies versus relief properties, geology-lithology, long-term uplift, dating, etc. Preliminary analysis of this database shows that spatial distribution of mass-movements is not homogeneous. Instead, we observed cluster of mass-movements following the main valleys or canyons. They mainly located at elevation between 1500 and 2000 m a.s.l. Interestingly, the largest landslides

(surface area > 50 km²) are disconnected to fluvial incision. They occurred within interfluvial areas. Few of the largest landslides cover alone more than 30 % of the total cumulated landslide area in this region and, on their own, might contribute at a first order to the relief erosion.



What are the main factors that trigger the giant-landslides in the Peruvian western Andes? The Aricota giant-landslide case study.

F. Delgado¹, S. Zerathe², S. Schwartz², C. Benavente¹, L. Audin², J. Carcaillet² and Aster Team³

¹Pontificia Universidad Católica del Perú, Av. Universitaria 1801, San Miguel-Lima, 15088 – Perú. delgado.f@pucp.edu.pe

²Univ. Grenoble Alpes, Univ. Savoie Mont Blanc, CNRS, IRD, IFSTTAR, ISTERre, 38000 Grenoble

³Aix-Marseille Univ., CNRS, IRD, Coll. France, UM 34 CEREGE, Technopôle de l'Environnement Arbois-Méditerranée, BP80, 13545 Aix-en-Provence, France

The central part of western Andes concentrates giant paleo-landslides that mobilized large volumes of rock, well preserved due to hyper arid climate of this region (Audin and Bechir, 2006; Pinto et al., 2008; Crosta et al., 2014; Crosta et al., 2015; Crosta et al., 2017; Mather et al., 2014; Zerathe et al., 2017) and bring us the opportunity to study the sequence of ancient events.

The main goal of this study is to identify the role of climate and tectonics phenomena's on the triggering of giant-landslides in Peruvian western Andes. We realized a multidisciplinary study on the Aricota landslide by using high-resolution DEM derived from Pléiades satellite image (Lacroix et al, 2016. Zerathe et al, 2016.) and coupled with cosmogenic nuclide methodology, We realize dating on the main body of landslides and main scarps in order to obtain chronological constraints of the gravitational destabilization events.

We identified two events: (1) a first event with an estimated volume of ~2 km³ that event generated an impressive dam in the main valley and formed a lake approximately 6 km long upstream; and (2) a second event of rocks avalanche with an estimated volume of ~0.3 km³. 10Be dating (17 samples) suggest ages of 17.9 ± 0.7 ka and 12.1 ± 0.2 ka (weighted mean and 1 sigma uncertainty of the weighted mean) for these two events. Comparing those mean ages with local paleoclimatic reconstructions, we noticed that the failures match well with two important wet events of the Altiplano: Heinrich 1 (14 - 18 ka) and Younger Dryas (11 - 13 ka), which correspond to the formation of the Taucu and Copiasa lakes respectively (Placzek et al., 2013). This suggests that the climate probably played an important role in the triggers of landslides. However, as several neotectonic faults also affect this area (in the 50 km of radius, e.g. Incapuquio fault or Purgatorio fault), we can't rule out a possible seismic trigger or even an earthquake/climate coupling.

On the western flank of the Andes, the Aricota landslide is one of the few dating events. Although there are numerous recognized paleo-landslides. So, other new landslides ages, should also allow us to know more about the origin of these phenomena in this arid region.

Differential exhumation driven by Tectonic processes in the Abancay deflection (Peruvian Andes)

B. Gérard¹, X. Robert¹, L. Audin¹, C. Gautheron², M. Bernet¹, C. Benavente³, F. Delgado³

¹Univ. Grenoble Alpes, Univ. Savoie Mont Blanc, CNRS, IRD, IFSTTAR, ISTERre, 38000 Grenoble, France

²GEOPS, Univ. Paris-Sud, CNRS, Université Paris-Saclay, 91405 Orsay, France

³INGEMMET, Instituto Geológico, Minero y Metalúrgico, Lima, Perú

The Abancay deflection (12-13.5°S), forming the northern edge of the Altiplano in the Central Andes of Peru, is a remarkable geomorphologic feature marking the along-strike segmentation of the Andes (Dalmayrac et al., 1980). Little is known about the timing and spatial distribution of exhumation in this peculiar part of the Eastern Cordillera for the last 40 Ma; however, it is characterized by 4 km-high relief and 2 km-deep gorges suggesting significant recent incision. To better constrain the exhumation and incision history of this northern edge of the Altiplano, we present apatite and zircon (U-Th)/He and fission-track data from 6 steep altitudinal profiles collected within the deflection (40 sampling sites). Thermochronology results highlight differential exhumation episodes between the Eastern Cordillera and the Altiplano with young thermochronological ages (<10 Ma) and older ones (>15 Ma) respectively. We processed these ages into QTQt (Gallagher, 2012) and PECUBE (Braun, 2003) to discuss and unravel the exhumation timing, magnitude and settings of this area. Data inversion reveals the (re)activation of the crustal scale Apurimac fault system tilting the entire deflection like a pop-up structure (< 10 Ma) leading to differential exhumation between the Eastern Cordillera and the Altiplano. We speculate that the Abancay deflection, with its “bulls-eye” morphology and the abrupt increase in exhumation rate < 10 Ma, may represent an Andean proto-syntaxis, somewhat similar to the syntaxes described in the Himalaya or Alaska (Zeitler et al., 2001).

Braun, J. Pecube, (2003). A new finite-element code to solve the 3D heat transport equation including the effects of a time-varying, finite amplitude surface topography. *Comput. Geosci.* 29, 787–794.

Dalmayrac, B., Laubacher, G. & Marocco, R., (1980). Géologie des Andes péruviennes.

Gallagher, K., (2012). Transdimensional inverse thermal history modeling for quantitative thermochronology. *J. Geophys. Res. Solid Earth* 117, 1–16.

Zeitler, P. K. et al. (2001). Erosion, Himalayan geodynamics and the Geomorphology of Metamorphism. *GSA TODAY* 4–9.

ANNEXES

Participation in papers:

Zerathe, S., Litty, C., Blard, P.H., Delgado, F., Audin, L., Carcaillet, J. & ASTER Team. (Submitted) Cosmogenic ^3He and ^{10}Be denudation rates in the Central Andes: comparison with a natural sediment trap over the last 18 ka. *Earth and Planetary Science Letters*

Aguirre, E., Benavente, C., Audin, L., Wimpenny, S., Baize, S., Rosell, L., ... & Palomino, A. (2021). Earthquake surface ruptures on the altiplano and geomorphological evidence of normal faulting in the December 2016 (Mw 6.1) Parina earthquake, Peru. *Journal of South American Earth Sciences*, 106, 103098.

Gérard, B., Audin, L., Robert, X., Gautheron, C., van der Beek, P., Bernet, M., ... & Delgado, F. (2021). Pliocene river capture and incision of the northern Altiplano: Machu Picchu, Peru. *Journal of the Geological Society*, 178(2).

Costa, C., Alvarado, A., Audemard, F., Audin, L., Benavente, C., Bezerra, F. H., ... & Garro, H. (2020). Hazardous faults of South America; compilation and overview. *Journal of South American Earth Sciences*, 104, 102837.

Minor revisions at Earth and Planetary Science Letters

Cosmogenic ^3He and ^{10}Be denudation rates in the Central Andes: comparison with a natural sediment trap over the last 18 ka --Manuscript Draft--

Manuscript Number:	EPSL-D-21-01480R1
Article Type:	Letters
Keywords:	Cosmogenic nuclide, denudation rate, ^{10}Be , ^3He , multiple-minerals, sediment budget, Central Western Andes
Corresponding Author:	Swann Zerathe, Ph.D ISTerre: Institut des Sciences de la Terre Grenoble, FRANCE
First Author:	Swann Zerathe, Ph.D
Order of Authors:	Swann Zerathe, Ph.D Litty Camille Blard Pierre-Henri Delgado Fabrizio Audin Laurence Carcaillet Julien ASTER Team
Abstract	<p>It is of major importance for Earth surface sciences to reconstruct denudation rates in the most precise and accurate way. For this, it can be useful to test on the same setting methods based on different assumptions, such as those relying on geomorphological and geochemical observations. Here, we use an exceptionally suited setting in the Locumba catchment (southwestern Peruvian Andes) that offers the unique opportunity to compare denudation rates derived from in situ cosmogenic ^3He and ^{10}Be with a geomorphological sediment budget integrated over the last 18 ka. The sediment budget is estimated by determining the volume of sediment trapped in the Aricota lake that formed 18 ka ago after the occurrence of a giant rockslide dam. We reconstructed the topography of the Locumba valley before the dam emplacement and established that the captured sediment volume is $0.8 \pm 0.1 \text{ km}^3$. Considering that the lake-water output is restricted to seepage through the dam and that overflow above the dam never occurred, this volume correctly represents the sediment flux integrated over the last 18 ka. Integrating this volume over the upstream catchment area ($\sim 1500 \text{ km}^2$), we derived a corresponding mean erosion rate of $30 \pm 9 \text{ mm.k}^{-1}$. Fluvial sediments feeding the Aricota lake were sampled to derive denudation rates from in-situ cosmogenic ^{10}Be in the silicates and from in-situ cosmogenic ^3He in the ferromagnesian minerals. Cosmogenic nuclide denudation rates from the main stream are 30 ± 2, 33 ± 2, 21 ± 1 and $82 \pm 5 \text{ mm.k}^{-1}$ for the ^{10}Be-quartz, the ^{10}Be-feldspar, the ^3He-amphibole and ^3He-pyroxene, respectively. The consistency between the cosmogenic nuclide denudation rates derived from ^{10}Be in the silicates and the erosion rate derived from our sediment budget shows that the ^{10}Be accurately estimates of the sediment flux. Additionally, this work provides the first successful application of ^{10}Be-feldspar nuclide-mineral pair to derive catchment-mean denudation rate and demonstrate that ^{10}Be-feldspar can thus be a good alternative in catchments dominated by volcanic rocks with no quartz. The discrepancies observed between the denudation rates derived from the ^3He-amphibole and ^3He-pyroxene couples require further studies.</p>

1 **Cosmogenic ^3He and ^{10}Be denudation rates in the Central Andes: comparison**
2 **with a natural sediment trap over the last 18 ka**

3
4 Zerathe Swann ^{1,*}, Litty Camille ¹, Blard Pierre-Henri ², Delgado Fabrizio ^{1,3}, Audin Laurence
5 ¹, Carcaillet Julien ¹, ASTER Team ⁴

6
7 ¹ ISTERre, IRD, CNRS, Univ. Grenoble Alpes, USMB, 38000 Grenoble, France.

8 ² CRPG, UMR 7358, CNRS, Université de Lorraine, 54501 Vandoeuvre-lès-Nancy, France.

9 ³ Especialidad Ingeniería Geológica, Facultad de Ciencias e Ingeniería. Pontificia Universidad
10 Católica del Perú, Av. Universitaria 1801, San Miguel, Lima 15088, Perú.

11 ⁴ Aix-Marseille Univ., CNRS, IRD, Coll. France, UM 34 CEREGE, Technopôle de
12 l'Environnement Arbois-Méditerranée, BP80, 13545 Aix-en-Provence, France. ASTER Team:
13 Georges Aumaître, Didier Bourlès, Karim Keddadouche

14
15 * Corresponding author: S. Zerathe

16 E-mail address: swann.zerathe@ird.fr

17
18 **Abstract**

19 It is of major importance for Earth surface sciences to reconstruct denudation rates in the most
20 precise and accurate way. For this, it can be useful to test on the same setting methods based on
21 different assumptions, such as those relying on geomorphological and geochemical
22 observations. Here, we use an exceptionally suited setting in the Locumba catchment
23 (southwestern Peruvian Andes) that offers the unique opportunity to compare denudation rates
24 derived from in situ cosmogenic ^3He and ^{10}Be with a geomorphological sediment budget
25 integrated over the last 18 ka. The sediment budget is estimated by determining the volume of

26 sediment trapped in the Aricota lake that formed 18 ka ago after the occurrence of a giant
27 rockslide dam. We reconstructed the topography of the Locumba valley before the dam
28 emplacement and established that the captured sediment volume is $0.8 \pm 0.1 \text{ km}^3$. Considering
29 that the lake-water output is restricted to seepage through the dam and that overflow above the
30 dam never occurred, this volume correctly represents the sediment flux integrated over the last
31 18 ka. Integrating this volume over the upstream catchment area ($\sim 1500 \text{ km}^2$), we derived a
32 corresponding mean erosion rate of $30 \pm 9 \text{ mm.k}^{-1}$. Fluvial sediments feeding the Aricota lake
33 were sampled to derive denudation rates from *in-situ* cosmogenic ^{10}Be in the silicates and from
34 *in-situ* cosmogenic ^3He in the ferromagnesian minerals. Cosmogenic nuclide denudation rates
35 from the main stream are 30 ± 2 , 33 ± 2 , 21 ± 1 and $82 \pm 5 \text{ mm.k}^{-1}$ for the ^{10}Be -quartz, the ^{10}Be -
36 feldspar, the ^3He -amphibole and ^3He -pyroxene, respectively. The consistency between the
37 cosmogenic nuclide denudation rates derived from ^{10}Be in the silicates and the erosion rate
38 derived from our sediment budget shows that the ^{10}Be accurately estimates of the sediment flux.
39 Additionally, this work provides the first successful application of ^{10}Be -feldspar nuclide-
40 mineral pair to derive catchment-mean denudation rate and demonstrate that ^{10}Be -feldspar can
41 thus be a good alternative in catchments dominated by volcanic rocks with no quartz. The
42 discrepancies observed between the denudation rates derived from the ^3He -amphibole and ^3He -
43 pyroxene couples require further studies.

44
45 Keywords: Cosmogenic nuclide, denudation rate, ^{10}Be , ^3He , multiple-minerals, sediment
46 budget, Central Western Andes

47

48 **1. Introduction**

49 Reconstructing denudation rates at different timescales in hyper-arid climates and tectonically
50 active settings like the western flank of the Peruvian Andes are particularly valuable. Indeed,

51 this allows to address the impact of climate and tectonic on denudation rates, a topic that
52 motivated long-standing debates (e.g. Herman and Champagnac, 2016; Willenbring and
53 Jerolmack, 2016). Additionally, the impact of climate and tectonic on erosion is often cited as
54 a driver for important feedbacks in the landscape and mountain structure evolution (e.g.
55 Whipple and Meade, 2004). Although observations suggest correlations between erosion rates
56 and precipitation rates or uplift rates, the respective amplitude of climatic and tectonic forcings
57 require more geological data to be properly documented. In this context, accurate estimates of
58 denudation rates at the millennial timescale are important (e.g. Mariotti et al., 2021). Recording
59 denudation at such timescales indeed offers the advantage to average and buffer the natural
60 variability of tectonic and climatic forcings. Moreover, this timescale is too short to be affected
61 by variations of the internal geodynamic flux.

62 To quantify long-term denudation rates, different methods are often applied, including:
63 thermochronology (0.1 to 100 Ma; i.e., Herman and Champagnac, 2016), cosmogenic nuclides
64 (1 to 1000 ka; i.e., Carretier et al., 2013), determination of solid and solute sediment fluxes in
65 a drainage basin (day to years; i.e., Guyot, 1993), estimates of total volume of sediment
66 deposited in lakes (years to millions of years; i.e., Svendsen et al., 1989) and reconstruction of
67 pre-eroded surfaces from Digital Elevation Models (>Ma; i.e., Riquelme et al., 2008). However,
68 only a few studies have used more than one of these techniques on the same setting to compare
69 and validate the obtained denudation rates results over long-time scales (i.e. Carretier et al.,
70 2013; Aguilar et al., 2014).

71 Additionally, denudation rates determined from cosmogenic nuclides have been mainly based
72 measuring ^{10}Be concentrations in quartz, as quartz rich lithologies are common on the Earth's
73 surface (e.g. Granger et al., 1996; Dunai, 2010). Only few studies have used other minerals than
74 quartz to calculate denudation rates (e.g. Ferrier et al., 2013; Litty et al., 2021) and, to our
75 knowledge, no study have used more than one mineral or multiple cosmogenic nuclides in the

76 same watershed. In the Andes, denudation rates were mostly determined using ^{10}Be -quartz (e.g.
77 Reber et al., 2017; Carretier et al., 2018).

78 On the southwestern flank of the Peruvian Andes, at latitude $\sim 17^\circ\text{S}$, the Aricota lake offers an
79 ideal opportunity to obtain and compare basin wide denudation rates using a several
80 cosmogenic nuclides and techniques. A giant landslide blocked the Locumba valley ~ 18 ka ago,
81 generating a large dam that triggered the formation of a 6 km long and 1.5 km wide lake (Figure
82 1; Delgado et al., 2020). Since the formation of the lake, two main tributary rivers, the Callazas
83 and Salado rivers, have transported sediments drained from a 1500 km² watershed. These
84 sediments have not been able to pass through the dam, and have thus continuously filled the
85 lake. Since the Aricota lake can be considered as an efficient sediment trap, the totality of its
86 sediment infill represents an accurate record of the denudation rate of the upstream catchment
87 integrated over the last 18 ka.

88 The purpose of this study is to compare the denudation rates obtained by two different
89 techniques: (1) the estimation of the total volume of the sediment accumulated in the Aricota
90 lake since its formation, 18 ka; (2) the cosmogenic ^{10}Be and ^3He concentrations measured in
91 different detrital minerals sampled in the main present-day rivers (quartz, feldspar, amphibole
92 and pyroxene).

93

94 **2. Geological settings**

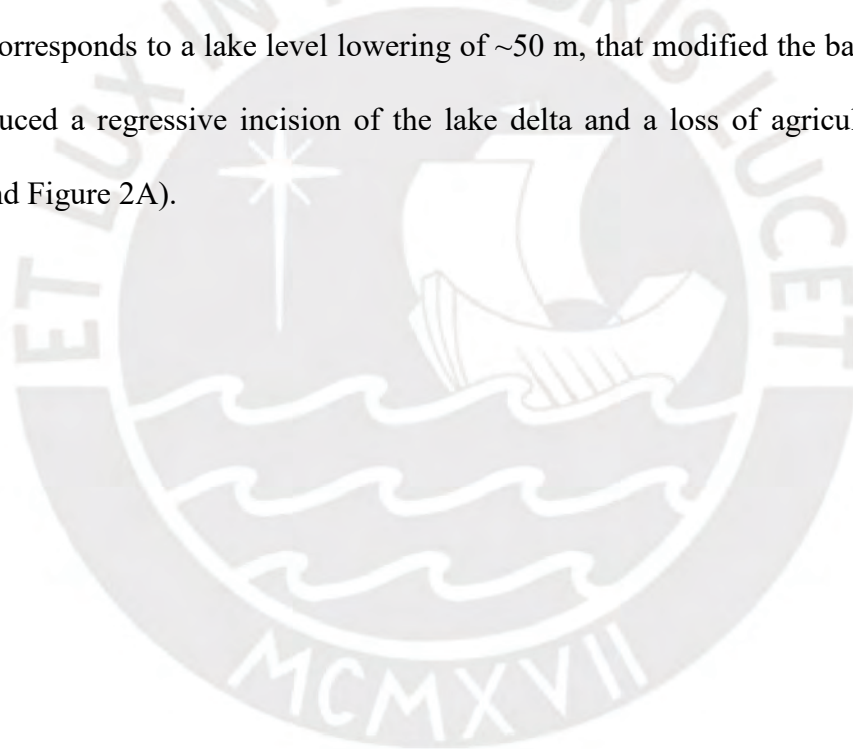
95 The Locumba valley is located in the South Peru at $\sim 17^\circ\text{S}$ latitude, along the Western flank of
96 the Central Andean Cordillera (Figure 1A). The geomorphology of the Central Cordillera shows
97 from West to East: (1) the coastal cordillera with a maximum elevation of 1000 m a.s.l., (2) the
98 Western Cordillera with elevations comprised between 1000 and 4500 m a.s.l., and (3) the
99 Altiplano plateau reaching 5000 m a.s.l. The western flank of the Andes is carved by deep
100 valleys and canyons related to a regional uplift and erosion (e.g. Thouret et al., 2017). The

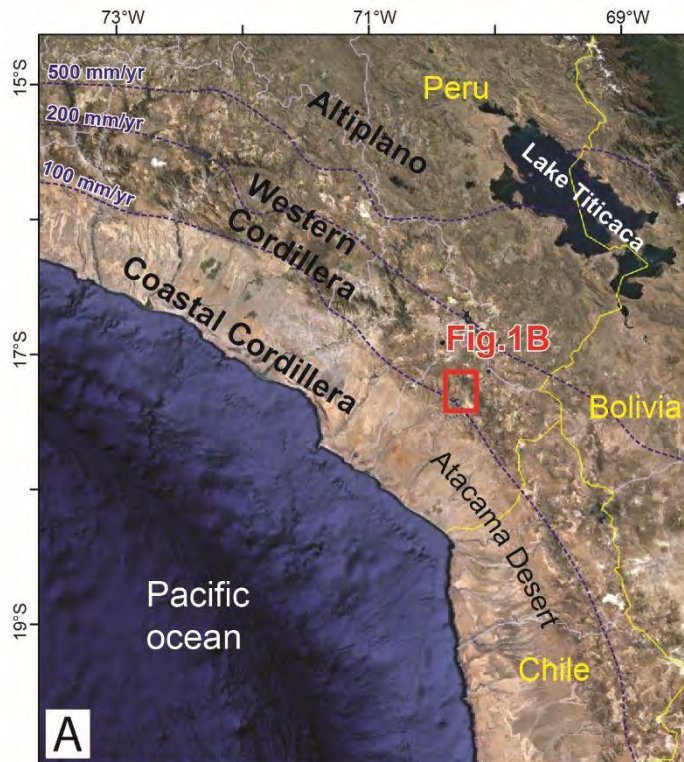
101 progressive onset of the Andean relief acted as an important topographic barrier prevented the
102 crossing of cloud and precipitations from the Amazonian basin (Houston and Hartley, 2003).
103 As a result of this Miocene uplift, hyper-arid conditions have developed and still currently
104 prevail in the so-called Atacama Desert (Figure 1A), one of the most arid and oldest deserts of
105 the world (e.g. Dunai et al., 2005). These hyper-arid conditions induce very low erosion rates
106 (typically 1–10 mm.k^a⁻¹ over the last Myrs ; Madella et al., 2018 and references therein) which
107 allows an exceptional preservation of landscapes over several millions of years (e.g. Dunai et
108 al., 2005). Contrasting with these dominantly dry conditions, records of extreme erosional
109 events, such as flash floods, debris flows or landslides linked to El Niño-La Niña oscillations
110 (ENSO) have been reported during the late Pleistocene in Southern Peru (e.g. Keefer et al.,
111 2003). Other evidences of more persistent humid conditions related to ENSO-like climate
112 configuration during previous interglacial periods are recorded as paleolakes extensions (e.g.
113 Ritter et al., 2018), alluvial fan (e.g. Ritter et al., 2019; Litty et al., 2019) and fluvial terrace
114 aggradations (e.g. Litty et al., 2018). The timings of those humid events are thought to have
115 persisted over millennial to plurimillennial periods (i.e. the Henrich events (H1: ca. 15-17 ka;
116 e.g. Martin et al., 2020) or the Ouki Event (ca. 100-120 ka; e.g. Placzek et al., 2013)) and are
117 found to be synchronous with the activity of some of the largest landslides inventoried in this
118 region (Thouret et al., 2017; Zerathe et al., 2017; Delgado et al., 2020).

119 In the Locumba valley, the giant Aricota rockslide, which occurred ~18 ka ago (Delgado et al.,
120 2020), created a ~2 km³ and 600 m high dam that blocked the path of the main river in the
121 valley (Figure 1B). Upstream of the dam, a 6 km long and 1.5 km wide lake formed. There is
122 no trace of overflow, nor of fluvial incision above the rockslide dam and the maximum elevation
123 of paleo shorelines and associated deposits remain several dozen meters below the minimum
124 elevation of the dam crest (Placzek et al., 2001; Delgado et al., 2020). The lake outflow occurred
125 strictly via seepage through the 1-km-wide dam (Placzek et al., 2001). Thus, the Aricota lake

126 acts as an efficient sediment trap since its formation. The two rivers feeding the lake are the
127 Callazas and Salado rivers (Figure 1B and Figure 2) which joined just upstream to the current
128 lake delta. These sediments are mainly composed of poorly sorted medium gravels, but also
129 includes finer grains (Placzek et al., 2001). The Locumba basin ranges from 2000 to 5900 m
130 a.s.l. and cover a total area of $\sim 1500 \text{ km}^2$. The Callazas and Salado sub-basins have an area of
131 1118 km^2 and 357 km^2 , respectively (Table 1). A hydroelectric plant siphons water from Lake
132 Aricota to provide power for the surrounding provinces and cities. This hydroelectric activity
133 has artificially lowered the lake from an initial volume of $\sim 800,000 \text{ m}^3$ in 1967, when the
134 hydroelectric plant was built, to an average volume of $\sim 140,000 \text{ m}^3$ in 2000 (Placzek et al.,
135 2001). This corresponds to a lake level lowering of $\sim 50 \text{ m}$, that modified the base level of the
136 river and induced a regressive incision of the lake delta and a loss of agricultural surfaces
137 (Figure 1B and Figure 2A).

138





139

140 *Figure 1: A) Study area location in the Central Western Andes and isohyets of annual precipitation; B) 3D*
 141 *GoogleEarth view of the Aricota rockslide dam and its lake (modified from Delgado et al., 2020). The blue circle*
 142 *locates a spring corresponding to the main seepage of the lake through the dam, feeding the lower Locumba*
 143 *river. Overflow of water above the dam never occurred since the dam emplaced (Placzek et al., 2001).*

144

145 The lithology of the upstream Locumba basin is dominated by Tertiary and Quaternary volcanic
146 and volcano-sedimentary rocks (Figure 2B). The Locumba river cuts into the stratigraphic
147 succession, from the valley bottom to the 4,500 m plateau: the lower unit, the Quellaveco
148 formation, is made of Cretaceous andesites, rhyolites and an intrusive granite (outcropping
149 north of the Aricota rockslide dam); then, the upper Tarata formation is composed of
150 Paleogene silt and shales; and, finally, the Neogene ignimbrites of the Huaylillas
151 formation unconformably covers these units and represents the majority of the outcrops (Figure
152 2B). This sequence is complete in the Salado tributary basin (eastern tributary), while, in the
153 lower part of the Callazas tributary basin (western tributary), the Miocene Huaylillas ignimbrite
154 is directly deposited on the Cretaceous Quellaveco andesite-rhyolite. The mechanical contrast
155 between the two lithologies favor the development of landslides that can reach the Callazas
156 river (Figure 2B, Delgado et al., 2020). Additionally, most of the upper part of the Callazas
157 tributary basin is incising into Pliocene andesitic lithologies that belong to the upper Barroso
158 formation, unconformably covering the sequence previously described. Finally, two active
159 volcanos belong to the Aricota lake basin: the Tutupaca (5815 m), in the western part of the
160 Callazas sub catchment, and the Yucamane (5550 m) that belongs to both sub-catchments
161 (Figure 2). The two volcanos are large conic edifices that have been built by discontinuous
162 volcanic activity from the middle Pleistocene to the Holocene. Their lithologies are dominated
163 by andesitic to dacitic lava sequences (Rivera et al., 2020 and Mariño et al., 2021). These
164 andesite-dacite volcanic sequences (Pliocene ages and younger) are dominated by a mineral
165 assemblage of plagioclase (10-20 %), amphibole (3-15 %), pyroxene (2-10 %), accessory
166 minerals and quartz (< 1%). The ignimbrite of the Huaylillas formation is the only layer that
167 contains significant amounts of quartz (5-15 %), along with plagioclase (10-30%), pyroxene (1
168 %), biotite and accessory minerals (< 1%).

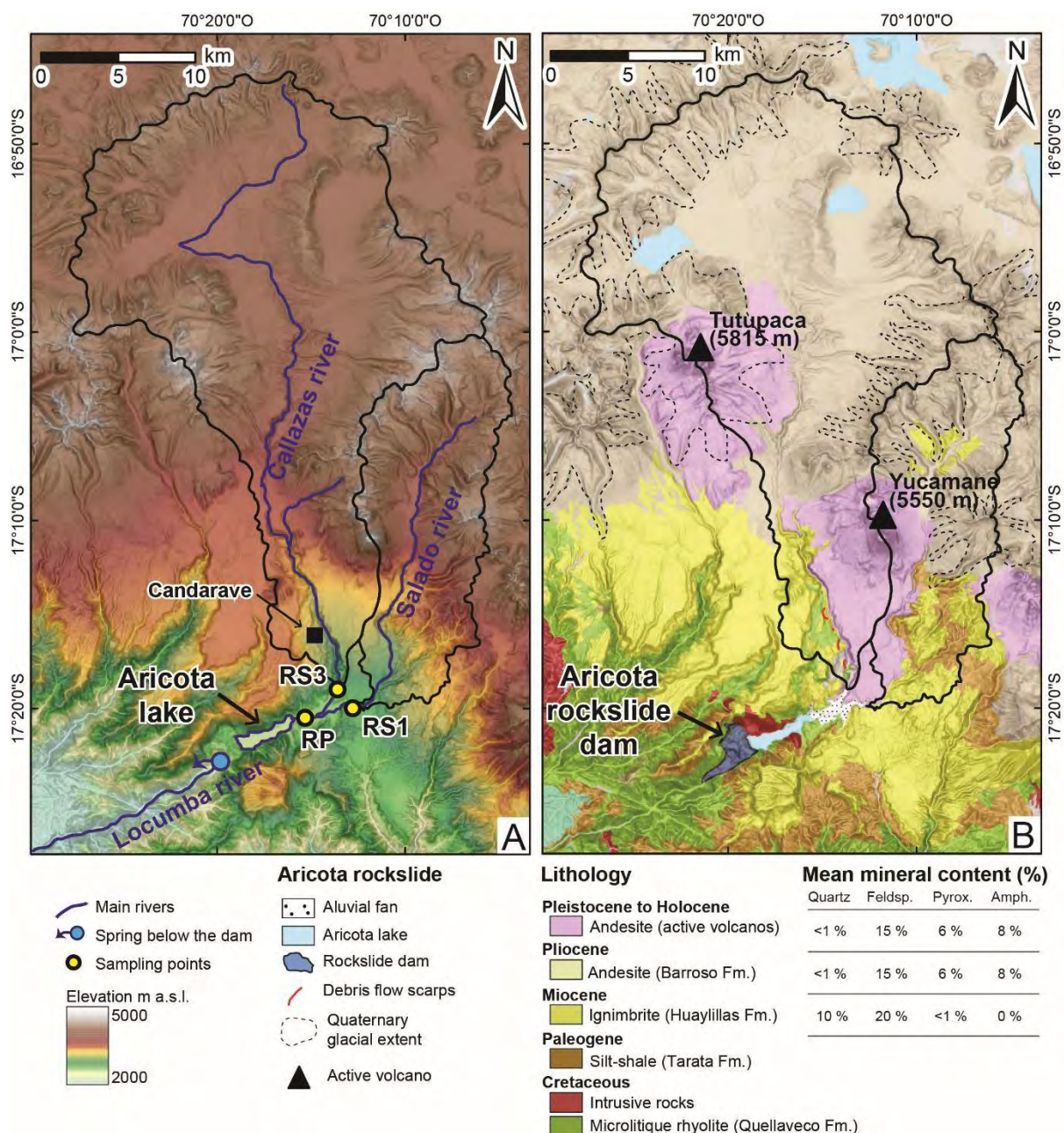
169 The detailed chronologies of lava and eruptions were established by Mariño et al. (2021) and
170 Rivera et al. (2020) for the Tutupaca and the Yucamane volcanos, respectively. During the
171 Holocene, the Yucamane volcano experienced at least 4-5 explosive events, with pyroclastic
172 flows and tephra's ejecta that probably reached a height of 4-5 km above the volcano (Rivera
173 et al., 2020). The Tutupaca volcano produced a large debris avalanche at 6-8 ka which spread
174 over 2-3 km on its south-eastern flank (Mariño et al., 2021). Later, 218 ± 14 yr BP (C-14), the
175 Tutupaca produced an historical eruption that triggered a debris avalanche ($<1 \text{ km}^3$) associated
176 to a pyroclastic eruption which spread over few kilometers along the eastern flank of the
177 volcano, up to the Callazas river (Samaniego et al., 2015).

178 Most of the Central Andes are currently unglaciated due to the arid conditions in this region.
179 However, since the Last Glacial Maximum the Central Andes experienced several glacial
180 advances and lake highstands during cooler and/or wetter episodes, due the combination of
181 orbital forcings and millennial-scale climate events (e.g. Martin et al., 2020). Moraines can be
182 identified in the head of the Callazas and Salado catchments (Mariño et al., 2021; Figure 2B).

183 To our knowledge, no dating of glacial advance was reported for this basin. However, those
184 moraines could be associated with the Last Glacial Maximum, which is dated in the Peruvian
185 Andes between 25 and 17 ka at similar elevations of about 4500 m a.s.l. (e.g. Bromley et al.,
186 2009).

187 Catchment-averaged denudation rates obtained from the lower Locumba valley (well
188 downstream to the Aricota dam) and from the adjacent valleys range from 10 to 30 mm.k^{-1}
189 (Reber et al., 2017).

190



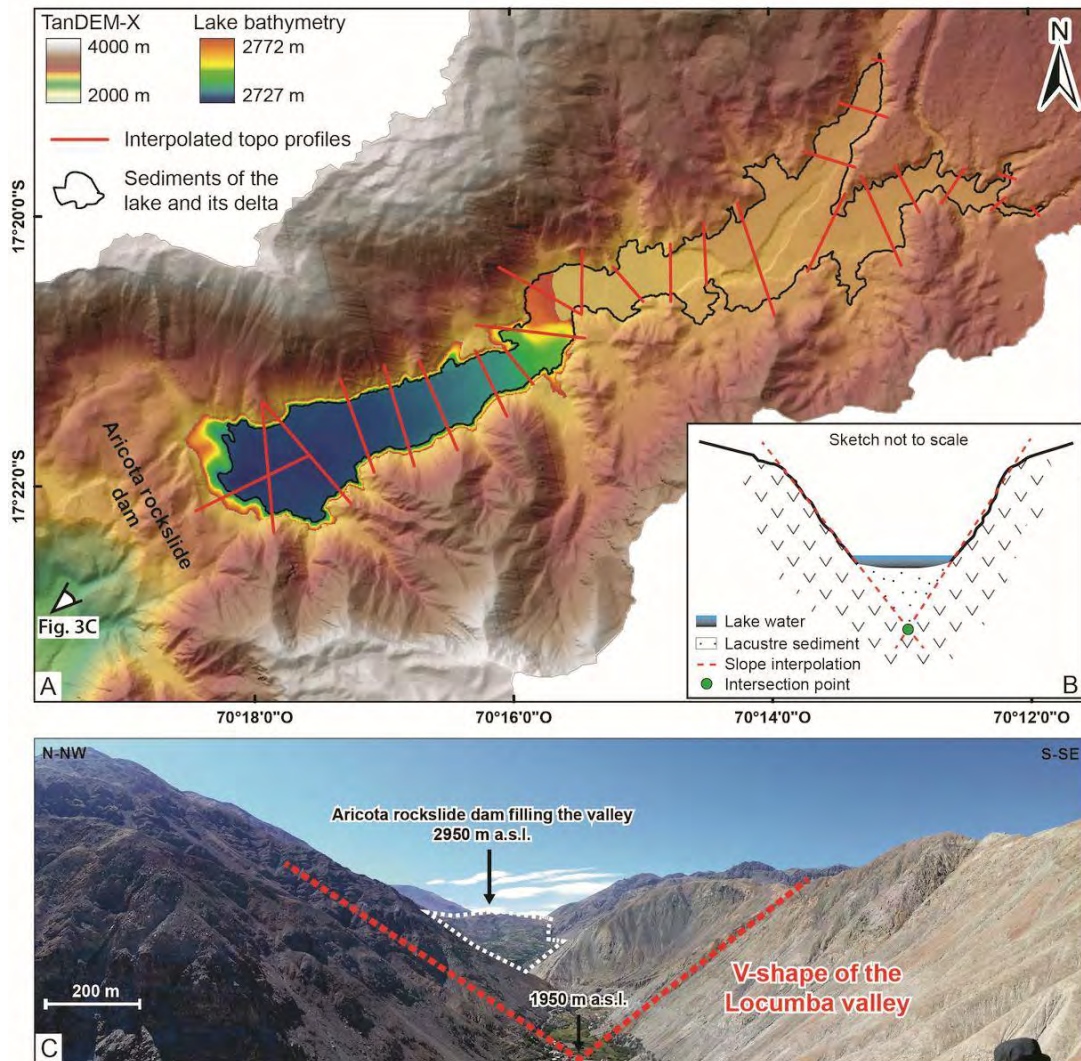
191
 192 *Figure 2: Settings of the upper Locumba basin. A) Hillshade map and elevations from the TanDEM-x DEM*
 193 *(12 m) showing the two tributaries of the upper Locumba basin, upstream to the Aricota lake. Three samples*
 194 *were collected: RP from the main stream, just above the current lake, and RS1 and RS3 from the eastern (Salado*
 195 *river) and the western (Callazas river) tributaries respectively. B) Lithological map of the area from the*
 196 *INGEMMET also showing the late Quaternary glacial extent through moraines mapping. Mineral content of*
 197 *the lithologies are from Rivera et al. (2020) and Mariño et al. (2021). Note that Paleogene Silt and Shale, as*
 198 *well as Cretaceous microlitique rhyolite, do not contain any phenocrysts larger than 100 microns.*

199
 200 **3. Methods**

201 **3.1. Estimation of the sediment volume accumulated upstream the Aricota rockslide**
202 **dam**

203 The volume of sediment trapped in the Aricota lake was computed by reconstructing the former
204 pre-dam V-shape fluvial valley (Figure 3C). Bathymetry was provided by the hydroelectric
205 company EGESUR (acquisition in October 2014, resolution 10 m; Gutierrez, 2014). The lake
206 currently reaches 45 m deep, with a relatively flat lake bottom (Figure 3A). We used the
207 Tandem-X DEM (TerraSAR-X add-on for Digital Elevation Measurements, acquisition in
208 2014, resolution 12 m) merged with the bathymetry to create a S1 DEM. We mapped the limit
209 of the accumulated sediments, including the emerged delta. In the lake, the bedrock-sediment
210 limit corresponds to the abrupt slope change between the steep valley flank and the flat bottom,
211 that is also visible in seismic profiles (Delgado et al., 2020 and references therein). Then, we
212 extracted 25 topographic profiles from the S1-DEM, perpendicularly to the lake elongation
213 length and to the delta (Figure 3A). Considering that the Locumba valley has a typical V-shape
214 fluvial profile (Figure 3C), we performed a linear fit on each valley flank until their intersection
215 at depth (Figure 3B). The intersection points correspond to the former valley bottom (Figure
216 3B). Then we used these points to rebuilt the former river profile and to create the synthetic
217 surface (S0) of the paleo-valley. Finally, we obtained the sediment volume by subtracting S1-
218 DEM by S0-DEM. The uncertainty on the vertical location of the intersection points was
219 propagated to derive an uncertainty on the sediment volume.

220



221
 222 *Figure 3: Methodology followed to estimate the volume of sediment trapped in the Aricota lake. A) Tandem-X*
 223 *DEM of the Locumba valley around the Aricota lake and lake bathymetry (provided by the company EGESUR).*
 224 *The red lines are the profiles used to interpolate the valley flanks below the lake bottom and the sediment delta.*
 225 *B) Sketch illustrating the valley slope interpolations allowing the reconstruction of the former valley shape*
 226 *(theoretical green intersection point). C) Panoramic view of the Aricota valley, downstream the Aricota*
 227 *rockslide dam, showing its V-shape (modified from Delgado et al., 2020).*

228

229 **3.2. Catchment-averaged denudation rates from cosmogenic ^3He and ^{10}Be**

230 In situ cosmogenic nuclides are produced in minerals of the Earth's surface, and this production
 231 decrease quickly below the air-rock interface (by an exponential factor each ~ 50 cm) (e.g.
 232 Dunai, 2010). These nuclides represent an accurate mean to determine denudation rates in a

233 landscape that is eroded at secular equilibrium (Dunai, 2010; equation 4). Such reconstructions
 234 were mainly based on ^{10}Be measured in quartz-rich lithologies. However, the upstream basin
 235 of the Aricota lake is mainly composed of basic and intermediate volcanic lithologies that are
 236 relatively poor in quartz. To obtain a better representativeness of the denudation rate over the
 237 entire catchment, we measured the ^{10}Be concentrations in quartz, but also in feldspar (Zerathe
 238 et al., 2017) and ^3He in amphibole and pyroxene (e.g. Litty et al., 2021).

239

240 3.2.1. Sampling

241 We collected three samples (Figure 2A, Table 1): RP are sediments representing the main
 242 Locumba river, just before its outlet in the Aricota lake, while samples RS1 and RS3 were
 243 collected few kilometers upstream, in the two tributaries of the Locumba river. Sediment
 244 sample RS1 is representative of the Salado river draining the eastern sub-basin and sample RS3
 245 is from the Callazas river, draining the western sub-basin (Figure 2A). About 3 kilograms of
 246 bedload sands were collected for each sample. The samples were sieved to retain the 0.2–0.5
 247 mm granulometric window. Then successive magnetic separations with a Frantz magnetic
 248 separator yielded different fractions enriched in amphibole - pyroxene and quartz - feldspar,
 249 respectively.

250

251 **Table 1: Sample location, corresponding catchment size and mineral-bearing areas in km^2 and corresponding**
 252 **percentage of the total catchment area.**

253

Sample label	Latitude ($^{\circ}\text{S}$)	Longitude ($^{\circ}\text{W}$)	Elevation (m a.s.l.)	Total catchment areas (km^2)	Mean catchment elevation (m a.s.l.)	Areas bearing quartz (km^2)	Areas bearing feldspar (km^2)	Areas bearing pyroxene and amphibole (km^2)
RP	17.34030	70.24937	2790	1470	4490	113 (8 %)	1409 (94 %)	1280 (85 %)
RS1	17.33285	70.21022	2880	357	4390	69 (19 %)	328 (92 %)	259 (73 %)
RS3	17.30760	70.22480	2882	1118	4561	44 (4 %)	1081 (97 %)	1021 (91 %)

254

255 3.2.2. *In-situ* ^{10}Be in quartz and in feldspar

256 The chemical extraction of ^{10}Be from quartz and feldspar was done at the GTC Platform of
257 the ISTERre laboratory (Grenoble, France). Quartz and feldspar were separated using the HF-
258 etching magnetite approach of Iacumin and Quercioli (1993). Grains were leached in HF-2%
259 for 2h, before being rinsed with water and dried. We then added about 100 mg of fine powder
260 of pure magnetite for ~100 gr of grains. The samples were then shaken and homogenized, the
261 general colors of the grains turning to light brown. At this stage, the feldspar minerals are
262 partially covered by magnetite powder while the quartz remains clean. Then, the Frantz
263 magnetic separator permitted to separate feldspar from quartz. Finally, the magnetite powder
264 was removed from the feldspar surfaces by dilute HCl leaching. Obtained separates were
265 carefully checked under binocular to ensure that they were almost pure minerals. Samples were
266 labelled RP-Q, RS1-Q, RS3-Q and RP-F, RS1-F, RS3-F for quartz and feldspar sub-samples,
267 respectively. Typical treated sample size of pure quartz and feldspars was ~10 g (Table 2). After
268 atmospheric ^{10}Be decontamination (by 3 sequential HF leaching), ~0.5 ml of ^9Be carrier
269 solution (998 mg.L^{-1} , Scharlab Be batch 14569501) was added and the samples were dissolved
270 in 40% HF.

271 Then beryllium was isolated following routine procedure using anion and cation exchange
272 columns followed by selective pH precipitation techniques for quartz. For feldspar, we applied
273 the updated protocol of Zerathe et al. (2017), which considers the high cationic content of
274 feldspar. This protocol notably uses sequential centrifugations after HF dissolution to remove
275 fluorides precipitates, pH-4 separation to remove Titanium and sequential repetition of cation
276 columns to ensure to reach a of high-purity Be fraction.

277 The beryllium hydroxides were precipitated, dried, and oxidized at 850°C during 6 hours into
278 BeO . $^{10}\text{Be}/^9\text{Be}$ ratio were measured at the French AMS National Facility, located at CEREGE
279 in Aix-en-Provence (Arnold et al., 2013). $^{10}\text{Be}/^9\text{Be}$ ratios were calibrated against the in-house
280 standard STD-11, using an assigned $^{10}\text{Be}/^9\text{Be}$ ratio of $(1.191 \pm 0.013) \times 10^{-11}$ (Braucher et al.,

281 2015), that is similar to the KNSTD07 calibration (Nishiizumi et al., 2007). Measured blank
282 $^{10}\text{Be}/^9\text{Be}$ ratios of the chemical procedure were $(5.2 \pm 2.3) \times 10^{-15}$ for the run of samples RP-Q,
283 RS3-Q, RS1-F and $(5.7 \pm 0.5) \times 10^{-15}$ for RS1-Q, RP-F and RS3-F, being one to two orders of
284 magnitude lower than the $^{10}\text{Be}/^9\text{Be}$ ratios of the measured samples. This implies that blanks
285 do not represent a significant source of uncertainty. Uncertainties on ^{10}Be concentrations
286 (reported as 1σ) are calculated according to the standard error propagation method using the
287 quadratic sum of the relative errors and include a conservative 0.5% external machine
288 uncertainty (Arnold et al., 2013), a 1.09 % uncertainty on the certified standard ratio, a 1σ
289 uncertainty associated to the mean of the standard ratio measurements during the measurement
290 cycles, a 1σ statistical error on counted events and the uncertainty associated with the chemical
291 and analytical blank correction.

292

293 3.2.3. *In-situ* ^3He in pyroxene and in amphibole

294 After a density separation in heavy liquids, pyroxenes and amphiboles were hand-picked under
295 a binocular microscope to obtain around 200 to 500 mg of pure minerals. Samples were labelled
296 RP-P, RS1-P and RP-A, RS1-A, RS3-A for pyroxene and amphibole separates respectively.
297 Unfortunately, we did not retrieve sufficient amount of pyroxene for the sample RS3-P, that
298 finally could not be processed. ^3He and ^4He concentrations were measured at the CRPG noble
299 gas platform, using an in house-tuned Helix SFT, following the procedures previously described
300 in Litty et al. (2021). For each sample, between 50 and 200 mg of pure mineral phenocrysts
301 (pyroxenes or amphiboles) were weighted and wrapped in tin foils. Each sample was then fused
302 in-vacuo for 15 min at 1400°C , using an in-house-built single vacuum induction furnace. ^3He
303 and ^4He blanks of this hot furnace procedure were $(3.6 \pm 1.1) \times 10^4$ at. and $(1.8 \pm 0.2) \times 10^9$ at.,
304 respectively, two to three orders of magnitude lower than the value of the measured samples.
305 This implies that blanks do not represent a significant source of uncertainty. The SFT sensitivity

306 was calibrated using a known amount of helium gas standard with a $^3\text{He}/^4\text{He}$ ratio of 20.63 Ra
307 (1 Ra= 1.384×10^{-6} is the atmospheric ratio) (Matsuda et al., 2002). Additionally, two aliquots
308 of the CRONUS-P pyroxene standard were analyzed during the same analytical session and
309 yielded a mean ^3He concentration of $(5.04 \pm 0.07) \times 10^9$ at.g $^{-1}$, in good agreement with the
310 average value reported from an inter-laboratory comparison (Blard, 2021).

311 The $^3\text{He}_{\text{tot}}$ measured by fusing the minerals is a three-component system that can be written e.g.
312 (Blard, 2021):

313

$$314 \quad ^3\text{He}_{\text{tot}} = ^3\text{He}_c + ^3\text{He}_{\text{nucl}} + ^3\text{He}_{\text{mag}} \quad (1),$$

315

316 where indices *c*, *nucl* and *mag* refer to the cosmogenic ^3He , the nucleogenic ^3He and the
317 magmatic component, respectively. To calculate the nucleogenic ^3He production rate ($P_{3\text{nucl}}$)
318 and its contribution ($^3\text{He}_{\text{nucl}}$) for each sample we use the excel spreadsheet of (Blard, 2021),
319 considering 1) the mean age of the lava crystallization determined here by (U-Th)/ ^4He dating,
320 2) the concentration of Li in each mineral sample measured by ICPOES, and 3) the major and
321 trace element concentrations measured in the bulk rock. Major, trace element and Li
322 concentrations in the pyroxene, amphibole and in the bulk sand were measured at the SARM-
323 CRPG facility (Nancy, France). The $^4\text{He}_{\text{tot}}$ in both pyroxene and amphibole is a two-component
324 system (Blard, 2021):

$$325 \quad ^4\text{He}_{\text{tot}} = ^4\text{He}_{\text{rad}} + ^4\text{He}_{\text{mag}} \quad (2),$$

326 where the indice *rad* refers to the radiogenic component. The mean age of the lava outcropping
327 in the catchment was evaluated using the (U–Th–Sm)/ $^4\text{He}_{\text{rad}}$ method (Blard, 2021). Assuming
328 that the magmatic component is negligible in those lithologies (Blard, 2021 and references
329 therein), the calculated ages are maximum. ^4He production rate (P_4) was estimated for each

330 sample from the equations of Farley (see in Blard, 2021). Mean lava ages (t_{eruption}) were then
331 computed using:

$$332 \quad t_{\text{eruption}} = {}^4\text{He}_{\text{rad}}/P_4 \quad (3)$$

333 where ${}^4\text{He}_{\text{rad}} = {}^4\text{He}_{\text{tot}}$. Corrections for α ejection and implantation between the phenocrysts and
334 the lava were applied (Blard, 2021).

335

336 3.2.4. Denudation rates calculation

337 The relationship between measured cosmogenic-nuclide concentration (C) and mean catchment
338 denudation rate (ϵ) can be expressed, in its simplest form, as (Brown et al., 1995):

$$339 \quad C = \sum P_i \Lambda_i / \epsilon \quad (4)$$

340 where P_i and Λ_i are the mean catchment production rate and the attenuation length,
341 respectively, of each particle (i : neutron, fast muon and slow muon) that contribute to the
342 production. Using Eq. (4) to quantify the mean denudation at catchment scales implies two
343 assumptions: (1) sediment storage within the catchment is limited and (2) loss induced by
344 radioactive decay of ${}^{10}\text{Be}$ is negligible since both the erosion time and the residence time of
345 sediment within the fluvial system are short. This is a reasonable assumption in high-relief
346 mountain settings such as the high elevation Peruvian Andes, where fluvial transport is expected
347 to be relatively rapid. In order to deduce catchment-wide denudation rates, a spatially averaged
348 cosmogenic nuclides production rate has been computed using Basinga software (Charreau et
349 al., 2019), based on a cell-by-cell approach with a 30 m digital elevation model. As
350 recommended when the used minerals are not homogeneously distributed over the catchment
351 (Charreau et al., 2019), we applied geological masks according to the mineralogical
352 assemblages known in the catchment in order to compute accurate production rates (Figure 2B
353 and Table 1). For all minerals, Paleogene and Cretaceous lithology were excluded from the
354 production rate calculation as they do not contain any phenocryst. Feldspars are almost

355 homogeneously distributed so no additional area was removed from the calculations. For quartz,
356 we selected only the areas corresponding to the Miocene ignimbrites of the Huaylilas formation
357 containing most of the quartz in the basin. Pyroxene and amphibole dominate in the Pliocene
358 and Pleistocene volcanic series (Figure 2B). Denudation rates for each nuclide-mineral pair
359 have been also computed without applying any mask for comparison. We used the modern
360 world-wide spallogenic production rate (i.e. induced by neutrons) at sea level and high latitude
361 of $4.11 \text{ atoms.g}^{-1}.\text{yr}^{-1}$ for ^{10}Be in quartz (Martin et al., 2017), $3.49 \pm 0.5 \text{ atoms.g}^{-1}.\text{yr}^{-1}$ for ^{10}Be
362 on feldspar (Zerathe et al., 2017) and $122 \pm 12 \text{ atoms.g}^{-1}.\text{yr}^{-1}$ for ^3He in both pyroxene and
363 amphibole (Martin et al., 2017). To compute the spatial correction factor, we used the time
364 dependent Lal-Stone scaling scheme, as implemented in CREp (Martin et al., 2017).

365

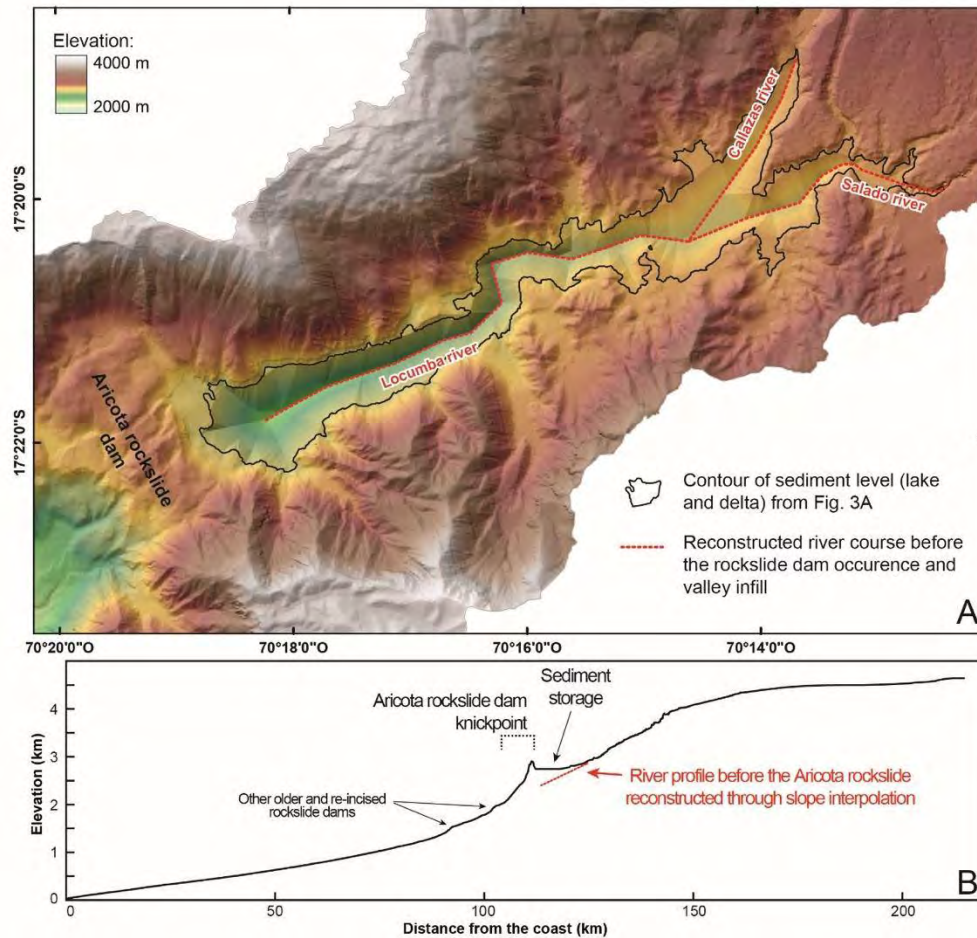
366 **4. Results**

367 **4.1. Sediment budget and derived catchment-averaged erosion rate**

368 The reconstructed DEM of the Locumba valley before the sediment accumulation is shown on
369 Figure 4A. To check the accuracy of this reconstruction, we plotted the portion of the river
370 profile reconstructed along with the current river profile of the whole Locumba basin (Figure
371 4B). We can observe a clear knickpoint produced by the Aricota rockslide dam in the center of
372 the current river profile. Downstream of this major knickpoint, smaller ones can be observed,
373 corresponding to older and partially re-incised rockslide dams (Delgado et al., 2020). The
374 portion of the river profile that has been reconstructed shows a good coherence and good
375 continuity with the longitudinal profile upstream and downstream of the Aricota rockslide,
376 validating the accuracy of our paleo-valley reconstruction.

377 We calculated a total volume of sediment (V_{sed}) of $0.8 \pm 0.1 \text{ km}^3$ accumulated behind the dam
378 by subtracting the S1-DEM by the S0-DEM. To derive an erosion rate from this volume, a
379 porosity correction can be applied. The porosity of the river sediment was measured on samples

380 RS1 and RS3 (following Missimer and Lopez, 2018) and yielded a value of 40 ± 10 %. This
381 value should be considered as a maximum estimate for the mean porosity in the lake sediment
382 because: (1) some finer sand fraction may have remained in suspension in the river, but be
383 deposited into the lake therefore reducing the mean porosity, and (2) sediment compaction into
384 the lake may further reduce the porosity. However, following the literature, the porosity of the
385 volcanic rocks outcropping in the Locumba catchment (i.e. mainly andesite and dacite) have
386 values that can range between 20 and 50 % (Heap et al., 2016 and references therein).
387 Considering that the porosity of the lake sediment and the eroded source rocks are both in the
388 same range, we assume that the volume of sediment trapped in the lake roughly equals the
389 volume of rock eroded in the catchment. To consider the any possible uncertainty associated to
390 the differential porosity, we propagated 10 % of additional uncertainty on the sediment volume.
391 Assuming an age of 17.9 ± 0.7 ka for the Aricota rockslide dam (Delgado et al., 2020),
392 corresponding to the lake initiation and thus the beginning of sediment accumulation (t), the
393 catchment-scale mean erosion rate (ϵ_{sed}) can be derived from the volume of eroded sediment
394 (V_{sed}) and the catchment area upstream to the dam ($A = 1470 \text{ km}^2$) such as $\epsilon_{\text{sed}} = (V_{\text{sed}}) / (t \times A)$.
395 We obtained an erosion rate of $30 \pm 9 \text{ mm.ka}^{-1}$.



396

397 **Figure 4: Reconstruction of the Locumba valley and river profile before the valley infill behind the Aricota**
 398 **rockslide dam. A) Hillshade view (TanDEM-X dem) showing the reconstructed valley flanks through slope**
 399 **interpolations below the current sediment level. B) Reconstructed river profile (in red) plotted along the long**
 400 **profile of the Locumba river.**

401

402 4.2. Cosmogenic nuclides-based catchment-averaged denudation rate

403 4.2.1. ^{10}Be results

404 Measured ^{10}Be concentrations range between $(1.36 \pm 0.14) \times 10^5$ and $(8.07 \pm 0.29) \times 10^5$ at.g $^{-1}$
 405 in quartz and between $(1.84 \pm 0.13) \times 10^5$ at.g $^{-1}$ and $(7.16 \pm 0.29) \times 10^5$ at.g $^{-1}$ in feldspar (Table
 406 2).

407

408 **Table 2: ^{10}Be measured in quartz and in feldspar.**

Sample	Mineral	Mass (g)	⁹ Be carrier (10 ¹⁹ atoms)	Total ¹⁰ Be counts	¹⁰ Be/ ⁹ Be ratio (10 ⁻¹³)	¹⁰ Be ^a (10 ⁵ at.g ⁻¹)
RP-Q ^b	Quartz	8.5780	3.3675	1271	1.789 ± 0.057	6.82 ± 0.24
RS1-Q ^c	Quartz	6.0263	3.4129	1235	1.483 ± 0.051	8.07 ± 0.29
RS3-Q ^b	Quartz	8.9790	3.3955	833	0.410 ± 0.029	1.36 ± 0.14
RP-F ^c	Feldspar	3.6429	3.3942	222	0.826 ± 0.058	7.16 ± 0.55
RS1-F ^b	Feldspar	6.6360	3.3648	478	0.943 ± 0.068	4.52 ± 0.36
RS3-F ^c	Feldspar	14.2379	3.4156	259	0.825 ± 0.057	1.84 ± 0.13

^a Concentration corrected from the blank, analytical uncertainties are 1σ and include the counting statistics, the machine stability (~0.5%) and the blank correction.

^b The ¹⁰Be/⁹Be blank ratio for those samples was $(5.2 \pm 2.3) \times 10^{-15}$.

^c The ¹⁰Be/⁹Be blank ratio for those samples was $(5.7 \pm 0.5) \times 10^{-15}$.

409 Taking into account geological masks, we obtained denudation rates of 30 ± 2 mm.ka⁻¹ and 33
410 ± 3 mm.ka⁻¹ for the main stream (RP) on quartz and feldspar, respectively (Table 3). For the
411 two tributary rivers: 1) denudation rates of 26 ± 2 mm.ka⁻¹ and 51 ± 5 mm.ka⁻¹ have been
412 calculated for RS1 (Salado River) on quartz and feldspar, respectively ; 2) denudation rates of
413 147 ± 18 mm.ka⁻¹ and 131 ± 13 mm.ka⁻¹ have been calculated for RS3 (Callazas River) on
414 quartz and feldspar, respectively.

415

416 4.2.2. ³He results

417 ³He and ⁴He results are presented in Table 4. Measured total ³He concentrations range between
418 $(4.06 \pm 0.12) \times 10^7$ and $(4.57 \pm 0.13) \times 10^7$ at.g⁻¹ in pyroxene and between $(1.04 \pm 0.03) \times 10^7$
419 and $(1.50 \pm 0.06) \times 10^7$ at.g⁻¹ on amphibole. Measured total ⁴He concentrations range between
420 $(3.17 \pm 0.03) \times 10^{12}$ and $(5.85 \pm 0.05) \times 10^{12}$ at.g⁻¹ in pyroxene and between $(1.41 \pm 0.01) \times 10^{12}$
421 and $(5.95 \pm 0.05) \times 10^{12}$ at.g⁻¹ in amphibole. Assuming that the magmatic ⁴He component is
422 negligible, we derived from the total ⁴He concentration and from the U-Th-Sm content of target
423 minerals and of the bulk sand (supplementary data), mean eruption ages ranging between $0.3 \pm$
424 0.1 and 1.6 ± 0.1 Ma. Those relatively young eruption ages are in good agreement with the
425 dominance of Pleistocene to Pliocene lava sequences in the upper Locumba basin (Figure 2B;

426 Rivera et al., 2020 and Mariño et al., 2021). Such young lava ages resulted in low contributions
 427 of nucleogenic ^3He ($^3\text{He}_n$), representing less than 1 % of the total ^3He concentrations.
 428 Considering geological masks, we calculated denudation rates of 21 ± 1 and 82 ± 5 mm.k.a^{-1} for
 429 the main stream (RP) from pyroxene and amphibole, respectively (Table 3). For the two
 430 tributary rivers: 1) a denudation rate of 57 ± 4 mm.k.a^{-1} have been calculated for RS1 (Salado
 431 River) from amphibole (the pyroxene was not measured due a lack of material) ; 2) denudation
 432 rates of 21 ± 1 and 68 ± 4 mm.k.a^{-1} have been calculated for RS3 (Callazas River) from pyroxene
 433 and amphibole, respectively.

434

435 **Table 3: Cosmogenic nuclide denudation rates in mm.k.a^{-1} derived from the different nuclide-mineral pairs.**
 436 **Note that denudation rates for ^{10}Be /feldspar were not recalculated with geological mask as the feldspar are**
 437 **homogeneously distributed over the Locumba catchment.**

438

Sample		^{10}Be denudation rates (mm.k.a^{-1})		^3He denudation rates (mm.k.a^{-1})	
		Quartz	Feldspar	Pyroxene	Amphibole
With geological mask	RP	30 ± 2	33 ± 3	21 ± 1	82 ± 5
	RS1	26 ± 2	51 ± 5	n.a.	57 ± 4
	RS3	147 ± 18	131 ± 13	21 ± 1	68 ± 4
Without geological mask	RP	40 ± 3	33 ± 3	18 ± 1	79 ± 4
	RS1	33 ± 2	50 ± 5	n.a.	53 ± 3
	RS3	208 ± 25	130 ± 12	21 ± 1	67 ± 4

446

447

448 **Table 4: ^3He and ^4He measured in pyroxene and amphibole.**

Sample	Mineral	Mass (mg)	$^4\text{He}_{\text{tot}}$ (10^{12} at.g $^{-1}$)	$^3\text{He}_{\text{tot}}$ (10^7 at.g $^{-1}$)	P_4^a (10^6 at.g $^{-1}$.yr $^{-1}$)	(U-Th-Sm)/ ^4He eruption age (Ma)	P_3^b (at.g $^{-1}$.yr $^{-1}$)	$^3\text{He}_n^c$ (10^5 at.g $^{-1}$)	% $^3\text{He}_n^c$ / $^3\text{He}_t$	$^3\text{He}_c^d$ (10^7 at.g $^{-1}$)
RP-P	Pyroxene	49.10	3.17 ± 0.03	4.57 ± 0.13	2.4 ± 0.4	1.3 ± 0.3	0.087	1.5	0.3	4.56 ± 0.13
RS1-P	Pyroxene	Not measured								

RS3-P	Pyroxene	52.70	5.85 ± 0.05	4.06 ± 0.12	Not measured					4.06 ± 0.12
RP-A	Amphibole	199.2	1.41 ± 0.01	1.04 ± 0.03	2.9 ± 0.4	0.5 ± 0.1	0.082	0.4	0.4	1.04 ± 0.03
RS1-A	Amphibole	58.00	1.65 ± 0.01	1.50 ± 0.06	6.6 ± 0.2	0.3 ± 0.1	0.057	0.2	0.2	1.50 ± 0.06
RS3-A	Amphibole	158.70	5.95 ± 0.05	1.27 ± 0.04	3.8 ± 0.1	1.6 ± 0.1	0.063	1.0	0.8	1.26 ± 0.04

449 ^a Calculated using equations of Farley (see in Blard, 2021), the U, Th and Sm content measured in phenocrysts
450 targets and bulk rock (supplementary data) and assuming a mean phenocryst radius of 250 ± 100 μm, which was
451 evaluated under a binocular microscope.

452 ^b Calculated using the equations of Andrews (1985) and Andrews et Kay (1982), the Li content of pyroxene and
453 major and trace composition of the bulk rock and assuming an eruption age obtained from the calculation of the
454 radiogenic ⁴He (supplementary data).

455 ^c ³He concentration (³He_n) obtained from P₃^b

456 ^d ³He concentration (³He_c) obtained after subtracting the nucleogenic ³He component (³He_n)^c to the total measured
457 ³He component (³He_t). The magmatic component was neglected.

458

459

460 5. Discussion

461 5.1. Erosion rate derived from sediment budget versus cosmogenic nuclide denudation 462 rates in the main stream

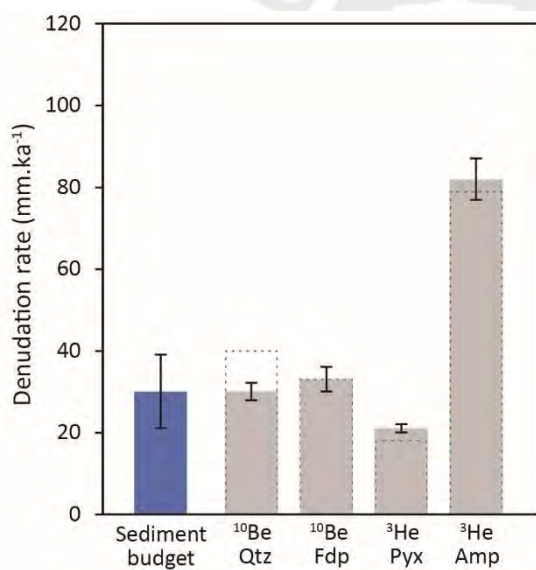
463 Denudation rates derived from cosmogenic nuclides integrate both mechanical erosion and
464 chemical weathering (e.g. Dunai, 2010), while the erosion rate derived from sediment budget
465 integrates the mechanical erosion only. As the chemical weathering of rocks occurs mainly by
466 water–rock interactions at the Earth’s surface, the short travel time of the sediments in the
467 Locumba basin, the young lithologies (mainly < 2 Ma), plus the semi-arid condition of this
468 region (rainfall < 500 mm.yr⁻¹) are in favor of a negligible weathering. Moreover, The Chemical
469 Index of Alteration (CIA) can be used to quantitatively evaluate the weathering (Nesbitt and
470 Young, 1982). CIA is defined as $Al_2O_3 / (Al_2O_3 \times CaO \times Na_2O \times K_2O) \times 100$ to consider the
471 elements that are easily leached from rocks. CIA values of about 50 indicate virtually no
472 weathering, whereas the value of 100 indicates intense weathering with complete removal of
473 alkali and alkaline earth elements. In our case, we obtained a CIA of ca. 59 using major element
474 compositions of rocks of the Locumba basin provided by Rivera et al. (2020) and Mariño et al.

475 (2021). These values indicate a negligible weathering. Therefore, erosion rate from the lake
476 sediment budget and cosmogenic nuclide denudation rates should be comparable as they both
477 integrate the mechanical erosion only.

478 As shown on Figure 5, the denudation rates derived from ^{10}Be -quartz ($30 \pm 2 \text{ mm.ka}^{-1}$), from
479 ^{10}Be -feldspar ($33 \pm 3 \text{ mm.ka}^{-1}$) are indistinguishable within uncertainties with the erosion rate
480 based on sediment budget ($30 \pm 9 \text{ mm.ka}^{-1}$). Integration times (t_i) associated with cosmogenic
481 nuclide denudation rates (ϵ) can be calculated by ($t_i = (\Lambda / \rho) / \epsilon$) where Λ is the neutron
482 attenuation length (160 g.cm^{-2}) and ρ the material density fixed at 2.7 g.cm^{-3} here. This implies
483 integration times of about 20 and 18 ka for the denudation rates from quartz and feldspar,
484 respectively. Given that this time range is similar to the age of the Aricota dam emplacement
485 (ca. 18 ka; Delgado et 2020), the sediment storage in the Aricota lake and those cosmogenic-
486 nuclide derived denudation rates represent the same integration time.

487 As feldspar is the mineral mostly represented and homogeneously distributed over the Locumba
488 catchment (Figure 2B), the consistency between the erosion rate from sediment budget and the
489 denudation rates from ^{10}Be -feldspar strongly suggests that a denudation rate of ca. 30 mm.ka^{-1}
490 is accurate for the Locumba basin over the last 20 ka. The consistency with the denudation rates
491 derived from ^{10}Be -quartz ($30 \pm 2 \text{ mm.ka}^{-1}$) also shows that the Miocene ignimbrite (bearing
492 quartz mostly) are eroding at almost the same rate than the Pliocene lava outcropping upstream.
493 The denudation rates deduced from ^3He in pyroxene and amphibole provided more contrasted
494 results. The denudation rate from ^3He -pyroxene are lower ($21 \pm 1 \text{ mm.ka}^{-1}$), although being
495 also compatible within uncertainties with the previous ones (Figure 5). Contrariwise, the
496 denudation rate derived from ^3He -amphibole are significantly higher ($82 \pm 5 \text{ mm.ka}^{-1}$).
497 Considering that the lava bearing the pyroxene and the amphibole also contains feldspar, the ^3He
498 denudation rates are at odd with the denudation rate of ca. 30 mm.ka^{-1} established from ^{10}Be -
499 feldspar. While the ^3He -pyroxene denudation rate is in reasonable agreement with those deduced

500 from ^{10}Be in quartz and feldspars, the ^3He -amphibole denudation rates hence seems to be
 501 overestimated. Several hypotheses can be explored to explain this discrepancy. i) This might
 502 be explained by differences between ^3He production rates in pyroxene and in amphibole. There
 503 are only few studies that documented ^3He production rate in amphibole (e.g. Amidon et al.,
 504 2012) and this mineral may have a highest Li-content and thus highest unrecognized
 505 nucleogenic contribution (Blard, 2021), especially when the mineral are hosted in U-rich bulk
 506 rock. ii) Another possible explanation can be that amphibole has a lowest ^3He retentivity than
 507 pyroxene but this should be further studied by acquiring specific additional experimental
 508 diffusion data. iii) Finally, this ^3He high denudation signal could be biased by a peculiar
 509 unknown amphibole-rich watershed area that buffers the signal.
 510



511
 512 **Figure 5: Erosion rate derived from sediment budget (in blue) compared to denudation rates derived from**
 513 **cosmogenic nuclide measurements (in grey) from the different nuclide-mineral pairs in the main stream**
 514 **(samples “RP”) and including geological masks (Table 3). Dashed bars indicate corresponding denudation**
 515 **rates calculated without considering geological masks. Acronyms Qtz, Fdp, Pyx and Amph stand for Quartz,**
 516 **Feldspar, Pyroxene and Amphibole, respectively.**

517

518 5.2. Variability of denudation rates derived from sub-catchments

519 Looking at ^{10}Be -quartz and ^{10}Be -feldspar results, the denudation rates obtained for the tributary
520 rivers show some variability. The values from the Salado river (RS1-Q = $26 \pm 2 \text{ mm.ka}^{-1}$ and
521 RS1-F = $51 \pm 5 \text{ mm.ka}^{-1}$, Table 3) are relatively close to the mean denudation rate of ca. 30
522 mm.ka^{-1} previously reported for the main stream. However, the denudation rates from the
523 Callazas river are much higher, with values of 147 ± 18 and $131 \pm 13 \text{ mm.ka}^{-1}$ for RS3-Q and
524 RS3-F, respectively. The mixing of cosmogenic nuclides concentrations at the scale of the basin
525 is based on the hypothesis that individual mineral grains supplied at different rates from
526 different source areas within the basin will be collected by the fluvial network, mixed in the
527 sediment load through fluvial processes and carried towards the basin outlet. Therefore, if this
528 mixing is satisfied, the cosmogenic nuclide concentration measured in an amalgam of alluvial
529 grains will likely represent the spatially averaged denudation rate over the upstream catchment
530 (Dunai, 2010). In that sense, downstream to a river junction theoretical denudation rate (ϵ_{theo})
531 should equal to the average of the denudations obtained in each tributary and weighted by their
532 areas (e.g. Binnie et al., 2006) such as $\epsilon_{\text{theo}} = (\epsilon_1 \times A_1 + \epsilon_2 \times A_2) / (A_1 + A_2)$, where the subscripts
533 correspond to each tributary basin. Applying this to our case, it returns theoretical denudation
534 rates for the main stream of 73 ± 8 and $112 \pm 11 \text{ mm.ka}^{-1}$ for RP-Q_{theo} and RP-F_{theo}, respectively,
535 that are not in agreement with the measured ones (Table 3). This suggests that denudation rates
536 derived from ^{10}Be -quartz and ^{10}Be -feldspar on the Callazas river are affected by local processes
537 and that ^{10}Be concentrations are anomalously low in those samples.

538 One possible explanation can be the presence of landslides and debris-flows that we identified
539 in the downstream part of the Callazas basin (Delgado et al., 2020; Delgado et al., in press).
540 Those landslides involve material from the quartz- and feldspar-bearing Miocene ignimbrite
541 (Figure 2B and Figure 6). Analysis of Google Earth images shows that those debris flows are
542 connected to the Callazas river (Figure 6), and that they may episodically supply quartz and
543 feldspar with very low ^{10}Be concentration to the river. This interpretation is also supported by

544 the fact that such high denudation rate is not recorded by the ^3He -pyroxene proxy ($\text{RS3-P} = 21$
545 $\pm 1 \text{ mm.ka}^{-1}$), that comes from other lithologies of the upper part of the basin, where no landslide
546 is reported. Sediment supply from landslides and mass-wasting processes is often mentioned to
547 discuss anomalously low cosmogenic nuclide concentrations in river sediment and inferred high
548 denudation rates (e.g. Stutenbecker et al., 2018). In our study case, we acknowledge that we do
549 not know much about the timing and frequency of those debris-flows. However, the fact that
550 this signal of high-denudation rate was not measured in the main stream below the river junction
551 suggests that the landslides are either recent (few hundred's years) or very episodic. This
552 conclusion is also supported by the very good agreement between the ^{10}Be -derived denudation
553 rates and those determined by the sediment budget of the Aricota lake investigated over ~ 20
554 ka.

555 Another possible interpretation for the lower ^{10}Be concentrations of the Callazas catchment can
556 be an anthropogenic effect, as mentioned by similar studies (e.g. Brardinoni et al., 2020 and
557 references therein). Together with the development of the Candarave village (Figure 1 and
558 Figure 6) during the last century, agriculture and new road openings were conducted in this area
559 that may have accelerated physical erosion, providing shielded, low ^{10}Be -bearing material, to
560 the fluvial network.

561



562

563 *Figure 6: Google Earth view of the lower Callazas basin were debris flows might supply quartz and feldspar*
 564 *with low ^{10}Be content (deeply buried) to the Callazas river.*

565

566 5.3. Geomorphological implications

567 The good correlation between (1) the sediment budget established in the Aricota lake trap and
 568 (2) the denudation rates derived from different pairs of cosmogenic nuclide-mineral sampled in
 569 its tributary, validates a mean denudation rate value of ca. 20-30 $\text{mm}\cdot\text{ka}^{-1}$ for the upper Locumba
 570 catchment, this value being integrated over the last 18 ka. Moreover, our results confirms that
 571 the ^{10}Be -quartz, ^{10}Be -feldspar and ^3He -pyroxene couples can accurately measure a catchment-
 572 mean denudation rate. Denudation rates of 20-30 $\text{mm}\cdot\text{ka}^{-1}$ are of the same magnitude as those
 573 documented by previous works in this region, which measured mean catchment denudations
 574 between 10 and 50 $\text{mm}\cdot\text{ka}^{-1}$, based on ^{10}Be -quartz in the southern Peru (Reber et al., 2017 and
 575 Starke et al., 2020). Reber et al. (2017) collected a stream-sediment sample in the same
 576 catchment as our study, in the lower Locumba valley (sample PRCME-401, lat.-long. 17.90°-
 577 70.95°, elevation ~400 m a.s.l.), reporting a mean ^{10}Be -quartz denudation rate of 12.5 ± 3.2
 578 $\text{mm}\cdot\text{ka}^{-1}$ for the whole Locumba catchment. The difference between our value (^{10}Be -quartz 30

579 $\pm 2 \text{ mm.ka}^{-1}$; Table 3) and the result of Reber et al. (2017) may result from the fact that this
580 previous study did not account for the presence of the Aricota dam in the middle part of the
581 catchment, hence ignoring the signal from upper part of the basin and the sediment flux
582 produced by the volcanos located upstream. Furthermore, it may have induced errors in the
583 estimation of the catchment mean production rate.

584 Finally, for detailed discussions about the new constraints provided by cosmogenic nuclide data
585 to unravel the respective role of climate and tectonic on the geomorphological evolution of the
586 Andes, the readers can refer to the throughout review of Carretier et al. (2018). Among others,
587 these authors suggest a significant contribution of extreme erosion events to the denudation in
588 the driest regions of the Central Andes. They also suggest that we need to better document the
589 role of large landslides in the long-term denudation. In the future, the joined use of multiple
590 nuclide-mineral pairs could help to better understand such complex denudation history, in
591 particular by offering the possibility to track the variability of the sediment source according to
592 the variability of its lithology (e.g. Hidy et al., 2018).

593

594 **6. Summary and conclusion**

595 We compared denudation rates derived from multiple cosmogenic nuclide-mineral pairs with
596 an estimation of fluvial sediment volume trapped behind the giant Aricota rockslide, that
597 completely dammed the Locumba valley (Central Andes) about 18 ka ago. The reconstruction
598 of the Locumba valley topography before the rockslide dam emplacement and estimation of the
599 sediment infill lead to an estimation of sediment volume of $0.8 \pm 0.1 \text{ km}^3$, implying a mean
600 erosion rate of $30 \pm 9 \text{ mm.ka}^{-1}$ when integrated over the upstream catchment area and an
601 accumulation period of 18 ka. The fluvial sediments currently feeding the Aricota lake were
602 sampled in the main stream and in its two upstream tributaries to derive cosmogenic nuclide
603 denudation rates from ^{10}Be in both quartz and feldspar and ^3He in both amphibole pyroxene.

604 Inferred denudation rates from the main stream were 30 ± 2 , 33 ± 2 , 21 ± 1 and 82 ± 5 mm.k^a
605 ¹ for the ¹⁰Be-quartz, the ¹⁰Be-feldspar, the ³He-amphibole and ³He-pyroxene, respectively. The
606 consistency between the denudation rates derived from ¹⁰Be cosmonuclide and the erosion rate
607 derived from the Aricota sediment budget shows that the ¹⁰Be can accurately estimate the
608 sediment flux in this volcanic catchment. Our results provide at the same time the first
609 successful use of ¹⁰Be-feldspar nuclide-mineral pair to derive catchment-mean denudation rate
610 which can be an interesting alternative in catchments where volcanic lithologies do not contain
611 quartz. The discrepancies obtained for the denudation rates derived from ferromagnesian,
612 especially from the ³He-amphibole, as thought to be related to specific ³He production-
613 diffusion mechanisms. Denudation rates derived from the tributaries return more contrasted
614 results, showing either denudation rates fully compatible with those obtained from the main
615 stream, or either significantly higher denudation rate that we attribute to landslides signatures.

616

617 **Acknowledgements**

618 All the data used to perform this study are available in the paper and in the supplemental
619 material. This research is part of the agreement between IRD and INGEMMET. This work was
620 supported by the TelluS Programs of CNRS/INSU. We acknowledge the German Aerospace
621 Centre (DLR) for providing the TANDEM-X DEM. The company EGESUR is thank for having
622 sharing the bathymetry data of the Aricota lake. The sample processing and chemical extraction
623 of the ¹⁰Be were performed at the GTC platform (ISTerre, Grenoble). We gratefully thank
624 Francis Coeur for the sample processing. The ¹⁰Be measurements were performed at the
625 ASTER AMS national facility (CEREGE, Aix en Provence) which is supported by the
626 INSU/CNRS, the ANR through the "Projets thématiques d'excellence" program for the
627 "Equipements d'excellence" ASTER-CEREGE action and IRD.

628 **References**

- 629 Aguilar, G., Carretier, S., Regard, V., Vassallo, R., Riquelme, R., Martinod, J., 2014. Grain size-
630 dependent ^{10}Be concentrations in alluvial stream sediment of the Huasco Valley, a semi-arid Andes
631 region. *Quat. Geochronol.* 19, 163–172.
- 632 Amidon, W. H., & Farley, K. A. (2012). Cosmogenic ^3He and ^{21}Ne dating of biotite and hornblende.
633 *Earth and Planetary Science Letters*, 313, 86-94.
- 634 Arnold, M., Aumaître, G., Bourlès, D.L., Keddaddouche, K., Braucher, R., Finkel, R.C., Nottoli, E.,
635 Benedetti, L., Merchel, S., 2013. The French accelerator mass spectrometry facility ASTER after
636 4 years: Status and recent developments on ^{36}Cl and ^{129}I . *Nuclear Instruments and Methods in*
637 *Physics Research Section B: Beam Interactions with Materials and Atoms* 294, 24-28.
- 638 Binnie, S. A., Phillips, W. M., Summerfield, M. A., & Fifield, L. K. (2006). Sediment mixing and basin-
639 wide cosmogenic nuclide analysis in rapidly eroding mountainous environments. *Quaternary*
640 *Geochronology*, 1(1), 4-14.
- 641 Blard, P.H. (2021). Cosmogenic ^3He in terrestrial rocks: A review. *Chemical Geology*, 120543.
- 642 Braucher, R., Guillou, V., Bourlès, D.L., Arnold, M., Aumaître, G., Keddadouche, K., Nottoli, E., 2015.
643 Preparation of ASTER in-house $^{10}\text{Be}/^9\text{Be}$ standard solutions. *Nuclear Instruments and Methods in*
644 *Physics Research Section B: Beam Interactions with Materials and Atoms*, 361, 335-340.
- 645 Brardinoni, F., Grischott, R., Kober, F., Morelli, C., & Christl, M. (2020). Evaluating debris- flow and
646 anthropogenic disturbance on ^{10}Be concentration in mountain drainage basins: implications for
647 functional connectivity and denudation rates across time scales. *Earth Surface Processes and*
648 *Landforms*, 45(15), 3955-3974.
- 649 Bromley, G. R., Schaefer, J. M., Winckler, G., Hall, B. L., Todd, C. E., & Rademaker, K. M. (2009).
650 Relative timing of last glacial maximum and late-glacial events in the central tropical Andes.
651 *Quaternary Science Reviews*, 28(23-24), 2514-2526.
- 652 Brown, E.T., Stallard, R.F., Larsen, M.C., Raisbeck, G.M., Yiou, F., 1995. Denudation rates determined
653 from the accumulation of in situ-produced ^{10}Be in the Luquillo Experimental Forest, Puerto Rico.
654 *Earth and Planetary Science Letters* 129, 193-202.

655 Carretier, S., Regard, V., Vassallo, R., Aguilar, G., Martinod, J., Riquelme, R., & Lagane, C. (2013).
656 Slope and climate variability control of erosion in the Andes of central Chile. *Geology*, 41(2), 195-
657 198.

658 Carretier, S., Tolorza, V., Regard, V., Aguilar, G., Bermúdez, M. A., Martinod, J., & Riquelme, R.
659 (2018). Review of erosion dynamics along the major NS climatic gradient in Chile and
660 perspectives. *Geomorphology*, 300, 45-68.

661 Charreau, J., Blard, P. H., Zumaque, J., Martin, L. C., Delobel, T., & Szafran, L. (2019). Basinga: A
662 cell- by- cell GIS toolbox for computing basin average scaling factors, cosmogenic production
663 rates and denudation rates. *Earth Surface Processes and Landforms*, 44(12), 2349-2365.

664 Delgado, F., Zerathe, S., Audin, L., Schwartz, S., Benavente, C., Carcaillet, J., Team, A. (2020). Giant
665 landslide triggerings and paleoprecipitations in the Central Western Andes: The aricota rockslide
666 dam (South Peru). *Geomorphology*, 350, 106932.

667 Delgado, F., Zerathe, S., Schwartz, S., Mathieux, B., Benavente, C. (2022). Inventory of large landslides
668 along the Central Western Andes (ca. 15° to 20° S): landslide distribution patterns and insights on
669 controlling factors. *Journal of South American Earth Sciences*, in press.

670 Dunai, T. J. (2010). *Cosmogenic nuclides: principles, concepts and applications in the earth surface*
671 *sciences*. Cambridge University Press.

672 Dunai, T.J., Gonzalez López, G.A., Juez-Larré, J., 2005. Oligocene–Miocene age of aridity in the
673 Atacama Desert revealed by exposure dating of erosion-sensitive landforms. *Geology* 33(4), 321-
674 324.

675 Ferrier, K. L., Perron, J. T., Mukhopadhyay, S., Rosener, M., Stock, J. D., Huppert, K. L., Slosberg, M.
676 (2013). Covariation of climate and long-term erosion rates across a steep rainfall gradient on the
677 Hawaiian island of Kaua ‘i. *Bulletin*, 125(7-8), 1146-1163.

678 Guyot, J. L., Jouanneau, J. M., Quintanilla, J., & Wasson, J. G. (1993). Dissolved and suspended
679 sediment loads exported from the Andes by the Beni river (Bolivian Amazonia), during a flood.
680 *Geodinamica Acta*, 6(4), 233-241.

681 Heap, M. J., Russell, J. K., & Kennedy, L. A. (2016). Mechanical behaviour of dacite from Mount St.
682 Helens (USA): A link between porosity and lava dome extrusion mechanism (dome or spine)?.
683 Journal of Volcanology and Geothermal Research, 328, 159-177.

684 Herman, F., & Champagnac, J. D. (2016). Plio- Pleistocene increase of erosion rates in mountain belts
685 in response to climate change. Terra Nova, 28(1), 2-10.

686 Hidy, A. J., Gosse, J. C., Sanborn, P., & Froese, D. G. (2018). Age-erosion constraints on an Early
687 Pleistocene paleosol in Yukon, Canada, with profiles of ^{10}Be and ^{26}Al : Evidence for a significant
688 loess cover effect on cosmogenic nuclide production rates. Catena, 165, 260-271.

689 Houston, J., Hartley, A.J., 2003. The central Andean west- slope rainshadow and its potential
690 contribution to the origin of hyper- aridity in the Atacama Desert. International Journal of
691 Climatology 23(12), 1453-1464.

692 Iacumin, P., Quercioli, C., 1993. A new technique for quantitative separation of quartz from feldspars.
693 European Journal of Mineralogy 5, 677-678.

694 Keefer, D.K., Moseley, M. E., DeFrance, S.D., 2003. A 38 000-year record of floods and debris flows
695 in the Ilo region of southern Peru and its relation to El Niño events and great earthquakes.
696 Palaeogeography, Palaeoclimatology, Palaeoecology 194(1-3), 41–77.

697 Litty, C., Charreau, J., Blard, P. H., Pik, R., & Nomade, S. (2021). Spatial variability of Quaternary
698 denudation rates across a volcanic ocean island (Santo Antão, Cape Verde) from cosmogenic ^3He .
699 Geomorphology, 375, 107557.

700 Litty, C., Schlunegger, F., Akçar, N., Lanari, P., Christl, M., & Vockenhuber, C. (2019). Possible
701 climatic controls on the accumulation of Peru's most prominent alluvial fan: The Lima
702 Conglomerate. Earth surface processes and landforms, 44(5), 991-1003.

703 Litty, C., Schlunegger, F., Akçar, N., Delunel, R., Christl, M., & Vockenhuber, C. (2018). Chronology
704 of alluvial terrace sediment accumulation and incision in the Pativilca Valley, western Peruvian
705 Andes. Geomorphology, 315, 45-56.

706 Madella, A., Delunel, R., Akçar, N., Schlunegger, F., & Christl, M., 2018. ^{10}Be -inferred paleo-
707 denudation rates imply that the mid-Miocene western central Andes eroded as slowly as today.
708 Scientific reports 8(1), 2299.

709 Mariño, J., Samaniego, P., Manrique, N., Valderrama, P., Roche, O., de Vries, B. V. W., Liorzou, C.
710 (2021). The Tutupaca volcanic complex (Southern Peru): Eruptive chronology and successive
711 destabilization of a dacitic dome complex. *Journal of South American Earth Sciences*, 109, 103227.

712 Mariotti, A., Blard, P. H., Charreau, J., Toucanne, S., Jorry, S. J., Molliex, S., Keddadouche, K., 2021.
713 Nonlinear forcing of climate on mountain denudation during glaciations. *Nature Geoscience*, 14(1),
714 16-22.

715 Martin, L.C.P., Blard, P.H., Balco, G., Lavé, J., Delunel, R., Lifton, N., Laurent, V., 2017. The CREp
716 program and the ICE-D production rate calibration database: A fully parameterizable and updated
717 online tool to compute cosmic-ray exposure ages. *Quaternary geochronology* 38, 25–49.

718 Martin, L. C., Blard, P. H., Lavé, J., Jomelli, V., Charreau, J., Condom, T., Keddadouche, K. (2020).
719 Antarctic-like temperature variations in the Tropical Andes recorded by glaciers and lakes during
720 the last deglaciation. *Quaternary Science Reviews*, 247, 106542.

721 Matsuda, J., Matsumoto, T., Sumino, H., Nagao, K., Yamamoto, J., Miura, Y., Kaneoka, I., Takahata,
722 N., Sano, Y., 2002. The $^3\text{He}/^4\text{He}$ ratio of the new internal He Standard of Japan (HESJ). *Geochem.*
723 *J.* 36 (2), 191–195.

724 Missimer, T. M., & Lopez, O. M. (2018). Laboratory measurement of total porosity in unconsolidated
725 quartz sand by two integrated methods. *J Geol Geophys*, 7(448), 2.

726 Nishiizumi, K., Imamura, M., Caffee, M. W., Southon, J. R., Finkel, R. C., & McAninch, J. (2007).
727 Absolute calibration of ^{10}Be AMS standards. *Nuclear Instruments and Methods in Physics*
728 *Research Section B: Beam Interactions with Materials and Atoms*, 258(2), 403-413.

729 Placzek, C., Quade, J., Betancourt, J.L., 2001. Holocene lake-level fluctuations of Lake Aricota,
730 southern Peru. *Quaternary research* 56(2), 181-190.

731 Placzek, C.J., Quade, J., & Patchett, P.J. (2013). A 130 ka reconstruction of rainfall on the Bolivian
732 Altiplano. *Earth and Planetary Science Letters*, 363, 97-108.

733 Reber, R., Delunel, R., Schlunegger, F., Litty, C., Madella, A., Akçar, N., & Christl, M. (2017).
734 Environmental controls on ^{10}Be - based catchment- averaged denudation rates along the western
735 margin of the Peruvian Andes. *Terra Nova*, 29(5), 282-293.

736 Riquelme, R., Darrozes, J., Maire, E., Hérail, G., & Soula, J. C. (2008). Long-term denudation rates
737 from the Central Andes (Chile) estimated from a Digital Elevation Model using the Black Top Hat
738 function and Inverse Distance Weighting: implications for the Neogene climate of the Atacama
739 Desert. *Andean Geology*, 35(1), 105-121.

740 Ritter, B., Binnie, S. A., Stuart, F. M., Wennrich, V., & Dunai, T. J. (2018). Evidence for multiple Plio-
741 Pleistocene lake episodes in the hyperarid Atacama Desert. *Quaternary Geochronology*, 44, 1-12.

742 Ritter, B., Wennrich, V., Medialdea, A., Brill, D., King, G., Schneiderwind, S., & Dunai, T. J. (2019).
743 Climatic fluctuations in the hyperarid core of the Atacama Desert during the past 215 ka. *Scientific*
744 *reports*, 9(1), 1-13.

745 Rivera, M., Samaniego, P., Vela, J., Le Penec, J. L., Guillou, H., Paquette, J. L., & Liorzou, C. (2020).
746 The eruptive chronology of the Yucamane-Calientes compound volcano: A potentially active
747 edifice of the Central Andes (southern Peru). *Journal of Volcanology and Geothermal Research*,
748 393, 106787.

749 Samaniego, P., Valderrama, P., Mariño, J., de Vries, B. V. W., Roche, O., Manrique, N., Malnati, J.
750 (2015). The historical (218±14 aBP) explosive eruption of Tutupaca volcano (Southern Peru).
751 *Bulletin of Volcanology*, 77(6), 1-18.

752 Stutenbecker, L., Delunel, R., Schlunegger, F., Silva, T. A., Šegvić, B., Girardclos, S., Christl, M.
753 (2018). Reduced sediment supply in a fast eroding landscape? A multi-proxy sediment budget of
754 the upper Rhône basin, Central Alps. *Sedimentary geology*, 375, 105-119.

755 Svendsen, J. I., Mangerud, J., & Miller, G. H. (1989). Denudation rates in the Arctic estimated from
756 lake sediments on Spitsbergen, Svalbard. *Palaeogeography, Palaeoclimatology, Palaeoecology*,
757 76(1-2), 153-168.

758 Starke, J., Ehlers, T. A., & Schaller, M. (2020). Latitudinal effect of vegetation on erosion rates
759 identified along western South America. *Science*, 367(6484), 1358-1361.

760 Thouret, J.C., Gunnell, Y., Jicha, B.R., Paquette, J.L., Braucher, R., 2017. Canyon incision chronology
761 based on ignimbrite stratigraphy and cut-and-fill sediment sequences in SW Peru documents
762 intermittent uplift of the western Central Andes. *Geomorphology* 298, 1-19.

- 763 Whipple, K. X., & Meade, B. J. (2004). Controls on the strength of coupling among climate, erosion,
764 and deformation in two- sided, frictional orogenic wedges at steady state. *Journal of Geophysical*
765 *Research: Earth Surface*, 109(F1).
- 766 Willenbring, J. K., & Jerolmack, D. J. (2016). The null hypothesis: globally steady rates of erosion,
767 weathering fluxes and shelf sediment accumulation during Late Cenozoic mountain uplift and
768 glaciation. *Terra Nova*, 28(1), 11-18.
- 769 Zerathe, S., Blard, P.H., Braucher, R., Bourlès, D., Audin, L., Carcaillet, J., Delgado, F., Benavente, C.,
770 Keddadouche, K., 2017. Toward the feldspar alternative for cosmogenic ^{10}Be applications.
771 *Quaternary Geochronology* 41, 83-96.





Earthquake surface ruptures on the altiplano and geomorphological evidence of normal faulting in the December 2016 (Mw 6.1) Parina earthquake, Peru

Enoch Aguirre^a, Carlos Benavente^{a,e,*}, Laurence Audin^b, Sam Wimpenny^c, Stéphane Baize^d, Lorena Rosell^a, Fabrizio Delgado^e, Briant García^{a,e}, Anderson Palomino^a

^a Instituto Geológico, Minero y Metalúrgico INGEMMET, Av. Canadá 1470 San Borja, Lima-Perú, Peru

^b Univ. Grenoble Alpes, Univ. Savoie Mont Blanc, CNRS, IRD, IFSTTAR, ISTerre, 38000, Grenoble, France

^c COMET, Bullard Laboratories, Department of Earth Sciences, University of Cambridge, UK

^d Institut de Radioprotection et de Sûreté Nucléaire (IRSN), BP 17, 92262, Fontenay-aux-Roses, France

^e Especialidad Ingeniería Geológica, Facultad de Ciencias e Ingeniería. Pontificia Universidad Católica del Perú, Av. Universitaria 1801, San Miguel, Lima, 15088, Peru

ABSTRACT

The 2016 Mw 6.1 Parina earthquake ruptured a shallow-crustal normal fault within the high Andes of south Peru. We use high-resolution DEMs and field mapping of the surface ruptures generated by the earthquake, in combination with **co-seismic** and **post-seismic** InSAR measurements, to investigate how different features of the geomorphology at Parina are generated by the earthquake cycle on the Parina Fault. We systematically mapped 12 km of NW-SE trending surface ruptures with up to ~27 cm vertical displacement and ~25 cm tensional opening along strike, separated by a gap with no observable surface ruptures. Co- and post-seismic InSAR measurements require slip below this gap in surface ruptures, implying that surface offsets observed in paleoseismic trenches may not necessarily be representative of slip at seismogenic depths, and will typically yield an underestimate of paleo-earthquake magnitudes. The surface ruptures developed along 10–20 m high cumulative scarps cutting through late Quaternary fluvio-glacial deposits and bedrock. The 2016 Parina earthquake did not rupture the full length of the late Quaternary scarps, implying that the Parina Fault does not slip in characteristic, repeat earthquakes. At Parina, and across most of the Peruvian Altiplano, normal faults are most-easily identified from recent scarps cutting late Quaternary moraine crests. In regions where there are no **recently-deposited** moraines, faults are difficult to identify and lack time constraints to quantify rates of fault slip. For this reason, current fault maps may underestimate the seismic hazard in the Altiplano.

1. Introduction

On the December 1, 2016 a rare, shallow M_w 6.1 earthquake was recorded in the Altiplano of southern Peru near the village of Parina (Fig. 1). The epicenter was located ~50 km west of Lampa village in a remote region of the plateau, though three fatalities and damage to local infrastructure were recorded (Llontop and Marrou, 2016). Body-waveform seismology and radar geodetic measurements have revealed that the earthquake ruptured a ~15 km-long, NW-SE striking normal fault, which trends sub-parallel to a well-documented system of normal faults cutting across the Altiplano known as the Cusco-Lagunillas Fault System (CLFS) (Fig. 1a; Wimpenny et al., 2018; Xu et al., 2019; Sébrier et al., 1985a,b; Benavente et al., 2013). Although an active fault map for the Peruvian Andes has been released by INGEMMET (Macharé et al., 2009; Benavente et al., 2013; 2017; INGEMMET, 2017), the Parina earthquake ruptured a previously-unmapped structure. This event provides a unique

opportunity to assess how key features of an earthquake, such as the fault location and the slip distribution, are related to the geomorphology and surface ruptures in the epicentral region, and to examine how earthquakes are preserved in the Altiplano landscape.

Whether fault-related geomorphology, such as fault scarps, accurately reflect the distribution of slip in past earthquakes is a particularly pertinent question for seismic hazard assessment in slowly-deforming regions like the Peruvian Altiplano. Seismicity in southern Peru is infrequent enough that the modern instrumental catalogue is a poor representation of the spatial distribution of active faults and the possible maximum magnitude of earthquakes on these faults, therefore paleoseismological methods must be used to complement the modern and historical catalogues (e.g. Schwartz, 1988). However, there are a number of limitations to using paleoseismological methods to infer past earthquake slip distributions and magnitudes (e.g. Ainscoe et al., 2018). For example, the fault

* Corresponding author. Instituto Geológico, Minero y Metalúrgico INGEMMET, Av. Canadá 1470 San Borja, Lima-Perú, Peru.
E-mail address: cbenavente@ingemmet.gob.pe (C. Benavente).

<https://doi.org/10.1016/j.jsames.2020.103098>

Received 19 May 2020; Received in revised form 13 November 2020; Accepted 8 December 2020

Available online 13 December 2020

0895-9811/© 2020 Published by Elsevier Ltd.

scarps generated by the two moderate-magnitude earthquakes to have occurred in the Peruvian Andes prior to the Parina event – the 1946 Ms 6.4 Ancash earthquake and the 1969 Mw 6.9 Huaytapallana (Pariahuanca) earthquake – both produced highly-segmented surface rupture traces with cumulative lengths far shorter than might be expected for earthquakes of their size (Wells and Coppersmith, 1994). The Ancash earthquake produced two 5 km-long sections of normal-faulting surface ruptures along the crest of Cerro Llamacorral, separated by a 12 km gap coincident with intervening river valleys (Bellier et al., 1991). Whilst the surface ruptures along the Huaytapallana Fault consisted of distinct segments 10 km-long and 6 km-long, separated by a 4 km-wide gap (Philip and Megard, 1977). From these rupture observations alone, it would not be possible to tell whether the gaps in the surface rupture traces reflected real along-strike variations in fault slip (e. g. due to a rupture barrier), erosional features, or a change in the material properties of the near-surface material. One way to assess

this particular limitation is by studying how slip in modern earthquakes relates to their surface ruptures and cumulative fault scarps.

In this study, we use new field measurements of the Parina earthquake surface ruptures, coupled with high-resolution DEMs of the cumulative fault scarps formed using drone photogrammetry, to examine the geomorphological evidence for faulting at Parina. We compare our scarp observations with previously-published measurements of co- and post-seismic ground deformation in the 2016 Parina earthquake from interferometric synthetic aperture radar (InSAR), to investigate how fault slip at depth relates to scarp formation and fault-related geomorphology at the surface. The accuracy and relative completeness of the surface rupture dataset, including field measurement and high-resolution DEM, also provides a unique opportunity to enrich the worldwide dataset of surface ruptures (SURE) (Baize et al., 2020).

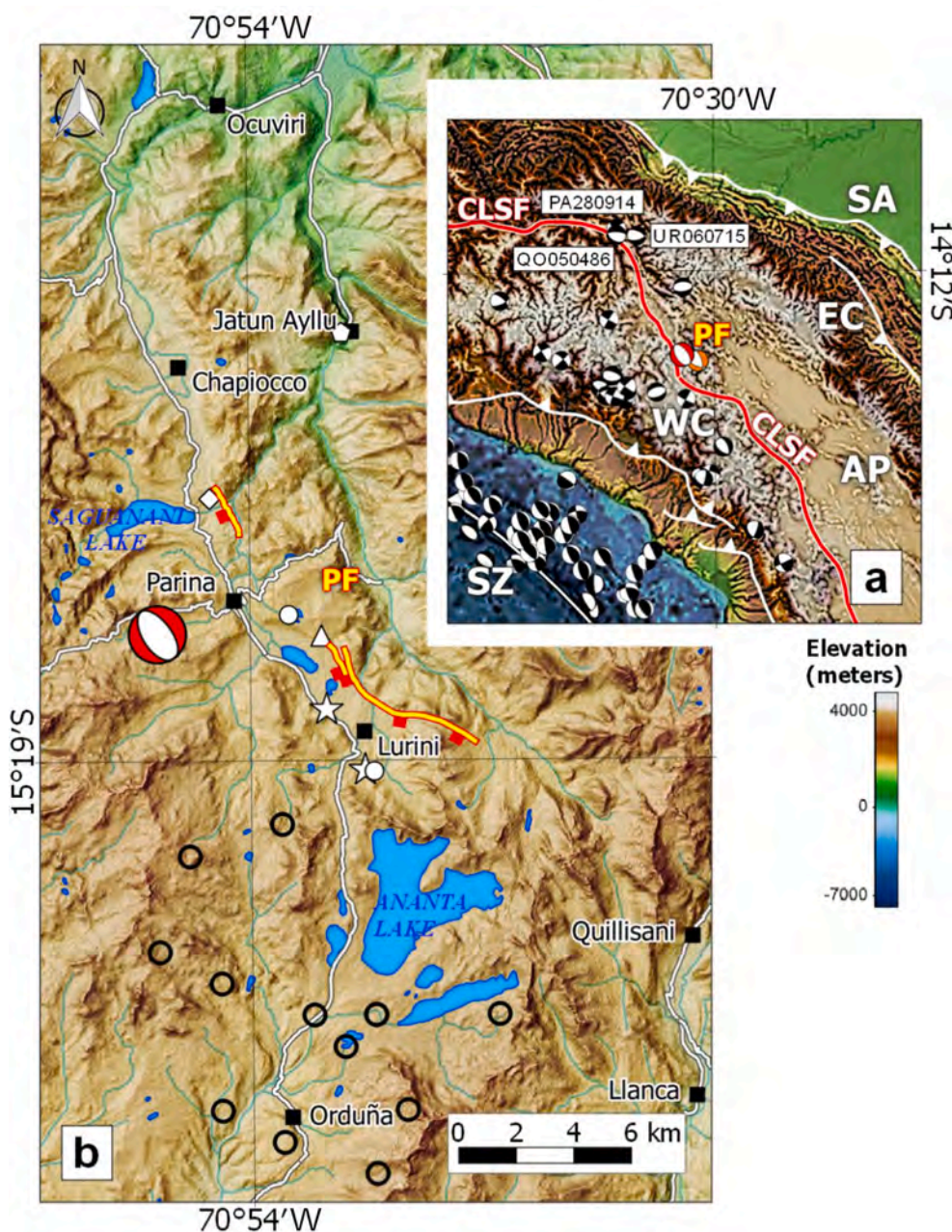


Fig. 1. a) Overview map of the Parina Fault scarp (in red). Inset (upper right) shows plate boundary setting, where (SA) Sub-andean zone, (EC) Eastern Cordillera, (AP) Altiplano, (WC) Western Cordillera, (SZ) Trench, (CLSF) for Cusco-Lagunillas Fault System and (PF) Parina Fault. The focal mechanisms seismic events shallower than 40 km hypocenter depth, with the red focal mechanism corresponding to the Parina earthquake, and the orange focal mechanism being an aftershock the next day. Note the events of Qoricocha (QO050486), Paruro (280,914) and Urcos (060,715) next to Cusco-Lagunillas Fault System (CLFS). All mechanisms are taken from the GCMT catalogue of Ekström et al. (2012) b) Close up view of the Parina Fault. White markers show the location of coseismic rock falls (pentagon), landslides (rhombus), soil liquefaction (circle), jumping stones (triangle) and crack openings (five-pointed star). Earthquake epicenters and aftershocks of the 2016 earthquake are shown as open circles. (For interpretation of the references to color in this figure legend, the reader is referred to the Web version of this article.)

2. Geological and seismotectonic setting

The Parina earthquake occurred within the northern Altiplano, a 350-450 km-wide plateau that extends ~1800 km along the backbone of the Andes, from southern Peru to northern Argentina. The Peruvian Altiplano is a low-relief basin at an average elevation of ~4500 m filled with Cenozoic sedimentary and volcanoclastic rocks that have been faulted and folded throughout the Miocene. Internal drainage and low topographic gradients in this region have precluded any deep fluvial dissection of the landscape, though periodic glaciation over the last ~100 ka has formed U-shaped valleys, moraines and drift sheets that dominate the surface morphology.

One of the most prominent structural features of the Peruvian Altiplano is the Cusco-Lagunillas Fault System (CLFS) (Ellison et al., 1989; Jaillard and Santander, 1992; Carlotto, 1998). The CLFS consists of a series of ~10–20 km-long, NW-SE trending normal faults (Fig. 1a) recognizable from their narrow hangingwall basins bound by uplifted and incised footwalls, as well as through Holocene fault scarps that often cut the Late Glacial Maximum moraines (Sébrier et al., 1985b; Mercier et al., 1992; Benavente et al., 2013a; Wimpenny

et al., 2020). Modern seismicity along the CLFS is sparse. Previous seismotectonic studies indicated that the northern section of the CLFS near Cusco had undergone extension in a Mb 5.3 normal-faulting earthquake that generated minor surface ruptures in 1986 (Cabrera and Sébrier, 1998) (see focal mechanism QO050486 in Fig. 1a). The only other moderate-magnitude (i.e. $M_w > 5$) earthquakes along the CLFS in the instrumental catalogue did not generate observable surface ruptures (see focal mechanism PA280914 and UR060715 in Fig. 1a). There have also been a number of historical reports of significant earthquakes along the CLFS, with Cusco being severely damaged in 1650 and 1950, as well as a cluster of earthquakes between 1939 and 1943 that damaged settlements further south-east along the Vilcanota river valley section of the CLFS (Ericksen et al., 1954; Silgado, 1978). The Parina earthquake is the first known $M_w > 6$ earthquake to rupture the CLFS in the modern instrumental era.

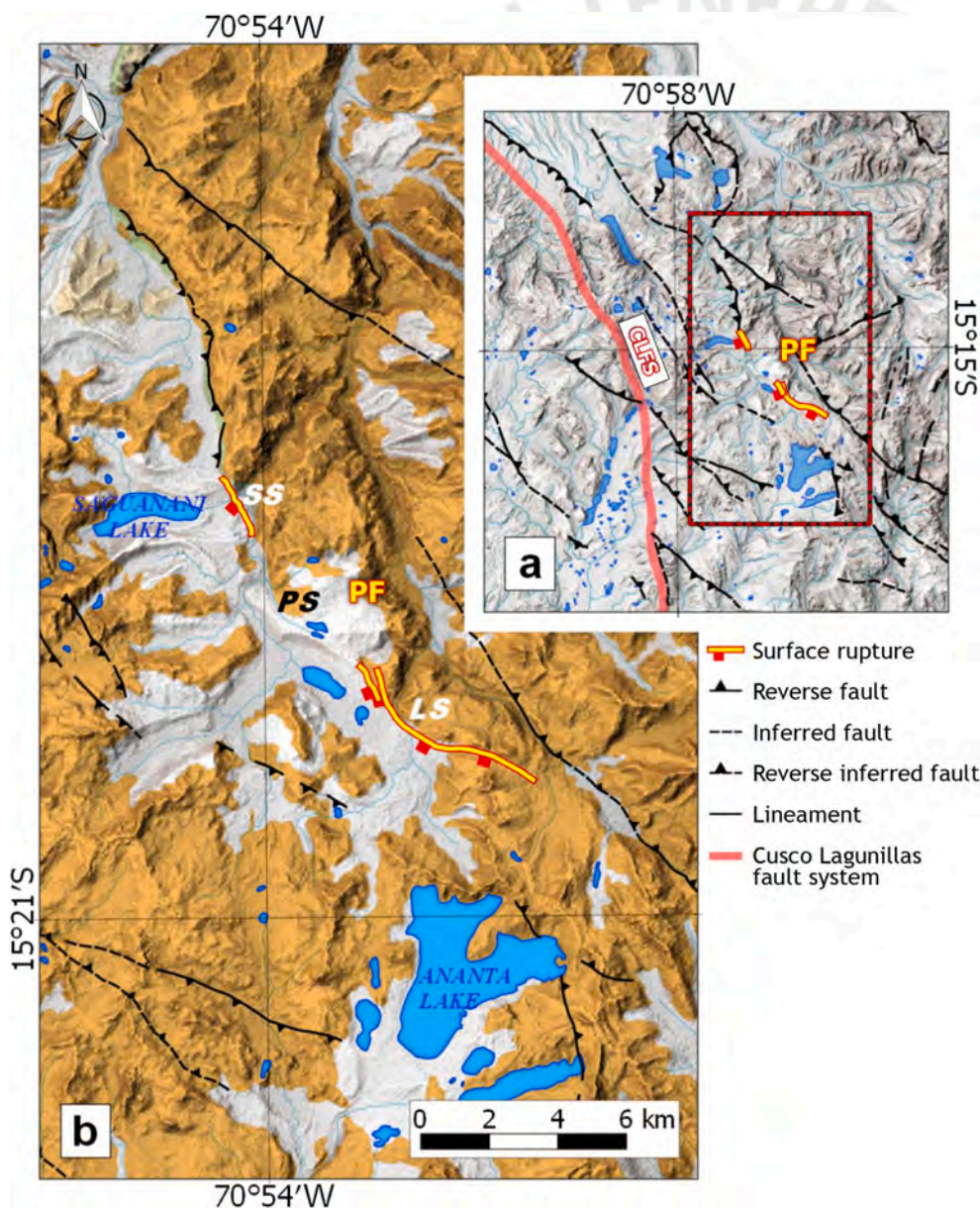


Fig. 2. a) Structural map in the Parina epicentral region. Inset (upper right), shows the Parina fault location respect to Cusco-Lagunillas Fault System (CLFS). b) Geology setting map (modified from INGEMMET, 2017). The yellow color represents Cenozoic volcanic rocks, while the gray color represents Quaternary deposits. Reverse faults are toothed black lines and the location of the surface rupture of 2016 event is shown by red and yellow line. Also shown are the segments of Parina Fault, Saguanani segment (SS), Parina segment (PS) and Lurini segment (LS). (For interpretation of the references to color in this figure legend, the reader is referred to the Web version of this article.)

3. Methods

3.1. Fieldwork

Three days after the earthquake in Parina, we organized a **post-seismic survey** of the epicentral area. On site, we mapped the surface ruptures generated by the earthquake, measured their height and tensional opening, collected an inventory of coseismic shaking effects along-strike (Fig. 3) and collected low-altitude drone imagery to form a high-resolution Digital Elevation Model (DEM), covering a surface area of $\sim 36 \text{ km}^2$ with detailed field inspection. The field evidence of earthquake-related shaking includes tensional cracks, liquefaction, and jumping stones. No rainfall occurred within the period between the earthquake and our first field study, thus both climate and limited anthropogenic activity in the area led to excellent preservation of the earthquake surface ruptures.

3.2. DEM construction and resolution

To examine the link between the surface ruptures and the cumulative fault scarps on the Parina Fault, we constructed a high-resolution DEM along the surface-rupture trace using the structure-from-motion technique with photographs collected from an eBee senseFly drone. The photographs were processed with the photogrammetry software Agisoft Photoscan (Agisoft, 2017). Ground control points were measured using differential GPS and used to guide the image matching and georeferencing. The resulting DEM has a 20 cm horizontal resolution and a $\sim 1 \text{ cm}$ vertical resolution between adjacent points (Westoby et al., 2012), and is complemented with orthomosaic color imagery at 4 cm/pixel resolution along the whole length of the surface ruptures (see Fig. 3b and c).

4. Observations

4.1. Surface ruptures and environment effects of the 2016 Parina earthquake

The surface ruptures generated by the Parina earthquake consisted of two NW-SE trending segments separated by a gap of 4 km, which we call the **Parina Gap** (Fig. 3a). The northern segment of surface ruptures (the Saguanani Segment, SS) is $\sim 2 \text{ km}$ long, whilst the southern segment (the Lurini Segment, LS) is $\sim 6 \text{ km}$ long, with both being defined by a semi-continuous trace of ruptures offsetting the surface sediment and bedrock.

4.1.1. Saguanani and Lurini segments

The Saguanani Segment, located at the northern end of the Parina Fault, displayed average vertical offsets across the surface ruptures of 3 cm, with maximum vertical offsets up to 8 cm (Figs. 4c and 5). The surface ruptures formed a series of sub-parallel, overlapping **strands that are best preserved** in sag ponds formed in the interfluvial crests between E-W trending moraine crests. The surface ruptures terminate at their southern end where they intersect a \sim NW-SE trending stream, and their northern termination occurs at the northern-most limit of lateral moraines around Lake Saguanani.

The Lurini Segment preserved far larger vertical and tensional offsets across the ruptures of up to 27 cm (Fig. 4a and b). Vertical and horizontal displacements across the ruptures decrease from a maximum in the middle of the Lurini Segment to a minimum at the tips of the segment with a **slip-length ratio of 5×10^{-5}** , matching the classic triangular shape expected for active normal faults (Cowie and Scholz, 1992) (see Fig. 5a and b). The northern $\sim 750 \text{ m}$ of the Lurini Segment consists of overlapping, sub-parallel strands of ruptures, whilst towards the south-east the remaining $\sim 5 \text{ km}$ of ruptures follow a single, curvilinear trace. The northern termination of the ruptures in the Lurini Segment occurs in a region coincident with sag small ponds and evidence for liquefaction, whilst the southern termination of the surface ruptures occurs where the fault trace crosses a stream.

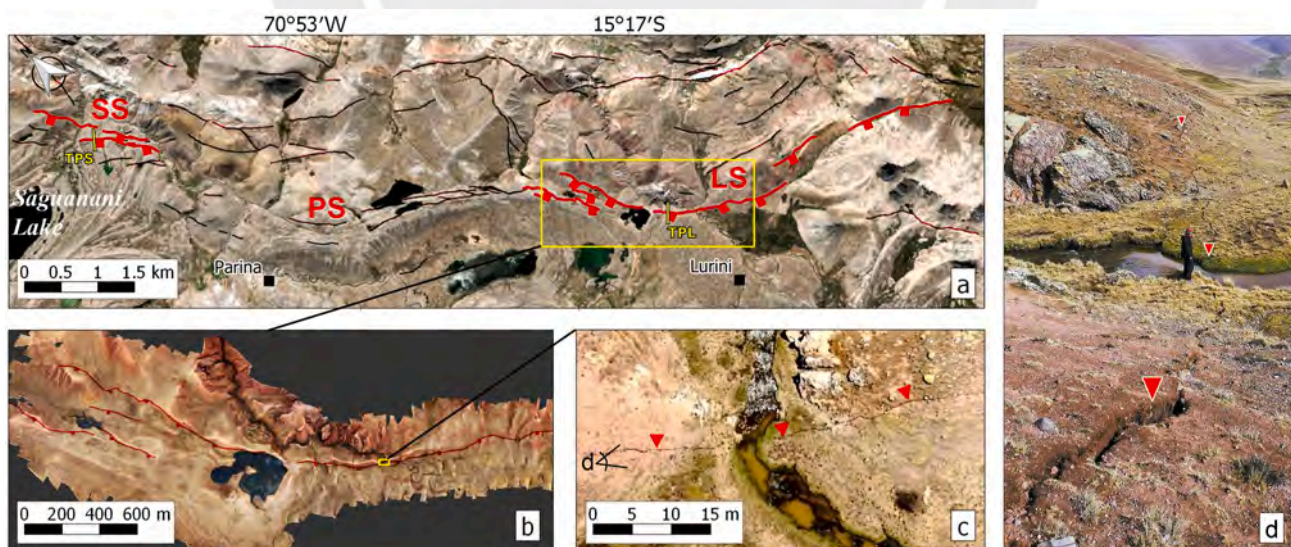


Fig. 3. a) Optical satellite imagery (from Google, DigitalGlobe) showing in red lines the Parina fault segments: Saguanani segment (SS), Parina segment (PS) and Lurini segment (LS). Black lines are Holocene tectonics scarps mapped during field work. Note that in the Parina segment there is no surface rupture trace. b) Red relief image map (RRIM) derived from the DEM (Chiba et al., 2007, 2008), built with photogrammetric surveyed data along the surface rupture (this study). Red lines are highlighting the surface rupture surveyed by foot along the fault trace. The location of the high-resolution DEM is highlighted by the yellow box in (a). c) Aerial photograph from the flying Ebee (4 cm in resolution). The footwall (top) and hanging wall (bottom) are limited by the scarp indicated by red triangles, note the scarp is cut by a stream, its flow direction is from south to north. The location of this drone image is outlined as a yellow box on (b). d) Surface offset associated to Parina earthquake; picture taken from western stream margin looking south-east along the scarp. Location is displayed in "d" letter in (c). (For interpretation of the references to color in this figure legend, the reader is referred to the Web version of this article.)



Fig. 4. Field photographs of coseismic surface ruptures and associated shaking effects. a) ~10 cm surface rupture, located in Lurini segment. b) ~27 cm surface rupture, located in Lurini segment. c) ~20 cm crack opening, located in Lurini segment. d) Sand boils west of the lake in Parina segment. e) Jumping stones, which are co-located with the sand boils, in Parina segment. f) Rockfall, which dammed the Jatun Ayllu River, some 12 km north of the epicenter. Note that near to surface rupture there is no more rock fall, probably due to the limited relief. See the yellow circle for the scale. (For interpretation of the references to color in this figure legend, the reader is referred to the Web version of this article.)

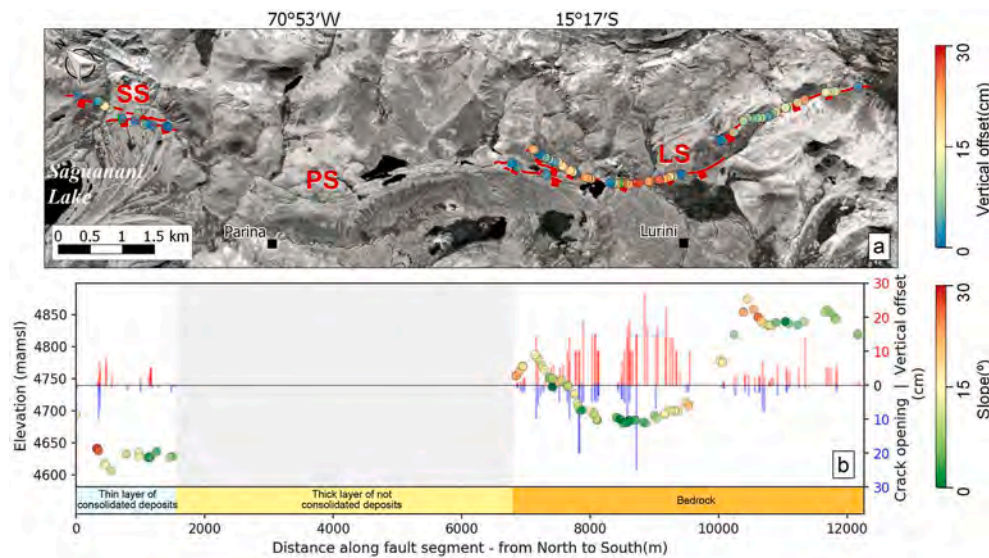


Fig. 5. a) Along-strike distribution of surface ruptures. Circles are sites where we measured the offset across the surface ruptures and are colored according to vertical offset. SS is the Saguanani segment, PS is the Parina segment and LS is the Lurini segment. b) Surface rupture data as a function of distance along the fault trace. The colored circles represent the surface slope at the location of each measurement of the surface rupture offset. Bars in red show the vertical offset measurements, and bars in blue show the crack opening measurements. The geology that the surface ruptures cut at the surface is shown below the profile in (b). (For interpretation of the references to color in this figure legend, the reader is referred to the Web version of this article.)

Along the Saguanani and Lurini Segments, the landscape has a low relief, and we did not observe any superficial mass movements with uphill extensional scars and downhill compressional bulges. A slope map generated from the high-resolution DEM shows that the slopes around the surface ruptures are below 15° on average, and that at Lurini, where vertical displacement is greatest, the topographic slope is at its lowest $<10^\circ$ (Fig. 5b). As slopes in granular material are generally stable at angles of repose $<30^\circ$, and the observation that regions with the highest slope angle have the smallest offsets across the surface ruptures, we believe that the first-order variations in displacement across the surface ruptures reflect variations in slip on the shallow portion of the Parina Fault, and not surface slope instability.

4.1.2. Parina Gap

Between the Saguanani and Lurini Segments there is a distinct gap in the mapped rupture trace. Although this gap does not show any evidence of surface rupture, we mapped several features that are commonly associated with near-field ground shaking within this region, such as sand boils (Fig. 4d and e) and jumping stones (Fig. 4e).

The sand boils are found within the hanging wall of the Parina Fault in areas of dry lake beds (Fig. 4d), are ~ 30 cm in diameter and are formed of medium-to-fine grained brown sands. In other settings, sand boils typically form through the ejection of fluidized sand through the shallow clay-rich sediments as a result of the shaking generated during an earthquake. This behavior of the near-surface sediment can last for a significant time after the seismic shaking, as the fine-grained sediments relax into a stable packing configuration and continue to expel pore waters (see Rodríguez-Pascua et al., 2015). The presence of sand boils within the Parina Gap is indicative of seismically-induced liquefaction around the Parina Fault in this area.

Jumping stones are volcanic boulders of ~ 20 – 30 cm diameter that are displaced laterally from their original resting place with no evidence of rolling along the sediment surface (Fig. 4e), indicating they have been lifted vertically and translated relative to the ground surface whilst in the air (e.g. King et al., 2018). We observe the jumping stones within the uplifted footwall of the Parina Gap and find they are consistently translated ~ 20 – 30 cm towards the south-east, which is roughly parallel to the fault trace inferred from the Saguanani and Lurini surface ruptures. For the stones to leave the ground surface means that the vertical ground acceleration exceeded 1 g during the earthquake. In addition, there must have been some horizontal component to the ground velocity either during the instant the stones left the ground surface, or whilst the stones were in the air.

4.1.3. Landsliding and rockfalls

The area near Parina is characterised by gentle relief. Nonetheless, we observed gravitational processes such as rock falls and small landslides in the epicentral region, in particular the Jatun Ayllu ravine (Fig. 1). This rockfall was located 13 km from the epicentral and covered a total area of ~ 0.60 km² (Fig. 4f). Rock falls were constituted of individual boulders or disrupted m-scale boulders (up to 10 m high) that descended slopes by rolling, jumping or free fall. This type of landslide was less common in comparison to shallow, disrupted landslides.

4.2. Late quaternary fault scarps on the Parina Fault

The surface ruptures formed in the 2016 Parina earthquake consistently follow ~ 5 to 20 m-high, pre-existing scarps cutting bedrock, alluvium and glacial deposits along the base of a ~ 150 m-high escarpment that marks the footwall of the Parina Fault. If these metre-high scarps are formed by repeated slip on the Parina Fault, the scarp heights correspond to a minimum vertical tectonic offset since the last period of glacial resurfacing and moraine formation at Parina. Exposure and radiocarbon dating of moraines in the nearby Cordillera Vilcanota suggest the last major episode of moraine deposition occurred during the Last Glacial Maximum ~ 10 – 45 ka (Clapperton, 1983), roughly placing the moraines and scarps as late Quaternary in age.

We used the high-resolution DEM to map the late Quaternary fault scarps and find that their along-strike distribution is similar to the surface ruptures generated by the 2016 Parina earthquake, but with some subtle differences (Fig. 7a,7 b). At Saguanani, the late Quaternary scarps form a series of sub-parallel strands that have offset the crests of nested lateral moraines and are directly coincident with the surface ruptures. We did not identify any late Quaternary scarps preserved in the Parina Gap – the same region there were no surface ruptures. In the Lurini Segment, late Quaternary fault scarps do outcrop along much of the surface rupture trace, but extend ~ 1 km further north-west than the 2016 surface ruptures, and do not occur along the ~ 1.5 km of the south-eastern end of the rupture trace.

We also extracted a series of topographic profiles across the late Quaternary fault scarps from our high-resolution DEM, in order to compare the along-strike scarp height distribution to the surface rupture heights. We calculate the scarp heights by using least-squares regression to fit lines to points above and below the scarp, and calculated the vertical separation of these lines. In many

places the scarp height variations may not reflect variations in fault throw, as erosional scouring within the hanging wall by axially-draining streams and deposition within small sag ponds may mask fault throw variations. We therefore only estimated scarp heights on selected surfaces that could be reliably correlated across the fault, such as moraine crests and abandoned fan surfaces (Fig. 6). As a result of this selective sampling, the along-strike distribution of late Quaternary scarp height measurements is far sparser than the surface rupture height distribution (compare Fig. 7d and e).

In the Saguanani Segment, we summed the vertical offsets across the sub-parallel fault scarps cutting late Quaternary moraine crests to estimate the cumulative vertical offset is between 5 and 15 m at different points along-strike. In the Luruni Segment

there are fewer places to make reliable scarp measurements, but the scarps are between 5 and 10 m-high. In contrast with the along-strike distribution of surface rupture heights in the 2016 Parina earthquake, the late Quaternary scarp heights do not increase towards the center of the Luruni Segment (Fig. 7d and e). Areas where the surface ruptures had the highest vertical offset and tensional opening do not necessarily correspond to where the Quaternary fault scarps were highest.

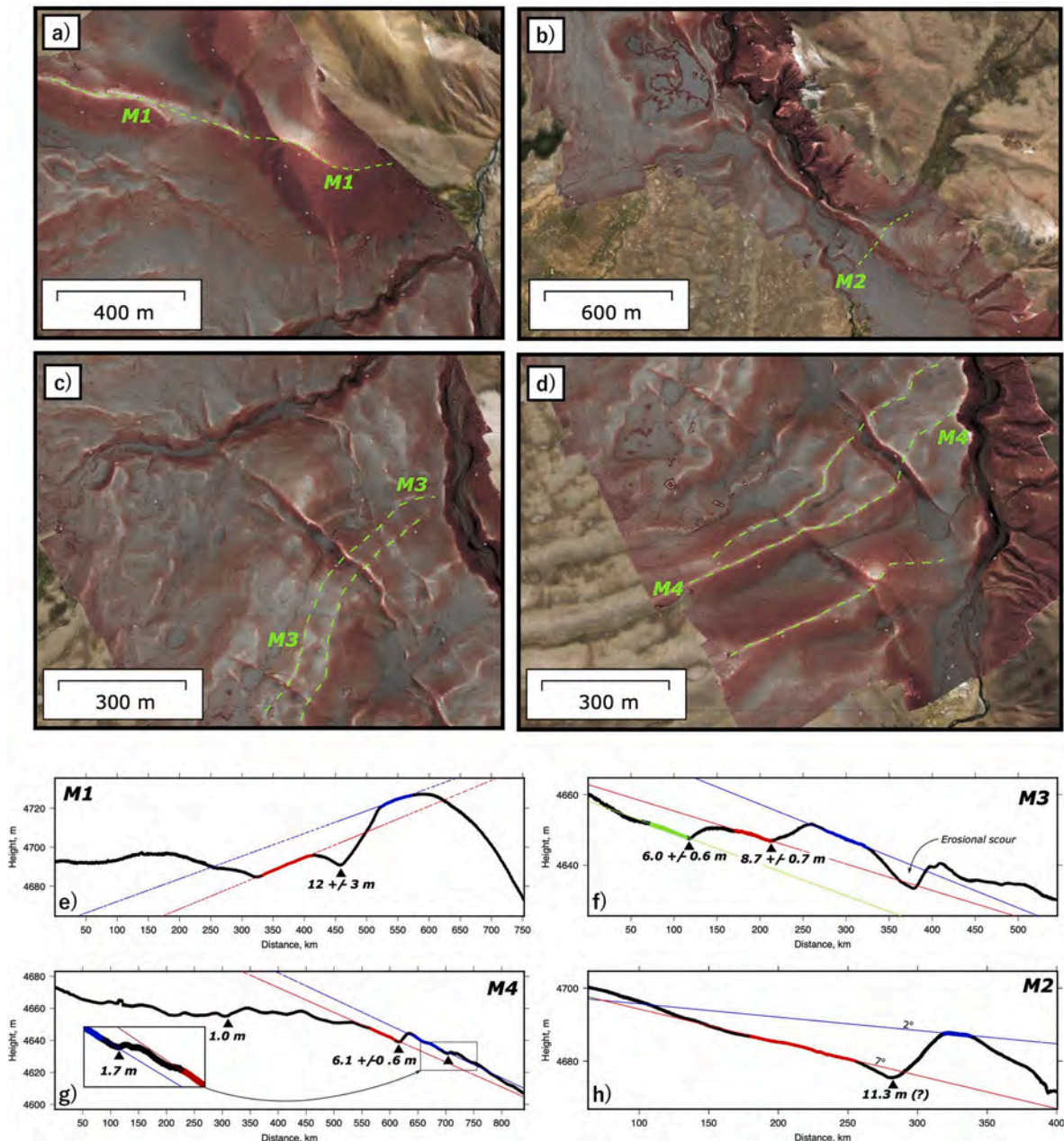


Fig. 6. Topographic profiles across the late Quaternary fault scarps extracted from high-resolution DEM. (a–d) Relief maps of the Parina late Quaternary scarps in the Saguanani (a,c,d) and Luruni (b) segments. Dashed green lines indicate profiles along surfaces or moraine crests that have been offset by the fault. Example topographic profiles are shown below. On the profiles, lines have been fit in a least-squares sense to points in the hangingwall (red) and footwall (blue), and the scarp height is measured as the vertical offset between these lines at the foot of the scarp. On low-dip angle surfaces ($<10^\circ$), the scarp height is similar to the fault throw to within $\pm 15\%$. (For interpretation of the references to color in this figure legend, the reader is referred to the Web version of this article.)

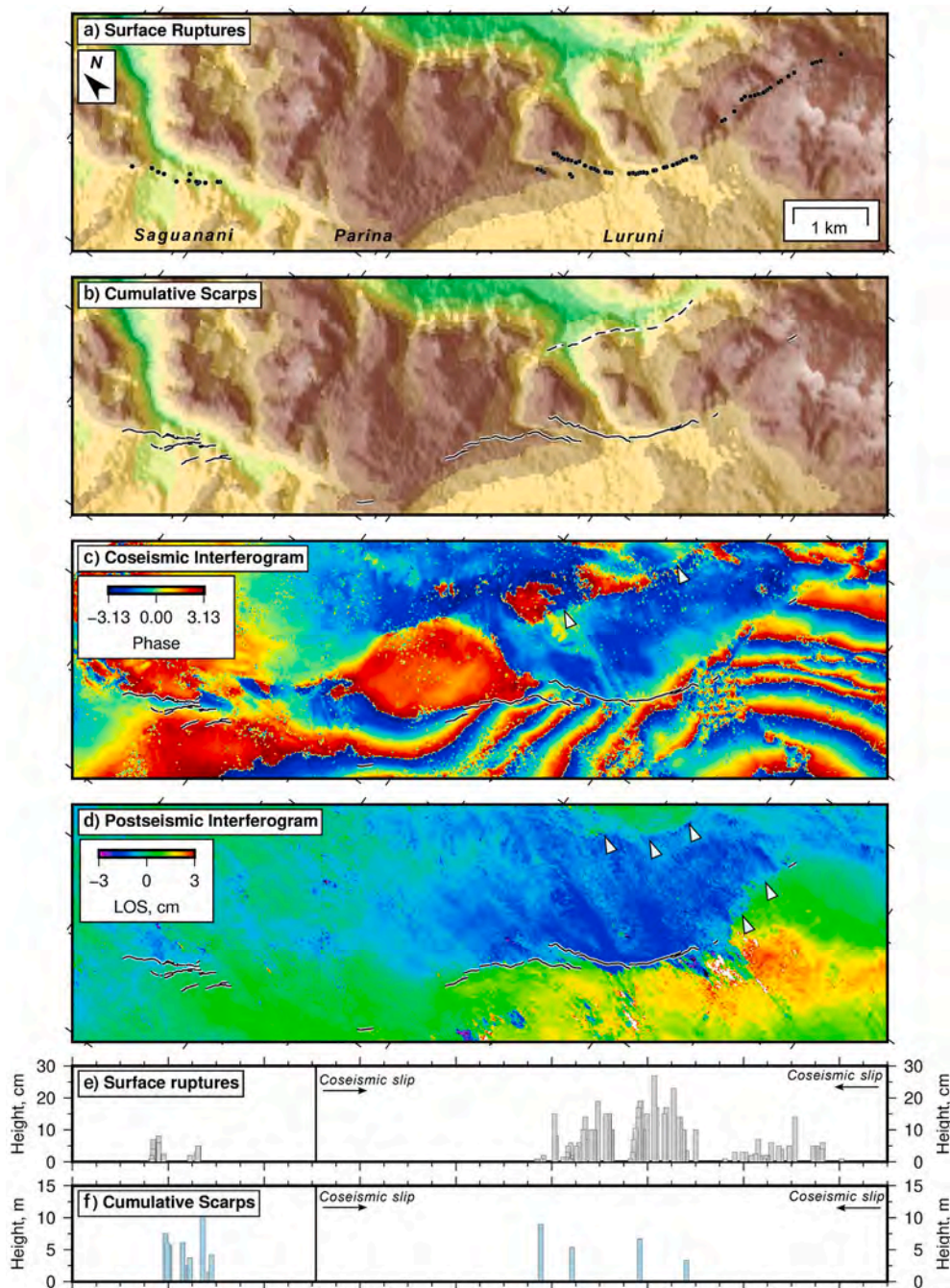


Fig. 7. Comparison of the topography with the surface ruptures, late Quaternary scarps, coseismic and **post-seismic** surface displacements. (a) SRTM 30 m topography with the mapped surface ruptures shown as black dots. (b) The same topography with mapped late Quaternary scarps shown as black lines. (c) Wrapped descending-track coseismic interferogram. (d) Unwrapped descending-track **post-seismic** interferogram between December 20, 2016 and June 30, 2017. (e) Along-strike distribution of coseismic surface rupture heights. (f) Along-strike distribution of cumulative scarp heights measured from offset moraine crests and fan surfaces using the high-resolution DEM.

5. Discussion

5.1. Surface ruptures, late quaternary scarps and slip on the Parina Fault

In this section we present a comparison between the surface ruptures and late Quaternary scarp heights mapped in this study, and the co- and post-seismic surface deformation recorded by InSAR from [Wimpenny et al. \(2018\)](#) to study how co- and post-seismic fault slip contribute to surface rupture formation and fault scarp growth.

The coseismic interferograms captured a relatively smooth pattern of surface displacement in the earthquake with 5–6 concentric fringes in the interferometric wrapped phase to the southwest of the mapped surface ruptures corresponding to ~15–20 cm of line-of-sight motion. Patches of low coherence in the interferogram visible as speckle within the fault hangingwall coincide with a marshy area that may have

undergone significant liquefaction ([Fig. 7d](#)). Interferogram fringes are truncated in the location of the surface ruptures on the Luruni Segment, but not on the Saguanani Segment, indicating that more slip reached the shallow fault zone at Luruni than Saguanani. In addition, the peak line-of-sight displacement at the center of the fringe pattern directly correlates with the location of the highest surface ruptures ([Fig. 7c,e](#)).

[Wimpenny et al. \(2018\)](#) and [Xu et al. \(2019\)](#) inverted the coseismic InSAR measurements for the geometry of the Parina Fault and the distribution of fault slip in the earthquake. Both studies found that the majority of fault slip (~50–70 cm) occurred between 3 and 10 km depth beneath the central Luruni Segment, whilst the InSAR data do not require any coseismic fault slip beneath the Saguanani Segment. Neither study required there to be slip within the top 2 km of the fault zone at any point along-strike, leading to the inference of a ‘shallow slip deficit’ (e.g. [Fialko et al., 2005](#); [Xu et al., 2019](#)). However, the fault dip

determined from the kinematic slip inversions (40°) and the maximum surface rupture height (27 cm) requires there was at least 35 cm of slip in parts of the shallow fault zone, highlighting the widely-recognized limitation of kinematic slip inversions using an elastic half-space Green's Function to accurately capture small-scale variations in near-surface fault slip.

Post-seismic slip may also contribute to the formation of surface ruptures and scarps. Post-seismic surface displacements measured from InSAR (Fig. 7d) indicate that the Luruni segment experienced ~7 cm of shallow afterslip between 0 and 3 km depth in the year following the earthquake coincident with the surface rupture trace (Wimpenny et al., 2018). Beneath the central part of the Parina Gap, ~2–4 cm of afterslip remained buried between ~2 and 5 km and did not reach the surface (Xu et al., 2019). There is little evidence for post-seismic deformation in the Saguanani Segment that could be related to shallow afterslip (Fig. 7d).

The comparison between the InSAR measurements, surface ruptures and fault scarps highlights a number of key features: (1) co- and post-seismic fault slip did occur at depth beneath the gap in the surface rupture trace, but this slip did not propagate to the surface in the 2016 earthquake, or in any scarp-forming earthquakes in the late Quaternary, (2) despite there being no resolvable co- or post-seismic slip beneath the surface ruptures of the Saguanani segment, late Quaternary scarps cutting lateral moraine crests in this area indicate there has been significant slip on this section of the Parina Fault in the late Quaternary, and (3) shallow post-seismic deformation can contribute a significant fraction (~20%) of fault scarp and surface rupture heights.

5.2. Preservation of surface ruptures, late quaternary scarps and surface geology

The kinematics and distribution of the surface ruptures and fault scarps at Saguanani and Luruni are independent of the topography, but vary along-strike in a manner that is not related to the first-order variation of slip at depth derived from the InSAR measurements. The prime example of this behavior is beneath the Parina Gap. There are subtle differences between the surface geology and conditions in the Saguanani-Luruni segments and the Parina Gap that may account for the along-strike variations in surface rupture and fault scarp preservation. At Saguanani and Luruni the surface geology consists of a thin veneer of unconsolidated sediments, including Last Glacial Maximum moraines and Pleistocene fluvio-glacial deposits that cover the bedrock, which can be seen exposed where streams cut through the fault footwall (Fig. 2b). In contrast, along the central Parina Gap, the extrapolated fault trace would cut through depressions filled with lacustrine and fluvio-glacial sediments dotted with small water bodies, suggesting the ground may be saturated in the near surface. We found evidence for this saturation when we attempted to trench a section of the fault near the north-western tip of the Luruni segment.

It seems likely that the 2016 Parina earthquake and previous late Quaternary earthquakes did not propagate to the surface in the Parina segment, either because of the quasi-plastic mechanical properties of the unconsolidated fluvio-glacial deposits, or because much of the near-surface material in the Parina segment liquefied during the earthquake, both of which prevent discrete ruptures forming. The observation that surface ruptures are absent in regions where liquefaction features are present suggests the latter of these two suggestions may be the dominant control at Parina.

The control of surface geological conditions on coseismic surface rupture patterns is well-documented. Khajavi et al. (2014) proposed that the thickness of the cover deposits or unconsolidated sediment is an important control on surface rupture on the Hope Fault, New Zealand. During the 2016 Amatrice-Norcia earthquake sequence, Pucci et al. (2017) and Civico et al. (2018) observed this same effect along the Laga Mts Fault and the Monte Vettore faults. Similarly, Moss et al. (2013) and Stanton (2013) concluded that the likelihood of rupture propagation to the surface is controlled by parameters such as the thickness and

stiffness of the surface cover.

Just as the surface ruptures are not formed everywhere up-dip of the main coseismic rupture area at depth, the late Quaternary scarps are also discontinuous along-strike and are only preserved in certain settings. At Parina, the best-preserved fault scarps are in the Saguanani Segment, where the fault has cut late Quaternary lateral moraines. This is a pattern recognized across much of south Peru and offers a general rule for mapping faults in the region: recently-active faults are best preserved in regions affected by recent glaciation. As the active normal faults have accommodated little finite extension, their footwalls are not always elevated relative to their hangingwall basin, and therefore the standard morphology associated with normal faults in faster-deforming parts of the world (e.g. Greece, western Turkey; Jackson et al., 1982; Hubert-Ferrari et al., 2002) is difficult to identify in the Altiplano of southern Peru. In addition, a previous phase of shortening in the late Miocene (Perez and Horton, 2014) has left remnant topography associated with upright anticlinal folding and footwall ridges that is often larger in amplitude than that formed by normal faulting meaning faults can be nearly impossible to identify from the regional topography alone. As a result, if most faults are only being preserved where they cut recently-deposited moraines, there is significant difficulty in understanding the along-strike continuity of the normal faults in the Peruvian Altiplano from geomorphology alone. Similarly, there is probably a significant sampling bias in fault mapping in the region related to where late Quaternary moraines are well preserved in the Altiplano.

5.3. The Parina earthquake surface ruptures and scaling relationships

In seismic hazard analyses, the maximum magnitude of a potential earthquake on a mapped fault is determined by comparing field observations of fault lengths and slip during individual events to empirical scaling relationships between M_w and length or slip (e.g. Wells and Coppersmith, 1994, hereafter W&C94). Such relationships are obtained after statistical analysis of a large number of previous events. However, there is a significant spread in the data used to construct these empirical relationships, and along-strike variations in near-surface geological conditions can significantly affect the size and outcrop of surface ruptures (Champenois et al., 2017; Ritz et al., 2020). Here, we compare our observations from the Parina earthquake to the W&C94 predictions.

The different values of surface rupture length (SRL), average displacement (AD) and maximum displacement (MD) for individual and combined segments are reported in Table 1. Note that to calculate the fault length including the Parina Gap, we argue that the fault remained buried at shallow depth because of the unfavorable surface geology, as suggested by the InSAR-derived coseismic source model. The final length is 12 km and we consider this to be representative of the surface rupture length in the scaling relationships.

Table 1

Data referring to the average displacement (AD), maximum displacement (MD) and the length of the surface rupture (SRL), in order to estimate the magnitude with Wells and Coppersmith (1994) approach for Saguanani (SS) and Luruni (LS) segments independently, totally with both segments and plus with Parina segment (PS).

Segments	AD (cm)	MD (cm)	SRL (km)	Mw from AD (Normal Fault, WC94)	Mw from MD (Normal Fault, WC94)	Mw from SRL (Normal Fault, WC94)
				(±0.33)	(±0.34)	(±0.34)
LS	6.8	27	6	6.0	6.2	5.9
Total SS + LS	6	27	7.7	6.0	6.2	6.0
Total SS + PS + LS	5.3	27	12	6.0	6.2	6.3

This simple analysis shows that the *Wells and Coppersmith (1994)* empirical scaling between fault slip, length and the resulting earthquake magnitude is accurate when using maximum displacement, giving Mw values close to actual instrumental measurement; total surface length at the surface and shallow subsurface fault (SS + PS + LS) scenario also gives a reasonable value. Using AD provides systematically lower prediction of the earthquake magnitude (Mw 6). Our conclusion is that, for moderate magnitude earthquakes such as that at Parina, the MD or SRL parameters of W&C94 appear to provide a reasonably accurate way of estimating the possible magnitude of earthquakes along faults.

5.4. Lessons for seismic hazard assessment

Two key results have come out of this study that provide new lessons on seismic hazard assessment from paleoearthquake data in the Peruvian Altiplano.

Firstly, there may be a significant preservation bias associated with Holocene normal faults in the Altiplano. Pleistocene glaciation deposited lateral moraines and drift sheets across much of the Altiplano that provide ideal marker surfaces to study faulting, and most of the active faults mapped to date are identified based on offset glacial deposits (e.g. *Benavente et al., 2013; Wimpenny et al., 2020*). In places where there are no glacial deposits, faults are far more difficult to identify as they have accommodated little finite slip, and fault maps may underestimate the number of potentially seismogenic faults in these areas.

Second, any along-strike variability and segmentation of paleoseismic surface ruptures may not accurately reflect along-strike variations in the earthquake rupture at depth. The surface scarps generated by the Parina earthquake were clearly split into two sections, separated by a gap of ~4 km, despite the slip at depth extending beneath the surface rupture gap. Therefore estimates of the size of past earthquakes based on the along-strike length of their rupture trace must take into account possible gaps caused by near-surface geology.

Surface rupture on shallow, continental faults poses a significant threat for transport infrastructure, villages and critical facilities such as gas pipelines (*Baize et al., 2020*). In Peru, this surface rupture hazard is rarely taken into account in hazard analyses. Probabilistic and empirical approaches to assessing hazard suffer due to the scarcity of data in the low-to-moderate magnitude range for shallow continental events, and often only consider the effect of the seismic waves. The lack of detailed surface rupture description thus results in poorly-constrained hazard assessment in the high Andes (*Yepes et al., 2016*) in comparison to our understanding of the hazard posed by megathrust ruptures on the subduction zone (*Audin et al., 2008*).

6. Conclusions

In this study, we have analysed the heterogeneous surface displacements generated by the moderate-magnitude Parina earthquake in the high Peruvian Andes through a combination of high-resolution DEMs, InSAR data and geological field investigation. We have demonstrated that both late Quaternary slip and the recent Mw 6.1 earthquake have occurred along a newly-identified normal fault, known as the Parina Fault. Similar faults elsewhere in the Peruvian Altiplano may pose a significant seismic hazard to the local population from the effects of shaking on infrastructure and from the secondary hazards of liquefaction and landsliding or rock falls, **particularly in towns and villages sat within hangingwall basins**. However, these faults may be difficult to map in regions where there has been no late Quaternary sedimentation, as the finite extension on the normal faults in the Altiplano is small owing to a recent change in the style of deformation in the region. **In regions where recent fault scarps can be identified**, detailed mapping of the coseismic surface ruptures highlighted that significant along-strike variability in the rupture heights can occur that is not correlated with along-strike changes in the **coseismic slip pattern** at depth, which would imply that trenching a single section of a fault may not accurately

reflect the magnitude of paleo-earthquake offsets on this fault, but could provide evidence on earthquake chronology.

The Parina event is a reminder that **shallow** earthquakes of moderate magnitude pose a real hazard to communities and infrastructure in the Altiplano – possibly greater than megathrust earthquakes on the subduction interface (*Costa et al., 2020*). The Parina event taught us that the reactivation of these intra-continental faults generates local accelerations >1 g. Many regions exist in the same regime, with little or no geodetically-measurable horizontal deformation, minimal current seismic activity, no documented paleoseismicity and geomorphology that has been shaped by many competing processes – not just faulting (for instance, in the French Alps: *Nocquet et al., 2016* or in Central USA: *Calais et al., 2016*). To better assess the seismic hazard in these regions, we must first develop an understanding of how active faulting is recorded in the landscape, both at long and short term.

Declaration of competing interest

The authors declare that they have no known competing financial interests or personal relationships that could have appeared to influence the work reported in this paper.

Acknowledgements

This work was supported by the INGEMMET (Geological Survey of Peru), IRD (Institut de Recherche pour le Développement), IRSN (Institute of Radiological Protection and Nuclear Safety) and the Cusco-PATA Project “Paleoseismology, Archeoseismology and Active Tectonics” (grant 006-2016-FONDECYT). SW thanks NERC-COMET and the British Geological Survey for PhD studentship funding. We also want to thank the authorities of the Province of Lampa-Puno, for providing facilities that permitted to develop the work. **The authors thank the Editor and to anonymous reviewer for constructive comments on this manuscript.**

References

- Agisoft, 2017. Agisoft PhotoScan Professional Edition. Agisoft. Retrieved from <http://www.agisoft.com/downloads/installer/>, Version 1.4.
- Ainscoe, E.A., Abdrakhmatov, K.E., Baikulov, S., Carr, A.S., Elliott, A.J., Grützner, C., Walker, R.T., 2018. Variability in surface rupture between successive earthquakes on the Susamyr Fault, Kyrgyz Tien Shan: implications for palaeoseismology. *Geophys. J. Int.* 216, 703–725 <https://doi.org/10/ggmr84>.
- Audin, L., Lacan, P., Tavera, H., Bondoux, F., 2008. Upper plate deformation and seismic barrier in front of Nazca subduction zone: the Chololo Fault System and active tectonics along the Coastal Cordillera, southern Peru. *Tectonophysics* 459 (1–4), 174–185 <https://doi.org/10/b9pr9z>.
- Baize, S., Nurminen, F., Sarmiento, A., Dawson, T., Takao, M., Scotti, O., et al., 2020. A worldwide and unified database of surface ruptures (SURE) for fault displacement hazard analyses. *Seismol. Res. Lett.* 91 (1), 499–520 <https://doi.org/10/ggbdx>.
- Bellier, O., Dumont, J.F., Sébrier, M., Mercier, J.L., 1991. Geological constraints on the kinematics and fault-plane solution of the quiches fault zone reactivated during the 10 November 1946 Ancash earthquake, northern Peru. *Bull. Seismol. Soc. Am.* 81 (2), 468–490.
- Benavente, C., Delgado, F., Taibe, E., Audin, L., Pari, W., 2013. *Neotectónica y Peligro Sísmico en el Región Cusco—Boletín Nro 55 Serie C*. INGEMMET. Retrieved from <http://repositorio.ingemmet.gob.pe/handle/ingemmet/296>.
- Benavente, C., Zerathe, S., Audin, L., Hall, S.R., Robert, X., Delgado, F., et al., 2017. Active transpressional tectonics in the Andean forearc of southern Peru quantified by ¹⁰Be surface exposure dating of an active fault scarp: active Tectonics in Southern Peru. *Tectonics* 36 (9), 1662–1678 <https://doi.org/10/gcg5jr>.
- Cabrera, J., Sébrier, M., 1998. Surface rupture associated with a 5.3-mb earthquake: the 5 April 1986 Cuzco earthquake and kinematics of the Chincheros-Quoricocha faults of the High Andes, Peru. *Bull. Seismol. Soc. Am.* 88 (1), 242–255.
- Calais, E., Camelbeeck, T., Stein, S., Liu, M., Craig, T.J., 2016. A new paradigm for large earthquakes in stable continental plate interiors: LARGE EARTHQUAKES IN SCRS. *Geophys. Res. Lett.* 43 (20) <https://doi.org/10.1002/2016GL070815>, 10,621–10,637.
- Carlotto, V., 1998. *Evolution andine et raccourcissement au niveau de Cusco (13°-16°S), Pérou: Enregistrement sédimentaire, chronologie, contrôles paléogéographiques, évolution cinématique*. Université Joseph-Fourier - Grenoble I. Retrieved from <https://tel.archives-ouvertes.fr/tel-00517507>.
- Champanois, J., Baize, S., Vallee, M., Jomard, H., Alvarado, A., Espin, P., et al., 2017. Evidences of surface rupture associated with a low-magnitude (Mw 5.0) shallow earthquake in the Ecuadorian Andes: andean earthquake surface rupture.

- J. Geophys. Res.: Solid Earth 122 (10), 8446–8458. <https://doi.org/10.1002/2017JB013928>.
- Chiba, T., Kaneta, S., Suzuki, Y., 2008. Red relief image map: new visualization method for three dimensional data. *Int. Arch. Photogram. Rem. Sens. Spatial Inf. Sci.* 37 (B2), 1071–1076.
- Chiba, T., Suzuki, Y., Hiramatsu, T., 2007. Digital terrain representation methods and red relief image map, A new visualization approach. *Map J. Jpn. Cartogr. Assoc.* 45 (1), 27–36. <https://doi.org/10.11212/jjca1963.45.27>.
- Civico, R., Pucci, S., Villani, F., Pizzimenti, L., De Martini, P.M., Nappi, R., the Open EMERGE Working Group, 2018. Surface ruptures following the 30 October 2016 Mw 6.5 Norcia earthquake, central Italy. *J. Maps* 14 (2), 151–160. <https://doi.org/10.1080/17445647.2018.1441756>.
- Clapperton, C.M., 1983. The glaciation of the Andes. *Quat. Sci. Rev.* 2 (2–3), 83–155.
- Costa, C., Alvarado, A., Audemar, F., Audin, L., Benavente, C., Bezerra, F.H., et al., 2020. Hazardous faults of South America; compilation and overview. *J. S. Am. Earth Sci.* 104, 102837 <https://doi.org/10/ghdn5r>.
- Cowie, P.A., Scholz, C.H., 1992. Growth of faults by accumulation of seismic slip. *J. Geophys. Res.: Solid Earth* 97 (B7), 11085–11095 <https://doi.org/10/ctnv2t>.
- Ekström, G., Nettles, M., Dziewoński, A.M., 2012. The global CMT project 2004–2010: centroid-moment tensors for 13,017 earthquakes. *Phys. Earth Planet. In.* 200–201, 1–9 <https://doi.org/10/gctpdx>.
- Ellison, R.A., Klinck, B.A., Hawkins, M.P., 1989. Deformation events in the andean orogenic cycle in the Altiplano and western Cordillera, southern Peru. *J. S. Am. Earth Sci.* 2 (3), 263–276 <https://doi.org/10/bc7f8w>.
- Ericksen, G.E., Concha, J.F., Silgado, E., 1954. The Cusco, Peru, earthquake of may 21, 1950. *Bull. Seismol. Soc. Am.* 44 (2A), 97–112.
- Fialko, Y., Sandwell, D., Simons, M., Rosen, P., 2005. Three-dimensional deformation caused by the Bam, Iran, earthquake and the origin of shallow slip deficit. *Nature* 435 (7040), 295–299 <https://doi.org/10/fh7bft>.
- Hubert-Ferrari, A., Armijo, R., King, G., Meyer, B., Barka, A., 2002. Morphology, displacement, and slip rates along the north anatolian fault, Turkey: the north anatolian fault. *J. Geophys. Res.: Solid Earth* 107 (B10), ETG 9-1-ETG 9-33. <https://doi.org/10/cr3t23>.
- INGEMMET, 2017. GEOCATMIN - SISTEMA DE INFORMACIÓN GEOLÓGICA Y CATASTRAL MINERO. Retrieved from. <http://geocatmin.ingemmet.gob.pe>.
- Jackson, J.A., Gagnepain, J., Houseman, G., King, G.C.P., Papadimitriou, P., Soufleris, C., Virieux, J., 1982. Seismicity, normal faulting, and the geomorphological development of the gulf of corinth (Greece): the corinth earthquakes of february and march 1981. *Earth Planet Sci. Lett.* 57 (2), 377–397 <https://doi.org/10/bbphj4>.
- Jaillard, E., Santander, G., 1992. La tectónica polifásica en escamas de la zona de Manazo—lagunillas (Puno, sur del Peru). *Bulletin de l'Institut Français d'Etudes Andines* 21 (1), 37–58.
- Khajavi, N., Quigley, M., Langridge, R.M., 2014. Influence of topography and basement depth on surface rupture morphology revealed from LiDAR and field mapping, Hope Fault, New Zealand. *Tectonophysics* 630, 265–284 <https://doi.org/10/f6gcwt>.
- King, T.R., Quigley, M.C., Clark, D., 2018. Earthquake environmental effects produced by the Mw 6.1, 20th May 2016 Petermann earthquake, Australia. *Tectonophysics* 747–748, 357–372 <https://doi.org/10/gbbhkp>.
- Llontop, J., Marrou, J., 2016. MOVIMIENTO SISMICO EN LA PROVINCIA DE LAMPA - PUNO (Informe de Emergencia No. 884). COEN - INDECI. Retrieved from. <https://www.indeci.gob.pe/objetos/alerta/MjUONG==/20161229211000.pdf>.
- Macharé, J., Escobar, B., Lenin, C., Audin, L., 2009. *Síntesis descriptiva del mapa neotectónico 2008—Boletín Nro 40 Serie C. INGENMET*. Retrieved from. <http://repositorio.ingemmet.gob.pe/handle/ingemmet/245>.
- Mercier, J.L., Sebrer, M., Lavenue, A., Cabrera, J., Bellier, O., Dumont, J.-F., Machare, J., 1992. Changes in the tectonic regime above a subduction zone of andean type: the Andes of Peru and Bolivia during the pliocene-pleistocene. *J. Geophys. Res.* 97 (B8), 11945 <https://doi.org/10/dmscwn>.
- Moss, R.E.S., Stanton, K.V., Buelna, M.J., 2013. The impact of material stiffness on the likelihood of fault rupture propagating to the ground surface. *Seismol. Res. Lett.* 84 (3), 485–488. <https://doi.org/10.1785/0220110109>.
- Nocquet, J.-M., Sue, C., Walpersdorf, A., Tran, T., Lenôtre, N., Vernant, P., et al., 2016. Present-day uplift of the western Alps. *Sci. Rep.* 6, 28404. <https://doi.org/10.1038/srep28404>.
- Perez, N.D., Horton, B.K., 2014. Oligocene-Miocene deformational and depositional history of the Andean hinterland basin in the northern Altiplano plateau, southern Peru: peréz and Horton: N. Altiplano tectonics. *Tectonics* 33 (9), 1819–1847 <https://doi.org/10/f6mw2s>.
- Phillip, H., Megard, F., 1977. Structural analysis of the superficial deformation of the 1969 Pariahuanca earthquakes (Central Peru). *Tectonophysics* 38, 259–278 <https://doi.org/10/cfzqb3>.
- Pucci, S., De Martini, P.M., Civico, R., Villani, F., Nappi, R., Ricci, T., et al., 2017. Coseismic Ruptures of the 24 August 2016, Mw 6.0 Amatrice Earthquake (Central Italy): M 6 EARTHQUAKE COSEISMIC RUPTURE IN ITALY. *Geophysical Research Letters* <https://doi.org/10/gcpx7f>.
- Ritz, J.-F., Baize, S., Ferry, M., Larroque, C., Audin, L., Delouis, B., Mathot, E., 2020. Surface rupture and shallow fault reactivation during the 2019 Mw 4.9 Le Teil earthquake, France. *Commun. Earth Environ.* 1 (1), 10 <https://doi.org/10/gbhhsj>.
- Rodríguez-Pascua, M.A., Silva, P.G., Pérez-López, R., Giner-Robles, J.L., Martín-González, F., Del Moral, B., 2015. Polygenetic sand volcanoes: on the features of liquefaction processes generated by a single event (2012 Emilia Romagna 5.9 Mw earthquake, Italy). *Quat. Int.* 357, 329–335 <https://doi.org/10/f63mm3>.
- Schwartz, D.P., 1988. Paleoseismicity and neotectonics of the Cordillera blanca fault zone, northern Peruvian Andes. *J. Geophys. Res.: Solid Earth* 93 (B5), 4712–4730 <https://doi.org/10/cmqvtr>.
- Sébrier, M., Mercier, J.L., Mégard, F., Laubacher, G., Carey-Gailhardis, E., 1985a. Quaternary normal and reverse faulting and the state of stress in the central Andes of south Peru. *Tectonics* 4 (7), 739–780 <https://doi.org/10/dv7bkj>.
- Sébrier, M., Mercier, J.L., Mégard, F., Laubacher, G., Carey-Gailhardis, E., 1985b. Quaternary normal and reverse faulting and the state of stress in the central Andes of south Peru. *Tectonics* 4 (7), 739–780 <https://doi.org/10/dv7bkj>.
- Silgado, E., 1978. Historia de los sismos más notables ocurridos en el Perú (1513–1974). *Serie C. Geodinámica e Ingeniería Geológica*, 3.
- Stanton, K.V., 2013. Investigation of Parameters Influencing Reverse Fault Rupture Propagation to the Ground Surface. California Polytechnic State University. Retrieved from. <http://digitalcommons.calpoly.edu/theses/1145/>.
- Wells, D.L., Coppersmith, K.J., 1994. New empirical relationships among magnitude, rupture length, rupture width, rupture area, and surface displacement. *Bull. Seismol. Soc. Am.* 84 (4), 974–1002.
- Westoby, M.J., Brasington, J., Glasser, N.F., Hambrey, M.J., Reynolds, J.M., 2012. 'Structure-from-Motion' photogrammetry: a low-cost, effective tool for geoscience applications. *Geomorphology* 179, 300–314 <https://doi.org/10/f4m7ct>.
- Wimpenny, S., Benavente, C., Copley, A., Garcia, B., Rossell, L., O'Kane, A., Aguirre, E., 2020. Observations and dynamical implications of active normal faulting in south Peru. *Geophys. J. Int.* ggaa144. <https://doi.org/10/ggqtsb>.
- Wimpenny, S., Copley, A., Benavente, C., Aguirre, E., 2018. Extension and dynamics of the Andes inferred from the 2016 Parina (huarichancara) earthquake. *J. Geophys. Res.: Solid Earth* 123 (9), 8198–8228, 10/gd4s3s.
- Xu, G., Xu, C., Wen, Y., Yin, Z., 2019. Coseismic and postseismic deformation of the 2016 MW 6.2 Lampa earthquake, southern Peru, constrained by interferometric synthetic aperture radar. *J. Geophys. Res.: Solid Earth* 124 (4), 4250–4272 <https://doi.org/10/gfxsdk>.
- Yepes, H., Audin, L., Alvarado, A., Beauval, C., Aguilar, J., Font, Y., Cotton, F., 2016. A new view for the geodynamics of Ecuador: implication in seismogenic source definition and seismic hazard assessment: Ecuador geodynamics and psha. *Tectonics* 35 (5), 1249–1279 <https://doi.org/10/f8vmj9>.



HAL
open science

Pliocene river capture and incision of the northern Altiplano: Machu Picchu, Peru

Benjamin Gérard, Laurence Audin, Xavier Robert, Cécile Gautheron, Peter van Der Beek, Matthias Bernet, Carlos Benavente, Fabrizio Delgado

► **To cite this version:**

Benjamin Gérard, Laurence Audin, Xavier Robert, Cécile Gautheron, Peter van Der Beek, et al.. Pliocene river capture and incision of the northern Altiplano: Machu Picchu, Peru. Journal of the Geological Society, Geological Society of London, 2021, 178 (2), pp.jgs2020-100. 10.1144/jgs2020-100 . hal-03470137

HAL Id: hal-03470137

<https://hal.archives-ouvertes.fr/hal-03470137>

Submitted on 8 Dec 2021

HAL is a multi-disciplinary open access archive for the deposit and dissemination of scientific research documents, whether they are published or not. The documents may come from teaching and research institutions in France or abroad, or from public or private research centers.

L'archive ouverte pluridisciplinaire **HAL**, est destinée au dépôt et à la diffusion de documents scientifiques de niveau recherche, publiés ou non, émanant des établissements d'enseignement et de recherche français ou étrangers, des laboratoires publics ou privés.



Pliocene river capture and incision of the northern Altiplano: Machu Picchu, Peru

Benjamin Gérard^{1*}, Laurence Audin¹, Xavier Robert¹, Cécile Gautheron², Peter van der Beek^{1,3}, Matthias Bernet¹, Carlos Benavente^{4,5} and Fabrizio Delgado^{4,5}


¹ Université Grenoble Alpes, Université Savoie Mont Blanc, CNRS, IRD, IFSTTAR, ISTERre, 38000 Grenoble, France

² Université Paris-Saclay, CNRS, GEOPS, 91405, Orsay, France

³ Institut für Geowissenschaften, Universität Potsdam, 14476 Potsdam, Germany

⁴ INGEMMET, Instituto Geológico, Minero y Metalúrgico, Lima, Perú

⁵ Facultad de Ciencias e Ingeniería, Pontificia Universidad Católica del Perú, Lima, Perú

 BG, 0000-0001-8143-8343; LA, 0000-0002-4510-479X; XR, 0000-0002-0567-7497; CG, 0000-0001-7068-9868;

PvdB, 0000-0001-9581-3159; MB, 0000-0001-5046-7520; CB, 0000-0002-2237-0016; FD, 0000-0003-2029-0191

Present address: BG, GET, Université de Toulouse, CNRS, IRD, UPS, (Toulouse), France

* Correspondence: benjamin.gerard.alpes@gmail.com

Abstract: The Abancay Deflection, forming the northern edge of the Altiplano in the Peruvian Andes, is a remarkable geomorphological feature marking the along-strike segmentation of the Andes. Little is known about the timing and spatial distribution of exhumation in this area. To constrain the exhumation history of the Abancay Deflection and its drivers, we present apatite (U–Th)/He and fission-track thermochronology data from samples collected along an elevation transect at Machu Picchu. Geomorphological analysis demonstrates recent and continuing drainage reorganization recorded by the spatial distribution of the normalized steepness index (k_{sn}) and normalized integrated drainage area (χ) parameters. Thermochronologically derived cooling rates are converted into exhumation using regionally constrained geothermal gradients between 16 and 26°C km⁻¹. Time–temperature inversions imply steady and slow exhumation (<0.05 km Ma⁻¹) between 20 and 4 Ma, followed by rapid exhumation (>0.9 km Ma⁻¹) since 4 Ma. The timing of rapid exhumation, combined with the geomorphological analysis, suggests that fluvial capture of the previously endorheic Altiplano by the Urubamba River drove recent incision and exhumation. Depending on the value of the geothermal gradient used, total exhumation since 4 Ma can be explained by river incision alone or requires additional exhumation driven by tectonics, possibly associated with movement on the Apurímac fault.

Supplementary material: Additional information is available at <https://doi.org/10.6084/m9.figshare.c.5177343>

Received 26 May 2020; **revised** 16 September 2020; **accepted** 15 October 2020

The Central Andes contain the second-highest and -widest plateau on Earth: the Altiplano. Topographic building-up of the Andes has occurred since at least the Cretaceous (*c.* 120–110 Ma; Jaillard and Soler 1996); the northern Altiplano acquired its modern elevation during the Miocene (Barnes and Ehlers 2009; Garzzone *et al.* 2017; Schildgen and Hoke 2018). Tectonic, climatic and erosional interactions affecting the Altiplano and its eastward border, the Eastern Cordillera (Fig. 1), have been extensively studied in the southern Central Andes of Bolivia and Argentina (e.g. Strecker *et al.* 2007). Pliocene canyon incision, potentially induced by global climate cooling, has been inferred for the Eastern Cordillera in southernmost Peru (Lease and Ehlers 2013). In contrast, the evolution of the northern edge of the Altiplano and the Eastern Cordillera further north in Peru remains poorly documented. This area is formed by the Abancay Deflection (Fig. 1; Dalmayrac *et al.* 1980), a major Andean transition zone that separates the wide Bolivian orocline (Central Andes) to the south from the narrower Northern Andes to the north. The Abancay Deflection has higher (*c.* 0.3 km) average elevation and is much more incised than the low-relief and internally drained Altiplano to the south (Fig. 1c). Palaeoaltimetry data (Picard *et al.* 2008; Sundell *et al.* 2019) and biodiversity records (Hoorn *et al.* 2010) suggest that the study area acquired its modern elevation of *c.* 4 km before 5 Ma. At the scale of the Central Andes, different potential uplift mechanisms have been proposed, including crustal shortening (Barnes and Ehlers 2009), lithospheric delamination (Garzzone *et al.* 2006) and crustal flow (Husson and Sempere 2003; for a review see Garzzone *et al.* 2017). Tectonic shortening was

transferred from the Altiplano to the Subandes of central Peru during the mid- to late Miocene (Horton 2005; McQuarrie *et al.* 2005; Espurt *et al.* 2011). The lack of structural, geomorphological and thermochronological data from the Eastern Cordillera, with only a few previous studies distributed around our study area (Fig. 1), however, renders the mode and timing of deformation transfer unclear (Gautheron *et al.* 2013). The mechanisms driving exhumation and surface uplift in the Abancay Deflection also remain enigmatic. The Machu Picchu Batholith, in the core of the Abancay Deflection, has been deeply incised by the Urubamba River and appears as a prime location to investigate the exhumation history of the Abancay Deflection and its drivers (Fig. 1). Here we present new apatite (U–Th)/He (AHe) and apatite fission-track (AFT) dates from the Machu Picchu Batholith. We use age–elevation relationships (AER; e.g. Fitzgerald and Malusà 2019) and inverse time–temperature modelling (QTQt; Gallagher 2012) to unravel the cooling and exhumation history of the core of the Abancay Deflection. As exhumation is generally driven by surface erosion, investigating the geomorphological evolution of an area is crucial to assess potential exhumation drivers. We couple the exhumation history to landscape evolution by extracting normalized steepness (k_{sn}) and the χ indices (Kirby and Whipple 2012; Perron and Royden 2013; Willett *et al.* 2014; Whipple *et al.* 2017) for the Urubamba drainage basin. These indices allow identification of slope anomalies (knickpoints) in the river profile and reorganization patterns between drainage basins, respectively. We combine these data to discuss potential mechanisms of Miocene to present exhumation in the Abancay Deflection.

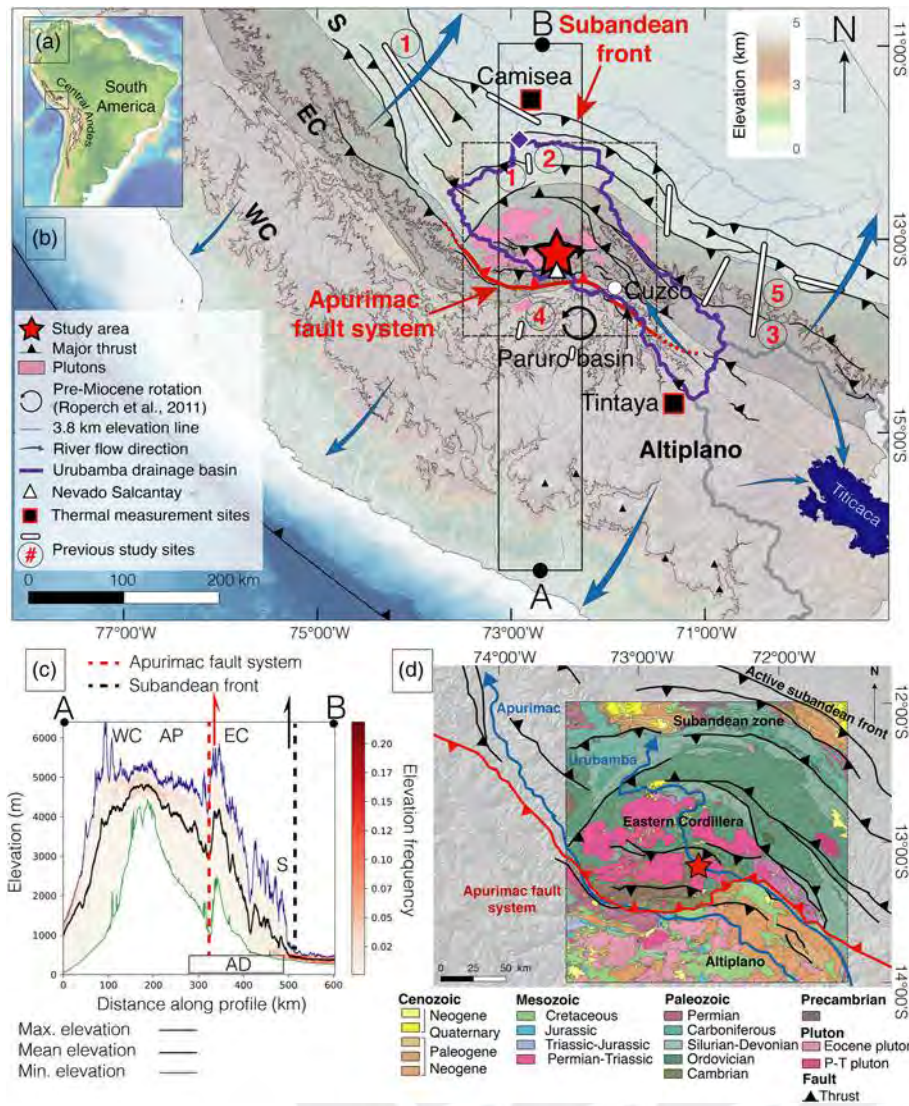


Fig. 1. Topography of the southern Peruvian Andes. (a) Location of the Central Andes within South America. The black line is the 3.8 km elevation contour outlining the Altiplano. (b) Study area (Abancay Deflection; black dashed square) showing location of sampling profile at Machu Picchu (red star) and major city (white circle). Pink areas correspond to Permo-Triassic intrusive rocks, including the sampled Machu Picchu Batholith. Grey shading indicates the Eastern Cordillera (EC). The rectangle AB is the location of the topographic swath profile displayed in (c). The Urubamba drainage basin is outlined by the purple contour and its outlet is indicated by the purple diamond. Geology was extracted from 1:100 000 scale INGEMMET maps. Red numbers refer to previous thermochronological studies. 1, Gautheron *et al.* (2013); 2, Espurt *et al.* (2011); 3, Lease and Ehlers (2013); 4, Ruiz *et al.* (2009); 5, Perez *et al.* (2016). (c) Abancay Deflection topography and relief: 100 km wide north–south-trending swath profile in southern Peru crossing the Abancay Deflection perpendicular to major east–west faults. A noteworthy feature is the abrupt morphological transition when crossing the Apurimac fault system (red dashed line) between the high and relatively flat Altiplano (AP) and the higher and much more incised Eastern Cordillera (EC) through the Abancay Deflection (AD). (d) Geological map of the Abancay Deflection. Geological map was compiled from 1:100 000 INGEMMET maps available at <http://geocatmin.ingemmet.gob.pe/geocatmin> and personal field observations. Other abbreviations: WC, Western Cordillera; S, Subandes.

Geological setting

The Abancay Deflection connects the Central and Northern Andes in Peru; its hinge-like character is emphasized by the $>45^\circ$ deflection of its fault pattern from the overall NNW–SSE axis of the range (Fig. 1; Marocco 1971). The Abancay Deflection records up to 65° of Eocene–Early Miocene (*c.* 40–20 Ma) rotation and marks the tectonic limit between the Bolivian orocline and the straight and narrow Northern Andes (Roperch *et al.* 2011). In the core of the Abancay Deflection, The Inca citadel of Machu Picchu is built on the Permo-Triassic granitic Machu Picchu Batholith (Eastern Cordillera; Fig. 1), emplaced at 222 ± 7 Ma (Carlier *et al.* 1982). The regional crustal-scale Apurimac fault system, *c.* 15 km south of the Machu Picchu Batholith, delimits two lithospheric blocks (Carlier *et al.* 2005) corresponding to two distinct lithotectonic domains: the Eastern Cordillera and the Altiplano (Fig. 1). The Altiplano is characterized by gentle relief and consists of Eocene plutons (50–30 Ma; Mamani *et al.* 2010) emplaced into Meso-Cenozoic sediments (Carlier *et al.* 1996; Fig. 1d). This domain was exhumed steadily at moderate rates (*c.* 0.2 km Ma⁻¹), at least between 38 and 14 Ma (Ruiz *et al.* 2009). In contrast, in the higher and deeply incised Eastern Cordillera, numerous Permo-Triassic batholiths emplaced into Paleozoic rocks (Mišković *et al.* 2009; Fig. 1d) crop out. The Eastern Cordillera is characterized by high elevation and relief, and contains the highest peaks east of the

Altiplano (e.g. Salcantay; 6.3 km a.s.l.; Fig. 1b). On average, the area presents elevation amplitude >1 km for a relief wavelength of *c.* 25 km (Supplementary Fig. 1). The lack of a Meso-Cenozoic sedimentary cover suggests that the Eastern Cordillera has been a long-lived structural high (Perez *et al.* 2016). Preliminary AFT ages of *c.* 2 Ma from two samples from the Machu Picchu Batholith, however, suggest unexpected rapid and recent exhumation (Kennan 2008).

The Urubamba River, flowing at the foot of Machu Picchu, drains both the Altiplano and the Eastern Cordillera towards the Amazon foreland (Figs 1b and 2a). The present-day climate of the Abancay Deflection is characterized by an abrupt latitudinal precipitation gradient, with rainfall decreasing from >2.5 m a⁻¹ in the Subandean domain to <0.5 m a⁻¹ in the Altiplano (Supplementary Fig. 2). The topography of the Abancay Deflection constitutes an effective orographic barrier causing this change in precipitation regime (Bookhagen and Strecker 2008; Insel *et al.* 2010), which has probably been in place since the late Miocene (Poulsen *et al.* 2010).

Methods

AHe and AFT systems record the thermal evolution of the upper *c.* 4 km of the crust, given their thermal sensitivity ranges spanning *c.* 40–80°C (e.g. Flowers *et al.* 2009; Gautheron *et al.* 2009; for a

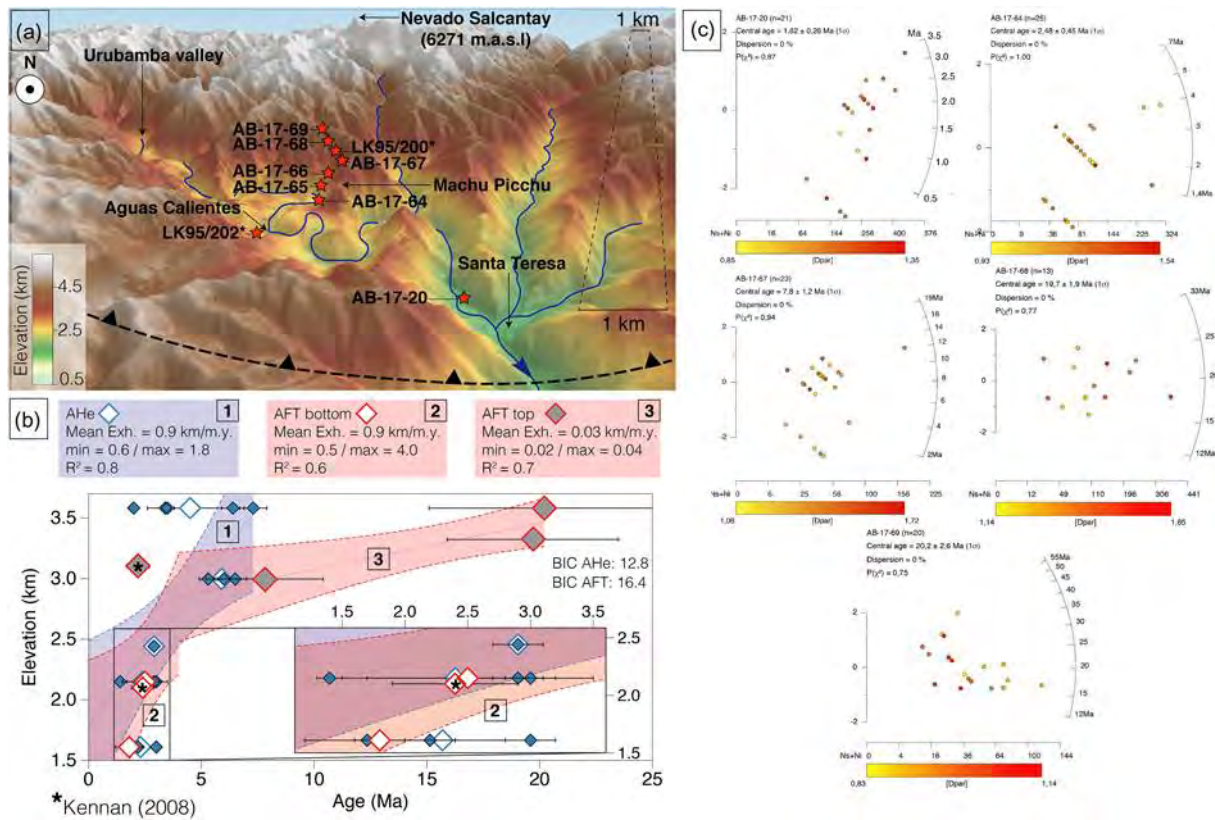


Fig. 2. Thermochronological data. (a) DEM (12 m resolution TanDEM-X data) focusing on the sample locations (red stars). The view is southward with the Urubamba River flowing toward the NW (blue arrow). The blind-thrust plotted is documented as an inherited structure into Paleozoic rocks. (b) Age v. elevation plot for AHe (blue diamonds), AFT bottom (white with red outline diamonds) and AFT top (grey with red outline diamonds). For AHe, filled diamonds represent single-grain ages and open diamonds represent mean AHe ages for each sample. Starred points are from Kennan (2008). Exh., exhumation rates inferred from the age–elevation relationship (AER; coloured dashed lines) with minimum and maximum values indicated by blue and red dotted lines (2σ confidence intervals) for AHe and AFT respectively. R^2 (correlation coefficient) for each segment and the Bayesian Information Criterion (BIC) are also indicated (see Glotzbach *et al.* 2011 for method). (c) AFT single-grain radial plots for each sample.

review see Ault *et al.* 2019), and *c.* 75–125°C (e.g. Brandon *et al.* 1998; Reiners and Brandon 2006), allowing the deciphering of exhumation linked to rock uplift and landscape evolution (e.g. Reiners and Shuster 2009; Ault *et al.* 2019). Here, we combine these data with geomorphological analyses to address landscape evolution and drainage reorganization in response to climatic and/or tectonic perturbations (e.g. Burbank and Anderson 2012).

Sampling strategy and sample preparation

Seven samples were collected from the Machu Picchu Batholith along the Inca trail from the town of Santa Teresa to the Phuyupatamarca Inca site, forming a 1.9 km elevation profile in the vicinity of Machu Picchu (Fig. 2a; Table 1). We sampled the freshest possible *in situ* outcrops encountered (Supplementary Data). Rock samples were crushed and sieved to extract the 100–

160 μm fractions, after which apatite crystals were concentrated using standard magnetic and heavy-liquid techniques.

Apatite (U–Th)/He (AHe) dating

Euhedral apatite crystals were carefully selected for AHe dating under a binocular microscope to identify minerals without fractures and/or inclusions that would skew the AHe age (Farley 2002). Among the seven samples, five yielded sufficient suitable apatite crystals for AHe dating, from which we extracted 15 single-grain ages. AHe measurements were performed at GEOPS (Université Paris Saclay, France). We determined the individual grain geometry and calculated the alpha-ejection correction factor using the Qt_FT program (Gautheron and Tassan-Got 2010; Ketcham *et al.* 2011). Individual apatite crystals were encapsulated in platinum tubes and were heated twice for 5 min under ultra-vacuum conditions at high temperature ($1050 \pm 50^\circ\text{C}$) using an infrared diode laser. The extracted ^4He gas was mixed with a known amount of ^3He ; the gas mixture was purified and analysed using a Prisma Quadrupole mass spectrometer. Subsequently, apatite crystals were dissolved in 50 μl of 5N HNO_3 solution containing known amount of ^{235}U , ^{230}Th , ^{149}Sm and ^{42}Ca ; an additional 50 μl of 5N HNO_3 was added to the solution. The solution was heated to 70°C for 3 h; after cooling, 900 μl of distilled water was added. The final solution was analysed using an ELEMENT XR inductively coupled plasma mass spectrometry system; the ^{238}U , ^{230}Th and ^{147}Sm concentrations were determined and apatite weight was estimated using the Ca content, following the method proposed by Evans *et al.* (2005). Standard Durango apatite crystals were analysed alongside the

Table 1. Sample locations and lithologies; all samples are from the Triassic granitic Machu Picchu pluton

Sample number	Latitude ($^\circ\text{S}$)	Longitude ($^\circ\text{W}$)	Elevation (m)
AB-17-20	13.14182	72.58376	1610
AB-17-64	13.18747	72.52931	2149
AB-17-65	13.18833	72.53428	2441
AB-17-66	13.19034	72.5369	2719
AB-17-67	13.19288	72.54157	2996
AB-17-68	13.2029	72.53497	3322
AB-17-69	13.20652	72.53204	3581

Table 2. QTQt parameters for data inversion

Parameters	Values or flags	References or justifications
Explored time interval (Ma)	0–50	Encompassing AHe and AFT data range
Explored temperature interval (°C)	0–140	Encompassing AHe and AFT closure temperature
Explored $\delta T/\delta t$ range (°C Ma ⁻¹)	1000	Maximum exploration; no constraints
Geothermal gradient (°C km ⁻¹)	25 ± 15	Broad range; the geothermal gradient measured at the site closest to our sampling is 16 ± 2°C km ⁻¹ (Henry and Pollack 1988)
Present-day surface temperature (°C)	25 ± 10	Gonfiantini <i>et al.</i> (2001)
Surface-temperature lapse rate (°C km ⁻¹)	6 ± 2	Estimated from Klein <i>et al.</i> (1999) and Gonfiantini <i>et al.</i> (2001)
Allow geothermal gradient to vary over time	Yes	Inversion output consistent with our geothermal gradient assumption
Reheating	No	No evidence for reheating event considering the time period explored
Number of iterations	300 000	
Etchant	5.5M	Sample preparation protocol
AFT annealing model	Ketcham <i>et al.</i> (2007)	Taking into account kinetic variability characterized by <i>D</i> _{par}
AHe radiation damage model	Gautheron <i>et al.</i> (2009)	Taking into account kinetic variability characterized by <i>eU</i>

eU, concentration of effective uranium.

unknowns to ensure data quality (Supplementary Table 1). The 1 σ error on each single-grain AHe age amounts to 8%, reflecting analytical error and uncertainty on the FT ejection factor correction. More details on the analytical procedure have been given by Recanati *et al.* (2017).

Apatite fission track (AFT) analysis

For AFT dating, apatite crystals were manually selected, mounted in epoxy resin and polished at the GTC platform (ISTerre, Grenoble, France). Among the seven samples, five presented sufficient suitable apatite crystals for AFT dating. AFT dating was performed using the external-detector method and ζ -calibration approach (Hurford and Green 1983). Spontaneous fission tracks were revealed by etching at 21°C for 20 s using a 5.5M HNO₃ solution. Induced tracks were implanted in an external mica-sheet detector by thermal-neutron irradiation at the FRM II reactor (Munich, Germany). Tracks were counted and lengths were measured at 1250 \times magnification under a Zeiss microscope. Simultaneous measurement of five Durango and five Fish Canyon Tuff age standards allowed a ζ -value of 275 ± 12 to be constrained for the operator, Benjamin Gérard. We used the BINOMFIT program (e.g. Ehlers *et al.* 2005) to calculate AFT central ages (Supplementary Data).

Interpreting age–elevation relationships (AER)

Age–elevation relationships (AER) provide a first-order estimate of apparent exhumation rates without requiring information on the thermal structure of the crust, with breaks in slope in AER allowing identification of changes in exhumation rate through time (e.g. Wagner *et al.* 1977; Fitzgerald and Malusà 2019). This approach, however, does not take into account potential inter-sample AHe/AFT kinetic variability and assumes a quasi-vertical profile (Stüwe *et al.* 1994). We fitted single- and multi-tier regressions to the AFT and AHe data from the altitudinal profile data using a Bayesian approach (Glotzbach *et al.* 2011); the best-fit AER was determined by minimization of the Bayesian Information Criterion (BIC; Schwarz 1978).

Time–temperature modelling

Time–temperature modelling with QTQt (Gallagher 2012) allows thermal histories to be inferred for individual samples, with the possibility of combining and processing multiple samples from an altitudinal profile. Parameters used for QTQt data inversion are

detailed in Table 2. We processed all AHe aliquots displayed in Table 3 and all AFT data presented in Table 4, including track-length measurements for sample AB-17-69 together. We extracted best-fitting thermal histories for the combined samples from the Machu Picchu profile, exploring the *T*–*t* space by calculating the likelihood for 300 000 iterations. We implemented the annealing model of Ketcham *et al.* (2007) and the radiation-damage model of Gautheron *et al.* (2009) for AFT and AHe respectively. We tested the influence of the AHe diffusion model on the inferred cooling history and found that this is insignificant in our case (Supplementary Fig. 9). We allowed the geothermal gradient to vary over time between commonly inferred values for the Eastern Cordillera (Henry and Pollack 1988; Barnes *et al.* 2008; Lease and Ehlers 2013); that is, between 10 and 40°C km⁻¹. The explored timespan starts at 50 Ma, twice the oldest thermochronological age, to take into account the earlier history. We implemented a surface-temperature lapse rate of *c.* 6°C km⁻¹, as determined for the eastern flank of the inter-tropical Andes (Gonfiantini *et al.* 2001).

Geomorphological analysis

For our geomorphological analysis, we used a 1 arc-second (*c.* 30 m) digital elevation model (DEM) derived from the Shuttle Radar Topography Mission (SRTM V4; Reuter *et al.* 2007) and 12 m resolution TanDEM-X data where available (Rizzoli *et al.* 2017). We extracted the Urubamba drainage basin, its associated drainage network and river longitudinal profiles with Whitebox GAT 3.4 (Lindsay *et al.* 2015; Fig. 1). We fixed the Urubamba basin outlet location to the Eastern Cordillera–Subandes boundary to avoid potential perturbations in the downstream river profile owing to surface uplift in the Subandean zone (e.g. Gautheron *et al.* 2013) and in the Amazon foreland (Fitzcarrald arch uplift; Espurt *et al.* 2007).

The normalized steepness index (*k*_{sn}) quantifies river gradients corrected for upstream drainage area and allows identification of abnormally steep river reaches or knickzones (Kirby and Whipple 2012). The map pattern of *k*_{sn} values in a catchment area is a powerful tool to determine active tectonic boundaries and/or edges of a metastable plateau consumed by regressive erosion with knickpoint retreat (Kirby *et al.* 2003; Wobus *et al.* 2006). We used Topotoolbox v.2 (Schwanghart and Scherler 2014) to extract *k*_{sn} values for the entire hydrographic network of the Urubamba, imposing a mean concavity value $\theta_{\text{ref}} = 0.45$ (Wobus *et al.* 2006).

The variable χ represents normalized integrated drainage area at any point in the river and has units of length (Perron and Royden

Table 3. Apatite (U–Th–Sm)/He data

Sample number	Morphology	Length (µm)	Width (µm)	Thickness (µm)	R_s (µm)	Weight (µg)	F_T	^4He (ncc STP g ⁻¹)	^{238}U (ppm)	^{232}Th (ppm)	^{147}Sm (ppm)	eU Th/U (ppm)	Age (Ma)	Corrected age (Ma)	$\pm 1\sigma$	
AB-17-20A	2b	156	115	107	74	4.3	0.81	15 283	47.4	193.0	59.0	4.1	94.0	1.4	1.7	0.1
AB-17-20B	1b + 1py	259	101	94	60	4.8	0.77	17 371	39.6	94.6	59.8	2.4	62.6	2.3	3.0	0.2
AB-17-20C	2b	126	120	99	69	3.1	0.80	16 046	76.4	3.3	58.1	0.0	77.5	1.7	2.2	0.2
AB-17-20															2.3*	0.5*
AB-17-64D	1b + 1py	209	113	89	57	3.7	0.75	9015	21.3	53.5	80.2	2.5	35.0	2.2	2.9	0.2
AB-17-64E	1b + 1py	179	96	90	56	2.9	0.75	9430	23.7	44.4	54.1	1.9	35.0	2.3	3.0	0.2
AB-17-64H	2b	102	118	139	70	3.6	0.80	5789	28.4	54.3	62.0	1.9	41.5	1.1	1.4	0.1
AB-17-64*															2.4*	0.7*
AB-17-65D	2b	205	151	141	97	9.6	0.85	3491	7.4	17.7	46.2	2.4	11.9	2.5	2.9	0.2
AB-17-65*															2.9*	0.2*
AB-17-67C	2b	154	108	84	58	2.8	0.76	14 056	17.5	48.1	53.8	2.7	29.3	4.0	5.3	0.4
AB-17-67D	1b + 1py	154	96	97	57	2.6	0.75	16 427	16.1	48.8	71.2	3.0	28.2	4.9	6.5	0.5
AB-17-67F	2b	104	112	72	72	3.6	0.80	45 191	69.1	33.5	19.3	0.5	77.2	4.8	6.0	0.4
AB-17-67*															5.9*	0.4*
AB-17-69B	1b + 1py	202	104	97	61	3.8	0.77	18 879	35.6	92.6	32.8	2.6	58.0	2.7	3.5	0.3
AB-17-69D	1b + 1py	212	92	66	43	2.2	0.68	17 806	16.6	55.8	82.4	3.4	30.4	4.9	7.3	0.6
AB-17-69E	1b + 1py	116	75	80	45	1.2	0.69	9998	11.1	31.5	47.1	2.8	18.9	4.4	6.4	0.5
AB-17-69I	2b	109	122	126	75	3.6	0.81	8191	14.2	42.2	74.1	3.0	24.4	2.7	3.4	0.2
AB-17-69J	2b	125	128	136	85	5.0	0.83	5001	13.9	45.1	78.1	3.2	24.8	1.6	2.0	0.1
AB-17-69*															4.5*	1.9*

Morphology refers to the apatite geometry. 2b, two broken faces; 1b + 1py, one broken face and one hexagonal pyramid. F_T , ejection correction factor; R_s , sphere equivalent radius of hexagonal crystal (Ketcham *et al.* 2011; Gautheron *et al.* 2012).

*AHe arithmetic mean value calculated for plotting (Fig. 2b) with associated error (standard deviation).

2013; Whipple *et al.* 2017). As it is predicted that drainage divides will migrate in the direction from lower to higher χ values, the pattern of χ values across drainage divides can be used to assess their present-day stability or evolution (Willett *et al.* 2014; Whipple *et al.* 2017). Combined with independent geomorphological evidence, such patterns can be extrapolated to infer recent drainage migration. We used Topotoolbox v.2 to calculate χ for the endorheic Altiplano and the neighbouring Urubamba basin, upstream of the 3.8 km elevation contour, and focus on the drainage divide equilibrium between these two drainage basins.

Results

Thermochronology data and modelling

We report 15 single-grain AHe ages (Table 3) and five AFT ages (Table 4) from five samples. We included two published AFT ages from the same zone (Kennan 2008) in our models (Table 4). Single-grain AHe and central AFT ages range from 1.4 ± 0.1 Ma to 7.3 ± 0.6 Ma ($\pm 1\sigma$) and from 1.8 ± 0.6 Ma to 20.2 ± 5.1 Ma ($\pm 2\sigma$), respectively (Tables 3 and 4; Fig. 2b and c). There is a consistent

increase in both AHe and AFT ages with elevation (Fig. 2b), with the AFT ages of the two highest samples being much older than all other AFT and AHe ages. AFT ages present a notable dispersion but pass the χ^2 test owing to the small number of spontaneous fission tracks in the crystals (Table 4). Only three track lengths were measured because of the young AFT ages and associated low track counts. Only the upper sample provided a mean track length (MTL) of $c. 12 \mu\text{m}$ (Table 4; Supplementary Table 2). Etch-pit widths (D_{par}), measured as a proxy for apatite composition, range between 0.97 and 1.46 μm (Table 4), suggesting that the analysed apatites are fluorapatites, characterized by rapid annealing compared with apatite crystals with higher D_{par} values (Donelick *et al.* 2005).

Bayesian AER modelling reveals that AHe ages are best fit by a single AER with a slope of $0.9^{+0.9}_{-0.3} \text{ km Ma}^{-1}$ between $c. 4$ and $c. 2$ Ma (Fig. 2b). In contrast, the AFT ages require a two-tier fit, with the higher elevation samples showing an AER with a slope of $0.03 \pm 0.01 \text{ km Ma}^{-1}$ ($c. 20$ to $c. 4$ Ma; Fig. 2b) and the lower elevation samples an AER with a slope of $0.9^{+3.1}_{-0.4} \text{ km Ma}^{-1}$ ($c. 4$ to $c. 2$ Ma; Fig. 2b); the latter is compatible with the AHe results.

Time–temperature inversions with QTQt reveal slow continuous cooling from $c. 20$ to 4.0 ± 0.6 Ma at a rate of $0.7 \pm 0.2^\circ\text{C Ma}^{-1}$,

Table 4. Apatite fission-track data

Sample number	n	ρ_s (10^5 cm^{-2})	N_s	ρ_i (10^5 cm^{-2})	N_i	ρ_d (10^5 cm^{-2})	P (χ^2)	Dispersion (%)	Central age (Ma)	$\pm 2\sigma$	U (ppm)	$\pm 1\sigma$	N D_{par}	$M D_{\text{par}}$ (µm)	n TL	MTL (µm)
AB-17-20	21	0.49	(51)	50.3	(5297)	13.8	87.5	0.4	1.8	0.6	55	2	67	1.16	n.d.	n.d.
AB-17-64	25	0.25	(31)	19.6	(2451)	14.2	99.8	0.2	2.5	1.0	21	1	76	1.21	n.d.	n.d.
AB-17-67	23	0.57	(41)	14.3	(1029)	14.3	93.5	0.6	7.8	2.6	15	1	89	1.35	n.d.	n.d.
AB-17-68	13	5.46	(154)	54.7	(1541)	14.3	76.8	0.2	19.7	3.8	57	3	74	1.46	n.d.	n.d.
AB-17-69	20	1.32	(78)	12.9	(763)	14.4	74.9	0.3	20.2	5.1	14	1	42	0.97	3	11.92
LK95/200*	30	n.r.	n.r.	n.r.	n.r.	n.r.	46.5	n.r.	2.2	0.5	n.r.	n.r.	n.r.	n.r.	n.r.	n.r.
LK95/202*	30	n.r.	n.r.	n.r.	n.r.	n.r.	97.0	n.r.	2.4	0.5	n.r.	n.r.	n.r.	n.r.	n.r.	n.r.

Fission-track age is reported as central age (Galbraith and Laslett 1993). Samples were counted dry with a BX51 Olympus microscope at 1250 \times magnification. Ages were calculated with the BINOMFIT program (Ehlers *et al.* 2005), using a zeta value of 275.18 ± 11.53 and the IRMM 540 uranium glass standard (15 ppm U). n , number of analysed grains; ρ_s , spontaneous track density; N_s , number of spontaneous tracks; ρ_i , induced track density; N_i , number of induced tracks; ρ_d , dosimeter tracks density; $P(\chi^2)$, probability of obtaining the χ^2 value for n degree of freedom ($n = \text{number of crystals} - 1$); $n D_{\text{par}}$, number of D_{par} measured; $M D_{\text{par}}$, mean D_{par} value (i.e. average etch pit diameter of fission track); n TL, number of track lengths measured; MTL, mean track lengths of horizontally confined tracks; n.d., no data; n.r., not reported.

*Previously published data (Kennan 2008). For samples LK95/200 and LK95/202, elevations are respectively 3.1 km and 2.1 km.

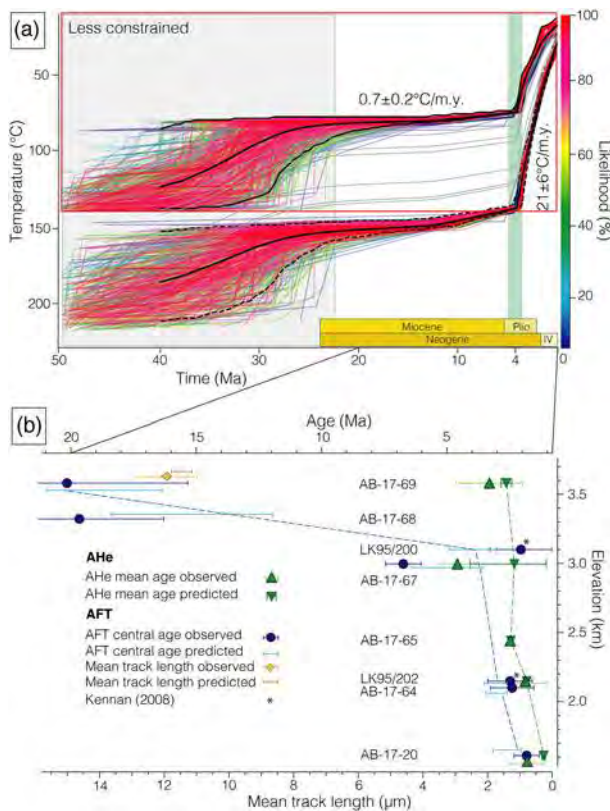


Fig. 3. Time–temperature (T – t) modelling. (a) Time–temperature paths obtained by inversion of AHe and AFT thermochronology data using QTQt. The red rectangle shows the explored T – t range for inversion. Coloured lines show the T – t paths for the top and the bottom samples with their respective likelihood (colour scale on right). Continuous and dashed black lines show the expected model and its 95% reliable interval for the thermal histories of the top and bottom samples, respectively. Grey lines represent the expected cooling paths for intermediate samples. The green vertical band indicates acceleration of cooling at 4.0 ± 0.6 Ma. Cooling rates derived from QTQt are indicated on the graph. (b) Fit of best-fit QTQt model predictions to the data for the Machu Picchu elevation profile.

increasing to $21 \pm 6^\circ\text{C Ma}^{-1}$ since *c.* 4 Ma (Fig. 3). AHe and AFT ages predicted by the best-fit model fit the observed ages within error.

Geomorphological analysis

The highest k_{sn} values ($>1000 \text{ m}^{0.9}$) in the Urubamba drainage basin are focused along a SW–NE band orthogonal to the drainage direction (Fig. 4b). This zone of high k_{sn} corresponds to kilometre-scale knickzones in the Urubamba main stem and its tributaries, where the rivers actively incise bedrock (Fig. 5c). In contrast, alluvial portions upstream (Fig. 5d) correspond to the lowest k_{sn} values ($<10 \text{ m}^{0.9}$; Fig. 4b). Along the drainage divide between the endorheic Altiplano and externally drained Urubamba drainage basins, χ values (calculated from a base level at 3.8 km) are noticeably higher in the Altiplano (*c.* 10^5 m) than in the Urubamba basin (*c.* 10^3 m ; Fig. 4c).

Discussion

Miocene–Present exhumation of the Machu Picchu Batholith

The data for both thermochronometric systems suggest rapid cooling starting at *c.* 4 Ma. It is reasonable to assume that the Machu Picchu Batholith did not experience reheating since the Miocene, considering the lack of evidence for volcanic activity and/or sedimentary burial (Perez *et al.* 2016). Magmatic activity in the Abancay Deflection ceased after *c.* 30 Ma (Mamani *et al.* 2010); any potential associated thermal perturbation would not have affected the Miocene thermal history. Nonetheless, to explore potential temporal variability of the geothermal gradient, we allow it to vary over time in the range $25 \pm 15^\circ\text{C km}^{-1}$ during time–temperature inversions. The model does not converge to a single range of palaeo-geothermal gradient estimates. As it is not possible to estimate the geothermal gradient accurately in the past, we consider it constant in time and space in the following calculations, following previous work (e.g. Barnes *et al.* 2012; Perez *et al.* 2016).

The value of the geothermal gradient is a crucial choice when translating cooling rates (inferred from time–temperature modelling) into exhumation rates. As the Abancay Deflection is devoid of direct measurements of its thermal structure, we explore two options

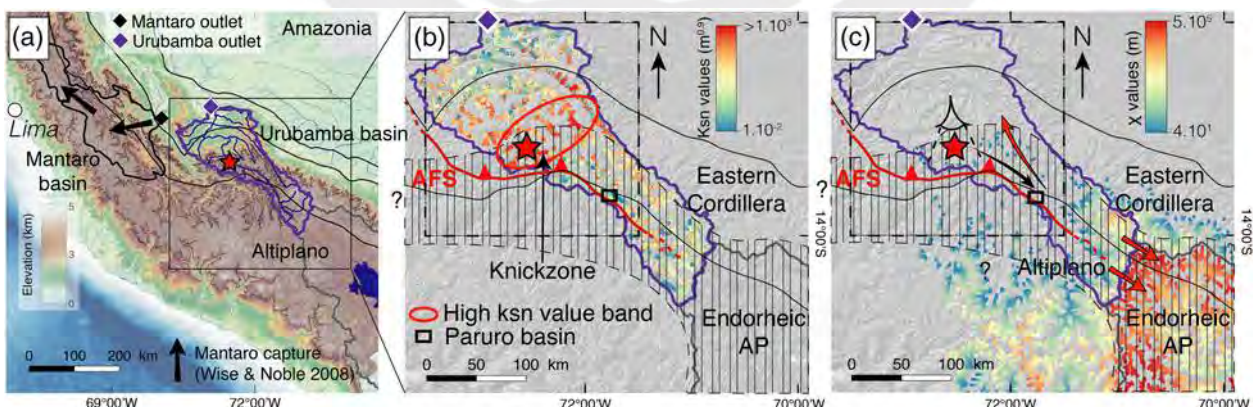


Fig. 4. Quantitative geomorphology of the Urubamba River drainage basin. (a) Urubamba (purple) and Mantaro (black) watershed locations in southern Peru. Blue lines are rivers. (b) k_{sn} map for the Urubamba drainage basin. Higher k_{sn} values (in warm colours) are aligned in a band orthogonal to the main elongation axis of the Urubamba drainage basin, suggesting capture of a palaeo-Altiplano (Wobus *et al.* 2003, 2006). (c) χ map for the Urubamba drainage basin. χ values were calculated with an elevation threshold of 3.8 km corresponding to the endorheic Lake Titicaca base level. The χ gradient across the drainage divide between the Urubamba and the endorheic Altiplano suggests that it is actively migrating southward (red arrows), implying continuing capture of the plateau. The black and the red curved arrows represent respectively the drainage direction for 9–7 Ma (Sundell *et al.* 2018) and for the present day. The ‘eye’ icon represents the view direction of the 3D DEM in Fig. 2a. In (a–c), the red star is the sample location close to Machu Picchu and the dashed black square is the Abancay Deflection. The grey polygon outlines the present-day endorheic Altiplano and the black-hatched polygon represents the ante-4 Ma northern extension of the palaeo-endorheic Altiplano. AFS, Apurimac fault system.

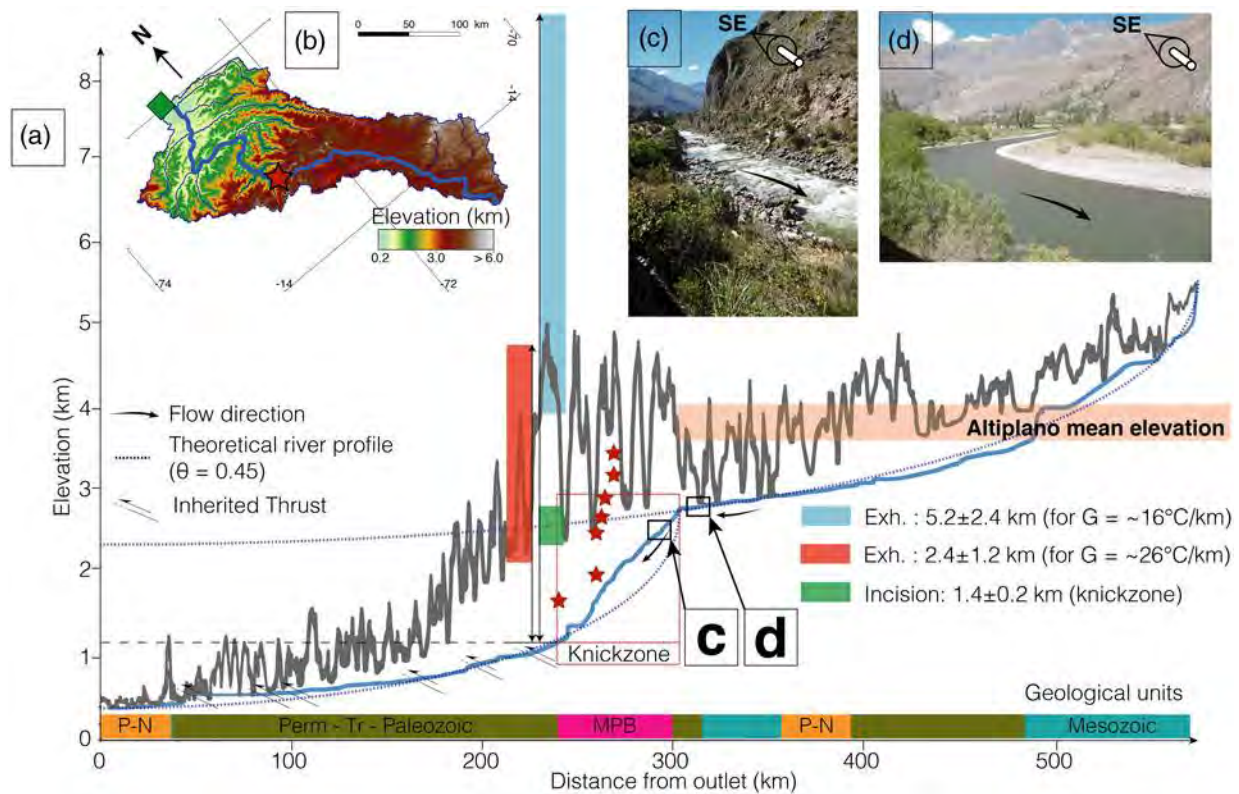


Fig. 5. (a) Urubamba river profile (blue) crossing the Machu Picchu Batholith. Red stars show projected location of the samples collected in this study. The orange horizontal band represents the mean elevation of the Altiplano (calculated from a swath profile) and the dark grey line is the mean topography in a 5 km swath following the Urubamba River. The blue and red vertical bands show the estimated total exhumation since 4 Ma for an assumed ‘cold’ and ‘warm’ geotherm, respectively, at the same location at the base of the knickzone. The green vertical band shows the minimum incision of the Urubamba River computed by the difference between the theoretical river profile reconstructed from the river profile above the knickzone and the present-day river profile at the foot of the knickzone. Vertical exhumation or incision rectangles are slightly shifted to avoid overprinting the signals displayed. Total exhumation is calculated taking into account minimum and maximum values for exhumation rates and timing of acceleration. The error on the incision estimate for the knickzone is propagated from a 15% uncertainty in the concavity value (θ) derived from river-profile fitting (Kirby and Whipple 2012). (b) DEM of the Urubamba drainage basin with its outlet (green diamond). The main Urubamba river (thick blue curve) is plotted in (a). The red star indicates the location of the knickzone and sampling profile. Inset photographs (c) and (d) show the morphological change of the Urubamba River from meandering upstream (d) to rapids in a canyon (knickzone; c). MPB, Machu Picchu Batholith; P-N, Paleo-Neogene.

to estimate the geothermal gradient in our study area. The first consists in using the nearest available measurements. Henry and Pollack (1988) reported a measured modern-day geothermal gradient of $c. 14^{\circ}\text{C km}^{-1}$ from the Tintaya mine on the Altiplano (Fig. 1), whereas Espurt *et al.* (2011) inferred a Miocene geothermal gradient of $c. 17^{\circ}\text{C km}^{-1}$ in the Camisea area in the Subandean domain (Fig. 1), leading to an estimated geothermal gradient of $16 \pm 2^{\circ}\text{C km}^{-1}$. The second option is to take into account more distant data available for the Eastern Cordillera of Bolivia, which suggest a somewhat higher geothermal gradient of $26 \pm 8^{\circ}\text{C km}^{-1}$ (Barnes *et al.* 2008). We will refer to these two estimates of the geothermal gradient as ‘cold’ (based on local data) and ‘warm’ (based on Barnes *et al.* 2008). Considering stable, linear and spatially uniform geothermal gradients of $16 \pm 2^{\circ}\text{C km}^{-1}$ or $26 \pm 8^{\circ}\text{C km}^{-1}$ (‘cold’ v. ‘warm’), we can translate the cooling rates from the time-temperature inversions to exhumation rates. Between $c. 20$ and $c. 4$ Ma, exhumation rates were $0.05 \pm 0.02 \text{ km Ma}^{-1}$ (‘cold’ gradient) or $0.03 \pm 0.01 \text{ km Ma}^{-1}$ (‘warm’ gradient); that is, very similar independent of the chosen geothermal gradient. For the period from $c. 4$ Ma to present day, however, the choice of geothermal gradient leads to significant differences in predicted exhumation rates. If the ‘cold’ gradient is used the exhumation rate is $1.3 \pm 0.6 \text{ km Ma}^{-1}$, whereas for the ‘warm’ gradient the exhumation rate decreases to $0.9 \pm 0.3 \text{ km Ma}^{-1}$. Both values are consistent within errors with those inferred from the AER analysis ($0.9_{-0.3}^{+0.9} \text{ km Ma}^{-1}$ for the AHe

data; Fig. 2b). In the following discussion, we will interpret exhumation rates values computed from QTQt cooling dynamic.

The local relief may also influence estimated exhumation rates, as topography deflects isotherms with an exponentially decreasing influence downward (Braun 2002; Braun *et al.* 2006). Therefore, the closure depth of thermochronometric systems is relief dependent, in particular for the lowest-temperature system (i.e. AHe). Using a relief wavelength $\lambda = 25 \pm 8 \text{ km}$ and relief amplitude $>1 \text{ km}$ (Supplementary Fig. 1) and the calculation method of Mancktelow and Grasemann (1997) (see also Braun *et al.* 2006), leads to deflections of the 100°C isotherm of 280–570 m depending on the chosen exhumation rate but does not significantly affect the exhumation-rate estimates.

Thus our thermochronology data from the Machu Picchu Batholith clearly show an $c. 30$ -fold increase in exhumation rate in the Pliocene, from <0.05 to $>0.9 \text{ km Ma}^{-1}$. Although the exact rate and amount of exhumation since this time depend on assumed values for the geothermal gradient and the influence of relief, the relative increase as well as its timing at $4.0 \pm 0.6 \text{ Ma}$ is robust.

Geomorphological evidence for capture of Altiplano drainage

The modern Abancay Deflection is externally drained and has anomalously high topography, high relief and outcropping

basement batholiths, in contrast to the neighbouring low-relief Altiplano (Fig. 1c). The Machu Picchu area is set within a SW–NE-trending band of high k_{sn} values (Fig. 4b), with much lower k_{sn} values found upstream in the Altiplano region. The Urubamba River, draining the Abancay Deflection, is one of the most distant tributaries of the Amazon. From its source in the Altiplano, it flows parallel to the Andean range at 3.8 km elevation for *c.* 150 km before it cuts the Machu Picchu Batholith in a >1 km deep canyon, associated with a major knickzone (Fig. 5). This knickzone appears to be confined to the Machu Picchu Batholith (Fig. 5a), which presumably has greater rock-strength than surrounding units. Although the SW–NE band of high k_{sn} values is mostly contained within intrusive rocks and metamorphic sediments (Fig. 1), these rocks also occur widely outside this band. Therefore, the band of high k_{sn} values does not appear to be purely lithologically controlled and presumably reflects a geomorphological or structural transition. In the absence of a major tectonic structure associated with it, we interpret the major knickzone associated with this band by base-level fall in the Urubamba river system owing to capture of a former endorheic catchment (which would have been a northward extension of the Altiplano; Fig. 4). Although we cannot determine the exact location of the river capture, it must have happened downstream of the present-day location of the knickzone. Capture is a continuing process, as shown by the pattern of χ values that points to drainage-divide migration toward the SE; that is, expansion of the Urubamba catchment to the detriment of the endorheic Altiplano (Fig. 4c). Although lithology does not appear to be a primary control on the pattern of k_{sn} values, headward propagation of incision from the foreland into the highlands may be stalling within the hard rocks of the Machu Picchu Batholith, limiting incision further upstream, as suggested by the alluvial river channels found upstream of the knickzone (Fig. 5c).

Miocene surface uplift of the northern Altiplano without exhumation

Our data imply slow exhumation between 20 and 4 Ma (*c.* 0.6 km in *c.* 16 myr), consistent with the record from the Altiplano to the south that suggests steady and moderate exhumation between 38 and 14 Ma (Ruiz *et al.* 2009; Supplementary Fig. 10). In contrast, the Eastern Cordillera record to the SE suggests significant Miocene exhumation (Lease and Ehlers 2013; Perez *et al.* 2016). Several palaeo-elevation estimates (e.g. Sundell *et al.* 2019) indicate that the elevation of both the Eastern Cordillera and the neighbouring Altiplano grew by *c.* 2 to *c.* 4 km between 20 and 5 Ma; the Abancay Deflection must have reached its present-day elevation before 5 Ma. Thus, slow exhumation of the core of the Abancay Deflection during the Miocene appears to be coeval with surface uplift of the northern Altiplano. Although a pulse of exhumation would be expected to accompany surface uplift, both the Abancay Deflection (this study) and the northern Altiplano (Ruiz *et al.* 2009) record steady and moderate exhumation rates. There are two potential explanations for diminished Miocene denudation within this rising orogen: (1) establishment of aridity owing to the development of an orographic barrier (Strecker *et al.* 2007), and/or (2) a high-elevation endorheic local base level. Provenance studies in the Paruro basin south of Cuzco, based on detrital zircon U–Pb dating (Sundell *et al.* 2018), suggest that the Machu Picchu area (specifically the Ollantaytambo Formation into which the Machu Picchu Batholith intruded; Bahlburg *et al.* 2006) was one of the numerous sources for late-Miocene (*c.* 9 to *c.* 7 Ma) Altiplano basin sediments. In contrast, rocks from the Machu Picchu area are currently exported toward the Amazon foreland via the modern Urubamba drainage network (Fig. 4c). This contrast implies a major drainage reversal since the late Miocene. The combined data strongly suggest that the Abancay Deflection (including the Machu Picchu Batholith) was

part of a slowly eroding endorheic environment during the Miocene, undergoing rock and surface uplift but little exhumation, as it was associated with a high-elevation local base level comparable with the present-day endorheic Altiplano.

Drivers of Pliocene exhumation

Our data suggest that exhumation rates increased dramatically at 4 Ma (Figs 2b and 3a). The total amount of exhumation since that time, however, depends on the assumed geothermal gradient. If the ‘cold’ Altiplano option is considered, total exhumation since *c.* 4 Ma amounts to 5.2 ± 2.4 km; in contrast, if the ‘warm’ Eastern Cordillera option is used, this number decreases to 2.4 ± 1.2 km. Regardless of the choice of geothermal gradient, these values are higher than those obtained in the Eastern Cordillera further south in Bolivia for the same period (*c.* 0.6 km Ma⁻¹; Lease and Ehlers 2013; Fig. 1, reference 3).

Fitting equilibrium profiles to the reaches of the Urubamba River above and below the knickzone (Kirby and Whipple 2012) allows us to derive a minimum depth of incision of 1.4 ± 0.2 km at the base of the knickzone (Fig. 5). This amount represents the height of the rock column above the present-day knickzone before incision. We suggest that the Urubamba River captured a former *c.* 3.8 km high endorheic drainage system of the Altiplano, initiating canyon carving at *c.* 4 Ma (Fig. 4). A similar scenario of endorheic basin capture and opening to the Amazon is recorded in the adjacent Mantaro River catchment to the north (Fig. 4a; Wise and Noble 2008).

Either climatic or tectonic changes could have further amplified incision. Two major but diachronous climatic events affected the Central Andes since the Miocene, both linked to emplacement and/or intensification of the South American monsoon leading to climate-driven incision of the Eastern Cordillera. The first is global Pliocene cooling between 4 and 2 Ma (Zhang *et al.* 2001), which has been interpreted as the remote driver for incision of canyons cutting perpendicularly through the Eastern Cordillera in southern Peru and Bolivia (Lease and Ehlers 2013). This cooling signal is even documented in northern Peru in the Cordillera Blanca area (Margirier *et al.* 2015). An older and more regional climatic event involves increased precipitation and possibly related intensified erosion in the Eastern Cordillera owing to surface uplift in the Central Andes during the Late Miocene (*c.* 10 to 6 Ma; Uba *et al.* 2007; Poulsen *et al.* 2010). This precipitation gradient pattern is still valid at present (Supplementary Fig. 2).

Whether incision was climatically amplified or not, a first-order observation from our data is that the reconstructed amount of incision (1.4 ± 0.2 km) overlaps the lower end of our exhumation estimate for a ‘warm’ geothermal gradient (2.4 ± 1.2 km; Fig. 5) but if a ‘cold’ geothermal gradient is assumed, the amount of canyon incision is significantly smaller than total exhumation at river level since 4 Ma (5.2 ± 2.4 km; Fig. 5). Some additional uplift will be caused by the isostatic response to mass removal by river incision. Zeilinger and Schlunegger (2007) quantified the maximum deflection owing to isostatic rebound to river incision for the Rio La Paz in the Bolivian Eastern Cordillera, a system similar in scale to the Urubamba River, and found that for an elastic thickness of 17.5 ± 2.5 km (Pérez-Gussinyé *et al.* 2008) this would be *c.* 0.2 km; that is, a negligible amount. Furthermore, glaciations could also promote erosion and incision. Postglacial isostatic rebound could potentially accelerate the surface uplift and exhumation. These observations are particularly true for fully glaciated area such as the Cordillera Blanca in northern Peru (Margirier *et al.* 2016). In contrast, present-day glaciers represent an insignificant part of our study area, as they occupy only >4.5 km elevation zones (Licciardi *et al.* 2009). In this intertropical context, they did not reach <4 km elevation in the past, with drier climatic conditions limiting their

spatial extent (Pleistocene; Fox and Bloom 1994). We thus do not take into account potential glacial influence on exhumation for the Machu Picchu region. A substantial amount of exhumation since 4 Ma (1.0 ± 1.4 km for the ‘warm’ geotherm case; 3.8 ± 2.6 km for the ‘cold’ geotherm case) thus has to be tectonic in origin. Knowledge of the (active?) tectonics of the Abancay Deflection remains limited because of its complex structural setting, dense vegetation and difficult access. Initiation of compression in the Subandean fold-and-thrust belt to the NE of the Abancay Deflection at *c.* 14 Ma is associated with thick-skinned tectonics (Espurt *et al.* 2011) that potentially could affect the basement of the Abancay Deflection. The diachronous *c.* 4 Ma acceleration of exhumation recorded in the Machu Picchu Batholith, in either of the hypotheses, suggests that the Abancay Deflection is tectonically decoupled from its surroundings. We propose activity of the Apurimac fault system to explain the additional post-Miocene exhumation (not explained by incision). Inherited normal faults reactivated as thrusts affecting the Eastern Cordillera are already documented further south in Bolivia (Perez *et al.* 2016), which could be comparable with the Apurimac fault system context. The structure of the Abancay Deflection developed by horizontal strike-slip faults with limited vertical motion during the Miocene (*c.* 20 to 4 Ma; Dalmayrac *et al.* 1980; Roperch *et al.* 2011; this study). A change to a more compressional setting at 4 Ma may have led to significant exhumation of the Abancay Deflection along the Apurimac fault system.

Conclusion

The opportunity to sample in the Machu Picchu Geopark provides a unique insight into a key area of the segmented Andean orogen: the Abancay Deflection. Our new thermochronology data and modelling from the Machu Picchu Batholith in the core of the Abancay Deflection reveal slow exhumation during the Miocene, despite evidence for both contemporaneous surface uplift and tectonic shortening of the northern Altiplano. This temporal decoupling of uplift and exhumation supports the hypothesis of an endorheic northern Altiplano prior to the Pliocene, as previously suggested from provenance data. Sediments seemed to be transported from the Eastern Cordillera toward the Altiplano in the late Miocene (Sundell *et al.* 2018) whereas the modern drainage direction is reversed toward the Amazon foreland. Geomorphological analysis of the Urubamba drainage basin suggests that it evolved through capture of an endorheic drainage system. At *c.* 4 Ma, drainage capture occurred close to our sampling location, resulting in base-level fall and causing a knickzone associated with significant incision to form at the point of capture. As a result of this increased focused incision, exhumation in this area increased since 4 Ma. The knickpoint has retreated toward the SE with the granite exposed all along the high-relief knickzone. The process driving exhumation is, however, probably more complex. As the total amount of exhumation may be larger than the maximum allowable amount of incision, depending on assumptions on the value of the geothermal gradient, additional tectonic uplift may be controlled by the Apurimac fault system.

Acknowledgments We thank SERNANP, INGEMMET (Cuzco-PATA convenio 006-2016-Fondecyt) and F. Astete (National Archaeological Park of Machu Picchu), for permission to work along the Inca trail and for provided facilities. We thank P. H. Leloup and G. Mahéo (Géode laboratory, Lyon) and the GTC platform (F. Coeur and F. Sénebier, ISTerre, Grenoble) for sample processing, as well as M. Balvay, R. Pinna-Jamme and F. Haurine for assistance during AFT and AHe dating. We also thank S. Hall, S. Noriega Londoño and an anonymous reviewer for instructive feedback on this paper.

Author contributions BG: conceptualization (equal), investigation (lead), supervision (equal), visualization (lead), writing – original draft (lead), writing – review & editing (equal); LA: conceptualization (equal), funding acquisition (lead), writing – review & editing (equal); XR: conceptualization

(equal), funding acquisition (lead), supervision (equal), visualization (equal), writing – review & editing (equal); CG: investigation (equal), writing – review & editing (equal); PvdB: investigation (equal), visualization (equal), writing – review & editing (equal); MB: investigation (equal), writing – review & editing (equal); CB: resources (supporting), writing – review & editing (supporting); FD: resources (supporting), writing – review & editing (supporting)

Funding This work was funded by the Agence Nationale de la Recherche (12-NS06-0005-01 for AHe analyses), Cuzco-PATA (006-2016-Fondecyt), Institut de Recherche pour le Développement, l’Institut des Sciences de la Terre and INSU.

Data availability All data generated or analysed during this study are included in this published article (and its supplementary information files).

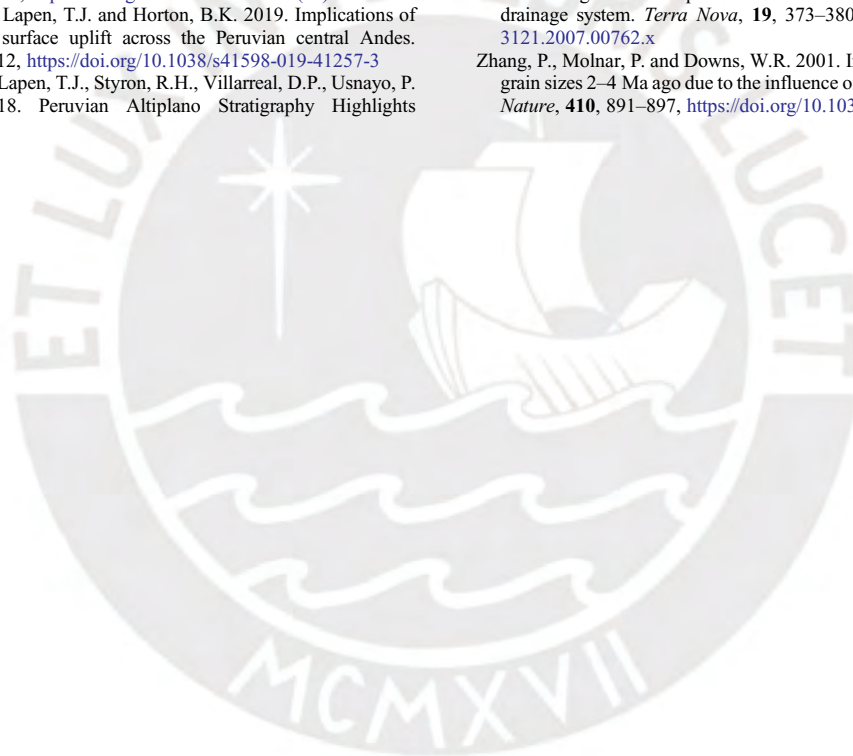
Scientific editing by Yuntao Tian

References

- Ault, A.K., Gautheron, C. and King, G.E. 2019. Innovations in (U–Th)/He, fission-track, and trapped-charge thermochronometry with applications to earthquakes, weathering, surface–mantle connections, and the growth and decay of mountains. *Tectonics*, **38**, 3705–3739, <https://doi.org/10.1029/2018tc005312>
- Bahlburg, H., Carlotto, V. and Cárdenas, J. 2006. Evidence of Early to Middle Ordovician arc volcanism in the Cordillera Oriental and Altiplano of southern Peru, Ollantaytambo Formation and Umachiri beds. *Journal of South American Earth Sciences*, **22**, 52–65, <https://doi.org/10.1016/j.jsames.2006.09.001>
- Barnes, J.B. and Ehlers, T.A. 2009. End member models for Andean Plateau uplift. *Earth-Science Reviews*, **97**, 105–132, <https://doi.org/10.1016/j.earscirev.2009.08.003>
- Barnes, J.B., Ehlers, T.A., McQuarrie, N., O’Sullivan, P.B. and Tawackoli, S. 2008. Thermochronometer record of central Andean Plateau growth, Bolivia (19.5°S). *Tectonics*, **27**, <https://doi.org/10.1029/2007TC002174>
- Barnes, J.B., Ehlers, T.A., Insel, N., McQuarrie, N. and Poulsen, C.J. 2012. Linking orography, climate, and exhumation across the central Andes. *Geology*, **40**, 1135–1138, <https://doi.org/10.1130/G33229.1>
- Bookhagen, B. and Strecker, M.R. 2008. Orographic barriers, high-resolution TRMM rainfall, and relief variations along the eastern Andes. *Geophysical Research Letters*, **35**, 1–6, <https://doi.org/10.1029/2007GL032011>
- Brandon, M.T., Roden-Tice, M.K. and Carver, J.I. 1998. Late Cenozoic exhumation of the Cascadia accretionary wedge in the Olympic Mountains, northwest Washington State. *Geological Society of America Bulletin*, **110**, 985–1009, [https://doi.org/10.1130/0016-7606\(1998\)110<0985:LCCEOT>2.3.CO;2](https://doi.org/10.1130/0016-7606(1998)110<0985:LCCEOT>2.3.CO;2)
- Braun, J. 2002. Quantifying the effect of recent relief changes on age–elevation relationships. *Earth and Planetary Science Letters*, **200**, 331–343, [https://doi.org/10.1016/S0012-821X\(02\)00638-6](https://doi.org/10.1016/S0012-821X(02)00638-6)
- Braun, J., van der Beek, P. and Batt, G. 2006. *Quantitative Thermochronology: Numerical Methods for the Interpretation of Thermochronological Data*. Cambridge, Cambridge University Press.
- Burbank, D.W. and Anderson, R.S. 2012. *Tectonic Geomorphology*, 2nd edn. Wiley–Blackwell, Chichester, <https://doi.org/10.1002/9781444345063>
- Carlier, G., Grandin, G., Laubacher, G., Marocco, R. and Mégard, F. 1982. Present knowledge of the magmatic evolution of the Eastern Cordillera of Peru. *Earth-Science Reviews*, **18**, 253–283, [https://doi.org/10.1016/0012-8252\(82\)90040-X](https://doi.org/10.1016/0012-8252(82)90040-X)
- Carlier, G., Lorand, J.P., Bonhomme, M. and Carlotto, V. 1996. A reappraisal of the Cenozoic inner arc magmatism in southern Peru: consequences for the evolution of the central Andes for the past 50 Ma. In: *Third International Symposium on Andean Geodynamics (ISAG)*. Saint Malo, 551–554.
- Carlier, G., Lorand, J.P., Liégeois, J.P., Fornari, M., Soler, P., Carlotto, V. and Cárdenas, J. 2005. Potassic–ultrapotassic mafic rocks delineate two lithospheric mantle blocks beneath the southern Peruvian Altiplano. *Geology*, **33**, 601–604, <https://doi.org/10.1130/G21643.1>
- Dalmayrac, B., Laubacher, G. and Marocco, R. 1980. *Géologie des Andes Péruviennes*. ORSTOM, Paris.
- Donelick, R.A., Sullivan, P.B.O. and Ketchum, R.A. 2005. Apatite Fission-Track Analysis. *Mineralogical Society of America and Geochemical Society, Reviews in Mineralogy and Geochemistry*, **58**, 49–94, <https://doi.org/10.2138/rmg.2005.58.3>
- Ehlers, T.A., Chaudhri, T., Kumar, S., Fuller, C.W., Willett, S.D., Ketchum, R.A. and Brandon, M.T. 2005. Computational Tools for Low-Temperature Thermochronometer Interpretation. *Mineralogical Society of America and Geochemical Society, Reviews in Mineralogy and Geochemistry*, **58**, 589–622, <https://doi.org/10.2138/rmg.2005.58.22>
- Espurt, N., Baby, P. *et al.* 2007. How does the Nazca Ridge subduction influence the modern Amazonian foreland basin? *Geology*, **35**, 515–518, <https://doi.org/10.1130/G23237A.1>
- Espurt, N., Barbarand, J., Roddaz, M., Brusset, S., Baby, P., Saillard, M. and Hermoza, W. 2011. A scenario for late Neogene Andean shortening transfer in

- the Camisea Subandean zone (Peru, 12°S): Implications for growth of the northern Andean Plateau. *Geological Society of America Bulletin*, **123**, 2050–2068, <https://doi.org/10.1130/B30165.1>
- Evans, N.J., Byrne, J.P., Keegan, J.T. and Dotter, L.E. 2005. Determination of Uranium and Thorium in Zircon, Apatite, and Fluorite: Application to Laser (U–Th)/He Thermochronology. *Journal of Analytical Chemistry*, **60**, 1159–1165, <https://doi.org/10.1007/s10809-005-0260-1>
- Farley, K.A. 2002. (U–Th)/He Dating: Techniques, Calibrations, and Applications. *Mineralogical Society of America and Geochemical Society, Reviews in Mineralogy and Geochemistry*, **47**, 819–844, <https://doi.org/10.2138/rmg.2002.47.18>
- Fitzgerald, P.G. and Malusà, M.G. 2019. Concept of the Exhumed Partial Annealing (Retention) Zone and Age-Elevation Profiles in Thermochronology. In: Malusà, M.G. and Fitzgerald, P.G. (eds) *Fission-Track Thermochronology and Its Application to Geology*. Springer, Cham, 165–189, https://doi.org/https://doi.org/10.1007/978-3-319-89421-8_9
- Flowers, R.M., Ketcham, R.A., Shuster, D.L. and Farley, K.A. 2009. Apatite (U–Th)/He thermochronometry using a radiation damage accumulation and annealing model. *Geochimica et Cosmochimica Acta*, **73**, 2347–2365, <https://doi.org/10.1016/j.gca.2009.01.015>
- Fox, N. and Bloom, A. 1994. Snowline Altitude and Climate in the Peruvian Andes (5–17°S) at Present and during the Latest Pleistocene Glacial Maximum. *Journal of Geography*, **103**, 867–885, https://doi.org/10.5026/jgeography.103.7_867
- Galbraith, R.F. and Laslett, G.M. 1993. Statistical models for mixed fission track ages. *International Journal of Radiation Applications and Instrumentation. Part, 21*, 459–470, [https://doi.org/10.1016/1359-0189\(93\)90185-C](https://doi.org/10.1016/1359-0189(93)90185-C)
- Gallagher, K. 2012. Transdimensional inverse thermal history modeling for quantitative thermochronology. *Journal of Geophysical Research: Solid Earth*, **117**, 1–16, <https://doi.org/10.1029/2011JB008825>
- Garzzone, C.N., Molnar, P., Libarkin, J.C. and MacFadden, B.J. 2006. Rapid late Miocene rise of the Bolivian Altiplano: Evidence for removal of mantle lithosphere. *Earth and Planetary Science Letters*, **241**, 543–556, <https://doi.org/10.1016/j.epsl.2005.11.026>
- Garzzone, C.N., McQuarrie, N. et al. 2017. Tectonic Evolution of the Central Andean Plateau and Implications for the Growth of Plateaus. *Annual Review of Earth and Planetary Sciences*, **45**, 529–559, <https://doi.org/10.1146/annurev-earth-063016-020612>
- Gautheron, C. and Tassan-Got, L. 2010. A Monte Carlo approach to diffusion applied to noble gas/helium thermochronology. *Chemical Geology*, **273**, 212–224, <https://doi.org/10.1016/j.chemgeo.2010.02.023>
- Gautheron, C., Tassan-Got, L., Barbarand, J. and Pagel, M. 2009. Effect of alpha-damage annealing on apatite (U–Th)/He thermochronology. *Chemical Geology*, **266**, 166–179, <https://doi.org/10.1016/j.chemgeo.2009.06.001>
- Gautheron, C., Tassan-Got, L., Ketcham, R.A. and Dobson, K.J. 2012. Accounting for long alpha-particle stopping distances in (U–Th–Sm)/He geochronology: 3D modeling of diffusion, zoning, implantation, and abrasion. *Geochimica et Cosmochimica Acta*, **96**, 44–56, <https://doi.org/10.1016/j.gca.2012.08.016>
- Gautheron, C., Espurt, N. et al. 2013. Direct dating of thick- and thin-skin thrusts in the Peruvian Subandean zone through apatite (U–Th)/He and fission track thermochronometry. *Basin Research*, **25**, 419–435, <https://doi.org/10.1111/bre.12012>
- Glotzbach, C., van der Beek, P.A. and Spiegel, C. 2011. Episodic exhumation and relief growth in the Mont Blanc massif, Western Alps from numerical modelling of thermochronology data. *Earth and Planetary Science Letters*, **304**, 417–430, <https://doi.org/10.1016/j.epsl.2011.02.020>
- Gonfiantini, R., Roche, M.-A., Olivry, J.-C., Fontes, J.-C. and Zuppi, G.M. 2001. The altitude effect on the isotopic composition of tropical rains. *Chemical Geology*, 147–167, [https://doi.org/10.1016/S0009-2541\(01\)00279-0](https://doi.org/10.1016/S0009-2541(01)00279-0)
- Henry, S.G. and Pollack, H.N. 1988. Terrestrial heat flow above the Andean Subduction Zone in Bolivia and Peru. *Journal of Geophysical Research: Solid Earth*, **93**, 15153–15162, <https://doi.org/10.1029/JB093iB12p15153>
- Hoom, C., Wesselingh, F.P. et al. 2010. Amazonia through time: Andean uplift, climate change, landscape evolution, and biodiversity. *Science*, **330**, 927–931, <https://doi.org/10.1126/science.1194585>
- Horton, B.K. 2005. Revised deformation history of the central Andes: Inferences from Cenozoic foredeep and intermontane basins of the Eastern Cordillera, Bolivia. *Tectonics*, **24**, 1–18, <https://doi.org/10.1029/2003TC001619>
- Hurford, A.J. and Green, P.F. 1983. The zeta age calibration of fission-track dating. *Chemical Geology*, **41**, 285–317, [https://doi.org/10.1016/S0009-2541\(83\)80026-6](https://doi.org/10.1016/S0009-2541(83)80026-6)
- Husson, L. and Sempere, T. 2003. Thickening the Altiplano crust by gravity-driven crustal channel flow. *Geophysical Research Letters*, **30**, 1–4, <https://doi.org/10.1029/2002GL016877>
- Insel, N., Poulsen, C.J. and Ehlers, T.A. 2010. Influence of the Andes Mountains on South American moisture transport, convection, and precipitation. *Climate Dynamics*, **35**, 1477–1492, <https://doi.org/10.1007/s00382-009-0637-1>
- Jaillard, E. and Soler, P. 1996. Cretaceous to early Paleogene tectonic evolution of the northern Central Andes (0–18°S) and its relations to geodynamics. *Tectonophysics*, **259**, 41–53, [https://doi.org/10.1016/0040-1951\(95\)00107-7](https://doi.org/10.1016/0040-1951(95)00107-7)
- Kennan, L. 2008. Fission track ages and sedimentary provenance studies in Peru, and their implications for Andean paleogeographic evolution, stratigraphy and hydrocarbon systems. In: *VIINGEPET, 13–17 October 2008*. Lima, Peru, **13**.
- Ketcham, R.A., Carter, A., Donelick, R.A., Barbarand, J. and Hurford, A.J. 2007. Improved modeling of fission-track annealing in apatite. *American Mineralogist*, **92**, 799–810, <https://doi.org/10.2138/am.2007.2281>
- Ketcham, R.A., Gautheron, C. and Tassan-Got, L. 2011. Accounting for long alpha-particle stopping distances in (U–Th–Sm)/He geochronology: Refinement of the baseline case. *Geochimica et Cosmochimica Acta*, **75**, 7779–7791, <https://doi.org/10.1016/j.gca.2011.10.011>
- Kirby, E. and Whipple, K.X. 2012. Expression of active tectonics in erosional landscapes. *Journal of Structural Geology*, **44**, 54–75, <https://doi.org/10.1016/j.jsg.2012.07.009>
- Kirby, E., Whipple, K.X., Tang, W. and Chen, Z. 2003. Distribution of active rock uplift along the eastern margin of the Tibetan Plateau: Inferences from bedrock channel longitudinal profiles. *Journal of Geophysical Research: Solid Earth*, **108**, <https://doi.org/10.1029/2001jb000861>
- Klein, A.G., Seltzer, G.O. and Isacks, B.L. 1999. Modern and last local glacial maximum snowlines in the Central Andes of Peru, Bolivia, and Northern Chile. *Quaternary Science Reviews*, **18**, 63–84, [https://doi.org/10.1016/S0277-3791\(98\)00095-X](https://doi.org/10.1016/S0277-3791(98)00095-X)
- Lease, R.O. and Ehlers, T.A. 2013. Incision into the eastern Andean Plateau during Pliocene cooling. *Science*, **341**, 774–776, <https://doi.org/10.1126/science.1239132>
- Licciardi, J.M., Schaefer, J.M., Taggart, J.R. and Lund, D.C. 2009. Holocene glacier fluctuations in the Peruvian Andes indicate northern climate linkages. *Science*, **325**, 1677–1679, <https://doi.org/10.1126/science.1175010>
- Lindsay, J.B., Cockburn, J.M.H. and Russell, H.A.J. 2015. An integral image approach to performing multi-scale topographic position analysis. *Geomorphology*, **245**, 51–61, <https://doi.org/10.1016/j.geomorph.2015.05.025>
- Mamani, M., Wörner, G. and Sempere, T. 2010. Geochemical variations in igneous rocks of the Central Andean orocline (13°S to 18°S): Tracing crustal thickening and magma generation through time and space. *Geological Society of America Bulletin*, **122**, 162–182, <https://doi.org/10.1130/B26538.1>
- Mancktelow, N.S. and Grasemann, B. 1997. Time-dependent effects of heat advection and topography on cooling histories during erosion. *Tectonophysics*, **270**, 167–195, [https://doi.org/10.1016/S0040-1951\(96\)00279-X](https://doi.org/10.1016/S0040-1951(96)00279-X)
- Margirier, A., Robert, X., Audin, L., Gautheron, C., Bernet, M., Hall, S. and Simon-Labric, T. 2015. Slab flattening, magmatism, and surface uplift in the Cordillera Occidental (Northern Peru). *Geology*, **43**, 1031–1034, <https://doi.org/10.1130/G37061.1>
- Margirier, A., Audin, L., Robert, X., Herman, F., Ganne, J. and Schwartz, S. 2016. Time and mode of exhumation of the Cordillera Blanca batholith (Peruvian Andes). *Journal of Geophysical Research: Solid Earth*, **121**, 6235–6249, <https://doi.org/10.1002/2016JB013055>
- Marocco, R. 1971. Etude géologique de la chaîne andine au niveau de la déflexion d'Abancay (Pérou). *Cahiers ORSTOM*, **3**, 45–58.
- McQuarrie, N., Horton, B.K., Zandt, G., Beck, S. and DeCelles, P.G. 2005. Lithospheric evolution of the Andean fold–thrust belt, Bolivia, and the origin of the central Andean plateau. *Tectonophysics*, **399**, 15–37, <https://doi.org/10.1016/j.tecto.2004.12.013>
- Mišković, A., Spikings, R.A., Chew, D.M., Košler, J., Ulianov, A. and Schaltegger, U. 2009. Tectonomagmatic evolution of Western Amazonia: Geochemical characterization and zircon U–Pb geochronological constraints from the Peruvian Eastern Cordilleran granitoids. *Geological Society of America Bulletin*, **121**, 1298–1324, <https://doi.org/10.1130/B26488.1>
- Perez, N.D., Horton, B.K., McQuarrie, N., Stübner, K. and Ehlers, T.A. 2016. Andean shortening, inversion and exhumation associated with thin- and thick-skinned deformation in southern Peru. *Geological Magazine*, **153**, 1013–1041, <https://doi.org/10.1017/S0016756816000121>
- Pérez-Gussinyé, M., Lowry, A.R., Phipps Morgan, J. and Tassara, A. 2008. Effective elastic thickness variations along the Andean margin and their relationship to subduction geometry. *Geochemistry, Geophysics, Geosystems*, **9**, <https://doi.org/10.1029/2007GC001786>
- Perron, J.T. and Royden, L. 2013. An integral approach to bedrock river profile analysis. *Earth Surface Processes and Landforms*, **38**, 570–576, <https://doi.org/10.1002/esp.3302>
- Picard, D., Sempere, T. and Plantard, O. 2008. Direction and timing of uplift propagation in the Peruvian Andes deduced from molecular phylogenetics of highland biotaxa. *Earth and Planetary Science Letters*, **271**, 326–336, <https://doi.org/10.1016/j.epsl.2008.04.024>
- Poulsen, C.J., Ehlers, T.A. and Insel, N. 2010. Onset of Convective Rainfall During Gradual Late Miocene Rise of the Central Andes. *Science*, **328**, 490–494, <https://doi.org/10.1126/science.1185078>
- Recanati, A., Gautheron, C. et al. 2017. Helium trapping in apatite damage: Insights from (U–Th–Sm)/He dating of different granitoid lithologies. *Chemical Geology*, **470**, 116–131, <https://doi.org/10.1016/j.chemgeo.2017.09.002>
- Reiners, P.W. and Brandon, M.T. 2006. Using Thermochronology To Understand Orogenic Erosion. *Annual Review of Earth and Planetary Sciences*, **34**, 419–466, <https://doi.org/10.1146/annurev.earth.34.031405.125202>
- Reiners, P.W. and Shuster, D.L. 2009. Thermochronology and landscape evolution. *Physics Today*, 31–36, <https://doi.org/10.1063/1.3226750>

- Reuter, H.I., Nelson, A. and Jarvis, A. 2007. An evaluation of void-filling interpolation methods for SRTM data. *International Journal of Geographical Information Science*, **21**, 983–1008, <https://doi.org/10.1080/13658810601169899>
- Rizzoli, P., Martone, M. *et al.* 2017. Generation and performance assessment of the global TanDEM-X digital elevation model. *ISPRS Journal of Photogrammetry and Remote Sensing*, **132**, 119–139, <https://doi.org/10.1016/j.isprsjprs.2017.08.008>
- Roperch, P., Carlotto, V., Ruffet, G. and Fornari, M. 2011. Tectonic rotations and transcurrent deformation south of the Abancay deflection in the Andes of southern Peru. *Tectonics*, **30**, <https://doi.org/10.1029/2010TC002725>
- Ruiz, G.M.H., Carlotto, V., Van Heiningen, P.V. and Andriessen, P.A.M. 2009. Steady-state exhumation pattern in the Central Andes – SE Peru. *Geological Society, London, Special Publications*, **324**, 307–316, <https://doi.org/10.1144/SP324.20>
- Schildgen, T.F. and Hoke, G.D. 2018. The topographic evolution of the central Andes. *Elements*, **14**, 231–236, <https://doi.org/10.2138/gselements.14.4.231>
- Schwanghart, W. and Scherler, D. 2014. TopoToolbox 2 – MATLAB-based software for topographic analysis and modeling in Earth surface sciences. *Earth Surface Dynamics*, **2**, 1–7, <https://doi.org/10.5194/esurf-2-1-2014>
- Schwarz, G.E. 1978. Estimating the dimension of a model. *Annals of Statistics*, **6**, 461–464, <https://doi.org/10.1214/aos/1176344136>
- Strecker, M.R., Alonso, R.N., Bookhagen, B., Carrapa, B., Hilley, G.E., Sobel, E.R. and Trauth, M.H. 2007. Tectonics and Climate of the Southern Central Andes. *Annual Review of Earth and Planetary Sciences*, **35**, 747–787, <https://doi.org/10.1146/annurev.earth.35.031306.140158>
- Stüwe, K., White, L. and Brown, R. 1994. The influence of eroding topography on steady-state isotherms. Application to fission track analysis. *Earth and Planetary Science Letters*, **124**, 63–74, [https://doi.org/10.1016/0012-821X\(94\)00068-9](https://doi.org/10.1016/0012-821X(94)00068-9)
- Sundell, K.E., Saylor, J.E., Lapen, T.J. and Horton, B.K. 2019. Implications of variable late Cenozoic surface uplift across the Peruvian central Andes. *Scientific Reports*, **9**, 1–12, <https://doi.org/10.1038/s41598-019-41257-3>
- Sundell, K.E., Saylor, J.E., Lapen, T.J., Styron, R.H., Villarreal, D.P., Usnayo, P. and Cárdenas, J. 2018. Peruvian Altiplano Stratigraphy Highlights Along-Strike Variability in Foreland Basin Evolution of the Cenozoic Central Andes. *Tectonics*, **37**, 1876–1904, <https://doi.org/10.1029/2017TC004775>
- Uba, C.E., Strecker, M.R. and Schmitt, A.K. 2007. Increased sediment accumulation rates and climatic forcing in the central Andes during the late Miocene. *Geology*, **35**, 979–982, <https://doi.org/10.1130/G224025A.1>
- Wagner, G., Reimer, G. and Jäger, E. 1977. Cooling ages derived by apatite fission track, mica Rb–Sr and K–Ar dating: the uplift and cooling history of the central Alps. *Memorie degli Istituti di Geologia e Mineralogia dell'Università di Padova*, **30**, 1–27.
- Whipple, K.X., Forte, A.M., DiBiase, R.A., Gasparini, N.M. and Ouimet, W.B. 2017. Timescales of landscape response to divide migration and drainage capture: Implications for the role of divide mobility in landscape evolution. *Journal of Geophysical Research: Earth Surface*, **122**, 248–273, <https://doi.org/10.1002/2016JF003973>
- Willett, S.D., McCoy, S.W., Perron, J., Goren, L. and Chen, C.Y. 2014. Dynamic reorganization of River Basins. *Science*, **343**, <https://doi.org/10.1126/science.1248765>
- Wise, J.M. and Noble, D.C. 2008. Late Pliocene inception of external drainage and erosion of intermontane basins in the highlands of Central Peru. *Revista de la Sociedad Geológica de España*, **21**, 73–91.
- Wobus, C.W., Hodges, K. and Whipple, K. 2003. Has focused denudation at the Himalayan topographic front sustained active thrusting near the Main Central Thrust? *Geology*, **31**, 861–864, <https://doi.org/10.1130/G19730.1>
- Wobus, C., Whipple, K.X. *et al.* 2006. Tectonics from topography: Procedures, promise, and pitfalls. *Geological Society of America, Special Papers*, **398**, 55–74, [https://doi.org/10.1130/2006.2398\(04\)](https://doi.org/10.1130/2006.2398(04))
- Zeilinger, G. and Schlunegger, F. 2007. Possible flexural accommodation on the eastern edge of the Altiplano in relation to focused erosion in the Rio La Paz drainage system. *Terra Nova*, **19**, 373–380, <https://doi.org/10.1111/j.1365-3121.2007.00762.x>
- Zhang, P., Molnar, P. and Downs, W.R. 2001. Increased sedimentation rates and grain sizes 2–4 Ma ago due to the influence of climate change on erosion rates. *Nature*, **410**, 891–897, <https://doi.org/10.1038/35073504>





Hazardous faults of South America; compilation and overview

Carlos Costa^{a,*}, Alexandra Alvarado^b, Franck Audemard^{c,1}, Laurence Audin^d,
 Carlos Benavente^e, F. Hilario Bezerra^f, José Cembrano^g, Gabriel Gonzálezⁱ, Myriam López^j,
 Estela Minaya^{k,2}, Isabel Santibañez^{g,2}, Julio Garcia^h, Mónica Arcila^j, Marco Pagani^h,
 Irene Pérez^l, Fabrizio Delgado^e, Mónica Paolini^{c,3}, Hernán Garro^a

^a Universidad Nacional de San Luis, San Luis, Argentina

^b Instituto Geofísico-Escuela Politécnica Nacional, Quito, Ecuador

^c (a) Fundación Venezolana de Investigaciones Sismológicas, Caracas, Venezuela

^d IRD-ISTerre, Grenoble, France

^e Instituto Geológico, Minerio y Metalúrgico, Lima, Peru

^f Universidad Federal do Rio Grande do Norte, Natal, Brazil

^g Pontificia Universidad Católica, Santiago, Chile

^h Centro de Investigación para la Gestión Integrada de Riesgo de Desastres, Universidad Católica del Norte, Antofagasta, Chile

ⁱ Servicio Geológico Colombiano, Bogotá, Colombia

^j Observatorio San Calixto, La Paz, Bolivia

^k GEM Foundation, Pavia, Italy

^l Instituto Nacional de Prevención Sísmica, San Juan, Argentina

ARTICLE INFO

Keywords:

Hazardous faults
 South America
 Neotectonics
 Seismic hazard

ABSTRACT

The heterogeneous South American geology has coined a wide variety of neotectonic settings where crustal seismogenic sources do occur. This fact has led to different approaches for mapping and inventory neotectonic structures. The South American Risk Assessment project promoted the discussion and update under uniform standards of the available information on neotectonic deformation, for its application in regional Probabilistic Seismic Hazard Assessments. As a result, 1533 hazardous faults have been inventoried onshore South America, 497 of them qualifying to feed the engine model driving probabilistic maps.

Main hazardous structures are concentrated throughout the eastern boundary of the Northern Andean Sliver and along the foreland-facing Andean Thrust Front. Space geodesy and seismicity illuminate the seismogenic significance of these deformation belts, although few neotectonic surveys have been conducted to date in the latter region. The characteristics of the main structures or deformation zones are here outlined according to their filiation to neotectonic domains, which are dependant on the geologic, seismotectonic, or morphotectonic settings in Andean and extra-Andean regions.

The knowledge accrued on the hazardous faults in South America here compiled, reinforces the fact that some of these structures constitute significant hazard sources for many urban areas and critical facilities and should be incorporated in seismic hazard assessments. However, the available fault data are insufficient in many cases or carry significant epistemic uncertainties for fault source characterization. This contribution aims to summarize the present knowledge on the South American hazardous faults as well as the main challenges for successful fault data incorporation into seismic hazard models.

* Corresponding author.

E-mail addresses: costa@unsl.edu.ar, mailcarloscosta@gmail.com (C. Costa).

¹ Now at Universidad Central de Venezuela, Caracas, Venezuela.

² Now as Independent Geologist.

³ Now at AguaEx, Santiago, Chile.

1. Introduction

The location and displacement record of fault sources constitute basic insights for seismic hazard assessment (SHA), helping to conduct more appropriate evaluations for a specific structure or region. This information is particularly relevant for areas where the recurrence interval of destructive earthquakes is larger than the time coverage provided by the seismic catalog, or whose slip rates can be barely measurable by instrumental networks. Thus, inventories under common compilation criteria of geologic structures with seismogenic significance in South America, constitute a basic supply for sound regional SHA which may also spotlight departure points for more detailed fault characterization studies.

The different seismotectonic and morphoclimatic settings in South America have traditionally resulted in heterogeneous criteria for mapping and interpreting neotectonic structures, particularly regarding the fault source geometry and activity rates. Many neotectonic or Quaternary-active structures have very limited information to date on their precise geometry, kinematics, and slip rates. Moreover, these attributes have usually been identified or suspected merely by fault/fold-related landforms or expert judgment, whereas no other data related to their activity or hazard are available. Accordingly, key parameters for fault source characterization such as slip rate and the 3D fault geometry (e.g. Basili et al., 2008; Haller and Basili, 2011; Pagani et al., 2015) carry high epistemic uncertainties or are absent for a significant number of structures.

A timely opportunity to update and review the existing data on the nature and distribution of onshore hazardous faults in South America has been the launching of the South America Risk Assessment project (SARA) (<https://sara.openquake.org/>), under the sponsorship of the Global Earthquake Model initiative (<https://www.globalquakemodel.org/>). The project was operative from 2014 to 2016 and aimed to estimate the regional hazard and risk through a probabilistic engine. The ultimate goal was to visualize the factors that increase the physical damage and decrease the resilience of populations to respond to and recover from damaging earthquake events.

The seismic hazard component of SARA addressed the harmonization of critical earthquake data sets, including crustal hazardous faults (SARA Topic 2), as one of the input layers of the SARA seismic hazard source model (SHSM) to calculate hazard and risk. The hazard or seismogenic capability of neotectonic structures (namely, those which have or are suspected to have slipped during the Quaternary), has been approached through characterization of their geometry, kinematics, and activity rate as main parameters. The other layers were historical and instrumental earthquake catalogs and recordings of local/national strong-motion. The project's main outcome has been the first regional probabilistic seismic hazard assessment (PSHA), with all data and tools placed in the public domain for data capture and representation (https://sara.openquake.org/hazard_rt7).

The SARA Topic 2 project activities have been focused on compiling the existing databases and in bridging the gap, whenever possible, between neotectonic information and the necessary data of faults sources required by the SARA SHSM. This contribution aims to summarize the main neotectonic settings in continental South America, relevant as to the occurrence of significant hazardous crustal structures, and to describe the criteria and strategies for data compilation. Such a goal implied to review and update the existing databases; to compile and elaborate new information and to upgrade many data by populating the required parameters for fault source modeling under homogeneous standards. The project also aimed to set up basic criteria to capture new GIS-based data, which can provide guidance for future research on these topics.

2. Tectonic outline of South America

As a response to contemporary geodynamical processes, neotectonic

deformation in South America is concentrated along the Andes (Fig. 1). Intraplate low strain regions comprising cratonic areas and related basins in extra-Andean South America constitute the major domain in terms of areal representation, but with few occurrences of hazardous faults in comparison to the Andes and peri-Andean regions.

The inherited geological and structural patterns and discontinuities of the Andes orogen, as well as the present plate tectonic setting, cause a wide variety of neotectonic environments in terms of both structural styles and strain rate, under different morphoclimatic conditions. These settings vary from an active subduction megathrust and onshore interplate borders, to slowly deforming internal regions. As for its present geodynamics, the Andean chain is characterized by the prevalence of strike-slip tectonics at its northern and southern extremes and by a typical oceanic-continental plate boundary throughout the Central Andes (Fig. 1).

The Andes have traditionally been divided into three main sectors, namely the Northern Andes, the Central Andes, and the Southern Andes (e.g. Gansser, 1973; Ramos, 1999) (Fig. 1). The Northern Andes, located north of the Gulf of Guayaquil (Fig. 2) are the result of the interactions between the Nazca, South American and Caribbean plates, involving a complex framework of tectonic blocks also related to the collision of island arcs (e.g. Ramos, 1999, 2009; Taboada et al., 2000; Audemard and Audemard, 2002; Audemard, 2014a; Arcila and Muñoz-Martin, 2020). Strike-slip tectonics is dominant near these plate boundaries throughout the Caribbean coast. Of particular relevance for the



Fig. 1. Main plate boundaries and geotectonic features of the continental South American Plate. Opposite red arrows point out boundaries between the Northern, Central, and Southern Andes domains. Yellow quadrangles show figures location. (For interpretation of the references to color in this figure legend, the reader is referred to the Web version of this article.)

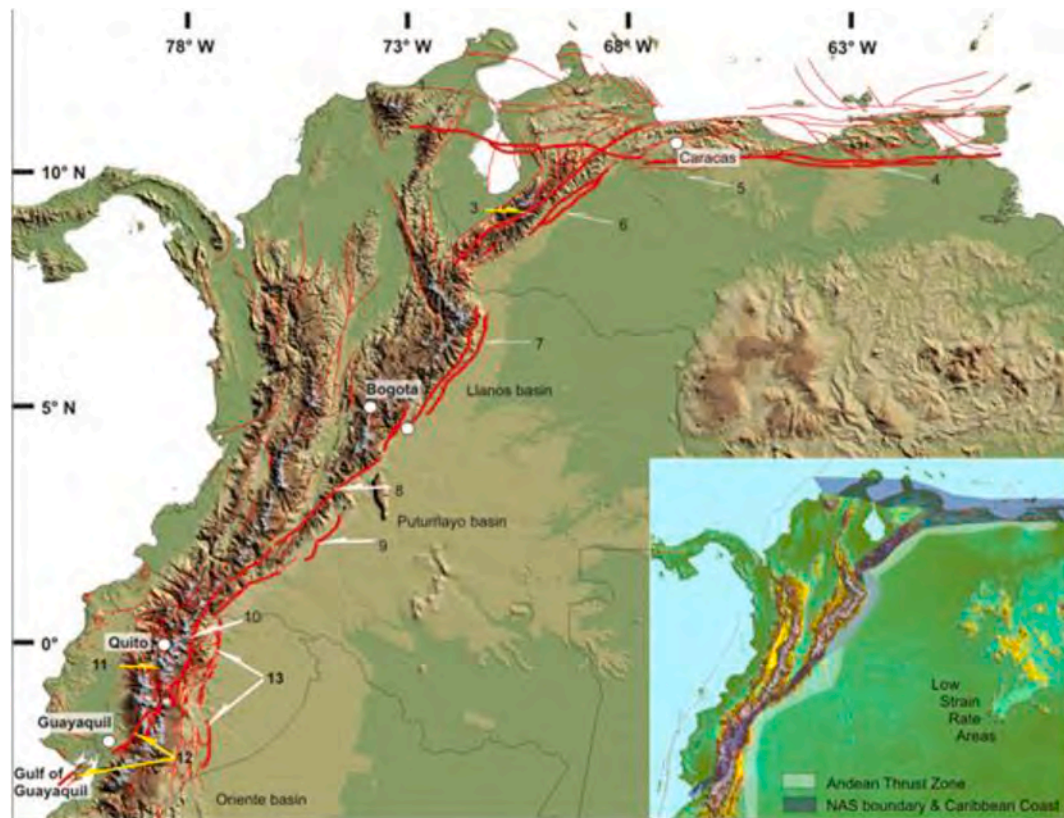


Fig. 2. Outline of the main hazardous fault systems (tick red lines) of the Northern Andes. 1. Oca-Ancón, 2. San Sebastian-El Pilar, 3. Boconó-Morón, 4. Campo Texas-Pedernales-Jusepin, 5. Frontal Thrusts, 6. South Andean Flexure Zone, 7. Eastern Frontal Thrust System, 8. Algeciras, 9. Amazonian Border, 10. Cosanga-Chingual, 11. Inter Andean Depression and Quito-Latacunga, 12. Pallatanga-Puná, 13. Subandean Thrust Zone. The inset shows the main neotectonic domains sketched in the text. See the location in Fig. 1. (For interpretation of the references to color in this figure legend, the reader is referred to the Web version of this article.)

occurrence of hazardous faults is the eastern boundary of the North Andean Sliver (NAS) or North Andean Block. This first-order deformation belt concentrates the escape to the north of the NAS as to stable South America (Pennington, 1981; Stephan et al., 1990; Bellier et al., 1989; Freymueller et al., 1993; Audemard, 1998; Nocquet et al., 2014; Alvarado et al., 2016; Mora-Páez et al., 2019a, 2020).

The Central Andes, between 4°S and 46°30' S are regarded as the typical Andean orogen, where mountain building and related processes are mainly driven by type-B subduction (Ramos, 1988, 1999; Gutscher et al., 2000) (Fig. 1). The main control of location and style of Quaternary deformation is exerted by the geometry of the subducted Nazca plate, determining several regions with distinct characteristics. Latitudinal segments with normal subduction angles show noticeable differences in spatial distribution and tectonic style of Quaternary deformation as regards to flat-subduction segments. This is mainly because neotectonic deformation is more efficiently transmitted to the foreland region in the latter (e.g. Jordan et al., 1983; Jordan and Allmendinger, 1986; Gutscher et al., 2000; Ramos et al., 2002).

South of 46°30'S, the Southern Andes are associated with ridge collision and kinematic interaction among the South American, Antarctica, and Scotia plates, determining the concentration of strike-slip deformation at the southern end of the continent (Dalziel et al., 1975; Cunningham, 1993; Klepeis, 1994; Ramos, 1999; Kraemer, 2003; Smalley et al., 2003) (Fig. 1).

Recent and ongoing deformation in the Pacific lowlands and Andean Forearc is a direct manifestation of interplate processes and seismicity at the Benioff zone (e.g. Allmendinger et al., 2005; Audin et al., 2008; Allmendinger and González, 2010; González et al., 2015; Benavente et al., 2017a). Major Quaternary structures at the eastern slope of the Andes instead, are related to crustal weaknesses rather than to interplate processes (Costa et al., 2006a and references therein).

The intraplate regions of cratonic South America expose a long-evolved Precambrian basement coexisting with sedimentary rocks deposited in pericratonic and rift basins. Neotectonic deformation has been described located on shear zones of pre-existing anisotropies of the basement rocks (e.g. Bezerra et al., 1998; Riccomini and Assumpção, 1999; Bezerra and Vita Finzi, 2000; Nogueira et al., 2010; Coelho et al., 1997; de Menezes et al.; Ramos et al.). Other neotectonic faults cut across pre-existing basement structures and form new faults (Bezerra et al., 2011).

3. Neotectonic domains

The diversity of geodynamic and geologic settings in space and time, determine a wide variety of neotectonic scenarios in continental South America. Similarities in the structural style of inventoried hazardous fault systems usually show a dependence upon the regional geology or their occurrence being constrained by morphostructural units. Such discrete areas are here conceived as *Neotectonic Domains*. This discrimination does not intend to cover the entire region or the occurrence of all hazardous faults known. It aims to introduce a geographic-based sketch to link the occurrence of main hazardous faults and neotectonic deformation zones with particular geologic, seismotectonic, and/or morphotectonic settings. Some domains are restricted to specific areas or major morphostructural provinces, whereas others overlap over different geologic and geodynamic environments.

The main *Neotectonic Domains* arising from the compiled data can be outlined as follows;

3.1. The Andean thrust zone

Although resulting from very variable geology, geologic evolution,

and plate interactions, the Andean foothills facing to the continental interiors from Venezuela to the Southern Patagonian Andes are characterized by an almost continuous zone with localized neotectonic crustal compression. Essentially a fold and thrust belt (FTB) of variable width, thickness, and net shortening (Figs. 1–6), only interrupted in the northern Pampean-Chilean flat-slab (27°–30°S).

Most structures are derived from FTB geometries, in some cases rooted in basement rocks and evolving from inverted Mesozoic faults (e.g. Fabre, 1983; Baby et al., 1992, 1997; 2018; Audemard and Audemard, 2002; Audemard, 2003; Mora et al., 2006, 2009, 2019; Zamora et al., 2009; Giambiagi et al., 2015; Folguera et al., 2015; Villegas-Lanza et al., 2016; McClay et al., 2018). These FTB have usually been formed from ~10 Ma to Present along the active Andean orogenic front (e.g. Mora et al., 2006, 2014; Ramos, 2009; Horton, 2018). Subandean thrust faults are commonly blind and related to piedmont anticlines. Although barely exposed at the surface, they can be imaged through gentle up-bulges or suspected from tilted alluvial surfaces in the piedmont alluvial planes and drainage anomalies (Dumont et al., 1991; Dumont, 1996; Audemard, 1999; Bes de Berc et al., 2005; Mugnier et al., 2006). The underlying causative structures have usually been illuminated through oil industry seismic lines.

In Venezuela, mountain building along the NE-SW trending Merida

Andes has been mainly driven by complex interactions between the Caribbean, South American, and Nazca plates with recent deformation concentrated along the Boconó Fault System (Fig. 2) (e.g. Pennington, 1981; Schubert, 1982; Freymueller et al., 1993; Audemard and Audemard, 2002; Trenkamp et al., 2002). However, the southeastern foothills of this mountain range are bounded by the South Andean Flexure Zone (Audemard and Audemard, 2002), which is rooted under this mountain range (Fig. 2). These contractional blind structures result from a complex flat and ramp geometries generally SE-vergent, which deform Quaternary alluvial terraces along the piedmont area (Audemard, 1999, 2003; Audemard et al., 2000; Audemard and Audemard, 2002) (Fig. 2). Similar thrust systems with opposite vergence appear at the northwestern foothills of the Merida Andes (De Toni and Kellogg, 1993; Audemard and Audemard, 2002; Duerto et al., 2006).

To the east of the Merida Andes and not directly related to the Andean chain, a main thrust boundary zone with general E-W trend results from shortening linked to the Caribbean-South America plates interaction along the Caribbean coast. In central-northern Venezuela, it is the southern boundary of the Caribbean nappes that overrode the continent in the Paleogene. Discontinuous reverse faults systems, such as Cantagallo and Frontal thrusts in central Venezuela (Audemard et al., 1988), and Campo Texas-Pedernales-Jusepin faults in eastern Venezuela

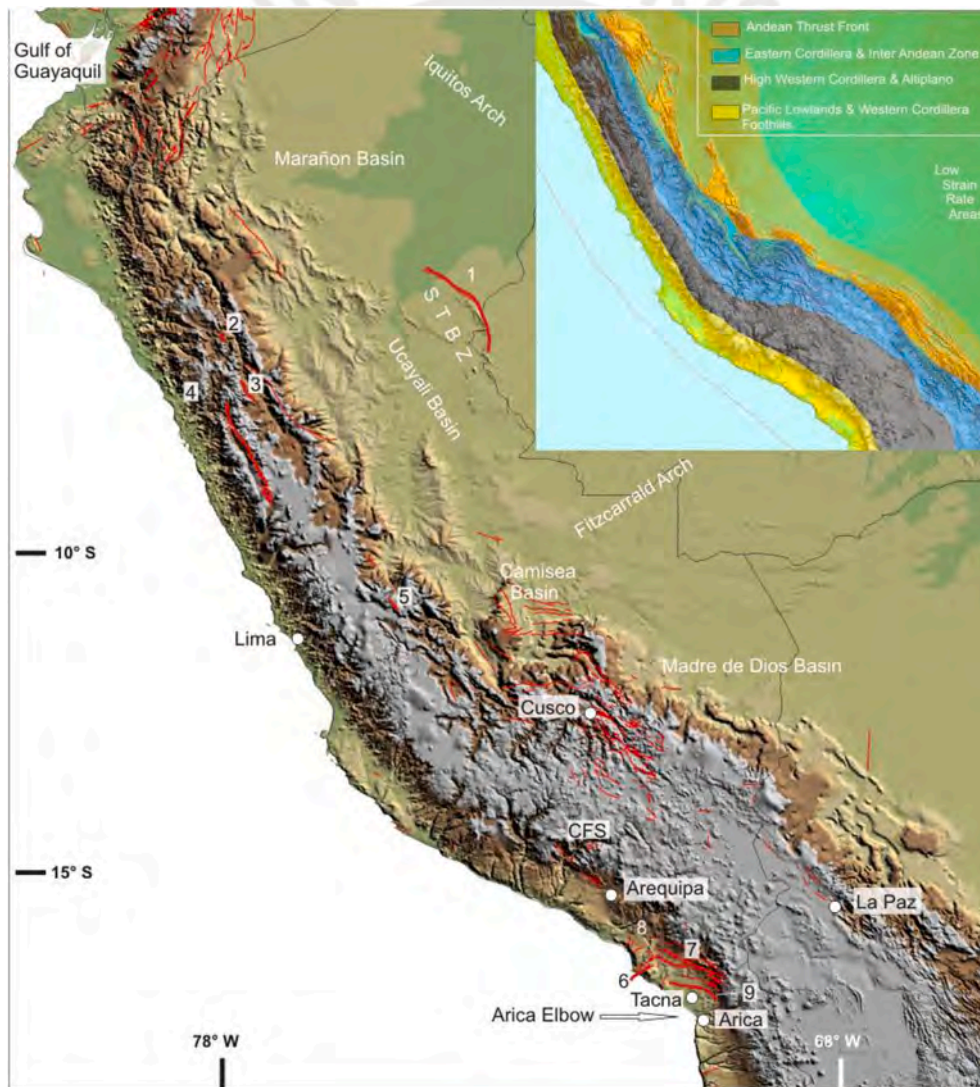


Fig. 3. Main hazardous faults and fault systems in the northern section of the Central Andes. 1. Subandean Tilted Block Zone, 2. Chaquilbamba, 3. Quiches, 4. Cordillera Blanca, 5. Huaytapallana, 6. Chololo, 7. Incahuico, 8. Purgatorio, 9. Sama-Calientes. The inset displays the neotectonic domains corresponding to this region. See the location in Fig. 1.

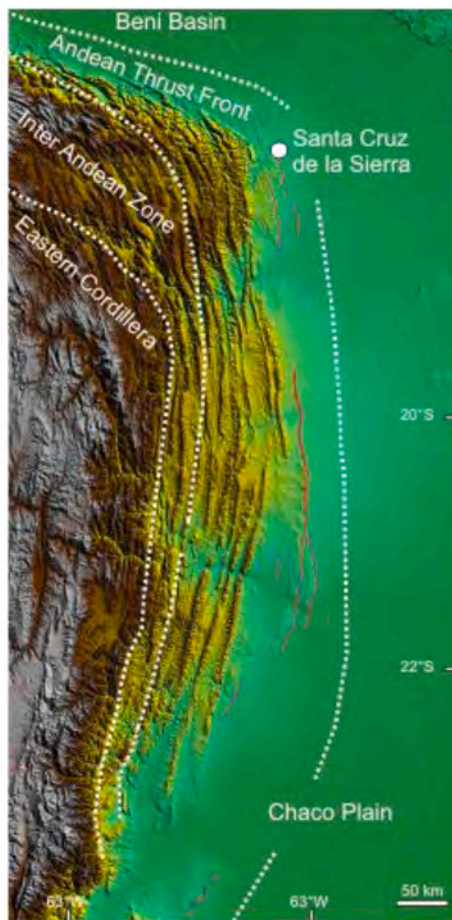


Fig. 4. SRTM image of the Andean Thrust Front and related neotectonic domains in the Bolivian Andes, depicting the Mandeyapeca Thrust System. Thrust traces according to the SARA T2 database and Weiss et al. (2015). See the location in Fig. 1.

(FUNVISIS, 1994; Singer et al., 1995; Wagner, 2004; Fajardo, 2015), extend up to the Atlantic coast and bound the southern coast of Trinidad (Fig. 2). In eastern Venezuela and southern Trinidad, this belt is accompanied by a trend of active oil-seeping mud volcanoes.

The Mérida Andes meets the Eastern Cordillera of the Colombian Andes in a structurally complex zone, where the Andean chain experiments two opposite right-angle bends as the dextral motion of the Boconó Fault System is being transferred into the Eastern Frontal Thrust System (EFTS) of the Eastern Cordillera in Colombia (Fig. 2). After a first bend to the south, this transfer is made possible by east-verging NNW trending thrusts in Colombia (Rodríguez et al., 2017). And after a second opposing bend, they connect with the EFTS through the NE trending Guaicaramo Fault System and related anticlines. These structures deform Pleistocene alluvial terraces (Paris and Sarria, 1986; Robertson, 1989, 2007; Vergara et al., 1995; Audemard, 1999; Diederix and Romero, 2009) with slip rates ~ 1.5 mm/a (Mora et al., 2010; Veloza et al., 2012; 2015, among others). This value is not much different from the one obtained for the South Andean Flexure Zone in Venezuela (Fig. 2), where Guzmán et al. (2013) estimated an uplift rate of 1.1 mm/a for the last 70 ka. Assuming a typical average dip of 30° for the master thrust zone, thus a slip rate ~ 2.5 mm/a can be expected. Historic and recent crustal earthquakes have occurred along this active front in Colombia such as the 1995 Mw 6.5 Tauramena earthquake (Dimaté et al., 2003).

Current tectonic activity is completely partitioned in the Mérida Andes (Audemard and Audemard, 2002; Audemard, 2009a). The Boconó fault takes most if not all the dextral slip while the South Andean

Flexure Zone and the northern FTB and the chain itself accommodate across-strike shortening. Dextral and reverse slip at the EFTS (Guaicaramo, Cusiana, Yopal, and others thrusts) in Colombia are not as clearly dissociated along the southern foothills of the Eastern Cordillera north of 4° N.

At $\sim 4^\circ$ N this compressive-transpressive bends slightly again to the NE-SW and Quaternary-active fault traces have been mapped through the inner Eastern Cordillera, merging with the dextral Algeciras Fault System (AFS) (Pennington, 1981; Taboada et al., 2000; Diederix and Romero, 2009; Diederix et al., 2019; Bohorquez et al., this volume), where Gómez et al. (2015) documented a transpressive duplex system between the AFS and the Guaicaramo Fault system. However, south of $\sim 4^\circ$ N, contractional neotectonic structures have also been reported along the Subandean zone, bounding the Garzón Massif on the east with the Putumayo basin (Mocoa and Amazonian Border Faults) (Paris and Romero, 1994; Paris et al., 2000; Robertson and Castiblanco, 2011; Veloza et al., 2012; Saeid et al., 2017; https://sara.openquake.org/hazard_rt2), indicating the southward continuation of the foothills contractional belt (Figs. 2 and 3).

Thrust faults, most of them blind, also prevail along the Ecuadorian foothills. These neotectonic structures are the outer bound of the Subandean Thrust Zone or Eastern Sub-Andean Thrust-and-Folds Belt (ESB), *sensu* Yepes et al. (2016), highlighted by bedrock uplifts, such as the Napo (i.e. Payamino, Pusuno and Sumaco faults) and Cutucú (Cutucú, Cangaime faults) uplifts (Fig. 3). Quaternary tectonic activity has been reported based on secondary evidence, drainage control, and coincidence with Neogene underlying structures (Ego et al., 1996; Egüez et al., 2003; Bès de Berc, 2003; Bès de Berc et al., 2005; Bernal et al., 2012).

South of the Gulf of Guayaquil (4° S), where the Carnegie ridge meets the trench, to $\sim 46^\circ$ S, the Andean Thrust Front lies in the Central Andes setting (Fig. 1). The thrust front has been migrating eastwards during the Cenozoic and in the Andes of Perú, Bolivia, and Argentina. Main Neogene shortening is recorded at the Eastern Cordillera but particularly at the Subandean zone (Fig. 3). The latter is the locus of active Andean growth and mountain building processes, as underlined by geodetic and seismologic data (Ramos, 1988, 1999; Kendrick et al., 1999, 2006; Gutscher et al., 2000; Taboada et al., 2000; Brooks et al., 2011; Nocquet et al., 2014; Alvarado et al., 2016).

The Central Andes of Perú exhibits a general NNW-SSE trend south of the gentle Huancabamba deflection (Fig. 3). The thrust front here lies above the Peruvian flat-slab segment (4° – 14° S), although the Subandean zone exhibits similar structural style as to the Northern Andes of Ecuador (Oriente basin) (Ham and Herrera, 1963; Ego et al., 1996; Baby et al., 1997). These areas are poorly surveyed as for neotectonic structures and the few ones compiled have insufficient and low-reliability data. Dumont et al. (1991) and Dumont (1996) outlined the Subandean Tilted Block Zone (STBZ) parallel to the Peruvian Subandean FTB, which is partly bounded by the Tapiche fault (Macharé et al., 2003, 2009a) (Fig. 3). According to these authors, neotectonic thrust activity along the STBZ controls major rivers patterns and migration, such as the Pastaza and Ucayali rivers to flow parallel to the STBZ, before merging into the Amazonas river and overpassing the forebulge of the Iquitos arch (Fig. 3).

The Peruvian flat-slab extends down to $\sim 14^\circ$ S, flanked to the south by major crustal-scale features, such as the Abancay deflection, the Camisea Subandean zone (Espurt et al., 2011) and the Fitzcarrald arch (Regard et al., 2009) (Fig. 3). Here, the Andean Thrust Front undergoes a local right angle deflection with many structures suspected to have sustained Quaternary activity (Ham and Herrera, 1963; Baby et al., 1997; Macharé et al., 2003, 2009a; Mora et al., 2009; Benavente et al., 2013; Regard et al., 2009; McClay et al., 2018, <https://www.ingemmet.gob.pe/mapa-neotectonico>; https://sara.openquake.org/hazard_rt2; <http://neotec-opendata.com/>).

The Andean chain notably widens south of the Abancay deflection above a normal subduction segment (14° – 27° S) (Fig. 4) and the Subandean thrust zone describes a gentle arc concave to the southwest with

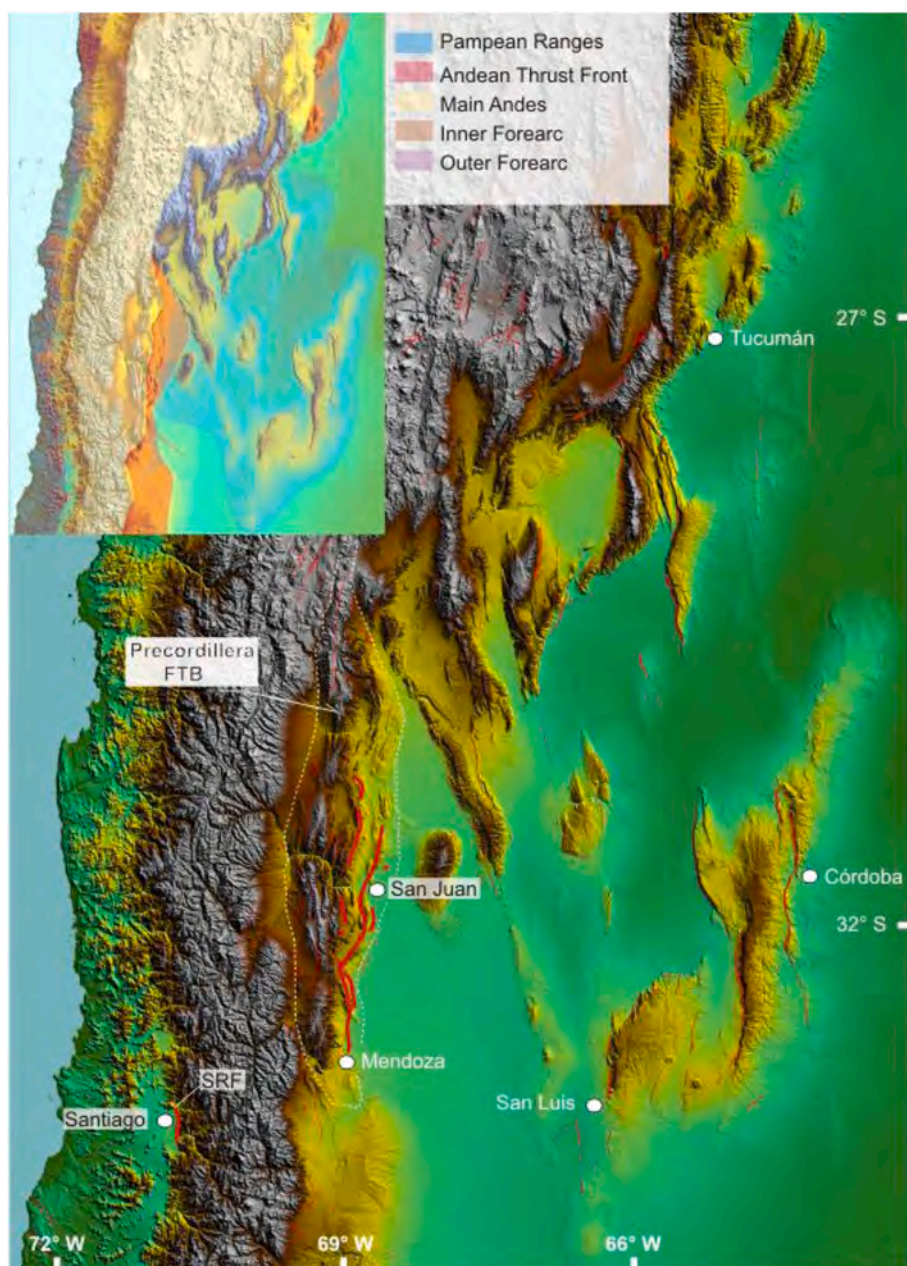


Fig. 5. The Andean broken foreland represented by the basement uplifts of the Pampean Ranges stands out in peri-Andean regions above the Pampean-Chilean flat subduction segment (27°–33°S). The main bounding faults compiled in this domain appear in thin red lines. The Andean Thrust Front is here located in the eastern part of the Precordillera FTB. SRF, San Ramón Fault. The inset shows the main neotectonic domains in this latitudinal section. See the location in Fig. 1. (For interpretation of the references to color in this figure legend, the reader is referred to the Web version of this article.)

a general NW trend. Almost none neotectonic structures have been compiled at the orogenic front between 14° and 18°S, a latitudinal segment coincident with the northern part of the Altiplano plateau and also characterized by an FTB style of Neogene deformation. Quaternary-active structures propagating eastward into flat Neogene sediments of the Beni basin has been suspected from subsurface data (Dumont, 1996; Baby et al., 1997; Gautheron et al., 2013; McClay et al., 2018; Rojas Vera et al., 2019) (Fig. 4) and suggested by the dynamics and adaptation of major (Dumont, 1996; Regard et al., 2009).

The Subandean zone of the Bolivian orocline bends to a general NNE direction in coincidence with the Arica elbow south of 18°S and extends down to 23°S (Argentina-Bolivia frontier zone). This segment corresponds to the widest, highest, and thickest Andean segment, whose retroarc orogenic belt has also accrued the highest Cenozoic shortening (Horton, 2018) (Fig. 4). The frontal deformation zone of the Andes can be recognized in the topography by a series of thin- and thick-skinned fault-related folds with parallel trends (Baby et al., 1992; Leturmy et al., 2000; Rocha and Cristallini, 2015; McClay et al., 2018; Giampaoli

and Rojas Vera, 2018; Rojas Vera et al., 2019). The outer thrust of this FTB corresponds to the Mandeyapeca Thrust System (MTS) (Moretti et al., 1996; Lavenu et al., 2000; Brooks et al., 2011; Weiss et al., 2015) (Fig. 4). Brooks et al. (2011) have suggested that the master faults underlying the orogenic wedge have the capability of producing large ($M_w > 8$) earthquakes. These authors derived a slip rate ~ 10 mm/a from geodetic data, corresponding to the locked portion of the detachment zone beneath the subandean zone. Weiss et al. (2015) refined Holocene dip-slip rates for the MTS, suggesting values of ~ 4.6 mm/a. This indicates that $\sim 1/2$ of both the mean geologic and geodetic shortening rates (~ 7 – 13 mm/a) are accommodated by dip-slip motion at the wedge-front, highlighting the significant threat that the MTS poses for this region.

Neogene shortening decrease from north to south along the Bolivian subandean zone (McClay et al., 2018; Giampaoli and Rojas Vera, 2018; Rojas Vera et al., 2019), although Holocene deformation has also been described at its southern tip in Argentina (Ramos et al., 2006).

The Andean Thrust Front progressively loses its typical topographic

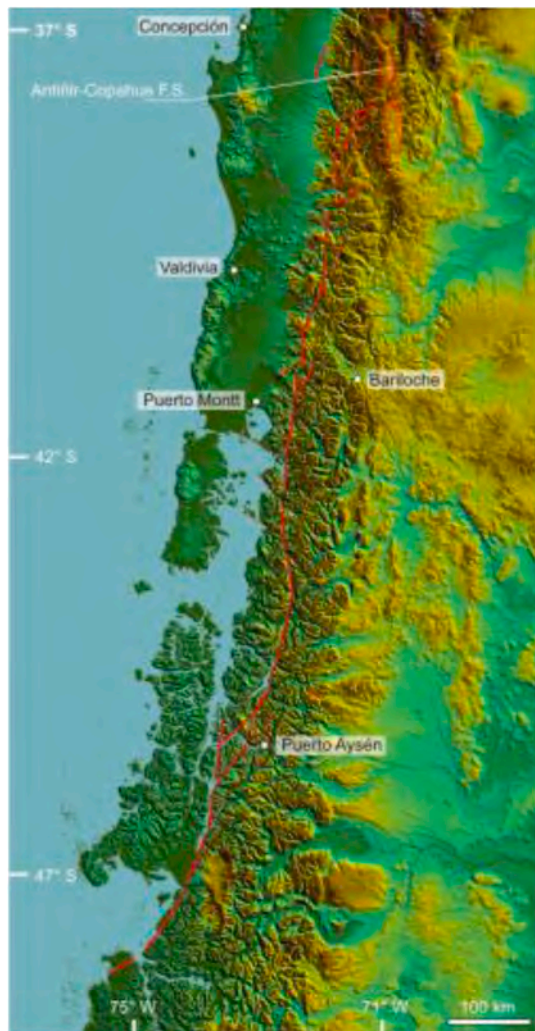


Fig. 6. SRTM image sketching the general trace of the Liqueñe Ofqui Fault System and its proposed continuation to the north into the Antifir-Copahue Fault System. See the location in Fig. 1.

imprint at the northern part of the Pampean-Chilean flat-slab (27°–33°S), where extra-Andean mountain building has been characterized by widespread Neogene broken-foreland basement uplifts (Pampean Ranges) during the last ~8Ma (Fig. 5) (e.g. Jordan and Allmendinger, 1986; Ramos et al., 2002; Costa, 1999; Costa et al., 2006a; Davila and Carter, 2013).

From a morphotectonic point of view, two main domains can be recognized along the Pampean-Chilean flat-slab. North of 29°–30°S, the Pampean Ranges are assembled to the Andean edifice, some of the uplifted basement blocks achieving an orogenic relief similar or even higher than the main Andean peaks (Ramos et al., 2004). The pattern of Quaternary faulting, characterized by short, distributed and not well spatially organized traces, suggests that the orogenic front is here characterized by a wide diffuse deformation zone (Costa et al., 2000a; García et al., 2013, 2017; Hongn et al., 2014; <https://sigam.segemar.gov.ar/visor/>) probably involving a thicker seismogenic crust. Conversely, south of 29°–30°S the frontal deformation zone of the Andes is concentrated at the Precordillera FTB foothills (Fig. 5), where an arid climate and suitable morphotectonic conditions favor the best exposures of the active orogenic front along the entire Andean chain (e.g. Bastías et al., 1984; Martos, 1987; Costa et al., 2000b, 2014a; 2015, 2019; Ahumada and Costa, 2009; Costa, 2009; Schmidt et al., 2011; Perucca and Onorato, 2011; Perucca et al., 2013; Audemard, 2014b; Audemard et al., 2016; Richard et al., 2019; Rimando et al., 2019). In this southern

part of the flat-slab segment, the Andean building is separated from the Pampean uplifts by a foreland basin (Fig. 5).

The Argentine Precordillera is a Palaeozoic orogen whose neotectonic deformation styles have been controlled by pre-Cenozoic structures, which result in a sharp change in the geometries and vergences of active thrusting north and south of 32°15'S (Cortés et al., 1999, 2006; Ahumada and Costa, 2009; Giambiagi et al., 2015; Costa et al., 2014a, 2019). Geodetic data suggests shortening rates of 4–7 mm/a (Kendrick et al., 1999, 2006; Brooks et al., 2003), although Quaternary shortening rates are variable, even within individual thrusts (Siame et al., 2002, 2005; 2006a; Schmidt et al., 2011; Rockwell et al., 2014; Costa et al., 2019; Richard et al., 2019; Rimando et al., 2019), highlighting the complexities for activity rates evaluation in these thrust systems. Most surveyed individual thrusts reveal shortening rates ~1 mm/a, suggesting that several active structures are accommodating the transient strain signal depicted by space geodesy. Geodetic data has also led to argue that the Andean hinterland behaves as a microplate at these latitudes (Brooks et al., 2003), although this interpretation is not necessarily endorsed by geologic data (García Morabito et al., 2020).

South of 33°S, another segment of normal subduction develops and the orogenic front becomes markedly less well exposed and characterized by east-directed blind thrusts (Cortés et al., 1999, 2006; García and Casa, 2014; Moreiras et al., 2014). An FTB style also characterizes the Andean foothills between 33° and 38°S with sparse evidence of neotectonic activity (Messenger, 2010; Messenger et al., 2010; Galland et al., 2007; Sagripanti et al., 2017, 2020; Colavitto et al., 2019; Mescua et al., 2019).

Neogene shortening in the Central Andes orogen decreases gradually to the south (Ramos et al., 2004). Between 38°S and the Fuegian Andes, the characteristics of the Andean front as for the occurrence of Quaternary fault activity has been poorly documented, except for the Antifir-Copahue Fault System (ACFS) in the northern Patagonian Andes and other isolated minor faults (Fig. 6) (https://sara.openquake.org/hazard_rt2). It has been claimed that the dominantly compressive ACFS merges to the south with the Liqueñe-Ofqui Fault System (Folguera et al., 2004, 2006; 2015; Melnick et al., 2006; Colavitto et al., 2020). At the southern continental end, the evolution of the Fuegian Andes foothills is closely related to the dynamics of the South America-Scotia plate margin (Fig. 7).

3.2. The North Andean Sliver boundary and the caribbean coast

Most significant hazardous faults in northernmost South America result from the complex interaction between the Caribbean, South America, and Nazca plates, involving the North Andean Block *sensu* Pennington (1981) or North Andean Sliver (NAS) *sensu* Nocquet et al.



Fig. 7. Main fault traces compiled for the Magallanes-Fagnano Fault System and modified after Sandoval and De Pascale (2020). See the location in Fig. 1.

(2014), where strike-slip faults largely prevail. This crustal block is escaping to the NNE concerning stable South America, involving a wide deformation belt where several minor blocks can be recognized mostly through tectonic geodesy data (Pennington, 1981; Aggarwal, 1983; Stephan et al., 1990; Audemard, 1993, 1998, 2002, 2009b, 2014; Freymueller et al., 1993; Kellogg and Vega, 1995; Taboada et al., 2000; Trenkamp et al., 2002; Alvarado et al., 2016; Mora-Paez et al., 2019a, 2020; Arcila and Muñoz-Martin, 2020). The main motion of the eastern NAS boundary and current interactions with the Southamerican plate is being accommodated onshore by several strike-slip fault systems running from the Caribbean coast down to the Ecuadorian-Colombian trench at the Gulf of Guayaquil (Stephan et al., 1990; Audemard, 1993, 2002, 2009b, Audemard, 2014a; Taboada et al., 2000; Dumont et al., 2005; Alvarado et al., 2016; Yepes et al., 2016; Baize et al., 2014, 2020).

In Venezuela, a significant part of this right-lateral motion takes place along the dextral Boconó- San Sebastián-El Pilar Fault System (Fig. 2) (Molnar and Sykes, 1969; Minster and Jordan, 1978; Schubert, 1979, 1982, 1984; Pérez and Aggarwal, 1981; Aggarwal, 1983; Soulas, 1986; Beltrán and Giraldo, 1989; Stephan et al., 1990; Audemard et al., 2006; Audemard, 2007). The strike-slip El Pilar-San Sebastián fault system runs mostly offshore with E-W general trend along the Venezuelan coastline with slip rates $\sim 9\text{--}10$ mm/a (Audemard et al., 2006 and references therein). Several historic earthquakes have taken place along them, being the last significant one, the Ms 6.8 1997 Cariaco earthquake (Audemard, 2002). These coastal fault systems bend into the NE-SW trending Boconó Fault System (BFS) (Schubert, 1980a, 1980b, 1982, 1984) (Fig. 2) which runs with a fairly axial position along the Andes of Mérida with Quaternary slip rates varying from 4 to 11 mm/a (Audemard, 1997; Audemard et al., 1999; Pouse-Beltrán et al., 2017, and references therein). Structural complexities along these major wrench fault systems determine transtensional and transpressional zones (Audemard et al., 2006), which have nested historic earthquakes (Audemard, 1997, 2002; 2007, Audemard, 2014a; Rodríguez et al., 2017).

The dextral motion of the BFS is being transferred by complex kinematic interactions at the Pamplona indenter to the Eastern Frontal Thrust System (EFTS) of the Eastern Cordillera in Colombia (Audemard, 2014a; Rodríguez et al., 2017), where this domain overlaps with the Andean Thrust Front domain from $7^{\circ} 30'$ to $4^{\circ}N$ (Fig. 2). South of this latitude this fault system bends to the NNE as it enters into the Eastern Cordillera, resuming the prevalence of dextral slip through the Algeciras Fault System (AFS) (Gómez et al., 2015; Diederix et al., 2019; Bohorquez et al., this volume, and references therein). This fault system as the main part of the NAS boundary is considered to continue through the Afiladores-Sibundoy faults (Paris et al., 2000; Velandia et al., 2005) and Chingual fault in Ecuador (Soulas et al., 1991; Egüez et al., 2003; Alvarado, 2009; Alvarado et al., 2016; https://sara.openquake.org/hazard_rt2; <http://neotec-opendata.com/>). The Chingual fault system is characterized by Quaternary slip rates ranging from 7 to 10 mm/a (Ego et al., 1995; Tibaldi et al., 2007).

According to Alvarado et al. (2016) and previous contributors, the eastern boundary of the NAS in the Ecuadorian Andes is constituted by the Chingual-Cosanga-Pallatanga-Puná (CCPP) fault systems (Fig. 2), which links different transpressive and contractional subsystems. West of the Cosanga and Pisayambo faults, the Interandean Depression (IAD) (Soulas et al., 1991; Lavenu et al., 1995; Egüez et al., 2003; Alvarado, 2009b; Alvarado et al., 2014) hosts contractional Quaternary deformation (Quito-Latacunga fault-fold system), where shortening rates of 1–4 mm/a have been estimated (Fiorini and Tibaldi, 2012; Alvarado et al., 2014; Champenois et al., 2017) (Fig. 2).

The Cosanga fault and the Quito-Latacunga faults and folds are almost N–S striking and are considered a transpressive segment of the NAS boundary. The former fault nucleated an Mw 5.0 earthquake in 2010 which ruptured at the surface (Champenois et al., 2017).

South of the IAD, the CCPP exposes dominant dextral strike-slip

along the Pallatanga fault (Soulas et al., 1991; Winter et al., 1993; Ego et al., 1996; Egüez et al., 2003; Alvarado, 2009c) where Holocene slip rates of 2.5–4.6 mm/a have been estimated (Winter et al., 1993; Baize et al., 2014, 2020). Paleoseismological investigation revealed large prehistoric earthquakes along the Pallatanga fault zone, bearing also records of the historic 1797 Riobamba event (Baize et al., 2014, 2020).

It is worth mentioning that even if the NAS eastern boundary concentrates the most significant hazardous faults in the Northern Andes, many other structures with documented Quaternary activity do occur in wide areas, particularly in western Colombia. Faults such as the Bucaramanga-Marta, Ibagué and Romeral Fault System, among other structures, play a role in accommodating neotectonic deformation with a prevalence of strike-slip movements (e.g. Diederix et al., 1987, 2011; Paris and Romero, 1994; Paris et al., 2000; Tibaldi and Romero, 2000; Diederix et al., 2006; Diederix et al., 2009; López, 2006; Osorio et al., 2008; Diederix and Romero, 2009).

In summary, the NAS east boundary constitutes a major tectonic feature in South America, particularly for hazardous faults occurrence and capability for generating large shallows crustal earthquakes. This deformation belt displays a general NE trend with dextral slip dominance, whereas, in areas with a dominant N–S strike, compressive sections prevail, like the EFTS in Colombia and the IAD-Cosanga fault in Ecuador.

3.3. The pacific lowlands and foothills of the Western Cordillera of the Central Andes

The peri-Andean zone from the pacific coast to the Andean foothills constitutes the main part of the Central Andes forearc (Fig. 1). This domain is very heterogeneous in terms of its geology, geomorphology, and occurrence of neotectonic structures. It overlaps several Andean segments with different subduction angles and orientations of the slip subduction vector. Certainly, it cannot be ascribed to a single domain and thus, the following outline merely constitutes a simplified approach for summarizing the occurrence of main hazardous faults throughout this environment.

Only a few data on the potential occurrence of hazardous faults have been compiled so far north of $17^{\circ}S$, although between $17^{\circ}S$ and the Arica elbow in the Perú-Chile border ($18^{\circ}30'S$) several neotectonic structures have been described depicting dominant NW striking faults with different kinematics. Some faults transversal to the coastline exhibits normal slip, such as the Chololo fault, which are thought to be related to the subduction dynamics (Audin et al., 2006, 2008, 2009a; Benavente et al., 2017a, 2017b) (Fig. 3). In the Western Cordillera foothills and nearby piedmont, compressive and transpressive fault systems have been reported (Incapuquio, Purgatorio, and Sama-Calientes fault systems), with slip rates $\sim 0.2\text{--}0.5$ mm/a, linked to the Andean chain bend at the Arica elbow (Audin et al., 2006, 2008, 2009b, 2009c, this volume; Hall et al., 2012; Benavente et al., 2017a, 2017b) (Fig. 3).

South of the Arica elbow in Northern Chile, regional-scale neotectonic deformation is characterized by N–S striking structures. First-order latitudinal tectonic segments occur throughout Chile, mostly due to subduction dynamics and inherited bedrock geology, resulting in different neotectonic deformation styles (Gutscher et al., 2000; Tassara and Yañez, 2003; Yañez et al., 2001; Yañez and Cembrano, 2004; Ramos, 2009).

Santibañez et al. (2019) divided the occurrence of Chilean neotectonic crustal faults in three longitudinal domains (N–S trending strips); namely the Outer-Forearc (OF), the Inner-Forearc (IF) and the Volcanic Arc (VA).

The Atacama Fault System (AFS) stands out in the OF domain (Fig. 8). This fault system, composed by multiple fault sections, runs ~ 1000 km in northern Chile from $20^{\circ}S$ to $30^{\circ}S$. It has a general N–S trend and an arcuate pattern concave to the west, sustaining locally Pliocene to Quaternary displacement mainly of extensional nature (Arabasz, 1968; Okada, 1971; Hervé and Thiele, 1987; Naranjo, 1987;

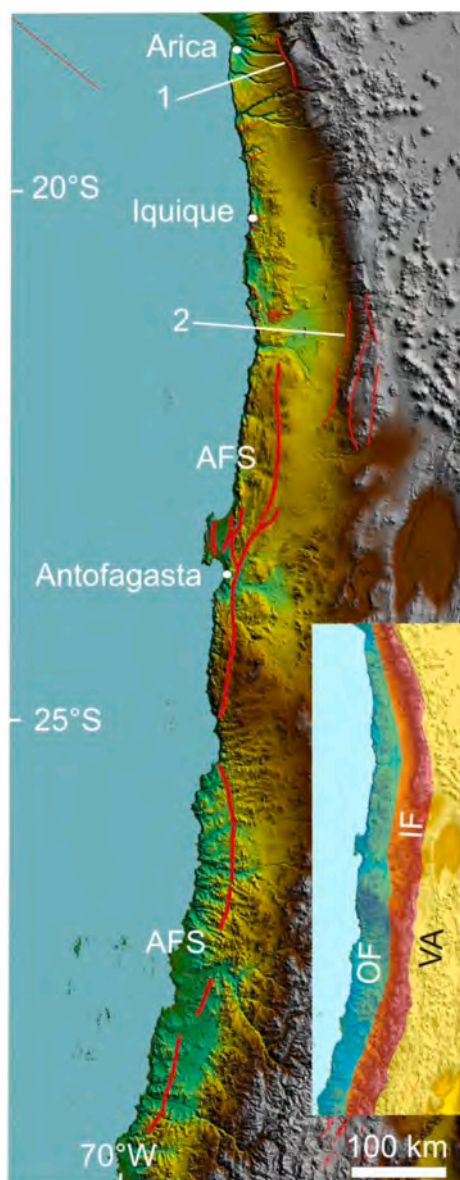


Fig. 8. Main traces compiled for the Atacama Fault System (AFS). 1. Western Andean Thrust, 2. Domeyko Fault System. Neotectonic domains in the inset. OF, Outer forearc, IF, Inner forearc, VA, Volcanic arc. See the location in Fig. 1.

González et al., 2003, 2008; Allmendinger and González, 2010; Cortés-Aranda et al., 2012). The best-known fault sections correspond to the Salar del Carmen and Mejillones faults, where Pleistocene-Holocene slip rates <1 mm/a and maximal magnitude $\sim M 7$ for paleo-earthquakes occurrence have been estimated (González et al., 2006; Cortés-Aranda et al., 2012; Ritz et al., 2019). South of Iquique (21°S), Pliocene to Quaternary strike-slip displacements along two NW-SE fault branches of the AFS have been documented by Carrizo et al. (2008). Furthermore, the Coastal Cordillera in northern Chile, between 19°S to 21° 30' S, exposes E-W reverse faults with neotectonic cumulative displacements up to 300 m. Some of these faults deform marine terraces and have been the locus of an Mw 6.7 earthquake (González et al., 2015). This N-S contraction is linked to the Nazca plate subduction along a concave to sea margin given by the Orocline bend of the Andes at this latitude (Allmendinger et al., 2005; González et al., 2015).

Trench-parallel normal faulting along the Coastal of Central Chile (34° 30'S) has been recently revealed by the reactivation of the Pichilemu Fault right after the 2010 Mw 8.8 Maule Earthquake. This extension is thought to be connected with coseismic and postseismic upper

plate extension promoted by unclamping of the megathrust (Aron et al., 2013, 2015). This fact underpins that independently of the local geological setting, hazardous faults located in the OF domain show a strong dependence on the subduction cycle.

The IF domain, according to Santibañez et al., (2019), extends along the Andes foothills and Chilean Precordillera (Fig. 8) through the Western Thrust System or Western Andean Thrust (WAT) (Muñoz and Charrier, 1996; David et al., 2005; García and Herail, 2005; Farías et al., 2005; Armijo et al., 2010; García et al., 2011) (Fig. 8). These structures are thought to have played an important role in the Altiplano uplift (Muñoz and Charrier, 1996), being its potential hazard underlined by historic earthquakes (Santibañez et al., 2019 and references therein). According to Armijo et al. (2015), the WAT is represented by discontinuous fault and fold systems, whose tectonic activity get younger to the south, involving neotectonic structures such as the Oxaya anticline, the Copaquilla-Tignamar thrusts, the Domeyko Fault System in northern Chile (Fig. 8), and the San Ramón Fault (SRF) further south (Fig. 5). The latter lies near the Santiago urban area in Central Chile exhibiting west-facing thrust scarps, at the boundary between the Central Depression and the Andes foothills (Lavenu et al., 2000; Rauld et al., 2006; Rauld, 2009; Armijo et al., 2010). Paleoseismological studies account for the occurrence of Late-Pleistocene-Holocene $\sim M 7.5$ earthquakes that ruptured along this fault, posing a significant threat for Santiago de Chile (Armijo et al., 2010; Vargas et al., 2014; Estay et al., 2016).

Further south, the most significant crustal neotectonic structure is developed in the VA domain and represented by the Liquiñe-Ofqui Fault System (LOFS) (Fig. 6). This NNE-striking fault system exhibits conspicuous regional-scale fault arrays, including horse-fault terminations and a central strike-slip duplex structure. The LOFS is a major crustal fault system with associated seismicity (e.g. Barrientos and Acevedo, 1992; Lange et al., 2008; Mora et al., 2010; Legrand et al., 2011; Agurto et al., 2012; Sielfeld et al., 2019), which accommodates dextral strike-slip displacement related to slip partitioning along more than 1200 km. (Hervé, 1976; Lavenu and Cembrano, 1999; Cembrano et al., 1996, 2002; Cembrano and Lara, 2009; Lara, 2009; Vargas et al., 2013).

Challenging morphoclimatic conditions and a dense vegetation cover have determined very scarce exposures along the LOFS, hampering to date a detailed mapping regarding its neotectonic activity. Numerical modeling of current slip rates led to estimate values in the order of 1–10 mm/a (Stanton-Yonge et al., 2016; Iturrieta et al., 2017), although field data suggest Late Quaternary slip rates in the range of 12–25 mm/a, meaning the LOFS being the fastest-moving crustal fault onshore South America (De Pascale et al., 2018; Astudillo et al., 2018). Apparent discrepancies with GPS velocities need to be yet accurately assessed, to unravel a possible slip deficit along the LOFS concerning its seismic cycle.

3.4. The high Western Cordillera of the Central Andes and the altiplano plateau

This domain comprises the high Western Cordillera and extends from the northernmost Central Andes in Perú down to the Arica elbow (Fig. 3), hosting some of the highest Andean peaks in the Cordillera Blanca of Perú. Normal faults highly prevail in the compiled Quaternary deformation, whose occurrence and evolution in these high-altitude areas is still a matter of debate (e.g. Dalmayrac and Molnar, 1981; McNulty and Farber, 2002; Margirier et al., 2017).

The Cordillera Blanca Fault System (Fig. 3) bounds the western flank of the homonymous cordillera, exhibiting outstanding examples of mountain front-scale morphologies driven by normal faulting (Sebrier et al., 1988; Schwartz, 1988; Macharé et al., 2003, 2009a; 2009b; Siame et al., 2006b; Margirier et al., 2017). Vertical slip rates range from 5.1 ± 0.8 to 0.6 ± 0.2 mm/a (Schwartz, 1988; Siame et al., 2006b; Margirier et al., 2017).

Another earthquake-related hazard became explicit in this high-

relief area when an Mw 7.9 subduction earthquake in 1970 triggered a deadly landslide, taking the life of near 10,000 people in (Plafker and Ericksen, 1978).

Historical surface ruptures, such as the Quiches fault related to the Ms 7.2 1946 Ancash earthquake (Doser, 1987; Bellier et al., 1991; Audin et al., 2009d) and suspected historical ruptures associated to the Chaquibamba fault (Bellier et al., 1989; Macharé et al., 2003, 2009c), both of extensional nature, are located in this domain.

In some areas of the Western Cordillera, the occurrence of Quaternary normal faults is related to deeply incised canyons and active volcanoes (i.e the Colca Canyon and the Huambo-Cabanaconde volcanic complex) (Fig. 3). A dynamic interplay in these settings among mountain uplift, high incision rates, and the flank collapse of active volcanic edifices, might enhance the geomorphic expression of surface faulting through deep-seated gravitational phenomena (Benavente et al., 2013; Wimpenny et al., 2020; García et al.,).

The high-relief areas of the Altiplano plateau are also characterized by Quaternary normal faulting, although the occurrence of neotectonic structures has not been yet properly surveyed (Sévrier et al., 1985; Lavenu et al., 2000; Macharé et al., 2003; Agurto et al., 2012; Aguirre et al., 2016; <https://www.ingemmet.gob.pe/mapa-neotectonico>; <http://neotec-opendata.com/>; https://sara.openquake.org/hazard_rt2). This high-altitude region (~3800 m on average) is characterized by endorheic basins and continues to the south into the Puna plateau in Argentina.

The majority of Quaternary faulting inventoried throughout the Altiplano is located around the Lake Titicaca area. Surface ruptures related to the 2016 Mw 6.1 earthquake has been reported for the Parina normal fault (Wimpenny et al., 2018, 2020; Aguirre et al., 2016). Wimpenny et al., (2020) reported a general ~ NNE-SSW Late Quaternary extension in the Peruvian Altiplano with fault slip rates in the range of 1–4 mm/a.

Little is known about the Quaternary faulting affecting the Puna plateau. The preliminary descriptions and general studies account for faults with different slip regimes, but lacking detailed parametric data (Costa et al., 2000a; Casa et al., 2014; García et al., 2017; <https://sigam.segemar.gov.ar/visor/>; https://sara.openquake.org/hazard_rt2).

3.5. The Eastern Cordillera and the Inter Andean zone of the Central Andes

This domain flanks the eastern Peruvian and the Bolivian Andes through the Bolivian orocline down to ~26° S in northern Argentina (Figs. 3 and 4). It extends above both flat-slab and normal subduction segments and Quaternary deformation is represented by different kinematic regimes, prevailing oblique-slip compressive and extensional structures, (Philip and Megard, 1977; Sévrier et al., 1985; Cabrera et al., 1987; Audin et al., 2009e; Macharé et al., 2009d; Benavente et al., 2013; García et al., 2017; Wimpenny et al., 2020).

The reverse-sinistral Huaytapallana fault (Fig. 3), which bounds the homonymous cordillera, was reactivated during the 1969 Ms 6.2 Parí-huanca earthquakes. It ruptured through scarps up to 2m high and sub metric sinistral component (Philip and Megard, 1977; Dorbath et al., 1991; Macharé et al., 2009d), testifying on the seismogenic capability of these faults. Interestingly, some rupture segments resemble single event scarps (like other surface ruptures, such as the Quiches fault), rather than long-evolved landforms.

Close to the subandean belt (Inter Andean zone), reverse faulting usually basement-cored are dominant (García et al., 2017; Rojas Vera et al., 2018).

3.6. The Pampean Ranges

The Pampean Ranges (Sierras Pampeanas) of Argentina constitutes the broken foreland of the southern Central Andes above the Pampean-Chilean flat-slab segment (27°–33°S, Fig. 5). Neogene mountain building in these former flat-lands was triggered by the subduction of the

aseismic Juan Fernández ridge, which started ~8 Ma in northern Chile and progressively moved south (e.g. Jordan et al., 1983; Jordan and Allmendinger, 1986; Gutscher et al., 2000; Yáñez et al., 2001; Ramos et al., 2002; Davila and Carter, 2013). These mountain blocks, bounded by reverse faults exhibit a notorious topographic asymmetry, being the Quaternary-active thrusts usually located at the foothills of the steep western slopes (e.g. Massabie, 1987; Fauqué and Strecker, 1987; Costa and Vita-Finzi, 1996; Costa, 1999, 2019; Costa et al., 2000a, 2001; 2014b, 2018, this volume; Casa, 2009; Casa et al., 2010; Costa, 2019; Rother et al., 2019). The youngest activity of fault systems bounding most Pampean Ranges seems to have migrated basin-wards during the Neogene block uplift (Costa, 2019).

Although ongoing deformation across the Pampean Ranges has not yet been suitably captured through satellite geodesy, some of these thrusts account for Holocene slip rates ~1 mm/a (Costa et al., 2018) and pose a seismic threat for urban areas and infrastructure (Costa et al.,). Paleoseismic studies suggest that Pampean faults can generate earthquake magnitudes similar to those structures in the Andean region, although with a longer recurrence interval (Costa et al., 2018, this volume).

3.7. The South America-Scotia plates transform boundary

This domain is exposed onshore at the southern tip of South America, in Tierra del Fuego island (Fig. 7). Sinistral-normal slip characterizes this deformation zone, concentrated throughout the Magallanes-Fagnano Fault System (MFFS), as indicated by seismicity, geophysical studies, GPS and field observations (Dalziel et al., 1975; Klepeis, 1994; Lodolo et al., 2003; Smalley et al., 2003, among others).

Despite difficult accesses and very scarce exposures, neotectonic evidence along this transform boundary has been described or suspected in the Chilean side (Winslow, 1982; Winslow and Prieto, 1991; Perucca and Bastías, 2008; Sandoval and De Pascale, 2020) and east of the Lake Fagnano in Argentina (Winslow, 1982; Costa et al., 2006b; Costa and Lara, 2009 and references below). In the latter area, trench studies highlighted prehistoric ruptures related to 3 or 4 earthquakes during the last ~8 ka, including the ruptures related to the two Mw 7.5 1949 events, with 1 m of coseismic vertical slip (Costa et al., 2006b). The prevalence of the vertical component recorded in the Lake Fagnano area is consistent with this fault segment being a transtensional zone of the transform boundary (Lodolo et al., 2003; Esteban et al., 2014, 2018; Roy et al., 2018, 2019).

Onorato et al. (2016, 2018, 2019, this volume) and Roy et al. (2019) reported Quaternary deformation related to the MFFS further to the east. The latter contribution estimated a 6.4 ± 0.9 mm/a left-lateral slip rate based on offsets of post-glacial morphologies, which are lined-up with GPS velocity models across the MFFS (Smalley et al., 2003). Sandoval and De Pascale (2020) suggested rates ranging from 10.5 ± 1.5 mm/a in Chile and 7.8 ± 1.3 mm/a east of Lake Fagnano, based on the interpretation of aerial images.

3.8. Slowly deforming regions

In intraplate South America, structures with Quaternary activity are located either on pre-existing Precambrian shear zones and metamorphic foliation or are newly formed structures that cut across the pre-existing Precambrian fabric. Several studies have highlighted their capability of producing surface ruptures and related phenomena (Bezerra and Vita Finzi, 2000; Bezerra et al., 2001, 2006, 2007, 2011; Ramos et al., this volume, among others). These intraplate regions comprise a much larger area than the entire Andean chain, but neotectonic data are patchy and most faults lack of slip-rate constraints. Estimated Quaternary rates are <0.1 mm/a and recurrence intervals presumably encompass 5–100 ka or more. For example, alluvial infill dating in the deformation zone of the Jundiaí fault (Fig. 9a) has led to estimate a mean recurrence period of 15.8 ka (Nogueira et al., 2010).

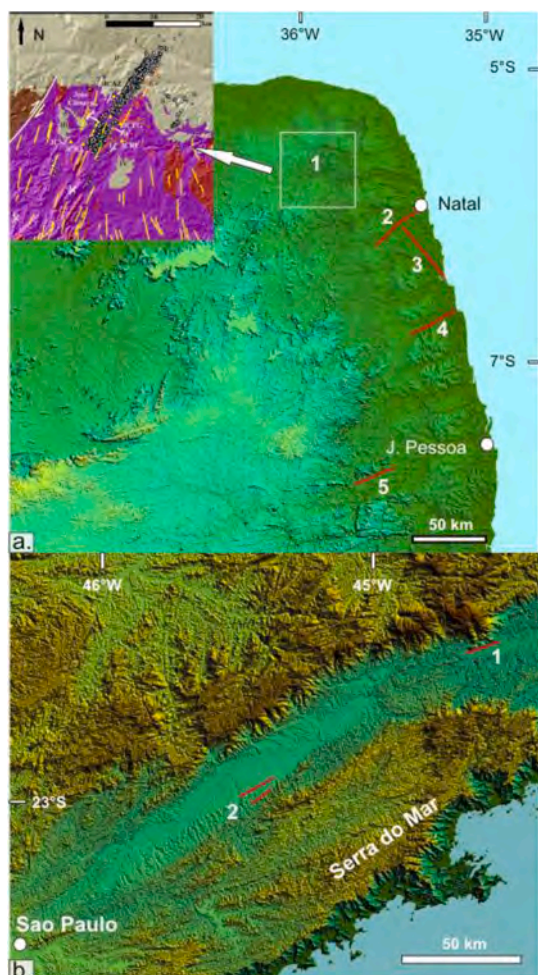


Fig. 9. a. Main faults compiled in northeast Brazil. 1. Samambaia (highlighted by shallow seismicity, modified after Bezerra et al., 2011), 2. Jundiá, 3. Boa Cica, 4., Canguaretama, 5. Cariata faults. b. Quaternary faults compiled in the Serra do Mar region, southeast Brazil., 1. Resende, 2. Taubate faults. See the location of both areas in Fig. 1.

Challenges for mapping neotectonic structures under common standards in cratonic-pericratonic regions, as for those applied for Andean settings, usually deal with the critical judgment of the preserved fault-related morphologies. Macroscale continuous linear features may result from old tectonic structures with inherited escarpments, being enhanced by fluvial systems. Whether or not these features have undergone Quaternary activity is often a matter of controversy, due to the lack of diagnostic data.

In the Brazilian platform, two main areas with Quaternary deformation has been documented with field support. In northeastern Brazil, the Samambaia fault shows prominent shallow seismicity illuminating the fault zone (Takeya et al., 1989; Bezerra et al., 2007; Ramos et al., this volume) (Fig. 9a). The Jundiá and Boa Cica faults are among the most important structures recording Holocene displacements, the former having a cumulated vertical slip of approximately 260 m on Miocene deposits (Bezerra and Vita Finzi, 2000; Bezerra et al., 2001, 2006) (Fig. 9a). Other important seismogenic faults in the region are the Pernambuco Lineament (Coelho et al., this volume) and the Riacho Fundo fault (Oliveira et al., 2015; Ramos et al., this volume). These structures, such as the Samambaia fault, reactivate Precambrian or early Cambrian fabrics and are underlined by recent seismic activity.

At the Serra do Mar (Fig. 9b), Quaternary faults reactivating Mesozoic rift structures have been described (Riccomini et al., 1989; Riccomini and Assumpção, 1999; Gontijo-Pascutti et al., 2010). They all

reactivated Mesozoic rift faults, which in turn have over imposed Precambrian shear zones of the Ribeira belt.

Quaternary deformations have been reported east of the Pampean Ranges in the Pampean plain (Fig. 10), related to propagating faults and usually interpreted through anomalous drainage pattern (Mon et al., 2005; Rossello et al., 2005; Brunetto and Iriondo, 2007; Mon and Gutiérrez, 2009; Brunetto et al., 2010, 2019; Peri and Rossello, 2010). The geometries, kinematics, and rates of activity of these subsurface structures are poorly known to date.

4. Strategies and methods for compiling hazardous faults

4.1. Definitions and criteria adopted

Hazardous structure and fault activity assessment. A Hazardous structure is a fault or fault-related-fold either outcropping or blind, capable of producing earthquakes of social/engineering concern in the future, and considered relevant as for seismic hazard implications. There is no consensus about a discrete timeline for defining whether a structure is potentially hazardous or not. For areas with medium to low strain rates, this means to include structures with activity during the Quaternary (~2.6 Ma). However, the Pliocene-Pleistocene boundary is poorly known in vast regions of South America. Besides, in key areas such as the Andean Thrust Front, this time window is represented by contemporaneous deformation and sedimentation, turning not very practical to define a time baseline. Therefore, it has been intended to also include in the inventory those structures affecting layers whose chronostratigraphy

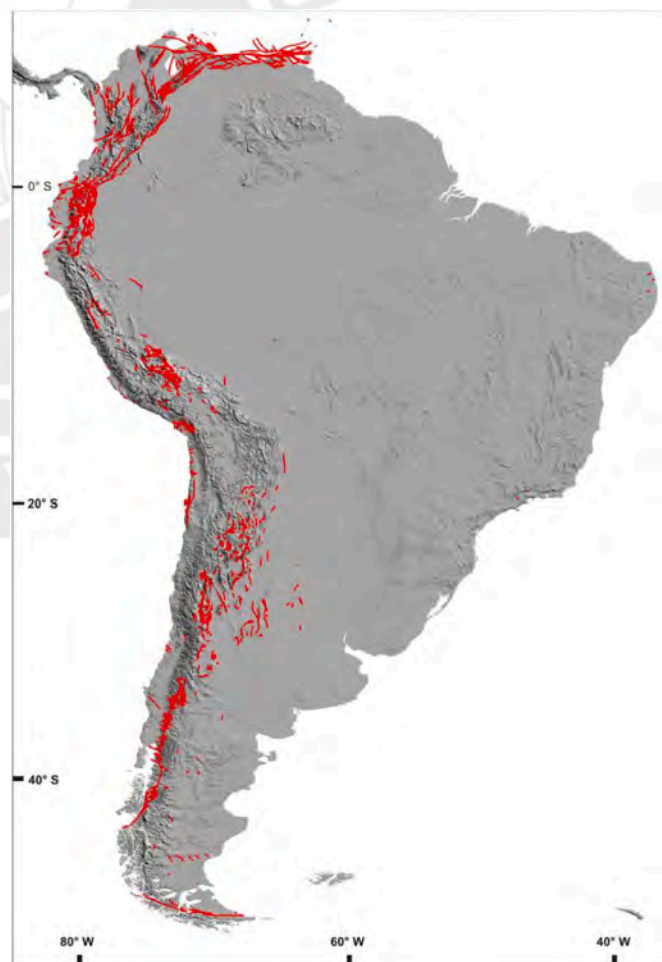


Fig. 10. Cartographic representation of the compiled structures under the activities of the SARA T2 project. See the text for details.

is doubtful, those affecting Miocene-Pliocene stratigraphic units, or those where young activity is suspected and Quaternary deformation markers are absent.

A hazardous structure is here considered as a synonym of neotectonic structures or Quaternary deformation *s.l.* SARA compilation has used a conservative approach, taking into account that fault maps for SHA should encompass a time interval that includes several earthquake cycles (Machette, 2000). Then, it is considered that the Quaternary period meets this standard even for long-recurrence interval faults. Overall, it has been intended to populate the database with information to be useful for different purposes and users in the future (territorial planning, critical facilities, geotechnical issues, etc.).

Fault activity assessment is here approached according to parameters related to the structure dynamics during the Quaternary (i.e. slip rate, age of the last movement). Aiming to favor homogeneous compilation criteria, it has not been relied on the heterogeneous criteria for systematizing fault activity. Common definitions of 'active fault' available in the scientific literature and promoted by regulatory agencies, usually constrain a specific timeline of interest for fault activity, such as the Holocene (11,7ka), the Late Pleistocene (125ka) or the Quaternary (~2.6 Ma) (e.g. Slemmons and de Polo, 1986; WSSPC, 1997; Machette, 2000; Haller et al., 1993; IAEA, 2010). Rating the hazard associated with a structure based on the age of the last movement may not be appropriate, particularly for regions of low to medium strain rates and long recurrence intervals (which represent most parts of continental South America). In these settings, the most active structure (in terms of the elapsed time since the last movement), might not be the most hazardous in terms of threat for rupture or ground shaking probabilities. Thus, adopting any particular definition for the term 'active fault', might not be suitable to characterize fault hazard throughout different seismotectonic settings.

Fault source. Fault surface with an assigned three-dimensional representation given by a generalized geometry, kinematics, area, and spatial coordinates within the seismogenic crust or at interplate boundaries. It is conceived to represent the surface where the earthquake slip and most of the released seismic energy is concentrated (Basili et al., 2008; Haller and Basili, 2011, among others).

Seismic-Hazard Source Model (SHSM). Computational engine for the description of the magnitude, location, and timing of expected earthquakes, based on a probabilistic approach and usually limited to those events that pose a significant threat. The SARA project relied on the OpenQuake platform for the calculation of hazard and risk, as well as for the generation of Probabilistic Seismic Hazard Assessment (PSHA) maps (i.e. Pagani et al., 2014, 2015).

4.2. Previous studies and data availability

The pre-existing neotectonic information in South America is very heterogeneous not only in terms of reliability and geographic coverage but also regarding the criteria applied for mapping Quaternary deformation. In wide areas, the compiled data are of a reconnaissance nature, largely based on remote sensing interpretation and general fieldwork.

The first regional cartographic attempt for compiling regional neotectonic information was under the framework of the SISRA Project (González-Ferrán, 1985), although the few Quaternary faults depicted were mostly derived from previous regional maps, without a relational database.

Venezuela, through the work of FUNVISIS, has been the pioneer country in developing regional neotectonic maps for supporting SHA since the 80s (e.g. Soulas, 1986; Beltrán, 1993, 1994; Audemard and Singer, 1996; Audemard, 2001, 2006). As a result, nationwide maps of Quaternary deformation and the seismogenic characterization of faults have been incorporated in the national seismo-resistant building code for Venezuela.

Systematic regional neotectonic compilations in South America started in the early 90s with the International Lithosphere Program

(World Map of Major Active Faults-ILP-II2) (Trifonov and Machette, 1993). This decade-long effort led to the development of country maps and inventories of Quaternary deformation, being the first experience attempting to inventory regional Quaternary deformation under common criteria (Audemard et al., 2000; Costa et al., 2000a, 2000b; Lavenu et al., 2000; París et al., 2000; Saadi et al., 2002; Egüez et al., 2003; Macharé et al., 2003). More than 300 Quaternary-active structures were compiled for South America and some countries of Central America (Cowan et al., 1998; Montero et al., 1998). The resulted database was updated and improved during the Multi Andean Project (MAP-GAC) (2005–2007), which contributed to the compilation of ~600 structures in Andean countries (PMA, 2009). Both projects relied on a GIS-based georeferenced mapping, linked to files depicting attributes for each mapped structure.

The end-products of ILP II2 and MAP projects were released as reports and maps with the structure surface characteristics and available knowledge on the fault trace and related data. These efforts focused on the terrain imprint of Quaternary fault traces, rather than on fault source geometry. Thus, some key data as for the SHA requirements, such as slip rate and the 3D structure geometry of faults were not available for a significant number of them. After these experiences, many initiatives have updated and expanded the information on Quaternary deformation under diverse digital platforms with a countrywide or regional scope (<https://sigam.segemar.gov.ar/visor/>; <https://www.ingemmet.gob.pe/mapa-neotectonico>; <http://neotec-opendata.com/>; <https://documents.ku.edu/ORGS/Academics/>).

4.3. Compilation strategies

The SARA Topic 2 project was conceived as a community-based effort involving local expertise and relying on regional networking. Data gathering relied on a responsible person with collaborators for each participating country (Argentina, Bolivia, Brazil, Chile, Colombia, Ecuador, Perú, and Venezuela). The first stage of the compilation involved a systematic inventory aimed to capture all available information on structures with evidence of Quaternary activity. However, as a conservative approach, the inventory also took into account presumably older structures in the following situations;

- Where regional low strain rates turned advisable to include structures with older activity (i.e. Late Pliocene) of potential significance for a wide range of possible applications (nuclear siting, territorial planning, etc.),
- When evidence for Quaternary activity was not conclusive, barely known or suspected to fall within the timeframe of interest,
- When the Pliocene-Pleistocene boundary was not properly established,

The inventoried structures were hierarchized at a second stage, by selecting those structures with available mandatory data for the characterization of fault sources (Table 1) as required by the SARA SHSM. Structures meeting at least one of the following criteria were included;

- Faults with slip rates >0.1 mm/a. This information applies to rates already available or estimated by compilers through quantitative-semi-quantitative data. Although rates derived from geological data were preferred, GPS-derived rates were also considered. For those structures with a wide rate range (i.e. 0.001–0,1mm/a), the higher value (or the preferred one if existing) was considered.
- Structures with Late Pleistocene activity or younger. Both confirmed and suspected.
- Structures confirmed or suspected to be the source for historical/instrumental seismicity with magnitude >5.5.

Structures have been inventoried as single or sectioned faults. Single faults are structures with a simple and essentially continuous trace

Table 1
Attribute table for data upload of the faults selected for feeding the SHSM. See text for explanation. The complete set of parametric data considered for compiling all structures is displayed in table S1 (supplementary data).

Attribute name	Object ID	Name	Strike	Slip type	Slip type (R)	Dip direction	Dip angle	Dip angle (R)	Dip direction	Dip angle	Dip angle (R)	Slip rate	Slip rate (R)	Age of last movement	Age of last movement (R)
Query name	ID_STR	STR_F_NAM	STR_F_SC	STR_F_ST	CF_F_ST	STR_F_DD	CF_F_DD	STR_F_DC	CF_F_DC	STR_F_DD	CF_F_DD	STR_F_SRC	CF_F_SRC	STR_F_ALM	CF_F_ALM
Attribute type	String	String	String-Integer	String	Integer	String-Integer	Integer	Integer	Integer	String-Integer	Integer	String-Integer	Integer	String	Integer

(observed or inferred), a concept that could be applied for a set of folds as well. Sectioned faults or faults systems with sections may correspond to km-scale gaps, step-overs, major changes in geometry (strike, dip, dip direction, rake) different fault splays or fault systems, or differences in key activity parameters (slip rate, recurrence interval, last event, etc.). Therefore, certain mapping attributes (i.e. age of last movement, trace characteristics) or parameters may vary for the different sections of a structure. For compilation purposes, the term “section” was here also applied to each trace of a fault assemblage grouped in plan view, such as flexural-slip faults or secondary splays of the main thrust. Key parameters of the selected structures were also displayed in complementary summary attribute tables (Table 1). A fault section essentially depicts geometric or kinematic characteristics of a structure, but it should not be regarded as fault segments or earthquake rupture segments (e. g. Schwartz and Sibson, 1989; McCalpin, 2009; DuRoss et al., 2016), because unitary surface rupture lengths remain unknown for most compiled structures.

Structure attributes were also designed to fault-related folds, although very few neotectonic folds have been incorporated into the database.

Compilers were requested to include structures regardless of data reliability, although a reliability rate (R) was assigned to the uploaded data (See Table 1).

4.4. Database structure

A relational database was designed to link the cartographic georeferenced representation of fault traces with the structure parameters (geometry, kinematic, geomorphology, paleoseismology, seismicity, and complementary information whenever available) (see supplementary information). The attribute table used for data upload included the key parameters for fault source characterization, such as fault strike and dip direction, slip sense, slip rate, and age of the last movement. The database was populated by both direct observations and measurements in the field (i.e. geometry and kinematics of faults and folds such as strike, dip, rake) and derivative parameters (slip rate, recurrence interval, age of last movement, 3D geometry, etc.). It is worth to note that most critical data as for fault source definition rely on derivative data.

Because of the continental scale representation, no direct differentiation of cartographic attributes (line styles, colors) has been included for the data visualization to distinguish parameters such as fault reliability, slip rate, and age of the last movement. But this differentiation is possible through informatic tools. To favor a straight-forward data entry for feeding the SHSM, the upload format of the structures selected was oriented to basic parameters for source characterization. Some general data (tectonic setting, geomorphic expression, etc.) were not taken into consideration at this stage.

The relational database allows to retrieve different fault parameters through a structured query language (SQL). Compilation relied on the upload of ESRI-shapefiles through a freeware software (QuantumGis) to enter/import the data for each structure in an attribute table.

5. Results

The compiled information for the SARA Topic 2 project, is the first open-source experience in South America in which fault data were considered as an input layer for feeding an SHSM. Moreover, it constitutes the first comprehensive state-of-the-art on neotectonic knowledge to date at a continental scale. The main efforts have been concentrated in database harmonization and population whenever possible with activity rates and 3D sources geometry.

During this 2-years long effort, 1523 structures and 3586 fault traces considered hazardous as for SHA purposes, have been compiled according to common criteria (Fig. 10). The project did not contemplate the generation of new field data, except for visits to specific sites. Thus, a significant part of the information was imported from existing databases

and bibliography. Not all the structures inventoried were considered as entry data for the SARA Open Quake engine, given that a significant number of inventoried structures did not meet the selected standards as for SHA or lack specific information for fault source characterization. Only 497 structures (~30% of the total population) met these criteria (Fig. 11). In many cases, the quantitative data for the key parameters were derived from qualitative estimates or expert judgment, assigning thus a low-reliability rate for these cases.

Almost all the structures inventoried are concentrated along the Andean chain, depicting at a synoptic view the major neotectonic framework of the Andes. Structures in the Northern Andes show an integrated arrangement of major faults, outlining the distribution of major hazardous faults with a dominance of strike-slip motion (Figs. 2 and 12). In contrast, most hazardous faults mapped in the Central Andes exhibit short individual lengths and a more distributed pattern in space, where

even major faults do not evidence regional continuity or integration into regional fault systems as in the Northern Andes. The different geometries of the subducting Nazca plate can be roughly recognized, highlighted for example by the propagation of Quaternary deformation into foreland areas at the Pampean-Chilean flat-slab in Argentina (Fig. 5). Here, the general arrangement in a plan view of the compiled data results in a triangular shape. The exception to these characteristics corresponds to the Atacama and Liquiñe-Ofqui fault systems in northern and southern Chile, respectively. Although integrated by many fault sections, these fault systems display a master deformation belt recognized along ~1000 km (Figs. 6 and 8).

Knowledge of the occurrence and characteristics of hazardous faults in the Southern Andes is still very incomplete (Figs. 6 and 7). The Magallanes-Fagnano Fault System, which represents the onshore transform boundary between the South American and Scotia plates (Fig. 7), is

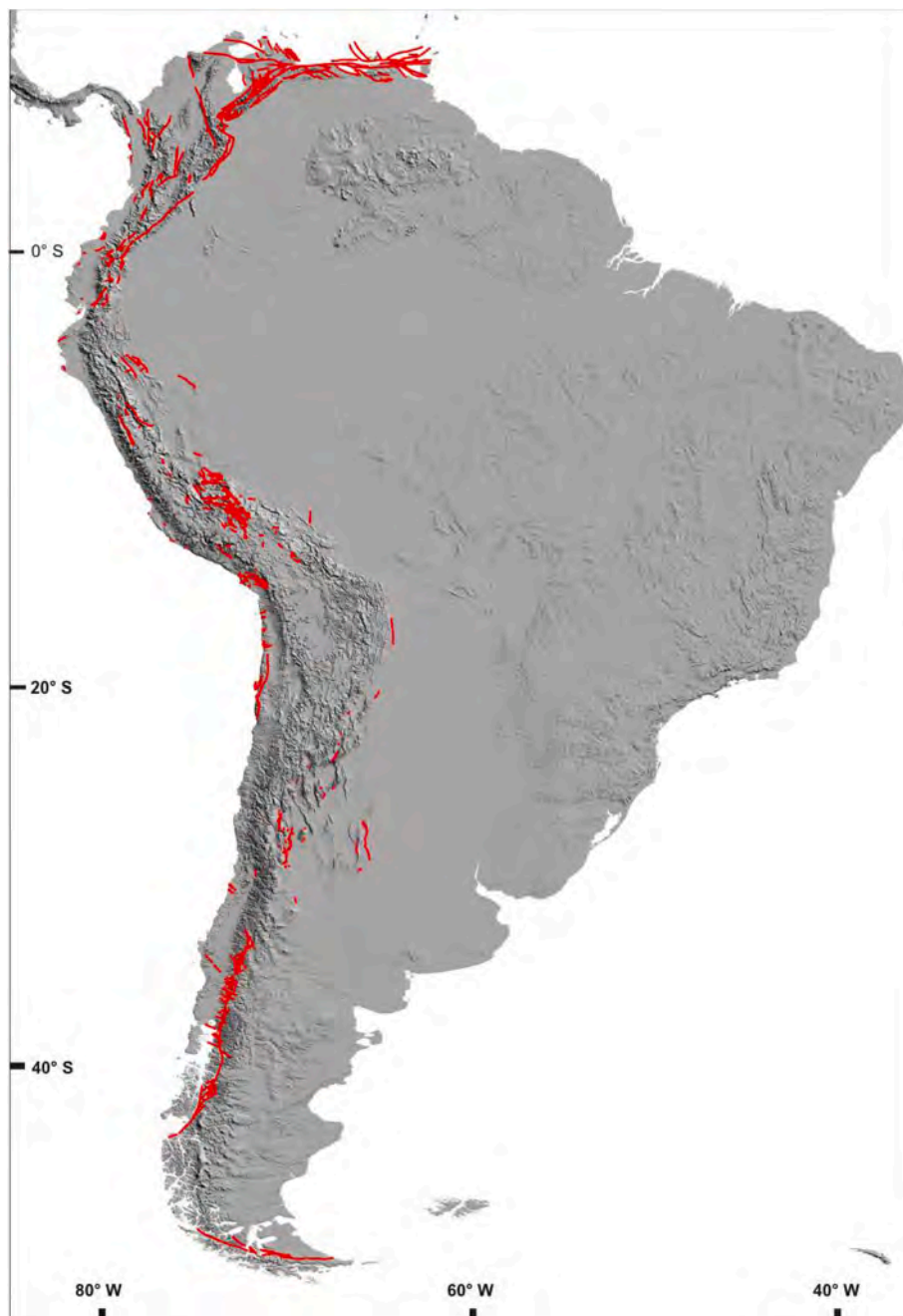


Fig. 11. Faults selected for incorporation to the SARA SHSM.



Fig. 12. Slip types of hazardous faults in Northern South America.

one of the very few places where punctual neotectonic studies have been conducted to date. This fault system has been the source of large historic earthquakes.

Neotectonic faults inventoried in cratonic regions constitute a much smaller population concerning the Andean region. However, some of these structures have generated surface deformation during the Quaternary.

Because estimation of slip rates has been addressed through derivative data and in some cases by expert judgment, these metadata might reflect either kinematic heterogeneities and/or data provider preferences. In any case, the filtering of the compiled faults according to their slip rate values also highlights the concentration of the structures with the higher rates along the NAS east boundary. (Fig. 13). Spatial variations of individual parameters may help to stand out heterogeneities in tectonic settings, as well as to point out that data harmonization is still required.

The main outcome of the data sets has been their integration as a data layer of the probabilistic seismic hazard assessment (PSHA) for South America generated through the OpenQuake engine for the SARA project (Fig. 14a). This map results from the integration of data layers provided by both historical and instrumental shallow seismicity, aside with hazardous faults information, and using a ground motion model considering the different regional tectonic regimes. Subduction and deep seismicity sources (e.g. Bucaramanga Nest) were not considered, with the aim of emphasizing the contribution of shallow sources to the seismic hazard computed along the Pacific coast. Details on the methodology behind the generation PSHA input model for South America can

be found at https://sara.openquake.org/hazard_rt7. The SARA T2 database can be accessed in electronic format at https://sara.openquake.org/hazard_rt2. Disaggregation of individual data layers allows identifying the contribution of crustal hazardous faults (Fig. 14b) to the estimated hazard, expressed as mean PGA (Peak Ground Acceleration) with 2% probability of exceedance in 50 years (a return period of 2.475 years). These results highlight the input of recognized hazardous faults for more realistic SHA, particularly for recurrence intervals >1ka, which characterize the vast majority of areas in South America. Fig. 14b also underscores that punctual data reporting high slip-rate faults (e.g. the Mandeyapecuá Thrust System), strongly influences SHA calculations (Fig. 14a).

The SARA T2 database can be accessed in electronic format at https://sara.openquake.org/hazard_rt2.

6. Concluding remarks

6.1. Data harmonization and completeness

Significant efforts were directed to elaborate and homogenize data sets compiled in different countries by different compilers. Although significant improvements have been achieved in comparison with pre-existing databases, many remaining issues still require further discussion and complementary data to homogenize parametric and cartographic information. Among these, the fault slip rate is a key parameter for SHA which conveys significant epistemic uncertainties to the compiled data.



Fig. 13. Slip rates of main inventoried faults.

Aside from remaining inconsistencies in data harmonization, the representation of hazardous faults is very heterogeneous particularly in terms of geographic coverage, availability, and/or data reliability. As the NAS east boundary in the Northern Andes, satellite geodesy indicates that transient strain is being concentrated nowadays at the Andean Thrust Front (Norabuena et al., 1998; Kendrick et al., 1999, 2006; Brooks et al., 2003, 2011; Weiss et al., 2015; Mora-Páez et al., 2019a). Accordingly, local studies conducted in the Subandean zone have unveiled very hazardous structures regarding their capabilities for producing large crustal earthquakes (Brooks et al., 2011; Weiss et al., 2015) (Fig. 4). However, the cartographic representation of this key area for SHA purposes is underrepresented by the regional neotectonic knowledge acquired to date.

Cartographic results also convey an unbalanced representation of hazardous faults when contrasting with specific areas where systematic neotectonic mapping has been carried out. For example, the detailed mapping of Quaternary faults around the Cusco region (Benavente et al., 2013) gave rise to a concentration of hazardous faults in this area at a regional scale (Figs. 3 and 11). This led to a biased view when contrasting with the much less populated surrounding areas (the compilation of neotectonic faults for the Arequipa region by Benavente et al., 2017a, was not yet available during the SARA project lifetime).

In summary, the compilation conducted provides a good representation of the current knowledge on the occurrence and characteristics of hazardous faults in continental South America. However, it does not necessarily provide an objective picture or balanced representation of the hazardous crustal structures existing in the region.

6.2. From neotectonic faults compilation to seismogenic sources characterization

The geological community has contributed particularly during the last 30 years to a better knowledge of the seismic hazard in South America through the identification of Quaternary deformation as potential fault sources. The neotectonic data accrued, from detailed scale surveys to regional scale cartography, constitute a significant input for applied earth sciences and engineering purposes. Many existing maps and parametric data of hazardous structures carry information on structure-activity through fault-related morphologies, but with few data depicting the characterization of fault sources. Thus, many SHA analyses have not considered hazardous faults as entry data or did so sparingly, partly because key fault data are absent or not available in an adequate format for SHA. Besides, the information of many faults lacks an appropriate uncertainty analysis of data, and the 3D source geometry (length and area) is poorly depicted or difficult to characterize. This turns many neotectonic data of limited application in PSHA and deterministic approaches.

Venezuela has conducted a nation-wide systematic effort since the 80s for translating neotectonic data into fault sources, and recent progress has been made in Ecuador and Colombia. The results achieved highlight the significance of setting institutionally-based and time-sustainable programs for the successful incorporation of fault source data in SHA models.

Approximately 30% of the total fault population inventoried has been incorporated into the generation of PSHA maps. A similar

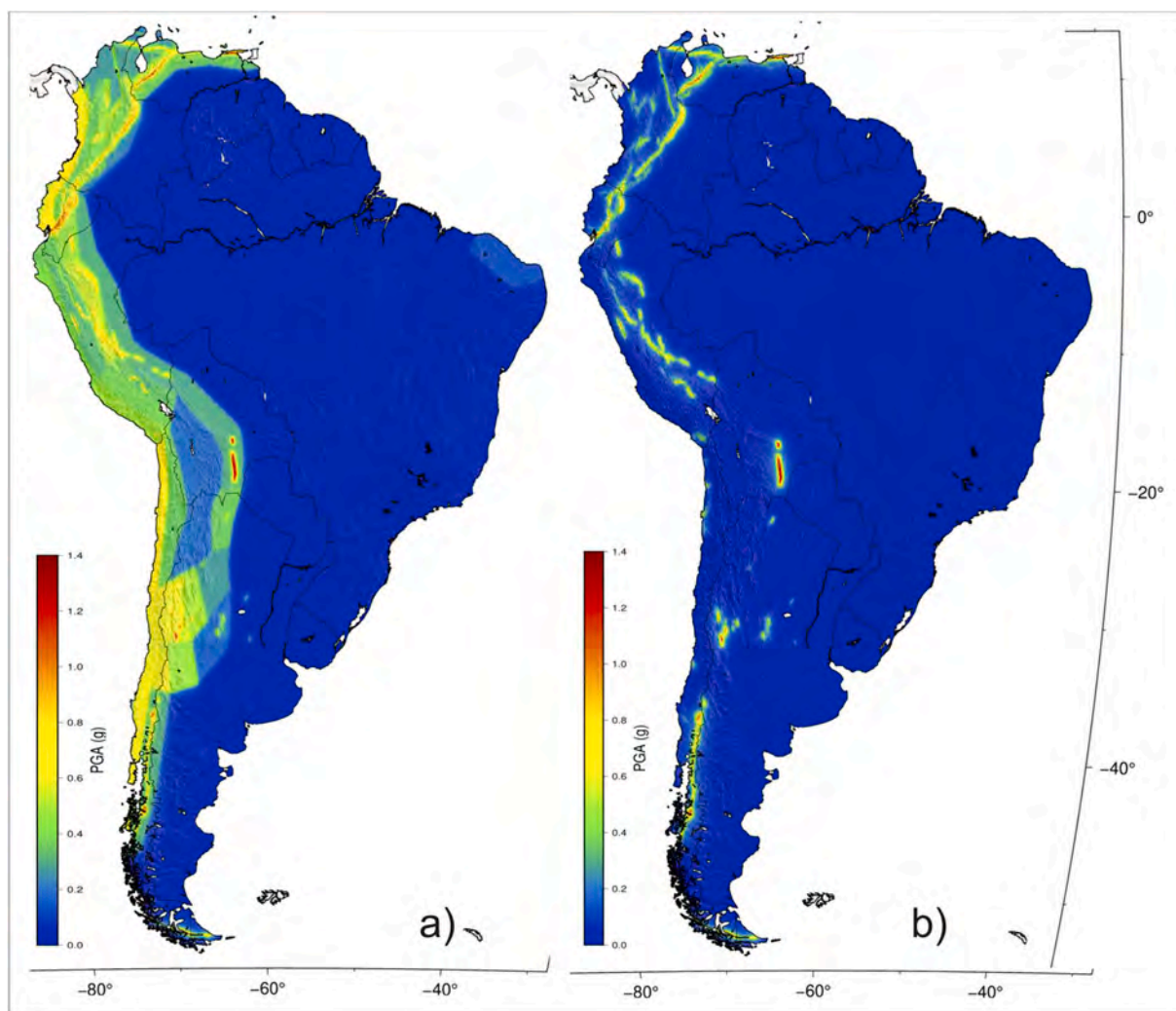


Fig. 14. Probabilistic Seismic Hazard Assessment maps resulting from the SARA project database obtained through the SARA SHSM. They depict expected PGA (Peak Ground Acceleration) on rock for 2% probabilities of exceedance in 50 years or equals to a 2.475 years return period, computing; a) seismicity and hazardous faults, b) hazardous faults.

percentage has resulted from the Quaternary deformation compiled in the United States incorporated into the USGS seismogenic source model (Haller and Basili, 1993). Aiming to increase the percentage of hazardous fault participation in SHSM, might help to organize future research paths and would be of relevance to SHA in South America.

6.3. Seismic hazard and risk in South America through the lens of a hazardous faults database

Subduction and interplate earthquakes are the most significant seismic threat for the region. However, historic destructive earthquakes related to shallow crustal sources ($\geq M 6.5$) have occurred onshore and the here compiled data underpin the seismogenic capability of many faults, even in low strain rate intraplate regions. The knowledge acquired also suggests that there is not necessarily a direct correlation between the fault activity rate and the threat that the fault implies. Many seismogenic capable fault zones may be characterized by current low or even no specific or localized seismicity and long recurrence intervals. Thus, they are probably barely noticeable in the landscape or even not studied yet.

Likewise, many of South America's capital cities are established nearby crustal fault sources, whose seismogenic capability is known or suspected, such as Caracas (Audemard et al., 2000; Rodríguez et al., 2016), Bogotá (Paris et al., 2000), Quito (Egüez et al., 2003; Alvarado

et al., 2014; Beauval et al., 2014; Yepes et al., 2016; Marinière et al., 2020), La Paz (Lavenu et al., 2000; Ramírez et al., 2009), and Santiago (Lavenu et al., 2000; Rauld et al., 2006; Rauld, 2009; Armijo et al., 2010; Vargas et al., 2014; Estay et al., 2016). Other hazardous faults occur near many large fast-growing cities, touristic places, or critical infrastructures, such as dams, pipelines, and even nuclear facilities (Costa et al., this volume). The estimated recurrence interval for most of these faults is much longer than the ~ 500 years spanning the historical period. This means that the last seismic event with surface deformation that these fault sources hosted, only affected at most a few dwellings. But the next one would probably hit urban areas with several million inhabitants, in most cases with inappropriate or inexistent building codes and/or poor observance of seismic safety procedures.

Studies in many of the here compiled hazardous faults have testified for their capability in generating large shallow crustal earthquakes with surface ruptures and related phenomena of social and engineering concern. This regional compilation spotlights that further studies are mandatory in many of them.

Declaration of competing interest

The authors declare that they have no known competing financial interests or personal relationships that could have appeared to influence the work reported in this paper.

Acknowledgments

Digital neotectonic data of national repositories have been kindly made available for this compilation by SEGEMAR, Argentina, OSC, Bolivia, SGC, Colombia, IG-EPN, Ecuador, INGEMMET, Perú, and FUNVISIS, Venezuela and constituted the departure base for this effort. The Pontificia Universidad Católica de Santiago, Chile was in charge of the project administration through J. Cembrano and I. Santibañez. We truly acknowledge the efficient editorial handling done by A. Folguera. The SARA project was funded by Swiss Re through the GEM Foundation.

References

- Aggarwal, Y., 1983. Neotectonics of the southern caribbean: recent data, new ideas. *Acta Cient. Venez.* 34 (1), 17.
- Aguirre, E., Benavente, C., Audin, L., Wimpenny, S., Baize, S., Rosell, L., García, B., Palomino, A., This Volume. Earthquake Surface Ruptures and Active Normal Faulting in the Altiplano in the December 2016 (Mw 6.1) Parina Earthquake in Peru. *Agurto, H., Rietbrock, A., Barrientos, S., Bataille, K., Legrand, D., 2012. Seismotectonic structure of the aysén region, southern Chile, inferred from the 2007 Mw=6.2 aysén earthquake sequence. Geophys. J. Int.* 190, 116–130.
- Ahumada, E., Costa, C., 2009. Antithetic linkage between oblique Quaternary thrusts at the Andean front, Argentine Precordillera. *J. South Am. Earth Sci.* 28, 207–216.
- Allmendinger, R., González, G., 2010. Neogene to Quaternary tectonics of the coastal Cordillera, northern Chile. *Tectonophysics* 495, 93–110.
- Allmendinger, R., González, G., Yu, J., Hoke, G.D., Isacks, B., 2005. Trench-parallel shortening in the northern Chilean forearc: tectonic & climatic implications. *Geol. Soc. Am. Bull.* 117, 89–104. <https://doi.org/10.1130/B25505.1>.
- Alvarado, A., 2009. Falla Chingual, Ecuador (EC-209). In: *Proyecto Multinacional Andino*. Ed. Atlas de deformaciones cuaternarias de Los Andes. SERNAGEOMIN, Publicación Geológica Multinacional, vol. 7. SERNAGEOMIN, pp. 250–253.
- Alvarado, A., 2009b. Sistema Quito, Ecuador. In: *Proyecto Multinacional Andino*. Ed. Atlas de deformaciones cuaternarias de Los Andes. SERNAGEOMIN, Publicación Geológica Multinacional, vol. 7, pp. 294–299.
- Alvarado, A., 2009c. Falla de Pallatanga, Ecuador (EC-67). In: *Proyecto Multinacional Andino*. Ed. Atlas de deformaciones cuaternarias de Los Andes. SERNAGEOMIN, Publicación Geológica Multinacional, vol. 7, pp. 142–146.
- Alvarado, A., Audin, L., Nocquet, J., Lagreuleit, S., Segovia, M., Font, Y., Lamarque, G., Yepes, H., Mothes, P., Rolandone, F., Jarrín, P., Quidelleur, X., 2014. Active tectonics in Quito, Ecuador, assessed by geomorphological studies, GPS data, and crustal seismicity. *Tectonics*. <https://doi.org/10.1002/2012TC003224>.
- Alvarado, A., Audin, L., Nocquet, J., Jaillard, E., Mothes, P., Jarrín, P., Segovia, M., Rolandone, F., Cisneros, D., 2016. Migration history of a continental plate boundary in Ecuador: delimiting the North Andean Sliver's eastern boundary with active faulting, seismicity, GPS and geology. *Tectonics* 35, 1048–1065.
- Arabasz, W., 1968. Geologic structure of the Tal-Tal area, northern Chile, in relation to the earthquake of December 28, 1966. *Bull. Seismol. Soc. Am.* 58, 835–842.
- Arcila, M., Muñoz-Martín, A., 2020. Integrated perspective of the present-day stress and strain regime in Colombia from analysis of earthquake focal mechanisms and geodetic data. In: Gómez, J., Pinilla-Pachon, A.O. (Eds.), *The Geology of Colombia, Volume 4 Qua-Ternary*. Servicio Geológico Colombiano, Publicaciones Geológicas Especiales, vol. 38. <https://doi.org/10.32685/pub.esp.38.2019.17>. Bogotá.
- Armijo, R., Rauld, R., Thiele, R., Vargas, G., Campos, J., Lacassin, R., Kausel, E., 2010. The West Andean thrust, the san Ramón Fault, and the seismic hazard for Santiago, Chile. *Tectonics* 29, 1–34.
- Armijo, R., Lacassin, R., Coudurier-Curveur, A., Carrizo, D., 2015. Coupled tectonic evolution of Andean orogeny and global climate. *Earth Sci. Rev.* 143, 1–25.
- Aron, F., Allmendinger, R., Cembrano, J., González, G., Yáñez, G., 2013. Permanent forearc extension and seismic segmentation: insights from the 2010 Maule earthquake, Chile. *J. Geophys. Res. Solid Earth* 118, 1–16.
- Aron, F., Cembrano, J., Astudillo, F., Allmendinger, R., Arancibia, G., 2015. Constructing forearc architecture over megathrust seismic cycles: geological snapshots from the Maule earthquake region, Chile. *Geol. Soc. Am. Bull.* 127 (3–4), 464–479.
- Astudillo, L., Cortés-Aranda, J., Melnick, D., Tassara, A., 2018. Holocene deformation along the Liqueñe – Ofqui fault zone, southern Chile: field observations and geomorphic analysis. 9th international INQUA meeting on paleoseismology. *Active Tectonics and Archeoseismology (PATA)* 25–27.
- Audemard, Franck, 1993. Néotectonique, Sismotectonique et Aléa Sismique du Nord-ouest du Vénézuéla (Système de failles d'Oca–Ancón). PhD thesis, Université Montpellier II, France, 369 pp + appendix. Univ. Montpellier.
- Audemard, F., 1997. Holocene and historical earthquakes on the Boconó fault system, southern Venezuelan Andes: trench confirmation. *J. Geodyn.* 24 (1–4), 155–167. [https://doi.org/10.1016/S0264-3707\(96\)00037-3](https://doi.org/10.1016/S0264-3707(96)00037-3).
- Audemard, F., 1998. Evolution Géodynamique de la Façade Nord Sud-américaine: nouveaux apports de l'Histoire Géologique du Bassin de Falcón, Vénézuéla. XIV Caribbean Geological Conference, Port of Spain. *Trinidad* 1995 (2), 327–340.
- Audemard, F., 1999. Morpho-structural expression of active thrust fault systems in the humid tropical foothills of Colombia and Venezuela. *Z. Geomorphol.* 118, 1–18.
- Audemard, F., 2001. Revisión y actualización de los parámetros sismogénicos de las fallas activas o potencialmente activas en Venezuela (Inf. Parcial Proy. INTEVEP 99-162). Informe Inédito de FUNVISIS para INTEVEP S.A. 24 pp + anexos.
- Audemard, F., 2002. Ruptura de los grandes sismos históricos venezolanos de los siglos XIX y XX, revelados por la sismicidad instrumental contemporánea. In: XI Congreso Venezolano de Geofísica, Caracas, Venezuela, Nov. 17–20, 2002 (8pp; Extended Abstract in CD).
- Audemard, F., 2003. Geomorphic and geologic evidence of ongoing uplift and deformation in the Mérida Andes, Venezuela. *Quat. Int.* 101–102C, 43–65. [https://doi.org/10.1016/S1040-6182\(02\)00128-3](https://doi.org/10.1016/S1040-6182(02)00128-3).
- Audemard, F., 2007. Revised seismic history of el Pilar Fault, northeastern Venezuela, from the Cariaco 1997 earthquake and recent preliminary paleoseismic results. *J. Seismol.* 11 (3), 311–326. <https://doi.org/10.1007/s10950-007-9054-2>.
- Audemard, F., 2009a. Flexura frontal surandina, Venezuela (VE-07). In: *Proyecto Multinacional Andino*. Ed. Atlas de deformaciones cuaternarias de Los Andes. SERNAGEOMIN, Publicación Geológica Multinacional, vol. 7, pp. 300–311.
- Audemard, F., 2009b. Key issues on the post-Mesozoic southern Caribbean plate boundary. In: James, K.H., Lorente, M.A., Pindell, J. (Eds.), *Origin and Evolution of the Caribbean Plate*, vol. 328. Geological Society, London, Special Publications, pp. 567–584. <https://doi.org/10.1144/SP328.23>.
- Audemard, F., 2014a. Active block tectonics in and around the Caribbean: a Review. In: Schmitz, M., Audemard, F.A., Urbani, F. (Eds.), *El Límite Noreste de la Placa Suramericana - Estructuras Litosféricas de la Superficie al Manto*, Editorial Innovación Tecnológica, Facultad de Ingeniería-Universidad Central de Venezuela/FUNVISIS. Geodynos.
- Audemard, F., 2014b. Segmentación sismogénica de la falla de Boconó a partir de investigaciones paleosísmicas por trincheras, Venezuela Occidental: ¿Migración de la ruptura hacia el noreste en tiempos históricos? *Revista Asociación Geológica Argentina* 71 (2), 247–259.
- Audemard, F.E., Audemard, F.A., 2002. Structure of the Mérida Andes, Venezuela: relations with the South America-Caribbean geodynamic interaction. *Tectonophysics* 345, 299–327.
- Audemard, F., Singer, A., 1996. active fault recognition in northwestern Venezuela and its seismogenic characterization: neotectonic and paleoseismic approach. In: ENGHDAI, E.R., CASTANO, J., BERROCAL, J. (Eds.), *Proceedings of the 1994 Regional Seismological Assembly in South America*, vol. 35. Geofísica Internacional, México, pp. 245–255, 3.
- Audemard, F.A., De Santis, F., Lugo, M., Singer, A., Costa, C., 1988. Estudio de Amenaza Sísmica para las Urbanizaciones "La Punta" y "Mata Redonda". FUNVISIS unpublished report, p. 188 al Sur de Maracay.
- Audemard, F., Pantosti, D., Machette, M., Costa, C., Okumura, C., Cowan, H., Diederix, H., Ferrer, C., participants of Sawop, 1999. Trench investigations along the Mérida section of the Boconó fault (central Venezuelan Andes), Venezuela. *Tectonophysics* 308, 1–21.
- Audemard, F., Machette, M., Cox, J., Dart, R., Haller, K., 2000. Map and database of quaternary faults in Venezuela and its offshore regions, p. 82. U.S. Geological Survey Open-File Report 00-018.
- Audemard, F., Singer, A., 2006. Quaternary faults and stress regime of Venezuela. *Revista Asociación Geológica Argentina* 61 (4), 480–491.
- Audemard, F., Perucca, L., Pantano, A., Avila, C., Onorato, M., Vargas, H., Alvarado, P., Viète, H., 2016. Holocene compression in the acequiñ valley (Andes Precordillera, San Juan province, Argentina): geomorphic, tectonic, and paleoseismic evidence. *J. S. Am. Earth Sci.* 67, 140–157.
- Audin, L., David, C., Hall, S., Farber, D., Hérail, G., 2006. Geomorphic evidences of recent tectonic activity in the forearc, southern Peru. *Rev. Assoc. Geol. Argentina* 61, 545–554.
- Audin, L., Laca, P., Tavera, H., Bondoux, F., 2008. Upper plate deformation and seismic barrier in front of Nazca subduction zone: the Chololo Fault System and active tectonics along the Coastal Cordillera, southern Peru. *Tectonophysics* 459, 174–185. <https://doi.org/10.1016/j.tecto.2007.11.070> (1–4) 1.
- Audin, L., Benavente, C., Macharé, J., 2009a. Falla Chololo (PE-42). In: *Proyecto Multinacional Andino (PMA)*, 2009. Atlas de deformaciones cuaternarias de los Andes, SERNAGEOMIN, vol. 7. Publicación Geológica Multinacional, pp. 202–207.
- Audin, L., Benavente, C., Macharé, J., 2009b. Falla de Purgatorio (PE-45). In: *Proyecto Multinacional Andino (PMA)*, 2009. Atlas de deformaciones cuaternarias de los Andes, SERNAGEOMIN, vol. 7. Publicación Geológica Multinacional, pp. 195–201.
- Audin, L., Benavente, C., Macharé, J., 2009c. Falla de Sama-calientes (PE-51). In: *Proyecto Multinacional Andino (PMA)*, 2009. Atlas de deformaciones cuaternarias de los Andes, SERNAGEOMIN, vol. 7. Publicación Geológica Multinacional, pp. 147–153.
- Audin, L., Benavente, C., Macharé, J., 2009d. Falla de Quiches (PE-08). In: *Proyecto Multinacional Andino (PMA)*, 2009. Atlas de deformaciones cuaternarias de los Andes, SERNAGEOMIN, vol. 7. Publicación Geológica Multinacional, pp. 190–194.
- Audin, L., Benavente, C., Macharé, J., 2009e. Falla de Tambomachay (PE-13a). In: *Proyecto Multinacional Andino (PMA)*, 2009. Atlas de deformaciones cuaternarias de los Andes, SERNAGEOMIN, vol. 7. Publicación Geológica Multinacional, pp. 202–207.
- Baby, P., Hérail, G., Salinas, R., Sempéré, T., 1992. Geometry and kinematic evolution of passive roof duplexes deduced from cross-section balancing-Example from the foreland thrust system of the Southern Bolivian Subandean Zone. *Tectonics* 11 (3), 23–536.
- Baby, P., Rochat, P., Mascle, G., Hérail, G., 1997. Neogene shortening contribution to crustal thickening in the back arc of the central Andes. *Geology* 25 (10), 883–886.
- Baby, P., Calderón, Y., Brusset, S., Roddaz, M., Bricchau, M., Eude, A., Calves, G., Quispe, A., Ramirez, L., Bandach, A., Bolaños, R., Hurtado, C., Louterbach, M., Espurt, N., 2018. The Peruvian sub-andean foreland basin system: structural overview, geochronologic constraints, and unexplored plays. In: Zamora, G., McClay, K.R., Ramos, V.A. (Eds.), *Petroleum Basins and Hydrocarbon Potential of*

- the Andes of Peru and Bolivia, vol. 117. Am. Assoc. Petrol. Geol. Memoir. <https://doi.org/10.1306/AAPG117>.
- Baize, S., Audin, L., Winter, T., Alvarado, A., Pilatasig, L., Taibe, M., Reyes, P., Kauffmann, P., Yepes, H., 2014. Paleoseismology and tectonic geomorphology of the Pallatanga fault (Central Ecuador), a major structure of the South-American crust. *Geomorphology* 237, 14–28.
- Baize, S., Audin, L., Alvarado, A., Jomard, H., Bablon, M., Champenois, J., Espin, P., Samaniego, P., Quidelleur, X., Le Pennec, J.-L., 2020. Active tectonics and earthquake geology along the Pallatanga fault, central Andes of Ecuador. *Front. Earth Sci.* 8, 193. <https://doi.org/10.3389/feart.2020.00193>.
- Barrientos, S., Acevedo, P., 1992. Seismological aspects of the 1988–1989 1013 Lonquimay (Chile) volcanic eruption. *J. Volcanol. Geoth. Res.* 1014, 73–87. [https://doi.org/10.1016/0377-0273\(92\)90075-0](https://doi.org/10.1016/0377-0273(92)90075-0), 53.
- Basili, R., Valensise, G., Vannoli, P., Burrato, P., Fracassi, U., Mariano, S., Tiberti, M., Boschi, E., 2008. The Database of Individual Seismogenic Sources (DISS), version 3: summarizing 20 years of research on Italy's earthquake geology. *Tectonophysics* 453, 20–43.
- Bastías, H., Weidmann, N., Pérez, M., 1984. Dos zonas de fallamiento Pliocuaternario en la Precordillera de San Juan, 2. 9° Congreso Geológico Argentino, Actas, pp. 329–341.
- Beauval, C., Marinière, J., Yepes, H., Audin, L., Nocquet, J.-M., *Alvarado, A., Baize, S., Aguilar, J., Singaicho, J.-C., Jomard, H., 2014. A New Seismic Hazard Model for Ecuador. *Bulletin of the Seismological Society of America*. <https://doi.org/10.1785/0120170259>.
- Bellier, O., Macharé, J., Sebrier, M., 1989. Extensión actual del norte Perú: estudio de la falla activa de Chalquibamba (Norte del Departamento de la libertad – Perú). *Sociedad Geológica del Perú. Boletín* 80, 1–12.
- Bellier, O., Dumont, J.F., Sèbrier, M., Mercier, J.L., 1991. Geological constraints on the kinematics and fault-plane solution of the Quiches fault zone reactivated during the 10 November 1946 Ancash earthquake, northern Peru. *Bull. Seismol. Soc. Am.* 81 (2), 468–490.
- (Comp.) Beltrán, C., 1993. Mapa Neotectónico de Venezuela. Scale 1 : 2,000,000. Funvisis.
- Beltrán, C., 1994. Trazas activas y síntesis neotectónica de Venezuela a escala 1 : 2.000.000. In: *Proceedings of VII Congreso Venezolano de Geofísica, Caracas*, pp. 541–547.
- Beltrán, C., Giraldo, C., 1989. Aspectos neotectónicos de la región nororiental de Venezuela. 7° Congreso Geológico Venezolano, *Proceedings* 3, 1000–1021.
- Benavente, C., Delgado, F., Taibe, E., Audin, L., Pari, W., 2013. Neotectónica y peligro sísmico en la región del Cusco. *INGEMMET. Boletín, Serie C: Geología Ambiental y Riesgo Geológico* 55, 245.
- Benavente, C., Delgado, G., García, B., Aguirre, E., Audin, L., 2017a. Neotectónica, evolución del relieve y peligro sísmico en la región Arequipa. *INGEMMET, Boletín Serie C: Geodin. Ing. Geol.* 64, 370.
- Benavente, C., Zerathe, S., Audin, L., Hall, S., Robert, X., Delgado, F., Carcaillet, J., Aumaitre, G., Bourlès, D., Keddadouche, K., 2017b. Active transpressional tectonics in the Andean forearc of southern Peru quantified by 10Be surface exposure dating of an active fault scarp. *Tectonics* 36, 1662–1678.
- Bernal, Carolina, Christopoul, Frederic, Soula, Jean Claude, Darrozes, Jose, Bourrel, Luc, Laraque, Alain, Burgos, Jose, Bes de Berc, Severine, Baby, Patrice, 2012. Gradual diversions of the Rio Pastaza in the Ecuadorian piedmont of the Andes from 1906 to 2008: role of tectonics, alluvial fan aggradation, and ENSO events. *International Journal of Earth Sciences*. <https://doi.org/10.1007/s00531-012-0752-9>.
- Bès de Berc, Severine, 2003. tectonique de chevauchement, surrection et incision fluviale. *Universite Toulouse III/P. Sabatier*.
- Bès de Berc, S., Soula, J.C., Baby, P., Souris, M., Christophoul, F., Rosero, J., 2005. Geomorphic evidence of active deformation and uplift in a modern continental wedge-top–foredeep transition: example of the eastern Ecuadorian Andes. *Tectonophysics* 399, 351–380. <https://doi.org/10.1016/j.tecto.2004.12.030>.
- Bezerra, F.H.R., Vita-Finzi, C., 2000. How active is a passive margin? Paleo-seismicity in northeastern Brazil. *Geology* 28, 591–594.
- Bezerra, F.H.R., Lima-Filho, F.P., Amaral, R.F., Caldas, L.H.O., Costa-Neto, L.X., 1998. Holocene coastal tectonics in NE Brazil. In: Stewart, I., Vita-Finzi, C. (Eds.), *Coastal Tectonics*, vol. 146. Geological Society of London, Special Publication, pp. 279–293.
- Bezerra, F.H.R., Amaro, V.E., Vita-Finzi, C., Saadi, A., 2001. Pliocene-Quaternary fault control of sedimentation and coastal plain morphology in NE Brazil. *J. S. Am. Earth Sci.* 14, 61–75.
- Bezerra, F., Ferreira, J., Sousa, M., 2006. Review of seismicity and neogene tectonics in northeastern Brazil. *Rev. la Asoc. Geol. Argentina* 61, 525–535.
- Bezerra, F.H.R., Takeya, M.K., Sousa, M.O.L., 2007. Coseismic reactivation of the Samambaia fault, Brazil. *Tectonophysics* 430, 27–39. <https://doi.org/10.1016/j.tecto.2006.10.007>.
- Bezerra, F., do Nascimento, A., Ferreira, J., Nogueira, F., Fuck, R., Brito Neves, B., Sousa, M., 2011. Review of active faults in the boroborema province, intraplate South America - integration of seismological and paleoseismological data. *Tectonophysics* 510, 269–290.
- Brooks, B., Bevis, M., Smalley, R., Kendrick, E., Manceda, R., Lauría, E., Maturana, R., Araujo, M., 2003. Crustal motion in the southern Andes (26°–36°S): do the Andes behave like a microplate? *G-cubed* 4, 1–14.
- Brooks, B.A., Bevis, M., Whipple, K., Arrowsmith, R., Foster, J., Zapata, T., Kendrick, E., Minaya, E., Echalar, A., Blanco, M., Euillades, P., Sandoval, M., Smalley, R., 2011. Orogenic-wedge deformation and potential for great earthquakes in the central Andean backarc. *Nat. Geosci.* 4, 380–383.
- Brunetto, E., Iriondo, M.H., 2007. Neotectónica en la Pampa Norte (Argentina). *Rev. Soc. Geol. Espana* 20 (1–2), 17–29.
- Brunetto, E., Iriondo, M.H., Zamboni, L., Gottardi, M.G., 2010. Quaternary deformation around the palo negro area, pampa norte, Argentina. *J. S. Am. Earth Sci.* 29, 627–641.
- Brunetto, E., Sobrero, F., Gimenez, M., 2019. Quaternary deformation and stress field in the río de la Plata craton (southeastern south America). *J. South Am. Earth Sci.* 91, 332–351.
- Cabrera, J., Sèbrier, M., Mercier, J., 1987. Active normal faulting in the high plateaus of central Andes: the Cusco region (Perú). *Ann. Tectonicae* 1 (2), 116–138.
- Carrizo, D., González, G., Dunai, T., 2008. Constricción Neógena en la Cordillera de la Costa Norte de Chile (20°30' 21°05'S), antearco externo de los Andes Centrales: neotectónica y datación de superficies con 21Ne cosmogénico. *Rev. Geol. Chile* 35 (1), 1–35.
- Casa, A., 2009. Sistema de fallas Aconquija (AR-02) In: *proyecto Multinacional Andino. In: Atlas de deformaciones cuaternarias de Los Andes. SERNAGEOMIN, Publicación Geológica Multinacional*, vol. 7, pp. 129–136.
- Casa, A., Yamin, M., Cegarra, Coppolecchia, M., Costa, C., 2010. Deformación cuaternaria asociada al frente de levantamiento oriental de las sierras de Velasco y Ambato. *Revista Asoc. Geol. Argentina* 67 (4), 425–438.
- Casa, A., Yamin, M., Cegarra, M., Wright, E., Coppolecchia, M., Costa, C., Hongn, F., Amengual, R., García, V., 2014. Actualización del SIG de las deformaciones cuaternarias de la República Argentina. 19th Congreso Geológico Argentino Abstracts in CD-ROM.
- Cembrano, J., Lara, L., 2009. The link between volcanism and tectonics in the Southern Volcanic Zone of the Chilean Andes: a review. *Tectonophysics* 471 (1–2), 96–113.
- Cembrano, J., Hervé, F., Lavenau, A., 1996. The Liquiñe-Ofqui fault zone: a long-lived intra-arc fault Zone in southern Chile. *Tectonophysics* 259, 55–66.
- Cembrano, J., Lavenau, A., Reynolds, P., Arancibia, G., Lopez, G., Sanhueza, A., 2002. Late Cenozoic transpressional ductile deformation north of the Nazca-South America-Antarctica triple junction. *Tectonophysics* 354, 289–314.
- Champenois, J., Baize, S., Vallee, M., Jomard, H., Alvarado, A.P., Espin, P., Ekström, G., Audin, L., 2017. Evidences of surface rupture associated with a low-magnitude (Mw5.0) shallow earthquake in the Ecuadorian Andes. *J. Geophys. Res.: Solid Earth* 122, 8446–8458. <https://doi.org/10.1002/2017JB013928>.
- Coelho, S., do Nascimento, A., Bezerra, F., Ferreira, P., da Fonsêca, J., Ferreira, J., this volume. Depth-dependent Stress and Faulting Style Change Associated with Intraplate Seismicity in the Pernambuco Lineament, (Brazil).
- Colavitto, B., Sagripanti, L., Fennell, L., Folguera, A., Costa, C., 2019. Evidence of Quaternary tectonics along Río Grande valley, southern Malargüe fold and thrust belt, Mendoza, Argentina. *Geomorphology*. <https://doi.org/10.1016/j.geomorph.2019.06.025>.
- Colavitto, B., Sagripanti, L., Jagoe, L., Costa, C., Folguera, A., 2020. Neotectonics in the northern Neuquén Andes of Argentina (37° - 38° S): new insights from a morphotectonic perspective. *J. S. Am. Earth Sci.*
- Cortés, J., Vinciguerra, P., Yamin, M., Pasini, M., 1999. Tectónica cuaternaria de la región Andina del Nuevo Cuyo (28–38LS). In: *Caminos, R. (Ed.), Geología Argentina. SEGEMAR, Buenos Aires*, pp. 760–778. *Analés* 29 (24), Sección 2B.
- Cortés, J., Casa, A., Pasini, M., Yamin, M., Terrizzano, C., 2006. Fajas oblicuas de deformación en Precordillera y Cordillera Frontal (31o 30' - 33o 30' S): controles Paleotectónicos. *Rev. Asoc. Geológica Argentina* 61, 639–646.
- Cortés-Aranda, J., González, G., Binnie, S., Ruth, R., Freeman, S., Vargas, G., 2012. Paleoseismology of the Mejillones fault, northern Chile: insights from cosmogenic 10Be and optically stimulated luminescence determinations. *Tectonics* 31 (2).
- Costa, C., 1999. Tectónica Cuaternaria en las Sierras Pampeanas. In: *Caminos, R. (Ed.), Geología Argentina. SEGEMAR, Buenos Aires*, pp. 779–784. *Analés* 29 (24), Sección 2B.
- Costa, C., 2009. Falla La rinconada (AR-22). In: *Proyecto Multinacional Andino (PMA), 2009. Atlas de deformaciones cuaternarias de los Andes, SERNAGEOMIN, Publicación Geológica Multinacional*, vol. 7, pp. 104–110.
- Costa, C., 2019. La Migración Del Frente De Corrimiento Neotectónico de las Sierras Pampeanas y su Imprinta morfológica. *Rev. Asoc. Geológica Argentina* 77, 315–325.
- Costa, C., Lara, L., 2009. Falla magallanes-fagnano (AR-56, CH-50). In: *Proyecto Multinacional Andino (PMA), 2009. Atlas de deformaciones cuaternarias de los Andes, SERNAGEOMIN*, vol. 7. *Publicación Geológica Multinacional*, pp. 254–258.
- Costa, C., Vita-Finzi, C., 1996. Late Holocene faulting in the southeast sierras Pampeanas of Argentina. *Geology* 24 (12), 1127–1130.
- Costa, C., Owen, L., Johnson, W., this volume. Quaternary deformation and seismogenic significance of the sierra chica fault system, (Argentina).
- Costa, C., Machette, M., Dart, R., Bastías, H., Paredes, J., Perucca, L., Tello, G., Haller, K., 2000a. Map and Database of Quaternary Faults and Folds in Argentina. U. S. Geological Survey Open-File Report 00-0108, p. 75.
- Costa, C., Gardini, C., Diederix, H., Cortés, J., 2000b. The andean orogenic front at sierra de Las peñas-las higuera, Mendoza, Argentina. *J. South Am. Earth Sci.* 13, 287–292.
- Costa, C., Murillo, V., Sagripanti, G., Gardini, C., 2001. Quaternary intraplate deformation in the southeastern Sierras Pampeanas, Argentina. *J. Seismol.* 5, 399–409.
- Costa, C., Audemard, F., Bezerra, F., Lavenau, A.A., Machette, M., París, G., 2006a. An overview of the main Quaternary deformation of South America. *Rev. Asoc. Geológica Argentina* 61, 461–479.
- Costa, C., Smalley, R., Schwartz, D., Stenner, H., Ellis, M., Ahumada, E., 2006b. Paleoseismic observations of an onshore transform boundary: the Magallanes-Fagnano fault, Tierra del Fuego. *Argentina* 61, 647–657.
- Costa, C., Ahumada, E., Gardini, C., Vazquez, F., Diederix, H., 2014a. Quaternary shortening at the orogenic front of the central Andes of Argentina (32°15'–32°40's): a field survey of the las peñas thrust system. *Geol. Soc. Spec. Publ.* 399 <https://doi.org/10.1144/SP399.5>.

- Costa, C., Massabie, A., Sagripanti, G., Brunetto, E., Coppolecchia, M., 2014b. Neotectónica. In: *Relatorio CGA. in Relatorio 19th Congreso Geológico Argentino, Geología y Recursos Naturales de la pcia. de Córdoba. R. Martino, A. Guesreschi*, pp. 725–746.
- Costa, C., Ahumada, E., Vázquez, F., Kröhlhng, D., 2015. Holocene shortening rates of an andean-front thrust, southern Precordillera, Argentina. *Tectonophysics* 664, 191–201.
- Costa, C., Owen, L., Ricci, W., Johnson, W., Halperin, A., 2018. Holocene activity and seismogenic capability of intraplate thrusts: insights from the Pampean Ranges, Argentina. *Tectonophysics* 737, 57–70. <https://doi.org/10.1016/j.tecto.2018.05.002>.
- Costa, C., Schoenbohm, L., Brooks, B., Gardini, C., Richard, A., 2019. Assessing quaternary shortening rates at an andean frontal thrust (32°30'S), Argentina. *Tectonics* 38, 3034–3051. <https://doi.org/10.1029/2019TC005564>.
- Cowan, H., Dart, R., Machette, M., 1998. Map of Quaternary faults and folds of Panama and its offshore regions. U.S. Geol. Survey Open-File Rep. 98–779 <https://doi.org/10.3133/ofr98779>.
- Cunningham, W., 1993. Strike-slip faults in the southernmost Andes and the development of the patagonian orocline. *Tectonics* 12 (1), 169–186.
- Dalmayrac, B., Molnar, P., 1981. Parallel thrust and normal faulting in Peru and constraints on the state of stress. *Earth Planet Sci. Lett.* 55, 473–481.
- Dalziel, I., Dott, R., Winn Jr., R., Bruhn, R., 1975. Tectonic relations of South Georgia to the southernmost Andes. *Geol. Soc. Am. Bull.* 86, 1034–1040.
- David, C., Audin, L., Comte, D., Tavera, H., Hérail, G., 2005. Crustal seismicity and active tectonics in the Arica bend forearc. In: 6th International Symposium on Andean Geodynamics. Extended Abstracts, Barcelona, pp. 206–210.
- de Menezes, E., do Nascimento, A., da Fonseca, J., Lima-Neto, H., Sousa, M., Ferreira, J., this vol. n. Recent Seismic Activity in Irauçuba Fault, Potiguar Basin, Brazil.
- Davila, Federico, Carter, Andrew, 2013. Exhumation history of the Andean broken foreland revisited. *Geology*. <https://doi.org/10.1130/G33960.1>.
- De Pascale, G.P., Froude, M., Penna, I., Hermanns, R., Moncada, D., Sepulveda, S., Persico, M., Petley, D., Vargas, G., Murphy, W., Paira, S., 2018. Preliminary Geologic Slip Rates along Andes Fastest Slipping Crustal Fault, the Lliquiñe-Ofqui Fault Zone (LOFZ), Patagonia, Chile. Poster Presentation at 2018 SCEC Annual Meeting.
- De Toni, B., Kellogg, J., 1993. Seismic evidence for blind thrusting of the northwestern flank of the Venezuelan Andes. *Tectonics* 12, 1393–1409.
- Diederix, H., Romero, J., 2009. Sistema de Fallas del Frente Oriental Andino (CO-29a y 29d). Proyecto Multinacional Andino (PMA), 2009. Atlas de deformaciones cuaternarias de los Andes, SERNAGEOMIN. Publicación Geol. Multinac. 7, 277–287.
- Diederix, H., Gómez, H., Khorzaji, J., Singer, A., 1987. Indicios neotectónicos de la falla de Ibagué en el sector Ibagué-Piedras, departamento Tolima, Colombia. *Rev. CIAF* 11 (1–3), 242–252.
- Diederix, H., Audemard, F., Osorio, J., Montes, N., Velandia, F., Romero, J., 2006. Modelado morfo-tectónico de la falla transcurrente de Ibagué, Colombia. *Rev. Asoc. Geol. Argent.* 61 (4), 492–503.
- Diederix, H., Romero, J., 2009. Falla de Algeciras (CO-29h). Proyecto Multinacional Andino (PMA), 2009. Atlas de deformaciones cuaternarias de los Andes, SERNAGEOMIN. Publicación Geol. Multinac. 7, 235–244.
- Diederix, H., Romero, J., Audemard, F., 2009. Falla de Ibagué (CO-35). Proyecto Multinacional Andino (PMA), 2009. Atlas de deformaciones cuaternarias de los Andes, SERNAGEOMIN. Publicación Geol. Multinac. 7, 226–234.
- Diederix, H., Torres, E., Hernández, C., 2011. Evidencia de la actividad de la falla de Bucaramanga durante el Pleistoceno superior basada en indicadores morfo-tectónicos y elementos de evolución del paisaje. 12° Congreso Colombiano de Geología Memorias, pp. 166–167.
- Diederix, H., Bohórquez, O.P., Mora-Páez, H., Peláez, J.R., Cardona, L., Corchuelo, Y., Ramírez, J., Díaz-Mila, F., 2019. The Algeciras Fault system of the upper magdalena valley, huila department. In: Gómez, J., Pinilla-Pachon, A.O. (Eds.), *The Geology of Colombia*, vol. 38. Publicaciones Geológicas Especiales SGC, pp. 497–531, 4 <https://doi.org/10.32685/pub.esp.38.2019.12>.
- Dimaté, C., Rivera, C., Tabaoda, A., Delouis, B., Osorio, A., Jimenez, E., Fuenzalida, A., Cisternas, A., Gomez, I., 2003. The 19 January 1995 Tauramena (Colombia) earthquake: geometry and stress. *Tectonophysics* 363, 159–180. [https://doi.org/10.1016/S0040-1951\(02\)00670-4](https://doi.org/10.1016/S0040-1951(02)00670-4).
- Dorbath, L., Dorbath, C., Jiménez, E., Rivera, L., 1991. Seismicity and tectonic deformation in the eastern cordillera and sub andean zone of central Perú. *J. S. Am. Earth Sci.* 4, 13–24.
- Doser, D.L., 1987. The Ancash Peru earthquake of November 19, 1946-Evidence for low-angle normal faulting in the high Andes of northern Peru. *J. Geophys. Res.* 91, 57–71.
- Duerto, L., Escalona, A., Mann, P., 2006. Deep structure of the Mérida Andes and sierra de Perijá mountain fronts, maracaibo basin, Venezuela. *AAPG (Am. Assoc. Pet. Geol.) Bull.* 90, 505–528.
- Dumont, J.F., 1996. Neotectonics of the Subandes-Braz, ilian craton boundary using geomorphological data-The Marañon and Beni basins. *Tectonophysics* 257, 137–151.
- Dumont, J.F., Deza, E., García, F., 1991. Morphostructural provinces and neotectonics in the Amazonian lowlands of Peru. *J. S. Am. Earth Sci.* 4, 373–381.
- Dumont, J.F., Santana, E., Vilema, W., Pedoja, E., Ordóñez, M., Cruz, M., Jiménez, N., Zambrano, I., 2005. Morphological and microtectonic analysis of quaternary deformation from puná and santa clara islands, Gulf of Guayaquil, Ecuador (south America). *Tectonophysics* 399, 331–350. <https://doi.org/10.1016/j.tecto.2004.12.029>.
- DuRoss, C., Personius, S., Crone, A., Olig, S., Hylland, M., Lund, W., Schwartz, D., 2016. Fault segmentation: new concepts from the wasatch fault zone, Utah, USA, *Journal of Geophys. Res. Solid Earth* 121, 1131–1157. <https://doi.org/10.1002/2015JB012519>.
- Ego, F., Sébrier, M., Yepes, H., 1995. Is the Cauca-Patia and Romeral fault system left-or right-lateral? *Geophys. Res. Lett.* 22, 33–36. <https://doi.org/10.1029/94GL02837>.
- Ego, F., Sébrier, M., Lavenue, A., Yepes, H., Eguez, A., 1996. Quaternary state of stress in the Northern Andes and the restraining bend model for the Ecuadorian Andes. *Tectonophysics* 259, 101–116.
- Egüez, A., Alvarado, A., Yepes, H., Machette, M., Costa, C., Dart, R., 2003. Database and map of quaternary faults and folds in Ecuador and its offshore region. U.S. Geological Survey Open-File Report 77, 03-289.
- Espurt, N., Barbarand, J., Roddaz, M., Brusset, S., Baby, P., Saillard, M., Hermoza, H., 2011. A scenario for late Neogene Andean shortening transfer in the Camisea sub-Andean zone (Peru, 12°S): implications for growth of the northern Andean Plateau, 123. *Bulletin of the Geological Society of America*. <https://doi.org/10.1130/B30165.1>, 9–10.
- Estay, N., Yáñez, G., Carretier, S., Lira, E., Manrique, J., 2016. Seismic hazard in low slip rate crustal faults, estimating the characteristic event and the most hazardous zone: study case San Ramón Fault, in southern Andes. *Nat. Hazards Earth Syst. Sci.* 16, 2511–2528.
- Esteban, F.D., Tassone, A., Isola, J.I., Lodolo, E., Menichetti, M., Lippai, H., Waldmann, N., Darbo, A., Baradello, L., Vilas, J.F., 2014. Basement geometry and sediment thickness of Lago Fagnano (Tierra del Fuego). *Andean Geol.* 41 (2), 293–313. [10.5027/andgeoV41n2-a02](https://doi.org/10.5027/andgeoV41n2-a02).
- Esteban, F.D., Tassone, A., Isola, J.I., Lodolo, E., Menichetti, M., 2018. Geometry and structure of the pull-apart basins developed along the western South American-Scotia plate boundary (SW Atlantic Ocean). *J. South Am. Earth Sci.* 83, 96–116. <https://doi.org/10.1016/j.jsames.2018.02.005>.
- Fabre, A., 1983. La subsidencia de la Cuenca del Cocuy (Cordillera Oriental de Colombia) durante el Cretáceo y el Terciario Inferior. Primera parte: estudio cuantitativo de Subsidencia. *Geol. Norandina* 8, 49–61.
- Fajardo, A., 2015. Neotectonic evolution of the Serranía del Interior range and Monagas Fold and Thrust Belt, Eastern Venezuela: morphotectonics, seismic profiles analyses and paleomagnetism. PhD dissertation. University of Pau, France.
- Fariás, M., Charrier, R., Comte, D., Martindot, J., Hérail, G., 2005. Late Cenozoic deformation and uplift of the western flank of the Altiplano: evidence from the depositional, tectonic, and geomorphologic evolution and shallow seismic activity (northern Chile at 19°30'S). *Tectonics* 24, 1–27.
- Fauqué, L., Strecker, M., 1987. Rasgos de neotectónica y avalanchas de roca producidas por terremotos en la vertiente Occidental de los Nevados del Aconquija, Provincia de Catamarca, Argentina, vol. 1. 10° Congreso Geológico Argentino, Actas, pp. 219–222.
- Fiorini, E., Tibaldi, A., 2012. Quaternary tectonics in the central interandean valley, Ecuador: fault-propagation folds, transfer faults and the cotopaxi volcano. *Global Planet. Change* 90, 91. <https://doi.org/10.1016/j.gloplacha.2011.06.002>.
- Folguera, A., Ramos, V.A., Hermanns, R.L., Naranjo, J., 2004. Neotectonics in the foothills of the southernmost Central Andes (37°–38° S): evidence of strike-slip displacement along the Antinir-Copahue fault zone. *Tectonics* 23, TC5008. <https://doi.org/10.1029/2003TC001533>.
- Folguera, A., Ramos, V., González Díaz, E., Hermanns, R., 2006. Miocene to quaternary deformation of the guanacos fold-and-thrust belt in the neuquén Andes between 37° S and 37° 30' S. *Geol. Soc. Am. Spec. Pap.* 407, 247–266. [https://doi.org/10.1130/2006.2407\(11](https://doi.org/10.1130/2006.2407(11)
- Folguera, A., Gianni, G., Sagripanti, L., Vera, E.R., Novara, I., Colavitto, B., Alvarez, O., Orts, D., Tobal, J., Introcaso, A., 2015. A review about the mechanisms associated with active deformation, regional uplift and subsidence in southern South America. *J. S. Am. Earth Sci.* 64, 511–529. <https://doi.org/10.1016/j.jsames.2015.07.007>.
- Freymueller, J.T., Kellogg, J.N., Vega, V., 1993. Plate motions in the north Andean region. *J. Geophys. Res.* 98, 21853–21863.
- FUNVISIS (Fundación Venezolana de Investigaciones Sismológicas), 1994. Estudio neotectónico y de geología de fallas activas de la región nororiental de Venezuela. Unpublished Report for Intevep 92-175 Project, p. 258.
- Galland, O., Hallot, E., Cobbold, P.R., Ruffet, G., de Bremond D'Arès, J., 2007. Volcanism in a compressional Andean setting: a structural and geochronological study of Tromen volcano (Neuquén province, Argentina). *Tectonics* 26, TC4010. <https://doi.org/10.1029/2006TC002011>.
- Gansser, A., 1973. Facts and theories on the Andes. *Journal of the Geological Society of London* 129 (1), 93–131.
- García, V., Casa, A., 2014. Quaternary tectonics and seismic potential of the Andean retrowedge at 33-34°S. *Geol. Soc. Spec. Publ.* 399, 311–327.
- García, M., Hérail, G., 2005. Fault-related folding, drainage network evolution and valley incision during the Neogene in the Andean Precordillera of Northern Chile January. *Geomorphology* 65 (3), 279–300. <https://doi.org/10.1016/j.geomorph.2004.09.007>.
- García, B., Benavente, C., Costa, C., Palomino, A., Rosell, L., This Volume Active Tectonics and Surface Ruptures Associated to Colca System Fault.
- García, M., Riquelme, R., Fariás, M., Hérail, G., Charrier, R., 2011. Late Miocene-Holocene canyon incision in the western Altiplano, northern Chile: tectonic or climatic forcing? *J. Geol. Soc.* 168, 1047–1060. <https://doi.org/10.1144/0016-76492010-134>. London.
- García, V.H., Hongn, F., Cristallini, E., 2013. Late Miocene to recent morphotectonic evolution and potential seismic hazard of the northern Lerma valley: clues from Lomas de Medeiros Cordillera Oriental, NW Argentina. *Tectonophysics* 608, 1238–1253.
- García, V., Casa, A., Hongn, F., Figueroa, S., Aranda, G., Escalante, L., Montero-López, C., Yamin, M., Amengual, R., Aramayo, A., 2017. Deformación cuaternaria. In: Muruaga, C.M., Grosse, P. (Eds.), *Ciencias de la Tierra y Recursos Naturales del NOA*.

- Relatorio del XX Congreso Geológico Argentino, vols. 624–645. San Miguel de Tucumán. ISBN 978-987-42-6666-8.
- García Morabito, E., Terrizzano, C., Zech, R., Yamín, M., Wüthrich, L., Christi, M., Ramos, V., Haghypour, N., Cortés, J., 2020. 10Be surface exposure dating reveals unexpected high deformation rates in the central Andean wedge interior. *Terra Nova* 1–16. <https://doi.org/10.1111/ter.12487>, 00.
- Gautheron, C., Espurt, N., Barbarand, J., Roddaz, M., Baby, P., Brusset, S., Tassan-Gotsand, L., Douville, E., 2013. Direct dating of thick- and thin-skin thrusts in the Peruvian Subandean zone through apatite(U-Th)/He and fission track thermochronometry. *Basin Res.* 25, 419–435. <https://doi.org/10.1111/bre.12012>.
- Giambiagi, L., Mescua, J., Bechis, F., Hoke, G., Suriano, J., Spagnotto, S., Moreiras, S., Lössada, A., Mazzitelli, M., Tournal, Folguera, A., Mardonez, D., Pagano, D., 2015. Cenozoic orogenic evolution of the southern central Andes (32–36°S). In: Folguera, A., Naipauer, M., Sagripanti, L., Ghiglione, C., Orts, D., Giambiagi, L. (Eds.), *Growth of the Southern Andes*. Springer Earth System Sciences, pp. 63–98. https://doi.org/10.1007/978-3-319-23060-3_4 (2016).
- Giampaoli, P., Rojas Vera, E., 2018. Fold growth and lateral linkage in the southern subandean fold-and-thrust belt of Argentina and Bolivia. AAPG Memoir 117, Petroleum Basins and Hydrocarbon Potential of the Andes of Peru and Bolivia, pp. 555–576.
- Gómez, L., Moreno, M., Hincapié, G., Buitrago, J., Cristancho, A., Patiño, A., Zafra, M., Cabrera, J.C., Quiñonez, C., 2015. *Geología de la Plancha 304 La Uribe, escala 1: 100.000*. Servicio Geológico Colombiano, Bogotá.
- Gontijo-Pascutti, A., Bezerra, F.H.R., La Terra, E., Almeida, J.C.H., 2010. Brittle reactivation of mylonitic fabric and the origin of the Cenozoic Rio Santana Graben, southeastern Brazil. *J. S. Am. Earth Sci.* 29, 522–536. <https://doi.org/10.1016/j.jsames.2009.06.007>.
- González, G., Cembrano, J., Carrizo, D., Macci, A., Schneider, H., 2003. Link between forearc tectonics and pliocene-quaternary deformation of the coastal cordillera, northern Chile. *J. S. Am. Earth Sci.* 16, 321–342.
- González, G., Dunai, T., Carrizo, D., Allmendinger, R., 2006. Young displacements on the Atacama Fault System, northern Chile from field observations and cosmogenic ²¹Ne concentrations. *Tectonics* 25, TC3006. <https://doi.org/10.1029/2005TC001846>.
- González, G., Gerbault, M., Martinod, J., Cembrano, J., Allmendinger, R., Carrizo, D., Espina, J., 2008. Crack formation on top of propagating reverse faults of the Chuculay Fault System northern Chile: insights from field data and numerical modeling. *J. Struct. Geol.* 30, 791–808.
- González, G., Salazar, P., Loveless, J., Allmendinger, R., Aron, F., Shrivastava, M., 2015. Upper plate reverse fault reactivation and the unclamping of the megathrust during the 2014 northern Chile earthquake sequence. *Geology* 43, 671–674.
- González Ferrán, O., 1985. Mapa Neotectónico preliminar para América del Sur, vol. 11. SISRA Project Series, p. 110 with Map.
- Gutscher, M.-A., Spakman, W., Bijwaard, H., Engdahl, E.R., 2000. Geodynamics of flat subduction; seismicity and tomographic constraints from the Andean margin. *Tectonics* 19 (5), 814–833.
- Guzmán, O., Vassallo, R., Audemard, F.A., Mugnier, J.-L., Oropeza, J., Yopez, S., Carcaillet, J., Alvarado, M., Carrillo, E., 2013. 10Be dating of river terraces of Santo Domingo river, on Southeastern flank of the Mérida Andes, Venezuela: tectonic and climatic implications. *J. S. Am. Earth Sci.* 48, 85–96. <https://doi.org/10.1016/j.jsames.2013.09.004>.
- Hall, S., Farber, D., Audin, L., Finkel, A., 2012. Recently active contractile deformation in the forearc of southern Peru. *Earth Planet Sci. Lett.* 337, 85–92. <https://doi.org/10.1016/j.epsl.2012.04.007>.
- Haller, K., Basili, R., 2011. Developing seismogenic source models based on geologic fault data. *Seismol Res. Lett.* 82, 519–525.
- Haller, K., Machette, M., Dart, R., 1993. Maps of major active faults, western hemisphere; international Lithosphere program (ILP) project II-2: guidelines for U.S. Database and map: U.S. Geological Survey Open-File Report 93–338, 45.
- Ham, C., Herrera, L., 1963. Role of subandean flat system in tectonics of eastern Peru and Ecuador. *Am. Assoc. Pet. Geol. Mem.* 2 <https://doi.org/10.1306/M2358.C6>.
- Hervé, F., 1976. Estudio geológico de la falla Liquiñe-Reloncaví en el área de Liquiñe; antecedentes de un movimiento transcurrente (Provincia de Valdivia). I Congreso Geológico Chileno Actas 1, pp. B39–B56.
- Hervé, F., Thiele, R., 1987. Estado de conocimiento de las megafallas en Chile y su significado tectónico. *Comunicaciones* 38, 7–91.
- Hong, F., Amengual, R., García, V., Yamín, M., Casa, A., 2014. Neotectónica del Valle Calchaquí. XIX Congreso Geológico Argentino, Abstracts in CD-ROM, pp. T6–T10.
- Horton, B., 2018. Sedimentary record of Andean mountain building. *Earth Sci. Rev.* 178, 279–309.
- IAEA (International Atomic Energy Agency), 2010. Seismic hazards in site evaluation for nuclear installations, Safety Standards Series No. SSG-9. <http://www-ns.iaea.org/sstandards/>, 60.
- Iturrieta, P., Hurtado, D., Cembrano, J., Stanton-Yonge, A., 2017. States of stress and slip partitioning in a continental scale strike-slip duplex: tectonic and magmatic implications by means of finite element modeling. *Earth Planet Sci. Lett.* 473, 71–82.
- Jordan, T., Allmendinger, R., 1986. The Sierras Pampeanas of Argentina-A modern analogue of Rocky Mountains foreland deformation. *Am. J. Sci.* 286, 737–764.
- Jordan, T., Isacks, B., Allmendinger, R., Brewer, J., Ramos, V., Ando, C., 1983. Andean tectonics related to the geometry of subducted Nazca plate. *Geol. Soc. Am. Bull.* 94, 341–361.
- Kellogg, J., Vega, V., 1995. Tectonic Development of Panama, Costa Rica, and the Colombian Andes: Constraints from Global Positioning System Geodetic Studies and Gravity, vol. 295. Special Paper Geological Society of America, pp. 75–90.
- Kendrick, E., Bevis, M., Smalley, Jr., R.F., Cifuentes, O., Galbán, F., 1999. Current rates of convergence across the Central Andes; estimates from continuous GPS observations. *Geophys. Res. Lett.* 26 (5), 541–544.
- Kendrick, E., Brooks, B., Bevis, M., Smalley, R., Lauria, E., Araujo, M., Parra, H., 2006. Active orogeny of the south-central Andes studied with GPS geodesy. *Rev. Asoc. Geol. Argentina* 61, 555–566.
- Klepeis, K., 1994. The Magallanes and Deseado fault zones: major segments of the South American-Scotia transform plate boundary in southernmost South America, Tierra del Fuego. *J. Geophys. Res.* 99 (22), 001–22,014.
- Kraemer, P., 2003. Orogenic shortening and the origin of the Patagonian orocline (56° S. Lat). *J. S. Am. Earth Sci.* 15 (7), 731–748. [https://doi.org/10.1016/S0895-9811\(02\)00132-3](https://doi.org/10.1016/S0895-9811(02)00132-3).
- Lange, D., Cembrano, J., Rietbrock, A., Haberland, C., Dahm, T., Bataille, K., 2008. First seismic record for intra-arc strike-slip tectonics along the Liquiñe-Ofqui fault zone at the obliquely convergent plate margin of the southern Andes. *Tectonophysics* 455, 14–24.
- Lara, L., 2009. Zona de falla Liquiñe-Ofqui. In: *Proyecto Multinacional Andino (PMA), 2009. Atlas de deformaciones cuaternarias de los Andes*, SERNAGEOMIN, vol. 7. Publicación Geológica Multinacional, pp. 215–218.
- Lavenau, A., Cembrano, J., 1999. Compressional and transpressional-stress pattern for Pliocene and quaternary brittle deformation in fore arc and intra-arc zones (Andes of central and southern Chile). *J. Struct. Geol.* 21, 1669–1691.
- Lavenau, A., Winter, T., Dávila, F., 1995. A pliocene-quaternary compressional basin in the interandean depression, Central Ecuador. *Geophys. J. Int.* 121, 279–300.
- Lavenau, A., Thiele, R., Machette, M., Dart, R., Bradley, L., Haller, K., 2000. Maps and database of quaternary faults in Bolivia and Chile, p. 50. U.S. Geological Survey Open-File Report 00-283.
- Legrand, D., Barrientos, S., Bataille, K., Cembrano, J., 2011. The fluid-driven tectonic swarm of fjordo aysen, Chile (2007) associated with two earthquakes (Mw=6.1 and Mw=6.2) within the Liquiñe-Ofqui fault zone. *Contin. Shelf Res.* 31 (3–4), 154–161.
- Leturmy, P., Mugnier, J., Vinour, P., Baby, P., Colletta, B., Chabron, E., 2000. Piggyback basin development above a thin-skinned thrust belt with two detachment levels as a function of interactions between tectonic and superficial mass transfer; the case of the Subandean Zone (Bolivia). *Tectonophysics* 320 (1), 45–67.
- Lodolo, E., Menichetti, M., Bartole, R., Ben-Avraham, Z., Tassone, A., Lippai, H., 2003. Magallanes-Fagnano continental transform fault (Tierra del Fuego, southernmost South America). *Tectonics* 22 (6), 1–26.
- López, M., 2006. Análisis de deformación tectónica en los piedemontes de las cordilleras Central y Occidental, Valle del Cauca, Colombia-Contribuciones paleosísmicas, vol. 113p. MSc Thesis Universidad EAFIT, Medellín.
- Mora, C., Comte, D., Russo, R., Gallego, A., Mocanu, V., 2010. Aysen seismic swarm (January 2007) in southern Chile: analysis using joint hypocentral determination. *J. Seismol.* 14 (4), 683–691.
- Macharé, J., Fenton, C., Machette, M., Lavenau, A., Costa, C., Dart, R., 2003. Database and map of quaternary faults and folds in Perú and its offshore region. U.S. Geological Survey Open-File Report 55, 03-451.
- Macharé, J., Benavente, C., Audin, L., 2009a. Síntesis Descriptiva del Mapa Neotectónico 2008. INGENMET, Boletín 40 Serie C, p. 102p.
- Macharé, J., Benavente, C., Audin, L., 2009b. Sistema de Fallas de la Cordillera Blanca (PE-07). Proyecto Multinacional Andino (PMA), 2009. Atlas de deformaciones cuaternarias de los Andes, SERNAGEOMIN. Publicación Geol. Multinac. 7, 208–214.
- Macharé, J., Benavente, C., Audin, L., 2009c. Falla de Chaquibamba (PE-04). Proyecto Multinacional Andino (PMA), 2009. Atlas de deformaciones cuaternarias de los Andes, SERNAGEOMIN. Publicación Geol. Multinac. 7.
- Macharé, J., Audin, L., Benavente, C., 2009d. Falla de Huaytapallana (PE-12).
- Machette, M., 2000. Active, capable, and potentially active faults - a paleoseismic perspective. *J. Geodyn.* 29, 387–392.
- Margirier, A., Audin, L., Robert, X., Pêcher, A., Schwartz, S., 2017. Stress field evolution above the Peruvian flat-slab (Cordillera Blanca, northern Peru). *J. South Am. Earth Sci.* 77, 58–69.
- Marinière, J., Nocquet, J.-M., Beauval, C., Champenois, J., Audin, L., Alvarado, A., Baize, S., Socquet, A., 2020. Geodetic evidence for shallow creep along the Quito fault, Ecuador. *Geophys. J. Int.* 220, 2039–2055, [10.1093/gji/ggz564](https://doi.org/10.1093/gji/ggz564).
- Martos, L., 1987. Evidencias de movimientos neotectónicos en una terraza de edad holocena / La Rinconada / San Juan / República Argentina. In: *Actas X Congreso Geol. Arg., 1 Asoc. Geol. Arg.*, pp. 263–265.
- Massabie, A., 1987. Neotectónica y sismicidad en la región de Sierras Pampeanas Orientales, sierras de Córdoba, Argentina, vol. 1. 10° Congreso Geológico Argentino, Actas, pp. 271–274.
- McCalpin, J. (Ed.), 2009. *Paleoseismology*, second ed. Academic Press, Amsterdam.
- McClay, K., Tamara, J., Hammerstein, J., Mora, A., Zamora, G., Uzbeda, H., 2018. Sub-Andean thick and thin-skinned thrust systems of Southeastern Peru and Bolivia - a review. *AAPG Mem* 117, 35–62.
- McNulty, B.A., Farber, D.L., 2002. Active detachment faulting above the Peruvian flat slab. *Geology* 30 (6), 567–570.
- Melnick, D., Charlet, F., Ehtler, H., De Batist, M., 2006. Incipient axial collapse of the main cordillera and strain partitioning gradient between the central and patagonian Andes, lago laja, Chile. *Tectonics* 25. <https://doi.org/10.1029/2005TC001918>.
- Mescua, J., Barriouevuo, M., Giambiagi, L., Suriano, J., Spagnotto, S., Stahlschmidt, E., de la Cal, H., Soto, J., Mazzitelli, M., 2019. Stress field and active faults in the orogenic front of the Andes in the Malargüe fold-and-thrust belt (35°–36°S). *Tectonophysics* 766, 179–193.
- Message, G., 2010. Signatures geomorphologiques de l'activité tectonique Plio-Quaternaire dans le Sud des Andes Centrales, Argentine. PhD Thesis. Université de Pau et des Pays Bas, p. 293p.
- Message, G., Nivière, B., Martinod, J., Lacan, P., Xavier, J., 2010. Geomorphic evidence for plio-quaternary compression in the andean foothills of the southern neuquén basin, Argentina. *Tectonics* 29, 1–18.

- Minster, J., Jordan, T., 1978. Present-day plate motions. *J. Geophys. Res.* B 83 B11, 5331–5354. <https://doi.org/10.1029/JB083iB11p05331>.
- Molnar, P., Sykes, L., 1969. Tectonics of the Caribbean and Middle America regions from focal mechanisms and seismicity. *Geol. Soc. Am. Bull.* 80 (9), 1639–1684. https://doi.org/10.1130/0016-7606_1969.
- Mon, R., Gutiérrez, A., 2009. The Mar Chiquita Lake: an indicator of intraplate deformation in the central plain of Argentina. *Geomorphology*. <https://doi.org/10.1016/j.geomorph.2009.04.009>.
- Montero, W., Denyer, P., Barquero, R., Alvarado, G., Cowan, H., Machette, M., Haller, K., Dart, R., 1998. Map and database of quaternary faults and folds in Costa Rica and its offshore regions. U.S. Geol. Survey Open-File Report 98–481, 65p.
- Mora, A., Parra, M., Strecker, M.R., Kammer, A., Dimaté, C., Rodriguez, F., 2006. Cenozoic contractional reactivation of Mesozoic extensional structures in the Eastern Cordillera of Colombia. *Tectonics* 25, TC2010. <https://doi.org/10.1029/2005TC001854>.
- Mora, A., Gaona, T., Kley, J., Montoya, D., Parra, M., Quiroz, L., Reyes, G., Strecker, M., 2009. The role of inherited extensional fault segmentation and linkage in contractional orogenesis: a reconstruction of lower cretaceous inverted rift basins in the Eastern Cordillera of Colombia. *Basin Res.* 21, 111–137.
- Mora, A., Baby, P., Roddaz, M., Parra, M., Brusset, S., Hermoza, W., Espurt, N., 2010. Tectonic history of the Andes and sub-Andean zones: implications for the development of the Amazon drainage basin. In: Hoorn, C., Wesselingh, F.P. (Eds.), *Blackwell*, pp. 38–60.
- Mora, A., Tesón, E., Martínez, J., Parra, M., Lasso, Á., Horton, B.K., Ketcham, R.A., Velásquez, A., Arias-Martínez, J.P., 2019. The eastern foothills of Colombia. In: Gómez, J., Mateus-Zabala, D. (Eds.), *The Geology of Colombia*, vol. 3. Servicio Geológico Colombiano, Pub. Geol. Esp, pp. 165–207. <https://doi.org/10.32685/pub.esp.37.2019.05>.
- Mora-Páez, H., Kellogg, J.N., Freymueller, J.T., Mencin, D., Fernandes, R.M.S., Diederix, H., LaFemina, P., Cardona-Piedrahita, L., Lizarazo, S., Pelaez-Gaviria, J.R., Diaz-Mila, F., Bohorquez-Orozco, O., Giraldo-Londoño, L., Corchuelo-Cuervo, Y., 2019a. Crustal deformation in the northern Andes - a new GPS velocity field. *J. S. Am. Earth Sci.* 89, 76–91.
- Mora-Páez, H., Kellogg, J.N., Freymueller, J.T., 2020. Contributions of space geodesy for geodynamic studies in Colombia: 1988 to 2017. In: Gómez-Tapias, J., Almanza, M.F., Ochoa-Yarza, A. (Eds.), *The Geology of Colombia*. Chap. 14 (in press).
- Moreiras, S., Giambiagi, L., Spagnotto, S., Nacif, S., Mescua, J., Toural, R., 2014. El frente orogénico activo de los Andes centrales a la latitud de la ciudad de Mendoza (32° 50'–33° S). *Andean Geol.* 41, 342–361.
- Moretti, I., Baby, P., Mendez, E., Zubieta, D., 1996. Hydrocarbon generation in relation to thrusting in the sub andean zone from 18 to 22° S – Bolivia. *Petrol. Geosci.* 2, 17–28.
- Mugnier, Jean Louis, Becel, David, Granjeon, Didier, 2006. Active tectonics in the Subandean belt inferred from the morphology of the Rio Pilcomayo (Bolivia). *Tectonics, Climate, and Landscape Evolution GSA SPECIAL PAPERS*. [https://doi.org/10.1130/2006.2398\(22\)](https://doi.org/10.1130/2006.2398(22)).
- Muñoz, N., Charrier, R., 1996. Uplift of the western border of the Altiplano on a west-vergent thrust system, Northern Chile. *J. S. Am. Earth Sci.* 9, 171–181.
- Naranjo, J., 1987. Interpretación de la actividad cenozoica superior a lo largo de la zona de falla Atacama, norte de Chile. *Rev. Geol. Chile* 31, 43–55.
- Nocquet, J.-M., Villegas-Lanza, J., Chlieh, M., Mothes, P., Rolandone, F., Jarrin, P., Cisneros, M., Alvarado, A., Audin, I., Bondoux, P., Martin, X., Font, Y., Régnier, M., Vallée, M., Tran, T., Beauval, C., Maguina Mendoza, T., Martinez, W., Tavera, H., Yepes, H., 2014. Motion of continental slivers and creeping subduction in the northern Andes. *Nat. Geosci.* <https://doi.org/10.1038/ngeo2099>.
- Nogueira, F., Bezerra, F., Fuck, R., 2010. Quaternary fault kinematics and chronology in intraplate northeastern Brazil. *J. Geodyn.* 49, 79–91. <https://doi.org/10.1016/j.jog.2009.11.002>.
- Norabuena, E., Lefler, G.L., Mao, A., Dixon, T., Stein, S., Sacks, I., Ellis, M., 1998. Space geodetic observations of nazca-south America convergence across the central Andes. *Science* 279, 358–362.
- Okada, A., 1971. On the Neotectonics of the Atacama Fault Zone Region. Preliminary Notes on Late Cenozoic Faulting and Geomorphic Development of Coast Range of Northern Chile. *Bulletin of the Department of Geography, Kyoto University*, pp. 47–65, 3.
- Oliveira, P.H.S., Ferreira, J.M., Bezerra, F.H.R., Assumpção, M., do Nascimento, A.F., Sousa, M.O.L., Menezes, E.A.S., 2015. Influence of the continental margin on the stress field and seismicity in the intraplate Acaraú Seismic Zone, NE Brazil. *Geophys. J. Int.* 202, 25–34. <https://doi.org/10.1093/gji/ggv211>.
- Onorato, R., Perucca, L., Coronato, A., Prezzi, C., Tejada, F., this volumen. Earthquake hazard, morphology, and displacement along the Scotia-South America plates boundary in Tierra del Fuego, (Argentina).
- Onorato, M.R., L Perucca, L., Coronato, A., Rabassa, J., López, R., 2016. Seismically-induced soft-sediment deformation structures associated with the Magallanes-Fagnano Fault System (Isla Grande de Tierra del Fuego, Argentina). *Sediment. Geol.* 344, 135–144.
- Onorato, M.R., Perucca, L.P., Coronato, A., 2018. Evidencias morotectónicas del Sistema de Falla Magallanes-Fagnano en la Isla Grande de Tierra del Fuego. VII Congreso Argentino de Cuaternario y Geomorfología. Puerto Madryn, Argentina.
- Onorato, M., Prezzi, C., Orgeira, M., Coronato, A., López, R., Magneres, L., 2019. Geophysical characterization of Udaeta Lake as a possible pull-apart basin associated to quaternary tectonic activity along Magallanes-Fagnano fault system. *Quat. Int.* <https://doi.org/10.1016/j.quaint.2019.06.025>.
- Osorio, J., Montes, N., Velandia, F., Acosta, J., Romero, J., Diederix, H., Audemard, F., Nuñez, A., 2008. Paleosismología de la falla de Ibaigüé. *Public. Esp. INGEOMINAS* 29, 240p (Bogotá).
- Pagani, M., Monelli, D., Weatherill, L., Danciu, H., Crowley, V., Silva, P., Henshaw, L., Butler, M., Nastasi, L., Panzeri, M., Simonato, D., Vigano, 2014. OpenQuake engine: an open hazard (and risk) software for the global earthquake model. *Seismol. Res. Lett.* 85 (3), 692–702. <https://doi.org/10.1785/0220130087>.
- Pagani, M., Garcia, J., Monelli, D., Weatherill, G., Smolka, A., 2015. A summary of hazard datasets and guidelines supported by the Global Earthquake Model during the first implementation phase. *Ann. Geophys.* 58 (1), S0108, 2015.10.4401/ag-6677 S0108.
- Paris, G., Romero, R., 1994. Fallas Activas en Colombia. *Bol. Geol. - Ingeominas* 34 (2–3), 3–26.
- Paris, G., Sarria, A., 1986. Proyecto Geofísico del Nordeste Colombiano-Neotectónica del Nororiente Colombiano: INGEOMINAS, Bogotá. Informe INGEOMINAS-ISA, p. 59.
- Paris, G., Machette, M., Dart, R., Haller, K., 2000. Map and database of quaternary faults and folds in Colombia and its offshore regions U.S., p. 66. Geological Survey Open-File Report 00-284.
- Pennington, W.D., 1981. Subduction of the eastern Panama basin and seismotectonics of northwestern South America. *J. Geophys. Res.* 86 (10), 753–10,770.
- Pérez, O., Aggarwal, Y., 1981. Present-day tectonics of southeastern Caribbean and northeastern Venezuela. *J. Geophys. Res.* 86 (10), 791–10,805.
- Peri, V.G., Rossello, E.A., 2010. Anomalías neotectónicas del drenaje del río Salado sobre las Lomas de Otumpa (Santiago del Estero y Chaco, Argentina) detectadas por procesamiento digital. *Rev. Asoc. Geol. Argent.* 66 (4), 636–648.
- Perucca, L., Bastías, H., 2008. Neotectonics, seismicity and paleoseismicity. Late Cenozoic of Patagonia and Tierra del Fuego. In: Rabassa, J. (Ed.), *Development in Quaternary Science Series*. Elsevier: Amsterdam, The Netherlands, pp. 73–94.
- Perucca, L., Onorato, R., 2011. Fallas con actividad cuaternaria en el corredor tectónico Matagusanos-Maradona-Acequiñon entre los ríos de La Flecha y del Agua. *Provincia de San Juan: Rev. Asoc. Geol. Argent.* 68, 39–52.
- Perucca, L., Audemard, F., Pantano, A., Avila, C., Onorato, M., Lara, G., Esper, 2013. Fallas cuaternarias con vergencias opuestas entre Precordillera Central y Oriental, provincia de San Juan. *Revista Asociación Geológica Argentina* 70 (2), 291–302.
- Philip, H., Megard, F., 1977. Structural analysis of the superficial deformation of 1969 Pariahuanca earthquakes (Central Perú). *Tectonophysics* 38, 259–278.
- Plafker, G., Erickson, E., 1978. Nevados huascarán avalanches, Peru. *Dev. Geotech. Eng.* 14A, 277–314. <https://doi.org/10.1016/B978-0-444-41507-3.50016-7>.
- Proyecto Multinacional Andino (PMA), 2009. Atlas de deformaciones cuaternarias de los Andes, SERNAGEOMIN. *Publicación Geol. Multinac.* 7, 154–159.
- Pousse-Beltran, L., Vassallo, R., Audemard, F., Jouanne, F., Carcaillet, J., Pathier, E., Volat, M., 2017. Pleistocene slip rates on the Boconó fault along the North Andean Block plate boundary, Venezuela. *Tectonics* 36, 1207–1231.
- Ramírez, V., Minaya, E., Teran, N., González, M., Hermanns, R., Clague, J., Cerritos, O., 2009. Sistema de fallas El Alto (BO-06). Proyecto Multinacional Andino (PMA), 2009. Atlas de deformaciones cuaternarias de los Andes, SERNAGEOMIN. *Publicación Geol. Multinac.* 7, 163–170.
- Ramos, V., 1988. The tectonics of the Central Andes; 30° to 33° S latitude. In: Clark, S., Burchfiel, C. (Eds.), *Processes in Continental Lithospheric Deformation*, vol. 218. Geological Society of America, Special Paper, pp. 31–54.
- Ramos, V.A., 1999. Plate tectonic setting of the andean cordillera. *Episodes* 22, 183–190.
- Ramos, V., 2009. Anatomy and global context of the Andes: main geologic features and the Andean orogenic cycle. *Mem. Geol. Soc. Am.* 204, 31–65.
- Ramos, G.V., de Castro, D.L., Bezerra, F.H.R., Ferreira, J.M., do Nascimento, A.F., Oliveira, P.H.S., Nogueira, F.C.C., This Volume. Intraplate Seismicity in the Equatorial Margin of Brazil Reactivates the Precambrian Basement Fabric.
- Ramos, V.A., Cristallini, E.O., Pérez, D.J., 2002. The pampean flat-slab of the central Andes. *J. S. Am. Earth Sci.* 15, 59–78.
- Ramos, V.A., Zapata, T., Cristallini, E., Introcaso, A., 2004. The andean thrust system -Latitudinal variations in structural styles and orogenic shortening. In: McClay, K. (Ed.), *Thrust Tectonics and Hydricarbon Systems*, vol. 82. AAPG Mem, pp. 30–50.
- Ramos, V., Alonso, R., Strecker, M., 2006. Estructura y neotectónica de las Lomas de Olmedo, zona de transición entre los sistemas Subandino y de Santa Bárbara, provincia de Salta. *Revista Asociación Geológica Argentina* 61 (4), 579–588.
- Rauld, R., 2009. Falla San Ramón, 137–140. Proyecto Multinacional Andino (PMA), 2009. Atlas de deformaciones cuaternarias de los Andes, SERNAGEOMIN. *Publicación Geol. Multinac.* 7, 137–141.
- Rauld, R., Vargas, G., Armijo, R., Ormeño, A., Valderas, C., Campos, J., 2006. Cuantificación de escapes de falla y deformación reciente en el frente cordillerano de Santiago. *Mem. XI Cong. Geol. Chileno* 2, 447–450.
- Regard, V., Lagnous, R., Espurt, N., Darrozes, J., Baby, P., Roddaz, M., Calderon, Y., Hermoza, W., 2009. Geomorphic evidence for recent uplift of the Fitzcarrald Arch (Peru); a response to the Nazca Ridge subduction. *Geomorphology* 107 (3–4), 107–117. <https://doi.org/10.1016/j.geomorph.2008.12.003>.
- Riccomini, C., Assumpção, M., 1999. Quaternary tectonics in Brazil. *Episodes* 22 (3), 221–225.
- Riccomini, C., Peggia, A., Saloni, J., Kohnke, M., Figueira, R., 1989. Neotectonic activity in the Serra do mar rift system (SE Brazil). *J. S. Am. Earth Sci.* 2 (2), 191–192.
- Richard, A., Costa, C., Giambiagi, L., Moreno, C., Ahumada, E., Vázquez, F., 2019. Neotectónica del extremo austral de la falla La Rinconada, Precordillera Oriental, provincia de San Juan. *Rev. Asoc. Geol. Argentina* 76, 24–39.
- Rimando, J., Schoenbohm, L., Costa, C., Owen, L., Cesta, J., Richard, A., Gardini, C., 2019. Late quaternary activity of the La Rinconada fault zone, san juan, Argentina. *Tectonics* 38, 916–940.
- Ritz, J.-F., Braucher, R., Bourlès, D., Delouis, B., Marquardt, C., Lavenu, A., Philip, H., Ortlieb, L., 2019. Slip rate of trench-parallel normal faulting along the Mejillones Fault (Atacama Fault System): relationships with the northern Chile subduction and implications for seismic hazards. *Terra. Nova* 31, 390–404.

- Robertson, K., 1989. Actividad neotectónica en el piedemonte de la Cordillera Oriental, sector Villavicencio-Tauramena, Colombia. 5° Congr. Col. Geol. Mem. 1, 171–192.
- Robertson, K., 2007. Morfotectónica y datos del fallamiento activo del piedemonte llanero, Colombia, Sudamérica. Cuadernos de Geografía 16, 109–120.
- Robertson, K., Castiblanco, M., 2011. Amenazas fluviales en el piedemonte amazónico colombiano. Cuadernos de Geografía 20 (2), 125–137.
- Rocha, E., Cristallini, E., 2015. Controls on structural styles along the deformation front of the Subandean zone of southern Bolivia. *J. Struct. Geol.* 73, 83–96.
- Rockwell, T., Ragona, D., Meigs, A., Owen, L., Costa, C., Ahumada, E., 2014. Inferring a thrust-related earthquake history from secondary faulting: a long rupture record of La Laja fault, San Juan, Argentina. *Bull. Seismol. Soc. Am.* 104, 269–284.
- Rodríguez, L., Ollarves, R., Audemard, F., Singer, A., Colón, S., Miró, C., Viète, H., 2016. Estudio paleosísmico en la traza activa de la falla El Ávila, Santa Rosa, Caracas, Venezuela. *Rev. Geogr. Venez.* 57, 39–57.
- Rodríguez, L.M., Diederix, H., Torres, E., Audemard, F.A., Hernández, C., Singer, A., Bohórquez, O., Yépez, S., 2017. Identification of the seismogenic source of the 1875 Cucuta earthquake on the basis of a combination of neotectonic, paleoseismologic and historic seismicity studies. *J. S. Am. Earth Sci.* <https://doi.org/10.1016/j.jsames.2017.09.019>.
- Rojas Vera, E., Giampaoli, P., Gobbo, E., Rocha, E., Olivieri, G., Figueroa, D., 2019. Structure and tectonic evolution of the Interandean and Subandean Zones of the central Andean fold-thrust belt of Bolivia. In: Horton, B., Folguera, A. (Eds.), *Andean Tectonics*. <https://doi.org/10.1016/B978-0-12-816009-1.00016-2>.
- Rossello, E.A., Mon, R., Bordarampé, C.P., Gutiérrez, A.A., 2005. Evidencias topográficas de actividad neotectónica en la llanura Chacoparanaense: consecuencias en la organización del drenaje de Mar Chiquita (Córdoba, Argentina). 10° Simposio Nacional de Estudios Tectónicos - 4° International Symposium of Tectonics. Boletín de Resúmenes Expandidos, pp. 205–208.
- Rothlis, L., Perucca, L., Santi Malnis, P., Alcacér, J., Haro, F., Vargas, N., 2019. Neotectonic, morphotectonic and paleoseismologic analysis of the las chacras fault system, sierras Pampeanas occidentales, san juan, Argentina. *J. South Am. Earth Sci.* 91, 144–153.
- Roy, S., Vassallo, R., Martinod, J., Ghiglione, M., Sue, C., 2018. Late-Quaternary to present-day continental strike-slip faulting of the Magallanes-Fagnano fault, system, Tierra del Fuego, Argentina. Proceedings 15th Congreso Geológico Chileno. <https://congresogeologicochileno.cl/wp-content/uploads/2018/12/Libro-de-Actas-XV-Congreso-Geologico-Chileno-2018-2.pdf>.
- Roy, S., Vassallo, R., Martinod, J., Ghiglione, M., Sue, C., Allemand, P., 2019. Co-seismic deformation and post-glacial slip rate along the Magallanes-Fagnano fault, Tierra del Fuego, Terra Nova, Argentina. <https://doi.org/10.1111/ter.12430>.
- Saadi, A., Machette, M.N., Haller, K.M., Dart, R.L., Bradley, L.-A., de Souza, A.M., 2002. Map and database of quaternary faults and lineaments in Brazil: U.S. Geological Survey Open-File Report 58, 02-230.
- Saeid, E., Bakioglu, K.B., Kellogg, J., Leier, A., Martínez, J.A., Guerrero, E., 2017. Garzón Massif basement tectonics: structural control on the evolution of petroleum systems in Upper Magdalena and Putumayo basins, Colombia. *Mar. Petrol. Geol.* 88, 381–401. <https://doi.org/10.1016/j.marpetgeo.2017.08.035>.
- Sagripanti, L., Colavitto, B., Jagoe, L., Folguera, A., 2017. A review about the quaternary upper-plate deformation in the Southern Central Andes (36–38° S): A plausible interaction between mantle dynamics and tectonics. *Journal South American Earth Sciences* 87, 221–231. <https://doi.org/10.1016/j.jsames.2017.11.008>.
- Sagripanti, L., Colavitto, B., Astori, A., Folguera, A., 2020. Quaternary deformation in the neuquén basin, explained by the interaction between mantle dynamics and tectonics. In: Kietzmann, D., Folguera, A. (Eds.), *Opening and Closure of the Neuquén Basin in the Southern Andes*. Springer, pp. 485–499. https://doi.org/10.1007/978-3-030-29680-3_21.
- Sandoval, F., De Pascale, G., 2020. Slip rates along the narrow Magallanes fault system, Tierra del Fuego region, Patagonia. *Sci. Reports Nat. Res.* <https://doi.org/10.1038/s41598-020-64750-6>.
- Santibáñez, I., Cembrano, J., García, T., Costa, C., Yáñez, G., Marquardt, C., Arancibia, G., González, G., 2019. Crustal faults in the Chilean Andes: geological constraints and seismic potential. *Andean Geol.* 46, 32–65.
- Schmidt, S., Hetzel, R., Mingorance, F., Ramos, V., 2011. Coseismic displacements and Holocene slip rates for two active thrust faults at the mountain front of the Andean Precordillera (~33° S). *Tectonics*. <https://doi.org/10.1029/2011TC002932>, 30, TC5011.
- Schubert, C., 1979. El Pilar fault zone, northeastern Venezuela: brief review. *Tectonophysics* 52, 447–455.
- Schubert, C., 1980a. Morfología neotectónica de una falla rumbo-deslizante e informe preliminar sobre la falla de Boconó, Andes meridionales. *Acta Cient. Venez.* 31, 98–111.
- Schubert, C., 1980b. Late Cenozoic pull-apart basins, Boconó fault zone, Venezuelan Andes. *J. Struct. Geol.* 2 (4), 463–468.
- Schubert, C., 1982. Neotectonics of the Boconó fault, western Venezuela. *Tectonophysics* 85, 205–220.
- Schubert, C., 1984. Basin formation along Boconó-Morón-El Pilar fault system, Venezuela. *J. Geophys. Res.* 89, 5711–5718.
- Schwartz, D.P., 1988. Paleoseismicity and neotectonics of the Cordillera Blanca fault zone, northern Peruvian Andes. *J. Geophys. Res.* 93 (B5), 4712–4730.
- Fault segmentation and controls of rupture initiation and termination. In: Schwartz, D., Sibson, R. (Eds.), *U.S. Geol. Survey Open-File Report* 89–315, 447p.
- Sébrier, M., Mercier, J., Mégard, F., Laubacher, G., Carey-Gailhardis, E., 1985. Quaternary normal and reverse faulting and the state of stress in Central Andes of South Peru. *Tectonics* 4 (7), 739–780.
- Sebrier, M., Mercier, J.L., Macharé, J., Bonnot, D., Cabrera, J., Blanc, J.L., 1988. The state of stress in an overriding plate situated above a flat slab: the Andes of Central Peru. *Tectonics* 7 (4), 895–928.
- Siame, L., Bellier, O., Sébrier, M., Bourlès, D., Leturmy, P., Pérez, M., Araujo, M., 2002. Seismic hazard reappraisal from combined structural geology, geomorphology and cosmic ray exposure dating analyses: the Eastern Precordillera thrust system (NW Argentina). *Geophys. J. Int.* 150, 241–260.
- Siame, L., Bellier, O., Sébrier, M., Araujo, M., 2005. Deformation partitioning in flat subduction setting: case of the Andean foreland of western Argentina (28° S–33° S). *Tectonics* 24, 1–27.
- Siame, L., Bellier, O., Sebrier, M., 2006a. Active tectonics in the Argentine Precordillera and western sierras Pampeanas. *Rev. Asoc. Geol. Argentina* 61, 604–619.
- Siame, L., Sébrier, M., Bellier, O., Bourlès, D., 2006b. Can Cosmic Ray exposure dating reveal the normal faulting activity of the Cordillera Blanca fault, Perú? *Rev. Asoc. Geológica Argentina* 61, 536–544.
- Siefeld, G., Lange, D., Cembrano, J., 2019. Intra-arc crustal seismicity: seismotectonic implications for the southern Andes volcanic zone, Chile. *Tectonics* 38, 552–578. <https://doi.org/10.1029/2018TC004985>.
- Singer, A., Beltrán, C., Rodríguez, J.A., 1995. Evidencias geomorfológicas de actividad neotectónica a lo largo de los corrimientos frontales de la Serranía del Interior en el oriente venezolano. In: 3rd. Geological Conference of the Geological Survey of Trinidad and Tobago.
- Slemmons, D., Depolo, C., 1986. Evaluation of active faulting and associated hazards. In: Wallace, R. (Ed.), *Active Tectonics*. NRC-NAS Studies in Geophysics, 45–62, Washington.
- Smalley Jr., R., Kendrick, E., Bevis, M., Dalziel, I., Taylor, F., Lauría, E., Barriga, R., Casassa, G., Olivero, E., Piana, F., 2003. Geodetic determination of relative plate motion and crustal deformation across the Scotia-South America plate boundary in eastern Tierra del Fuego. *G-cubed* 4 (9), 1070. [10.1029/2002GC000446](https://doi.org/10.1029/2002GC000446).
- Soulas, J.-P., 1986. Neotectónica y tectónica activa en Venezuela y regiones vecinas. 6° Congreso Geológico Venezolano, Proceedings 10, 6639–6656.
- Soulas, J.-P., Egüez, A., Yepes, H., Pérez, H., 1991. Tectónica activa y riesgo sísmico en Los Andes Ecuatorianos y el extremo sur de Colombia. *Boletín Geológico Ecuatoriano* 2 (1), 3–11.
- Stanton-Yonge, A., Griffith, W., Cembrano, J., St-Julien, R., Iturrieta, P., 2016. Tectonic role of margin parallel and margin-transverse faults during oblique subduction in the southern volcanic zone of the Andes: insights from boundary element modeling. *Tectonics* 35, 1990–2013.
- Stephan, J.-F., Mercier de Lepinay, B., Calais, E., Tardy, M., Beck, C., Carfantán, J.-C., Olivet, J.-M., Vila, J.-M., Bouysse, P., Mauffret, A., Bourgeois, J., Thery, J.-M., Tournon, J., Blanchet, R., Dercourt, J., 1990. Paleogeodynamics maps of the Caribbean: 14 steps from lias to present. *Bulletin Société Géologique de France* 6, 915–919.
- Taboada, A., Rivera, L.A., Fuenzalida, A., Cisternas, A., Philip, H., Bijwaard, H., Olaya, J., Rivera, C., 2000. Geodynamics in northern Andes: subductions and intracrustal deformations (Colombia). *Tectonics* 19, 787–813.
- Takeya, M., Ferreira, J.M., Pearce, R.G., Assumpção, M., Costa, J., Sophia, C.M., 1989. The 1986–1988 intraplate earthquake sequence near João Câmara, NE Brazil—Evolution of seismicity. *Tectonophysics* 167, 117–131.
- Tassará, A., Yáñez, G., 2003. Relación entre el espesor elástico de la litosfera y la segmentación tectónica del margen andino (15–47° S). *Rev. Geol. Chile* 30 (2), 159–186. <https://doi.org/10.5027/andgeoV30n2-a02>.
- Tibaldi, A., Romero, J., 2000. Morphometry of late Pleistocene-Holocene faulting and volcanotectonic relationship in the southern Andes of Colombia. *Tectonics* 358–377.
- Tibaldi, A., Rovida, A., Corazzato, C., 2007. Late Quaternary kinematics, slip-rate and segmentation of a major Cordillera-parallel transcurrent fault: the Cayambe-Afladores-Sibundoy system, NW South America. *J. Struct. Geol.* 29, 664–680.
- Trenkamp, R., Kellogg, K., Freymueller, J., Mora-Paez, H., 2002. Wide plate margin deformation, southern Central America and northwestern South America, CASA GPS observations. *J. S. Am. Earth Sci.* 15, 157–171.
- Trifonov, V.G., Machette, M.N., 1993. The world map of major active faults project. *Ann. Geofis.* 36 (3–4), 225–236.
- Vargas, G., Rebolledo, S., Sepúlveda, S., Lahsen, A., Thiele, R., Townley, B., Padilla, C., Rauld, R., Herrera, M., Lara, M., 2013. Ruptura sísmica submarina, tectónica y volcanismo activo a lo largo de la falla Liquiñe-Ofqui e implicancias para el peligro sísmico en los Andes Patagónicos. *Andean Geol.* 40, 141–171.
- Vargas, G., Klinger, Y., Rockwell, T., Forman, S., Rebolledo, S., Baize, S., Lacassin, R., Armijo, R., 2014. Probing large intra-plate earthquakes at the west flank of the Andes. *Geology* 42, 1083–1086.
- Velandia, F., Acosta, J., Terraza, G., Villegas, H., 2005. The current tectonic motion of the Northern Andes along the Algeciras fault system in SW Colombia. *Tectonophysics* 399, 313–329.
- Veloza, Gabriel, Styron, Richard, Taylor, Michael, Mora, Andr[es], 2012. Open-source archive of active faults for northwest South America. *GSA Today* 22. <https://doi.org/10.1130/GSAT-G156A.1>.
- Veloza, G., Taylor, M., Mora, A., Gosse, J., 2015. Active mountain building along the eastern Colombian Subandes: a folding history from deformed terraces across the Tame anticline, Llanos Basin. *Bull. Geol. Soc. Am.* <https://doi.org/10.1130/B31168.1>.
- Vergara, H., Taboada, A., Romero, J., Paris, G., Castro, E., 1995. In: Valdírri, J., Ingeominas (Eds.), *Neotectónica del Borde Llanero: Resultados preliminares. Seminario de sismotectónica del Borde Llanero Colombiano*, p. 115 (Bogotá).
- Villegas-Lanza, J., Chlieh, M., Cavalíe, O., Tavera, H., Baby, P., Chire-Chira, J., Nocquet, J., 2016. Active tectonics of Peru: heterogeneous interseismic coupling along the Nazca megathrust, rigid motion of the Peruvian Sliver, and Subandean shortening accommodation. *Journ. Geoph. Res. Solid Earth* 121 (10), 7371–7394.

- Wagner, R., 2004. Estudio Estructural Regional y Análisis de Deformaciones Recientes en el Frente de Montaña de La Serranía Del Interior Oriental y en la parte Norte de la Subcuenca de Maturín. Unpublished undergraduate thesis. Universidad Central de Venezuela, Caracas, Venezuela.
- Weiss, J., Brooks, B., Arrowsmith, R., Vergani, G., 2015. Spatial and temporal distribution of deformation at the front of the Andean orogenic wedge in southern Bolivia. *J. Geophys. Res. Solid Earth* 120, 1909–1931. <https://doi.org/10.1002/2014JB011763>.
- Wimpenny, S., Copley, A., Benavente Escobar, C.L., Aguirre, E., 2018. Extension and dynamics of the Andes inferred from the 2016 Parina (huarichancara) earthquake. *J. Geophys. Res.: Solid Earth* 123 (9), 8198–8228.
- Wimpenny, S., Benavente, C., Copley, A., Garcia, B., Rossell, L., O’Kane, A., Aguirre, E., 2020. Observations and dynamical implications of active normal faulting in South Peru. *Geophys. J. Int.* 222 (1), 27–53. <https://doi.org/10.1093/gji/ggaa144>.
- Winslow, M., 1982. The structural evolution of the Magallanes basin and neotectonics of the southernmost Andes. In: Craddock, C. (Ed.), *Antarctic Geoscience*. University of Wisconsin, pp. 143–154.
- Winslow, M., Prieto, X., 1991. Evidence of Active Tectonics along the Strait of Magellan, Chile. 6° Congreso Geológico Chileno, Resúmenes Expandidos, pp. 654–655.
- Winter, T., Avouac, J., Lavenue, A., 1993. Late Quaternary kinematics of the Pallatanga strike-slip fault (Central Ecuador) from topographic measurements of displaced morphological features. *Geophys. J. Int.* 115, 905–920.
- WSSPC (Western States Seismic Policy Council), 1997. Active Fault Definition for the Basin and Range Province, WSSPC 97-1 White Paper, 3pp.
- Yáñez, G., Cembrano, J., 2004. Role of viscous plate coupling in the late Tertiary Andean tectonics. *J. Geophys. Res.* 109 (B02407), 1–21.
- Yáñez, G., Ranero, C., Von Huene, R., Diaz, J., 2001. Magnetic anomaly interpretation across the southern Central Andes (328–33.58S): the role of the Juan Fernandez ridge in the late Tertiary evolution of the margin. *J. Geophys. Res.* 106, 6325–6345.
- Yepes, H., Audin, L., Alvarado, A., Beauval, C., Aguilar, J., Font, Y., Cotton, F., 2016. A new view for the geodynamics of Ecuador: implication in seismogenic source definition and seismic hazard assessment. *Tectonics* 35, 1249–1279.
- Zamora, G., Zapata, T., Ramos, V., Rodríguez, F., Bernardo, L., 2009. Evolución tectónica del frente Andino en Neuquén. *Rev. Asoc. Geol. Argentina* 65, 192–203.

